

A PHYSICAL HYDROGEOLOGICAL AND HYDROCHEMICAL  
STUDY OF GROUNDWATER/SURFACE WATER  
INTERACTION IN A GRANITIC TERRAIN  
IN EASTERN NEWFOUNDLAND

CENTRE FOR NEWFOUNDLAND STUDIES

**TOTAL OF 10 PAGES ONLY  
MAY BE XEROXED**

(Without Author's Permission)

HERBERT SCOTT SCHILLEREFF







National Library  
of Canada

Acquisitions and  
Bibliographic Services Branch

395 Wellington Street  
Ottawa, Ontario  
K1A 0N4

Bibliothèque nationale  
du Canada

Direction des acquisitions et  
des services bibliographiques

395, rue Wellington  
Ottawa (Ontario)  
K1A 0N4

1980-1981

1980-1981

## NOTICE

The quality of this microform is heavily dependent upon the quality of the original thesis submitted for microfilming. Every effort has been made to ensure the highest quality of reproduction possible.

If pages are missing, contact the university which granted the degree.

Some pages may have indistinct print especially if the original pages were typed with a poor typewriter ribbon or if the university sent us an inferior photocopy.

Reproduction in full or in part of this microform is governed by the Canadian Copyright Act, R.S.C. 1970, c. C-30, and subsequent amendments.

## AVIS

La qualité de cette microforme dépend grandement de la qualité de la thèse soumise au microfilmage. Nous avons tout fait pour assurer une qualité supérieure de reproduction.

S'il manque des pages, veuillez communiquer avec l'université qui a conféré le grade.

La qualité d'impression de certaines pages peut laisser à désirer, surtout si les pages originales ont été dactylographiées à l'aide d'un ruban usé ou si l'université nous a fait parvenir une photocopie de qualité inférieure.

La reproduction, même partielle, de cette microforme est soumise à la Loi canadienne sur le droit d'auteur, SRC 1970, c. C-30, et ses amendements subséquents.

Canada

**A PHYSICAL HYDROGEOLOGICAL AND HYDROCHEMICAL STUDY OF  
GROUNDWATER/SURFACE WATER INTERACTION IN A GRANITIC  
TERRAIN IN EASTERN NEWFOUNDLAND**

by

© Herbert Scott Schillereff, B.S., M.Sc.

A thesis submitted to the School of Graduate Studies  
in partial fulfillment of the requirements for the degree of  
Doctor of Philosophy

Department of Earth Sciences  
Memorial University of Newfoundland

1992

St. John's

Newfoundland





National Library  
of Canada

Acquisitions and  
Bibliographic Services Branch

395 Wellington Street  
Ottawa, Ontario  
K1A 0N4

Bibliothèque nationale  
du Canada

Direction des acquisitions et  
des services bibliographiques

395, rue Wellington  
Ottawa (Ontario)  
K1A 0N4

*Author's consent*

*by the author*

The author has granted an irrevocable non-exclusive licence allowing the National Library of Canada to reproduce, loan, distribute or sell copies of his/her thesis by any means and in any form or format, making this thesis available to interested persons.

L'auteur a accordé une licence irrévocable et non exclusive permettant à la Bibliothèque nationale du Canada de reproduire, prêter, distribuer ou vendre des copies de sa thèse de quelque manière et sous quelque forme que ce soit pour mettre des exemplaires de cette thèse à la disposition des personnes intéressées.

The author retains ownership of the copyright in his/her thesis. Neither the thesis nor substantial extracts from it may be printed or otherwise reproduced without his/her permission.

L'auteur conserve la propriété du droit d'auteur qui protège sa thèse. Ni la thèse ni des extraits substantiels de celle-ci ne doivent être imprimés ou autrement reproduits sans son autorisation.

ISBN 0-315-86680-2

Canada

## ABSTRACT

This thesis presents a hydrogeological and hydrochemical investigation of groundwater and surface water interaction in a fractured granite terrain, within the Seal Cove River valley in eastern Newfoundland. The overall approach for this work was to first determine the structural geologic framework of the study area and surrounding region, then use this framework as a basis for interpreting the physical, hydrochemical and isotopic responses of groundwater and surface water to hydrologic stress, and for numerical simulations of groundwater flow in the study area.

The Seal Cove River valley study area (referred to as the SCRv) is 81.7 ha. in size and includes a 1.44 km reach of a branch of the Seal Cove River, with a 300 m x 50 m beaver pond midway along this reach. Lithologically homogeneous granitic rocks occur in glaciated outcrops on over 30% of a hillside above the study reach and sporadically on the valley floor. Overburden consists of thin glacial drift and peat deposits. Geophysical surveys indicate that the buried granite surface is essentially flat, dipping on average 0.5 degrees toward the north-northwest.

The structural geologic framework was compiled from air photos, outcrop mapping and scanline fracture surveys across the pluton, and core logging in the SCRv. The Holyrood pluton intrudes multiply-deformed volcanic rocks of the Harbour Main Group and lies within the Conception Bay Anticlinorium, bounded to the east and west by the Topsail and Duffs Faults. Within the pluton, fracture lineaments and the regional mesoscopic fracture system both show preferred

northerly, northeasterly and southeasterly strikes. Trace length and fracture frequency patterns show little variation in western parts of the pluton (including the SCR.V area). There are no obvious variations in structural trends on a macroscopic scale in the vicinity of the SCR.V.

In the SCR.V, three subvertical mesoscopic fracture sets are identified based on cluster analysis of scanline data. These sets correspond with orientations of subsurface fractures and macroscopic fracture in the SCR.V and with the regional fracture system. A fourth set comprises subhorizontal sheeting joints. Mesoscopic fracture trace lengths and spacings tend to vary smoothly across the SCR.V without significant variation within or between subvertical fracture sets.

The major boundary faults are interpreted to predate the Holyrood pluton, acting as feeders for the sill-like intrusion. Siluro-Devonian reactivation of these faults is interpreted to have generated the tectonic fracture system in the pluton (and the SCR.V). A kinematic deformation model for the pluton is presented in which the regional tectonic fracture system formed as Riedel and secondary P-shear fractures during a single phase of progressive, left-lateral bulk simple shear. This model is the only detailed analysis of deformation in the pluton to date.

The structural framework implies that 1) groundwater flow around the SCR.V occurs primarily in a shallow or intermediate flow systems; 2) near-surface mesoscopic fractures and subvertical macroscopic fault and fracture zones are the likely principal conduits for shallow groundwater flow in the SCR.V; 3) fracture-controlled hydraulic properties of the granite (e.g. hydraulic conductivity) can be assumed to be uniform around the SCR.V (at scales of 10's to 100's of meters); and 4) the present SCR.V fracture data set is inadequate for sophisticated



determination of directional permeability in the granite (e.g. by permeability tensor formulation or fracture network analysis), requiring a simpler approach in formulating input parameters for numerical models of groundwater flow in the SCR.V. Use of the more sophisticated methods mentioned above would require a more complete and unbiased characterization of fracture geometry than is available here, i.e. a statistical description of the geometry of subhorizontal fractures (Set 4), and unbiased estimates of fracture spacing for all sets.

The physical hydrogeologic setting of the SCR.V appears to be simple. Overburden materials are more permeable than the fractured granite, with injection test results showing an overall decrease of granite permeability with depth. Organic clay-silt pond sediments are less permeable than near-surface granite, forming a local semi-confining layer. Downward gradients are present on the hillslope, while horizontal or upward (artesian) gradients are present on the valley bottom. Hydraulic gradients and equipotential surfaces in the granite suggest that groundwater flows toward the stream reach and that a hillslope recharge zone expands streamward during storm response. The hydrogeologic and topographic setting supports an assumption that the SCR.V behaves as a hydrologic catchment, with vertical no-flow boundaries beneath the surface catchment boundaries.

Measurements at eight seepage meter/mini-piezometer locations around the beaver pond, six multilevel piezometers in bedrock in the south end of the SCR.V, a series of rain gauges on the hillslope and valley bottom, and at three rectangular weirs along the study reach are used to describe hydrologic responses to precipitation in the SCR.V. Seepage flux and piezometric variations correlate with seasonal rainfall changes and individual storm hydrographs, suggesting that surface waters and groundwaters are coupled during response to hydrologic stress.

Rapid hydraulic head transfer and groundwater displacement in bedrock is

interpreted to occur by the filling and draining of highly permeable fractures in the granite. Physical hydrologic measurements also suggest that groundwater flux from the fractured granite should not be ignored in hydrologic mass budgets, but that direct runoff may dominate stormflow at this site.

The hydrochemical setting of the SCR.V reflects local climate and geology. Rain waters are Na-Cl type and stream waters are dilute. Dilute, Ca-HCO<sub>3</sub> type groundwaters suggest that the shallow flow system in the SCR.V is meteorically-driven, actively-flushed and only slightly evolved.

Transient mass balance methods which are substantially different from conventional mass balance approaches are developed for performing transient hydrograph separations along a stream reach. Two groundwater compositional groups (near-stream and valley-bottom types) are recognized in the SCR.V. During weak hydrologic stress, groundwater compositional changes are subtle and suggest that separate fracture plumbing systems may exist near the stream at scales of a few meters. In response to storm stress, stream-ward displacement of compositionally heterogeneous groundwaters is followed by subsurface mixing with shallow recharging groundwater or rain. Evidence of changing groundwater compositions during stormflow suggests that low flow stream compositions may not be reliable estimators of discharging groundwater compositions throughout stormflow.

Hydrograph separation results for two autumnal 1986 and 1987 runoff events indicate that the groundwater component of peak stormflow ranges from 40% to 95%, depending on the tracer species used (conductivity, chloride or oxygen-18). Specific conductivity is probably non-conservative as a tracer due to

dissolution of biosalts (e.g. potassium salts on vegetative litter) by surficial runoff water. The timing of storm runoff and the composition and proportion of the groundwater component is likely controlled by the location of most concentrated rainfall stress in the assumed catchment. Predominant groundwater components in early storm runoff suggests that runoff events in the SCRVR do not follow the conventional pattern where direct channel precipitation and surface runoff dominates early runoff and subsurface (groundwater) flow dominates peak runoff.

Steady state, two-dimensional numerical simulations of groundwater flow in the SCRVR indicate that surface and subsurface hydraulic measurements at low flow are internally consistent. These results also suggest that the catchment area actually contributing groundwater to the study reach may be smaller than originally assumed, and that groundwater flow transverse to the valley occurs predominantly at shallow depths (up to 50-100 m below surface), as predicted from the structural geologic framework. Results of three-dimensional steady-state simulations are physically realistic and match (within an order of magnitude) measured hydraulic heads and seepage fluxes at the stream and low flow stream discharges. These results also support the size and shape of the assumed catchment, contrary to initial two-dimensional model results. Incorporation of horizontal permeability anisotropy, inferred from fracture frequency data, does not substantially change three-dimensional model results as compared with an isotropic case. Inclusion of hydraulic properties for principal macroscopic fractures in the study area into the three-dimensional model produces mild perturbations in equipotential patterns at the scale of the assumed catchment.

This thesis documents the importance of adopting a multidisciplinary approach for investigating groundwater/surface water interaction in areas of



fractured, low permeability rock, where geologic factors strongly influence groundwater flow. The transient mass balance methods developed here were applied with mixed success, but would be expected to produce improved results with better poised and more well-documented storm events, and may be usable in other settings. A fracture filling and draining mechanism adequately explains rapid hydraulic head changes and groundwater displacement at this site. In addition, combined physical, chemical and isotopic results indicate that groundwater and surface water in the SCRv are strongly coupled during response to hydrologic stress. Finally, useful inferences concerning catchment-scale groundwater flow and the influences of permeability anisotropy and the macroscopic fracture system were obtained from two- and three-dimensional steady-state numerical simulations of hydraulic head in the SCRv.

## ACKNOWLEDGEMENTS

Funding for this study was provided through Natural Sciences and Engineering Research Council of Canada (NSERC) Strategic Grant G1183 with Dr. John E. Gale as principal investigator, and through NSERC Operating Grants to Dr. Gale and Dr. John A. Welhan. Further support was provided through a Memorial University Graduate Fellowship and in the form of flight time from two Sealand Helicopters Scholarships.

The supervisory committee for this thesis consisted of Drs. John Gale, John Welhan, and Tom Calon (Department of Earth Sciences), and Dr. Leonard Lye (Memorial University, Faculty of Engineering). Dr. Gale helped formulate the original concept for this study and provided logistical, administrative and overall supervisory support. His detailed review of parts of this thesis is appreciated. Dr. Welhan supervised the hydrochemical and isotopic components of this thesis, and contributed in many other ways. His long hours collaborating with the author to refine a new sample preparation method for oxygen-18 isotope analysis and in review of portions of this thesis are greatly appreciated. Dr. Tom Calon provided useful commentary on the structural geologic components of this thesis as well as much needed encouragement and support, especially during the latter stages of thesis preparation. Dr. Leonard Lye provided assistance in the statistical analysis of hydrologic data, especially in normalizing diverse types of data for comparison purposes. In addition to the above committee, Mr. Jim Waterhouse (Memorial University, Faculty of Engineering) helped supervise field hydrologic components during early stages of this thesis, and Dr. Colin Banfield (Memorial University, Department of Geography) assisted in various aspects of rainfall measurement

and interpretation of precipitation data. This thesis in its final form was not reviewed by the supervisory committee prior to submission.

The following people assisted with field work as paid personnel and are gratefully acknowledged: Stuart Thomson, Glenn Bursey, Don Cameron, Robert MacLeod, David Briggins, Beverly Chapman, Lorne Boone, Frank Mooney, Gerry Whelan, Janet Galloway and Karen Stapleton. Mr. Doug Belshaw (of Solinst Inc.) provided assistance in fabrication of multilevel piezometer packers. Field hydrologic instruments for this study were borrowed from the Newfoundland Department of Environment and Lands, Groundwater Division, and from Environment Canada, Atmospheric Environment Service, Scientific Services branch. Water samplers were kindly loaned for this study by the Environment Protection Service. Technical services personnel of the Faculty of Engineering at Memorial University (S.J. Carew Building) contributed greatly in the fabrication and maintenance of field equipment. Their prompt assistance on numerous occasions and generous donation of bits and pieces kept field work going and is gratefully acknowledged.

Numerous people assisted in laboratory or technical aspects of this thesis work and their efforts are thankfully acknowledged. Principal among them were Jerry Pulchan, Gert Andrews, Dr. P. Morin, Dr. M. Bruce-Lockhart, David van Everdingen, Lisa Gardner, Dave MacNeil and Wilf Marsh. Robert MacLeod (Memorial University) and Arlen Harbaugh (U.S. Geological Survey) provided valuable computing assistance. Pat Browne and Maureen Moore, of the Department of Earth Sciences at Memorial, smoothed many an administrative obstacle during this thesis work.



For providing pleasant social and musical diversion from thesis work, I would like to acknowledge the friendship and support of one-time fellow graduate students: Jack Botsford, John Tuach, Scott Swinden, Tom Lane and Paul Myrow, as well as the remaining members of J.T. and The Rabbits, and Tickle Harbour.

Above and beyond the contributions of people mentioned above, I would like to express my appreciation for the love and long-standing support of my wife, Bridget Neame, during this thesis work. I am sure this thesis would not have been completed without her active participation in maintaining a counterbalance and warm family environment in the face of what too often threatened to become all-consuming.

Finally, this thesis is dedicated to my mother and father, whose worldly insight and courage have been a source of inspiration and strength.

## TABLE OF CONTENTS

	<u>Page</u>
<b>ABSTRACT .....</b>	ii
<b>ACKNOWLEDGEMENTS.....</b>	viii
<b>TABLE OF CONTENTS .....</b>	xi
<b>LIST OF TABLES .....</b>	xv
<b>LIST OF FIGURES .....</b>	xvii
<b>LIST OF PLATES .....</b>	xxvi
<b>CHAPTER 1 - INTRODUCTION</b>	
<b>1.1 Background .....</b>	1
<b>1.2 Objectives and scope .....</b>	5
<b>1.3 Thesis organization .....</b>	8
<b>1.4 Previous work .....</b>	10
1.4.1 Geology of the Holyrood pluton .....	10
1.4.2 Characterization and hydrogeological significance of fracture geometry .....	11
1.4.3 Catchment response to hydrologic stress .....	13
1.4.4 Numerical modelling of flow systems in hydrologic catchments ..	15
<b>CHAPTER 2 - STRUCTURAL GEOLOGICAL FRAMEWORK OF THE SEAL COVE RIVER VALLEY AND SURROUNDING REGION</b>	
<b>2.1 Introduction .....</b>	17
2.1.1 General statement .....	17
2.1.2 Geological setting of the Holyrood pluton .....	18
2.1.3 Data sources and limitations .....	20
<b>2.2 Fracture geometry within the Holyrood pluton .....</b>	24
2.2.1 Structural framework of the pluton.....	24
2.2.2 Regional fracture geometry in the Holyrood pluton .....	25
Air photo lineaments .....	25
Mesoscopic fracture orientations .....	28
Fracture trace lengths and frequencies .....	31
2.2.3 Fracture geometry in the Seal Cove River valley .....	35

Macroscopic and mesoscopic fracture orientations .....	35
Fracture trace lengths .....	44
Fracture spacings .....	50
<b>2.3 Discussion .....</b>	<b>55</b>
2.3.1 Brittle deformation history of the Holyrood pluton .....	55
2.3.2 Influences on variability of fracture geometry within the Holyrood pluton .....	59
2.3.3 Principal hydrogeological implications .....	61
 <b>CHAPTER 3 - GROUNDWATER FLUX AND PIEZOMETRIC RESPONSE TO PRECIPITATION IN THE SEAL COVE RIVER VALLEY</b>	
<b>3.1 Introduction .....</b>	<b>63</b>
3.1.1 General statement .....	63
3.1.2 Physical hydrogeologic setting of the study area .....	63
3.1.3 Basis for treating the study area as a hydrologic catchment .....	66
3.1.4 Permeability of bedrock and overburden in the study area .....	67
<b>3.2 Instrumentation and data collection .....</b>	<b>69</b>
3.2.1 Bedrock piezometers.....	69
3.2.2 Groundwater flux .....	71
3.2.3 Rainfall and streamflow .....	74
<b>3.3 Groundwater flux response to precipitation .....</b>	<b>75</b>
<b>3.4 Piezometric response to precipitation .....</b>	<b>80</b>
3.4.1 Seasonal piezometric response to precipitation .....	80
3.4.2 Short-term piezometric response to precipitation .....	80
3.4.3 Correlation of piezometric responses .....	84
3.4.4 Three-dimensional variation of hydraulic head .....	86
<b>3.5 Mechanism of groundwater response to precipitation .....</b>	<b>91</b>
<b>3.6 Conclusions and inferences .....</b>	<b>93</b>
 <b>CHAPTER 4 - HYDROCHEMICAL AND ISOTOPIC RESPONSE OF SURFACE WATERS AND GROUNDWATERS TO PRECIPITATION IN THE SEAL COVE RIVER VALLEY</b>	
<b>4.1 Introduction .....</b>	<b>95</b>
4.1.1 General statement .....	95
4.1.2 Hydrochemical setting of the study area .....	96



<b>4.2 Methods</b> .....	98
4.2.1 Hydrologic measurements and water sampling .....	98
4.2.2 Reach mass balance methods .....	101
<b>4.3 Analysis of groundwater compositions in the study area</b> .....	107
4.3.1 Organization of groundwater data sets .....	108
4.3.2 Description of groundwater types and compositional variations ..	108
4.3.3 Groundwater mixing relationships .....	116
<b>4.4 Analysis of stormflow in the study area</b> .....	121
4.4.1 Description of storm runoff events .....	121
4.4.2 Bulk inflow analysis .....	125
4.4.3 Reach hydrograph separation .....	131
4.4.4 Controls on groundwater stormflow components .....	138
<b>4.5 Comparison of hydrochemical and physical responses to hydrologic stress in the study area</b> .....	141
4.5.1 Timing and duration of groundwater responses .....	141
4.5.2 Comparison of hydrograph separation results with physical hydrologic response to storms .....	142
4.5.3 Compatibility of hydrochemical and physical response mechanisms in the SCR V .....	144
<b>4.6 Conclusions</b> .....	146

## **CHAPTER 5 • NUMERICAL SIMULATIONS OF GROUNDWATER FLOW IN THE SEAL COVE RIVER VALLEY**

<b>5.1 Introduction</b> .....	149
5.1.1 General statement.....	149
5.1.2 Computer code used in numerical simulations .....	
<b>5.2 Two-dimensional simulation of groundwater flow in the study area</b> ....	150
5.2.1 Two-dimensional modelling approach .....	150
5.2.2 Mesh configuration, boundary conditions and input parameters	151
5.2.3 Two-dimensional model results and discussion .....	157
<b>5.3 Three-dimensional simulation of groundwater flow in the study area</b> ..	161
5.3.1 Three-dimensional modelling approach .....	161
5.3.2 Mesh configuration and boundary conditions.....	163
5.3.3 Input parameters .....	164
5.3.4 Three-dimensional model results .....	175
5.3.5 Limitations of three-dimensional model results .....	189

5.4 Hydrogeological inferences based on numerical modelling results .....	191
5.4.1 Effective size of the groundwater catchment for the study reach .....	191
5.4.2 Uniformity of groundwater flux along study reach .....	192
5.5 Conclusions .....	196
 <b>CHAPTER 6 - THESIS SUMMARY AND CONCLUSIONS</b>	
6.1 Thesis summary .....	198
6.2 Thesis conclusions .....	213
 REFERENCES .....	 215
 APPENDIX A - Geophysical Surveys in the Seal Cove River Valley - Procedures and Results .....	 226
APPENDIX B - Scanline Fracture Mapping in the Holyrood Pluton - Procedures and Results .....	242
APPENDIX C - Core Logging in the Seal Cove River Valley - Procedures and Results .....	274
APPENDIX D - Method for Correction of Orientation Bias in Fracture Surveys in the Seal Cove River Valley .....	323
APPENDIX E - Injection Testing in the Seal Cove River Valley - Procedures and Results .....	328
APPENDIX F - Estimation of Permeability of Glacial Drift in the Seal Cove River Valley - Procedures and Results .....	345
APPENDIX G - Construction and Installation of Multilevel Piezometers in the Seal Cove River Valley .....	350
APPENDIX H - Factors Affecting Implementation of Reach Mass Balance Methods .....	358
APPENDIX I - Alterations to the Computer Code used for Three- Dimensional Numerical Simulations of Groundwater Flow in the Study Area .....	368
APPENDIX J - Hydrochemical Data .....	370

## LIST OF TABLES

<u>Table</u>	<u>Page</u>
2.1 Summary of results of cluster analysis of scanline fractures in the Seal Cove River valley .....	37
2.2 Descriptive statistics of the distributions of trace length for each fracture set from combined scanline data in the Seal Cove River valley. ....	47
2.3 Descriptive statistics of the distributions of spacing (SPAC) and log-spacing (LSPAC) for each fracture set from combined scanline data in the Seal Cove River valley .....	53
3.1 Borehole injection test information for the study area. ....	69
4.1 Hydrologic characteristics of rainfalls referred to in this study .....	122
4.2 Input data and hydrograph separation results for four 1987 runoff events in the Seal Cove River valley sampled at peak discharge. ....	139
5.1 Summary of parameters used for numerical models along profiles A-A' and B-B' in the study area .....	155
5.2 Recharge rates and cell designations for 3D models in this study. Values "1" and "5" represent recharge rates of 1% and 5% of average annual precipitation applied to the top active cell at that location. Bold numbers indicate locations where constant heads were imposed at the top active cell. Double underlined numbers indicate locations designated as river cells. ....	166
5.3 Summary of data used to construct fracture frequency rosette from scanline data in the SCR.V. ....	174
5.4 Summary of simulated flow rates along sections of the study reach..	195
A1 Comparison of calculated $\rho_1$ , $\rho_2$ and depth values for EM station 82. For $\rho_1$ changes of two orders of magnitude, $\rho_2$ values change by less than a factor of two. ....	228
A2 Direct probe survey data and results. ....	232
A3 Refraction seismic survey data and results. ....	233

<b>A4</b>	Electromagnetic survey data and results. ....	234
<b>B1</b>	Scanline fracture data for the Seal Cove River valley. ....	258
<b>C1</b>	Fracture data for borehole H2 in the Seal Cove River valley. ....	295
<b>C2</b>	Fracture data for borehole H4 in the Seal Cove River valley. ....	307
<b>D1</b>	Listing of FORTRAN code "TERZAGHI" used for implementing the Terzaghi orientation bias correction. ....	325
<b>E1</b>	Injection test data for borehole M1 in the Seal Cove River valley. ..	334
<b>E2</b>	Injection test data for borehole M2 in the Seal Cove River valley. ..	335
<b>E3</b>	Injection test data for borehole M3 in the Seal Cove River valley. ..	336
<b>E4</b>	Injection test data for borehole H2 in the Seal Cove River valley. ..	337
<b>E5</b>	Injection test data for borehole H4 in the Seal Cove River valley. ..	340
<b>E6</b>	Summary of bedrock permeabilities calculated from injection test data in the Seal Cove River valley (note: "BTOC" = below top of casing). ....	343
<b>F1</b>	Summary of grain size distribution characteristics and estimated hydraulic conductivities for glacial drift in the SCR.V. ....	349
<b>G1</b>	Summary of locations, orientations and depths for boreholes instrumented with multilevel piezometers in the Seal Cove River valley. ....	354
<b>H1</b>	Contrast/error ratios for flow ( $Q_o-Q_i$ ) and composition ( $C_k-C_r$ ) contrasts at peak flow for storm runoff data sets used in this study. ....	362
<b>I1</b>	Alterations to the computer code MODFLOW to produce HETMOD. The revisions are easily recognizable in the context of the subroutine listings provided in the MODFLOW documentation. ....	369

## LIST OF FIGURES

Figure	Page
1.1 Location and setting of the Seal Cove River valley study area in eastern Newfoundland. ....	4
1.2 Interrelationships of major study components for this thesis. Arrows indicate directions of principal information transfer. ....	7
2.1 Regional geologic map of the Avalon Peninsula showing the major lithologic units and structural features around the Holyrood pluton (adapted from Brueckner (1979) and King (1988)). ....	19
2.2 Equal-area, lower hemisphere stereoplots of fracture orientations at a test outcrop (site 7); (a) total fracture population; (b) scanline data (scanlines orientations shown as solid circles); (c) scanline data corrected for orientation bias (described in text). All plots constructed using the same contour function increment (0.1) using methods of Fisher et al. (1986). ....	23
2.3 (a) Distribution of air photo lineaments across the northern part of the Holyrood pluton (solid, fracture lineaments; dashed, soil morphological or vegetation lineaments). Grid of 36 subareas (italic numbers) used for azimuth comparisons in (b). Numbered circles are scanline survey sites. The SCR V is located in subarea 16. (b) Azimuthal rose plots of fracture lineaments in subareas shown in (a). "ND" refers to no fracture lineament data for subareas 28 and 35. ....	26 27
2.4 Equal-area, lower hemisphere stereoplots of fracture orientations measured at 33 scanline survey sites (open circles) across the northern part of the Holyrood pluton. All plots constructed using the same contour function increment (0.1) using methods of Fisher et al. (1986). ....	29
2.5 Contour map of mean bulk trace length for all scanline survey sites across the pluton. Contour interval is 0.5 m. Sites labelled by circled numbers are referred to in text. ....	32
2.6 Contour map of mean bulk fracture frequency for all scanline survey sites across the pluton. Contour interval is 0.5 m. Sites labelled by circled numbers are referred to in text. ....	34



<b>2.7</b>	Summary of fracture orientations in the Seal Cove River valley compiled from air photo, outcrop and scanline mapping data. Equal-area, lower hemisphere stereoplots of scanline fractures were all constructed with the same contour function increments (0.1) using methods of Fisher et al. (1986); orientations of scanlines shown as solid square points on the plots. ....	36
<b>2.8</b>	(a) Eigenvalue ratio plot (after Woodcock and Naylor, 1983) for fracture pole clusters determined from scanline data in the Seal Cove River valley. S1, S2 and S3 refer to eigenvalues for mean pole of each cluster. ....	39
	(b) Equal-angle, lower hemisphere stereoplot of the mean poles of clusters determined for scanline data in the Seal Cove River valley. Fracture sets assigned based on groupings of mean poles as described in text. ....	40
<b>2.9</b>	Equal-area, lower hemisphere stereoplots of fracture poles for successive ten meter segments in borehole H2 (a-f) and borehole H4 (g-l) in the Seal Cove River valley. Plunge and trend of the boreholes are indicated by bold points on the plots. ....	41
<b>2.10</b>	Equal-area, lower hemisphere stereoplots showing associations of fracture orientations with fracture termination style (a-d) and mineral infilling (e,f) for scanline data in the Seal Cove River valley. ....	43
<b>2.11</b>	Trace length histograms for scanline data in the Seal Cove River valley, subdivided by fracture set and level of censoring. ....	46
<b>2.12</b>	Contour maps of mean trace lengths at scanline survey sites in the Seal Cove River valley, for fracture set 1 (a); set 2 (b); and set 3 (c). Contour interval is 0.5 m. Grid numbers refer to UTM coordinates. ....	49
<b>2.13</b>	Frequency histograms for spacings between consecutive fractures of the same fracture set, determined from scanline data in the Seal Cove River valley. ....	52
<b>2.14</b>	Contour maps of mean spacing at scanline survey sites in the Seal Cove River valley, for fracture set 1 (a); set 2 (b); and set 3 (c). Contour interval is 0.2 m. Grid numbers refer to UTM coordinates. ....	54
<b>2.15</b>	Senses of motion and relative age relationships for fractures across the northern part of the Holyrood pluton, compiled from air photo,	

	outcrop mapping and scanline survey data. Kinematics of the regional left-lateral shear deformation model are shown in the inset. ....	57
3.1	Topography, drainage, access and instrument locations for the Seal Cove River valley study area. M and H symbols are multilevel piezometers, W symbols are weirs, R symbols are rain gauges, and D symbols are locations where glacial drift was sampled. ....	64
3.2	Plot of log intrinsic permeability versus depth for boreholes in the Seal Cove River valley which were injection tested. The regression line (with 95% confidence limits) was fitted through all the data. ....	68
3.3	Schematic diagram of multilevel piezometers used in this study. Piezometric intervals are shown in black (where bounded by chemical packers) or stipple (where bounded by bentonite seals). M holes are vertical; H holes are inclined to the southeast at angles shown beneath the labels. Ground elevations (meters a.s.l.) are given in parentheses. ..	70
3.4	Variation of discharge seepage fluxes (a, b) and mini-piezometer hydraulic gradients (c) in the beaver pond in the study reach. Seepage flux data from Sep. 15-16, 1986 (solid circles) shown at left edge of (a); rainfall shown at bottom of (a); seepage meter (SM) and mini-piezometer (MP) locations shown in (b). ....	72
3.5	Maps of contoured discharge seepage flux at the beaver pond during October 7-28, 1987. Contour interval is 10 ml/m/hr. Grid numbers refer to UTM coordinates (meters). Seepage collection dates and accumulated rainfall during those periods are shown for each map. Fracture lineaments in (d) (dashed, inferred; dotted, assumed) are extrapolated from those shown in Figure 2.7. ....	77
3.6	Variation of piezometric levels at all of the multilevel piezometers for the 1987 monitoring period. Single numbers refer to piezometric intervals (e.g. "2" refers to interval I2). Correlation coefficients ( $R^2$ ) for responses of intervals within piezometers are shown at right (e.g. within piezometer M3 (c), $R^2$ for responses in intervals I2 and I4 is 0.96). ....	81
3.7	Piezometric variations (a) and hydraulic gradients (b) in piezometer H4 and variation in streamflow (c) during October, 1987. ....	83
3.8	Detailed piezometric variations in piezometers H4 (a) and H2 (b) in response to the October 22, 1987 storm. ....	85

3.9	(a) Responses to precipitation at selected piezometric intervals; and (b) at selected seepage flux, piezometric and stream flow measurement points in the SCR.V during the 1987 monitoring period. Responses have been standardized to unitless z values (described in text). Correlation coefficients between response trends are shown at the upper left of each plot. ....	87
3.10	Vertical components of hydraulic gradients in bedrock piezometers before storm hydrograph and during peak stormflow in response to the October 22, 1987 storm. Arrows indicate discharge (up) or recharge (down), with gradient values given next to arrowheads. ....	89
3.11	Equipotential maps (a, b and c) and inferred hinge line locations (d) for two horizontal planes in the shallow subsurface in the SCR.V. The two planes (at 90 m and 84 m above sea level) are depicted in relation to the piezometers in (a). Equipotential patterns before and during response to the October 22, 1987 storm (a, b) and for both planes at low flow conditions (c) on September 2, 1987) suggest that groundwater flow during was northwesterly-directed toward the stream. ....	90
4.1	Seasonal variation of conductivity and oxygen-18 for rainfalls in the SCR.V in 1986 and 1987. Oxygen-18 values display no obvious summer enrichment and autumn depletion trends (in contrast to seasonal secular trends indicated by global precipitation data; e.g. Dansgaard, 1964). ....	97
4.2	Conceptual diagram illustrating the reach hydrologic approach. Upstream features numbered on the inflow hydrograph are discussed in the text. ....	102
4.3	Schematic diagrams depicting the concept of a bulk inflow chemical path (a) and the application of a bulk inflow chemical path (b) for indicating runoff compositions entering a reach during stormflow. ....	105
4.4	Plot of conductivity versus chloride (a) and trilinear plot of cation concentrations (b) for rain, stream and groundwaters in the SCR.V. ....	109
4.5	Variations in groundwater oxygen-18 and conductivity during a low rainfall summer period in 1986 (a, b) and in response to rainfalls in September 1987 after a dry summer period (c, d). Groundwater flow conditions at the piezometers are indicated in (c). ("BOTT" indicates that both recharge and discharge gradients were developed within the piezometer). ....	111

4.6	Variations of stream flow (a), stream chemistry (b) and groundwater chemistry (c) in response to rainfall on September 27, 1986. ....	114
4.7	Variations of stream flow (a), stream chemistry (b) and groundwater chemistry (c) in response to rainfall on October 22, 1987. Weighted three-point running average and associated $\pm 2\sigma$ uncertainty limits for M112 groundwater compositions highlight the oxygen-18 enrichment and subtle conductivity decrease during response to the storm event. ....	115
4.8	Groundwater mixing relationships in response to rainfalls on September 15, 1987 (a), September 27, 1986 (b) and October 22, 1987 (c). Interpretation of the diagrams is described in the text. ....	117
4.9	Reach section description and hydrographs for the Sep. 27, 1986 and Oct. 22, 1987 study storms (a), bulk inflow plot for the Oct. 22, 1987 storm (b), and bulk inflow plots for different reach sections and different tracer combinations for the Sep. 27, 1986 storm. Description and interpretation of these plots are given in the text. ....	126
4.10	Bulk inflow plot for four runoff events at peak flow conditions in 1987. ....	130
4.11	Hydrograph separation results for the Oct. 22, 1987 storm using oxygen-18 (a) and conductivity (b) tracers. ....	132
4.12	Hydrograph separation results for the Sep. 27, 1986 storm using oxygen-18, conductivity and chloride tracers (columns) for full, upper and lower reach sections (rows). For example, plot (b) shows separation results for the full reach using conductivity as a tracer. ....	135
5.1	Configuration of 2D model profiles and 3D model grid in the Seal Cove River valley area. Numbers on map borders are UTM coordinates in meters. Topographic contours are in meters above sea level. ....	152
5.2	Physical configuration of model mesh for profile A-A' (a) and B-B' (b). Numbers at bottom of mesh are model column numbers. Small crosses in Figure 5.3 correspond with central nodes of these mesh cells. ....	153
5.3	2D simulation results for case 1 (a), case 2 (b), case 3 (c) and case 4 (d). Numbers at left show elevation above sea level	

	(meters). Numbers at bottom show width of profiles (meters). Small crosses are nodes at center of model cells. ....	158
<b>5.4</b>	3D model grid showing macroscopic fractures included in model, cells designated as containing such fractures, and the assumed catchment boundary (for reference). ....	165
<b>5.5</b>	Conceptual approach for formulating horizontal hydraulic conductivity values for cells containing macroscopic fractures in the 3D model. ....	168
<b>5.6</b>	Fracture frequency versus log hydraulic conductivity (K) for borehole injection test data in the SCR.V. Individual borehole data are given separate symbols, as shown. A least squares regression line is fitted through all data. ....	171
<b>5.7</b>	Rosette of fracture frequency for each scanline in the SCR.V. Key numbers 1-23 refer to individual scanlines as listed in Table 5.3. Points 17 and 20 are treated as outliers, as discussed in the text. ....	173
<b>5.8</b>	Simulated hydraulic heads (dashed contours) for layers 2 (a), 3 (b), 4 (c), 5 (d) and 6 (e) for the isotropic 3D model (no incorporation of macroscopic fractures). Heads are in meters above sea level. The boundary of the assumed catchment is shown by a solid line. ...	176
<b>5.9</b>	Simulated hydraulic heads (dashed contours) for layers 2 (a), 3 (b), 4 (c), 5 (d) and 6 (e) for the anisotropic 3D model (no incorporation of macroscopic fractures). Heads are in meters above sea level. The boundary of the assumed catchment is shown by a solid line. ...	179
<b>5.10</b>	Simulated hydraulic heads (dashed contours) for layers 2 (a), 3 (b), 4 (c), 5 (d) and 6 (e) for the anisotropic 3D model (incorporating macroscopic fractures). Heads are in meters above sea level. The boundary of the assumed catchment is shown by a solid line. ...	182
<b>5.11</b>	Simulated vertical component of hydraulic gradient (dashed contours) between layers 2 and 3 (a) and between layers 4 and 5 (b) for the isotropic model case (no macroscopic fractures). Negative values indicate recharge areas (cross-hatched); positive values indicate discharge areas. The boundary of the assumed catchment is shown by a solid line. ....	186
<b>5.12</b>	Simulated vertical component of hydraulic gradient (dashed contours) between layers 2 and 3 (a) and between layers 4 and 5 (b) for the anisotropic model case (no macroscopic fractures). Negative values indicate recharge areas (cross-hatched); positive	

	values indicate discharge areas. The boundary of the assumed catchment is shown by a solid line. ....	187
5.13	Simulated vertical component of hydraulic gradient (dashed contours) between layers 2 and 3 (a) and between layers 4 and 5 (b) for the anisotropic model case (with macroscopic fractures). Negative values indicate recharge areas (cross-hatched); positive values indicate discharge areas. The boundary of the assumed catchment is shown by a solid line. ....	188
5.14	Simulated groundwater flux for sections of the study reach in the SCRV. Most points show discharge into the reach section; those with "R" indicate simulated recharge from that reach section. Points representing measured seepage flux, and calculated discharge flux at M1 are also shown. Results for three model cases are shown and are discussed in the text. ....	193
A1	Surface topography, geophysical survey station locations, and peat and outcrop distribution on the valley floor in the study area. ....	237
A2	Comparative results of overburden thicknesses at stations where true depth to bedrock is known. Station abbreviations along bottom: HS (hammer seismic), EM (electromagnetic), DP (direct probe), H3 (borehole H3). ....	238
A3	Contoured bedrock surface elevations (m.a.s.l.) on the valley floor of the Seal Cove River valley, compiled from combined geophysical and direct probe records. ....	239
A4	Overburden isopach map for the valley floor in the study area, compiled from geophysical and direct probe survey data. Contours in meters. ....	240
A5	Perspective view of the buried granite surface on the valley floor, viewed toward the northeast at 30° inclination. Vertical exaggeration is 12:1. ....	241
B1	(a-c) Scanline trace maps for survey site 16 in the Seal Cove River valley. ....	246
B2	Scanline trace map for survey site 17 in the Seal Cove River valley. ....	249
B3	Scanline trace map for survey site 18 in the Seal Cove River valley. ....	250

<b>B4</b>	Scanline trace map for survey site 19 in the Seal Cove River valley. ....	251
<b>B5</b>	(a,b) Scanline trace maps for survey site 21 in the Seal Cove River valley. ....	252
<b>B6</b>	Scanline trace map for survey site 44 in the Seal Cove River valley. ....	254
<b>B7</b>	Scanline trace map for survey site 49 in the Seal Cove River valley. ....	255
<b>B8</b>	Scanline trace map for survey site 54 in the Seal Cove River valley. ....	256
<b>B9</b>	Scanline trace map for survey site 54 in the Seal Cove River valley. ....	257
<b>C1</b>	Schematic diagram showing the geometric relationships between components of the impression packer used in this study. Packer, pipe mandrel mounting string, indenter hardware and related hardware are omitted for clarity. ....	276a
<b>C2</b>	Fracture core log for borehole M1 .....	280
<b>C3</b>	Fracture core log for borehole M2 .....	281
<b>C4</b>	Fracture core log for borehole M3 .....	282
<b>C5</b>	Fracture core log for borehole H2 .....	283
<b>C6</b>	Fracture core log for borehole H4 .....	290
<b>E1</b>	Schematic diagram of constant head injection test set up .....	332
<b>E2</b>	Schematic diagram of falling head injection test set up in inclined borehole H4. Set up for borehole M2 was identical except borehole was vertical. ....	333
<b>F1</b>	Grain size distribution curves for glacial drift samples collected in the Seal Cove River valley. ....	348
<b>G1</b>	Schematic diagrams of piezometric interval locations and depths, and plumbing details for multilevel piezometers in boreholes M1 (a), M2 (b), M3 (c), H2 (d) and H4 (e). ....	355



G2	Schematic diagram of piezometric interval locations and depths, and construction details for the multilevel piezometer in borehole H3. ....	357
H1	Plot of deuterium versus oxygen-18 showing the location of selected rain, stream and groundwaters from the Seal Cove River valley with respect to global and local meteoric water lines. ....	360

## LIST OF PLATES

<u>Plate</u>		<u>Page</u>
<b>2.1</b>	Outcrop in the Holyrood granite pluton showing undulating subhorizontal sheeting joints. Apertures in such joints are commonly open, with gaps up to 10 mm or more. Note the active water seepage from the horizontal joints on the rock face. The person is holding a meter stick for scale. ....	25b
<b>2.2</b>	Traces of typical subvertical fractures in the granite. Apertures in such subvertical fractures in the pluton are commonly microscopic. Differential erosion has resulted in minor surface depressions marking these fractures. Marker pea is 12 cm long. ....	25c

## CHAPTER 1

### INTRODUCTION

#### 1.1 Background

Understanding surface water/groundwater interaction and the response of small catchments to hydrologic stress (e.g. precipitation) has become increasingly important in recent years for a variety of contaminant hydrology, water resource and land use issues. Specific examples are the effects of acid precipitation on stream runoff chemistry (e.g. Bottomley et al., 1984) and aquatic life (e.g. Baker and Schofield, 1982; Gunn and Keller, 1984) and the anthropogenic impacts of forestry or road-building practices on the quality and quantity of storm runoff (e.g. King and Tennyson, 1984; Harr, 1986).

Within the field of catchment hydrology, much effort has been focused on understanding mechanisms of streamflow generation in a variety of hydrogeologic settings (e.g. Sklash and Farvolden, 1979; Kennedy et al., 1986; Pearce et al., 1986). Yet for small catchments underlain by well-exposed, fractured, low-permeability rock (e.g. granite), the physical and hydrochemical response to hydrologic stress remains poorly understood. This is because most experimental catchments are either heavily forested (e.g. Sklash and Farvolden, 1979; DeWalle et al., 1988) or underlain predominantly by porous media (e.g. Pilgrim et al., 1978; Anderson and Burt, 1982), or both (e.g. Pearce et al., 1986; Mulholland et al.,

1990), with very few catchments sited in granitic terrain (e.g. Christophersen et al., 1990). In addition, many surface water-groundwater interaction studies utilize physical hydrogeologic measurements, such as hydraulic head or seepage flux, made at widely-spaced time intervals. Such an approach may provide useful information in certain cases where porous media flow dominates. However, it would fail to document the variability in these parameters during response to hydrologic stresses where both hydraulic heads and permeability are highly variable, either in porous media (e.g. Lee and Hynes, 1978) or in a fractured rock terrain as described here.

The setting of experimental study catchments, conventionally in headwater regions of drainage basins, also restricts the types of analyses that can be conducted in those catchments and the range of terrains where the results can be applied. Small headwater catchments are commonly used due to their hydrologic simplicity which supports assumptions of steady-state conditions in the implementation of mass balance techniques such as chemical and isotopic hydrograph separation. Yet downstream reaches of streams, being the areas most likely to undergo development or changes in land use, are the areas where catchment response and streamflow generation information is most needed. Furthermore, a transient mass balance approach, which is inherently more realistic than a steady-state approach for quantitatively analyzing rapidly changing stream flow and chemistry terms during storm runoff events, has not been possible in conventional headwater catchment studies since there has been no practical way to estimate change-in-storage as required in transient mass balance equations.

Fractures are known to control fluid flux and flow directions through rocks of low matrix permeability, such as granite (e.g. Hsieh et al., 1985; Gale et al., 1987; Neuman, 1987). It follows that the confidence that can be placed in values of fracture-controlled fluid flow properties, such as permeability and anisotropy,

where these properties are extrapolated through a rock mass, depends on the nature and variability of fracture geometry throughout the rock mass. In most catchment studies, bedrock characteristics such as fracture patterns or changes in lithology have been neglected or given cursory mention, due to the belief that groundwater contributions from fractured low-permeability bedrock are negligible during storm runoff events. This view may be reasonable for catchments where the interaction of shallow groundwater and surface water occurs dominantly within thick soil zones or sequences of unconsolidated overburden. However, it may not be valid in areas of well-exposed, fractured granite where groundwater efflux along highly-permeable fractures or faults may be substantial.

The above paragraphs point out the need for further investigation of surface water-groundwater interaction which (i) is sited in a well-exposed, fractured low-permeability rock (e.g. granitic) terrain, (ii) documents response to precipitation in a catchment area which is not geographically restricted to the headwater region of a drainage basin, and (iii) which utilizes a transient mass balance approach and incorporates hydrologically significant bedrock structural features. The study area for this thesis is located within the Seal Cove River drainage basin on the Avalon Peninsula in eastern Newfoundland (Figure 1.1). The Seal Cove River valley study area (SCRV) consists of a section of hillslope and valley bottom, and provides an excellent opportunity for such an investigation. The SCRV is underlain by lithologically homogeneous granitic bedrock of the Precambrian Holyrood pluton. Extensive granite exposures in and around the SCRV make this region amenable to detailed geologic mapping and analysis of fracture geometry, which in turn provides a framework for interpreting physical hydrologic and hydrochemical variations, and for constraining numerical simulations of shallow groundwater flow within the study area. Based on

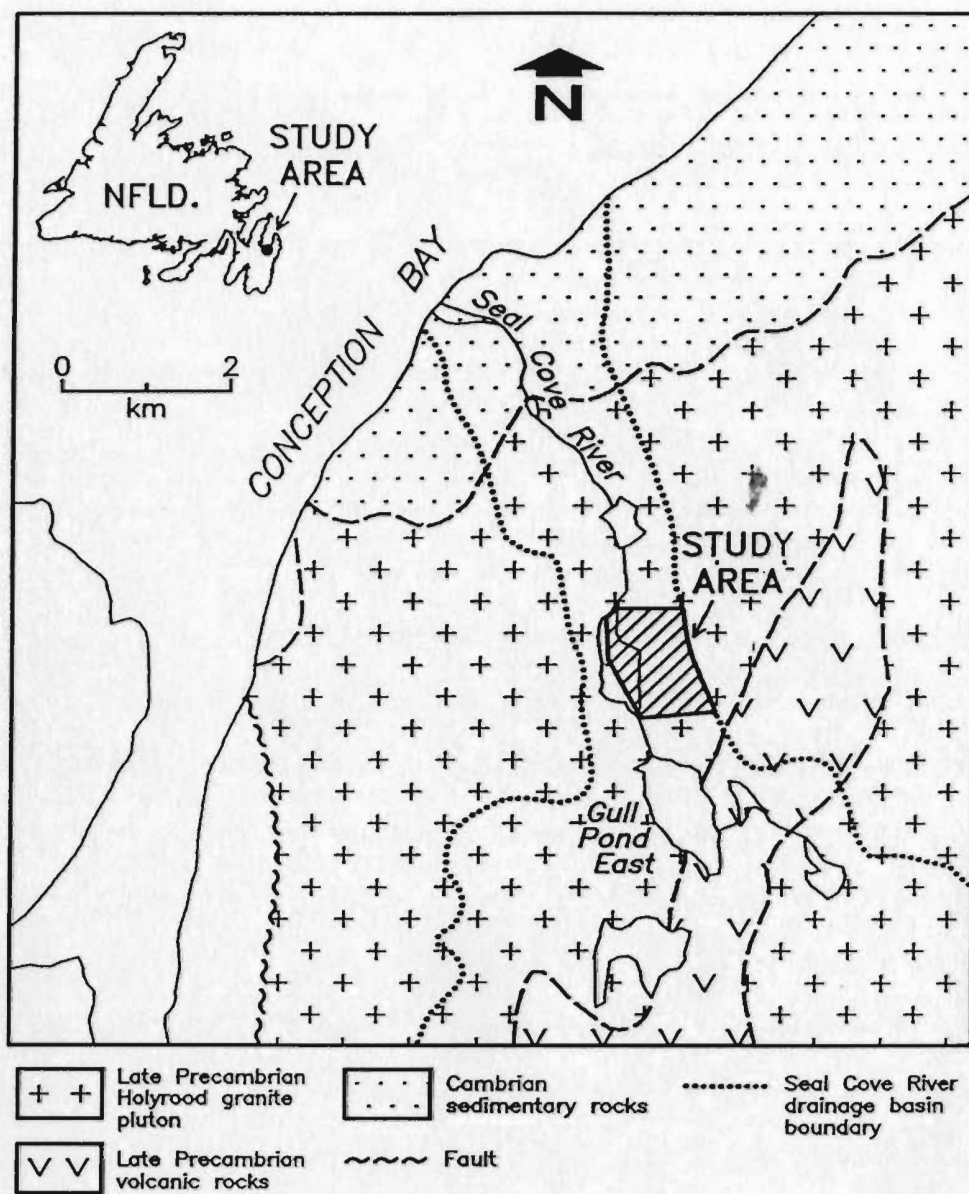


Figure 1.1 - Location and setting of the Seal Cove River valley study area in eastern Newfoundland.

topographic and geologic characteristics, the SCRV can be assumed to behave as a hydrologically isolated catchment area within the Seal Cove River drainage basin, but far removed from the headwater region. By monitoring stream flow and sampling stream water along a small pristine reach of the Seal Cove River flowing through the study area, it is possible to estimate changes in mass and flow storage within this study reach. This in turn permits the use of transient mass balance techniques for investigating stormflow generation in this study.

## **1.2 Objectives and scope**

The objectives of this thesis are:

1. To develop a more thorough understanding and exposition of fracture geometry (e.g. orientation, trace length, spacing) in granitic rocks, both at the surface and the shallow subsurface; and to use the geologic and bedrock structural features in and around the study area as a framework for interpreting groundwater/surface water interaction to hydrologic stress in the SCRV.
2. To provide a clearer understanding of the magnitude and timing of the physical reaction of surface water and shallow groundwater in a fractured granite terrain to storm events and seasonal precipitation changes; to use measurements of seepage fluxes in the study reach, piezometric levels in bedrock piezometers, stream flow and rainfall, made at intervals that are consistent with the duration and rate of change of hydrologic stresses; and to describe the physical mechanisms of groundwater response to such stress in the SCRV.
3. To investigate the hydrochemical interaction between surface waters and



groundwaters in a catchment specifically sited in well-exposed granitic terrain, using measurements of rain, stream and groundwater chemistry and isotopic composition under low flow and stormflow conditions. Specific aims are to (i) interpret compositional variations and mixing relationships between shallow groundwaters sampled in boreholes in the SCR, (ii) determine the components of storm runoff generated along the stream reach, and (iii) compare the hydrochemical and physical response to hydrologic stress in the SCR. A further objective is to theoretically develop transient mass balance methods for interpreting chemical changes and determining stormflow components along a stream reach and practically implement these methods using data in this thesis.

4. To use fracture and hydrogeologic data in constraining boundary conditions for two- and three-dimensional steady state numerical simulations of shallow groundwater flow in the SCR. These models are aimed at (i) determining the internal consistency of physical hydrologic measurements and (ii) to test inferences, based on physical hydrogeologic and hydrochemical responses to hydrologic stress in the SCR, concerning the effective size of the area contributing to stormflow, and the shape and distribution of recharge and discharge areas and shallow groundwater flow paths in the assumed catchment.

This thesis attempts to integrate the fields of geology (augmented by geophysics), hydrogeology and hydrochemistry within the field, laboratory and numerical modelling components shown in Figure 1.2. The hallmarks of this thesis are (i) the siting of this hydrological investigation specifically within a well-exposed granitic area, a setting which has previously received considerably less attention than areas underlain by porous media; (ii) the development, analysis and implementation of transient mass balance methods (based on a stream reach)

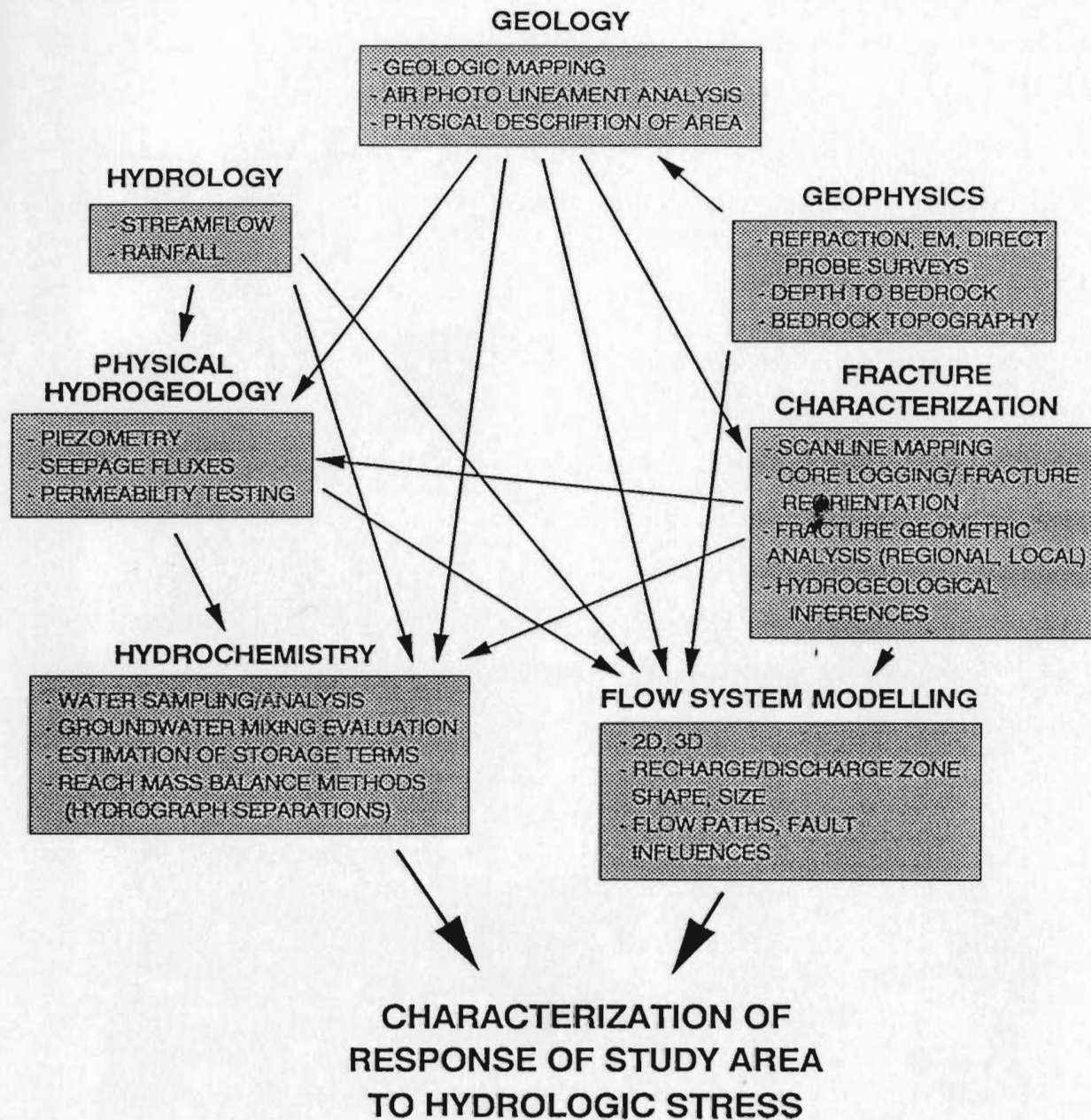


Figure 1.2 - Interrelationships of major study components for this thesis. Arrows indicate directions of principal information transfer.

which have the potential for markedly expanding the range of hydrologic settings where mass balance techniques can be applied, and (iii) the application of a strongly multidisciplinary approach to a hydrologic study, in accord with recent appeals stressing the value of this strategy (e.g. Freeze, 1990; Church et al., 1990). The development and use of transient mass balance equations for purposes of hydrograph separation along a stream reach under stormflow conditions has not been done before to my knowledge (see Section 1.4.3) and can be considered the key contribution to science in this thesis. It is recognized that in a multidisciplinary thesis study there is an inherent risk that some study components may not be developed to their fullest potential. However, the benefits of an integrated, broad-based understanding of the study area are considered to outweigh possible limitations in detailed scope. The current level of understanding of the geology and physical hydrogeology of the SCR/V are considered adequate to make at least a preliminary interpretation of the hydrochemistry and overall response to precipitation in the SCR/V.

### **1.3 Thesis organization**

This thesis is subdivided into six chapters. Chapter 1 presents a background to this study, detailed thesis objectives and organization, and previous work relating to the multi-disciplinary components of this work.

Chapter 2 describes the geology and fracture geometry within the Holyrood pluton and in the SCR/V, based on regional and detailed geologic field mapping, scanline fracture surveys and core logging in the SCR/V. Areal variations in fracture geometry are compared at macroscopic and mesoscopic scales in order to place the SCR/V in a regional structural geologic context. Cluster analysis techniques are used to define subvertical fracture sets in the SCR/V for further detailed statistical analysis. The brittle deformation history of the pluton and factors influencing the variability of fracture geometry are discussed, and

hydrogeological implications of the bedrock structures in and around the SCR V are presented. Data in this chapter constitute a geologic structural framework for interpreting physical hydrogeology and hydrochemistry data and for constraining numerical models of groundwater flow in subsequent chapters.

In Chapter 3, the physical and hydrogeological setting of the SCR V is described along with the basis for treating the area as a hydrologic catchment. Detailed physical responses of groundwater and surface water to hydrologic stress in the SCR V are presented and interpreted, based on field measurements of rainfall, streamflow, seepage fluxes and piezometric levels. Correlations between the surface water and groundwater responses are evaluated and three-dimensional variations of hydraulic head during hydrologic stress are discussed. Physical mechanisms of groundwater response to precipitation are proposed which are consistent with the geologic framework presented in Chapter 2.

In Chapter 4, the hydrochemical and isotopic (oxygen-18 and deuterium) responses of rain, stream and groundwaters in the SCR V to hydrologic stress are described and interpreted. Transient reach mass balance methods are developed and implemented in this chapter. Groundwater mixing patterns are investigated in an effort to constrain input parameters for these methods. Results and limitations of hydrograph separations for two major storm runoff events in the study area are discussed. The compatibility of both physical and hydrochemical responses to precipitation in the SCR V, based on results from Chapters 3 and 4, are evaluated at the end of Chapter 4.

In Chapter 5, the input parameters for numerical models are developed, boundary conditions are described and results of two- and three-dimensional steady state simulations of the groundwater flow system in the SCR V are presented and interpreted. These results are used to evaluate the internal consistency of seepage flux and piezometric measurements in the SCR V, to

determine the shape and location of recharge and discharge zones in the assumed catchment, and to infer the influence of major fractures on the shallow groundwater flow system in the SCR.V.

Chapter 6 is a summary of this thesis and its principal conclusions.

A series of appendices present the following supplementary information:

- procedures, analytical techniques and results for various field methodologies used in this thesis,
- construction details for field instrumentation,
- a derivation of the reach mass balance equations and a discussion of their implementation (both in the SCR.V and in other settings), and,
- details of computer codes used in this thesis.

#### **1.4 Previous work**

Prior to work for this thesis, there were no geological or hydrogeological studies dealing specifically with the SCR.V. The previous work presented below is subdivided according to the broad components of this thesis. The contributions of some of these studies and other pieces of work are discussed further in the appropriate parts of this study.

##### **1.4.1 Geology of the Holyrood pluton**

The regional geology of the Holyrood pluton was described by Rose (1952), McCartney (1967) and King (1982, 1988), with the petrology of the intrusion investigated by Hughes (1971), Strong et al. (1974) and Strong and

Minatides (1975). Recent age dates have been reported by Krogh et al. (1983). Regional geophysical surveys indicating the thickness or extent of the pluton have been presented by Weaver (1967), Hodych and Weir (1972), Miller and Pittman (1982) and Miller (1983). Models for the tectonic and petrogenetic history of the pluton have been proposed by Hughes and Brueckner (1971), King (1982) and O'Brien et al. (1983). However, the present study presents the only detailed analysis of fracture patterns and brittle deformation history within the pluton to date.

#### 1.4.2 Characterization and hydrogeological significance of fracture geometry

Fracture survey techniques using scanline methods at surface outcrops or underground drift wall mapping have been described by a variety of workers, e.g. Hudson and Priest (1979), Priest and Hudson (1981), Rouleau et al. (1981), LaPointe and Hudson (1985). Survey techniques used in this study are an amalgamation of these methodologies and International Society for Rock Mechanics (ISRM, 1978) guidelines. Borehole impression packing methods used here were adapted from those of Barr and Hocking (1967). Borehole fracture logging and reorientation methods have been described by Goodman (1976) and Gale (1981).

Studies dealing with sources of error affecting fracture surveys and the various methods of correction for these errors include Terzaghi (1965), Cruden (1977), Baecher and Lanney (1978), Baecher (1980), Baecher and Einstein (1981), and Priest and Hudson (1981).

Recently, there has been a growing number of studies dealing with

statistical analysis of fracture geometry for hydrogeological purposes, e.g. Doe, et al. (1982), Gale and Rouleau (1983), Rouleau (1984), LaPointe et al. (1984), LaPointe and Ganow (1984), and Gale et al. (1987). Definition of systematic fracture sets by orientation is a fundamental step in proceeding with these types of statistical analysis. Various methods for defining fracture sets have been proposed, including visual observation of fracture pole clusters on stereoplots (e.g. Turner and Weiss, 1963; Phillips, 1972), visual observation augmented by designation of linear set boundaries on stereoplots (e.g. Rouleau, 1984), or a numerically-based clustering approach based on a mode analysis (Shanley and Mahtab, 1976). An up-dated version of the clustering algorithm (for personal computer; Gillett, 1987) was used in this study.

Variability of fracture geometry (i.e. orientation, trace length, spacing or fracture frequency) in crystalline rock terrains has been discussed in the context of defining fracture domains, describing influences of lithologic changes or major structures on fracture patterns, or describing variations of fracture patterns with depth by Stone (1980), Dugal et al. (1981), Mahtab and Yegulalp (1984), Seeburger and Zoback (1982), Stone et al. (1984) and Raven and Gale (1986). Brisbin (1980) and Segall and Pollard (1983) have discussed the origin, development and nomenclature of joints in granite.

The hydrogeological significance of fracture geometry in crystalline rocks has been well-documented in studies characterizing equivalent continuous porous medium directional permeabilities based on discrete fracture data (e.g. Snow, 1969; Gale, 1982), developing stochastic fracture networks for numerical fluid flow modelling (e.g. Long et al., 1982; Rouleau, 1984), or describing porosity characteristics of fractured granites (e.g. Knapp, 1975; Gale et al., 1987).

Variation of permeability in crystalline rocks with depth (Davis and Turk, 1964; Snow, 1968; Raven and Gale, 1977) has been attributed to decreases in fracture density, aperture or size with depth (Gale and Rouleau, 1986). Correlations between permeability and fracture frequency have been discussed by LaPointe and Ganow (1984), LaPointe et al. (1984) and Gale and Rouleau (1986). Gale (1982) presents a useful overview of permeability characteristics in fractured rock and discusses influencing factors other than fracture geometry, such as in situ stresses, distribution of fracture aperture and degree of fracture interconnection.

#### 1.4.3 Catchment response to hydrologic stress

A wide variety of hydrograph separation studies using chemical and stable isotope (deuterium and oxygen-18) tracers have indicated the importance of "old water" (i.e. stored in the subsurface prior to a storm event) during storm flow (e.g. Dincer et al., 1970; Sklash and Farvolden, 1979; Bottomley et al., 1984; Hooper and Shoemaker, 1986; Kennedy et al., 1986). Approaches to determining more than two stormflow components (i.e. old (groundwater) and new (event) water) have relied on direct determination of additional flow components (e.g. DeWalle et al., 1988; Swistock et al., 1989). Genereux and Hemond (1990) presented a three tracer method, using naturally-occurring radon-222 and two injected stream tracers, for determining the components of lateral inflow to a stream reach at low flow under steady-state conditions. While their approach produces a composition for lateral inflow to a stream reach, similar to the type of results produced by a mass balance method discussed in this thesis (bulk inflow analysis), their presentation did not extend to transient hydrologic conditions during stormflow, as is done in this thesis. To my knowledge, there have been no previous studies utilizing transient mass balance equations for purposes of hydrograph separation



along a stream reach under stormflow conditions, as is attempted in this study.

Hydrologic studies involving stream reaches have also included investigations of in-stream transport processes (e.g. McKnight and Bencala, 1990), stream contaminant sedimentation (Berndtsson, 1990), groundwater/stream interaction in semi-arid regions (Cooley and Westphal, 1974), and mathematical steady-state models of rainfall-runoff processes along a reach (Dunne et al., 1991). Pinder and Jones (1969) reported increases in solute concentration at successive sampling points along a small stream in Nova Scotia, attributing this to differences in groundwater composition or discharge along the stream reach. Rodhe (1987), as described by Wels et al. (1991), estimated time-varying compositions of groundwater contributing to streamflow, within a finite groundwater reservoir model under stormflow conditions using a trial and error technique with total groundwater volume as the variable. Bencala et al. (1987) used a steady-state chemical mass balance equation to determine the chemistry of groundwater inflows to a stream reach. Space et al. (1991) used deuterium in a two-component steady-state mixing model to estimate groundwater inflow to a stream reach under drought conditions with no surface runoff. Yoneda et al. (1991) used incremental radon-222 samples along a 20 km long stream reach to identify locations of groundwater inflow zones to the stream. Burt (1979) and Anderson and Burt (1982) evaluated contributions of soil zone throughflow to a short (60 m) stream reach at the base of a grassy hillslope. By attributing hydrograph features to different hillslope runoff mechanisms (initial overland flow, delayed throughflow), they were implicitly treating the hillslope as a catchment area, broadly similar to the way the SCRIV is treated in this thesis.

Hydrometric techniques have been used to identify the importance of near-

surface and subsurface flow paths (e.g. Pilgrim et al., 1978; Sklash et al., 1986) and principal physical runoff mechanisms, such as saturated overland flow in near-stream areas (variable source areas), during stormflow generation (e.g. Hewlett and Hibbert, 1967; Dunne and Black, 1970; Freeze and Banner, 1970). Ward (1982) presents a useful overview of runoff mechanisms and related terminology for simple headwater catchments. Prompt near-stream piezometric responses to precipitation have been shown by Lee and Hynes (1978), Sklash and Farvolden (1979) and Mulholland et al. (1990), although the piezometers in these studies were placed in overburden deposits and not in fractured granite as in this study. Lee (1977) and Lee and Cherry (1978) described techniques for measuring seepage fluxes between shallow groundwater and surface water (ponds or streams). Variability of seepage fluxes have been investigated by Lee and Hynes (1978), Lee and Cherry (1978), Lee et al. (1980) and Krabbenhoft and Anderson (1986).

#### 1.4.4 Numerical modelling of flow systems in hydrologic catchments

There have been many previous studies in the numerical simulation of groundwater flow and rainfall-runoff processes in hydrologic catchments and hill slopes. Some examples are the works of Freeze (1971, 1972a, 1972b, 1980), examining baseflow contributions to streamflow, and overland flow and variable source area runoff mechanisms and controlling factors; that of Sklash and Farvolden (1979), using hypothetical watershed profiles to simulate the development of their proposed near-stream groundwater ridge in response to rainfall; and that of Smith and Hebbert (1983), simulating the dynamic hydraulic interaction between unsaturated and saturated zones within a hillslope soil zone. Such studies have generally been generic, i.e. specific to no particular rock type or

geologic terrain, or have utilized experimental catchments underlain by porous media.

More recently, flow system modelling studies have been conducted specifically within fractured crystalline rock terrains (e.g. Gale et al., 1987; Forster and Smith, 1988a, 1988b). Gale et al. (1987) presented two- and three-dimensional, steady state simulations of regional groundwater flow around a test mine in Sweden, using equivalent porous media permeability and porosity characteristics developed from detailed studies at the mine to set input parameters, and using measured groundwater inflows in the mine for model calibration. Forster and Smith (1988a, 1988b) developed a two-dimensional coupled fluid flow and heat transfer model for groundwater flow within hypothetical mountain massifs to investigate the influences of a wide range of topographic, geologic, climatic and regional heat flux factors. Aspects of the conceptual approaches of such studies in fractured low-permeability rock, e.g. decrease of equivalent porous media permeability with depth and incorporation of the hydraulic properties of large discrete fracture zones within that permeability field, are also relevant in the SCR V and are included in numerical modelling done in this thesis.

## CHAPTER 2

### STRUCTURAL GEOLOGIC FRAMEWORK OF THE SEAL COVE RIVER VALLEY AND SURROUNDING REGION

#### 2.1 Introduction

##### 2.1.1 General statement

Fluid flow properties of granitic rocks are predominantly controlled by the nature and geometric variability of the fracture systems within such rock masses. Variability of fracture geometry commonly accompanies changes in lithology or structural style, e.g. fracture orientations may deviate from regional patterns near pluton contacts or vary with changes in regional fold style, and fracture density may increase in proximity to major faults (e.g. Balk, 1937; Dugal et al., 1981; Stone et al., 1984; Raven and Gale, 1986). Hence, when a fractured rock mass is described for hydrogeological purposes, it is important that the fracture system be described in both a regional and local geologic context so that fracture-controlled hydraulic properties, which are commonly determined at only a few locations, can be extrapolated throughout the rock mass with a sound physical basis.

The purpose of this chapter is to provide such a physical framework for the later components of this study by describing and interpreting the structural geology and fracture geometry of the northern part of the Holyrood pluton and of the SCRV. The northern part of the pluton is included in order to identify any

regional structural trends and thus better describe structures within the SCRV. The general geology of the Holyrood pluton, and sources and limitations of data used in this chapter are described immediately below. Descriptions of regional and local fracture geometry within the pluton are then presented, focusing on orientation, trace length, fracture frequency and fracture spacing. Procedures and results for scanline fracture surveys, core logging, and correction of orientation bias in fracture surveys are presented in Appendices B, C and D, respectively. A history of brittle deformation in the northern part of the pluton and the major influences on variability of fracture geometry within the pluton are discussed. Finally, hydrogeological implications stemming from these observations and interpretations are presented. Fracture characteristics bearing on boundary conditions and input parameters for numerical modelling are readdressed in Chapter 5.

### 2.1.2 Geologic setting of the Holyrood pluton

The SCRV lies within the northern part of the late Precambrian Holyrood Intrusive Suite (King, 1988) in eastern Newfoundland (Figure 2.1). The pluton crops out discontinuously over an area of approximately 60 km x 20 km (King, 1980) and is inferred to extend beneath Conception Bay (Miller, 1983) for a total area of about 1340 km<sup>2</sup>. Gravity modelling infers that the northern part of the pluton is at most 1.8 km thick (Hodoch and Weir, 1972; Miller and Pittman, 1982), hence has the form of a large laccolith or sill (width-to-thickness ratio approximately 10:1). The pluton consists mainly of medium-grained, massive, pink to grey granite with minor aplite and felsite dikes, and lesser medium-grained quartz monzonite, quartz diorite and gabbro. In the SCRV, bedrock consists primarily of massive pink granite and lesser felsic and mafic dikes. Primary mafic

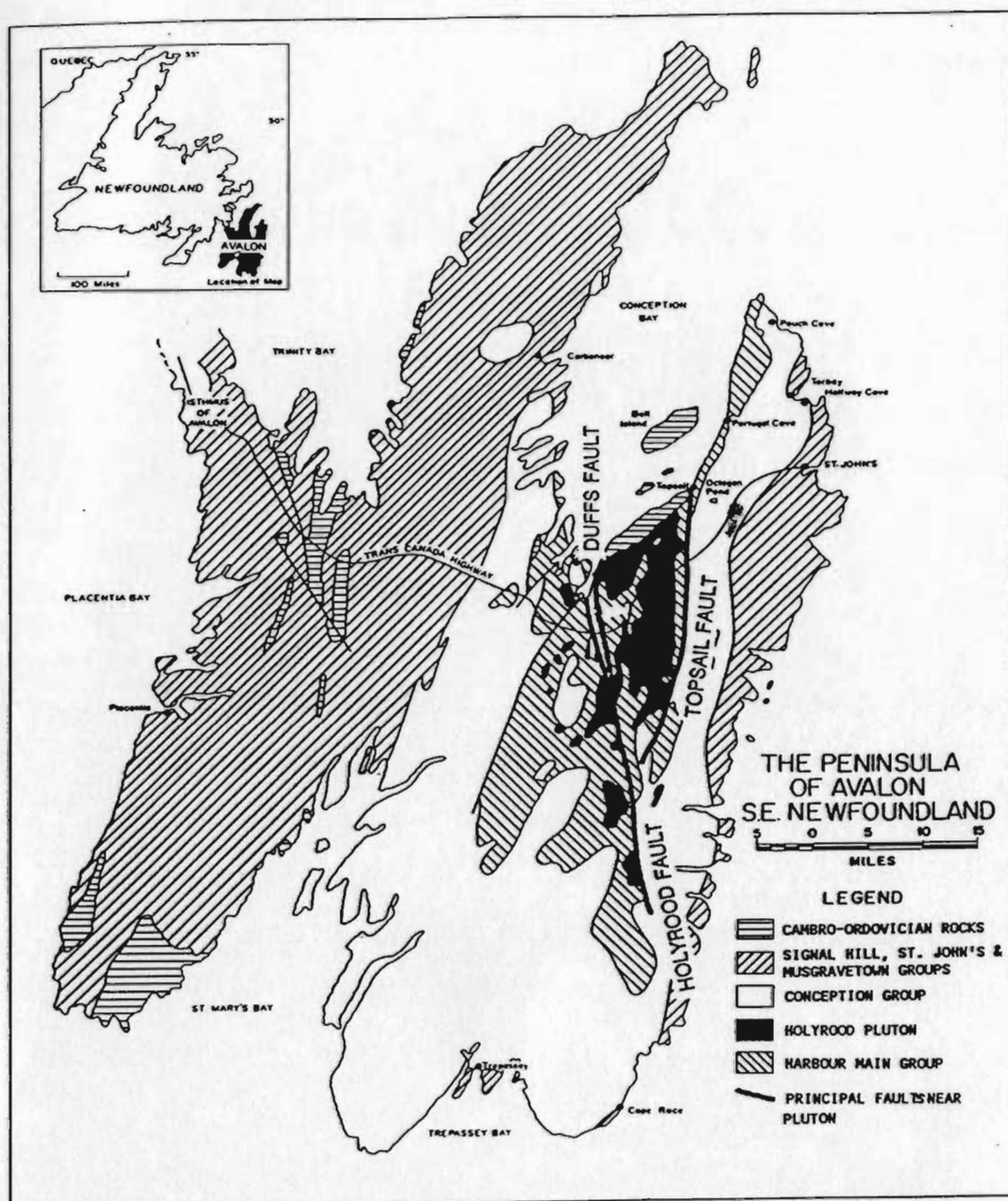


Figure 2.1 - Regional geologic map of the Avalon Peninsula showing the major lithologic units and structural features around the Holyrood pluton (adapted from Brueckner (1979) and King (1988)).

minerals in the granite are altered to secondary minerals, mainly chlorite, while the feldspars are partly altered to clay minerals, such as kaolinite. Krogh et al. (1983) determined a U/Pb (zircon) age date of 620 (+2.2, -1.7) Ma for granitic rocks in the pluton.

The pluton intrudes multiply-deformed volcanic, volcanoclastic and related sedimentary rocks of the late Precambrian Harbour Main Group and is nonconformably overlain by tilted middle to late Cambrian sedimentary rocks of the Adeytown Group (King, 1988) near the Conception Bay coast (Figure 2.1). Abundant volcanic roof pendants in the northern part of the Holyrood pluton (Hughes, 1971) indicate that the present erosional surface coincides approximately with the emplacement roof of the intrusion.

Wisconsinan glaciation in this region formed a series of linear valleys trending northwards toward Conception Bay (Henderson, 1972). The valley floors are typically covered with quartzo-feldspathic drift with granitic boulders while the ridge crests are eroded, showing ice erosion features such as striations, chatter marks and roche moutonnée. The drift is likely derived from the pluton, as glacial transport distances on the Avalon Peninsula are typically less than 1 km (D. Liverman, pers. commun.).

### 2.1.3 Data sources and limitations

Geological and fracture data for this thesis were obtained by 1) air photo analysis, 2) outcrop mapping, 3) scanline fracture surveys and 4) logging of reoriented core. The aims, general methods of collection, and limitations of these data are discussed below.

Analysis of air photos (1:12,500-scale in colour) and outcrop mapping data documented the occurrence, orientation and general character of macroscopic and mesoscopic structures. To minimize errors in determining lineament azimuths on the air photos, only lineaments 75 m long or longer were used for air photo analysis. Because most outcrops in this region are less than 25 m across, this means that very few fractures between 25 m and 75 m long were directly observed in this study. To avoid mistaking glacial features for true fracture lineaments, only lineaments exposed in and extending from bedrock areas were used. Ground truth checking indicated that these types of lineaments represent actual fractures. Fracture lineaments within the Holyrood pluton generally have amplitude-length ratios of less than 0.02 indicating, by their lack of deflection around topographic contours, that the underlying fractures are subvertical (Ragan, 1973). Large subhorizontal fractures do occur (visible at road cuts and hillside exposures), but are not recognizable on air photos, hence were not included in the air photo analysis. In addition, azimuth comparisons for lineaments are qualitative only, as discussed below.

Detailed geologic mapping (at 100 outcrops across the pluton; 52 in the SCR V) was carried out to document lithologic contact relationships and general fracture characteristics, such as dominant orientations, termination styles, infilling mineralogy, relative ages, and sense and orientation of fault displacement.

Following geologic mapping, scanline fracture surveys were conducted at a 33 sites across the pluton (nine in the SCR V area) to provide a data base for statistical fracture analysis. Most survey sites were located on glacially-denuded hilltops. This preferential use of hilltop exposures may have resulted in an under-sampling of fault zones and associated dense fracturing,



which are commonly located in morphological depressions (e.g. Raven and Gale, 1977). The degree of this type of sample bias in the SCRVS is unknown, but is probably not significant since a range of hilltop, hill slope and valley bottom exposures are combined to form the SCRVS scanline fracture data set.

The representiveness of the scanline methods used in this study was tested by mapping all of the fractures within a 20 m x 20 m test outcrop (survey site 7), then applying normal scanline techniques and comparing the results. Stereoplots for the fracture population and the scanline sample (Figures 2.2 a and b, respectively) have nearly identical patterns and relative pole cluster densities, suggesting that the scanline methods provided a representative sample at this site and, by inference, at the other survey sites.

Scanline data from site 7 were also used to test the effects of scanline orientation bias (Terzaghi, 1965; see Appendix D), which is caused by inadequate sampling of fractures making small angles with a sampling line. Fractures within about  $25^\circ$  of a sample line are said to fall within a "blind zone" where sampling is effectively nil. Stereoplots of uncorrected and corrected scanline data from site 7 (Figures 2.2b and 2.2c, respectively) are nearly identical, with very few new fracture orientations generated by the correction algorithm ( $< 9\%$  of uncorrected total). This is attributed to the practice used here of laying out scanlines perpendicular to the principal fracture sets and pooling the data so that fractures in blind zones for single scanlines (indicated in Figure 2.2c) are sampled by the other scanline(s). Based on these test results, the effects of orientation bias on the sampling of steeply dipping fractures at site 7, and by inference at other scanline survey sites across the pluton, are considered to be negligible.

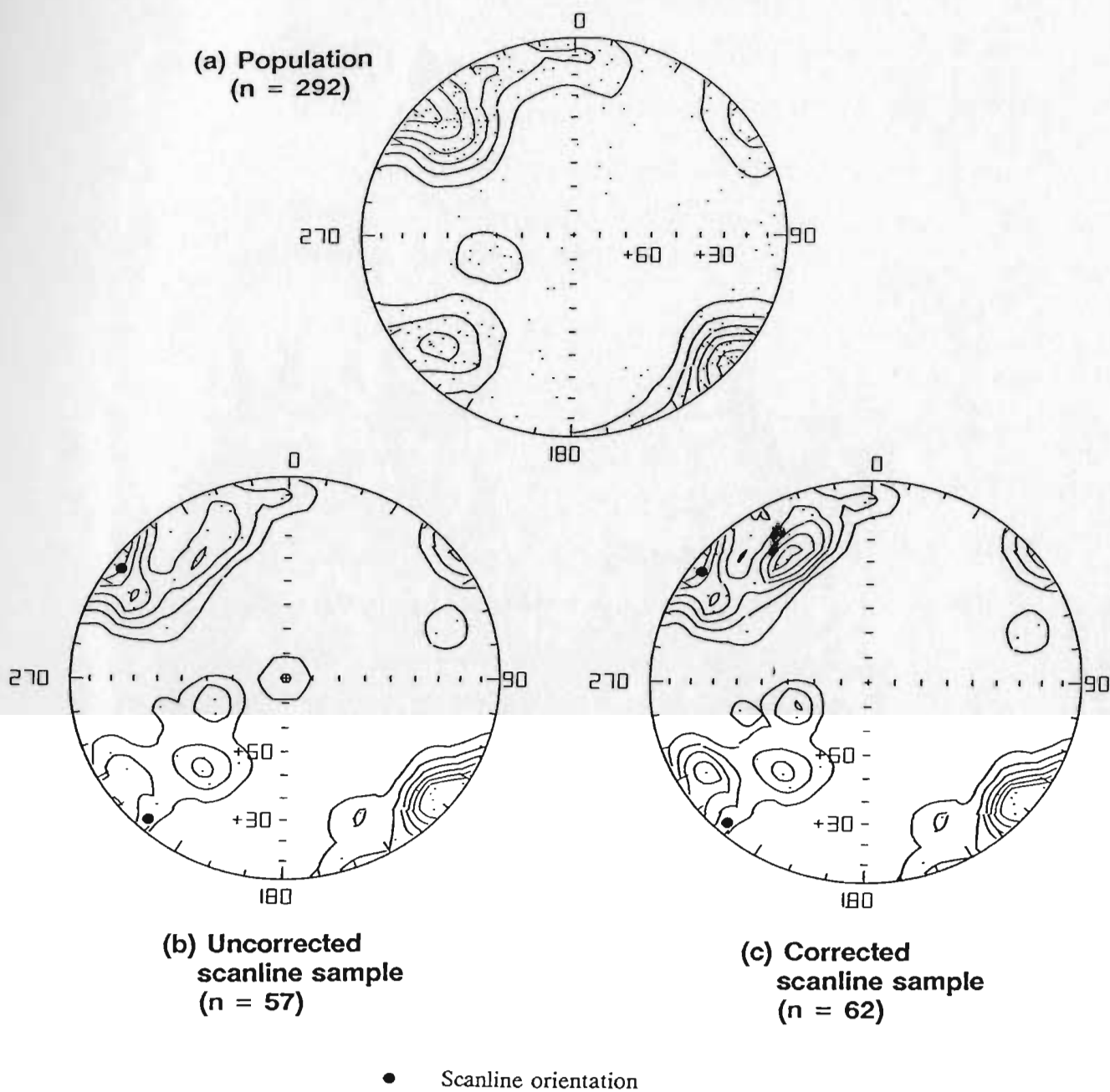


Figure 2.2 - Equal-area, lower hemisphere stereoplots of fracture orientations at a test outcrop (site 7); (a) total fracture population; (b) scanline data (scanline orientations shown as solid circles); (c) scanline data corrected for orientation bias (described in text). All plots constructed using the same contour function increment (0.1) using methods of Fisher et al. (1986).

Since the survey outcrops were flat-lying (dips less than 20°), subhorizontal fractures were inherently under-sampled by scanline methods. Because of this, subhorizontal fracture characteristics were estimated using direct observations at vertical exposures and core fracture measurements. Subsurface fracture orientations were determined by reorienting core from inclined boreholes H2 and H4 in the SCR (Appendix C). However, it was not possible to reorientate all of the core from these holes due to gaps in recovery caused by lost or ground core during drilling. In addition, the uncertainties in core fracture orientations are large (estimated to be  $\pm 10^\circ$  or more in dip magnitude and dip direction) compared with more precise scanline fracture measurements ( $\pm 2^\circ$  for subvertical fractures at flat subhorizontal outcrops). For these reasons, scanline data were used exclusively here for defining subvertical fracture sets and in the statistical analysis of fracture geometry.

## **2.2 Fracture geometry within the Holyrood pluton**

### **2.2.1 Structural framework of the pluton**

The Holyrood pluton and the volcanic host rocks of the Harbour Main Group form the core of the Conception Bay anticlinorium (King, 1988), a major north northeast-trending tectonic feature in the eastern Avalon Zone of Newfoundland. This setting and the occurrence of tilted sedimentary rock units above the granite suggest that the pluton itself may be warped. As possible evidence of this, the northeast-trending tongue of volcanic rocks, sited east of the SCR (Figure 2.1), may represent a synformal erosional remnant of volcanic roof rock.

The major brittle structures in the region are north-trending, subvertical faults (e.g. Topsail Fault, Holyrood Fault, Duffs Fault; Figure 2.1) which are interpreted to bound and predate intrusion of the pluton (King, 1988; A. King, pers. commun.). Within the pluton, brittle structures include a full range of fault and shear zones, shear joints, tension gashes, veins, and sheeting fractures (collectively referred to here as fractures). These structures were formed during emplacement, tectonic deformation, and uplift and erosion of the pluton, with ages ranging from Precambrian to Recent times. In outcrop, the tectonic fractures commonly display strain transfer zones, en echelon patterns and arcuate horsetail terminations, which are used to indicate relative senses of shear. Plates 2.1 and 2.2 show typical fractured outcrops in the granite. Fracture apertures were visually estimated to be fractions of a millimeter for tectonic fractures, and up to 10 mm or more for sheeting fractures. Quantitative measurement of fracture apertures and their variability was not within the scope of this study. Faults and fracture zones in outcrop are typically less than one meter wide, without densely fractured adjacent halo zones, and contain angular breccia or comminuted brittle fault gouge. Ductile strain is rare in the pluton, limited to mineral alignment and shearing within cognate mafic inclusions in the granite.

Regional fracture geometry in the pluton is described below, focusing on 1) macroscopic fracture patterns (from air photo lineament analysis), 2) mesoscopic fracture orientations (from scanline data), for comparison with macroscopic fracture patterns, and 3) trace lengths and fracture frequencies (also from scanline data), for assessing regional trends in fracture size and abundance. Following this, detailed analyses of fracture orientation, trace length and spacing are presented for the SCR, and geometric variations within the SCR are compared with regional trends.

### 2.2.2 Regional fracture geometry in the Holyrood pluton

#### Air photo lineaments

The distribution of fracture lineaments in the northern part of the pluton is shown in Figure 2.3a, along with a grid of 1.5 km x 2 km subareas used for comparison of lineament azimuths in Figure 2.3b.

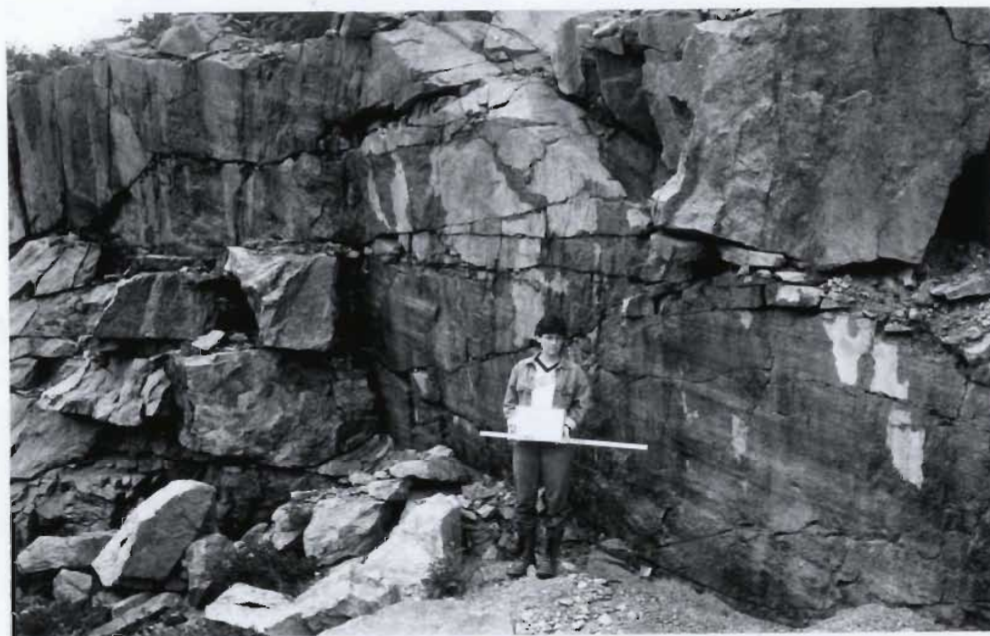


Plate 2.1 - Outcrop in the Holyrood granite pluton showing undulating subhorizontal sheeting joints. Apertures in such joints are commonly open, with gaps up to 10 mm or more. Note the active water seepage from the horizontal joints on the rock face. The person is holding a meter stick for scale.



Plate 2.2 - Traces of typical subvertical fractures in the granite. Apertures in such subvertical fractures in the pluton are commonly microscopic. Differential erosion has resulted in minor surface depressions marking these fractures. Marker pen is 12 cm long.



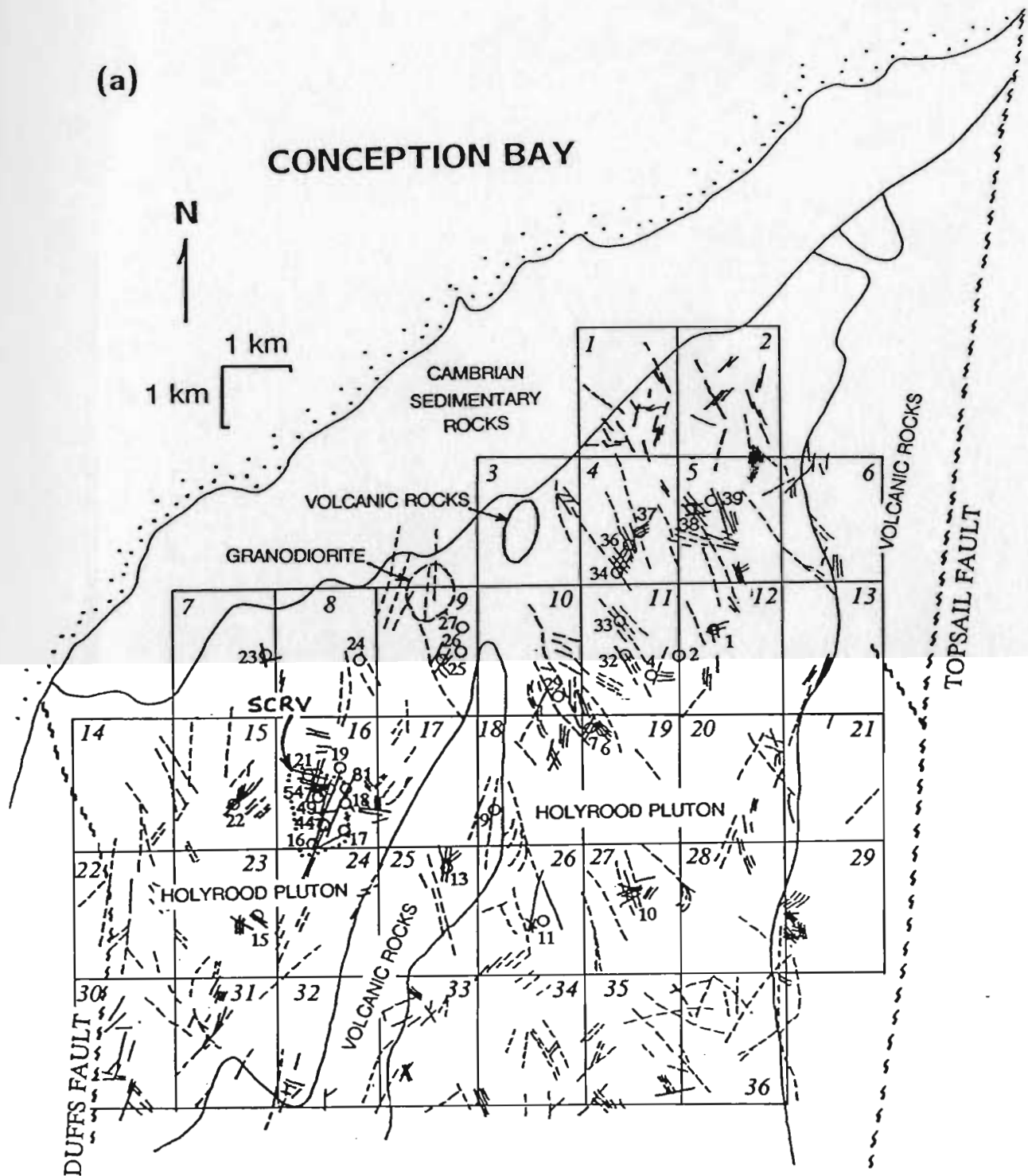


Figure 2.3 - (a) Distribution of air photo lineaments across the northern part of the Holyrood pluton (solid, fracture lineaments; dashed, soil morphological or vegetation lineaments). Grid of 36 subareas (italic numbers) used for azimuth comparisons in (b). Numbered circles are scanline survey sites. The SCR is located in subarea 16.



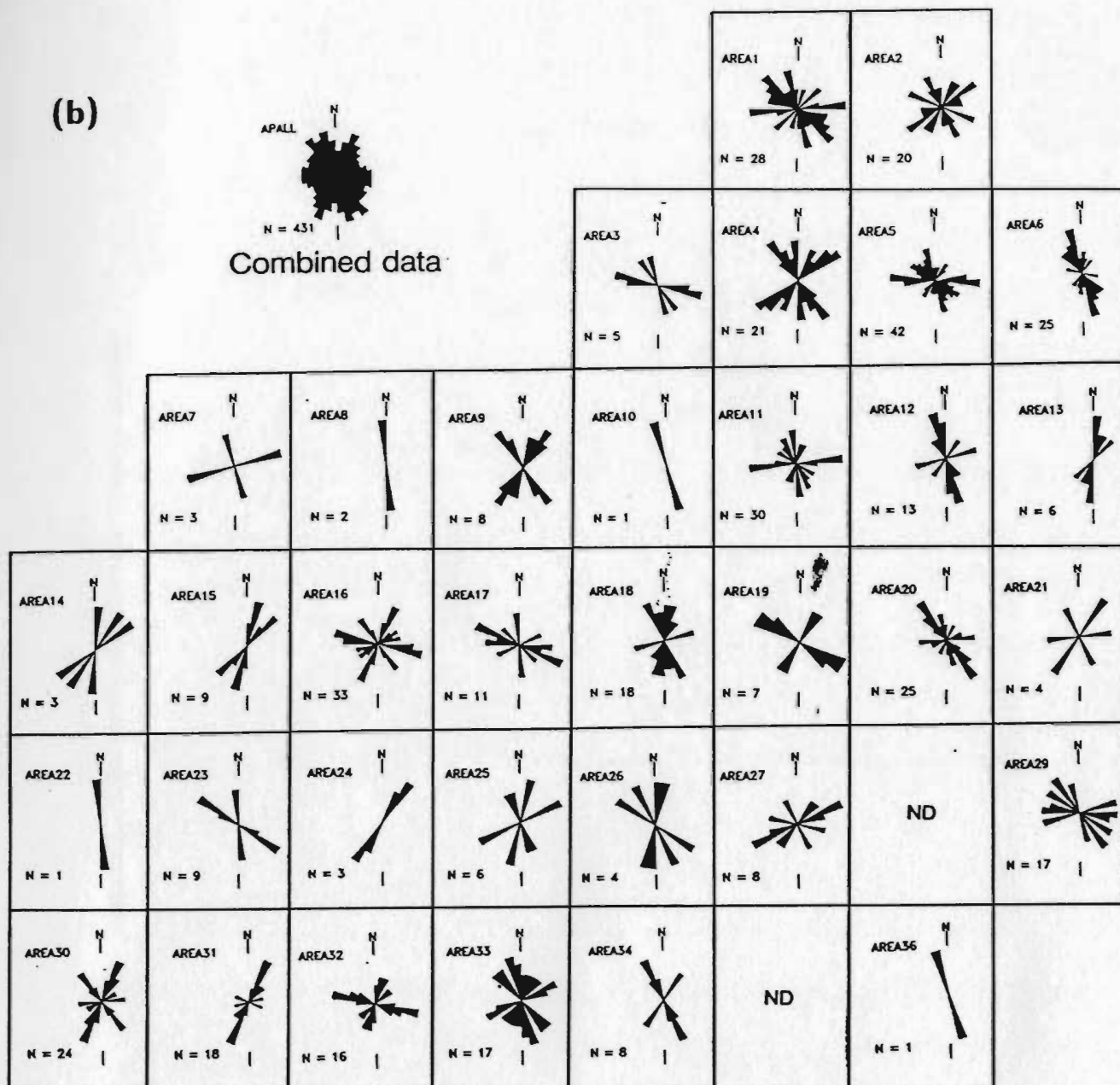


Figure 2.3 - (b) Azimuthal rose plots of fracture lineaments in subareas shown in (a). "ND" refers to no fracture lineament data for subareas 28 and 35.

Throughout the pluton, where lineaments extend from bedrock exposures into covered areas, they display morphological expressions such as small scarps, narrow valleys or subtle changes in vegetation pattern. The lineaments are generally short, with a mean length for all data of only 177 m and a maximum length of only 1750 m. Preferred lineament azimuths are toward the northeast ( $030^\circ$ ), east ( $100^\circ$ ), and southeast ( $160^\circ$ ). Two or all three of these preferred azimuths are developed at locations widely distributed around the pluton (i.e. subareas 1, 4, 5, 9, 11, 12, 16, 18, 19, 20, 21, 30 and 34; Figure 2.3b), suggesting that the faults or fracture zones underlying these lineaments have generally consistent orientations throughout the pluton. Mean lineament lengths in the subareas in Figure 2.3 are also uniform, ranging from 100-250 m (except in subareas 16, 22, 25 and 26 where mean lengths range from 375-488 m). This general uniformity of lineament geometry is important for interpreting the brittle deformation history of the pluton and comparing fracture geometry at different scales, as discussed below.

Fracture lineaments generally trend parallel with the northerly-trending pluton contacts and lithologic boundaries in the region and visibly cross lithologic contacts only in a few isolated areas (e.g. subareas 30, 32 and 33; Figure 2.3). Subareas 6, 18, 22, 25 and 32 also show development of contact-parallel lineaments within volcanic host rocks, up to 300 m from the pluton contact. Lineaments in subarea 15 occur parallel to a family of northeast-striking basalt dikes which intrude the granite. The influence of lithologic contacts on fracture geometry in the pluton is further discussed below.

#### Mesoscale fracture orientations

Figure 2.4 shows stereoplots of poles to fractures measured by scanline

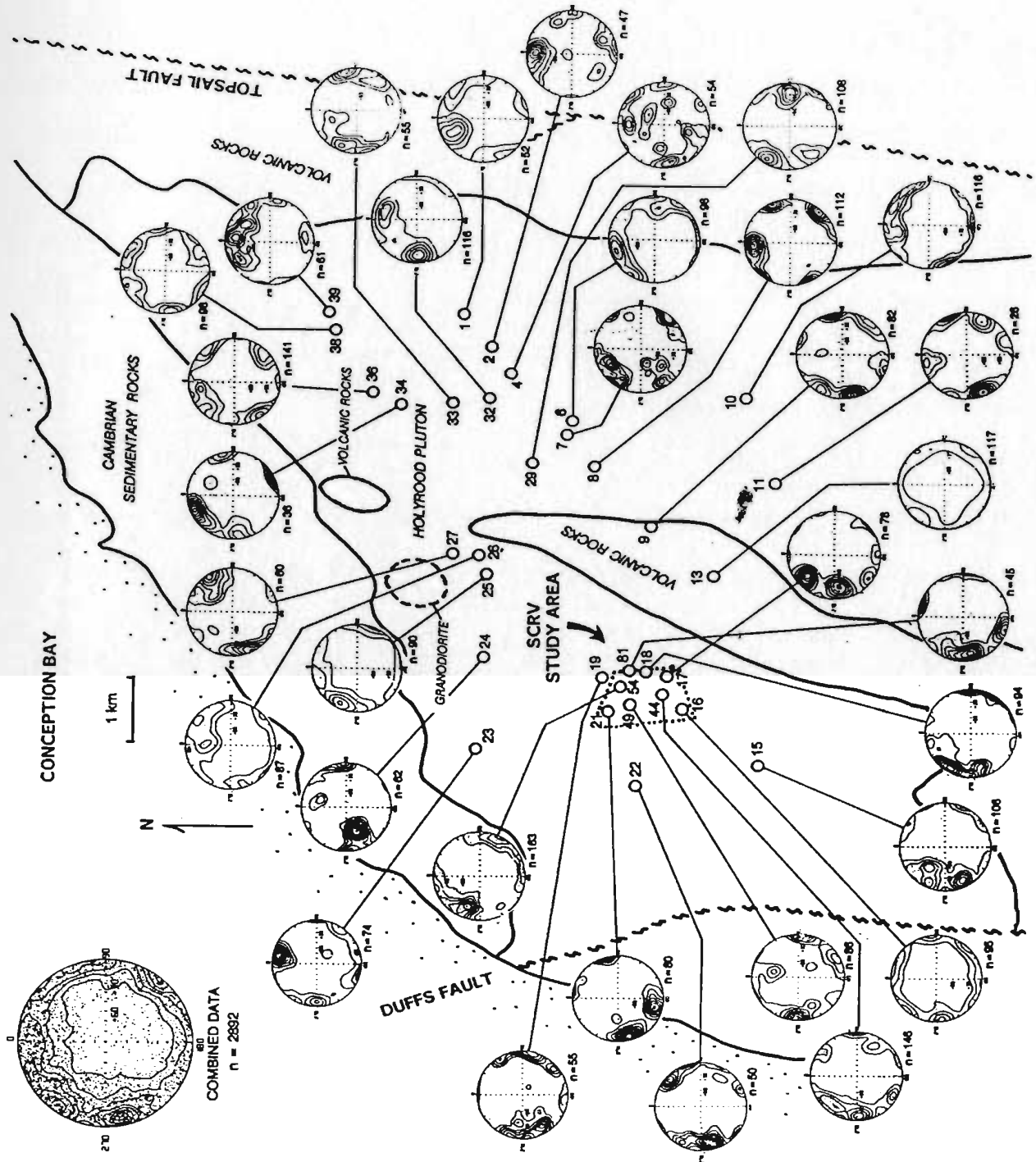


Figure 2.4 - Equal-area, lower hemisphere stereoplots of fracture orientations measured at 33 scanline survey sites (open circles) across the northern part of the Holyrood pluton. All plots constructed using the same contour function increment (0.1) using methods of Fisher et al. (1986).

surveys across the Holyrood pluton. Data from all sites (except site 13) show clear modes and are non-random at 5% (or less) significance level, as indicated by a series of randomness tests conducted as part of the cluster analysis techniques (Gillett, 1987) used here. Combined fracture orientation data (inset, Figure 2.4) show preferred strikes to the north, northeast and to a lesser extent to the southeast, which correspond with the preferred azimuths of composite fracture lineament data (Figure 2.3b). As with the fracture lineaments, mesoscopic fractures display consistent orientations at locations widely distributed around the pluton (i.e. sites 8, 9, 11, 15, 16, 17, 18, 33, 34, 38, 44 and 49). This suggests that both macroscopic and mesoscopic fractures developed with similar and generally consistent orientations throughout the pluton. Regional fracture orientations are further discussed below in describing a regional deformation mechanism for the northern part of the Holyrood pluton.

Data from individual scanline survey sites also show varying effects of changes in lithology on local fracture orientations. For example, at site 9 (Figure 2.4), fractures overprint a diffuse granite/volcanic contact zone and cross the zone at an oblique angle without deviation from the regional trends. At sites 26 and 27, subvertical fractures strike dominantly to the north-northwest, also at high angles to granite/granodiorite contacts within the pluton to the northwest and granite/volcanic contacts to the southeast. These cases suggest that lithologic changes in and around the pluton may not strongly influence local fracture orientations.

The influence of simple faulting on local fracture orientations is displayed at site 34, situated between two northwest-trending faults which lie approximately 100 m apart. There, subvertical fractures strike dominantly east-northeast and are

parallel with short fracture lineaments extending between the faults. The mesoscopic fractures and short lineaments are likely part of an envelope of parasitic fractures or cross faults between the larger faults. At nearby sites 36 and 33, east-northeast fractures are only weakly to moderately developed, supporting the assertion that fracture orientations at site 34 are locally fault-controlled.

Influences of complex structural and lithologic changes at outcrop scale are shown by fracture data from site 13, where volcanic rocks contain structurally intercalated granitic and granodioritic rocks along a series of local high-angle faults. At site 13, fractures are random at the 5% significance level which likely reflects the lumping of fractures from a number of diverse small structural domains within the outcrop.

#### Fracture trace lengths and frequencies

Figure 2.5 shows contours of bulk fracture trace length determined from scanline survey data across the pluton. Bulk trace length is the average of all trace lengths measured along all scanlines at a particular survey site and is used here to infer regional variations in average mesoscopic fracture size. Trace lengths for individual fracture sets in the SCRV are described further below. The distribution functions of bulk trace length and bulk fracture frequency, as used here, are unknown. Average values for these terms are used here primarily to show relative differences across the northern part of the pluton. Contours on both Figures 2.5 and 2.6 were computer-generated with the SURFII graphics package, using a conventional approach involving the weighted average of control points to generate a contouring grid. Contours on Figures 2.5 and 2.6 which trend perpendicular to the north and east pluton contacts are artifacts of the contouring process caused by sparse data and are ignored.

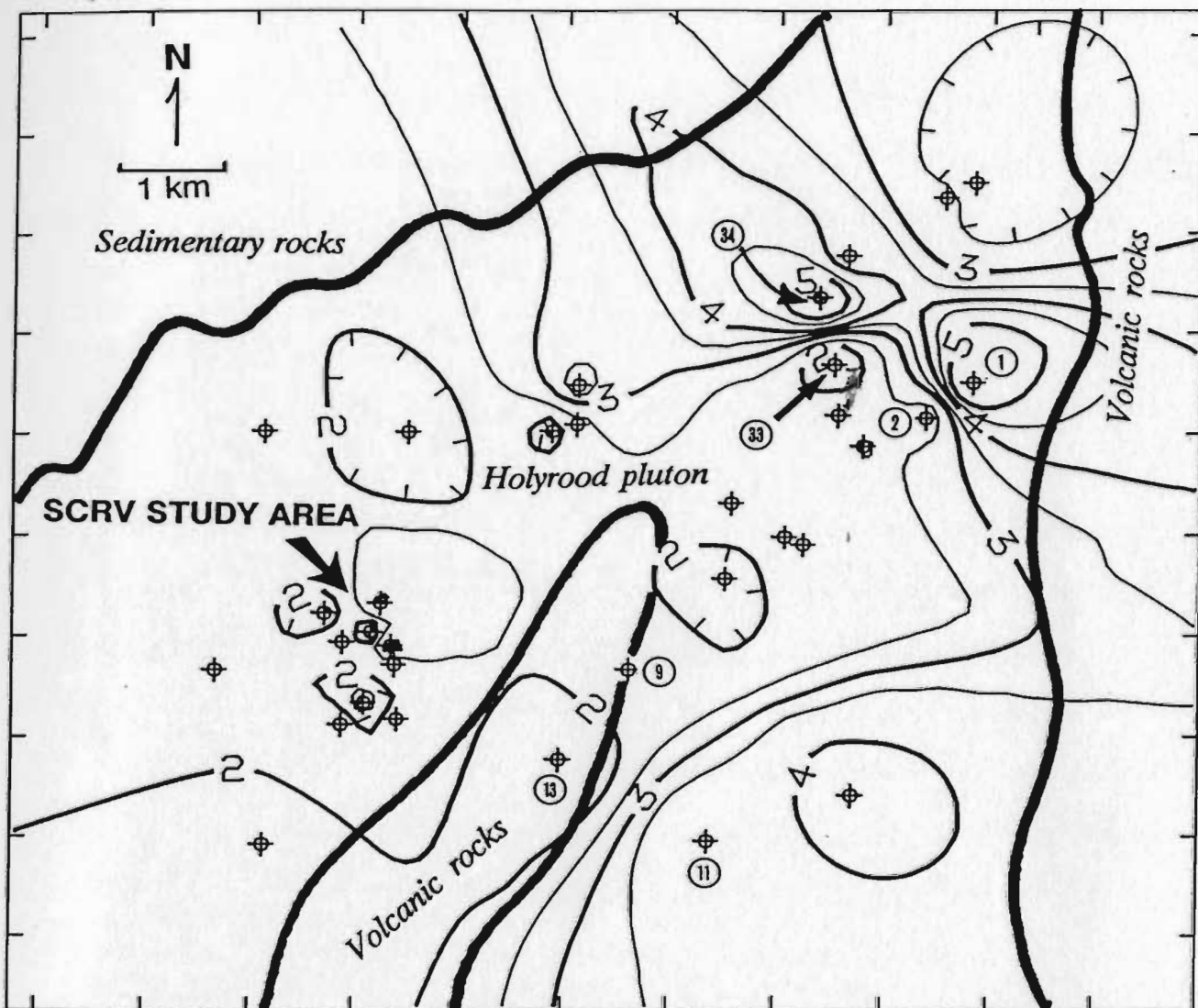


Figure 2.5 - Contour map of mean bulk trace length for all scanline survey sites across the pluton. Contour interval is 0.5 m. Sites labelled by circled numbers are referred to in text.

Bulk trace lengths in Figure 2.5 vary from 0.79 m (site 44) to 5.55 m (site 34), with an average for all sites of 2.57 m. The bulk trace lengths range consistently around 2-3 m in the western part of the study area, but are more variable to the east. For example, bulk trace length drops from over 5.5 m at site 34 to less than 1.8 m at site 33, less than 1 km away. Lack of pronounced lithologic changes between areas of abrupt bulk trace length variation in the eastern part of the pluton suggests that these variations are structurally controlled, possibly due to proximity of the Topsail Fault (Figure 2.1). By contrast, the contour pattern around sites 9, 11 and 13 in Figure 2.5 appears to be concordant with the pluton contact suggesting that trace lengths there may be controlled by lithologic changes in the granite (e.g. finer grain sizes) near the diffuse contact.

Figure 2.6 shows contours of bulk fracture frequency determined from scanline survey data across the pluton. Bulk fracture frequency was determined by dividing the total number of fractures measured at a particular site by the total scanline length, and it is used here to infer regional variations in average fracture density. This usage of bulk fracture frequency (and bulk trace length above) is similar to the approach used by Stone (1980) and Stone et al. (1984) to assess regional fracture characteristics in a granitic pluton. Fracture frequency for fracture sets in the SCRV are described in terms of spacing below.

Bulk fracture frequencies in Figure 2.6 range from 0.94/m (site 1) to 4.92/m (site 54), with an average for all sites of 2.21 fractures per meter. Bulk fracture frequency tends to vary inversely with bulk trace length across the pluton. This inverse relationship is expectable since where fracture density is high, fractures will tend to more commonly abut each other leading to shorter average trace lengths.



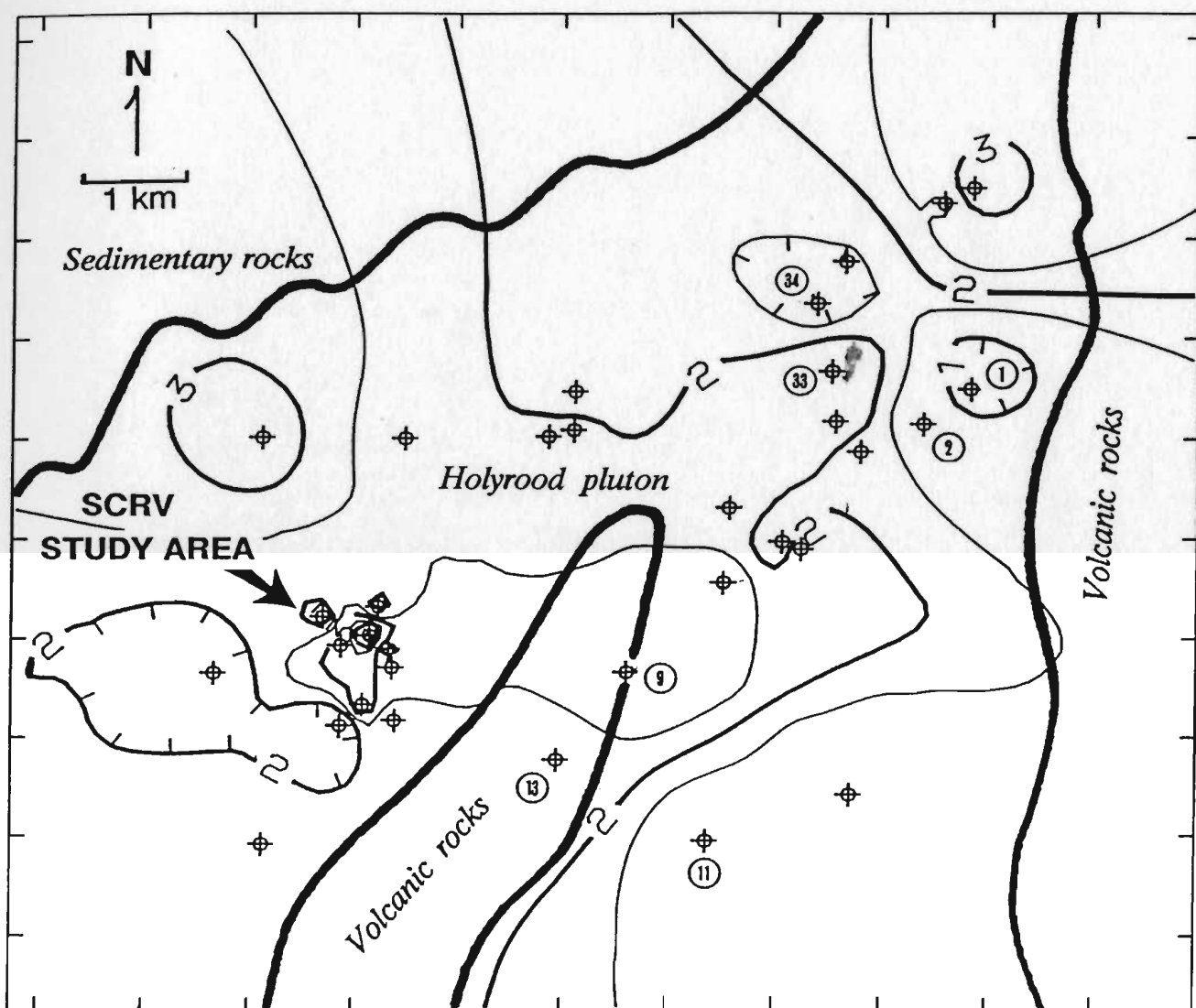


Figure 2.6 - Contour map of mean bulk fracture frequency for all scanline survey sites across the pluton. Contour interval is 0.5/m. Sites labelled by circled numbers are referred to in text.



### 2.2.3 Fracture geometry in the Seal Cove River valley

#### Macroscopic and mesoscopic fracture orientations

Figure 2.7 shows fracture orientations in the SCR V compiled from air photo, outcrop mapping and scanline survey data. The fracture system is dominated by subvertical strike-slip faults and large fractures striking mainly to the northeast ( $025^{\circ}$ ), east ( $105^{\circ}$ ) and southeast ( $155^{\circ}$ ) and which are traceable as air photo lineaments. Preferred azimuths for fracture lineaments in the SCR V (rose diagram in Figure 2.7; also subarea 16 in Figure 2.3b) are very similar to those for combined lineament data across the pluton (rose diagram in Figure 2.3b). Field evidence for both left-lateral and right-lateral senses of strike-slip fault motion includes common subhorizontal slickensides and polished fracture surfaces (both in outcrop and in core) and orientations of mesoscopic Riedel shear fractures. Riedel fracture sets, indicating left-lateral dominantly strike-slip displacement sense, were observed in the SCR V around north-trending macroscopic fractures in at least three locations. In addition, en echelon fracture patterns, "horse tail" feather fractures, and en passant transfer zones in outcrop all indicate that strike-slip motion is the characteristic displacement style for subvertical fractures in the SCR V.

Three subvertical fracture sets were defined with scanline fracture data in the SCR V using the cluster analysis techniques of Gillett (1987). With this approach, fracture pole clusters are defined by minimizing an objective function which depends on angular deviations of poles within clusters and of mean poles between clusters. Three to seven unimodal clusters were defined for data sets from each of the nine scanline survey sites around the SCR V, for a total of 30 clusters (Table 2.1). An eigenvalue ratio plot (after Woodcock and Naylor, 1983)

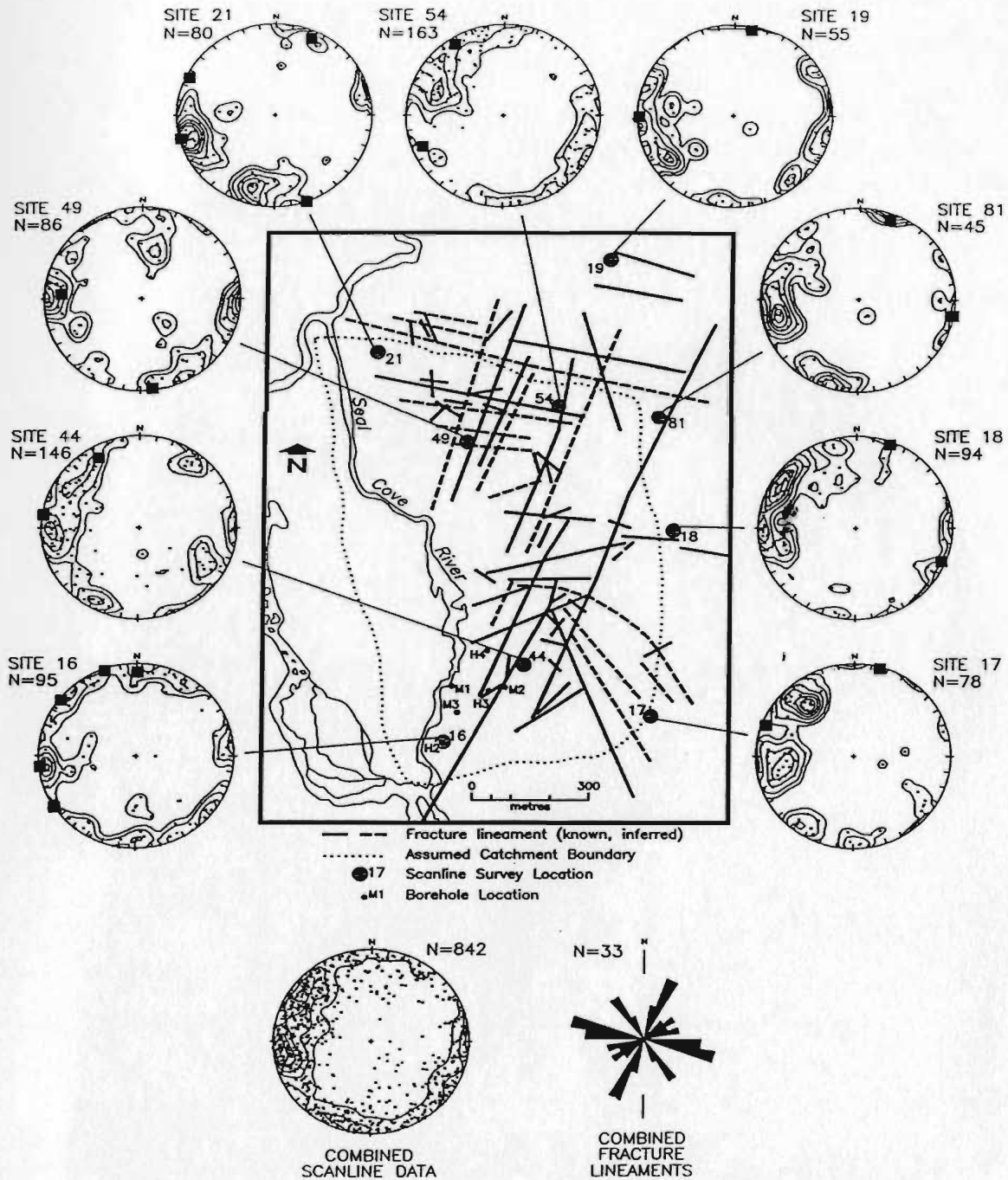


Figure 2.7 - Summary of fracture orientations in the Seal Cove River valley compiled from air photo, outcrop and scanline mapping data. Equal-area, lower hemisphere stereoplots of poles to scanline fractures were all constructed with the same contour function increments (0.1) using methods of Fisher et al. (1986); orientations of scanlines shown as solid square points on the plots.

Table 2.1 - Summary of results of cluster analysis of scanline fractures in the Seal Cove River valley. Mean trend and plunge refers to poles to fractures in the clusters.

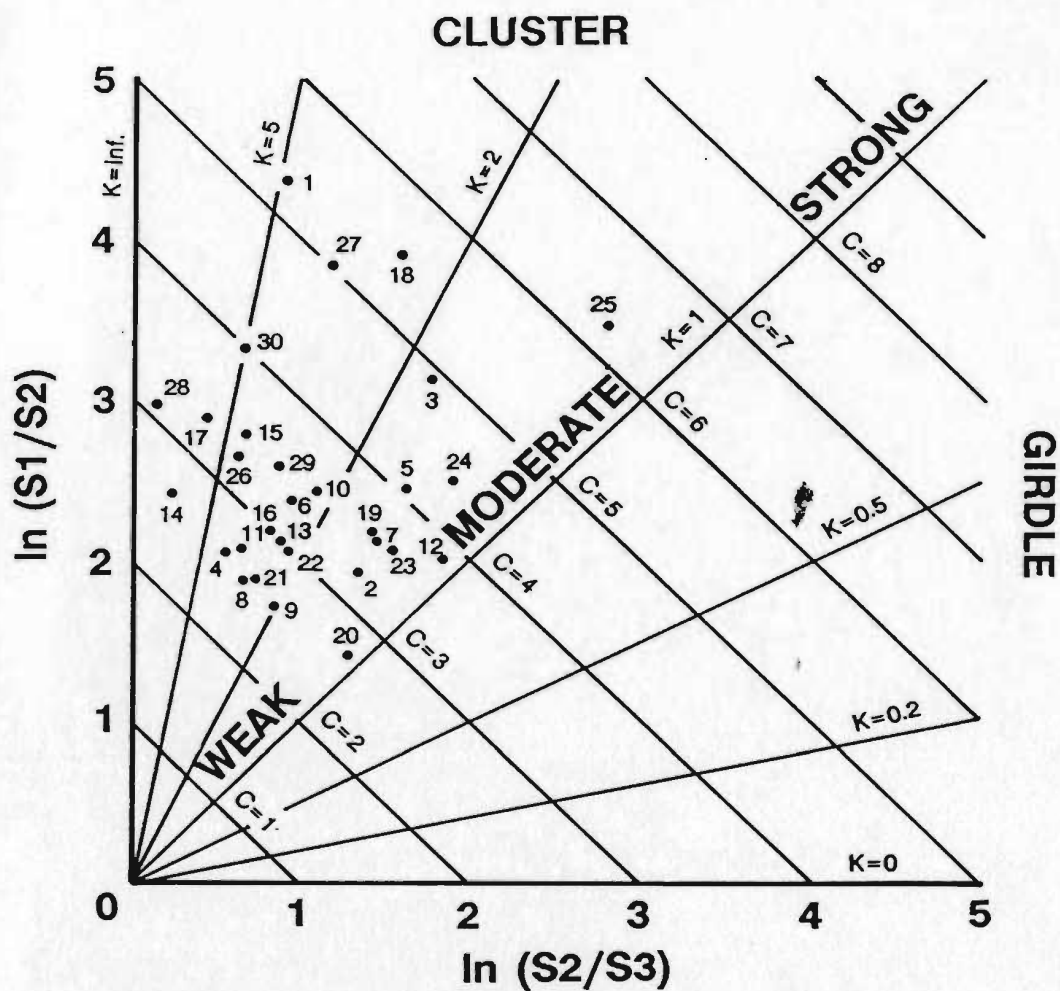
<u>Cluster</u> <u>number</u>	<u>Survey</u> <u>site</u>	<u>n</u>	<u>Mean</u> <u>trend</u>	<u>Mean</u> <u>plunge</u>	<u>Cluster</u> <u>number</u>	<u>Survey</u> <u>site</u>	<u>n</u>	<u>Mean</u> <u>trend</u>	<u>Mean</u> <u>plunge</u>
1	16	6	156	6	16	21	35	188	16
2	16	32	265	11	17	44	21	210	16
3	16	20	132	0	18	44	10	36	17
4	16	37	195	1	19	44	21	123	32
5	17	12	203	11	20	44	94	289	17
6	17	36	318	11	21	49	25	155	14
7	17	30	263	23	22	49	45	271	9
8	18	18	0	17	23	49	16	15	35
9	18	76	289	12	24	54	18	86	16
10	81	14	198	8	25	54	11	132	8
11	81	31	273	18	26	54	34	356	2
12	19	7	155	9	27	54	12	116	19
13	19	26	279	4	28	54	9	236	9
14	19	22	237	16	29	54	66	301	18
15	21	45	255	14	30	54	13	290	49

shows that these clusters are weak to moderately strong (Figure 2.8a). Figure 2.8b shows a stereoplot of the mean poles of all the clusters defined in the SCR.V. Fracture sets 1, 2 and 3 were visually assigned to groupings of these mean poles. Fractures in the clusters assigned to a particular set were then pooled for further statistical analysis. Six clusters (numbers 14, 18, 23, 24, 28 and 30) do not readily fit into these groupings. Of these, four clusters (18, 23, 28 and 30) are small ( $n = 6-16$ ) and the other two clusters (14 and 24) belong to separate survey sites. Hence, no one survey site has fractures which differ systematically and in large numbers from the overall pattern in the SCR.V.

The mean poles for combined fractures in sets 1, 2 and 3 have trends and plunges of 273/14 (set 1), 193/5 (set 2) and 126/10 (set 3). Comparison of stereoplot contour patterns and modal concentrations for survey sites around the SCR.V (Figure 2.7) shows that all three subvertical fracture sets occur throughout the study area, with variation in the relative dominance of sets but only minor variation in set orientations. In addition, the mean set orientations correspond with preferred fracture lineament azimuths in the SCR.V (Figure 2.7) and with the regional combined mesoscopic (Figure 2.4) and combined macroscopic (Figure 2.3b) fracture patterns. These similarities are used to infer that there has been no obvious reorientation of the fracture system in the SCR.V (e.g. due to folding or fault reactivation) compared with the regional fracture system. The significance of local and regional similarities in fracture geometry is further discussed below.

Figure 2.9 shows stereoplots of subsurface fracture orientations for boreholes 112 and 114, with data subdivided in 10 m increments. Collar locations for all SCR.V boreholes are shown in Figure 2.7; borehole orientations and depths are summarized in Appendix G (Table G1). Subvertical fracture orientations in

# EIGENVALUE RATIO GRAPH



Strength factor  $C = \ln(S1/S3)$

Shape factor  $K = [\ln(S1/S2)]/[\ln(S2/S3)]$

Figure 2.8 - (a) Eigenvalue ratio graph (after Woodcock and Naylor, 1983) for fracture pole clusters determined from scanline data in the Seal Cover River valley. S1, S2 and S3 refer to eigenvalues for mean pole of each cluster.

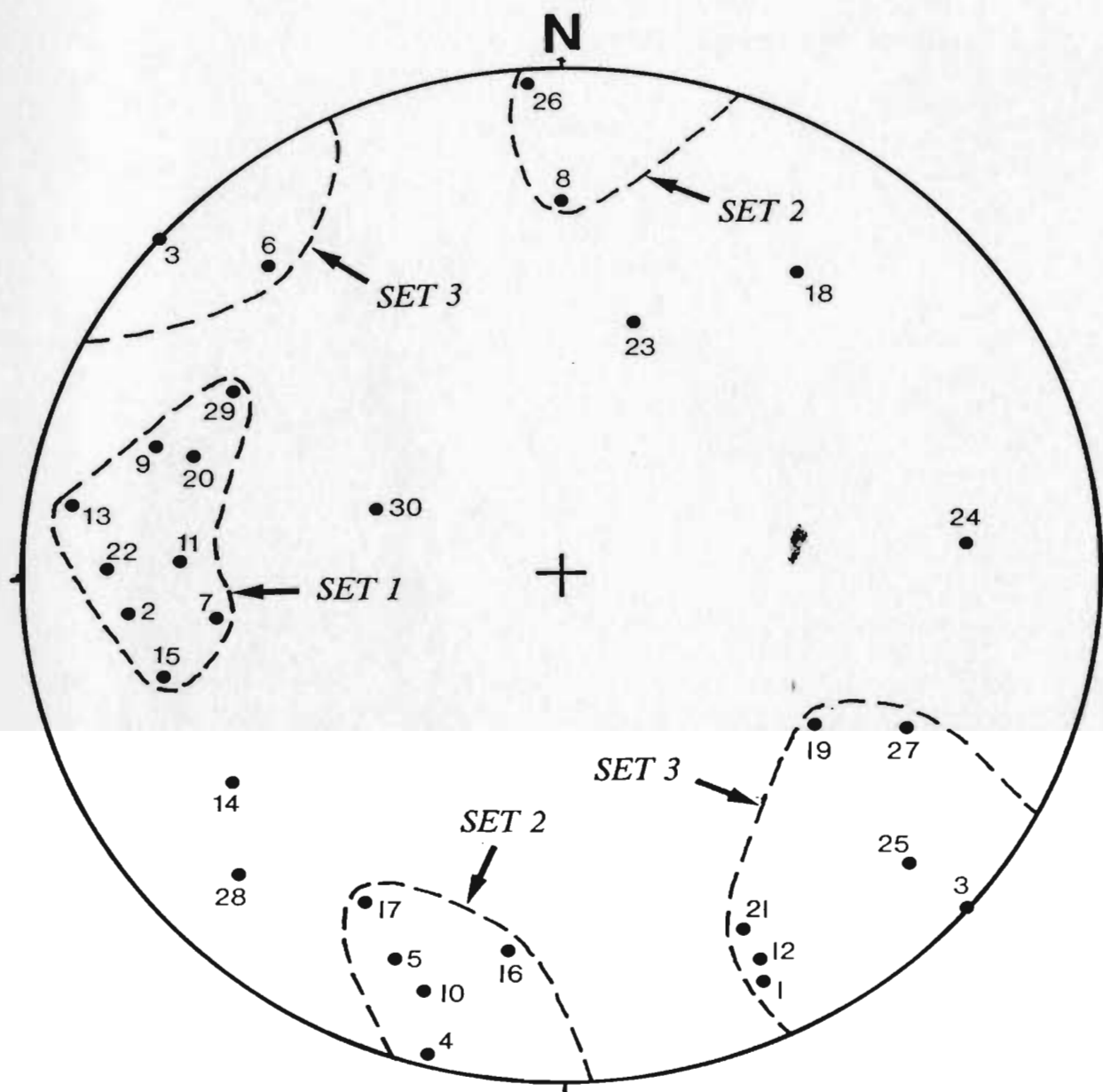


Figure 2.8 - (b) Equal-angle, lower hemisphere stereoplot of the mean poles of clusters determined for scanline data in the Seal Cove River valley. Fracture sets assigned based on groupings of mean poles as described in text.

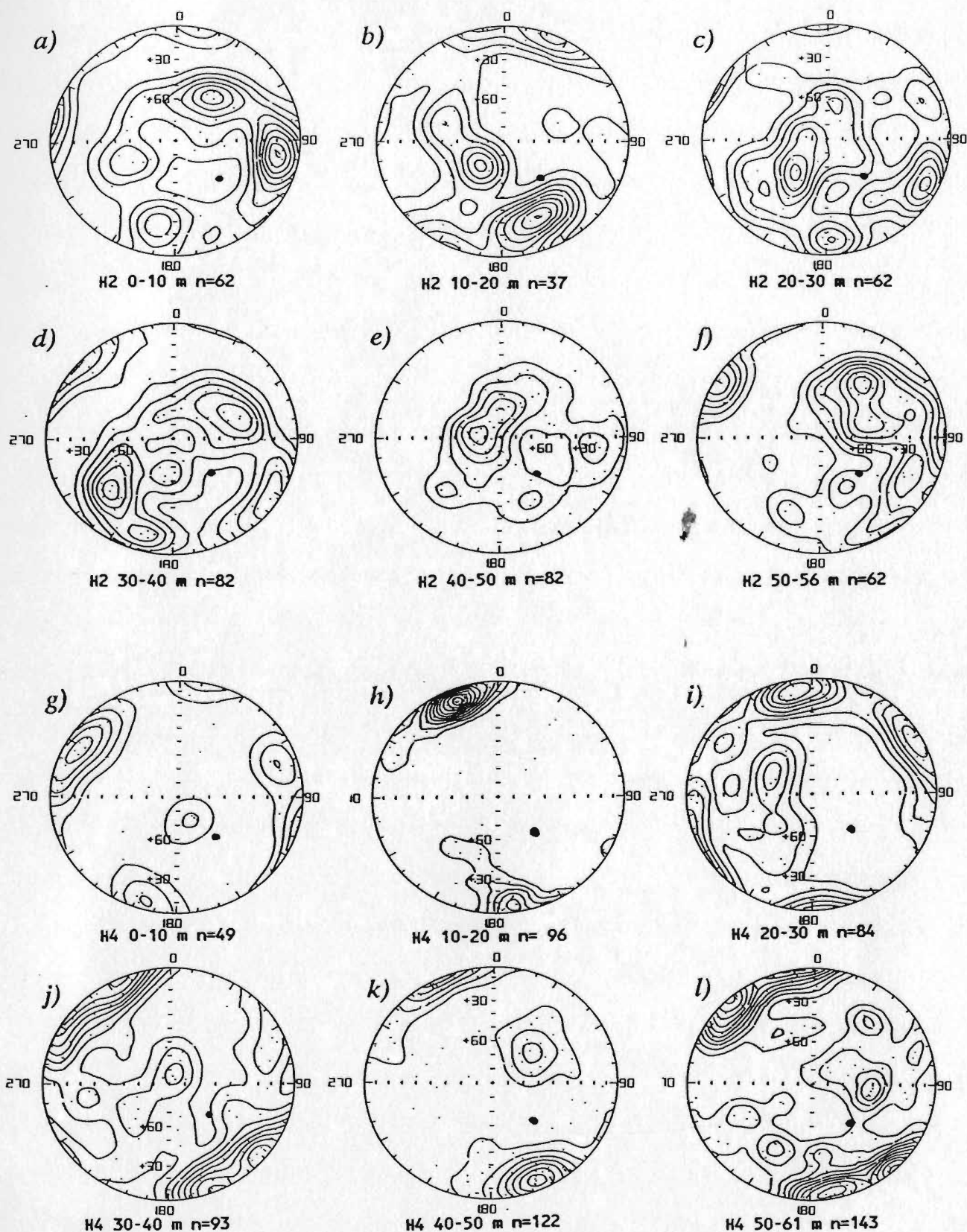


Figure 2.9 - Equal-area, lower hemisphere stereoplots of fracture poles for successive ten meter segments in borehole H2 (a-f) and borehole H4 (g-l) in the Seal Cove River valley. Plunge and trend of the boreholes indicated by bold points on the plots.

H2 (Figure 2.9 a-f) are generally consistent in the upper 40 m and below 50 m, with stereonet modes in the south and east-southeast quadrants corresponding with sets 2 and 3. In H4 (Figure 2.9 g-l), northeasterly-striking subvertical fractures corresponding with set 3 dominate throughout the hole, while fractures corresponding with set 1 are conspicuous only between 20-30 m depth (Figure 2.9i). In general, Figure 2.9 indicates the subvertical fractures can be reasonably assigned to fracture sets defined using surface scanline data and tend to display consistent orientations to depths of over 60 m, although there is variation in the relative dominance of sets within and between holes similar to the areal variation of fracture orientations between scanline sites. Subhorizontal fractures occur in nearly all levels of H2 and H4, and dominate at 40-50 m depth in H2 (Figure 2.9e). These subhorizontal fractures match field observations of sparse sheeting joints on the hillside in the SCRV, and collectively the subhorizontal fractures are considered to form a fourth fracture set with an approximately vertical mean pole. A more precise mean orientation is not determinable here due to the uncertainties in core fracture orientations and lack of statistically valid sampling of subhorizontal fractures by scanline methods (mentioned above).

Relative ages for subvertical fracture sets in the SCRV can be inferred by associations of fracture orientations with termination style. Termination style refers to the manner in which a fracture ends (depicted schematically in Figures 2.10 a-d), i.e. both ends free; both ends abutting other fractures at high angles (H-junction); one end abutting another fracture at a high angle (T-junction); or one end meeting another fracture at a low angle (splay). Figure 2.10b shows that fractures showing T-junction terminations most commonly occur in set 1. Assuming that younger fractures abut older (pre-existing) fractures, this infers that set 1 abuts and is relatively younger than set 2 or set 3. However, H-junction



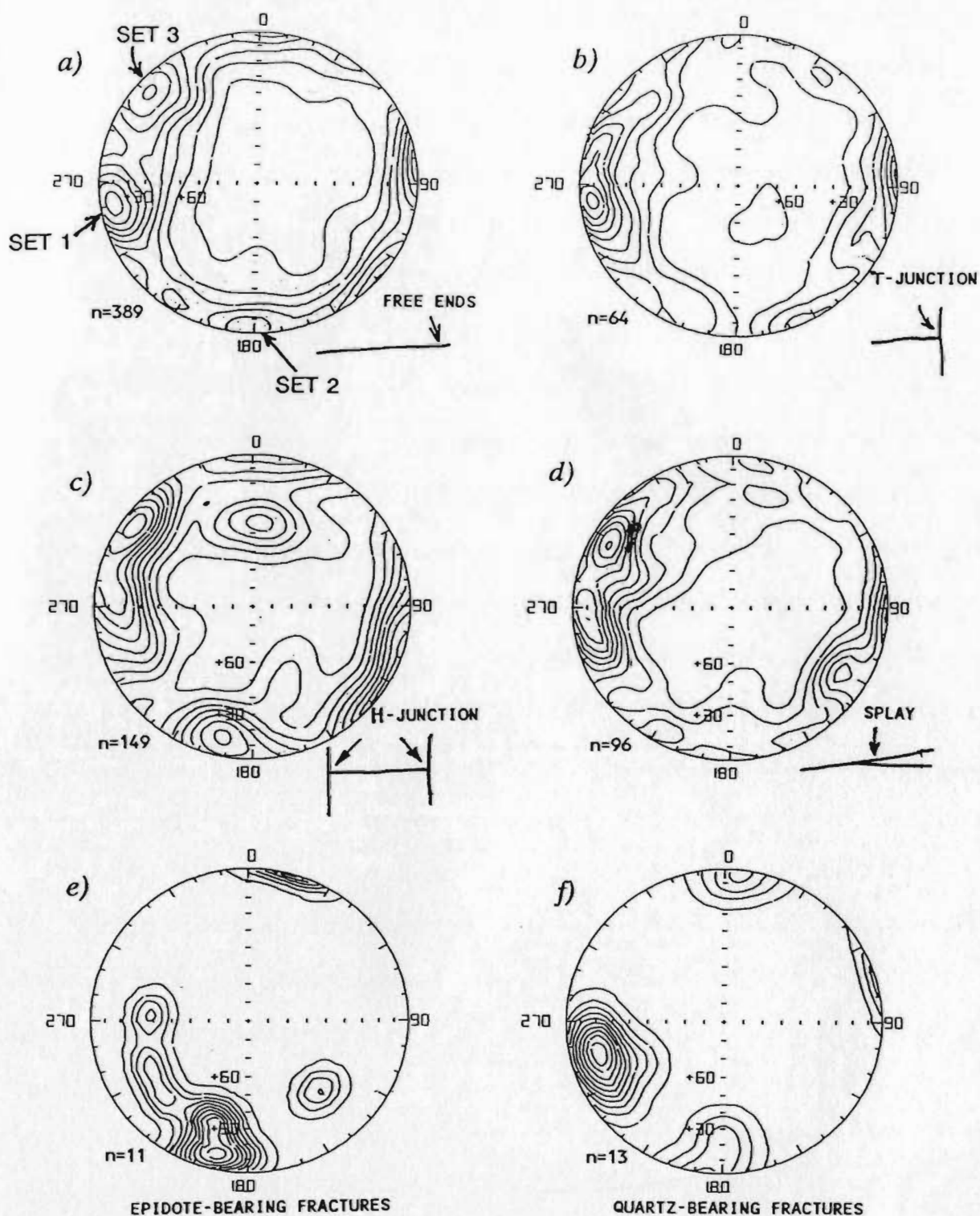


Figure 2.10 - Equal-area, lower hemisphere stereoplots showing associations of fracture orientations with fracture termination style (a-d) and mineral infilling (e-f) for scanline data in the Seal Cove River valley.

terminations (Figure 2.10c) are shown by fractures in sets 1, 2 and 3, inferring that subvertical fractures in the SCR/V underwent essentially coeval formation, abutting each other during progressive propagation. This is consistent with the generally coeval age relations shown by subvertical tectonic fractures throughout the pluton (discussed below).

Kamineni et al. (1980) and Stone et al. (1984) have used fracture infilling mineralogy in granitic rocks to distinguish fractures formed early in the cooling history of a pluton, which contain high-temperature minerals such as epidote, quartz or chlorite, from later-formed fractures containing only lower-temperature minerals such as clays, gypsum or iron oxides. Figures 2.10e and 2.10f shows that epidote and quartz tend to occur preferentially in fractures assignable to sets 2 and 1, respectively, suggesting that these sets may have formed earlier than set 3. However, the data in these two figures represent a very small proportion ( $< 2\%$ ) of the total scanline data in the SCR/V, so this interpretation may be misleading. Hematite and chlorite are nearly ubiquitous filling minerals in sets 1, 2 and 3, supporting the interpretation based on termination style above that subvertical fractures formed coevally in the study area. It should be noted that clayey fault gouge or fracture infilling is rare within the SCR/V, both for surface and subsurface fractures (see Appendices B and C). Only one fault with clayey gouge was encountered (along borehole H13; Figure 2.7).

#### Fracture trace lengths

In order to analyze trace lengths statistically, it is important to address sampling biases which may be present, such as censoring bias, truncation bias and size bias (e.g. Baecher and Lanney, 1978; Rouleau, 1984). Censoring bias occurs where one or both ends of a trace are unexposed, leading to underestimation of

mean trace length. Truncation bias occurs where trace lengths less than a certain minimum measured length (here set to 0.5 m for expediency of field measurements) are ignored, leading to overestimation of mean trace length. Hence, truncation and censoring biases tend to offset each other. Trace length statistics presented below (Table 2.2) have been corrected for censoring and truncation bias following the methods of Rouleau and Gale (1985) and Baecher and Lanney (1978).

Size bias occurs where long fractures are preferentially exposed and intersected by scanlines (Priest and Hudson, 1981; Rouleau, 1984). The use of semi-trace lengths, i.e. those on only one side of a scanline, has been proposed to more accurately describe trace lengths where size bias is important (e.g. Cruden, 1977; Priest and Hudson, 1981). However, this approach assumes that semi-trace lengths of the same fracture on opposite sides of a scanline are independent of each other, which may not be physically reasonable, and requires a constant censoring point, i.e. always at the same length value, which is not applicable to irregularly shaped outcrops. In addition, it is unclear what effect the use of semi-traces has on censoring and truncation corrections. Finally, at all outcrops in the SCR V area, small fractures far outnumber major fractures suggesting that size bias is probably not severe. For these reasons, and since there is no simple method to account simultaneously for progressive censoring, truncation and size biases in exponential or log-normal trace length distributions (Rouleau, 1984), no correction for trace length size bias has been made in this study.

Figure 2.11 shows histograms of fracture trace lengths in the SCR V area, compiled using pooled scanline data from all scanline sites (Figure 2.7). Results were subdivided by subvertical fracture set and level of censoring (i.e. whether

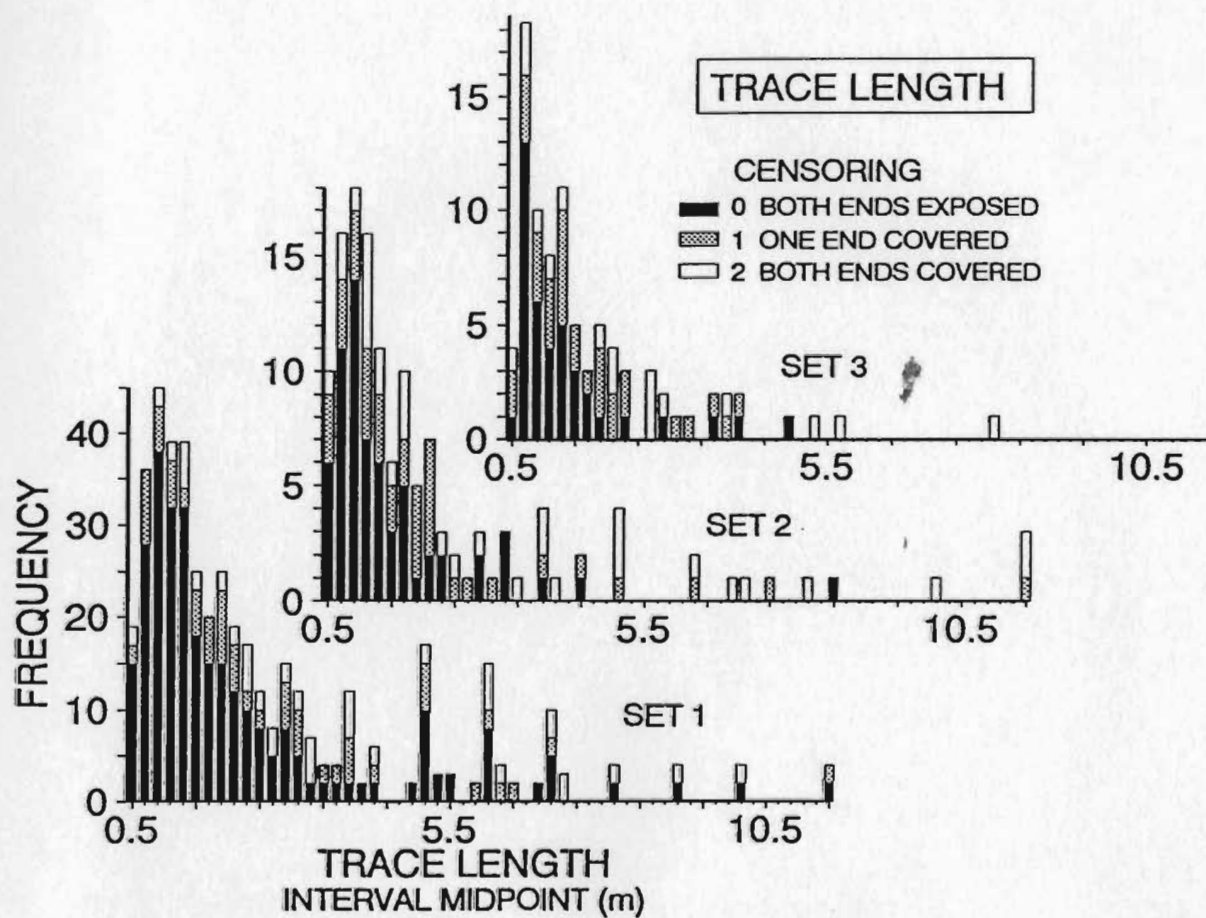


Figure 2.11 - Trace length histograms for scanline data in the Seal Cove River valley subdivided by fracture set and level of censoring.

Table 2.2 - Descriptive statistics of the distributions of trace length for each fracture set from combined scanline data in the Seal Cove River valley.

STATISTICS	SET 1	SET 2	SET 3
Total no. obs.	366	135	88
Mean (m)	2.30	2.27	1.71
St. dev. (m)	2.04	2.67	1.36
Maximum (m)	14.5	20.0	8.0
Sum length (m)	842.4	306.3	150.7
No. obs. with censoring = 0	277	65	40

#### ESTIMATES OF BIAS-CORRECTED PARAMETERS

##### Exponential model<sup>1</sup>

Mean (m)	2.54	4.21	3.27
----------	------	------	------

##### Log-normal model<sup>2,3</sup>

Mean (LN)	0.534	0.430	0.295
St. dev. (LN)	0.752	0.815	0.676
Mean (m)	2.26	2.14	1.69
St. dev. (m)	1.97	2.08	1.29

---

<sup>1</sup> For exponential model, mean is equal to standard deviation.

<sup>2</sup> For log-normal model, mean (LN) and st. dev. (LN) are of log-transformed trace lengths.

<sup>3</sup> Mean (m) and st. dev. (m) for log-normal model were calculated for original distribution from (LN) values using methods described by Rouleau (1984).

one, both or no trace ends are exposed). The left-skewed histogram shapes suggest that exponential or log-normal models can be fitted to the trace length distributions. Table 2.2 shows that for each fracture set the arithmetic mean is approximately equal to the mean estimated for a log-normal distribution, while the mean estimated for an exponential distribution is markedly greater. In addition, the tendency in this case for set 1 to have the largest mean value and set 3 the smallest is not shown by the exponential means. These differences are attributed to a poor fit of the data with an exponential model, although no goodness-of-fit tests have been done. Log-normal trace length distributions have been previously reported for line-sampled fractures (e.g. Priest and Hudson, 1981; Warburton, 1980a, 1980b), and the likelihood of similar distributions for trace lengths here suggest that subvertical fractures in the SCRV follow geometric patterns typically observed in granite rock masses.

Trace length statistics were indeterminate for subhorizontal fractures in the SCRV due to inadequacies in sampling (mentioned above). In another study of fracture geometry in granitic rock (Rouleau and Gale, 1985), trace lengths for well-exposed subhorizontal fractures (mapped on drift walls underground) had similar statistical characteristics as subvertical fractures. However, lacking further data, the statistical characteristics and distribution of subhorizontal fractures in the SCRV remains unknown.

In an effort to determine areal variations in average fracture length around the SCRV, mean trace lengths for each subvertical set at each survey site were plotted (Figure 2.12). Figures 2.12 and 2.13 were computer-generated in similar fashion as Figures 2.5 and 2.6 above. Due to the small number of control points (9), these maps are considered to provide only general indications of areal variation in fracture size. Figure 2.12 shows that trace lengths vary smoothly

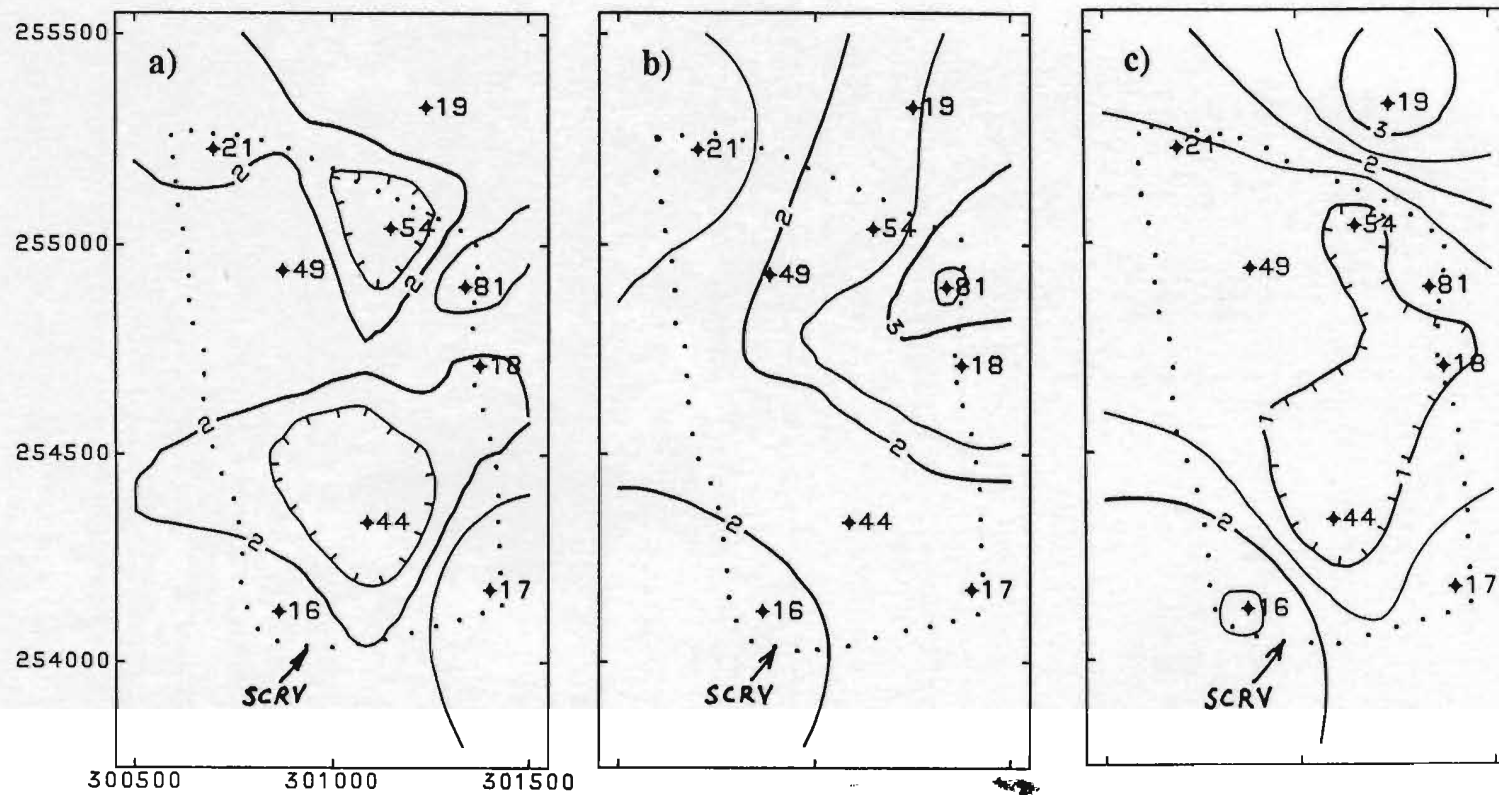


Figure 2.12 - Contour maps of mean trace lengths at scanline survey sites in the Seal Cove River valley, for fracture set 1 (a); set 2 (b); and set 3 (c). Contour interval is 0.5 m. Grid numbers refer to UTM coordinates.

across the SCR.V, with different contour patterns for each set. Mean trace lengths range from 1.12-2.83 m (set 1), 1.43-2.56 m (set 2) and 0.76-2.53 m (set 3), with standard deviations of 1.5-1.6 m for all points (values for site 81 (Figure 2.12b) and site 19 (Figure 2.12c) discounted due to small numbers of data). Hence, the areal variation of mean trace length values for a given set and between sets falls within two standard deviations of the mean trace length value at any given site. This suggests that trace length variations across the SCR.V, both within and between subvertical fracture sets, are not significant.

#### Fracture spacings

As a measure of fracture abundance within the SCR.V, fracture spacing was determined from scanline data using the relation  $S = d \cos\theta$ , where  $S$  is fracture spacing between adjacent members of a fracture set,  $d$  is the distance along a sampling line between adjacent fractures in a given set and  $\theta$  is the angle between the sample line and the mean pole of the set (after Kiraly, 1970; ISRM, 1978). Scanline rather than core fracture data were used to compute spacings because scanline survey sites were more widely distributed around the SCR.V than the boreholes, so that scanline data better represent areal variations in fracture abundance, and because the available borehole fracture data were considered too incomplete and imprecise for calculation of meaningful spacing values.

It is recognized that spacings determined from scanline data are biased to some degree since fractures shorter than the minimum measured trace length (0.5 m here) are not included in spacing calculations. However, the consistency of fracture orientations and mean trace lengths between the survey sites suggests that this spacing bias may be approximately uniform across the study area. Hence, scanline data in this study are used to indicate relative variations in spacing



characteristics within the SCR.V.

Figure 2.13 shows histograms of fracture spacings in the SCR.V area, compiled using pooled scanline data from all scanline sites (Figure 2.7) and subdivided by fracture set. Table 2.3 shows descriptive statistics for these spacing data and parameters for exponential, Weibull and log-normal theoretical models of the empirical distributions. Kolmogorov-Smirnov D statistics (Table 2.3), determined following the methods of Rouleau (1984), indicate that 1) an exponential model fits sets 1 and 2 well, but does not fit set 3 at all, 2) a Weibull model fits the data moderately well, with levels of significance around 0.05 or above, but 3) a log-normal model best fits the spacing data from all sets, with levels of significance greater than 0.20. Log-normal spacing distributions in fractured granite has been reported by others (e.g. Rouleau and Gale, 1985), although exponential distributions have been most commonly reported for fracture spacings (e.g. Mahtab et al., 1973; Priest and Hudson, 1976; Wallis and King, 1980; and others). This variability tends to support the assertion of Priest and Hudson (1981) that parent distributions may vary with different rock types and geologic settings.

As with trace length, spacing statistics were indeterminate for available data on subhorizontal fractures in the SCR.V. Direct observations at vertical exposures indicate that spacings of subhorizontal fractures in the SCR.V range from 0.1-3 m, with an approximate mean spacing of 0.5 m.

Relative areal variations in fracture abundance across the SCR.V were investigated by contouring values of mean spacing for each set at each survey site (Figure 2.14). The contour patterns in Figure 2.14 vary smoothly across the study

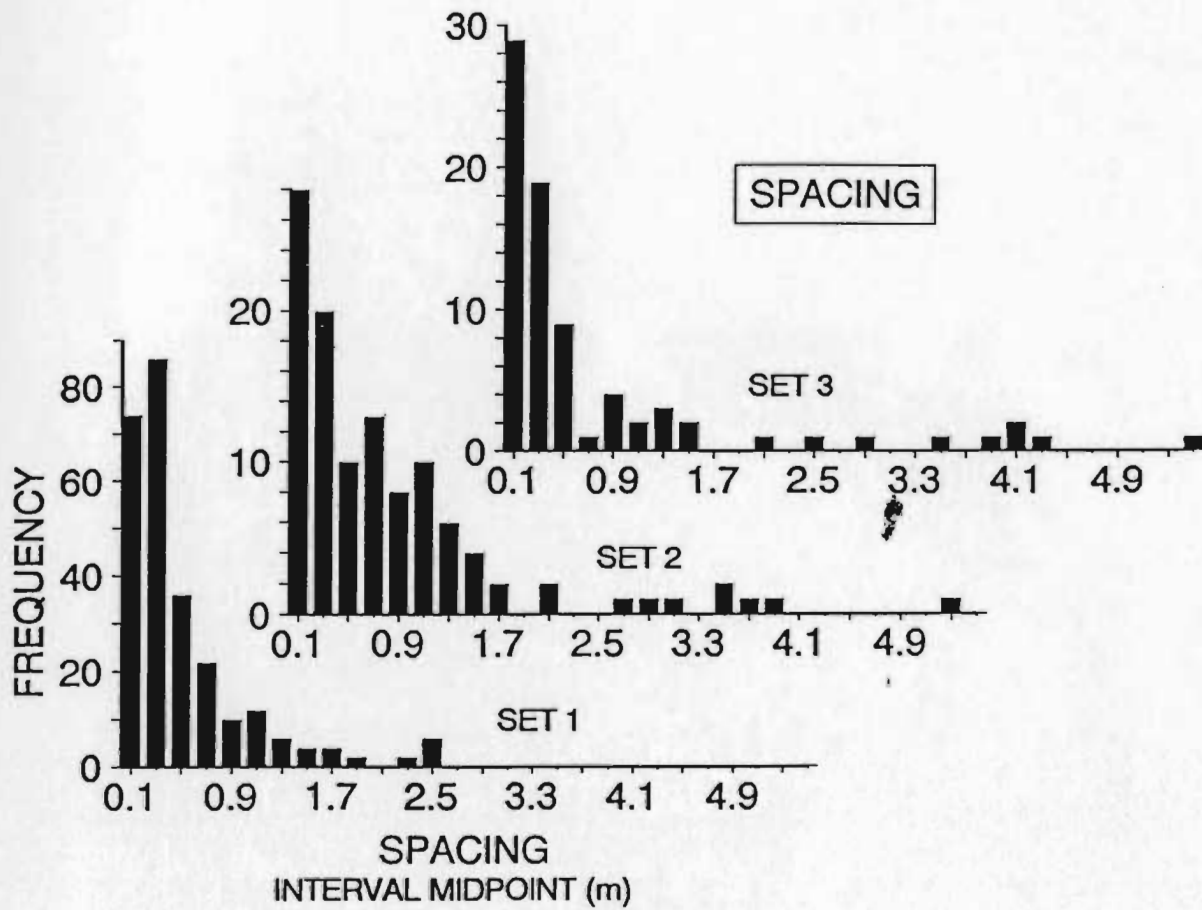


Figure 2.13 - Frequency histograms for spacings between consecutive fractures of the same fracture set, determined from scanline data in the Seal Cove River valley.

Table 2.3 - Descriptive statistics of the distributions of spacing (SPAC) and log-spacing (LSPAC) for each fracture set from combined scanline data in the Seal Cove River valley

STATISTICS	Set 1		Set 2		Set 3	
	SPAC	LSPAC	SPAC	LSPAC	SPAC	LSPAC
Total No. Obs.	256	256	111	111	74	74
Mean (m)	0.48	-1.17	0.82	-0.77	0.82	-0.91
St. dev. (m)	0.49	0.96	0.92	1.15	1.17	1.14
Maximum (m)	2.58	0.95	5.30	1.67	5.43	1.69
Minimum (m)	0.01	-4.65	0.01	-4.61	0.03	-3.51
Skewness	2.34	-0.36	2.35	-0.43	2.27	0.57
Weibull						
Shape (c)	1.114		0.975		0.833	
Scale (b)	0.498		0.808		0.730	
<hr/>						
D-statistic and [P(>D)]*						
exponential	0.0609		0.0712		0.2200	
	[>.20]		[>.20]		[<.01]	
normal		0.0214		0.0400		0.1051
		[>.20]		[>.20]		[>.20]
Weibull	0.0762		0.0529		0.1415	
	[.10]		[>.20]		[>.05]	

\*Results (significance level) of the Kolmogorov-Smirnov goodness-of-fit test for the exponential, log-normal and Weibull models

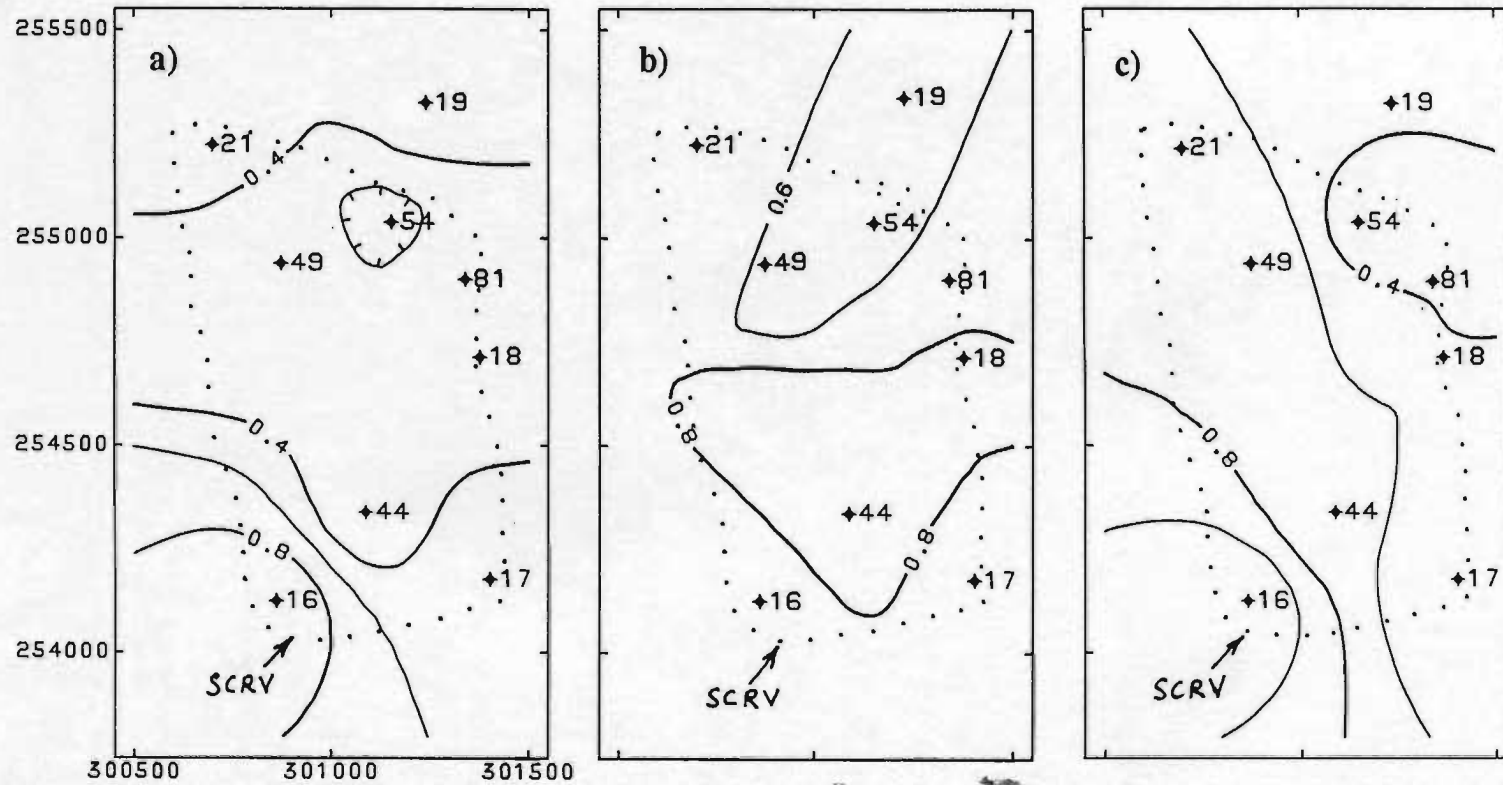


Figure 2.14 - Contour maps of mean spacing at scanline survey sites in the Seal Cove River valley, for fracture set 1 (a); set 2 (b); and set 3 (c). Contour interval is 0.2 m. Grid numbers refer to UTM coordinates.

area, with different patterns for each fracture set. However, as in Figure 2.13, the range of mean spacing values within a given set falls within two standard deviations of the mean spacing value at any control point. Based on these data, there appears to be no significant variation of mean spacing for a given set across the SCR.V.

## **2.3 Discussion**

### **2.3.1 Brittle deformation history of the Holyrood pluton**

To meaningfully interpret the fracture geometry for the pluton described above and to infer hydrogeological characteristics for the rock mass in and around the SCR.V, it is useful to describe the brittle deformation history for the northern part of the Holyrood pluton. This deformation history is described here in terms of 1) the evolution of the major faults bounding the pluton, 2) tectonic fracturing after pluton emplacement, and 3) post-tectonic effects of uplift, erosion and glaciation. Structures which are unlikely to significantly affect fluid flow within the fractured granite, such as localized ductile deformation within mafic inclusions or healed autobrecciation in the granite, are not considered.

The principal faults in the region, the Topsail and Duffs/Holyrood Faults (Figure 2.1), are interpreted to bound the northern part of the Holyrood pluton (King, 1988) and likely originated prior to intrusion of the granite. These findings are suggested by sedimentological differences in pre-granitic rocks east and west of the pluton, which infer a faulted upland sediment source, and also by the likelihood that the faults acted as feeder conduits for the pluton (A.F. King, pers. commun.). Post-intrusion reactivation of these major faults is indicated by

offsets outlined by the regional distribution of granite bodies and by the displacement of sedimentary rocks younger than the pluton in areas south of the study area (King, 1988). The offset of Cambrian sedimentary rocks by the Topsail Fault (Figure 2.1) also indicates a post-lowermost Palaeozoic fault movement. This reactivation is significant in that it is interpreted to have controlled the development of the regional tectonic fracture system within the pluton, as described below.

Tectonic fracture development within the Holyrood pluton can be related to the accretion of rocks in eastern Newfoundland onto the Appalachian Orogen by left-lateral strike-slip motion during the Siluro-Devonian Acadian Orogeny (Kent and Opdyke, 1978). Northwest-directed compressional stresses associated with this event (King, 1982) are interpreted to have generated regional northeast-trending folding in the Avalon Zone (e.g. Williams and Bursnall, 1988). These stresses, acting obliquely on the pre-existing, north-trending boundary faults, are interpreted here to have induced a regional, left-lateral shear couple within the Holyrood pluton, leading to development of the tectonic fracture system.

Evidence for this is shown in Figure 2.15 which summarizes the principal orientations, senses of motion and relative ages for fractures and faults across the pluton. These fractures can be interpreted as a system of Riedel and secondary P-shear fractures formed in response to left-lateral, bulk simple shear within the pluton. Supporting this model, mesoscopic Riedel shear fractures were directly observed adjacent to north-trending, left-lateral strike-slip faults in the SCRV. Kinematic relationships for this deformation model are shown in Figure 2.15 (inset) and have been described for other rock types and supported by clay model studies (e.g. Tchalencho, 1968; Harris and Cobbold, 1984). Minor differences

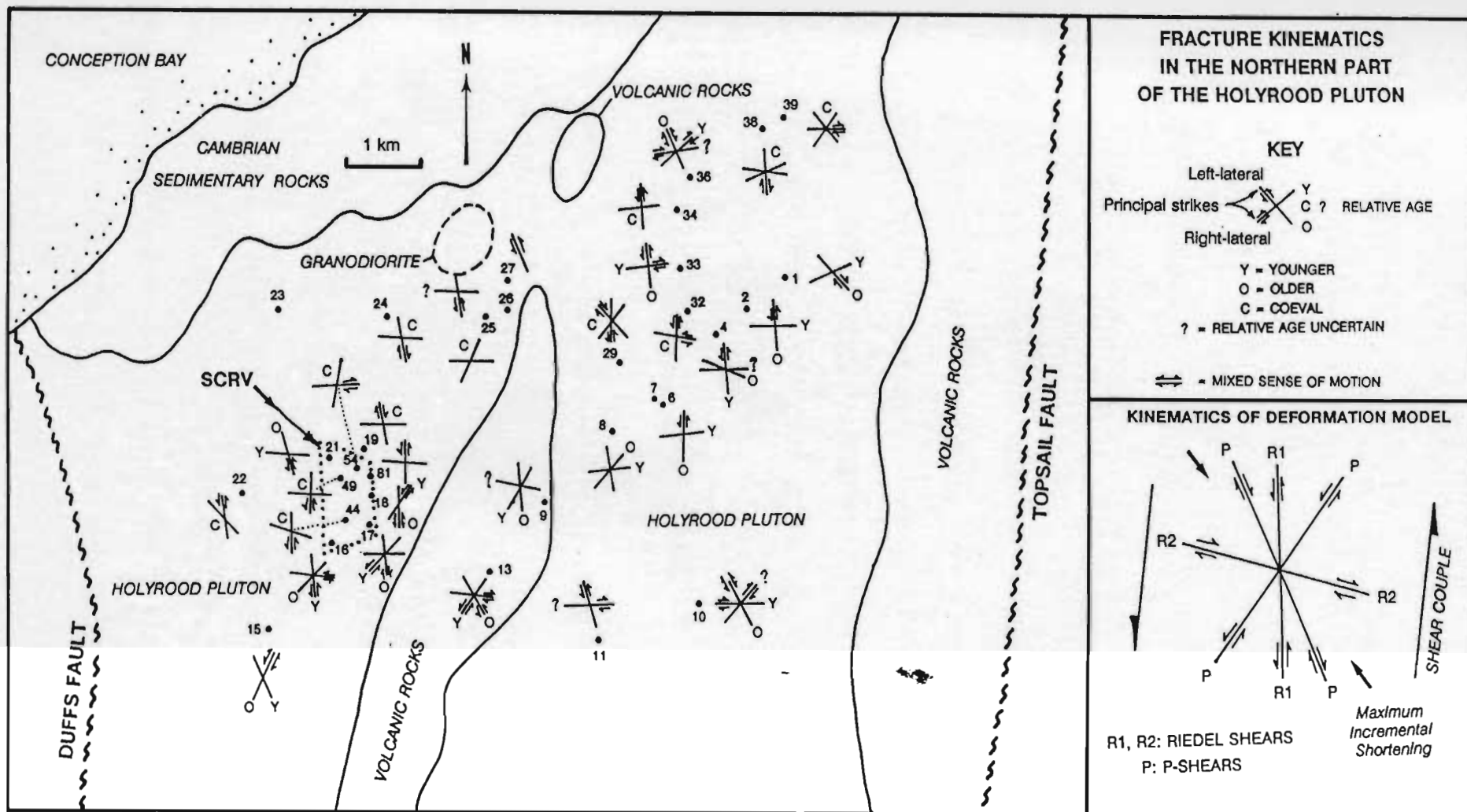


Figure 2.15 - Senses of motion and relative age relationships for fractures across the northern part of the Holyrood pluton, compiled from air photo, outcrop mapping and scanline survey data. Kinematics of the regional left-lateral shear deformation model are shown in the inset.

which exist between the actual and expected fracture orientations (e.g. the presence of east-northeast-striking fractures at sites 1, 33, 34 and 36; Figure 2.15) can be attributed to local deviations in the stress field or to rotation of early-formed fractures during progressive shearing.

Fracture age relationships (Figure 2.15), compiled assuming that younger about older fractures, indicate no consistent sequence of tectonic fracture formation within the pluton, even though clay model studies (Tchalencho, 1968) suggest that Riedel fractures tend to form prior to P-shear fractures. Field evidence suggests that the many subvertical shear fractures in the pluton are coeval, with fractures of diverse strikes commonly crossing each other within the same outcrop. This coeval nature is consistent with inferences from observations of termination style and fracture infilling mineralogy, described above. Taken together, these indicators suggest that shear fractures in the Holyrood pluton are genetically related, formed as part of a single progressive deformation event.

Post-tectonic sheeting fractures in the pluton (including the subhorizontal fractures in the SCR/V) are attributed to release of vertical stress during uplift and erosion (described, for example, by Jahns (1943) and Johnson (1970)), probably enhanced by cycles of loading and unloading due to glaciation. An alternative hypothesis is that some of these fractures may have formed parallel to the roof of the pluton during emplacement (described, for example, by Balk, 1937). However, this interpretation is unlikely here since the subhorizontal fractures are almost always dilational, commonly open (at surface exposures), totally devoid of high-temperature minerals (e.g. epidote and vein quartz), and show no sign of having undergone the tectonic shear event interpreted to have generated the subvertical fracture system in the pluton.



### 2.3.2 Influences on variability of fracture geometry within the pluton

Understanding the dominant influences on the variability of fracture geometry within the northern part of the Holyrood pluton serves 1) to further define the structural setting of the SCR, i.e. whether it is concordant with regional trends or anomalous within the pluton, and 2) to link key features of the brittle deformation history with inferences of current hydrogeological properties of the granite in the SCR. Assessment of such influences is constrained in this study by the density and distribution of fracture survey points, which is in turn controlled by the extent of exposure. For example, detailed transects across pluton contacts or major boundary faults were not possible. In addition, the area of most dense control (i.e. the SCR) is underlain by homogeneous granitic rock and is distant from the major boundary faults, so is not well situated for investigating lithological or structural controls on fracture geometry in the pluton.

However, within these constraints and in the context of the deformation history described above, it is still possible to make the following main points regarding variability of fracture geometry in the study region:

- 1) The lack of major lineaments over 2 km long and the general consistency of fracture orientations at macro- and mesoscopic scales within the northern part of the Holyrood pluton suggests that the pluton deformed as a contiguous rigid body within a regional stress regime, without developing major contrasting fracture domains. The lack of conspicuous, systematic shifts in regional fracture orientations on either side of the narrow belt of volcanic rocks east of the SCR (Figure 2.4) further indicates that any possible warping of the pluton is either very mild or occurred prior to tectonic fracturing.

- 2) Limited field evidence, coupled with the deformation model proposed above, infers that deviations of fracture orientations from regional trends tend to be localized (i.e. at scales of tens of meters) and principally controlled by the presence of macroscopic faults. However, it is difficult to distinguish structural from lithologic controls on fracture orientations in the northern part of the Holyrood pluton due to the dominant northerly trends of both faults and lithologic contacts in this region.
- 3) The fracture system in the SCR.V appears to be concordant with the regional deformation pattern, at least in the western portions of the pluton. The increased variability of bulk trace length and fracture frequency toward the eastern side of the pluton (Figures 2.5 and 2.6) indicates greater structural complexity there than in the area immediately around the SCR.V. As speculation, this greater variability to the east may be due to irregular thickness of the pluton there, leading to variations in fracture sizes and abundances due to local stress concentrations during deformation.
- 4) Due to limited, shallow subsurface fracture data in this study ( $\leq 60$  m depth, in the SCR.V only), it was not possible to correlate surface and deep subsurface fracture orientations to determine how the fracture system may vary with depth away from the pluton roof (now approximately at the erosion surface). However, the proposed model of regional strike-slip simple shear acting on the thin, tabular and generally lithologically homogeneous northern part of the Holyrood pluton infers that subvertical fracture orientations are likely to be consistent from surface to base of the pluton. The shortness of air photo fracture lineaments in the pluton (mean for all data of 177 m) suggests that these macroscopic subvertical fractures terminate within the pluton, without forming

major tectonic discontinuities (like the Topsail or Duffs Faults) within the pluton.

### 2.3.3 Principal hydrogeological implications

The observation that major faults, likely to fully penetrate the Holyrood pluton, are absent from the northern part of the intrusion implies that there are no direct, high-permeability hydrologic conduits from the surface to host rocks below the pluton. The relatively simple deformation history and fracture system in the pluton, compared with the multiply-deformed (and presumably more densely fractured) heterogeneous volcanic host rocks of the Harbour Main Group, suggests that the Holyrood pluton may act as a semi-confining hydrostratigraphic unit within the regional groundwater flow regime.

In the SCR.V, the consistency of fracture orientations at different scales and from surface to depths of 60 m, and the lack of significant trace length and spacing variability between survey sites implies that fracture-controlled hydraulic rock mass properties (e.g. hydraulic conductivity) are likely to be developed in a uniform manner around the study area. Hence, for a first approximation, it is reasonable to extrapolate hydraulic properties, measured or determined at a few points, to areas throughout the remainder of the SCR.V. This is the approach taken in the numerical simulations of groundwater flow in the SCR.V (Chapter 5).

Within the SCR.V fracture system, dilational sheeting joints (commonly with open apertures at the surface) and subvertical macroscopic fractures and fracture zones (predominantly filled with brittle fault breccia) are likely to be the principal conduits for shallow groundwater flow (i.e. to depths in the range of tens to a few hundred meters). The fault along borehole H13, marked by a short (75

m) lineament (Figure 2.7) and filled with clayey gouge, may represent a local barrier to groundwater flow, although, as mentioned above, this fault is anomalous.

Finally, the lack of a statistical description of the subhorizontal fractures (set 4) and the bias present in spacings determined from scanline data in the SCR.V means that the present fracture data for the SCR.V are inadequate for determining directional permeability characteristics of the granite by, for example, calculating a three-dimensional permeability tensor (e.g. Snow, 1969) or using a fracture network approach (e.g. Gale and Rouleau, 1986). Because of these limitations, simpler approaches are necessary for determining directional permeability for purposes of numerical modelling of groundwater flow in the SCR.V (described in Chapter 5). In addition, considering the data limitations and qualitative nature of set 4 in this study, no attempt was made to define a representative elementary area or volume for individual fracture sets or the fracture system in the SCR.V as a whole.

### **CHAPTER 3**

## **GROUNDWATER FLUX AND PIEZOMETRIC RESPONSE TO PRECIPITATION IN THE SEAL COVE RIVER VALLEY**

### **3.1 Introduction**

#### **3.1.1 General statement**

In this chapter, the physical interaction of surface water and groundwater in the SCRV in response to differing hydrologic stresses is investigated, using measurements of seepage fluxes, piezometric levels, stream flow and rainfall made under a variety of stormflow and low flow conditions. These data are used to describe the magnitude and timing of the reaction of surface water and near-surface groundwater to storm events and seasonal precipitation changes and to infer the principal mechanism of groundwater response within the fractured granite to precipitation. Results and inferences presented in this chapter, along with the structural geologic framework described in Chapter 2, form the starting point for discussion of the chemical and isotopic response of the system to hydrologic stress, presented in Chapter 4. The material presented in this chapter along with the two-dimensional modelling results in Chapter 5 come from an unpublished journal manuscript by H.S. Schillereff, J.E. Gale and J.A. Wellman.

#### **3.1.2 Physical hydrogeologic setting of the study area**

The study area (shown by dotted line, Figure 3.1) encompasses 81.7 ha of hillslope and valley bottom within the Seal Cove River valley and includes a 1.44 km reach of a branch of the Seal Cove River. A small, shallow, abandoned

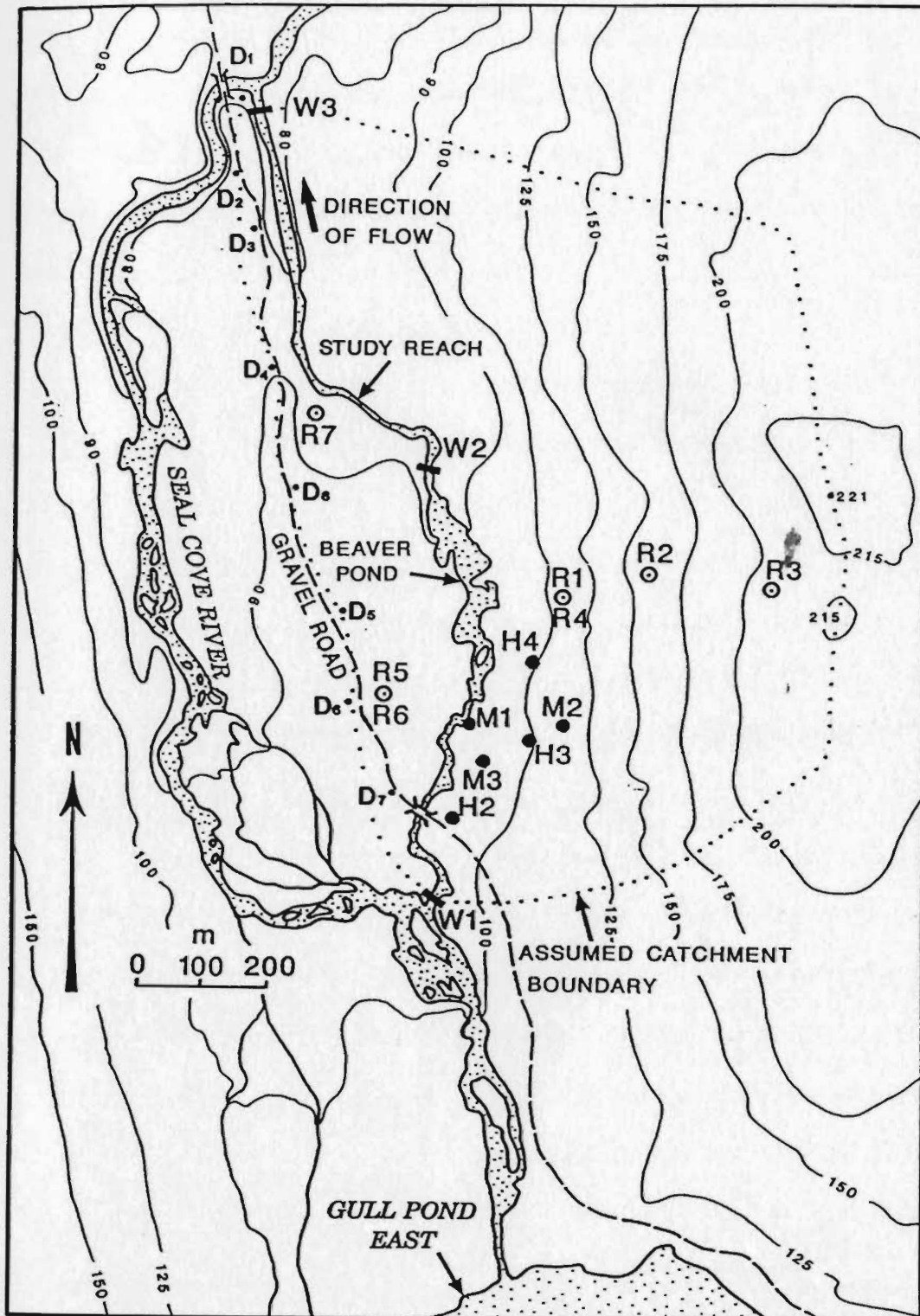


Figure 3.1 - Topography, drainage, access and instrument locations for the Seal Cove River valley study area. M and H symbols are multilevel piezometers, W symbols are weirs, R symbols are rain gauges, and D symbols are locations where glacial drift was sampled.

beaver pond (300 m x 50 m in size; <1.5 m deep) occurs approximately midway along this reach. The southern edge of the study area is about 600 m from Gull Pond East (Figure 3.1), a large pond (nominally 1 km x 1.5 km) in the Seal Cove River valley drainage basin. Approximately 25% of the outflow from Gull Pond East flows into the study reach (the remaining 75% flows into the western branch on the opposite side of the valley).

Granitic rocks of the Holyrood pluton are exposed at glaciated outcrops on over 30% of the hillside and sporadically on the valley floor. Bedrock in this area is lithologically homogeneous and contains only minor, sporadic felsic dikes. Glacial drift partly covers the granitic bedrock in the valley and consists of unstratified, poorly-sorted, quartzo-feldspathic silt, sand and gravel, mainly 1-3 m thick (locally up to 8 m; see Appendix A). Patchy peat deposits, occurring principally along the upper part of the stream reach and pond in the study area, are commonly 0.2-0.6 m thick (locally up to 1.5 m). Geophysical surveys (Appendix A) indicate that the buried granite surface is essentially flat, dipping on average 0.5 degrees toward the north-northwest. Sediments in the small pond along the reach consist of unconsolidated, organic-rich silt and clay, from 0.2-0.8 m thick. Based on direct measurements and field observations, sand and gravel lenses do not occur in the pond sediments, but may occur in shallow isolated depressions at the granite surface beneath the pond sediments. A discontinuous mat of decayed vegetation and arkosic sandy gravel up to 0.5 m thick occurs on the hillslope.

Vegetation in the area consists mainly of small spruce and fir trees, alder and tamarack bushes, and ground juniper. The climate in the region is a cool, moist, maritime type with a mean annual precipitation of about 1300 mm (1000 mm as

rainfall and 300 mm equivalent as snow).

### 3.1.3 Basis for treating the study area as a hydrologic catchment

The study area is considered to constitute a small catchment (Figure 3.1) which is hydrologically distinct from the rest of the valley. Hydrologic no-flow boundaries are assumed to exist under the crest of the hillslope east of the study reach, under the local ridge of glacial drift along the central axis of the valley to the west, and along lines perpendicular to topographic contour lines at the north and south limits of the catchment.

Groundwater boundaries are assumed to be vertical and to directly underlie corresponding surface-water boundaries. This assumption is based on the fact that fractures in the bedrock are primarily subvertical and the absence of any obvious inclined structural or lithological features which could enlarge or reduce the groundwater catchment area compared with the surficial boundaries. Along the western catchment boundary on the valley bottom, the local surface water divide is assumed to directly overlie a groundwater divide. This is supported by calculations, based on Dupuit flow conditions in glacial drift above the flat buried granite surface, indicating that leakage between the branches of the Seal Cove River is negligible (less than 3% of low flow discharge from the study reach).

Using a partial-valley catchment implies that inter-basin flow and groundwater flow from headwater regions of the Seal Cove River drainage basin into the study area are negligible, compared with flow generated within the study area. Significant inter-basin flow into the study area is unlikely since the glaciated valleys parallel and adjacent to the SCRV all drain to the north, with similar



elevations and topographic gradients. Groundwaters from headwater regions of the Seal Cove River drainage basin are assumed to discharge mainly into Gull Pond East before reaching the assumed catchment. This is suggested by shape of upstream portions of the Seal Cove River drainage basin which narrows sharply toward Gull Pond East. Finally, calculations using measured permeabilities in the study area show that possible topographically-driven groundwater flux from Gull Pond East into the assumed catchment is less than 10% of that likely to be derived from the hillslope within the catchment.

#### 3.1.4 Permeability of bedrock and overburden in the study area

As a preamble to this chapter and later parts of this thesis, it will be useful at this point to summarize permeabilities measured in the granite and estimated for the glacial drift in the SCR.V.

Bedrock permeabilities were measured in a series of boreholes in the study area (M and H locations, Figure 3.1) using constant-head or falling-head injection tests, prior to installation of multilevel piezometers in the boreholes. Injection test procedures and results are presented in Appendix E. Table 3.1 summarizes test information. Borehole H3 was inadvertently drilled within a fracture zone with crumbly fault gouge and could not be tested due to caving hole conditions. Injection test results for granite the SCR.V (Figure 3.2) show local permeability variability between individual test intervals, but an overall tendency for decreasing permeability with depth, as indicated by the regression line and 95% confidence lines for the predicted mean values. It is recognized that high permeability fractures will predominantly control water flow through the rock mass near the test intervals. However, the persistence and interconnectivity of such high

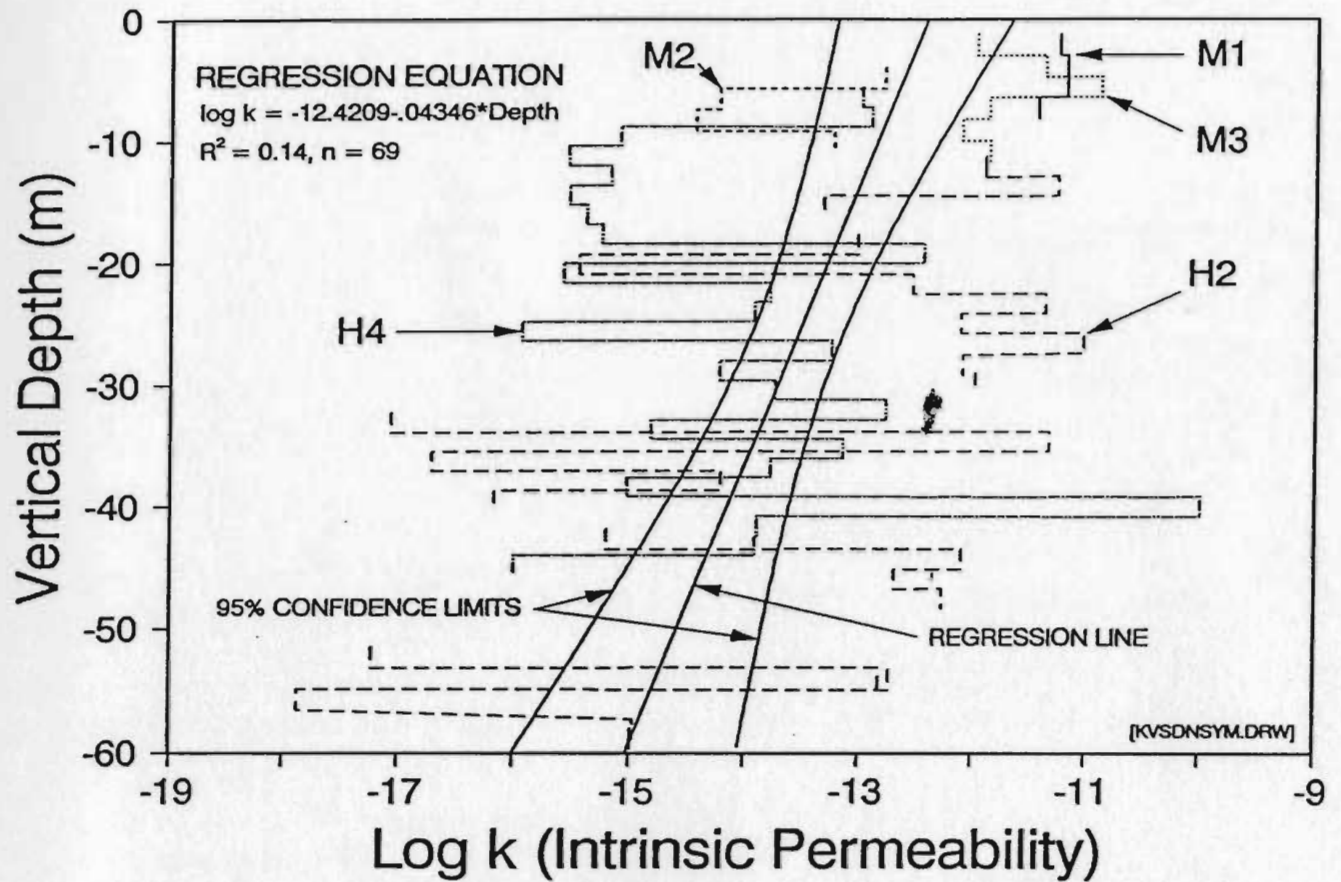


Figure 3.2 - Plot of log intrinsic permeability versus depth for boreholes in the Seal Cove River valley which were injection tested. The regression line (with 95% confidence limits) was fitted through all the data.

permeability fractures away from the test intervals are unknown. Hence, all injection test data, including both low and high permeability zones, were used in the regression analysis, to best represent the overall permeability of the rock mass. A similar high degree of permeability variability between intervals in such tests has been reported elsewhere (e.g. Gale, 1981; Gale and Rouleau, 1986). Hence, the low correlation coefficient shown in Figure 3.2, while indicating there is not rigorous statistical support for decreasing permeability with depth, can be considered typical for field borehole injection test results. Given that permeability decreases with depth have been reported for granitic rocks in a number of other studies (e.g. Davis and Turk, 1964; Snow, 1968; Raven and Gale, 1977), it is reasonable to use Figure 3.2 as a guide for permeability variations with depth in this thesis.

---

Table 3.1 - Borehole injection test information for the study area

---

Hole	Length (m)	Inclina- tion (°)	Diameter (mm)	No. test Intervals	Interval Length (m)	Test type*
M1	10.06	90	48	4	1.74	C
M2	12.19	90	48	4	1.74	C,F
M3	14.20	90	48	4	1.74	C
I12	78.06	53	76	29	2-2.05	C
I13	28.34	55	60	-	-	untested
I14	61.02	53	60	26	2.00	F

---

\* C = constant-head test; F = falling-head test

---

Hydraulic conductivities for glacial drift in the SCRVR were determined using the methods of Masch and Denny (1966), based on sieve analysis (Appendix F) of drift samples collected at eight locations around the valley floor (D locations, Figure 3.1). Hydraulic conductivities for the drift range from  $9.4 \times 10^{-6}$  to  $2.8 \times 10^{-5}$  m/s, with a geometric mean of  $1.6 \times 10^{-5}$  m/s.

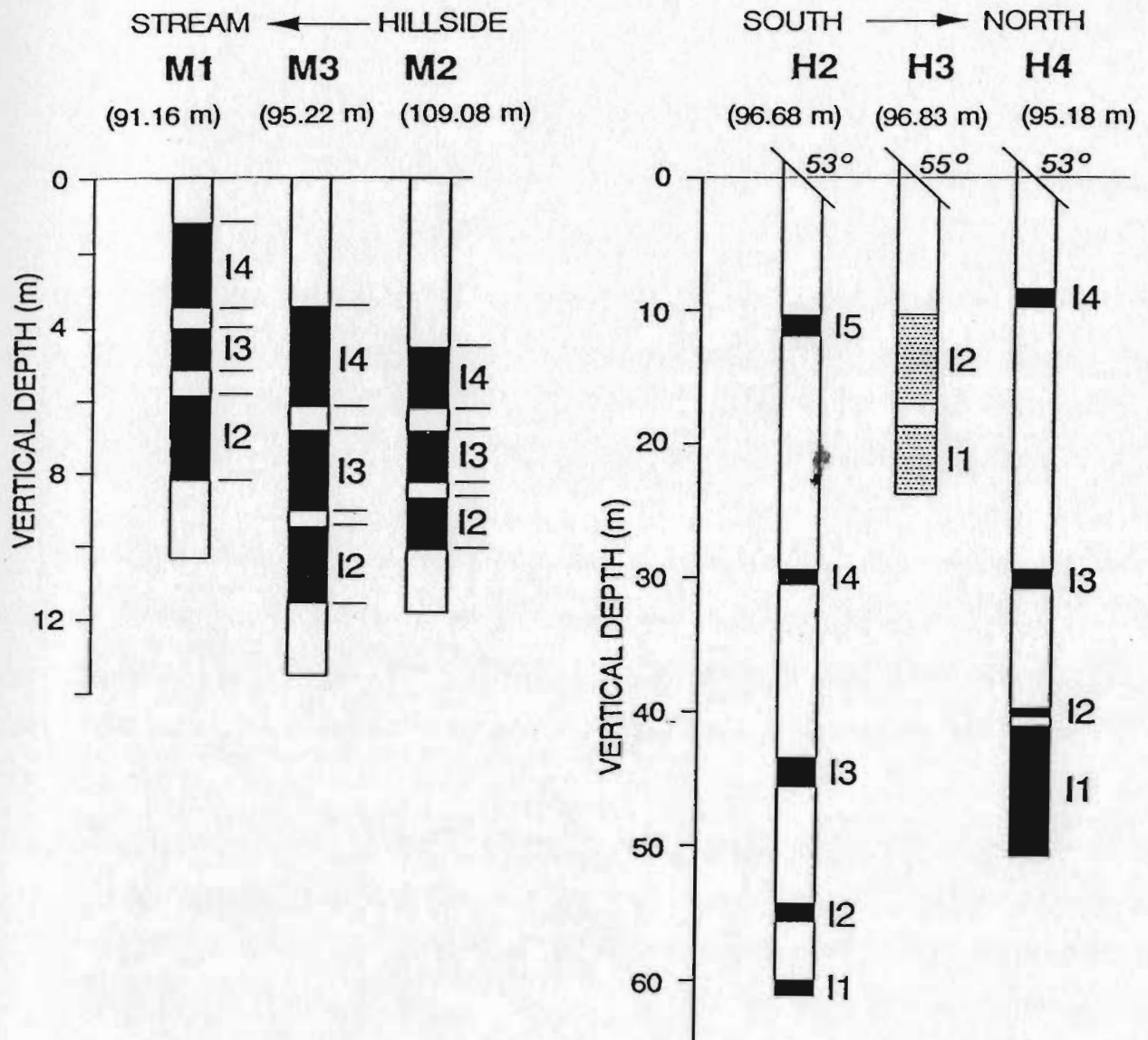


Figure 3.3 - Schematic diagram of multilevel piezometers used in this study. Piezometric intake intervals (labelled) are shown in black (where bounded by chemical packers) or stipple (where bounded by bentonite seals). M holes are vertical; H holes are inclined to the southeast at angles shown beneath the hole labels. Ground surface elevations (meters a.s.l.) are given in parentheses.

### 3.2 Instrumentation and data collection

#### 3.2.1 Bedrock piezometers

Multilevel piezometers were installed in granite bedrock in the southern part of the study area (M1, M2, M3, H2, H3 and H4; Figure 3.1), with piezometric intervals located in zones of high injection test permeability. Figure 3.3 shows schematic diagrams and depths of the piezometers, displayed from left to right by increasing distance from the stream (M piezometers) and by relative location south to north (H piezometers). The piezometers contain 2-5 intake intervals, numbered sequentially from bottom to top (i.e. H1 is deepest; H5 shallowest). For conciseness, the piezometric intervals are referred to here in abbreviated form, e.g. H2H5 refers to interval H5 in the piezometer in borehole H2. Details of piezometer construction and installation are given in Appendix G. All piezometers except H3 consisted of bundled standpipes rising through a PVC pipe string, with intervals isolated by expanding chemical packers (after Cherry and Johnson, 1982). Caving hole conditions in H3 prevented the use of chemical packers, hence this hole was instrumented with two separate standpipes, each jetted into clean silica sand backfill and isolated with bentonite seals. Leakage past the chemical packers or bentonite seals in the piezometers was negligible, as indicated by minimal head changes observed in non-pumped intervals during piezometer development and groundwater sampling.

Piezometric data were collected manually, using electrical water level tapes, at daily or weekly intervals from August-October, 1986; from July-October, 1987; and at half-hour to hour intervals during storm events in October, 1987.

#### 3.2.2 Groundwater flux

Eight seepage meter/mini-piezometer nests were installed at approximately

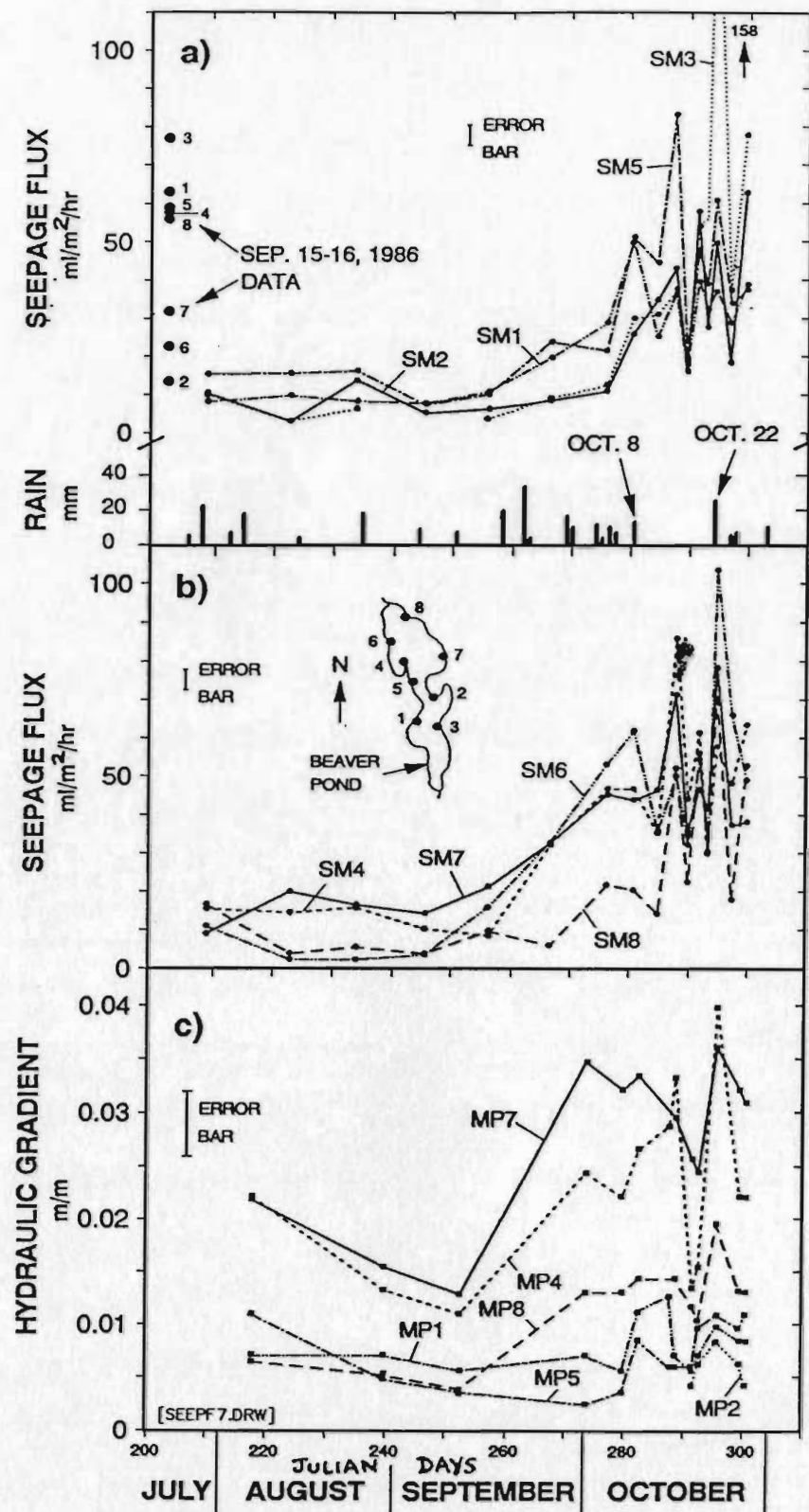


Figure 3.4 - Variation of discharge seepage fluxes (a, b) and mini-piezometer hydraulic gradients (c) in the beaver pond in the study reach. Seepage flux data from Sep. 15-16, 1986 (solid circles) shown at left edge of (a); rainfall shown at bottom of (a); seepage meter (SM) and mini-piezometer (MP) locations shown in (b).

100 m intervals around the edge of the beaver pond (locations shown in Figure 3.4b) using methods described by Lee (1977) and Lee and Cherry (1978). Mini-piezometers were completed to depths of 0.4-0.8 m below the pond bottom. All of the nests were located in similar settings 1-2 m from the edge of the pond, in 0.28-0.42 m of water. Due to the very slight slope of the pond bottom and shallow pond depth ( $< 1.5$  m), and due to time and logistical limitations during field work, transects of seepage meters were not installed across the pond. Flux variations due to slope of the pond bottom (e.g. Lee, 1977) were assumed to be negligible. Pond sediments are homogeneous in appearance, composition and permeability (described below). No highly permeable lenses were found, i.e. such as those reported to produce anomalous flux and gradient readings in seepage meter studies (Krabbenhoft and Anderson, 1986). For these reasons, seepage flux variations between nest locations were assumed to adequately represent areal variations of groundwater discharge from bedrock into the pond as a whole. Weir data (see below) were not considered useable to corroborate the magnitude of overall seepage flux into the pond, since there was no weir sited at the inlet to the pond. However, supporting the representivity of the seepage meters, it should be noted that three-dimensional model results in Chapter 5 show that simulated efflux into the whole pond very closely matches the average seepage flux value from the eight meters.

Seepage volumes and mini-piezometer levels were measured over a two-day experimental period in September, 1986, then at regular one to two week intervals during the summer, 1987, and 1-5 day intervals during October, 1987. Mini-piezometers MP3 and MP6 ceased functioning during 1987, so only data from the remaining six mini-piezometers were recorded. For expediency, mini-piezometer levels were measured directly above the pond surface, rather than with a suction manometer device as described by Lee and Cherry (1978). Calibration tests in a wave tank indicated that this direct measurement method was only slightly less

precise (about  $\pm 2$  mm) than the manometer method (about  $\pm 1.5$  mm). However, due to the large uncertainty in hydraulic gradients calculated from field measurements (up to  $\pm 0.005$  m/m) and the uncertain degree of sealing around the mini-piezometers (described below), gradients from these mini-piezometer data are only used qualitatively here.

Due to time limitations, field permeability tests through the mini-piezometers were not conducted. Hydraulic conductivities for the organic mud pond sediments encountered at the seepage meter/mini-piezometer nests were estimated based on slopes of regression lines of flux versus gradient plots for 1987 data and ranged from  $10^{-6}$  to  $10^{-7}$  m/s. As a check of these estimates, falling head permeability tests were conducted on sediment cores obtained with thin-walled drive tubes at locations 1, 4, and 7. The sampled sediments all consisted of tan to dark brown, soft clay, with 37-46% organic content by weight. The measured hydraulic conductivities were similar to each other ( $3.6$ - $9.3 \times 10^{-8}$  m/s, with a geometric mean of  $6.0 \times 10^{-8}$  m/s) and were one to two orders of magnitude smaller than the regression-based values, which are effectively field scale estimates. Although estimates of hydraulic conductivity at laboratory and field scales are expected to differ somewhat (e.g. de Marsily, 1986), the large differences here suggest that the regression-based conductivity estimates were too high and, in turn, that heads measured in the field were too low. This is consistent with installation difficulties with the mini-piezometers.

The pond sediments are extremely soft and the mini-piezometers could be pulled out by hand with only moderate effort, suggesting that collapse of the mud annulus and sealing of the standpipe was incomplete. The mini-piezometers were also easily agitated by wind and wave agitation, and by foot pressure during measurements. These factors point to the likelihood of partial leakage along the piezometer tube and poor isolation of the tip, leading to erroneously low head measurements. It should be noted that regardless of which range of hydraulic



conductivity is adopted for the pond sediments, the interpretations presented below relating to the pond sediments are not substantially altered.

### 3.2.3 Rainfall and streamflow

Rainfall was recorded using Sangamo<sup>R</sup> recording rain gauges (R1, R2, R3 in 1986; R5 and R7 in 1987) and a standard rain gauge (R4 in 1986; R6 in 1987) at locations shown on Figure 3.1. All gauges were placed in clearings 15-25 m wide, surrounded by sheltering vegetation. The gauges recorded rainfall in 0.2 mm increments, over seven-day periods. Cumulative rainfall was read manually (to the nearest 0.1 mm) at the standard gauge after each rainfall event.

Streamflow was measured using sharp-edged, contracted, rectangular weirs, nominally 2 m wide, at locations W1, W2 and W3 (Figure 3.1). Water height was measured with a Stevens<sup>R</sup> float recorder mounted above a stilling well located upstream of each weir. Recorders were accurately referenced to weir crest elevations using levelling equipment to ensure precise discharge determinations. The intake for each stilling well was located 3 m upstream of the weir to avoid head loss due to stream velocity at the approach to the weir. Because heavy Spring runoff in both 1986 and 1987 overtopped channel banks and flooded each weir, only summer and autumn storm flows were measurable. The timing and duration of stormflow were determined from hydrographs created from digitized float recorder records. It should also be noted that the upstream weirs (W1 and W2) do not specifically bound the beaver pond, so discharges through these weirs could not be used to check seepage flux magnitudes into the beaver pond.

### 3.3 Groundwater flux response to precipitation

Measured seepage flux at a given location represents an average of the

actual fluxes developed there during the collection period. For this reason, fluxes are plotted at times corresponding with the mid-point of collection periods (Figures 3.4a and 3.4b). In contrast, hydraulic gradients determined from mini-piezometer measurements are essentially instantaneous values and are plotted at the actual times of measurement (Figure 3.4c). These gradients steadily decreased during the summer, 1987, then roughly doubled after mid-September, 1987, with a sharp pond-wide increase due to the October 22 storm. While the overall pattern of gradient variations mimics that of seepage flux, little significance is attached to detailed gradient variations (e.g. during the October 10-20 period) due to uncertainties about the sealing around the mini-piezometers.

Groundwater discharge at the eight seepage meters in the beaver pond in 1987 (Figures 3.4a and 3.4b) was low from July to mid-September, ranging from 3 to 20 ml/m<sup>2</sup>/hr, then increased from mid-September to early November, ranging from 20 to 158 ml/m<sup>2</sup>/hr. Figures 3.4a and 3.4b also show greater variability of fluxes between mid-September and early November, in terms of both time and location, as compared with the July to mid-September period. This trend of increasing magnitude and variability corresponds with increased rainfall (top of Figure 3.4b) and, by inference, increased groundwater recharge and decreased evapotranspiration following the dry summer period. The 1987 autumn fluxes were in the same range as those for mid-September 1986 (shown in Figure 3.4a). However, the summer period in 1986 was wetter than in 1987, with cumulative rainfalls during June-August equal to 119% and 89%, respectively, of the cumulative 30-year average rainfalls for these months (Environment Canada, Atmospheric Environment Service, pers. commun.). The similarity of autumn fluxes for both years thus suggests that the dry summer conditions in 1987 had little prolonged effect on groundwater discharge fluxes.

Figures 3.4a and 3.4b show variability of fluxes around the pond, with some seepage meters producing consistently low fluxes (SM2 and SM8) and others consistently high fluxes (SM4 and SM7) throughout the monitoring period. This variation is consistent with the variability of fracture permeability (Figure 3.2b). However, permeability variations do not adequately explain the response at seepage meters SM3 and SM6. They had the lowest fluxes during the summer yet the highest fluxes during the autumn. Hence their response appears to depend in part on seasonal rainfall amount.

Figure 3.5 shows a series of contour maps of seepage flux for the period October 7-28, 1987, which illustrate the variability of groundwater discharge during individual storm events. Significant rainfalls occurred on October 8 (13.0 mm) and October 22 (22.6 mm). The 13.4 mm rainfall accumulation for October 23-27 period (Figure 3.5h) consists of 3.1 mm at the end of the October 22 storm and 10.3 mm from two small events on October 25 and 27.

Response to the October 8 rainfall is limited to slight flux increases at SM1, SM5 and SM6 (Figure 3.5a) as compared with the immediate post-storm period (October 10-15; Figure 3.5b) when rainfall was negligible. This subdued short-term response is consistent with the findings of Lee et al. (1980) that small rainfalls induce only minimal seepage flux responses. However, fluxes during the dry period October 10-20 (Figures 3.5b-3.15f, and 3.4a and 3.4b) rose and fell systematically at all seepage meters in a damped, cyclical manner, which may constitute a longer-term response to the October 8 rainfall. No significant rainfall or anomalous barometric pressure changes occurred during this period, and both streamflow and bedrock piezometry (Figures 3.6 and 3.7 below) displayed a steady decline during this post-storm period. These flux variations can not be attributed

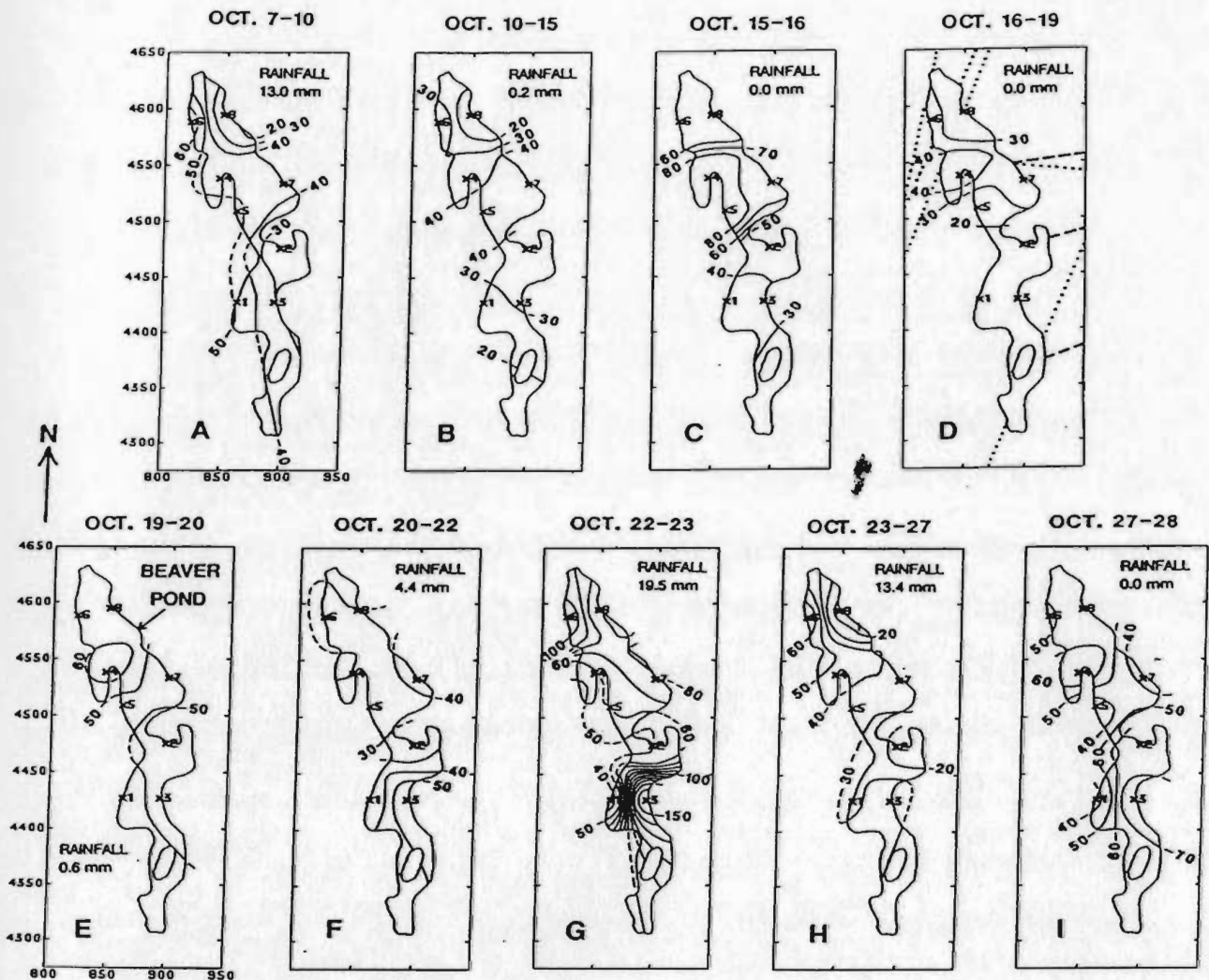


Figure 3.5 - Maps of contoured discharge seepage flux at the beaver pond during October 7-28, 1987. Contour interval is 10 ml/m<sup>2</sup>/hr. Grid numbers refer to UTM coordinates (meters). Seepage collection dates and accumulated rainfall during those periods are shown for each map. Fracture lineaments in (d) (dashed, inferred; dotted, known) are extrapolated from those in Figure 2.7.

to spurious measurements since they were observed at all seepage meters. In addition, no evolving gases were observed emanating from the pond sediments or collected in the seepage meters, which might cause erratic flux readings. The variations exceed the  $\pm 10$ -15% range commonly associated with background flux measurements (David Lee, pers. commun., 1988) and, in addition, the cycles span several days, hence can not be explained by diurnal flux variations due to vegetation (described, for example, by Lee and Hynes, 1978).

These cyclical post-storm flux variations were most likely caused by excess pore pressures at the granite/pond sediment interface. A simple force balance shows that a pore pressure equal to 1.08 m of head, developed at the base of 0.5 m of pond sediments overlain by 0.5 m of water (i.e. 0.08 m of head above the pond surface), would induce heaving of the pond sediments. At piezometer M1, collared in the fractured granite near stream level just upstream of the pond (Figure 3.1), heads in the shallowest interval (I4; 1.52-3.52 m deep) were 0.2-0.25 m above the pond surface during October, 1987 (Figure 3.6a below). This artesian condition infers that pore pressures beneath the pond sediments were in the right range to induce heaving of the pond sediments. Bedrock hydraulic conductivities at M1 (nominally  $3$  to  $5 \times 10^{-5}$  m/s) are approximately three orders of magnitude greater than those measured for the pond sediments. Hence the sediments form a semi-confining layer, conducive to the build up of excess pore pressures. In addition, the low porosity for fractured granites (typically 1% or less) means that heaving of the overlying sediments would tend to be cyclical, with rapid release and rapid recovery of pore pressure beneath the pond, controlled by overall declining bedrock pore pressures following a storm. This hypothesis is supported by an oscillation in the trend of standardized SM6 seepage fluxes above and below the steadily recessing piezometric levels at M1 following the October 8

storm, as shown in Figure 3.9b. The consistency of the occurrence of the oscillating fluxes at all seepage meters suggests there might be many small "heave" zones, rather than just a few major zones, possibly controlled by microtopography at the granite interface.

In contrast to the October 8 storm, the October 22 rainfall produced immediate and pronounced flux increases at all seepage meter locations (Figure 3.5f and 3.5g). Flux responses were prompt enough that the dense contour pattern developed during rainfall (Figure 3.5g) appears to have been already developing soon after the onset of rainfall (Figure 3.5f). Groundwater discharge flux decreases due to a rapid increase in stream stage during stormflow, as described by Lee and Hynes (1978) for a stream channel, probably did not occur at the pond. This is because stage increases in the pond (with large surface area) during rainfall are inherently less than in a stream channel (with smaller surface area), hence rapid development of head, opposing normal upward gradient into the pond, does not develop. Flux increases were concentrated around SM3 and SM6 (Figure 3.5g), with strong flux gradients (up to  $4 \text{ ml/m}^2/\text{hr}$  per meter of horizontal distance) developed between SM3 and adjacent seepage meters. Flux increases dissipated rapidly after the storm so that fluxes during October 23-27 (Figure 3.5h) were similar to pre-storm values. The prompt groundwater discharge increases for this storm were therefore spatially variable and short lived, lasting only approximately one day after rainfall ceased. Since monitoring ended on October 28, it is not known if longer-term rise and fall cycles, similar to those during the October 10-20 period, developed after the October 22 storm.

### 3.4 Piezometric response to precipitation

#### 3.4.1 Seasonal piezometric response to precipitation

In 1987, hydraulic heads in the six bedrock multilevel piezometers (Figure 3.6) declined steadily from July to mid-September, with individual storm events producing short-term deviations from this overall recession. The heads then rose sharply in mid-September and remained elevated through the end of the monitoring period in early November. The declining hydraulic heads during the dry summer months document the lowering of the water table in the granite and coincide with streamflow recession in the stream reach. As with seepage flux, the elevated heads during the autumn period correlate with increased rainfall. Piezometric variations in 1986 were consistent with those in 1987, but are not shown since piezometric measurements were less frequent, rainfall was less variable and the monitoring period was shorter than in 1987.

#### 3.4.2 Short-term piezometric response to precipitation

Figures 3.7 and 3.8 document the following characteristics of piezometric response in the study area to individual storms during October, 1987:

- 1) piezometric levels rose promptly, within hours after the start of rainfall, and dissipated in a matter of days;

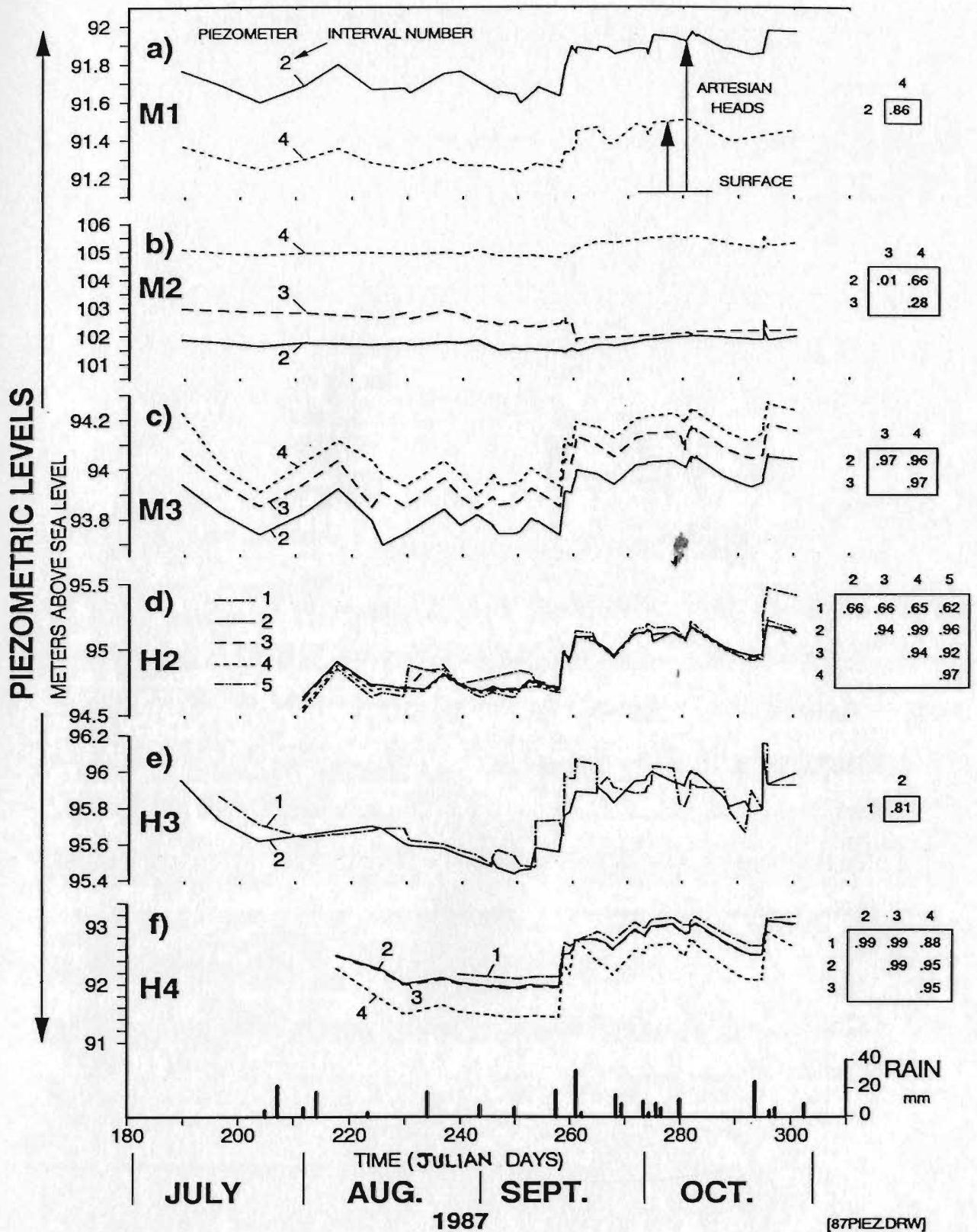


Figure 3.6 - Variation of piezometric levels at all of the multilevel piezometers for the 1987 monitoring period. Single numbers refer to piezometric intervals (e.g. "2" refers to interval I2). Correlation coefficients ( $R^2$ ) for responses of intervals within piezometers are shown at right (e.g. within piezometer M3 (c),  $R^2$  for responses in intervals I2 and I4 is 0.96).



- 2) increases in piezometric level became disproportionately greater with increasing rainfall amount;
- 3) the magnitude of hydraulic head changes diminished with depth in H4 (to a depth of 45 m), but not in H2 (to a depth of 60 m).

Figures 3.7a shows that piezometric levels increased promptly in response to rainfalls on October 8 and October 22, 1987, respectively. Figure 3.8 shows that heads in H2 and H4, to depths of 60 m, started to rise within 12 hours after the start of rainfall, i.e. in the middle of the October 22 storm event. Similar responses were observed in all other piezometers except M2. At M2, increases in piezometric level for this storm were delayed for approximately 12 hours compared with other piezometers. Permeabilities within the 8 m injection-tested section of M2 varied by two orders of magnitude ( $1.6 \times 10^{-13}$  to  $3.6 \times 10^{-15}$  m<sup>2</sup>) indicating that abrupt variations in hydraulic connectivity between fractures exist over short distances in that hole. This, plus the low range of permeabilities, may partly explain the slower piezometric response at M2. In addition, a thick unsaturated zone at M2 (4 m compared with zones 1 m or less at other piezometers) may have contributed to longer infiltration times and to the delay in piezometric response.

Time-lag characteristics of the instruments themselves did not contribute significantly to observed delays in piezometric response to rainfall. This is indicated by rapid responses of water levels in standpipes during sampling as well as short calculated time lags for all piezometers (Hvorslev, 1951), on the order of seconds to minutes. Piezometric recession after rainfall is clearly shown on Figure 3.7a for the period after the October 8 storm. This implies that increases in water table elevation due to infiltration dissipated rapidly, in a matter of days.

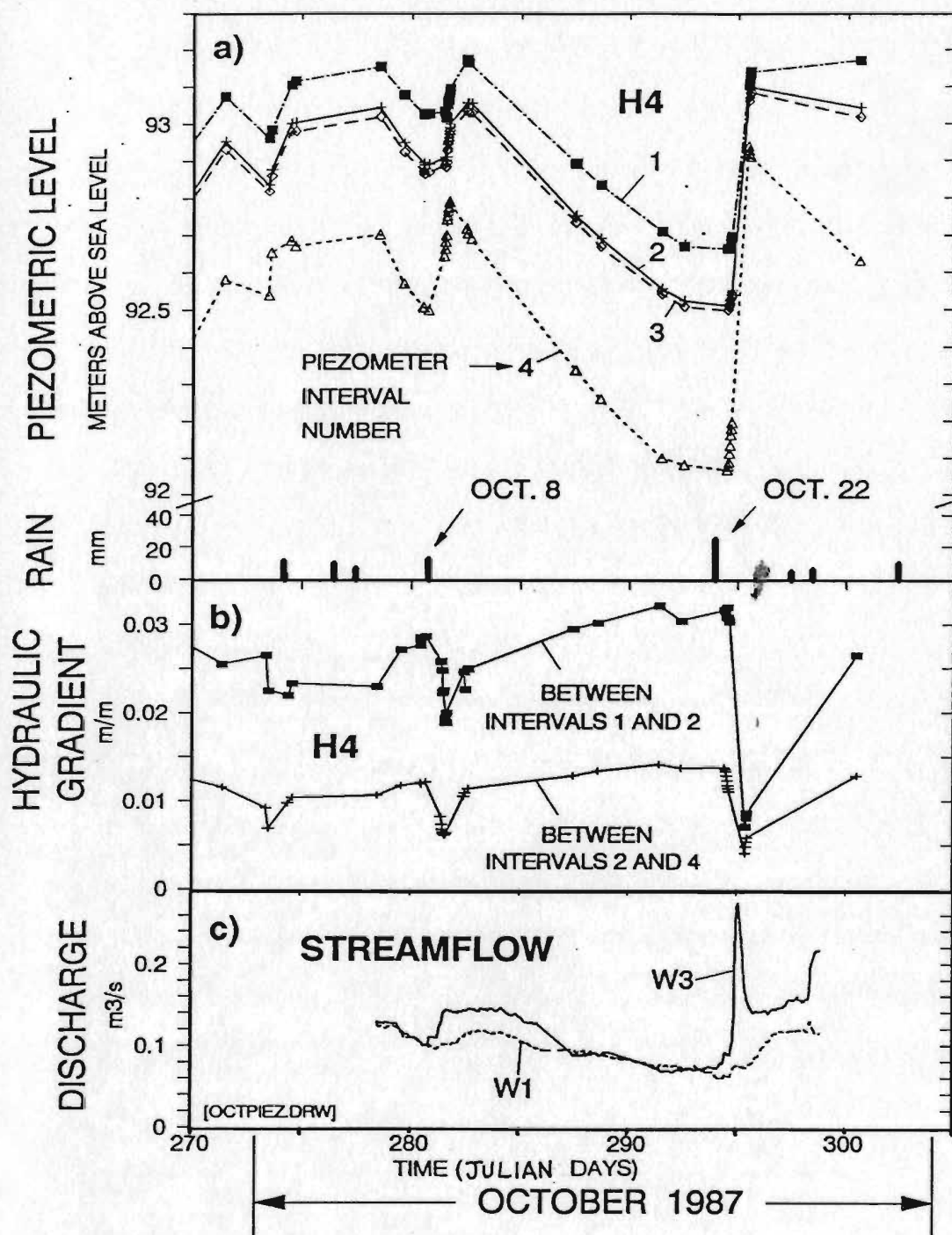


Figure 3.7 - Piezometric variations (a) and hydraulic gradients (b) in piezometer H4 and variation in streamflow (c) during October, 1987.

Figure 3.7a also shows a relationship between the magnitude of piezometric response and rainfall amount. For the 13.0 mm October 8 rainfall, piezometric levels in interval I4 of H4 rose 0.3 m, while in this same interval, a 0.9 m increase was measured for the 22.6 mm October 22 rainfall. Hence, while rainfall amounts roughly doubled, piezometric rise tripled. It should be noted that ground conditions were drier before the October 22 storm than before the October 8 storm, as indicated by rainfall records and by the greater degree of piezometric recession prior to the October 22 storm (Figure 3.7a). In addition, the October 22 rainfall was more intense (average 1.5 mm/hour) than the October 8 rainfall (average 0.9 mm/hour). These observations suggest that higher rainfall intensity, enhanced infiltration capacity and a depressed water table all contributed to the larger piezometric response to the October 22 storm.

Finally, Figure 3.8a shows that hydraulic heads in the shallowest interval (I4) of H4 rose 0.9 m in response to the October 22 storm, while in the deepest interval (I1) they rose just under 0.5 m. In contrast, head increases were similar for all intervals (I1-I5) in H2 (Figure 3.8b). This differing response with depth, suggesting a more efficient transfer of hydraulic head in the vicinity of H2, is consistent with higher permeabilities at H2 compared with those at H4 (Figure 3.2b).

#### 3.4.3 Correlation of piezometric response

The degree of correlation of hydraulic head responses between intervals in individual piezometers in response to precipitation is indicated by the correlation coefficients ( $R^2$ ) given at the right of Figure 3.6. The  $R^2$  values were obtained by linear regression of heads measured within minutes of each other in different

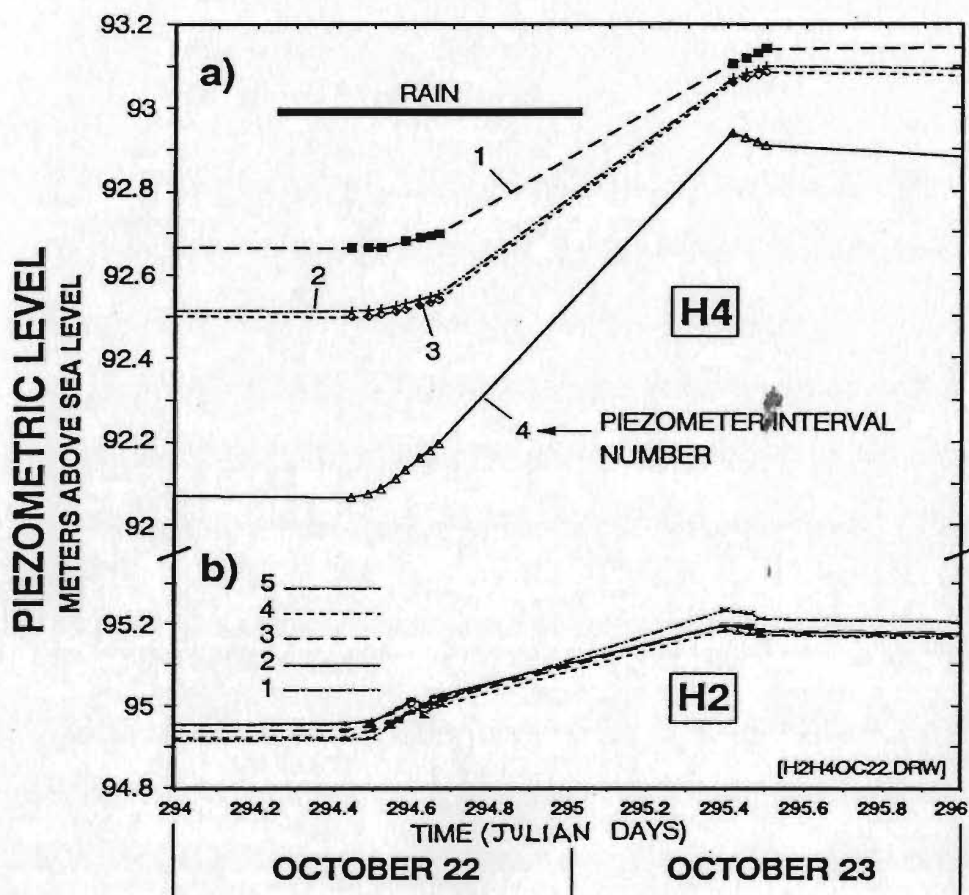


Figure 3.8 - Detailed piezometric variations in piezometers H4 (a) and H2 (b) in response to the October 22, 1987 storm.

intervals. Correlation was strong ( $R^2 = 0.80-1.00$ ) in most piezometers (except at M2 and the bottom of H4), indicating that transient heads were efficiently transferred through the granite from the surface to 60 m depth. Low  $R^2$  values are interpreted to mean that local hydraulic connection was poor, as manifested by injection test permeabilities. For example, the relatively low permeabilities at M2 correspond with low  $R^2$  values (0.01-0.66).

Figure 3.9 shows comparative changes of piezometric levels, seepage fluxes, mini-piezometer gradients and streamflow in response to precipitation during the 1987 monitoring period. To facilitate comparison, these data have been standardized to a unitless variable ( $z$ ), with mean of zero and standard deviation of one (after Bethea et al., 1985). Correlation coefficients for the trends of these transformed hydrologic data are given in the upper left corners of Figures 3.9a and 3.9b.

Figure 3.9a shows that all of the piezometers (except M2) responded similarly to seasonal precipitation trends and showed a moderate to strong degree of correlation ( $R^2 = 0.44-0.97$ ). This implies that factors affecting long-term changes in hydraulic heads in the granite operated uniformly throughout the instrumented area. Figure 3.9b shows that piezometric, seepage flux, mini-piezometer gradient and streamflow changes were similar in response to seasonal precipitation trends. The moderately strong correlation ( $R^2 = 0.74-0.80$ ) between piezometric and streamflow observations suggests that surface waters and shallow groundwaters in the study area interacted closely and responded in similar fashion to hydrologic stress.

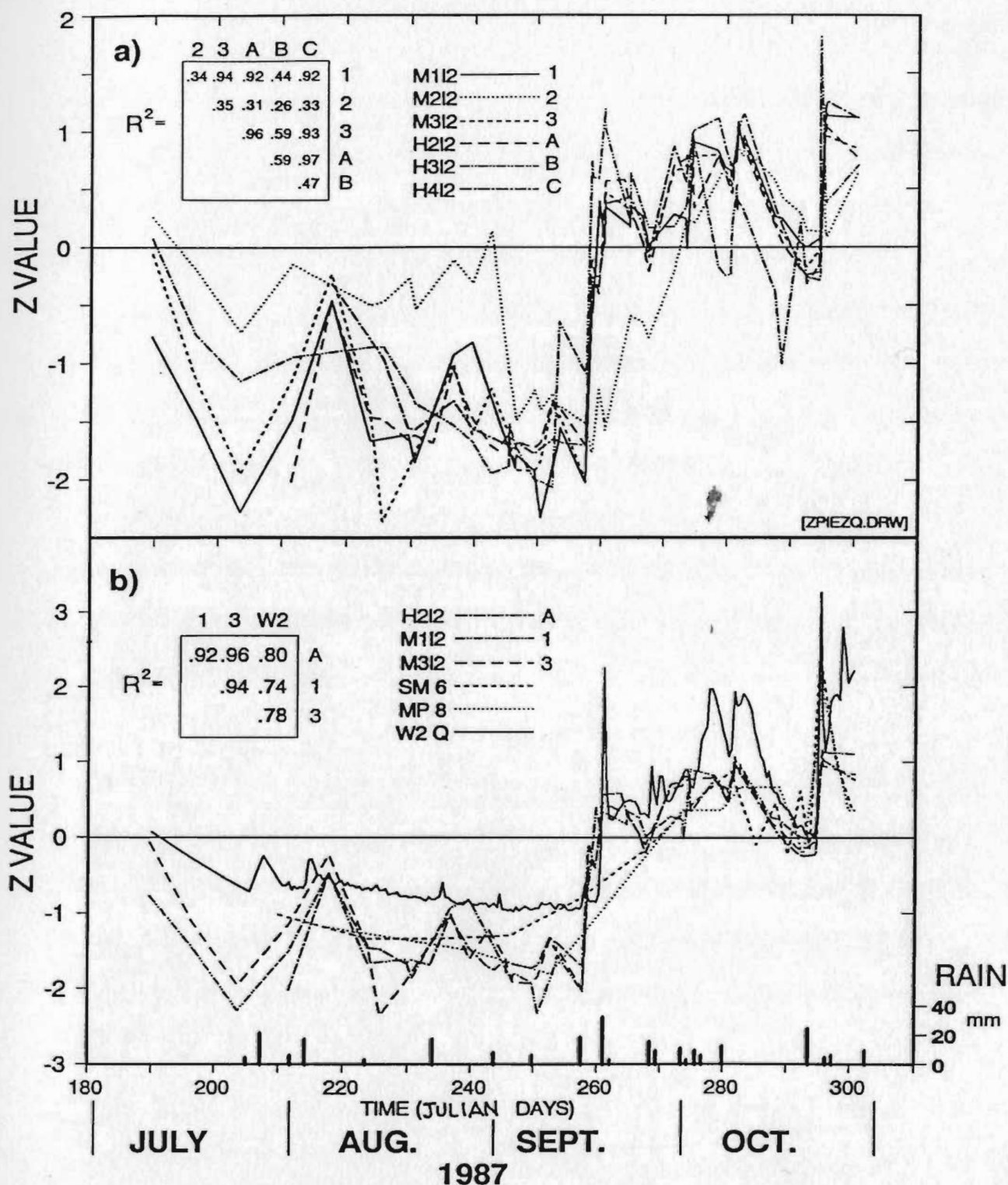


Figure 3.9 - (a) Responses to precipitation at selected piezometric intervals; and (b) at selected seepage flux, piezometric and stream flow measurement points in the SCRVS during the 1987 monitoring period. Responses have been standardized to unitless z values (described in text). Correlation coefficients between response trends are shown at the upper left of each plot.

#### 3.4.4 Three-dimensional variation of hydraulic head

In Figure 3.10, strong downward gradients at M2 (up to 0.83), strong upward gradients at M1 (up to 0.11), and much smaller downward or upward gradients at the other piezometers suggest the development of a recharge zone on the hillslope, a discharge zone near the stream and a zone of approximately horizontal flow in intervening areas. Slight gradient variations with depth occur but are negligible in H2. Figure 3.10 also shows that downward gradients increased (at M2 and M3) and upward gradients decreased (at M1 and H4) in response to the October 22, 1987 storm. This infers that the recharge zone may have expanded toward the stream during response to the storm. Gradient reversals, from discharge to recharge (at H3 and upper levels of H2), imply that a hinge surface, separating the recharge and discharge zones, migrated past H3 and H2 in response to this storm.

Figure 3.11 shows equipotential maps constructed using heads determined by linear interpolation of measured piezometric levels both within and between piezometers. Hinge lines (intersections of the hinge zones with the horizontal planes) were constructed by superimposing the maps for both planes and joining points with the same equipotential value. Since the map constructions are highly simplified (based on only five control points), they must be viewed as providing only very general information on head distribution and behaviour. Figure 3.11 depicts equipotential contours in the shallow granite subsurface, on horizontal planes at 84 and 90 m elevations, before, and in response to, the October 22, 1987 storm (Figures 3.11a and 3.11b), at low flow (Figure 3.11c) and approximate hinge line locations (Figure 3.11d). Figures 3.11a, 3.11b and 3.11c show that the equipotential surfaces on both planes sloped gently to the northwest, both before



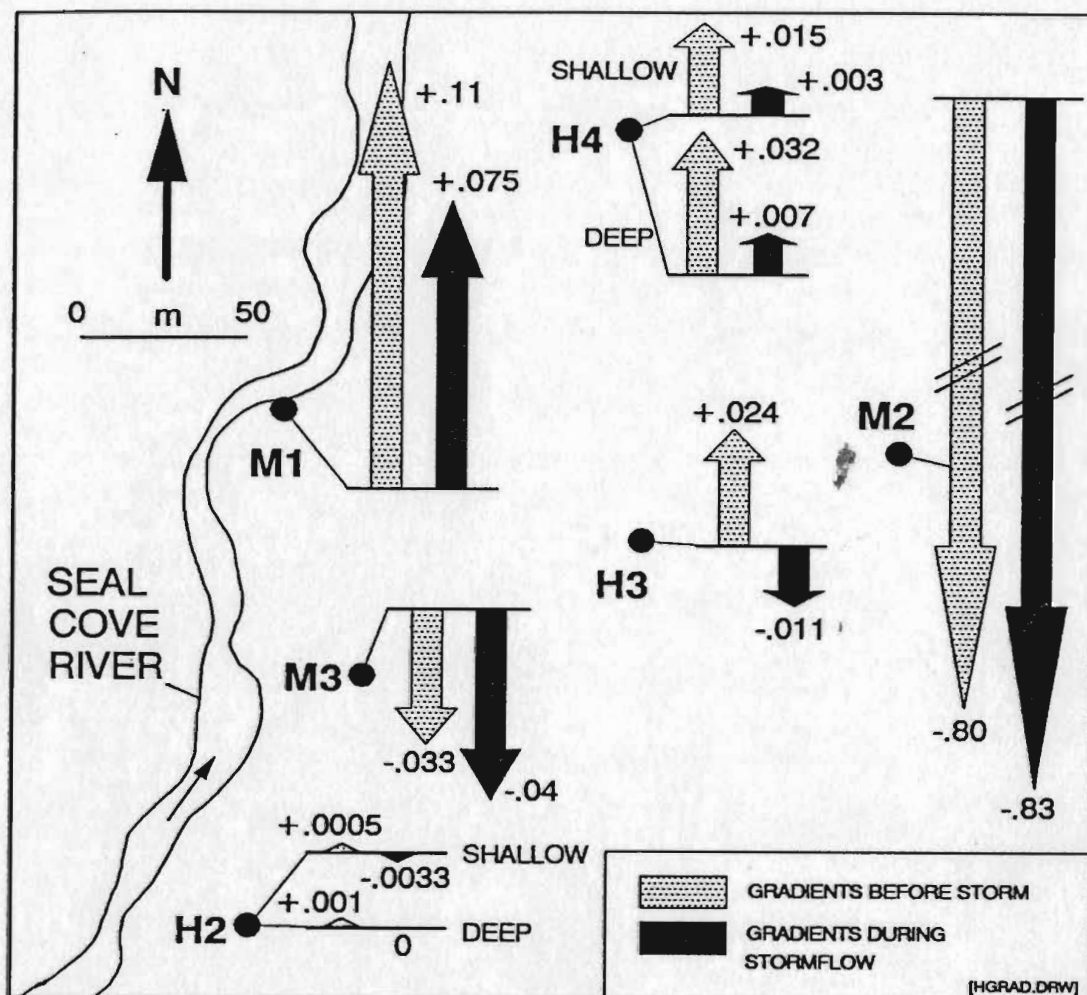


Figure 3.10 - Vertical components of hydraulic gradients in bedrock piezometers before storm hydrograph and during peak stormflow in response to the October 22, 1987 storm. Arrows indicate discharge (up) or recharge (down), with gradient values given next to arrowheads.



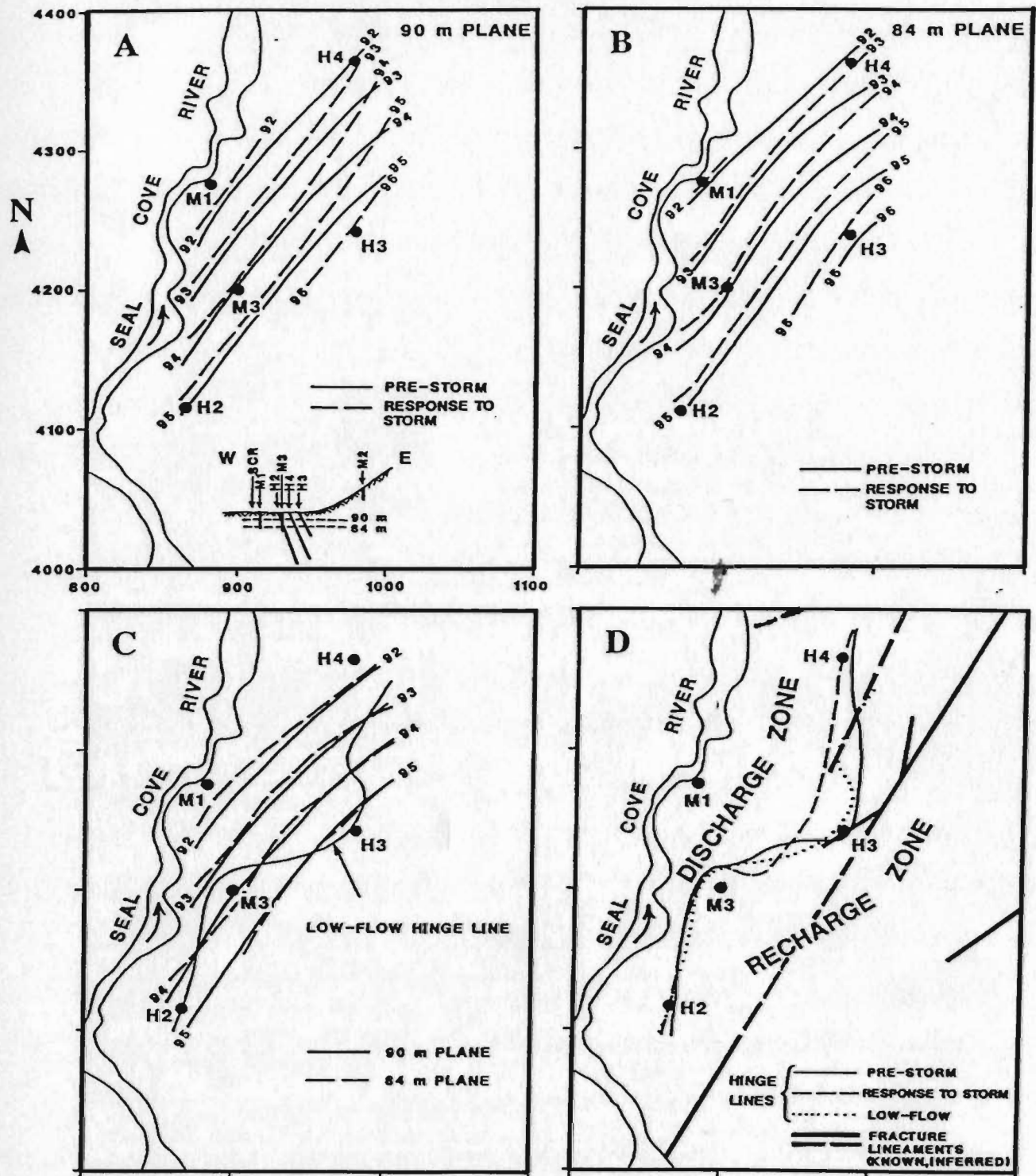


Figure 3.11 - Equipotential maps (a, b and c) and inferred hinge line locations (d) for two horizontal planes in the shallow subsurface in the SCR. The two planes (at 90 m and 84 m above sea level) are depicted in relation to the piezometers in (a). Equipotential patterns before and during response to the October 22, 1987 storm (a, b) and for both planes at low flow conditions (c) on September 2, 1987) suggest that groundwater flow during was northwesterly-directed toward the stream.

and in response to a storm and under low flow conditions. The orientation of these surfaces suggests that groundwater flow was directed from the hillslope toward the stream. Actual flow directions have not been drawn since the degree of anisotropy in the fractured granite is unknown. Figure 3.11d shows that the low flow and pre-storm hinge lines roughly coincided and that the shift of the recharge zone toward the stream was apparently greatest in the northern part of the instrumented area. To the south, all of the hinge lines roughly coincide and deviate sharply away from the base of the hillslope (which trends through H3 and H4). There were no obvious surface topographic features which could have contributed to these differences in hinge line location. The hinge lines between H3 and M3 were collinear with a fracture lineament passing through H3 inferring that individual fracture zones may influence hinge line locations.

### **3.5 Mechanism of groundwater response to precipitation**

Results presented here support the concepts of rapid transfer of heads through the saturated zone (e.g. Pilgrim et al., 1978) and prompt displacement of groundwater to surface waters (e.g. Sklash and Farvolden, 1979; Sklash et al., 1986) in response to rainfall. An important difference here is that groundwater flow occurs in fractured granite where matrix permeability is extremely low (less than  $E-18 \text{ m}^2$ ). Hence, the only mechanism for rapid head transfer and groundwater displacement in the study area in response to precipitation is the filling and draining of fractures. Draining of fractures is supported by direct observations of water seeping from joints at hillside outcrops and emptying from shallow sub-surface fractures into open boreholes after storms.

Intuitively, the most permeable fractures in an area, here assumed to be the

open subhorizontal fractures and subvertical faults and fracture zones described in Chapter 2, will tend to form primary conduits for infiltration and groundwater recharge and discharge. Weyer and Karrenburg (1970) and Weyer (1972) have discussed the possibility that rapid groundwater discharge from major faults after storm events contributes to observed stream response. The principal implications of a fracture filling/draining mechanism dominated by highly permeable fractures in the study area are that:

- 1) open, near-surface fractures, e.g. sheeting joints with gapped apertures, may allow very high groundwater velocities and hence the movement of shallow groundwater over much greater distances during storm runoff events than would be expected in areas where porous media flow dominates;
- 2) it is possible that a relatively small number of large permeable fractures (possibly on the order of a few hundred), with spacings on the order of 5-10 m, may effectively control the response to precipitation of groundwater at deeper levels of the saturated zone and groundwater-stream interconnection; and,
- 3) because of the contrast between matrix and fracture permeabilities in the granite, the water table in the SCRVS comprises an interconnected lattice of free surfaces in near-surface fractures, rather than an essentially continuous water surface, as conventionally conceived for porous media. Hence, in fractured rock settings, the timing and magnitude of changes in the water table due to hydrologic stress will tend to vary depending on the variability in the spacing and hydraulic connectivity between fractures.

The fracture filling and draining mechanism proposed here is compatible with

"piston flow" displacement of groundwater in response to rainfall, as hypothesized by Pearce et al. (1986) and others. A principal tenet of the piston flow hypothesis is that groundwater moves along flow paths, in this case the fracture system in granitic bedrock, in serial fashion with incomplete mixing of successive parcels of water. Groundwater mixing in the SCR, at a scale of a few meters and in terms of the study reach as a whole, is discussed in Chapter 4. In addition, it will be shown in Chapter 5 that the catchment area actually contributing water to the study reach may be smaller than the topographic limits of the assumed catchment shown in Figure 3.1. This, along with the possibility of high groundwater flow velocities, suggests that groundwater contributing to the reach during stormflow likely originates promptly from valley bottom and near-stream areas, rather than from distal hilltop locations.

### **3.6 Conclusions and inferences**

Measured increases in groundwater discharge in response to storms and the linkage of surface and groundwater masses demonstrated above shows that groundwater should not be ignored in water budgets for the study area. Groundwater terms are therefore necessary in flow and chemical mass balance analyses of the study area presented in the next chapter. In addition, a fracture filling and draining mechanism proposed here for groundwater response to precipitation implies that conventional porous medium concepts of groundwater flow, such as slow groundwater velocities and a continuous, smoothly-varying water table, may not apply in granite in the SCR at scales of tens of meters or less.

The physical hydrogeological evidence presented in this chapter can be used

to infer that stormflow contributed from the assumed catchment adjacent to the study reach is dominated by direct runoff from the assumed catchment rather than displaced groundwater. This is based on 1) the degree of granite exposure and thinness of cover materials (suggesting low infiltration capacity), 2) direct observations of overland flow on the hillslope during storm runoff, 3) sharp peaks in storm hydrographs developed along the stream reach, and 4) low magnitudes of discharge seepage flux in the pond and stream. The composition of stormflow and the consistency of physical, chemical and isotopic responses to hydrologic stress in the SCR V will be addressed in the next chapter, using the structural geologic and physical hydrogeologic data and interpretations discussed up to this point as an interpretive framework.

## **CHAPTER 4**

### **HYDROCHEMICAL AND ISOTOPIC RESPONSE OF SURFACE WATER AND GROUNDWATER TO PRECIPITATION IN THE SEAL COVE RIVER VALLEY**

#### **4.1 Introduction**

##### **4.1.1 General statement**

This chapter presents a description and interpretation of the hydrochemical and isotopic (oxygen-18 and deuterium) responses of surface water and groundwater to precipitation in the SCRV, with the aim of more clearly understanding the overall response of the assumed catchment to hydrologic stress. To investigate hydrochemical and isotopic responses in the study area, rainfall and stream flow were measured and rain, stream and groundwaters were sampled during low flow and stormflow conditions in 1986 and 1987. These data are used here to 1) investigate groundwater compositional variations and mixing relationships, 2) determine the components of storm runoff generated along the study reach, and 3) evaluate the consistency of hydrochemical and isotopic responses with the physical hydrologic responses to precipitation in the study area described in Chapter 3.

The reach hydrologic approach used here for determining stormflow runoff components differs substantially from conventional headwater approaches for studying catchment response to precipitation (e.g. Dincer et al., 1970; Sklash et al.,

1976). Transient mass balance methods have been developed for interpreting chemical changes in a stream reach and for performing chemical and isotopic hydrograph separations for stormflow generated along a reach. These methods are summarized below and discussed in detail in Appendix II.

#### 4.1.2 Hydrochemical setting of the study area

The hydrochemical setting of the SCR V reflects the humid temperate marine climate in eastern Newfoundland as well as the geologic materials underlying the study area. Rain waters are dilute Na-Cl type, with chloride likely derived from marine aerosols generated at the coast 4 km away. In addition, oxygen-18 values measured for individual rainfalls in this study varied widely ( $> 10$  o/oo range) with no obvious seasonal secular variation observed in the SCR V during the monitoring periods (Figure 4.1). This can be attributed to erratic fluctuations between marine and terrestrially-derived air masses accompanying the highly-changeable climatic conditions in eastern Newfoundland.

Stream and groundwaters in the SCR V are dilute, reflecting the low solubility of silicate minerals in the granite and glacial drift. Low flow stream waters have oxygen-18 and deuterium values (in per mille) around -5.7 o/oo and -46 o/oo, respectively (described below), which are enriched 0.5 o/oo (in oxygen-18) and 4.5 o/oo (in deuterium) compared to shallow groundwaters discharging along the reach. This is likely due to evaporative fractionation of Gull Pond East waters (the major contributor to the study reach at low flow, as described in Chapter 3) and means that low flow stream compositions do not represent discharging groundwater compositions along the study reach.

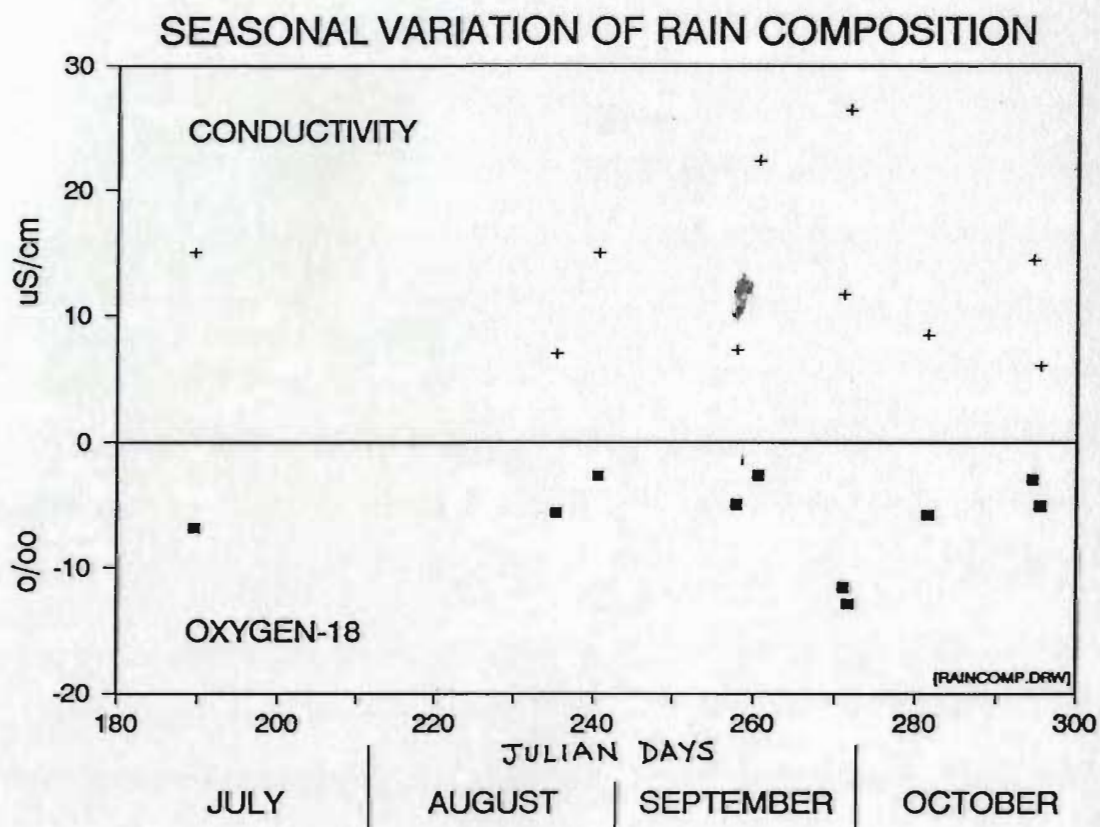


Figure 4.1 - Seasonal variation of conductivity and oxygen-18 for rainfalls in the SCR V in 1986 and 1987. These SCR V data display no obvious seasonal secular trends (e.g. summer enrichment and autumn depletion of oxygen-18 as shown by global precipitation data; e.g. Dansgaard, 1964).



As suggested in Chapter 3, groundwaters following deep flow paths and originating in headwater regions of the Seal Cove River drainage basin or adjacent basins probably do not contribute substantially to the hydrologic mass budget in the SCR. This is supported by a comparison of groundwater compositions in a 150 m-deep borehole in the Holyrood pluton 3 km north of the SCR (drilled as part of other graduate research in the Department of Earth Sciences at Memorial University) with those sampled in the SCR.

Groundwaters from lower levels of that hole, interpreted to be discharging from a regional flow system in the Seal Cove River drainage basin (N. Sargent, pers. commun.), are at or near calcite saturation and have chloride concentrations 5-10 times and specific conductances 2-3 times greater than groundwaters sampled in the SCR.

## 4.2 Methods

### 4.2.1 Hydrologic measurements and water sampling

Hydrologic measurements and water sampling for this study were carried out during August-October, 1986, and June-November, 1987, with infrequent preliminary groundwater sampling in 1985. Stormflows were not measurable during winter and spring periods due to freeze-up or high-discharge snow melt runoff, which flooded the weirs. Due to field monitoring and sampling difficulties, data for only two well-documented storm runoff events (starting September 27, 1986 and October 22, 1987) and four other 1987 events at peak flow conditions (described below) were available for study using reach mass balance methods.

Groundwater samples were collected during stormflow and low flow conditions throughout the monitoring period.

Rainfall was measured using standard and recording tipping-bucket rain gauges (R locations, see Figure 3.1). Stream flow was measured at three sites along the study reach using sharp-edged, contracted, rectangular weirs (W locations, see Figure 3.1) and Stevens strip chart recorders (Type F in 1986, Type E in 1987) with floats mounted in stilling wells. Discharge precisions were  $\pm 0.005$  m<sup>3</sup>/s in 1986 and  $\pm 0.011$  m<sup>3</sup>/s in 1987 (precisions differ because of differing gear ratios available for the float recorders).

Rain samples were collected from the standard gauge within 0.7-75 hours after rainfall events ended. Incremental rain samples, which can reveal time-varying rain compositions during storm events (e.g. McDonnell et al., 1990), were not collected, hence it was assumed that any given composite rain sample represents rain composition throughout that particular rainfall event. Isotopic fractionation of rain samples while in the gauge prior to collection was considered to be negligible (Appendix H).

Stream waters were sampled at the weirs, manually during low flow and automatically, using rain-activated CAN-AM<sup>R</sup> and ISCO<sup>R</sup> samplers, at 1-3 hour intervals during stormflow. The samplers were set to pre-rinse their intake tubes between each sample to avoid cross-contamination of samples.

Groundwaters in the granite were sampled to depths of up to 50 m from three open boreholes in 1985 (H2, H3 and H4; Figure 3.1) and six multilevel piezometers installed in these and other holes in 1986 and 1987 (H2, H3, H4, M1,

M2 and M3; Figure 3.1). Samples were collected from packed-off sections in open holes using gas-drive bladder pumps and from piezometer interval standpipes using peristaltic pumps and gas-drive samplers (Robin et al., 1982). Prior to sampling, each standpipe was purged to remove stagnant water. At piezometer M1, groundwaters were collected automatically using a Phillips sampler, at 3-6 hour intervals during storm runoff events in September and October, 1987. With this sampler, standpipe purging was not possible, so initial samples, corresponding to cumulative volumes equal to the interval standpipe volume, were discarded from each suite.

Several hundred stream, groundwater and rain samples were analyzed for oxygen-18 and conductivity, with subsets analyzed for major anion and cation concentrations and deuterium. Oxygen-18 was analyzed using CO<sub>2</sub> equilibration techniques using a sample preparation technique (Welhan and Schillereff, in prep.) which facilitates the analysis of large numbers of samples. Typical  $\pm 2\sigma$  measurement precisions were  $\pm 0.15$  o/oo or better, based on replicate standard analyses. Deuterium was analyzed at the Environmental Isotope Laboratory of the University of Waterloo, with  $\pm 2\sigma$  precisions of  $\pm 2$  o/oo. Conductivity (specific conductance) was measured using a portable Cole-Parmer meter (1985) and a laboratory-grade Radiometer CDM-3 meter (1986 and 1987). Conductivities for the 1986 samples were normalized to the 1987 values (1985

samples were not kept, so their conductivities could not be normalized). Measurement precisions ( $\pm 2\sigma$ ) were 0.5% of the conductivity value. Major anion concentrations were measured using high-pressure liquid chromatography (HPLC), yielding  $\pm 2\sigma$  precisions of  $\pm 0.1$  mg/l for chloride. Major cation concentrations were determined by flame atomic absorption, with  $\pm 2\sigma$  precisions of  $\pm 0.6$  (Ca),  $\pm 0.04$  (Mg),  $\pm 0.02$  (Na) and  $\pm 0.04$  (K) mg/l. Water samples collected early in this study were not handled or stored following standard protocols for cation analysis. The integrity of cation analyses of these samples was investigated by plotting the sum of cation meq/l versus conductivity for all analyses. Analyses plotting two or more standard deviations away from a regression line through all the data were rejected (equal to 7% of all cation data).

#### 4.2.2 Reach mass balance methods

Reach mass balance methods developed for this study are based on the premise that flow and mass inputs at the inflow end of a stream reach can be subtracted from those at the outflow end to determine contributions from a catchment adjacent to the reach (Figure 4.2). The reach hydrograph, defined by the ordinal difference between superposed outflow and inflow hydrographs, represents stream flow generated from the assumed catchment adjacent to the study reach.

The reach hydrologic approach differs substantially from conventional mass balance approaches for studying stream flow generation in the following ways:

- 1) By using measurements at inflow and outflow ends of a reach, rather than at a single outflow point from a basin, storage terms can be estimated for the reach

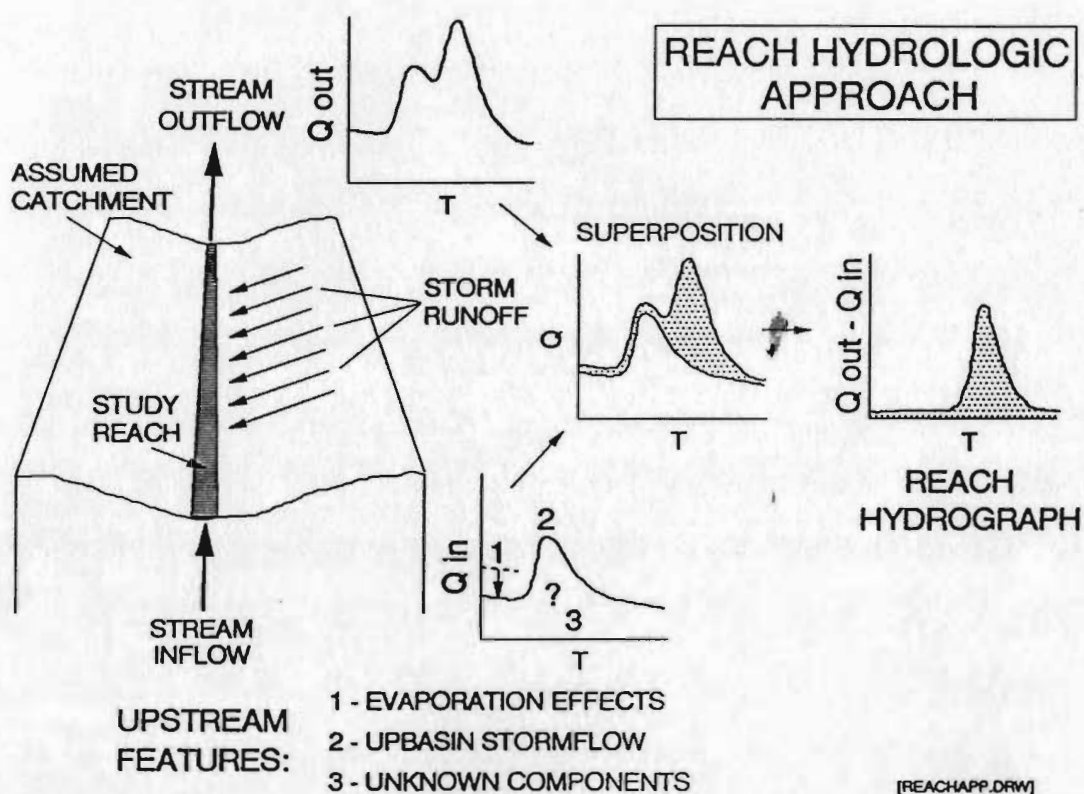


Figure 4.2 - Conceptual diagram illustrating the reach hydrologic approach. Upstream features numbered on the inflow hydrograph are discussed in the text.

channel and transient mass balance equations can be used. Thus, assumptions of steady-state conditions, necessary in conventional mass balance approaches, are not required. A transient mass balance approach is intuitively desirable in performing hydrograph separations since both stream discharge and composition can change rapidly during stormflow, especially at the outlet of a stream reach.

2) By measuring stream inflow and composition, variations in stream flow generated upstream of the study reach can be accounted for in the mass balance equations. Examples of such variations are stream composition changes due to evaporation, changes in stream discharge due to stormflow generated upstream, or variable ratios of stormflow components in upbasin storm runoff.

3) Knowing inflow and outflow mass fluxes for a reach and the composition of (new) rain water, it is possible, using methods described below, to specify varying compositions of pre-storm groundwater (old water) discharging into a study reach during stormflow. Thus, compositions of groundwater entering the reach need not be assumed or approximated from baseflow stream compositions, as is commonly done (e.g. Sklash et al., 1976; Hooper and Shoemaker, 1986).

Transient flow and mass balances for a stream reach can be expressed as:

$$Q_i + Q_g + Q_r - Q_o = \Delta V / \Delta t \quad [1]$$

$$C_i Q_i + C_g Q_g + C_r Q_r - C_o Q_o = \Delta(C_v V) / \Delta t \quad [2]$$

where,  $Q$  is discharge,  $C$  is concentration,  $V$  is volume in the reach channel, subscripts  $i$ ,  $o$ ,  $g$ ,  $r$  and  $v$  refer to stream inflow and outflow, groundwater (old pre-storm water), surface runoff (new event water), and average reach volume,

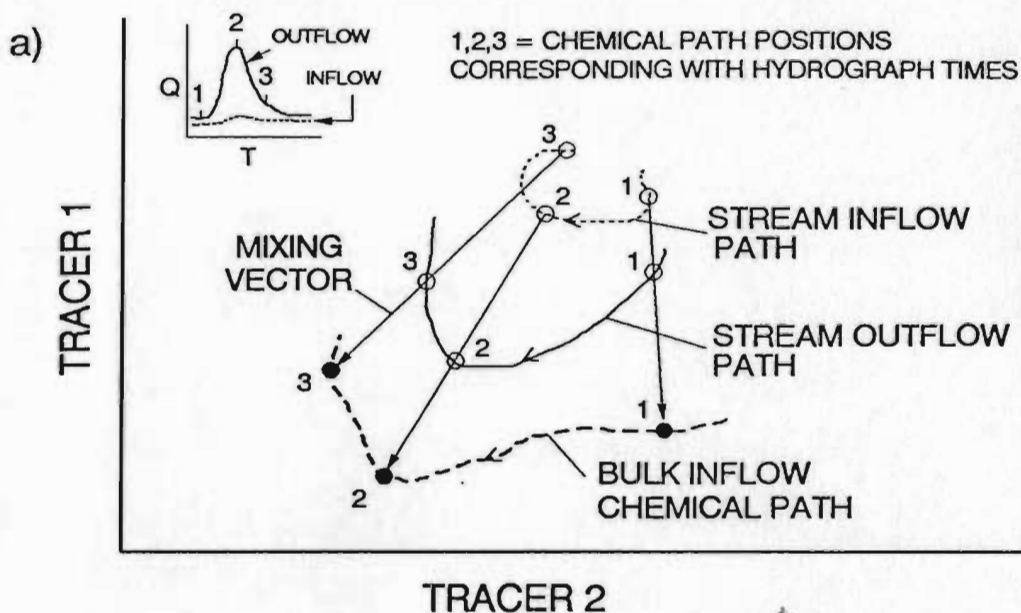
respectively, and the " $\Delta/\Delta t$ " notation refers to rate of change with time, approximated using finite differences. In this study, two related methods are developed from these equations - one for investigating compositional changes in a reach during stormflow using two independent tracers (referred to here as bulk inflow analysis) and the other for performing hydrograph separations of storm runoff generated along the reach, utilizing the results of bulk inflow analysis.

Figure 4.3 depicts the concepts of bulk inflow analysis, and is to be interpreted as follows. Inflow and outflow stream compositions along a reach will tend to follow different chemical paths (labelled in Figure 4.3a) during storm runoff, when compositionally different water from a catchment adjacent to the reach. Mixing vectors have been constructed passing through coeval points on these stream chemical paths. These vectors terminate at the bulk composition of water which flowed into the reach at any given time. The bulk compositions collectively form a bulk inflow chemical path. An equation for calculating bulk inflow compositions was derived from equations [1] and [2] by combining the flow terms  $Q_g$  and  $Q_r$  into a bulk inflow term,  $Q_{bi}$ , and the mass terms  $C_g Q_g$  and  $C_r Q_r$  into a bulk inflow mass term,  $C_{bi} Q_{bi}$ , then solving for bulk inflow composition ( $C_{bi}$ ):

$$C_{bi} = \{C_o Q_o + C_v (\Delta V / \Delta t) + V (\Delta C_v / \Delta t) - C_i Q_i\} / (Q_o + \Delta V / \Delta t - Q_i). \quad [3]$$

In Figure 4.3b, the position of a bulk inflow path with respect to composition fields for runoff waters is used to indicate the types and relative proportions of waters flowing into the reach from the adjacent catchment at different times during stormflow. For example, if compositions A and C in Figure 4.3b represent groundwater types and composition B represents rain, then bulk

### CONCEPT OF BULK INFLOW CHEMICAL PATH



### APPLICATION OF BULK INFLOW CHEMICAL PATH

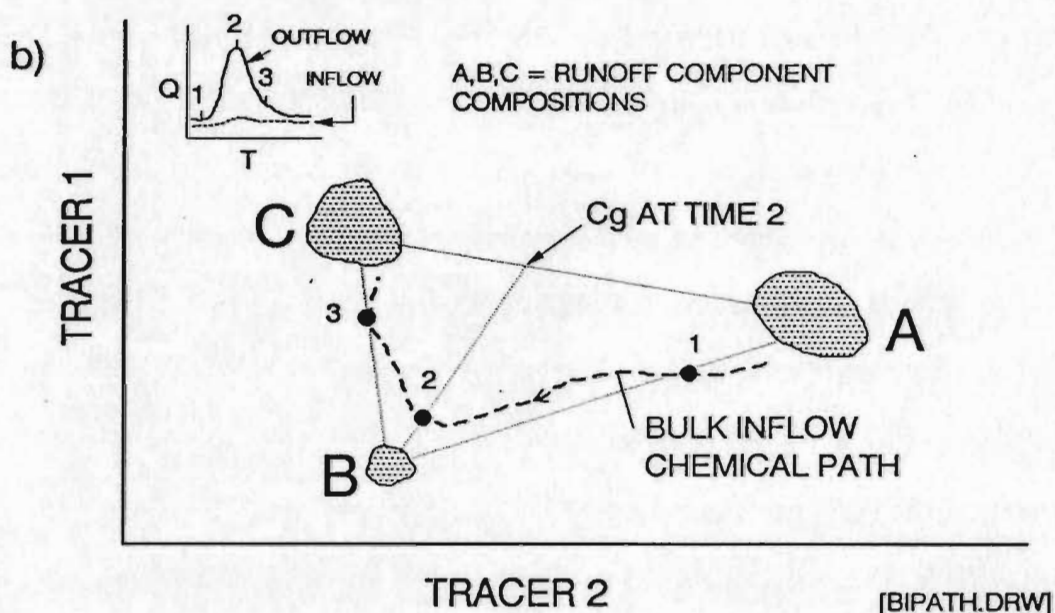


Figure 4.3 - Schematic diagrams depicting the concept of a bulk inflow chemical path (a) and the application of a bulk inflow chemical path (b) for indicating runoff compositions entering a reach during stormflow.



inflow would consist of an A+B mix dominated by groundwater A at time 1, an A+B+C mix dominated by rain water at time 2 and a C+B mix dominated by groundwater C at time 3. Groundwater (old water) compositions ( $C_g$ ) to use for hydrograph separation would in this case be composition A at time 1, an A:C mix (about 40:60) at time 2 and composition C at time 3. Bulk inflow analysis can also indicate the presence of unmeasured runoff compositions. For example, if groundwater A was considered to be the only pre-storm water source contributing to stormflow, the shift away from the A+B mixing line (i.e. at time 3) would indicate that another composition (i.e. C) was contributing to runoff.

A transient reach hydrograph separation equation was derived by combining equations [1] and [2], expanding  $\Delta(C_v V)/\Delta t$  as  $C_v(\Delta V/\Delta t) + V(\Delta C_v/\Delta t)$  and solving for groundwater (old water) discharge,  $Q_g$ :

$$Q_g = \{ \Delta V/\Delta t (C_v - C_r) + V(\Delta C_v/\Delta t) + Q_o(C_o - C_r) - Q_i(C_i - C_r) \} / (C_g - C_r) \quad [4]$$

where all terms are as defined above. An important limitation in using  $C_g$  values determined from bulk inflow analysis is that when the tracer coordinate values for  $C_g$  are independently used in equation [4], the calculated  $Q_g$  values are identical. This is a mathematical artifact of the derivation of equations [3] and [4] from the same mass balance equations ([1] and [2]) and means that the hydrograph separation results using tracer 1 cannot be used to corroborate those of tracer 2 when  $C_g$  is determined from bulk inflow analysis using the two tracers.

The principal assumptions made in developing and applying equations [3] and [4] are:

- 1) evaporative flow and mass losses from the reach are negligible during

stormflow;

- 2) sufficient contrasts exist between values of  $Q_o$  and  $Q_i$  and between values of  $C_g$  and  $C_r$  so that equations [3] and [4] are stable and yield acceptable precisions throughout stormflow;
- 3) flow and mass routing times along the reach are negligible compared with the duration of stormflow, i.e. changes at successive weirs along the reach can be considered coeval,
- 4) the entire study reach is effluent at all times, and,
- 5) inflow water to the reach (either stream inflow or lateral runoff) completely and promptly moves through and out of the reach without prolonged residence time in stagnant areas. Supporting this, the stream and beaver pond do not have heavy vegetation along their banks (which might slow stream velocity and increase residence time; Jim Hendry, pers. commun., 1992) and the beaver pond is continually cleared by through-flowing stream discharge.

The validity of these assumptions in the SCRIV, along with methods used in this study for evaluating transient storage terms ( $V$ ,  $\Delta V/\Delta t$ ,  $C_v$  and  $\Delta C_v/\Delta t$ ), are discussed in Appendix II. For clarity in the text below, it should be noted that  $Q_o$ - $Q_i$  and  $C_g$ - $C_r$  terms are referred to as flow and composition contrasts, respectively. The contrasts required to achieve acceptable reach hydrograph separation precisions are addressed in Appendix II.

Sensitivity analyses were performed on equation [4] by varying individual terms within their error range and noting effects on calculated  $Q_g$  values. These analyses indicate that reach hydrograph separation results are most stable 1) for storms where contrasts between  $C_g$  and  $C_r$  are greatest, 2) around peak flow, where contrasts between stream inflow and outflow discharges are greatest, and 3)

where stream inflow discharge remains low throughout stormflow. It is useful to note that sufficient contrast between  $C_g$  and  $C_i$  is not required, since stream inflow discharge ( $Q_i$ ) and mass ( $C_i$ ) terms are removed during application of the mass balance equations for the stream reach. Sensitivity analysis of the steady state hydrograph separation equation in the literature (e.g. Sklash et al., 1976) also shows that separation results are most stable around peak flow where contrasts between the mass fluxes of runoff components are greatest.

#### **4.3 Analysis of groundwater compositions in the study area**

To identify groundwater compositions involved in storm runoff (i.e. those to use as "runoff component composition" fields as in Figure 4.3b) and to discuss groundwater mixing relationships and the responses of groundwater compositions to hydrologic stress in the SCR V, it is necessary to describe groundwater compositional groups and the direction, magnitude and timing of groundwater compositional variations in the study area. These groundwater features are presented in this section and serve as a basis for analysis of stormflow in the SCR V presented in Section 4.4.

##### **4.3.1 Organization of groundwater data sets**

Groundwater compositional data for the SCR V are presented below in the form of discrimination diagrams (Figure 4.4) for identifying compositional groups in the study area and as variations with time (Figure 4.5, 4.6c and 4.7c) during a range of summer and autumn hydrologic conditions.

Figures 4.5a and b represent low rainfall (low stream flow) conditions

during the summer of 1986, while Figures 4.5c and d represent the transition from dry summer conditions to wetter autumn conditions in 1987. Groundwater variations during response to rainfall are presented for the September 27, 1986 and October 22, 1987 events in Figures 4.6c and 4.7c, respectively. Stormflow variations (Figures 4.6a and 4.6b) and stream compositional variations (Figures 4.6b and 4.7b) are discussed below in Section 4.4.

#### 4.3.2 Description of groundwater types and compositional variations

Groundwaters sampled in the SCRv are  $\text{Ca-HCO}_3$  type and are undersaturated with respect to calcite and amorphous silica, as indicated by solution modelling using the code PHREEQE (Parkhurst et al., 1980). This suggests that SCRv groundwaters are only slightly evolved and part of a meteorically-driven, actively-flushed, shallow flow system. Details of PHREEQE model input parameters and a complete listing of hydrochemical data used in this thesis are presented in Appendix J.

Trends in Figure 4.4a suggest that two main groundwater compositional groups occur in the SCRv - a group representing valley bottom and hillslope groundwaters (collectively identified by the M112-M2 trend) and a group representing very shallow, near-stream groundwaters (M114 trend).

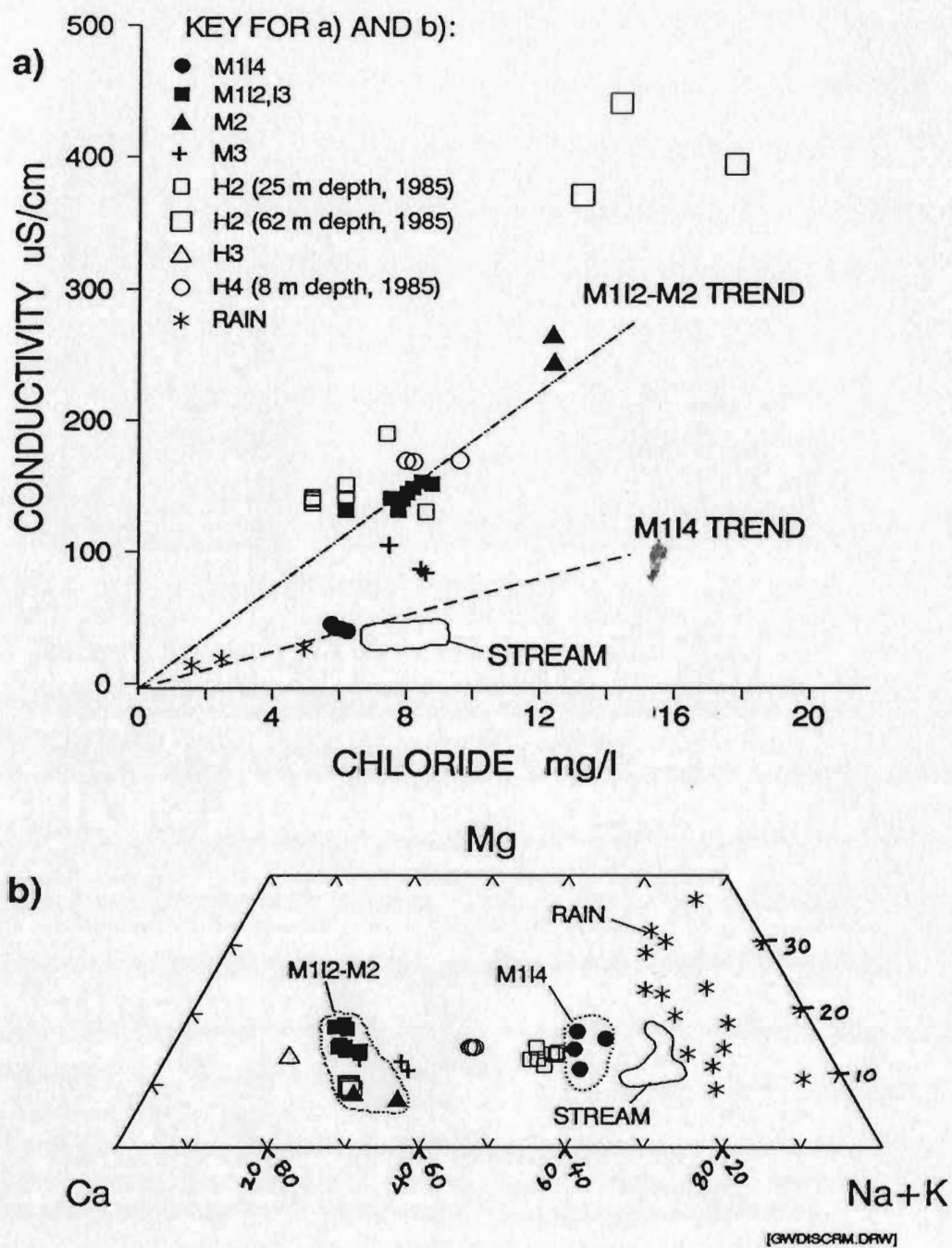


Figure 4.4 - Plot of conductivity versus chloride (a) and trilinear plot of cation concentrations (b) for rain, stream and groundwaters in the SCR.V.

The 1985 conductivities in Figure 4.4a are not normalized to the other data but fall generally along the M112-M2 trend. The presence of two groundwater compositional groups in the SCRv is also indicated by separate M114 and M112-M2 cation compositional fields in Figure 4.4b. As shown in Figure 4.4a and in oxygen-18-conductivity diagrams below (Figure 4.8), M112 and 13 groundwaters represent the approximate average compositions for shallow valley bottom groundwaters in the SCRv. Because of this, and due to the constant discharging conditions at M1 (described in Chapter 3), M114 and M112,13 groundwater compositions are used as runoff component fields in bulk inflow analysis in Section 4.4 below. It will be seen that these are reasonable choices given the range of uncertainty in bulk inflow chemical paths.

Groundwater compositional variations during the low rainfall period in the summer 1986 (Figure 4.5a and b) were subtle, with oxygen-18 changes of  $<0.5$  ‰ and conductivity changes of  $<5$   $\mu\text{S}/\text{cm}$  at M3 and  $<10$   $\mu\text{S}/\text{cm}$  at M1. Most of the oxygen-18 variations were near the magnitude of the  $\pm 2\sigma$  measurement uncertainties (shown as dotted error bars in these and other data figures). Systematic oxygen-18 enrichment and conductivity decreases at M3 for seven days following the small August 28 rainfall (10.2 mm) were likely due to infiltration of dilute, enriched rain water at M3 where recharge conditions prevailed. The systematic oxygen-18 depletion (up to 0.45 ‰) at M1 intervals during September 4-5 (M114 and M112 coincide on September 5) is notable since this did not coincide with any pronounced hydrologic stress. This was possibly due to the discharge of poorly mixed groundwater in the fractured granite past M1 toward the stream. Subtle compositional variations at M1 and M3 during a rainless period from July 8-16, 1987 (not shown here) were of similar magnitude ( $<0.5$

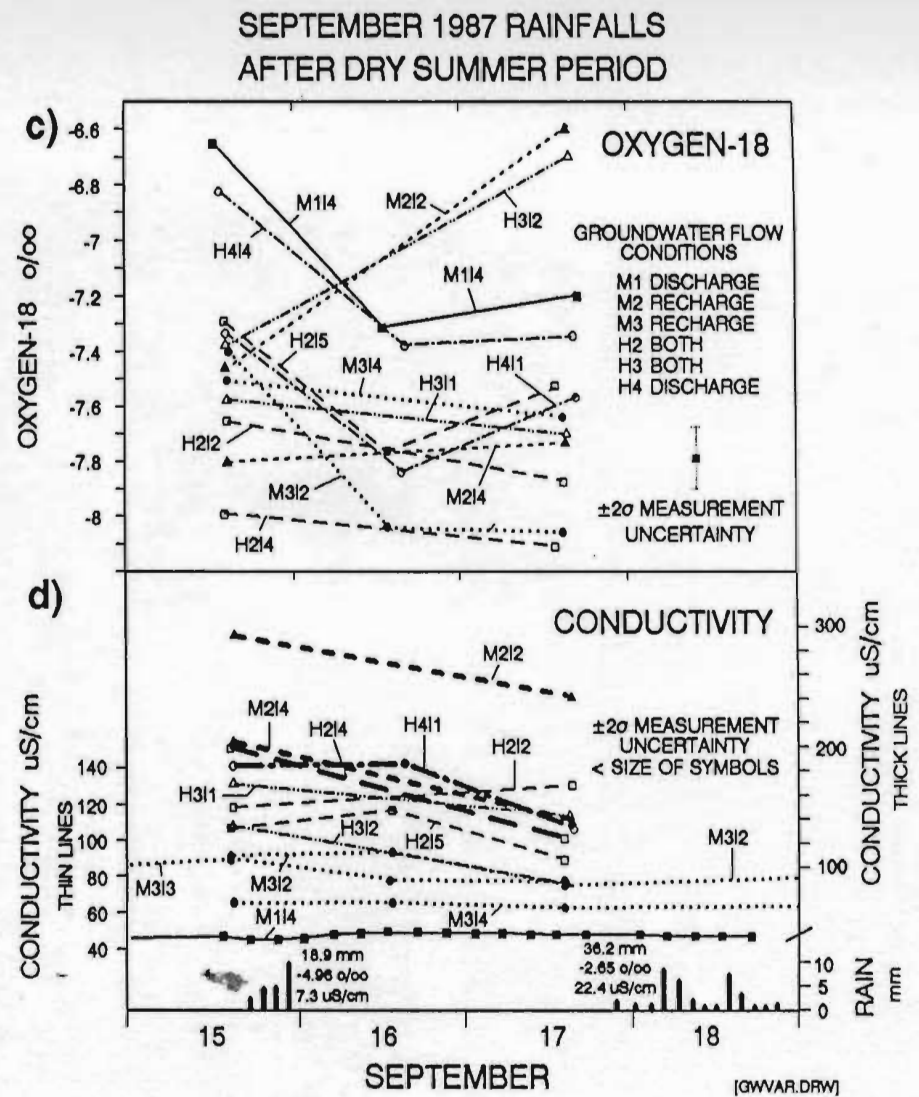
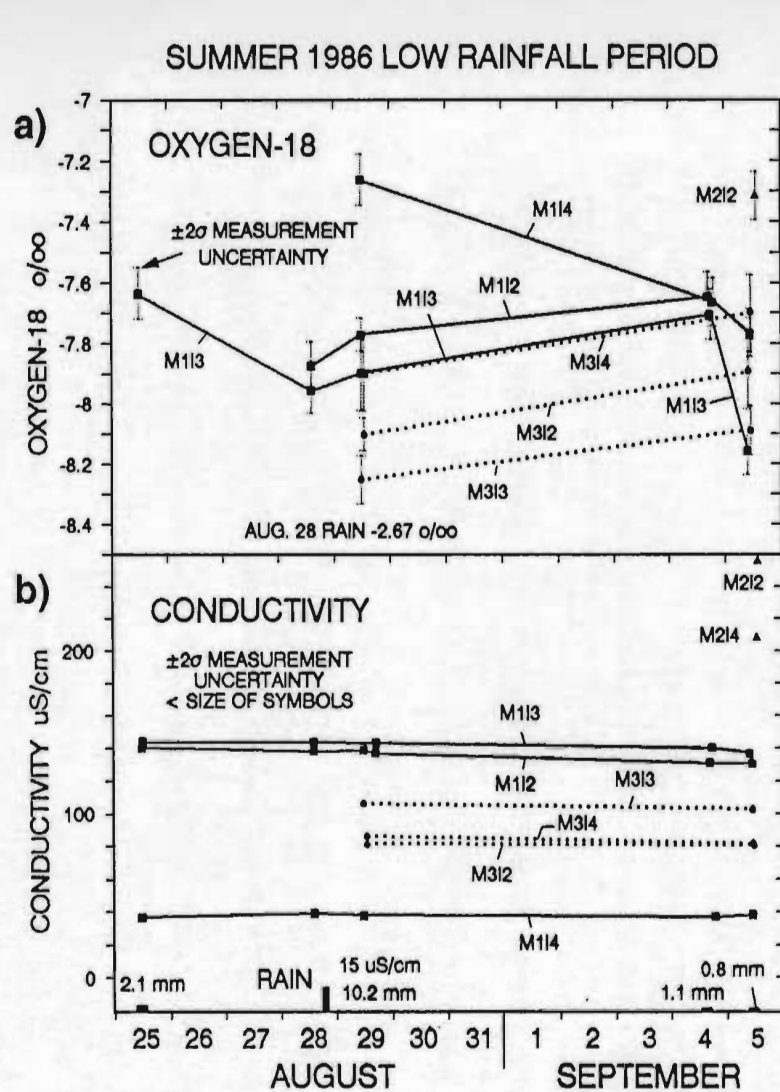


Figure 4.5 - Variations in groundwater oxygen-18 and conductivity during a low rainfall summer period in 1986 (a, b) and in response to rainfalls in September 1987 after a dry summer period (c, d). Groundwater flow conditions at the piezometers are indicated in (c). ("BOTH" indicates that both recharge and discharge gradients were developed within the piezometer).

o/oo and  $<6 \mu\text{S}/\text{cm}$ ) to those shown in Figure 4.5a and b.

Groundwater compositional variations in response to rainfall in mid-September, 1987 (Figure 4.5c and d) are marked by subtle changes during rainfall but substantial changes afterwards. Sequential samples from M114 (Figure 4.5d) show weak but well-defined conductivity decreases ( $<1.5 \mu\text{S}/\text{cm}$ ) during the September 15 rainfall. However, due to lack of similar sequential sampling at other piezometers, it is unknown if this apparent rapid compositional response occurred throughout the instrumented area.

More pronounced and widespread variations occurred during the two day period after the September 15 rainfall. Groundwaters sampled on September 16 tend to show oxygen-18 depletion (by 0.47-0.66 o/oo) and conductivity increases (of 0.5-10.4  $\mu\text{S}/\text{cm}$ ), compared with pre-storm values on September 15. Groundwaters sampled on September 17 show oxygen-18 enrichment (up to 0.27 o/oo) or a sharp decrease in rate of depletion (at M312), and conductivity decreases (of 1-53  $\mu\text{S}/\text{cm}$ ) compared with September 16 values. The widespread, systematic nature of the composition changes between September 15-16 and between September 16-17 suggests that similar changes also occurred in intervals not sampled on September 16 (e.g. at M212, H312, H212, etc.). Collectively, the observed compositional changes record a shift in the types of water mixing into piezometric intervals in the SCR.V between one and two days after rainfall. Mixing relationships determined for these variations, along with those for the September 27, 1986 and October 22, 1987 storm runoff events (described below), will be used to describe a characteristic two-stage response of groundwater compositions to storm stress in the SCR.V.



During the September 27, 1986 runoff event, M1 groundwater compositions (Figure 4.6c) showed systematic oxygen-18 depletion (by 0.27-0.66 ‰), reaching a maximum four days after rainfall, followed by slight enrichment. M1 groundwater conductivities showed subtle, nonsystematic changes ( $<3 \mu\text{S}/\text{cm}$ ) two days after rainfall, then systematic decreases (of 3.6-17.9  $\mu\text{S}/\text{cm}$ ) between two and four days after rainfall, followed by mild increases (of 0.7-7.9  $\mu\text{S}/\text{cm}$ ). Small chloride changes ( $<0.8 \text{ mg}/\text{l}$ ) generally correspond with the conductivity variations. The oxygen-18 and conductivity trends suggest that the groundwater compositional response at M1 lasted at least four days after the start of the September 27, 1986 rainfall. It is not known if similar prolonged responses occurred after the September 15 or October 22, 1987 rainfalls, due to interference from subsequent rainfall (September 17) and shorter record lengths for these runoff events.

During response to the October 22, 1987 storm event, M1 groundwater compositions (Figure 4.7c) showed oxygen-18 enrichment (0.76 ‰) and mild conductivity decreases ( $\leq 2 \mu\text{S}/\text{cm}$ ) at M112, while at M114, oxygen-18 changes were not significant and conductivities increased slightly. To more clearly reveal the M112 trends, three-point running averages, weighted by the magnitude of uncertainties in the raw data (after Taylor, 1982, p. 150), are shown in Figure 4.7c. Notably, the M112 changes appear to have begun just after the onset of rainfall (as with M114 conductivity decreases during the September 15, 1987 event; Figure 4.5d) and before the start of the storm hydrograph. This timing suggests that early composition changes in shallow, near-stream groundwaters for these runoff events in the SCR V were in rapid response to rainfall stresses and not due to stream water-groundwater interaction during the hydrograph rising limb (e.g. emplacement of bank storage). This point will be further discussed below (bank storage along the study reach is addressed in Appendix II). Due to less frequent

## SEPTEMBER 27, 1986 RAINFALL EVENT

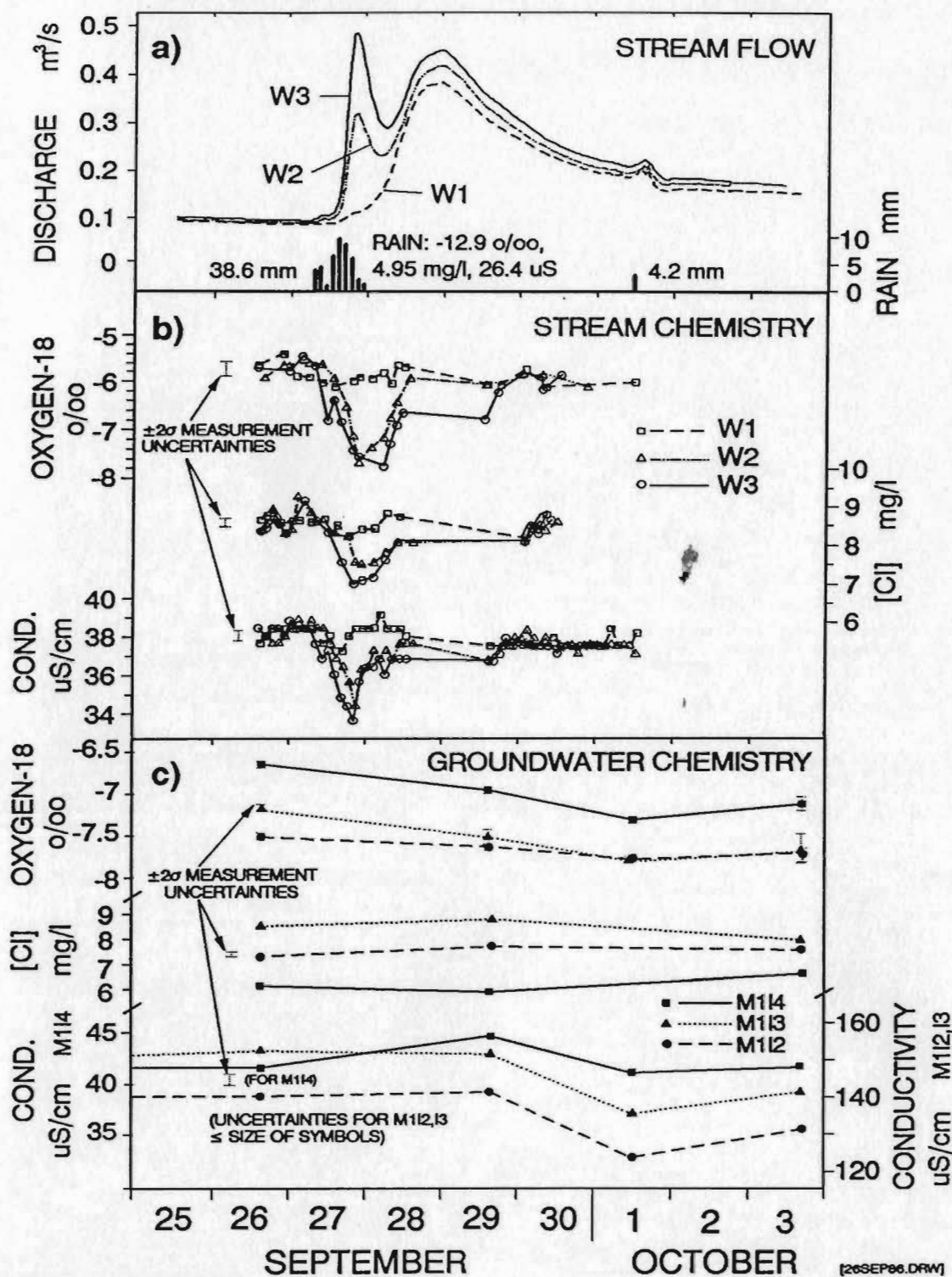


Figure 4.6 - Variations of stream flow (a), stream chemistry (b) and groundwater chemistry (c) in response to rainfall on September 27, 1986.

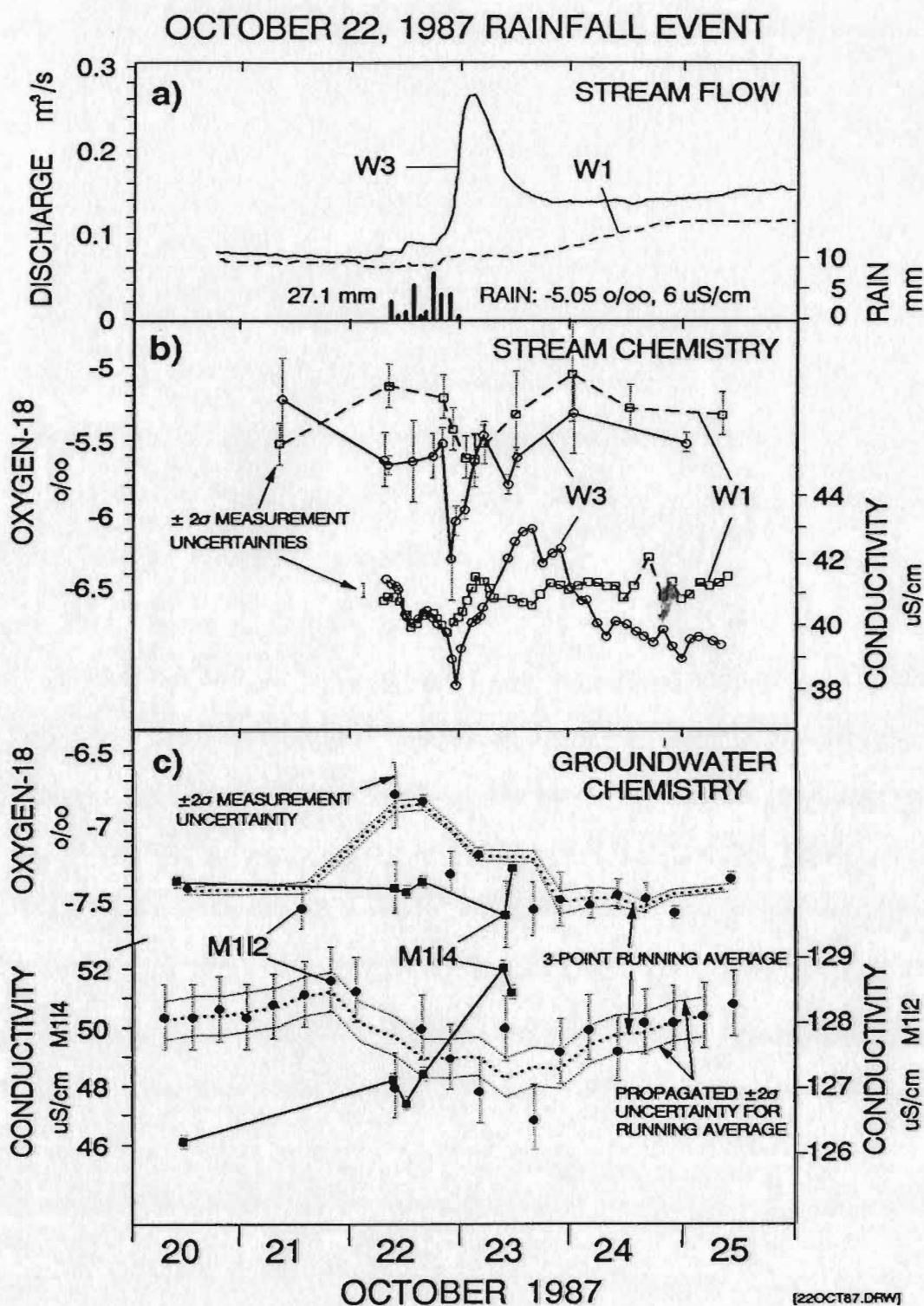


Figure 4.7 - Variations of stream flow (a), stream chemistry (b) and groundwater chemistry (c) in response to rainfall on October 22, 1987. Weighted three-point running average and associated  $\pm 2\sigma$  uncertainty limits for M1I2 groundwater compositions highlight the oxygen-18 enrichment and subtle conductivity decrease during response to the storm event.

groundwater sampling, it is unknown if similar variations occurred with the onset of the September 27, 1986 rainfall (Figure 4.6c).

#### 4.3.3 Groundwater mixing relationships

To further investigate groundwater compositional variations in response to precipitation in the SCR, groundwater mixing relationships were analyzed for the September 27, 1986, and September 15 and October 22, 1987 runoff events. These relationships are used to identify common features of groundwater compositional response to storm stress in the SCR.

Figure 4.8 presents the results of groundwater mixing analyses using oxygen-18-conductivity variations for the above runoff events. The mixing analyses are based on relationships between directed mixing lines and their error ranges (shown as the patterned wedges in Figure 4.8) and groundwater compositional fields (shown as open fields in Figure 4.8). All of these features are explicitly labelled in Figure 4.8a. The groundwater fields were compiled from all 1986-87 SCR groundwater data (the few 1985 data were excluded since conductivities were not normalized to 1987 data). Figure 4.8 should be interpreted as follows. The mixing lines pass through points defined by groundwater compositions present at different times in a given piezometric interval. The mixing lines point towards compositional fields for waters which could have mixed into that sampling interval to produce the observed compositional changes. The error ranges for the mixing lines represent the maximum errors possible in constructing the lines, based on the extreme values of the  $\pm 2\sigma$  uncertainties for the data points. Different shading patterns for the error ranges are used to identify different time intervals in relation to the onset of

rainfall. These time intervals along with line types used to identify different piezometric intervals are given in a key for each plot in Figure 4.8. By focusing on the direction of the patterned wedges and their intersection with compositional fields for potential mixing waters, the interpretation of groundwater mixing relationships presented in Figure 4.8 should be clear.



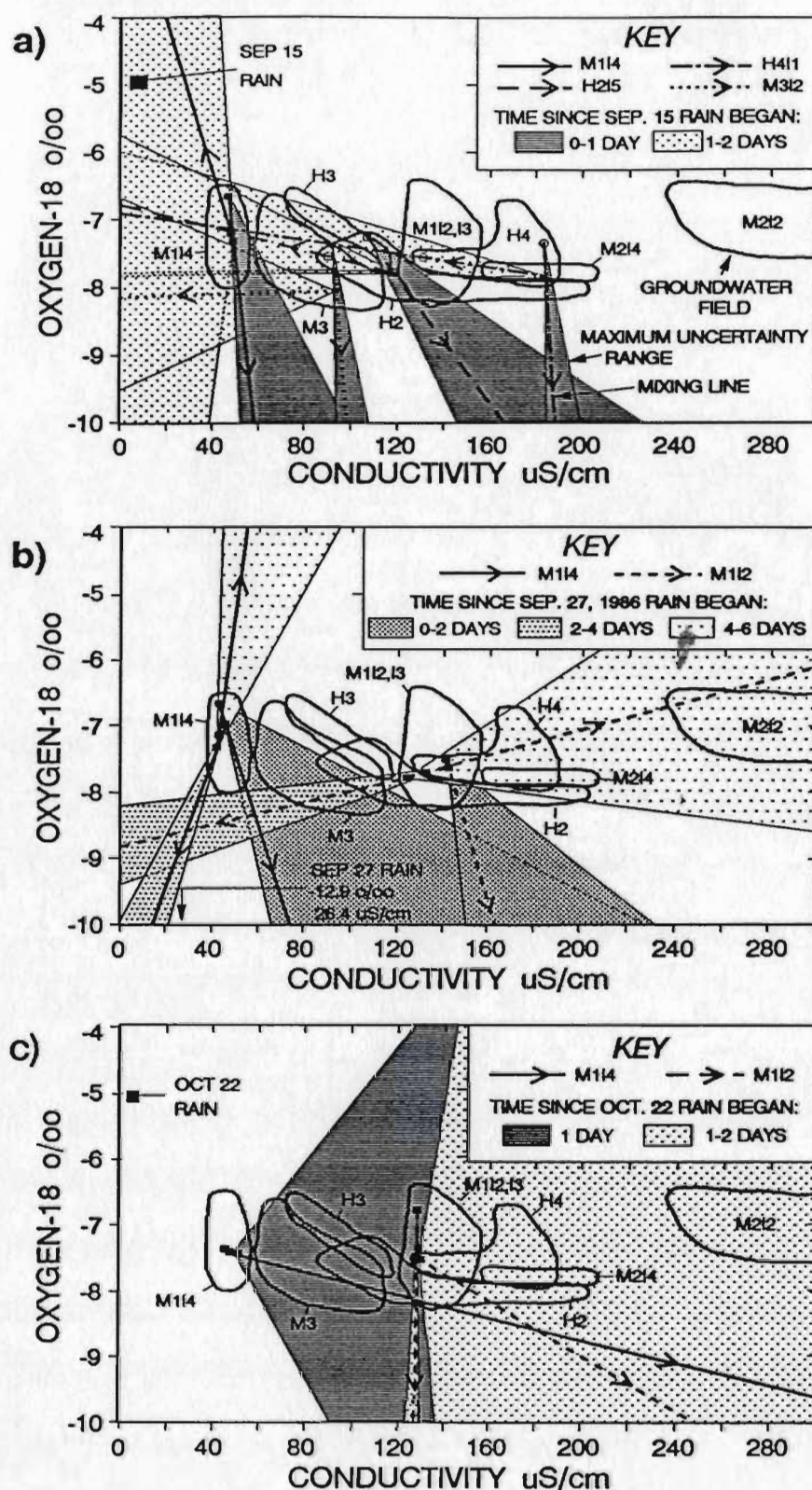


Figure 4.8 - Groundwater mixing relationships in response to rainfalls on September 15, 1987 (a), September 27, 1986 (b) and October 22, 1987 (c). Interpretation of the diagrams is described in the text.

September 15, 1987 runoff event

Groundwater mixing for the September 15, 1987 runoff event is presented first (Figure 4.8a) since a wide variety of piezometric intervals are represented and the mixing patterns are conspicuous. Mixing lines are shown for all piezometric intervals where composition changes were documented during the September 15-16 and 16-17 periods in Figure 4.5c and d (i.e. at M1I4, H2I5, H4I1 and M3I2).

The pronounced shift from downwards-directed mixing lines (during the first day after rainfall) to left-directed mixing lines in Figure 4.8a documents a general trend towards mixing of groundwaters in the SCR V with shallow recharging groundwaters or rain water on the second day following this rainfall. Mixing between groundwaters and rain water during the first day after rainfall is not indicated for any of the piezometric intervals, including at M3 where recharge gradients prevailed. In this light, it is interesting to infer the mixing behaviour at other piezometric intervals, especially at M2I2 and H3I2 showing substantial post-storm enrichment (Figure 4.5c). If M2I2 and H3I2 compositions followed a post-storm depletion-enrichment trend similar to that for the four intervals included in Figure 4.8a), then their oxygen-18 enrichment during the second day after rainfall would have been around 1 ‰, i.e. stronger than at the other intervals. This stronger enrichment is consistent with strong recharge gradients developed at M2 (around 0.8 m/m; e.g. Figure 3.10) and with the location of H3 (also with a recharge gradient during storm response as inferred from the October 22, 1987 storm response; Figure 3.10) down-gradient from M2 at the base of the hillslope.

#### September 27, 1986 runoff event

Figure 4.8b shows groundwater mixing relationships at M114 and M112 in response to the September 27, 1986 rainfall. Mixing at M113 (not shown) mimics the M112 trends. For the 0-2 day interval, mixing trends down and to the right of the rain composition, suggest that mixing at M114 and M112 did not involve rain water. This pattern is consistent with mixing trends during initial response to the September 15, 1987 rainfall (i.e. 0-1 day period; Figure 4.8a). For the 2-4 day interval in Figure 4.8b, mixing at M114 could have involved rain water as well as other M114 compositions and mixing at M112 could have involved H2-, M3- or other M112,13 compositions. This shift toward mixing with shallow recharging groundwaters or rain is the same pattern developed during the secondary response to the September 15, 1987 rainfall. For the 4-6 day interval in Figure 4.8b, mixing at M114 involved only other M114 compositions, whereas mixing at M112 could have involved H4, M2 or other M112,13 compositions. Implications regarding travel distances and rates of shallow groundwater flow stemming from this possible late-stage arrival at the stream of groundwaters originating at the hillslope (i.e. at M2) during this runoff event are discussed below.

#### October 22, 1987 runoff event

Figure 4.8c shows groundwater mixing relationships for M114 and M112 in response to the October 22, 1987 rainfall. Because of the mild variations in M114 oxygen-18 and M112 conductivity (Figure 4.7c), mixing trends are weakly defined and have broad uncertainty ranges. Nevertheless, the direction of mixing trends down or to the right, away from the October 22 rain composition, suggests that rain water was not involved in mixing at M114 during the first day or at M112



during the first two days after rainfall began.

#### Common responses of SCR/V groundwater compositions to storm stress

Determining common or characteristic responses of groundwater compositions to hydrologic stress in the SCR/V is constrained by the small number of data sets available in this study and the limited areal extent of sampling in the instrumented area (except for the September 15, 1987 runoff event; Figure 4.5c and d). Other constraints are the lack of data for winter or spring periods, the shallow depths of groundwater sampling (<50 m, most <15 m), and scarcity of sequential sample suites with short collection time intervals. Nevertheless, within these constraints, common features of groundwater compositional response during stormflow conditions in the study area can be identified as described below.

Persistent compositional differences within piezometers (e.g. at M1 or M3; Figures 4.4, 4.5 and 4.6) supports a hypothesis that shallow groundwaters in the SCR/V are inhomogeneous and move within separate plumbing systems at small spatial scales (i.e. on order of a few meters). This is consistent with the fracture filling/drainage mechanism proposed for the physical response of groundwater to storm stress (Chapter 3) and will be further discussed below.

Groundwater compositional variations due to storm stress can start soon after the onset of rainfall and persist for up to four days or more. Groundwater mixing during storm stress in the SCR/V appears to progress in two stages:

- 1) an initial response, ending approximately 1-2 days after start of rainfall, during which compositionally heterogeneous groundwaters, adjacent to sampling intervals, are displaced in stream-ward directions, without mixing with rain water; followed by,

2) a secondary response, ending approximately 4 days after the start of rainfall, during which mixing shifts to involve more near-surface or recharging groundwaters, or rain water.

This two-stage response was noted for runoff events with wide ranging rainfall amounts and antecedent moisture conditions (i.e. for the September 15, 1987 rainfall - 18.9 mm, very dry beforehand; and the September 27, 1986 rainfall - 38.6 mm, moderately wet beforehand; see Table 4.1). This suggests that the presence or absence of this two-stage pattern does not depend strongly on these hydrologic parameters. The absence of a clear secondary response to the October 22, 1987 storm is likely due to the concentration of that rainfall in areas away from the study reach in the assumed catchment (as described below), so that abundant recharging groundwater or rain water would not have been available to mix into near-stream M1 intervals.

Finally, possible late-stage arrival of hillslope-derived groundwaters at the stream reach (for the September 27, 1986 event) may constitute a third storm response stage. Transit from the hillslope to the stream (a distance of 100 m or more) in four days requires average groundwater velocities on the order of 25 m per day. Such velocities would be considered abnormally high for most porous unfractured media, but are possible within the open, near-surface fracture system present in the study area (Chapter 2).

#### **4.4. ANALYSIS OF STORMFLOW IN THE STUDY AREA**

##### **4.4.1 Description of storm runoff events**

Table 4.1 - Hydrologic characteristics of rainfalls referred to in this study

<u>Rainfall date</u>	<u>Duration (hours)</u>	<u>Depth (mm)</u>	<u>Average intensity (mm/hour)</u>	<u>Antecedant moisture conditions</u>
<u>1986</u>				
Aug. 28	18.3	10.2	0.56	62/21* (dry)
Sep. 17	21.1	24.2	1.15	61/39 (dry)
Sep. 27	16.6	38.6	2.33	94/10 (mod. wet)
<u>1987</u>				
Jul. 5	26.0	33.9	1.30	29/22 (very dry)
Aug. 23	9.5	18.1	1.91	64/20 (dry)
Sep. 15	10.0	18.9	1.89	46/23 (very dry)
Sep. 17	24.0	36.2	1.51	65/2 (wet)
Sep. 26	6.0	15.8	2.63	84/8 (wet)
Oct. 8	8.5	10.0	1.18	120/7 (wet)
Oct. 22	18.5	27.1	1.46	67/13 (mod. dry)

\* antecedant moisture ratio, defined here as total rainfall (mm) over preceding 30 days divided by number of days since rainfall exceeded 10 mm

The September 27, 1986 and October 22, 1987 storm runoff events are used here for detailed bulk inflow and hydrograph separation analysis. In addition, data for four other runoff events in 1987, collected under peak flow conditions, were analyzed to illustrate limitations in the application of bulk inflow analysis and to provide additional stormflow generation information.

Stream flow and stream chemistry variations for the September 27, 1986 and October 22, 1987 runoff events are shown in Figures 4.6 and 4.7, respectively. For both events, runoff from the assumed catchment generated sharp hydrograph peaks lasting approximately one day (Figures 4.6a and 4.7a). A large floodwave from upstream passed through the reach during the September 27, 1986 event, but did not appear during the October 22, 1987 event. This indicates that the September 27, 1986 rainfall was more extensive on upper parts of the Seal Cove River drainage basin than was the October 22, 1987 rainfall. The lag time between the September 27, 1986 rainfall and arrival of the floodwave can be attributed to flood routing time within upper parts of the basin and within Gull Pond East, or to later rainfall within the headwater regions compared with the study area, or both. Flow and mass inputs for this lagged inflow are removed from those of the assumed catchment by the application of the reach mass balance equations.

For both events, stream composition changes increased in magnitude downstream from weir W1, indicating that chemical mass flux was added to the reach from the assumed catchment. The generally subtle compositional variations at W1 are assumed to reflect the insensitivity of outflow compositions from Gull Pond East to individual storm events and to the only minor amounts of rapid runoff added to the stream between Gull Pond East and W1 (as suggested by

topography and increased vegetation on the hillslope just south of the study area).

Along the study reach, stream chemistry changes commenced with the start of rainfall for both storms but reached extreme values earlier during October 22, 1987 storm runoff (at times corresponding with the rising limb) than during the September 27, 1986 runoff event (at or just after peak stormflow). This reflects differences in the timing and sources of stream flow generation for these two storms which may be attributed to the differences in rainfall distribution within the assumed catchment. This is further shown by the timing of peak flow in relation to rainfall for the two events. The initial peak flow for the September 27, 1986 storm hydrograph (at W2 and W3, Figure 4.6a) coincided with rainfall, while peak flow for the October 22, 1987 storm hydrograph (at W3, Figure 4.7a) occurred after rainfall had ceased. This difference suggests that the September 27, 1986 rainfall was likely concentrated near the study reach, producing prompt stormflow, whereas the October 22, 1987 rainfall was likely concentrated away from the stream (i.e. on the hillslope), with stormflow lagged by increased travel time to the reach. Actual rainfall distributions for these storms cannot be directly compared because there were too few rain gauges used and the gauges were deployed in different patterns in 1986 and 1987 (Figure 3.1).

Finally, rainfall amount was greater and antecedent moisture conditions were damper for the September 27, 1986 event than for the October 22, 1987 event (Table 4.1). These factors, along with the stormflow and inferred rainfall distribution differences mentioned above, suggest that the hydrologic stresses induced in the SCR by these two storms were fundamentally different. This manifests itself in the form of differing groundwater mixing patterns (described above). The compositions and proportions of groundwater runoff components

during both events are discussed below.

#### 4.4.2 Bulk inflow analysis

##### Description of bulk inflow plots

Figure 4.9 shows results of bulk inflow analyses for the September 27, 1986 and October 22, 1987 runoff events, while Figure 4.10 shows results for the four runoff events in 1987 sampled at peak flow. These results are discussed in turn in this section and used to interpret hydrograph separation results in Section 4.4.3.

The numbered points on Figures 4.9b-h represent bulk inflow compositions for corresponding numbered times on the pertinent hydrographs in Figure 4.9a. Uncertainties for bulk inflow compositions (dotted bars) represent  $\pm 2\sigma$  uncertainties propagated through equation [3] (above). Bulk inflow compositions with large uncertainties spanning the entire range of the plots (e.g. point 1 for the October 22, 1987 stormflow) were omitted for clarity. Due to lack of stream chloride data, there are no bulk inflow compositions for point 7 in Figures 4.9d, f and h.

Rain compositions for each particular event and compositional fields for groundwaters possibly discharging into the stream (M114 and M112,13) are included in the bulk inflow plots. Bulk inflow compositions (within their uncertainty ranges) in Figure 4.9 generally trend along or between rain-M114 groundwater or rain-M112,13 groundwater mixing lines, supporting the use of these M1 groundwater fields as likely compositions of groundwater stormflow components. Further supporting this usage, M112,13 groundwater compositions

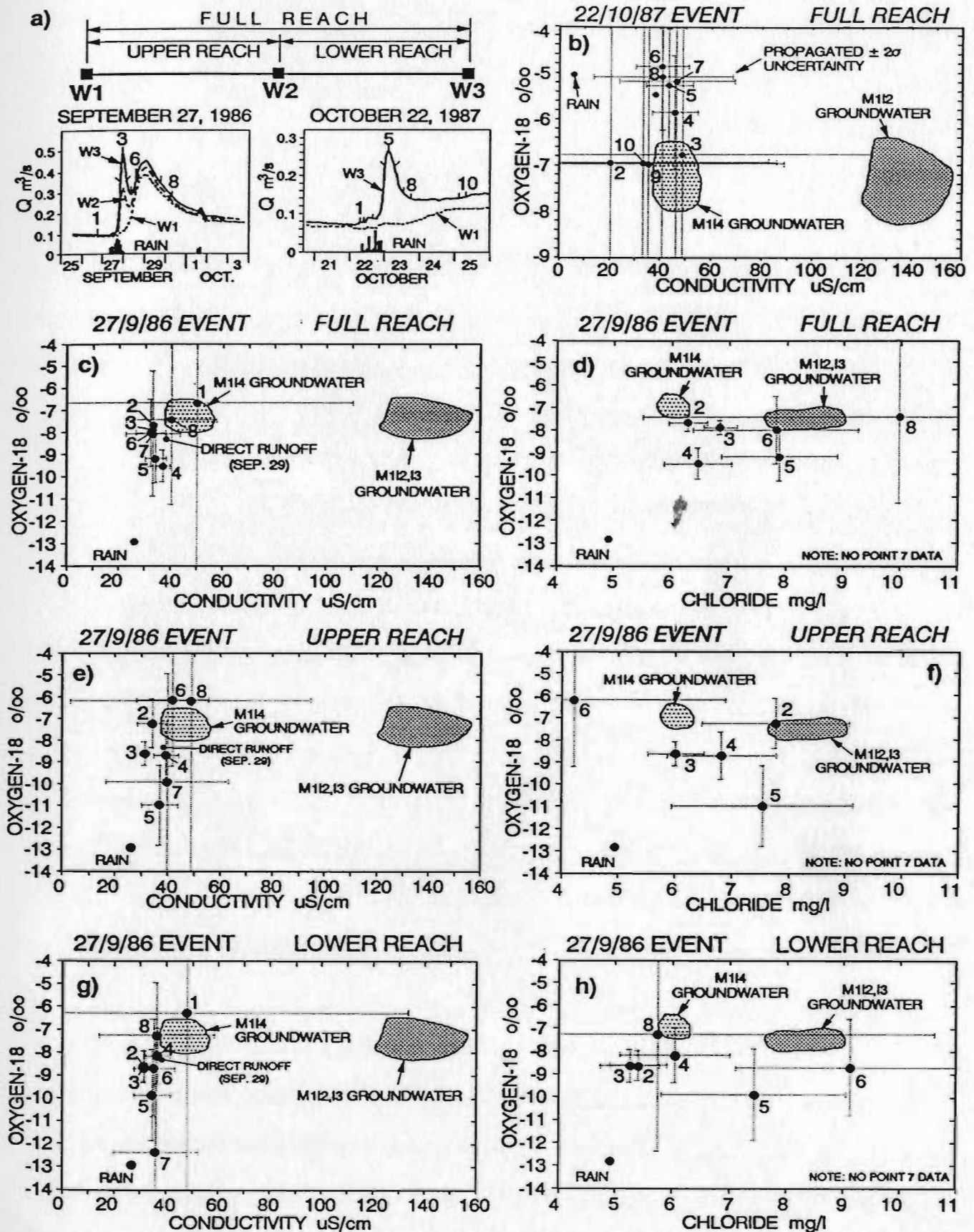


Figure 4.9 - Bulk inflow plots for the October 22, 1987 (b) and September 27, 1986 (c-h) runoff events. Labelling for reach sections and reference times for hydrographs are shown in (a). Interpretation of plots is described in the text.

can be considered to represent the average valley bottom groundwater compositions, as mentioned above.

#### Bulk inflow analysis for the October 22, 1987 runoff event

Bulk inflow for the October 22, 1987 runoff event is analyzed first since its storm hydrograph is simple. Figure 4.9b shows that bulk inflow composition uncertainties are lowest around peak flow (points 4, 5 and 6), which is a direct result of increased contrasts between stream discharge at W1 and W3. At other times during the storm hydrograph, bulk inflow compositions have large uncertainties and cannot be used to unequivocally specify runoff component mixtures in the reach. As an example, the large uncertainty for point 3 means that bulk inflow during rainfall and before the rising limb could have been dominated by rain (as direct channel precipitation) or a mixture of rain with M114 or, equally, with M112 groundwater. However, the tendency for bulk inflow compositions during pre- and post-hydrograph periods (i.e. points 2, 3, 9 and 10) to cluster around the M114 field and the progression of bulk inflow compositions away from the M114 field during peak flow (i.e. points 4, 5 and 6) suggest that M114 groundwaters dominated bulk inflow into the reach before and after peak October 22, 1987 stormflow.

Points 4, 5 and 6 in Figure 4.9b can be interpreted to indicate a progression towards mixing between rain and M112,I3 groundwater during peak stormflow. This, taken together with the inferences above, suggests that groundwaters discharging into the study reach shifted from M114-compositions before and during the October 22, 1987 rainfall, to M112,I3-compositions during peak stormflow, then back to M114-compositions after stormflow. Groundwater



components for this runoff event can thus be considered to range between limits defined by hydrograph separation results using measured M114 and M112 groundwater compositions for the  $C_g$  term in the reach mass balance (equation 4).

#### Bulk inflow analysis for the September 27, 1986 runoff event

Bulk inflow compositions on the oxygen-18-conductivity plots (Figures 4.9c, e and g) suggest that M114-type groundwater dominated discharge to the reach during low flow (e.g. point 1, Figure 4.9c) and recession (e.g. point 8, Figures 4.9e and g) periods. This is similar to the inferred M114 groundwater domination of bulk inflow before and after the October 22, 1987 stormflow peak above.

Well-constrained bulk inflow compositions during the rising limb and at peak flow (points 2 and 3, respectively) in Figures 4.9c, e and g plot slightly to the left of a mixing zone between the September 27 rain composition and the M114 groundwater field. This suggests that bulk inflow during these times comprised rain water mixed with near-stream (M114-type) groundwaters with slightly lower conductivities than those delineated within the plotted M114 field. This is plausible given the time-varying heterogeneity of groundwater compositions in the study area (described above) and the probability that samples from M114 may not fully represent very near-stream groundwaters along the reach.

An alternate possibility, that mixing during the rising limb and peak flow involved compositions in the M114 field and a different rain composition (or compositions), seems unlikely for the following reasons. The September 27, 1986 rain composition is well-constrained by two oxygen-18 and four conductivity measurements, with uncertainty ranges smaller than the size of the rain symbol in

the figures. The possibility that early September 27, 1986 rainfall may have been initially much more enriched in oxygen-18, so that points 2 and 3 in Figures 4.9c, e or g could fall along more gently-sloping "initial rain"-M114 groundwater mixing lines, seems unlikely as this would require excessive depletion ( $\geq 4$  o/oo) during subsequent rainfall to produce the measured rain oxygen-18 value (-12.9 o/oo).

In contrast to trends in Figures 4.9c, e and g, bulk inflow compositions in the oxygen-18-chloride plots (Figures 4.9d, f and h) are more scattered and lie between rain-M114 groundwater and rain-M112,13 groundwater mixing lines, suggesting that a mixture of M114 and M112-type groundwaters contributed to storm runoff during and after peak stormflow. In Figure 4.9f, point 6 is probably spurious due to the fact that stream discharges at this time (on rising limb of inflow floodwave; Figure 4.9a) were rapidly changing and very nearly identical. Trends in Figures 4.9d, f and g, taken with the inferred M114 domination during low flow periods, suggests that groundwaters discharging into the study reach may have shifted toward domination by M112,13 (i.e. valley bottom) compositions during peak stormflow, similar to trends for the October 22, 1987 event above. Differences between bulk inflow trends using chloride or conductivity tracers paired with oxygen-18 are likely due to non-conservative behaviour of conductivity during the September 27, 1986 stormflow (further discussed below).

#### Bulk inflow analysis for the ancillary 1987 runoff events

Figure 4.10 is a bulk inflow plot for the four 1987 runoff events measured at peak stormflow and illustrates the effects of different flow and composition contrasts on the ability to specify bulk inflow mixing components. Bulk inflow composition uncertainty is smallest for the September 17 event since the flow

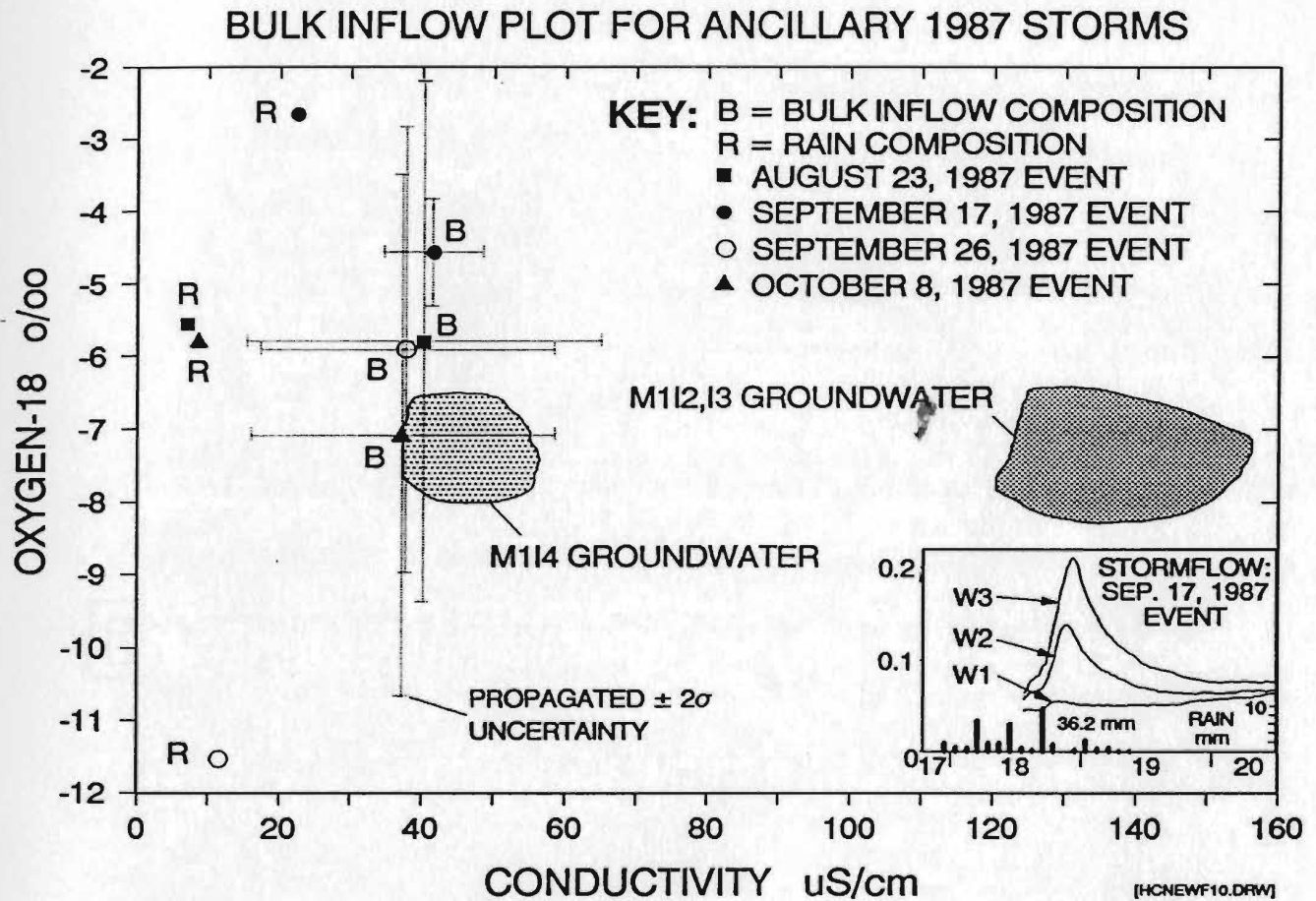


Figure 4.10 - Bulk inflow plot for four runoff events at peak flow conditions in 1987.

contrast was largest for that storm compared with the other storms (Table 4.2). The bulk inflow composition for the September 17 event suggests that bulk inflow included both M114 and M112,13 groundwater compositions, which is consistent with other bulk inflow mixing results above.

Bulk inflow compositions for the August 23 and October 8 events are too poorly constrained to specify groundwater types involved in storm runoff due to insufficient flow contrasts (Table 4.2), although they are consistent with inflow of rain and M1-type groundwaters. For the September 26 event, it is interesting to note that, even though the bulk inflow composition is highly uncertain, its relation with the strongly depleted September 26 rain composition indicates that bulk inflow at that time involved predominantly rain and M114-type groundwater. This shows that, in special cases where flow contrasts are low but runoff chemistry is well-poised and composition contrasts are high, bulk inflow analysis can still indicate the types of water involved in runoff, even though hydrograph separation results (requiring adequate combined flow and composition contrasts) may be poorly constrained.

#### 4.4.3 Reach hydrograph separation

Figures 4.11 and 4.12 show reach hydrograph separation results for the October 22, 1987 and September 27, 1986 runoff events, respectively. In these figures, reach  $Q$  represents the difference between outflow and inflow stream discharges along the reach and  $Q_g$  stands for the groundwater component of reach  $Q$ . Direct precipitation onto the reach channel for these events was 0.007-0.02 m<sup>3</sup>/s, based on rainfall intensity and reach channel area (17721 m<sup>2</sup>), which is less than or equal to reach  $Q$  uncertainty. Hydrograph separation results were

# **HYDROGRAPH SEPARATIONS FOR THE OCTOBER 22, 1987 EVENT**

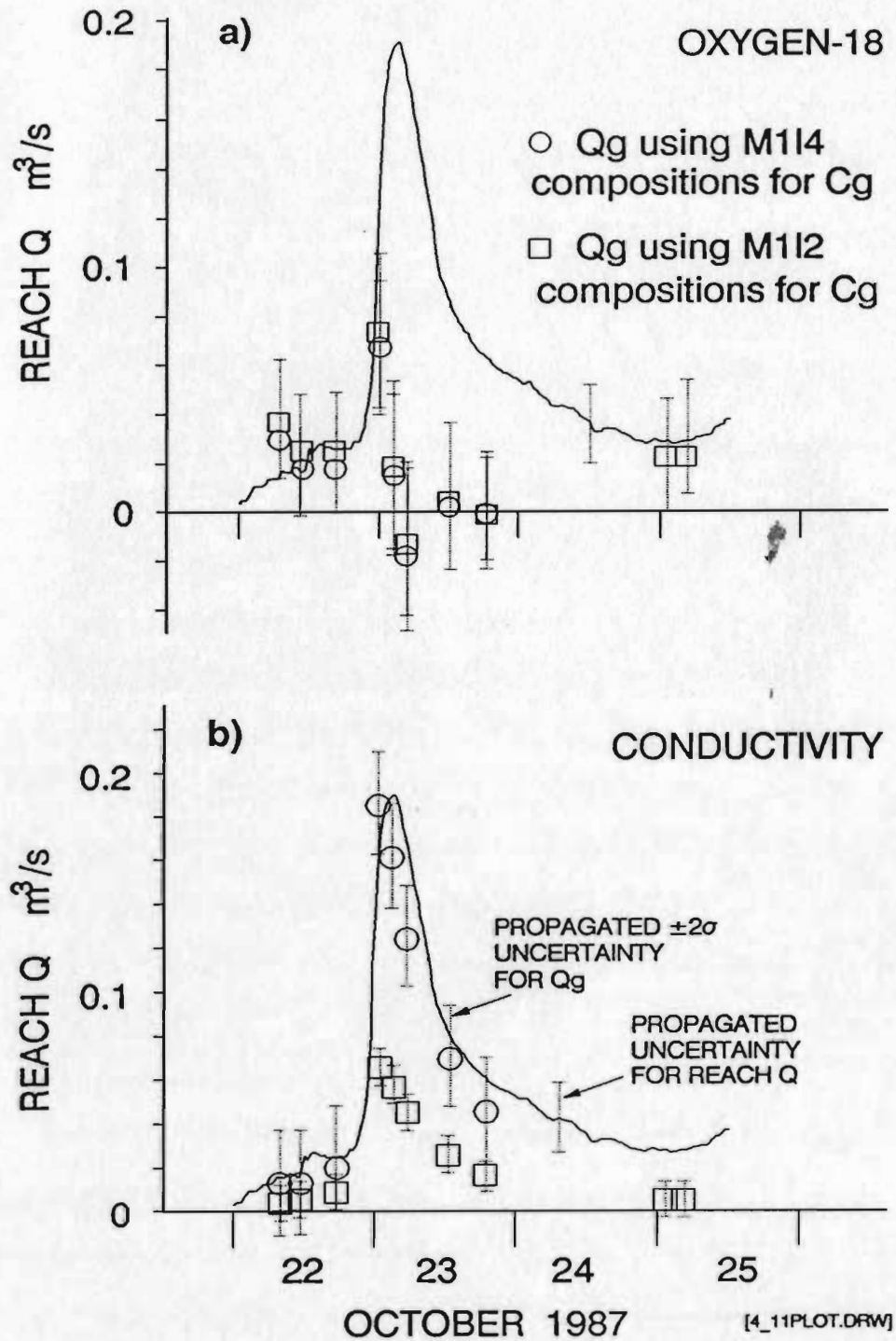


Figure 4.11 - Hydrograph separation results for the October 22, 1987 runoff event using oxygen-18 (a) and conductivity (b) tracers.

determined using M114 and M112 groundwater compositions for the  $C_g$  term in equation [4] since these compositions are assumed to represent the range of groundwaters discharging into the reach, as mentioned above. Actual groundwater runoff proportions are interpreted to lie along or between the separation trends for M114 and M112 groundwaters, as discussed below.

#### Hydrograph separation for the October 22, 1987 runoff event

Hydrograph separation for the October 22, 1987 runoff event using oxygen-18 as a tracer (Figure 4.11a) indicates low (or impossible negative)  $Q_g$  values during peak flow and falling limb periods, whether M114 or M112 compositions are used for  $C_g$  in equation [4]. These results can be attributed to the marginal oxygen-18 compositional contrast for this event (compositional contrast/error ratio equals 11 (Table H1) compared with minimum recommended range of 10-15; Appendix H). Similarly,  $Q_g$  values at peak flow using deuterium as a tracer (not shown) are also near zero (slightly negative) and can also be attributed to insufficient compositional contrast (contrast/error ratio of 3.8; Table H1). Thus, isotopic values during peak flow periods of the October 22, 1987 runoff event are considered to be poorly poised for hydrograph separation. These results are included here for completeness, and to illustrate some effects of insufficient compositional contrast.

However, there is some useful information in the results shown in Figure 4.11a. These separation results are physically reasonable up to the start of the rising limb and during post-hydrograph recession (i.e. on October 25, Figure 4.11a). This is likely due to lack of abundant surface runoff during these periods, hence lack of instability in the separation equation due to low groundwater-rain composition contrast. These results suggest that groundwater formed essentially 100% of runoff during rainfall and early stages of the rising limb of the reach hydrograph. The significance of this is discussed below.

Separation results for the October 22, 1987 runoff event using conductivity as a tracer (Figure 4.11b) are physically reasonable throughout stormflow. Following the inferences of bulk inflow analysis for this event, the M114-type groundwater dominated runoff during rainfall and formed 100% of stormflow on the lower rising limb. Figure 4.11b shows that at peak flow, groundwater discharge dominated by M112-type compositions formed only about 30% of peak stormflow derived from the assumed catchment. However, actual groundwater proportions at peak flow may have been greater, as discussed further below.

After peak flow, the return of runoff to 100% M114-type groundwater by October 25 is assumed to have been gradual. Although no M114-based  $Q_g$  values are available for October 25, the spread of M112-based and M114-based  $Q_g$  values during the falling limb suggests that M114-dominated groundwater discharge would have constituted 100% of reach Q on October 25.

#### Hydrograph separation for the September 27, 1986 runoff event

Figure 4.12 shows separation results for the September 27, 1986 storm, subdivided by tracer (oxygen-18, conductivity and chloride) and reach segment (full, upper and lower reach). Results using the three tracers are described below and used to compare groundwater runoff components along different reach segments, to discuss non-conservative tracer behaviour, and to illustrate the imprecise or impossible  $Q_g$  values resulting from the low chloride composition contrast during this runoff event.



## HYDROGRAPH SEPARATIONS FOR THE SEPTEMBER 27, 1986 EVENT

- Qg using M114 compositions for Cg
- Qg using M112 compositions for Cg
- ↑ Indicates Qg >> reach Q for that time (hence Qg not plotted)
- ┘ Propagated  $\pm 2\sigma$  uncertainty for Qg

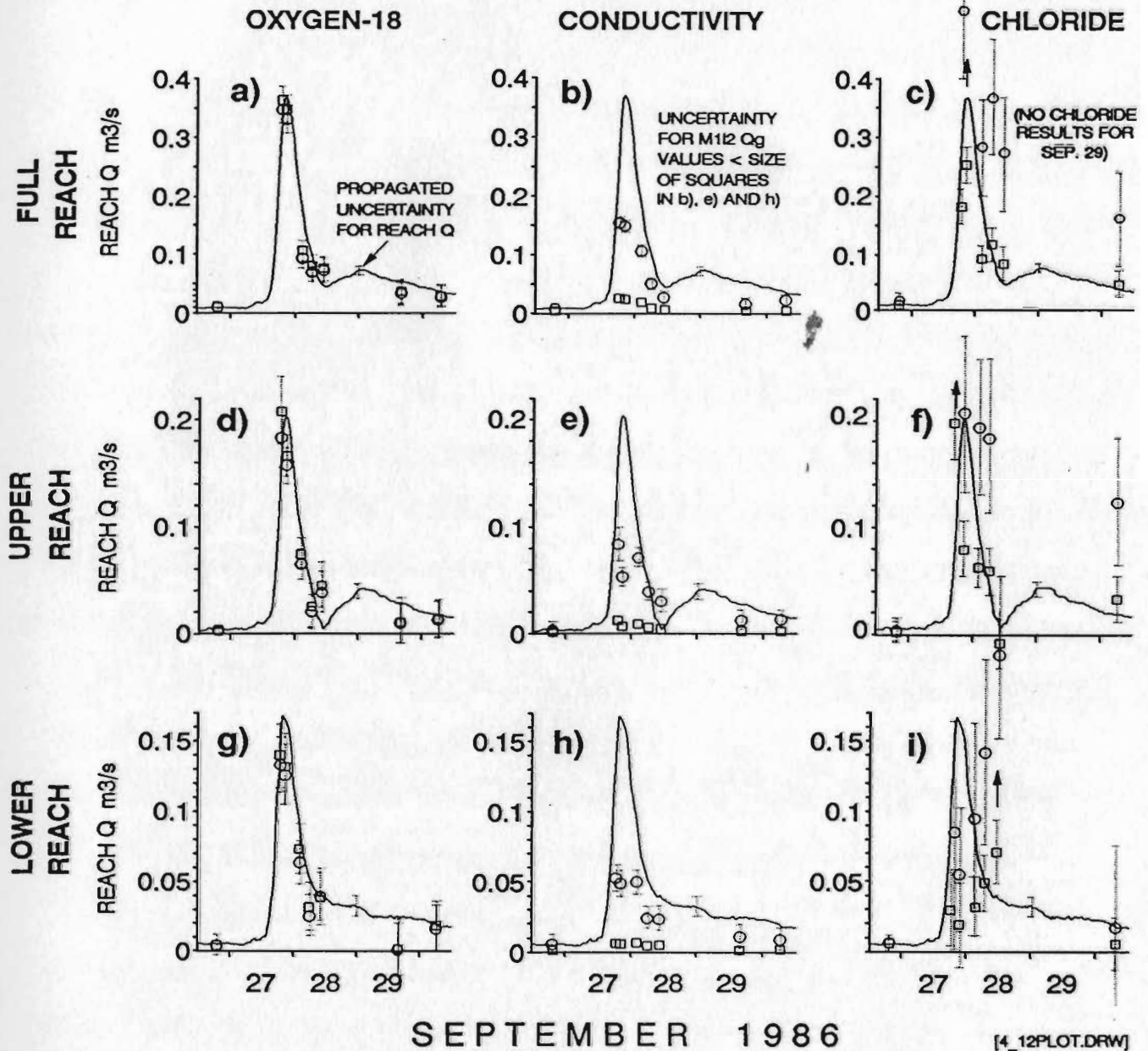


Figure 4.12 - Hydrograph separation results for the September 27, 1986 runoff event using oxygen-18, conductivity and chloride tracers (columns) for full, upper and lower reach sections (rows). For example, plot (b) shows separation results for the full reach using conductivity as a tracer.



Separation results using oxygen-18 as a tracer (Figures 4.12a, d and g) indicate that groundwater dominated runoff during rising limb, peak discharge and falling limb periods. The similarity of M114- and M112-based results in Figures 4.12a, d and g can be attributed to the small difference between measured M114 and M112 groundwater oxygen-18 values (-6.8 o/oo versus -7.6 o/oo (nominal), respectively; Figure 4.6c) compared with the contrast of these oxygen-18 values with the strongly depleted September 27 rain value (-12.9 o/oo). Assuming that groundwater discharge around peak flow was dominantly of M112 composition (as inferred from bulk inflow analysis), groundwater proportions based on oxygen-18 were of the order of 80-95% at peak stormflow. Separation results at peak flow using deuterium as a tracer were similar (not shown). After the steep falling limb,  $Q_g$  values are weakly constrained, due to reduced flow contrasts and lack of stream chemistry data during the September 28-29 period (Figure 4.6b), but permit an interpretation that runoff trended back to 100% M114-type groundwater by September 30. The similarity of groundwater runoff proportions for the upper and lower reach sections suggests that runoff processes from the assumed catchment may have operated uniformly along the reach during this event, at least at the scale of the reach sections.

The separation results at peak flow for the Sep. 27, 1986 event are considered the most reliable and significant in this study. Their reliability derives from the use of an isotopic tracer and the degree of flow and composition contrasts present for most of the runoff event. The dominance of groundwater at peak stormflow indicated by these results tends to refute, for this storm, the hypothesis proposed at the end of Chapter 3 that direct runoff dominates stormflow in the SCR. The separation results tend to break down, however, along the upper reach after peak flow due to inadequate flow contrasts. This

coincides with the rising limb of the delayed inflow hydrograph from upstream sources. The apparent near-zero reach discharge value on September 28 for the upper reach is simply an artifact of the subtractive superposition method of determining the reach discharge hydrograph.

Separation results based on conductivity (Figures 4.12b, e and h) differ substantially from those based on oxygen-18 in that conductivity-based  $Q_g$  values are much lower overall and show a significant spread depending on whether M114 or M112 compositions are used for the  $C_g$  term in equation [4]. The overall lower  $Q_g$  values in Figures 4.12b, e and h can be attributed to non-conservative behaviour in the conductivity of surface runoff during stormflow. Viewing equation [4], it can be seen that a rise in runoff conductivity (i.e. increase in  $C_r$  value) would lead to decreases in all of the compositional difference terms (e.g.  $C_o - C_r$ ,  $C_g - C_r$  etc.). However, since stream conductivities were lower than groundwater conductivities, the compositional difference terms in the numerator of equation [4] would decrease faster than the denominator, leading to overall decrease in calculated  $Q_g$  value. This also can explain the very low M112-based  $Q_g$  values using conductivity (open squares in Figures 4.12b, e and h). Since M112 groundwater conductivities were substantially greater than stream conductivities (Figure 4.6), a rise in  $C_r$  value would decrease the numerator in equation [4] but produce very little decrease in the denominator, so that calculated  $Q_g$  would be driven to very low values.

Conductivity increases in surface runoff are commonly attributed to dissolution of biosalts at the land surface during transit to the stream (e.g. Pilgrim et al., 1979). This was probably the case for this event as well, since cation (Mg and K) concentrations in stream waters increased during peak stormflow on

September 27-28 (not shown). The likely non-conservative behaviour of conductivity as a tracer for this event suggests that the conductivity-based separation results for the October 22, 1987 event may also be too low to some degree. Thus the actual groundwater runoff component during peak October 22, 1987 runoff may have been higher, even dominating reach stormflow as shown by the oxygen-18 based results for the September 27, 1986 event. However, the degree of non-conservative behaviour for conductivity may vary from storm to storm depending on antecedent moisture, pre-storm biosalt concentrations and the distribution of rainfall which would affect contact time of surface runoff with those biosalts. The complex interplay of these factors is too poorly known for these two runoff events to permit a more rigorous comparison of the conductivity-based separation results. In addition, there are simply too few runoff data sets available to adequately assess the typical behaviour of conductivity as a tracer in the SCR.V.

Separation results using chloride as a tracer (Figures 4.12c, f and i) are more erratic and have much larger propagated uncertainties than do results based on the other tracers. This is attributed to the low chloride contrasts between flow components for this event (contrast/error ratio of 6.7 at peak flow; Table H1) and inherent measurement noise due to the low chloride concentrations in all the waters. This chloride behaviour is probably inherent in SCR.V groundwaters due to low overall chloride concentrations, leading to chronically low confidence in chloride-based separation results for this study area.

#### Hydrograph separation for the ancillary 1987 runoff events

Table 4.2 gives groundwater proportions for four runoff events in 1987

sampled at peak flow. Separation precisions for all but the September 17, 1987 storm are unacceptably coarse (i.e.  $> \pm 15\%$ ) due to inadequate flow or composition contrasts, or both. These results illustrate how separation precisions vary with the degree to which the contrast/error ratios differ from the minimum recommended range of 10-15 (Appendix H). The need for combined adequate flow and composition contrasts is illustrated by results for the September 26 event where the small flow contrast (contrast/error ratio of 3) leads to large separation uncertainties ( $\pm 63$  and  $\pm 97\%$  for conductivity and oxygen-18 tracers) even though the composition contrasts are adequately large.

#### 4.4.4 Controls on groundwater stormflow components in the study area

Hydrograph separation results above suggest that M114-type groundwater dominates runoff on the rising limb of storm hydrographs but that M112-type groundwaters (i.e. valley bottom groundwaters) contribute to stormflow during peak flow. A likely control of the composition and proportion of the groundwater

Table 4.2 - Input data and hydrograph separation results for four 1987 runoff events sampled at peak discharge in the Seal Cove River valley.

Storm Date:                      23 Aug 87      17 Sep 87      26 Sep 87      8 Oct 87

Input data<sup>1</sup>

$Q_3$ m <sup>3</sup> /s	.0488	.2106	.0973	.1408
$Q_1$ m <sup>3</sup> /s	.0134	.0559	.0544	.1005
$C_3$				
Conductivity ( $\mu$ S/cm)	40.0	41.5	40.9	39.9
Oxygen-18 (o/oo)	-5.77	-4.40	-5.97	-5.96
$C_1$				
Conductivity ( $\mu$ S/cm)	39.7	41.7	43.4	41.0
Oxygen-18 (o/oo)	-5.70	-3.93	-6.02	-5.51
$C_g$				
Conductivity ( $\mu$ S/cm)	42.5	70	44.0	43.3
Oxygen-18 (o/oo)	-7.07	-7.25	-7.36	-7.65
$C_r$				
Conductivity ( $\mu$ S/cm)	7.0	22.4	11.7	8.5
Oxygen-18 (o/oo)	-5.55	-2.65	-11.56	-5.80
Vol. m <sup>3</sup>	7060	7670	7100	7200

Composition and flow contrasts

$C_g$ - $C_r$ contrast/error ratio				
Conductivity	126	168	115	123
Oxygen-18	7	22	20	9
Flow contrast/error ratio				
$Q_3$ - $Q_1$	2	10	3	3

Hydrograph separation results<sup>2</sup>

Groundwater component at peak runoff

(Cond.)	93 $\pm$ 75%	40 $\pm$ 8%	81 $\pm$ 63%	82 $\pm$ 65%
(O-18)	15 $\pm$ 107%	40 $\pm$ 14%	135 $\pm$ 97%	76 $\pm$ 117%

<sup>1</sup> subscripts 1, 3, g and r stand for weir W1, weir W3, groundwater and rain, respectively.  $C_g$  values for the Aug. 23, September 26 and October 8 events are M114 groundwater compositions; for the September 17 event they represent a 25:75 mix of M114 and M112,13 groundwaters as inferred by bulk inflow analysis.

<sup>2</sup>  $\Delta V/\Delta t$  and  $\Delta C/\Delta t$  terms assigned values compatible with those at peak flow for main study storms.

in peak runoff in the SCR V is the location of most concentrated rainfall stress within the assumed catchment, described previously. For the October 22, 1987 event, the lagging of the hydrograph peak behind rainfall and the dominance of M112(13)-type groundwaters at peak flow are consistent with the focusing of hydrologic stresses away from the study reach causing stream-ward displacement of distal valley-bottom groundwaters (represented by M112(13) compositions).

In contrast, the prompt hydrograph response during the September 27, 1986 rainfall and the apparently larger role of M114-type groundwaters in peak runoff are consistent with the focusing of hydrologic stresses near the stream for that event. The lack of abundant surface runoff indicated by the oxygen-18-based separation results (Figures 4.12a, d and g) suggests that the September 27, 1986 rainfall largely infiltrated into the peat/drift deposits, displacing very near-stream (M114-type) groundwaters into the reach. This process is reasonable since the rainfall intensity was low (average of 2.33 mm/hour; Table 4.1) and would not likely have exceeded the infiltration capacity of the surficial materials. In addition, substantial infiltration during this event is consistent with mixing of rain into the M114 interval 2-4 days after rainfall began, suggested by groundwater mixing relationships (Figure 4.8b).

The style of hydrologic stress for the September 17, 1987 event may have been intermediate between that of the September 27, 1986 and October 22, 1987 events, as inferred from the relatively short lag of the storm hydrograph (inset, Figure 4.10) behind rainfall.

Finally, the domination of early storm runoff by groundwater for both the main study storms suggests that storm runoff in the SCR V may not follow a

stormflow cycle, as described for example by Poinke et al. (1988), in which direct channel precipitation and surface runoff dominate early runoff and subsurface water (groundwater) dominates runoff at and after peak flow. Groundwater domination of early stormflow in the SCR/V can be attributed to extremely responsive groundwater displaced from shallow, open fractures in near-surface granite. This is consistent with observations and inferred mechanisms of physical response of groundwater during storm events, discussed in the next section.

#### **4.5 Comparison of hydrochemical and physical responses to hydrologic stress in the study area**

In an attempt to understand the integrated hydrochemical and physical responses to hydrologic stress in the SCR/V, these responses are compared below in terms of timing and duration, comparability of hydrograph separation results with physical observations, and compatibility of hydrochemical responses with physical response mechanisms.

##### **4.5.1 Timing and duration of groundwater responses**

Prompt, rain-triggered groundwater compositional changes in the SCR/V, such as at M114 during the September 15, 1987 rainfall or at M112 during the October 22, 1987 event, are most likely due to transfer of hydraulic head down into the fractured granite during infiltration with associated displacement of local heterogeneous groundwater past piezometric sampling points. These early groundwater responses to storm stress are apparently not due to direct mixing with rain water or, in the very near-stream setting, to stream stage changes in the reach (i.e. due to ephemeral influent flow through the stream bed).

For the October 22, 1987 runoff event, both the groundwater compositional variations at M112 and pronounced seepage flux increases at the beaver pond had similar durations, lasting about one day after the start of rain. This suggests that displacement of shallow, compositionally heterogeneous groundwater in the near-stream granite can be physically linked with corresponding groundwater discharge through the pond sediments. For all runoff events monitored in the SCR.V, piezometric levels after peak hydrologic stress decreased to pre-storm levels in a matter of days. Thus, groundwater compositional changes occurring within the same time frame (e.g. those occurring four days after the September 27, 1986 rainfall) can be reasonably attributed to late-stage physical perturbations of shallow groundwater in response to storms. However, since groundwater compositional changes may also occur under low flow conditions (e.g. suggested by the summer 1986 oxygen-18 data, Figure 4.5a), it is difficult to specify, with current data, when storm-induced groundwater compositional changes cease in the SCR.V and when any possible seasonal secular variations in groundwater compositions (mentioned in Section 4.4 above) would regain dominance.

#### 4.5.2 Comparison of hydrograph separation results with physical hydrologic response to storms

Runoff coefficients for the assumed catchment, i.e. the ratio of volume of total stormflow generated along the reach to total rainfall volume over the assumed catchment, ranged from 0.2-0.53 for runoff events monitored in this study. For the September 27, 1986, September 17, 1987 and October 22, 1987 storms, runoff coefficients along the reach were 0.53, 0.49 and 0.43, respectively. These values are consistent with hypotheses (presented above) relating proximity of rainfall hydrologic stress to the stream reach with the lag time between rainfall and peak stormflow. Rainfall concentrated near the reach (e.g. September 27,



1986 event) promptly produced the highest observed runoff coefficient, while response to rainfall focused away from the reach (e.g. October 22, 1987 event) was lagged and had a lower runoff coefficient.

For runoff events monitored in this study, peak stormflows along the upper and lower reach sections were within  $\pm 15\%$  of each other. This suggests that rainfall distribution along the length of the assumed catchment, along with other controls on runoff distribution such as hillslope morphology, fracture patterns in the granite, overburden thickness and distribution, and vegetation, lead to uniform runoff magnitudes along the study reach. This inference is supported by the uniformity of stormflow generation along different reach subsections for the September 27, 1986 event (described above) and by results of two-dimensional numerical simulations of groundwater flow (presented in the next chapter). However, response to hydrologic stress in the assumed catchment must certainly vary with scale, with responses at scales of meters to a few tens of meters tending to show strong spatial variability. This is consistent with the inference of separate fracture plumbing systems around M1, based on groundwater mixing relationships, and also the spatial variability shown by seepage fluxes in response to the October 22, 1987 event (Chapter 3), with fluxes changing by a factor of  $>4$  over horizontal distances of  $<40$  m.

The magnitudes of groundwater discharge based on reach hydrograph separation can be quantitatively compared with physical measurements for the October 22, 1987 runoff event. Discharge seepage fluxes at the beaver pond measured during October 22-23 (corresponding with hydrograph times 2 to 7 in Figure 4.9a) averaged  $2.14 \times 10^{-8} \text{ m}^3/\text{m}^2 \cdot \text{s}$ . This gives an average groundwater discharge rate over the entire pond surface area ( $11030 \text{ m}^2$ ) of  $2.36 \times 10^{-4} \text{ m}^3/\text{s}$  for this period. Corresponding groundwater discharge into the stream channel can be estimated using the hydraulic conductivity at M1 ( $6 \times 10^{-5} \text{ m/s}$ ) and the average upward gradient ( $0.0925 \text{ m/m}$ ) during this peak flow period, giving an average discharge flux into the stream channel of  $5.55 \times 10^{-6} \text{ m}^3/\text{m}^2 \cdot \text{s}$ . Over the entire

stream channel surface area ( $6720 \text{ m}^2$ ), and including the discharge rate from the beaver pond, this gives an average groundwater discharge rate over the entire study reach of  $0.0375 \text{ m}^3/\text{s}$ . In comparison, the average groundwater discharge rate based on hydrograph separation results is  $0.0403 \text{ m}^3/\text{s}$ , determined using the area under the groundwater hydrograph for the October 22-23 period.

The close agreement of these estimates (within 7.5% of each other) tends to corroborate the October 22, 1987 hydrograph separation results based on conductivity and shows that most groundwater (99.5%) was discharged into the reach channel rather than the beaver pond. This latter point is also consistent with the semi-confining nature of the pond bed sediments, invoked to explain cyclic discharge fluxes through the pond bed sediments in Chapter 3. A similar comparison as above for the September 27, 1986 storm was not possible since there were no seepage flux measurements nor hydraulic gradient data at M1 at peak flow available.

#### 4.5.3 Compatibility of hydrochemical and physical response mechanisms in the SCR V

As concluded in Chapter 3, the principal physical mechanism of groundwater response in bedrock to storm stress in the SCR V is the filling and draining of fractures, allowing rapid head transfer and groundwater displacement in the granite. A secondary mechanism of cyclical, post-storm heaving in the beaver pond sediments likely has little impact on hydrochemical changes in the stream since (as described above) the magnitude of groundwater discharge into the beaver pond is negligible.

Groundwater mixing relationships and hydrograph separation results described in this chapter are compatible with the fracture filling and draining mechanism. The prompt displacement of groundwater in stream-ward directions at the onset of rain and the predominance of groundwater in early storm runoff

imply that the most active zone of groundwater flow is primarily in open fractures near the surface. In addition, the possibility of late-stage arrival of hillslope-derived groundwaters in response to storms requires travel times which are physically reasonable only within the context of rapid drainage through a permeable, near-surface fracture system.

It should be noted, however, that an alternate view for interpreting hydrochemical variations in the SCR V is possible. The isotopic heterogeneity of SCR V groundwaters, notably those in near-stream discharge areas, likely reflects variations of input compositions (infiltration) and lack of complete mixing during travel in the fracture system between recharge and discharge areas. The groundwater mixing trends described above may in part reflect long-term seasonal input variations to the flow system and partial damping by relatively slow advective and dispersive mixing processes in the subsurface. This would argue against mixing of contemporary rain water with near-stream shallow groundwaters (e.g. at M114, 2-4 days after the September 27, 1986 rainfall; Figure 4.8b) as well as the rapid transit of hillslope groundwaters to the stream. Whether or not infiltrating rain water actually mixes with valley bottom groundwaters during short-term response to storm stress, rapid storm-induced changes in groundwater composition can be considered to occur due to displacement of heterogeneous groundwaters around sampling intervals in response to prompt, ephemeral rises in piezometric levels. This may be superimposed on a steadier, slower flow regime between storms.

Proper testing of the relative importance of event-based versus seasonal variations in the hydrochemical and physical responses of groundwater to hydrologic stresses in the SCR V would require long-term rainfall/rain composition records (i.e. for at least a year) to document actual seasonal input variations, along with regular groundwater monitoring and sampling within the full suite of piezometric intervals to document in-transit damping effects. Because available data are much more limited than this, a quantitative analysis of

groundwater velocities and residence times within the fractured granite was not attempted here. In this vein, it should be noted that correlation of isotopic variations in valley-bottom groundwaters with previous seasonal secular variations in rainfall composition (e.g. ascribing isotopic enrichment of groundwaters collected in the fall to arrival of seasonally-enriched summer infiltrate) may be inherently unworkable in the SCR. This is due to an apparent lack of well defined seasonal variation in rain compositions in the SCR (suggested by data in Figure 4.8), attributable to the highly changeable climatic conditions in this region regardless of season. Similar large variations in rainfall isotopic composition on time scales of days with no seasonal dependence have also been observed elsewhere (e.g. Heathcote and Lloyd, 1986).

#### 4.6 Conclusions

Mass balance methods developed here permit the study of chemical variations and stormflow components along a stream reach, for areas where a hydrologically-isolated catchment can be assumed to exist adjacent to the study reach. This reach approach is a major departure from conventional methods for studying storm runoff, in which study areas are generally restricted to headwater portions of drainage basins. The reach approach is potentially of greater practical use since it is generally in down-stream areas where the need for information on storm runoff quality and quantity is greatest (i.e. for land-use decisions, or to determine the effects of road construction, mining, logging, etc.).

Incorporation of transient conditions in these methods offers a more realistic expression of changing stream flow and chemistry during runoff events. Within the reach hydrologic approach, transient storage terms in the reach channel can be measured or approximated. Complex stream inflows as well as variable rainfall distribution can also be analyzed with these methods. However, the use of subtractive superposition to manipulate hydrographs may not be valid during the steep rising limb of an upbasin floodwave as it propagates downstream

along the reach. For this latter reason, as well as the requirement of sufficient combined flow and runoff component composition contrasts, the best-suited runoff events for these methods are those producing low, steady inflows and simple, large outflows.

The requirement for adequate flow as well as compositional contrasts means that hydrograph separations at the beginning and end of major runoff events are weakly constrained (since flow contrasts are low at those times). In addition, relatively large rainfalls are required (about 20 mm or greater in the SCR V) to produce adequate flow contrasts. These points highlight the need for the most precise streamflow measurement possible at low flow (e.g. via compound weirs) for best results using these methods.

Bulk inflow analysis offers the potential for identifying time-varying compositions of groundwater actually entering the reach during stormflow, thus constituting a substantial improvement over conventional methods based on pre- and/or post-storm stream compositions.

The compatibility of hydrochemical and physical hydrologic variations in the SCR V study area indicates that surface water and shallow groundwater are strongly coupled in their response to hydrologic stress. Groundwater runoff components for the September 27, 1986 and October 22, 1987 events range up to 80-95% of peak stormflow and differ in part depending on the location of principal hydrologic stress in the SCR V (i.e. near to or far from the stream reach). The large groundwater component indicated by oxygen-18 separation results for the September 27, 1986 event suggests that the well-exposed granite hillslope does not necessarily lead to surface runoff-dominated storm flow in the study area, as hypothesized in Chapter 3. Conductivity was shown to act non-conservatively compared with oxygen-18 in hydrograph separations for the September 27, 1986 event. However, the degree of non-conservative behaviour of conductivity in surface runoff during the October 22, 1987 event is unknown since,

due to inadequate composition contrasts, there are no useable separation results based on oxygen-18 (or deuterium) to serve as a reference. Finally, there are too few runoff data sets in this study to properly assess the typical behaviour of conductivity as a tracer for hydrograph separation at this site.

The likely composition of groundwater runoff in the SCRV, including very near-stream (M114-type) and valley-bottom (M112,13-type) groundwaters, suggests that groundwater discharging to the study reach originates primarily in valley-bottom locations. Arrival of hillslope-derived groundwater during late stages of storm response cannot be ruled out and is physically possible only within interconnected, open fractures such as in the shallow subsurface in the SCRV. The similarity of groundwater discharges along the reach subsections for the September 27, 1986 event further suggests that groundwater discharge to the reach occurs primarily along numerous, interconnected, shallow open fractures (i.e. sheeting joints) rather than from drainage from a few large, deep subvertical faults. The local groundwater flow system most strongly interacting with the study reach may therefore be restricted to near-surface regions in the granite. These and other hypotheses regarding groundwater flow paths and the effect of large subvertical fractures on that flow are investigated by numerical simulation in Chapter 5.

## CHAPTER 5

### NUMERICAL SIMULATION OF GROUNDWATER FLOW IN THE SEAL COVE RIVER VALLEY

#### 5.1 Introduction

##### 5.1.1 General statement

This chapter presents a description and interpretation of steady-state, two-dimensional (2D) and three-dimensional (3D) numerical simulations of groundwater flow in the Seal Cove River valley study area. These simulations are aimed at determining the internal consistency of physical hydrologic measurements made in the SCR, to infer the shape and distribution of recharge and discharge areas in the assumed catchment, and to evaluate the influence of major fractures on the shallow groundwater flow system in the SCR. In addition, model results are used to make inferences regarding the effective size of the groundwater catchment for the study reach and the uniformity of groundwater discharge along the study reach.

Equivalent porous media permeabilities were used in all of the simulations. At this scale of modelling and considering the data density in the study area, this

approach was the only justifiable one. Further details of 2D and 3D modelling approaches, including use of measured permeability and fracture characteristics in formulating input parameters, are presented below.

#### 5.1.2 Computer code used in numerical simulations

A modular three-dimensional finite-difference groundwater flow code, MODFLOW (McDonald and Harbaugh, 1988), was used for numerical simulations. This code is widely used and has been verified against a variety of analytical solutions. MODFLOW was used unaltered for the 2D simulations. However, for some of the 3D simulations, MODFLOW had to be modified to accommodate the permeability characteristics of cells containing fracture zones (described in detail in Section 5.3). Details of revisions to MODFLOW and testing of the revised code are described in Appendix I.

### 5.2 Two-dimensional simulation of groundwater flow in the study area

#### 5.2.1 Two-dimensional modelling approach

The specific objective of 2D modelling was to determine if hydraulic heads and discharge fluxes to the study reach, simulated under steady-state conditions using measured permeabilities as input parameters, were reasonable and consistent with measured artesian heads at the stream and seepage fluxes at the beaver pond. To do this, two parallel model profiles were constructed perpendicular to the stream, passing through piezometer M1 (A-A') and through the beaver pond (B-B'). Recognizing that there is limited control along these profiles, these were considered the best placement to use what control points were available and to orient the profiles along the general direction of groundwater flow to the study reach. These 2D models were calibrated using piezometric and seepage flux measurements at low flow prior to the October 22, 1987 storm.



### 5.2.2 Mesh configuration, boundary conditions and input parameters

Configurations of the 2D profiles in the SCR V are shown in Figure 5.1. The profiles extend beyond the limits of the assumed catchment so that simulation results within the catchment are not artificially perturbed by model edge effects. The model meshes for profiles A-A' and B-B' are shown in Figure 5.2. Note that vertical exaggeration is 2.5:1. Each model is divided into six layers to a total depth of 500 m below surface (Table 5.1) and contains 38 (A-A') or 29 (B-B') columns, with widths ranging from 5 to 100 m. Both models are 50 m in north-south breadth. Columns were narrowest in the valley for detailed head resolution.

The thickness for layer 1 (overburden) in the models was based on geophysical survey results, whereas thicknesses for layers 2-5 in the granite were chosen for convenience and do not reflect any hydrostratigraphic divisions. Layer 2 is thin in the valley so that calibration, based on near-surface measurements at M1 and at the seepage meters, would be meaningful. Layer 2 thickens away from the valley so that, for modelling purposes, the simulated water table remains within or above layer 2. Layer 3 thicknesses were chosen so that the bottom of layer 3 and the boundaries of layers 4-6 occurs at constant depths below surface, for purposes of assigning hydraulic conductivities to the three deep layers (described below).

Boundary conditions for the models are as closely related to the local hydrogeologic conditions as possible. The sides of each profile are designated as no-flow boundaries, based on topography and surface drainage. A no-flow boundary at the bottom of each profile sets an arbitrary lower limit to the shallow

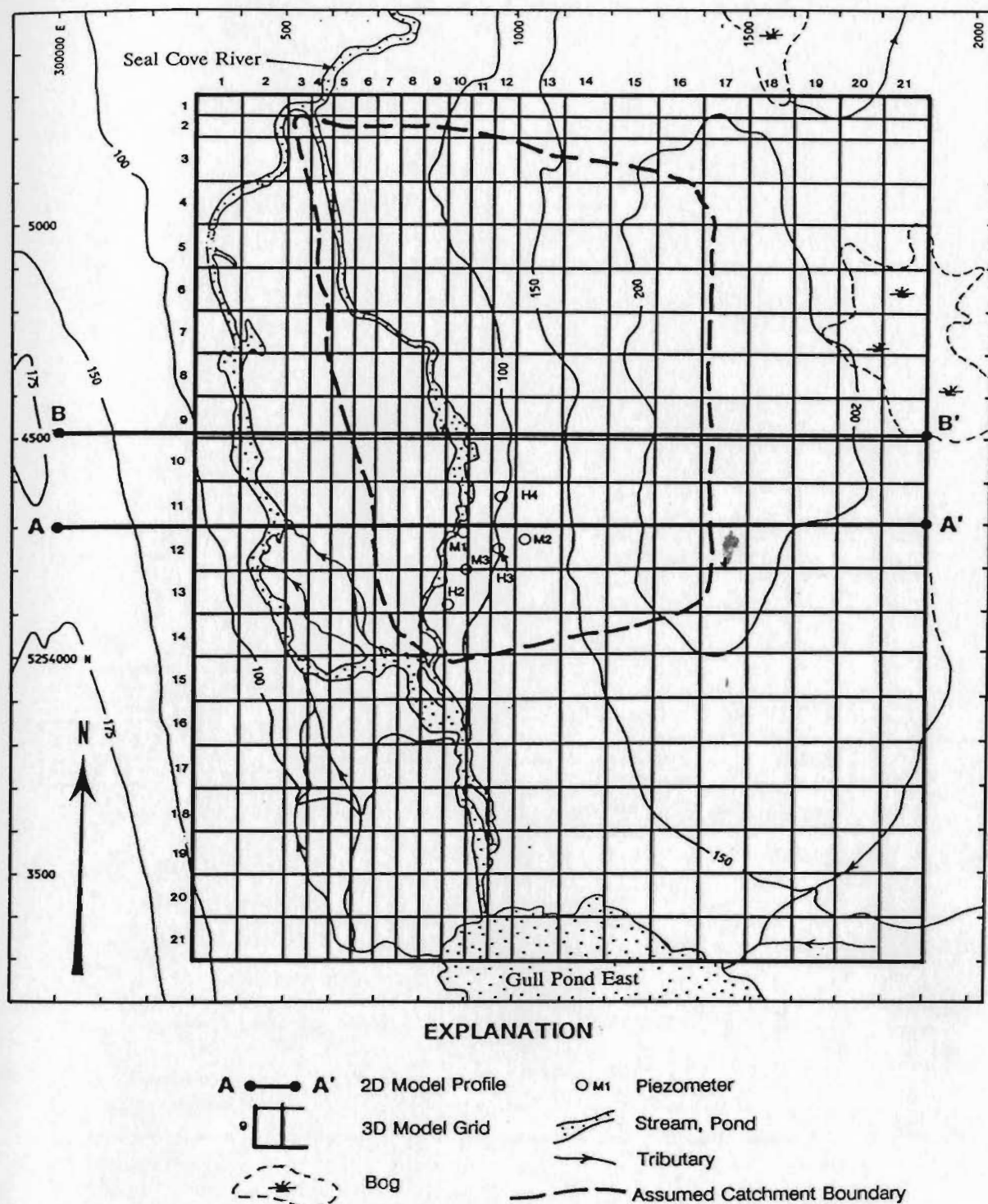


Figure 5.1 - Configuration of 2D model profiles and 3D model grid in the Seal Cove River valley area. Numbers on map borders are UTM coordinates in meters. Topographic contours are in meters above sea level.

a)

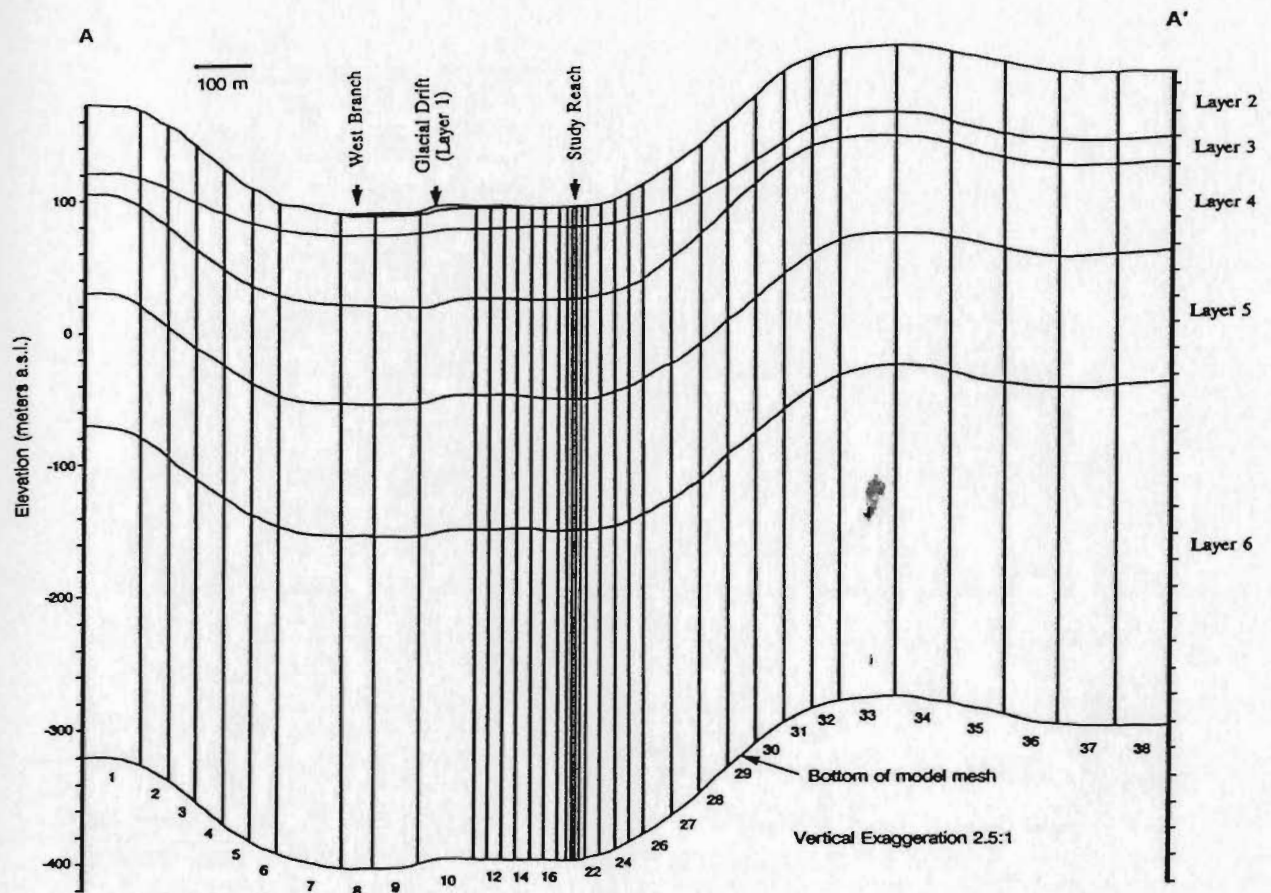


Figure 5.2 - Physical configuration of model mesh for profile A-A' (a) and B-B' (b). Numbers at bottom of mesh are model column numbers. Small crosses in Figure 5.3 correspond with central nodes of these mesh cells.

b)

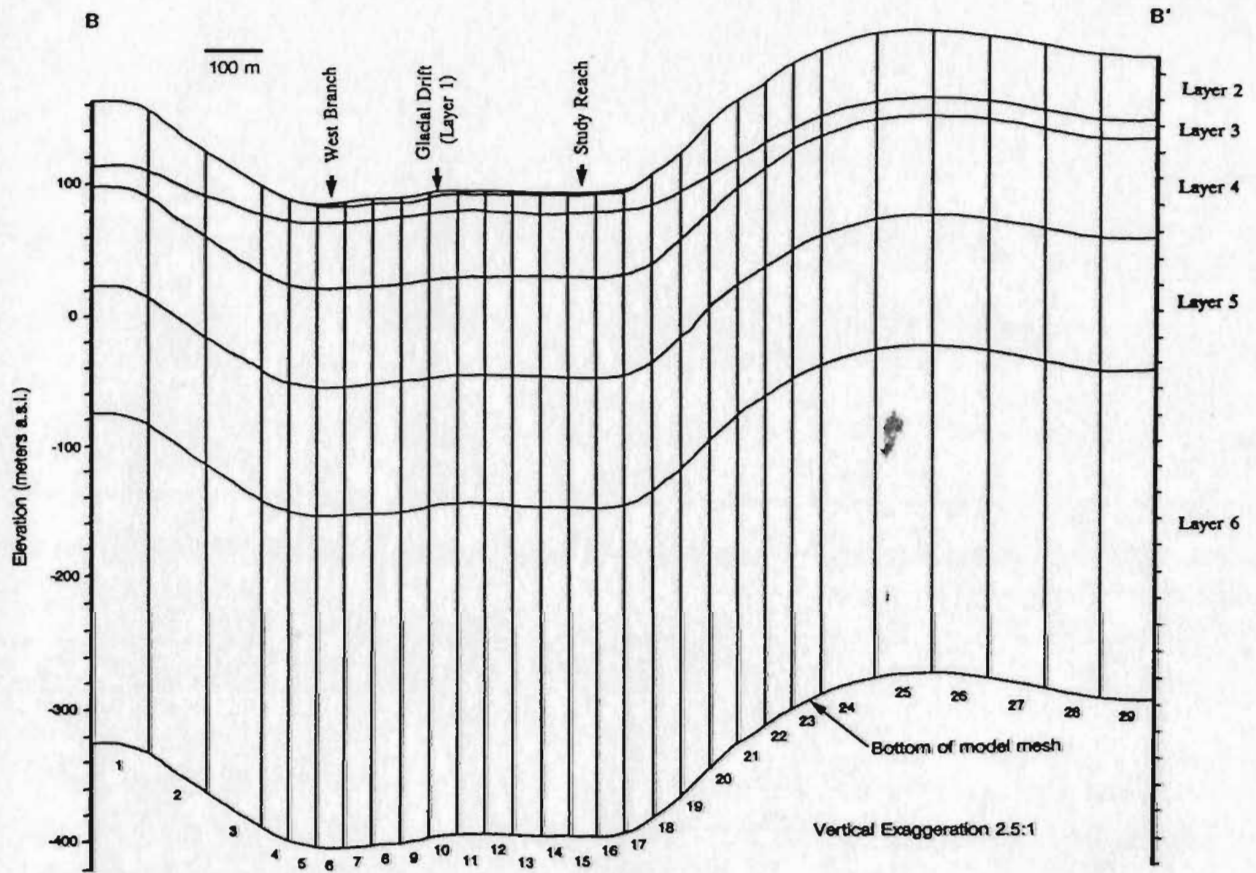


Figure 5.2 (continued)

Table 5.1 - Summary of parameters used for numerical models along profiles A-A' and B-B' in the study area

	<u>Case 1</u>	<u>Case 2</u>	<u>Case 3</u>	<u>Case 4</u>
Profile	A-A'	A-A'	B-B'	B-B'
Recharge rate <sup>1</sup>	1%/5%	1%/5%	1%/5%	1%/5%
Hydraulic conductivity <sup>2</sup> (m/s) for layers 2, 3	Reg'n line <sup>3</sup>	Lower Conf. limit <sup>4</sup>	Reg'n line	Lower Conf. limit
-----				
<u>For all cases:</u>	Material	Hydraulic cond. (m/s)	Thickness (m)	
Layer 1	drift	$6.7 \times 10^{-4}$ <sup>5</sup>	0-4	
Layer 2	granite	(above)	50(hilltop)- 15(valley) <sup>6</sup>	
Layer 3	granite	(above)	15(hilltop)- 50(valley)	
Layer 4	granite	$1.6 \times 10^{-9}$ <sup>7</sup>	75	
Layer 5	granite	$4.2 \times 10^{-10}$	100	
Layer 6	granite	$4.3 \times 10^{-11}$ <sup>7</sup>	250	

=====  
<sup>1</sup> Based on climatological and regional stream runoff characteristics and expressed as % of average annual rainfall; 1% on bare granite slopes, 5% elsewhere

<sup>2</sup> Porous media hydraulic conductivity as described in Section 3.1.4

<sup>3</sup> Values determined from regression line on Figure 3.2

<sup>4</sup> Values determined from lower 95% confidence limit on Figure 3.2

<sup>5</sup> Average value for glacial drift as described in Section 3.1.4

<sup>6</sup> Variable thickness assigned for modelling purposes to ensure that the water table was always within or above layer 2

<sup>7</sup> Values for deep layers assigned by reference to data used in modelling of granite at Stripa, Sweden (Gale et al., 1987)

groundwater flow system to be modelled. Cells in the model mesh containing the west branch of the Seal Cove River as well as those containing marshy areas at the east end of both profiles (i.e. where specific flow information to and from the cell was not needed) were assigned constant heads equal to surface water elevation above sea level. Cells containing the study reach channel (in A-A') or the beaver pond (in B-B') were designated as "river" cells, for which MODFLOW reports net flow rate to and from the cell and allows incorporation of the thickness and permeability of the pond sediments. Cells containing the beaver pond were assigned a layer 1 hydraulic conductivity (K) of  $6.0 \times 10^{-8}$  m/s, the geometric mean value from permeability tests on pond sediment cores. Sensitivity tests show that simulated groundwater fluxes into these cells are insensitive to the assigned K value, changing only about 5% for an order of magnitude change in K.

Depth-dependant hydraulic conductivities were assigned to layers 2 and 3 based on measured permeabilities in boreholes in the SCR/V as shown in Figure 3.2. The permeability ranges which yield the best match of model results with calibration parameters are discussed below. Hydraulic conductivities were assigned to each of the three deep layers (constant within each layer, Table 5.1), by reference to data used in modelling groundwater flow in granite at Stripa, Sweden (Gale et al., 1987). Since bedrock permeabilities in the models decrease with depth, a modelling option assuming unconfined conditions was used.

Recharge rates are commonly difficult to specify for catchment-scale groundwater flow models. Recharge rates used here were estimated using average annual precipitation data, based on thirty-year normals from the Atmospheric Environment Service (Environment Canada). Assuming that actual evapotranspiration equals about 470 mm per year out of the average annual precipitation for this region of about 1300 mm (Mr. Stuart Porter, Atmospheric Environment Service, pers. commun.), this leaves about 830 mm for total average annual runoff. Considering the high runoff coefficients for steep terrain, such as in the SCR/V, and negligible infiltration during periods of freeze up, it can be

further assumed that 90-95% of total average annual runoff occurs as surface runoff, leaving about 65 mm as average annual recharge. Using this as a rough guide, recharge rates for the models were set at 5% and 1% of average annual precipitation for vegetated areas and bare rock slopes, respectively.

### 5.2.3 Two-dimensional model results and discussion

Figures 5.3 shows 2D model results, expressed as contoured hydraulic heads, for four cases representing different hydraulic conductivity ranges assigned to profiles A-A' and B-B'. Cases 1 and 3 represent results using hydraulic conductivities based on the regression line through measured permeability data in Figure 3.2. Cases 2 and 4 represent corresponding results based on the lower 95% confidence limit in Figure 3.2.

For cases 1 and 3 (Figures 5.3a and c), simulated heads are too low, i.e. the water table is strongly depressed (tens of meters deep beneath the hilltops) and the artesian head by the stream along A-A' is an order of magnitude lower than that measured at M1. In contrast, for cases 2 and 4 (Figures 5.3b and d), simulated heads are too high (i.e. heads in mid-valley between the branches of the Seal Cove River are artesian), the water table at the hilltops occurs at very shallow depths (<1 m below surface at its highest point) and, along A-A', artesian heads at the stream are 3-4 times greater than those measured at M1. Hence, the narrow permeability range between the regression line and lower confidence limit in Figure 3.2 brackets the values required to produce simulated heads which are both reasonable throughout the profiles and consistent with artesian heads measured at M1.



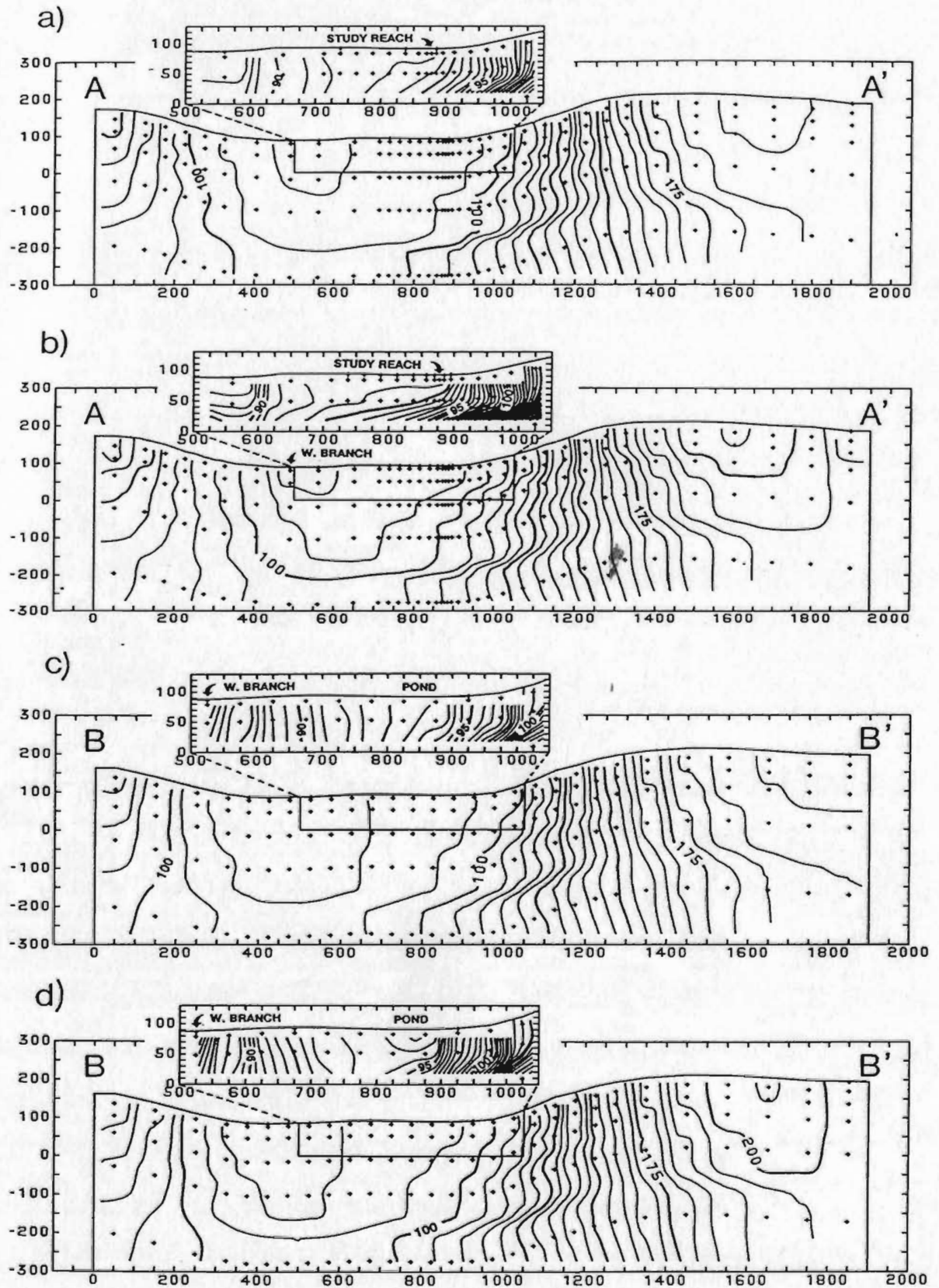


Figure 5.3 - 2D simulation results for case 1 (a), case 2 (b), case 3 (c) and case 4 (d). Numbers at left show elevation above sea level (meters). Numbers at bottom show width of profiles (meters). Small crosses are nodes at center of model cells.



The magnitudes of groundwater discharge to the study reach show little variation for cases 1-4 and are consistent with measured seepage fluxes and low flow stream discharges. For cases 1 and 2 (and for trials not shown here with vertical anisotropies ( $K_z/K_x$ ) of 10 and 0.32), discharge rates into the cell containing the study reach range between  $4.5\text{--}4.7 \text{ E-}5 \text{ m}^3/\text{s}$ . When these discharge rates are extrapolated to the full reach length (1440 m), the cumulative discharge into the reach ( $0.0013 \text{ m}^3/\text{s}$ ) is within an order of magnitude of stream discharges actually measured along the reach at low flow ( $0.005\text{--}0.009 \text{ m}^3/\text{s}$ ). For cases 3 and 4, groundwater discharge rates into the beaver pond range from  $4.0\text{--}4.2 \text{ E-}5 \text{ m}^3/\text{s}$  which, over the area of the pond, corresponds with an average groundwater discharge flux of  $1.59\text{--}1.69 \text{ E-}8 \text{ m}^3/\text{m}^2\cdot\text{s}$ . These simulated groundwater fluxes are extremely close to measured average seepage flux at the pond (around  $1.1 \text{ E-}8 \text{ m}^3/\text{m}^2\cdot\text{s}$ ) at low flow.

Equipotential patterns for each case in Figure 5.3 show similar overall characteristics, i.e. recharge areas at the hilltops, a principal discharge area at the west branch of the Seal Cove River, a local discharge area developed around the study reach (inset profiles), and shallow heads forming a local water table high between the study reach and west branch of the Seal Cove River. These patterns suggest that groundwater recharging near the hilltop east of the study reach may flow under the study reach and discharge into the west branch of the Seal Cove River. Model groundwater discharge rates into the west branch (about  $6 \text{ E-}5 \text{ m}^3/\text{s}$ ) are 28-50% greater than those discharging into the study reach or beaver pond ( $4\text{--}4.7 \text{ E-}5 \text{ m}^3/\text{s}$ ). Based on these patterns, it can be concluded that the catchment area actually contributing groundwater to the study reach may be smaller than originally assumed, with dominant flow restricted to depths on the order of 50-100 m below surface. These concepts are further discussed in light of

3D model results below.

The internal consistency of hydraulic heads and discharge fluxes simulated using the narrow permeability range described above, with measured artesian heads at M1, seepage fluxes at the beaver pond and low flow discharge along the study reach suggest the following:

- 1) Measured injection test data adequately represent the range of equivalent porous media permeabilities present in the granite to depths of 60 m in the SCR V and a representation of permeability variations with depth using simple linear regression of combined injection test data is a valid approach at this site. This result forms the basis for assigning hydraulic conductivities to layers 2 and 3 in the 3D models.
- 2) The limited number of locations where hydraulic head and seepage flux were directly measured in the discharge zone along the study reach are adequate for constraining simulations of average groundwater discharge from the assumed catchment. In addition, the similarity of simulated discharge fluxes for both profiles suggests that average groundwater discharge may be uniform along the length of the reach. This is assessed below using 3D model results.

### 5.3 Three-dimensional simulation of groundwater flow in the study area

#### 5.3.1 Three-dimensional modelling approach

The 3D modelling presented here expands on the 2D model results in an effort to investigate groundwater flow characteristics of the entire assumed catchment and immediate surrounding area. Steady-state 3D simulations of hydraulic head in the study area are performed both with and without incorporation of horizontal permeability anisotropy and hydraulic characteristics for the principal macroscopic fractures in the SCR.V. Contoured hydraulic heads in model layers are then compared to assess the degree to which anisotropy or the macroscopic fractures influence the overall groundwater flow pattern and the areal distribution of recharge and discharge zones within the assumed catchment. In addition, simulated net flow rates into "river" cells are used to assess the uniformity of groundwater fluxes along the study reach.

Anisotropic permeability of the fractured granite is the most difficult input parameter to characterize for modelling of groundwater flow in the SCR.V. This is due to the diverse factors which control anisotropic permeability in fractured low-permeability rocks, such as in situ effective normal stress on fractures, variations in fracture aperture, and the degree of fracture interconnection (e.g. Gale, 1982), for which there are no data currently available for the study area. To introduce the approach used here for approximating permeability anisotropy, it is useful to review other approaches and why they are considered unworkable with the current data set for the SCR.V.

Anisotropic permeability has been expressed mathematically in the form of

a second-rank tensor, compiled assuming that the rock mass contains planar, infinite fractures with uniform orientations within well-defined sets and known apertures (e.g. Snow, 1969). However, the assumption of continuous fractures is a major limiting factor in applying this approach to real fracture systems (Gale et al., 1987). In addition, fracture aperture distributions are not currently known in the SCR.V.

Permeability tensors have also been determined for a field site using cross-hole injection test data (e.g. Hsieh and Neuman, 1985) and by combined analysis of single- and cross-hole injection test data (Neuman, 1987). However, cross-hole testing was not conducted in the SCR.V and would not likely produce useable results for the above techniques due to the large distances (an order of magnitude or more greater than in the above studies) between the present SCR.V boreholes.

Numerous workers have used numerical or physical fracture network models, based on statistical characterization of fracture geometry (i.e. orientation, trace length, spacing), to determine directional permeability characteristics of fractured rock (e.g. Hudson, 1982; Long et al., 1982; Rouieau, 1984; LaPointe and Hudson, 1985; Gale et al., 1987; Long and Billaux, 1987; Odling and Webman, 1991). However, as mentioned in Chapter 2, the fracture data base for the SCR.V is not considered to be sufficiently well-defined, due mainly to the lack of a statistical description of subhorizontal fractures (set 4) and biases present in spacings determined from scanline data, to apply such methods.

In the absence of applicable sophisticated methods, a simple approach for approximating permeability anisotropy is adopted here, based on the relationship of permeability and fracture frequency. Several workers have observed that

maximum permeability of fractured rock mass is perpendicular to maximum fracture frequency, at scales larger than individual fractures (e.g. Boom, 1983; LaPointe et al., 1984; LaPointe and Ganow, 1984). LaPointe and Ganow (1984) also demonstrated at one study site, where the prominence of individual fracture sets varies from place to place (as in the SCRV), that the aggregate fracture characteristics and the maximum permeability direction are regionally consistent with each other. Aggregated fracture frequency for the SCRV, and permeability anisotropy inferred from it, are presented and discussed further below. Limitations of the 3D modelling approach used here are addressed in Section 5.3.5 below.

### 5.3.2 Mesh configuration and boundary conditions

The 3D model grid used here (Figure 5.1) contains 21 rows and 21 columns (row numbers to the left and column numbers at the top of the grid). As with the 2D models, the 3D grid extends outside the assumed catchment boundary to avoid model edge effects within the assumed catchment and in order to incorporate areas where water table elevations are known (e.g. streams, pond, boggy areas, etc.). Column widths are narrowest (50 m) in the valley for detailed head and groundwater flux resolution along the study reach. The 3D mesh contains six layers (as in the 2D models), consisting of an upper layer of overburden (layer 1) and five layers in granite bedrock (layers 2-6), to a total depth of 500 m. The distribution and thickness of layer 1 was determined from inspection of air photos, direct observation and from the results of the geophysical surveys (Appendix A). The thicknesses of layers 2-6 were assigned the same way as for the 2D models (Table 5.1).

The sides and bottom of the 3D mesh are designated as no-flow boundaries. In addition, surface cells containing the west branch of the Seal Cove River, Gull Pond East, minor tributaries and boggy areas at the northeast corner of the mesh were assigned fixed head values equal to the elevations of the surface water surface above sea level. While a no-flow boundary is not strictly valid for the western side of the grid (obliquely transecting the hillslope above the west branch of the Seal Cove River), it was felt that the widespread constant-head cells throughout the western part of the valley floor would swamp any anomalous effects of this. A no-flow boundary along the southern side of the mesh is consistent with calculations indicating minimal inflow into the study area from Gull Pond East as discussed in Chapter 3.

For simplicity, only macroscopic fractures over 300 m long were used in the 3D model (Figure 5.4) and these fractures were assumed to extend vertically from the top of layer 2 to the bottom of the model mesh. Where a fracture lineament crosses the very tip of a cell (e.g. southeast corner of row 6, column 13), the effects are assumed to be minimal in that cell as a whole and are ignored.

### 5.3.3 Input parameters

The key input parameters required by MODFLOW for the type of steady state 3D simulations presented here are hydraulic conductivity in each layer, and permeability anisotropy for the rock mass and for cells containing macroscopic fractures. These parameters are discussed under separate headings below.

Cell coordinates and elevations were determined from an enlarged topographic map (1:5000 scale) of the area. Recharge rates for the 3D models were assigned the same way as for the 2D model profiles. The distribution of recharge rates (Table 5.2) depends on surface slope, exposure and vegetation.

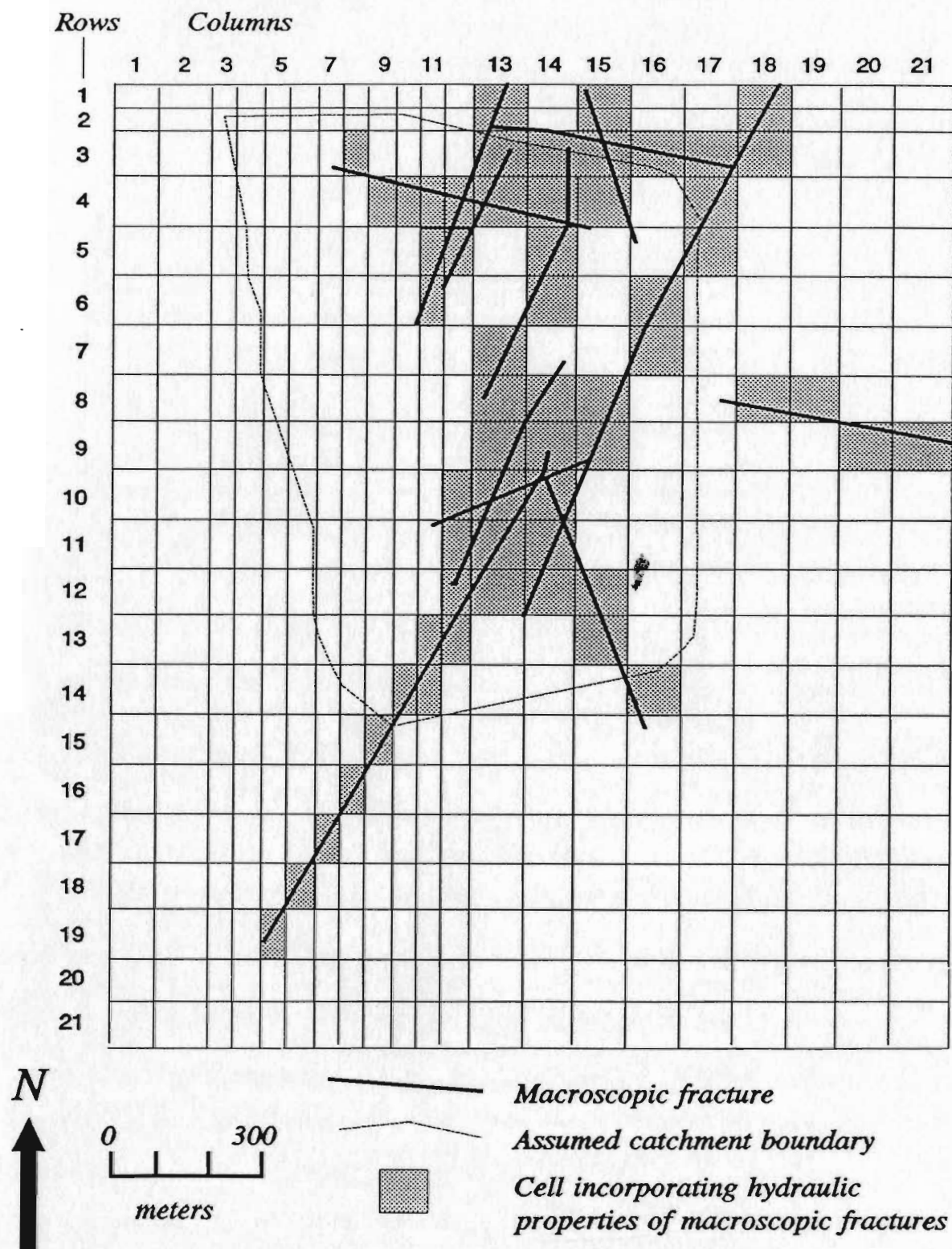


Figure 5.4 - 3D model grid showing macroscopic fractures included in model, cells designated as containing such fractures, and the the assumed catchment boundary (for reference).





which was determined using air photos, topographic maps and by direct observation. Starting hydraulic heads for all layers were set several meters above surface elevation. During solution iterations, these heads decreased toward their final steady state values. Since a modelling option for unconfined conditions was used, the final heads in the uppermost active layer (layer 1 or 2) represent the elevation of the water table.

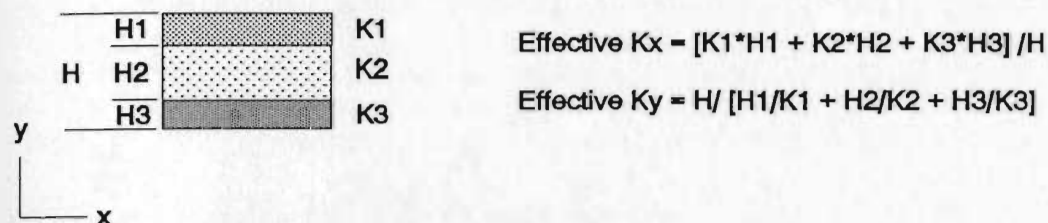
#### Hydraulic conductivity in each layer

Hydraulic conductivity for layer 1 (overburden) was assigned the same value shown in Table 5.1.

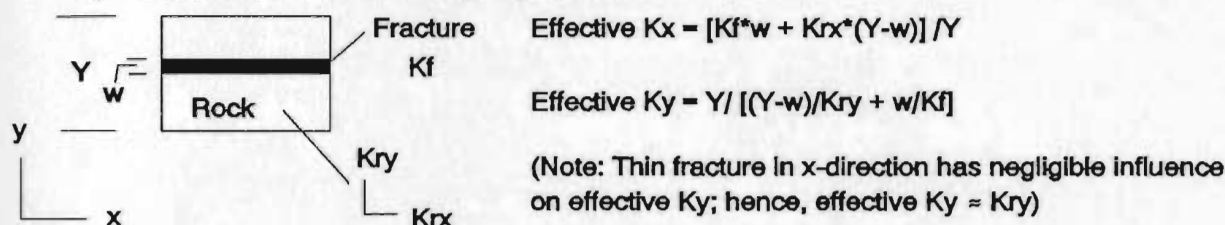
Hydraulic conductivities for cells not containing macroscopic fractures in layers 2-6, labelled  $K_r$ , were assigned in accord with the 2D model results. For layers 2 and 3,  $K_r$  values for a given depth were assigned at random from the corresponding permeability range between the regression line and lower confidence limit in Figure 3.2. The uniformity of bedrock lithology and fracture geometry (at the scale of the 3D model) supports this extrapolation of injection test permeability data throughout the 3D model region.  $K_r$  values for layers 4-6 were assigned values as shown in Table 5.1. Vertical hydraulic conductances between bedrock layers were calculated using  $K_r$  values. Permeability anisotropy within the bedrock layers (discussed below) was used to define horizontal hydraulic conductivities in the row ( $K_{rx}$ ) and column ( $K_{ry}$ ) directions.

Hydraulic conductivities for bedrock cells containing macroscopic fractures were formulated as shown in Figure 5.5. The macroscopic fractures are assigned

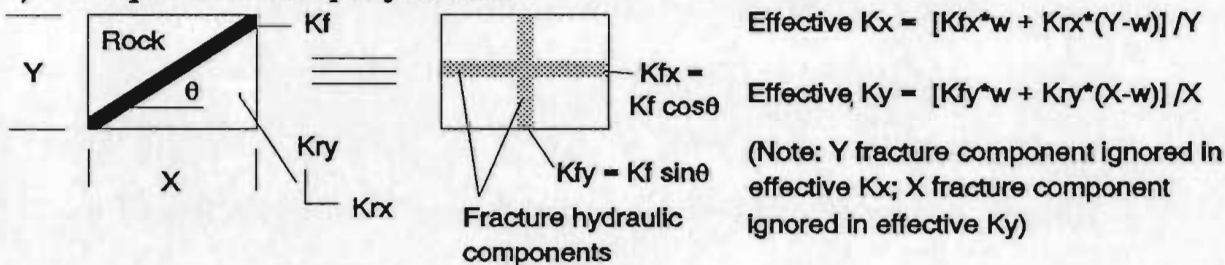
a) *Stratified porous media analogy (after Terzaghi and Peck, 1968)*



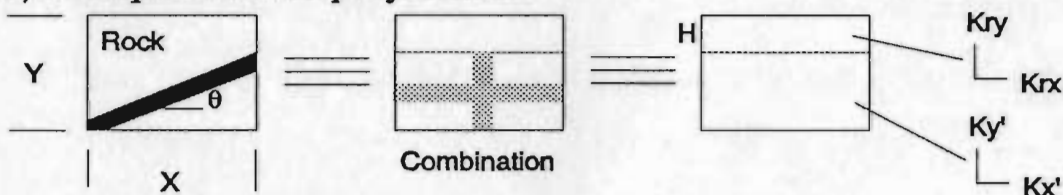
b) *Concordant macroscopic fracture*



c) *Oblique macroscopic fracture*



d) *Oblique macroscopic fracture*



Note: If fracture partly transects cell in x-direction, then analogously:

$$\text{Cell effective } K_x = X / [H/K_{rx} + (X - H)/K_{x'}]$$

$$\text{Cell effective } K_y = [K_{ry}(H) + K_{y'}(X - H)] / X$$

Figure 5.5 - Conceptual approach for formulating horizontal hydraulic conductivity values for cells containing macroscopic fractures in the 3D model.

an average width of 0.2 m (determined from scanline survey data) and are assumed to have equivalent porous media hydraulic conductivities ( $K_f$ ) 1000 times greater than the  $K_r$  values. This  $K_f/K_r$  ratio is in accord with the porous, brecciated nature of faults and fracture zones observed in the SCR V (indicative of increased permeability over the mesoscopically-fractured rock mass), and is consistent with similar ratios used in other modelling studies (e.g. Forster and Smith, 1988; Gale et al., 1987; Odling and Webman, 1991).  $K_f$  is also assumed to be isotropic.

In Figure 5.5, macroscopic fractures are treated as thin, highly-permeable layers within the rock mass and the effective hydraulic conductivities for cells containing such fractures are calculated using principles for combining the permeabilities of stratified porous media. It should be noted that, in the MODFLOW algorithms, hydraulic conductivity is considered homogeneous within any given cell. Hence, the precise location of macroscopic fractures within cells (depicted in Figure 5.4) is of no direct consequence to the model solution; it is the contribution of  $K_f$  to the effective hydraulic conductivity of a cell in the row direction (referred to here as  $K_x$ ) and column direction ( $K_y$ ) that is important for modelling purposes.

Figure 5.5a shows hypothetical stratified porous media and equations for effective  $K_x$  and  $K_y$ . Where a macroscopic fracture is oriented parallel to cell walls (Figure 5.5b), equations for effective  $K_x$  and  $K_y$  are analogous to those in Figure 5.5a. Note that a thin, highly-permeable layer parallel to, say, the  $x$ -direction has little influence on the effective  $K_y$  value, hence effective  $K_y \approx K_r$ .

In cases where a fracture obliquely transects a cell (Figure 5.5c and 5.5d),

the fracture would effectively make contributions to local flow both in the x- and y-directions. One way to represent this for modelling purposes is to resolve the fracture into two layers in the cell, one parallel to the x-direction and the other parallel to the y-direction, so that  $K_{fx} = K_f \cos\theta$  and  $K_{fy} = K_f \sin\theta$ , respectively, as shown. This approach of resolving fracture hydraulic properties into orthogonal components has been used elsewhere (e.g. Odling and Webman, 1991). In Figure 5.5c, equations for effective  $K_x$  and  $K_y$  involve these conceptual layers (parallel to the x- and y-directions, respectively) and ignore the companion layer (based on the arithmetic simplification shown in Figure 5.5b). Incomplete transection of a cell, e.g. in the y-direction in Figure 5.5d, is dealt with by shortening the conceptual fracture layer in that direction. Combining hydraulic conductivities for the part of the cell containing no macroscopic fracture (in this case, the top) with the effective  $K_x$  and  $K_y$  for the fracture-bearing part of the cell gives the effective  $K_x$  and  $K_y$  for the entire cell.

For cells containing multiple macroscopic fractures, effective  $K_x$  and  $K_y$  are determined by subdividing the complex cell into simple units similar to those shown in Figure 5.5, then combining the effective permeabilities of the subunits to obtain the effective permeabilities for the entire cell.

#### Anisotropy for the rock mass and for cells containing fracture zones

A first approximation of horizontal permeability anisotropy for the rock mass in the SCRV is developed from fracture frequencies determined from scanline survey data. In an effort to identify relationships between fracture frequency and measured permeabilities in the SCRV, Figure 5.6 was constructed from borehole logs and all available injection test data. Figure 5.6 shows a weak

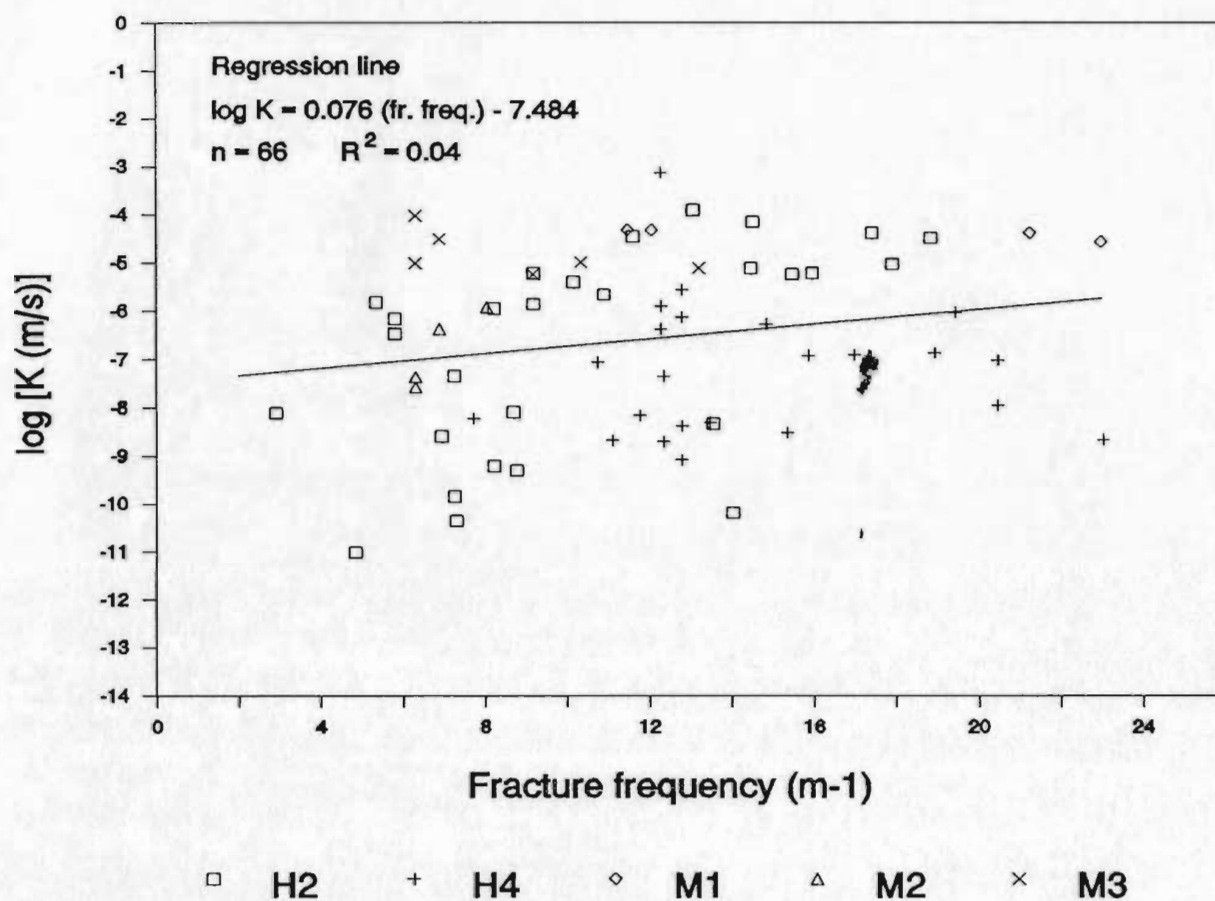


Figure 5.6 - Fracture frequency versus log hydraulic conductivity (K) for borehole injection test data in the SCRV. Individual borehole data are given separate symbols, as shown. Least squares regression line is fitted through all data.

positive correlation between fracture frequency and injection test permeability, as has also been reported elsewhere (e.g. Gale and Rouleau, 1986). The weak correlation is attributed to unequal contributions from individual fractures to flow behaviour at the scale of the test intervals (nominally 2 m). It is recognized that the permeability-fracture frequency correlation lacks statistical rigor. Still, lacking an alternate approach useable with the current data set, the permeability-fracture frequency relationship has been adopted to provide a guideline for the hydraulic behaviour of the rock mass at the scale of the 3D model.

Figure 5.7 shows a fracture frequency rosette compiled from all the scanline survey data in the SCR.V. Each symmetrical pair of rosette points represents the fracture frequency, calculated from all of the fractures ( $\geq 0.5$  m long) encountered along a given scanline, plotted along the azimuthal trend of that scanline. Table 5.3 summarizes data used to construct Figure 5.7. Points 17 and 20 appear to be outliers and are considered to be spurious. By combining the fracture frequency points for the remaining scanlines (dashed line), it can be seen that the maximum fracture frequency direction is approximately east-west, with an average value of about 3 fractures per meter. This corresponds with the north-south striking fracture set 1, which also shows the most dense pole clusters in the SCR.V (Figures 2.7 and 2.8b). The minimum fracture frequency direction is approximately north-south, with an average value of about 1.5 fractures per meter.

Based on Figure 5.7, and the approach of LaPointe and Ganow (1984) described above, the maximum and minimum horizontal permeability directions in bedrock in the SCR.V are inferred to be north-south (parallel to model columns) and east-west (parallel to model rows), respectively. Considering the common, coeval genetic history interpreted for all subvertical fractures in the SCR.V (and

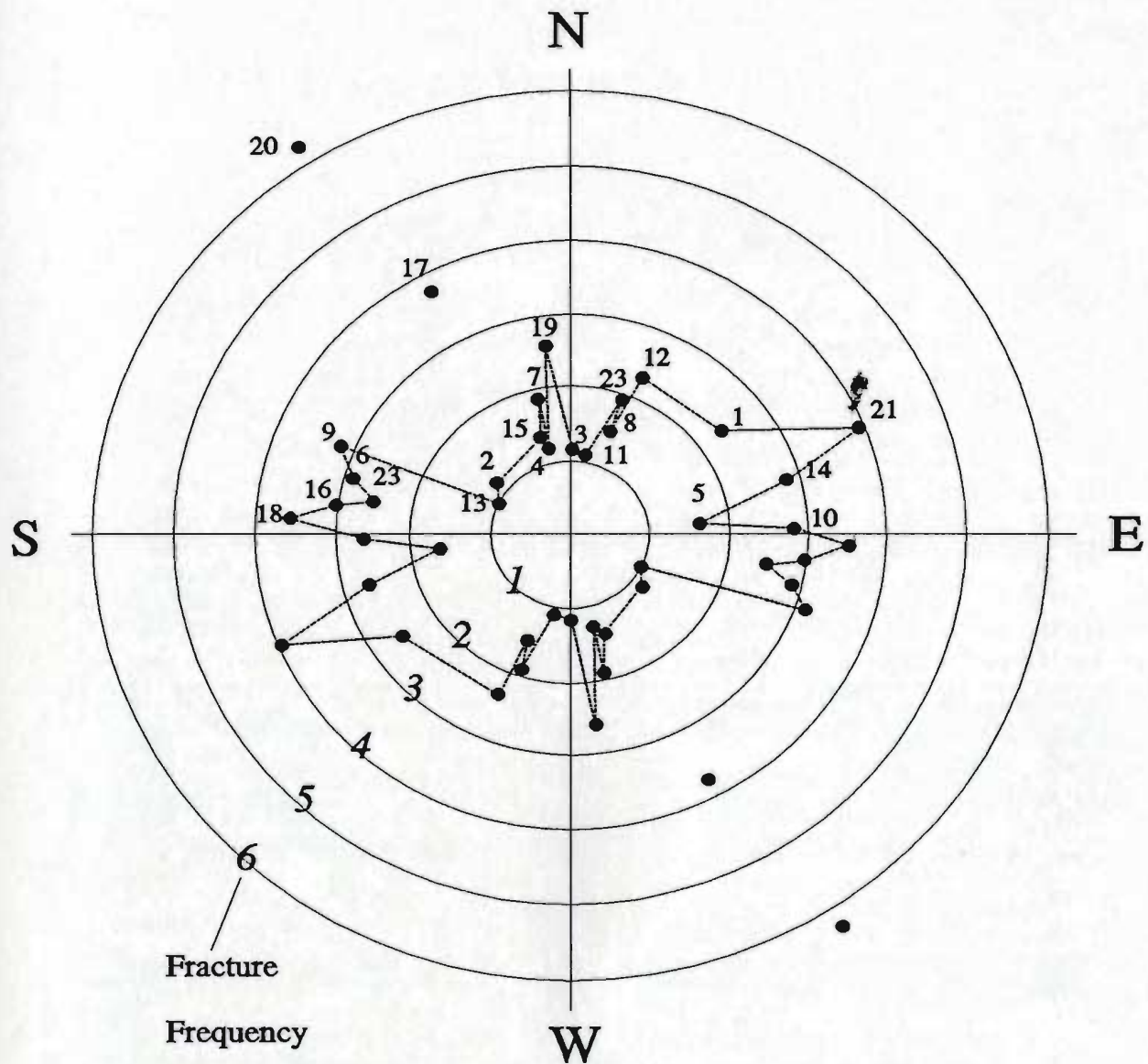


Figure 5.7 - Rosette of fracture frequency for each scanline in the SCR. Key numbers 1-23 refer to individual scanlines as listed in Table 5.3. Points 17 and 20 are treated as outliers, as discussed in text.

Table 5.3 - Summary of data used to construct fracture frequency rosette from scanline data in the SCRV.

Survey Site	Photo No.	Scanline Letter	Ref. Number (Fig. 5.7)	Azimuth (0-360°)	Scanline Length (m)	No. of Fractures	Fracture Frequency (m <sup>-1</sup> )
16	0228	A	1	237	10.0	25	2.50
		B	2	308	14.0	16	1.14
	0231	A	3	000	13.0	15	1.15
	0235	A	4	340	17.6	22	1.25
		B	5	264	13.0	21	1.62
17	0303	A	6	290	20.0	56	2.80
		B	7	190	13.2	25	1.89
18	0315	A	8	020	21.0	32	1.52
		B	9	113	21.0	65	3.10
19	0334	A	10	269	15.0	39	2.60
		B	11	010	15.0	16	1.07
21	0415	A	12	023	12.0	28	2.33
		B	13	295	12.0	12	1.00
	0417	A	14	255	10.0	26	2.60
		B	15	161	10.0	14	1.40
44	1406	A	16	278	12.0	36	3.00
		B	17	332	10.5	39	3.71
49	1229	A	18	274	14.5	51	3.52
		B	19	173	13.7	35	2.55
54	1321	A	20	327	12.5	78	6.24
		B	21	248	12.5	49	3.92
81	0324	A	22	100	10.0	25	2.50
		B	23	019	10.0	19	1.90



lacking specific information on the relative permeability of individual fracture sets) it is further assumed that the subvertical fractures in the SCRVR all contribute to flow in an approximately equal manner, at least at the scale of the 3D model. Hence, the permeability anisotropy ratio ( $K_y/K_x$  or  $K_{vd}/K_{hw}$ ) for the 3D models is based on the fracture frequency ratio and assigned a value of 2:1.

#### 5.3.4 Three-dimensional model results

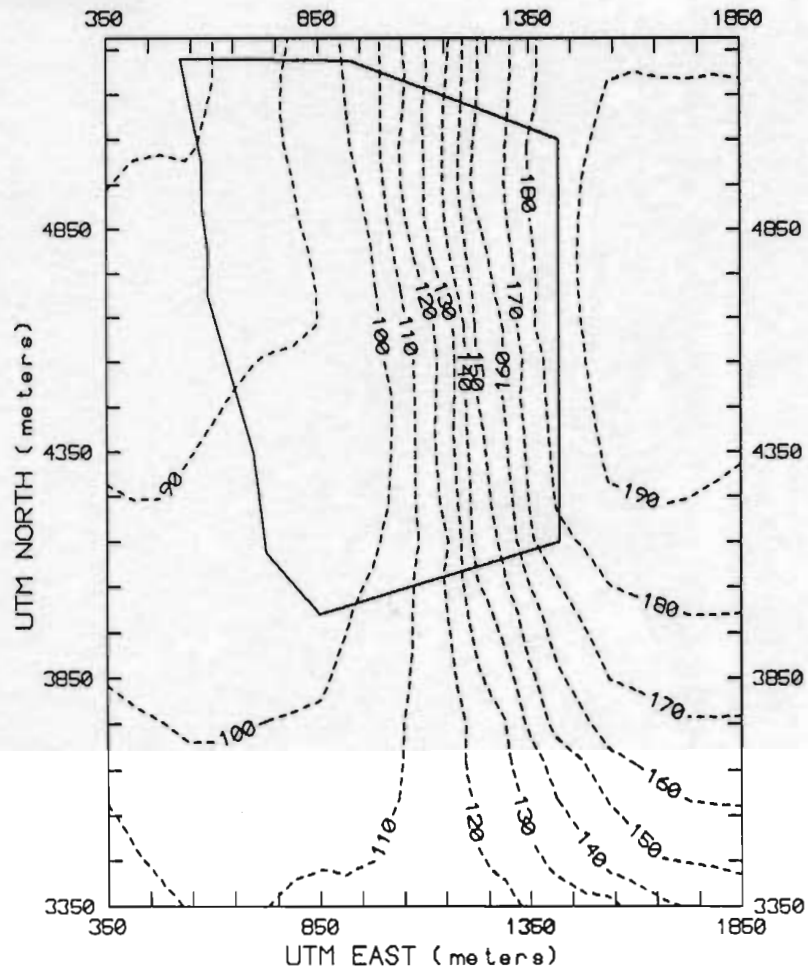
Results of three 3D model cases are presented below:

- Case 1: isotropic conditions, with  $K_y/K_x$  equal to one and no incorporation of hydraulic properties of macroscopic fractures (Figure 5.8);
- Case 2: anisotropic conditions, with  $K_y/K_x$  equal to two and no incorporation of hydraulic properties of macroscopic fractures (Figure 5.9);
- Case 3: anisotropic conditions, with  $K_y/K_x$  equal to two and incorporation of cell-specific hydraulic properties of macroscopic fractures (Figure 5.10).

The code MODFLOW was used for cases 1 and 2; the code HETMOD (Appendix I) was used for case 3. In all cases, mass balance discrepancies for the simulations (balance of cumulative inflows and outflows for all the model cells) were negligible (less than 0.5 %).

Figures 5.8, 5.9 and 5.10 present simulated hydraulic heads for the bedrock layers in the 3D mesh, in meters above sea level. Due to an operational limitation of MODFLOW, which unavoidably induced apparent desaturation of many cells in the thin overburden material in the 3D models, layer 1 results were very sparse and are not presented. All contour maps were produced using

a) ISOTROPIC CASE (NO FRACTURES) - LAYER 2



b) ISOTROPIC CASE (NO FRACTURES) - LAYER 3

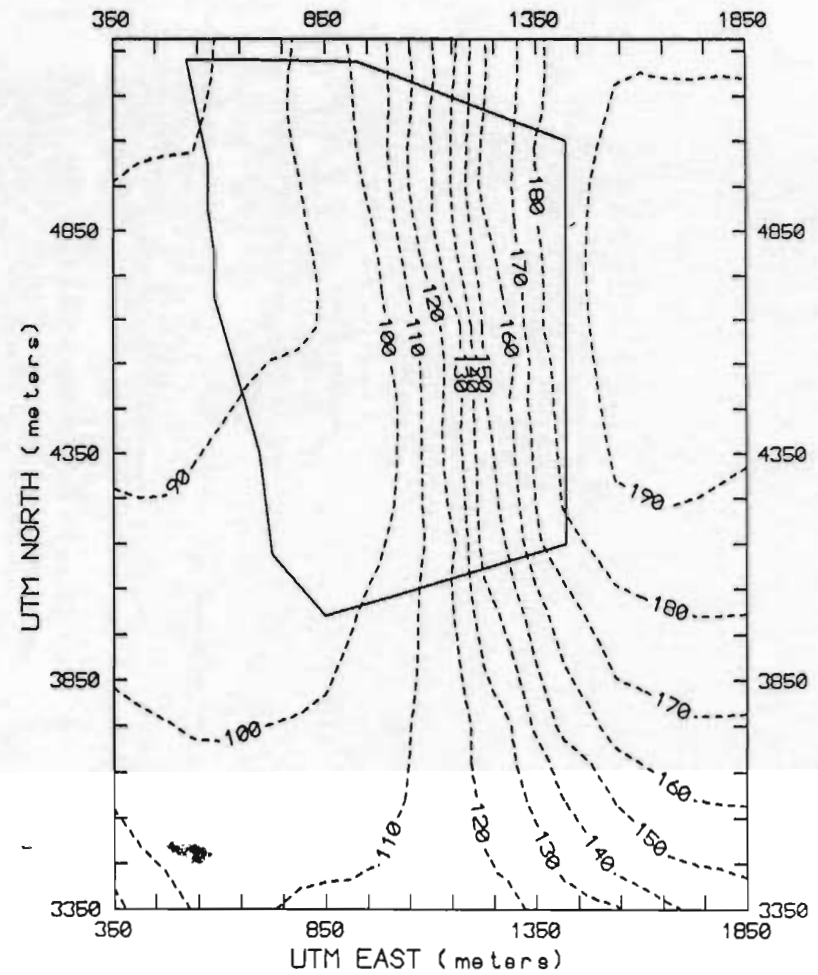


Figure 5.8 - Simulated hydraulic heads (dashed contours) for layers 2 (a), 3 (b), 4 (c), 5 (d) and 6 (e) for the isotropic 3D model (no incorporation of macroscopic fractures). Heads are in meters above sea level. The boundary of the assumed catchment is shown by a solid line.

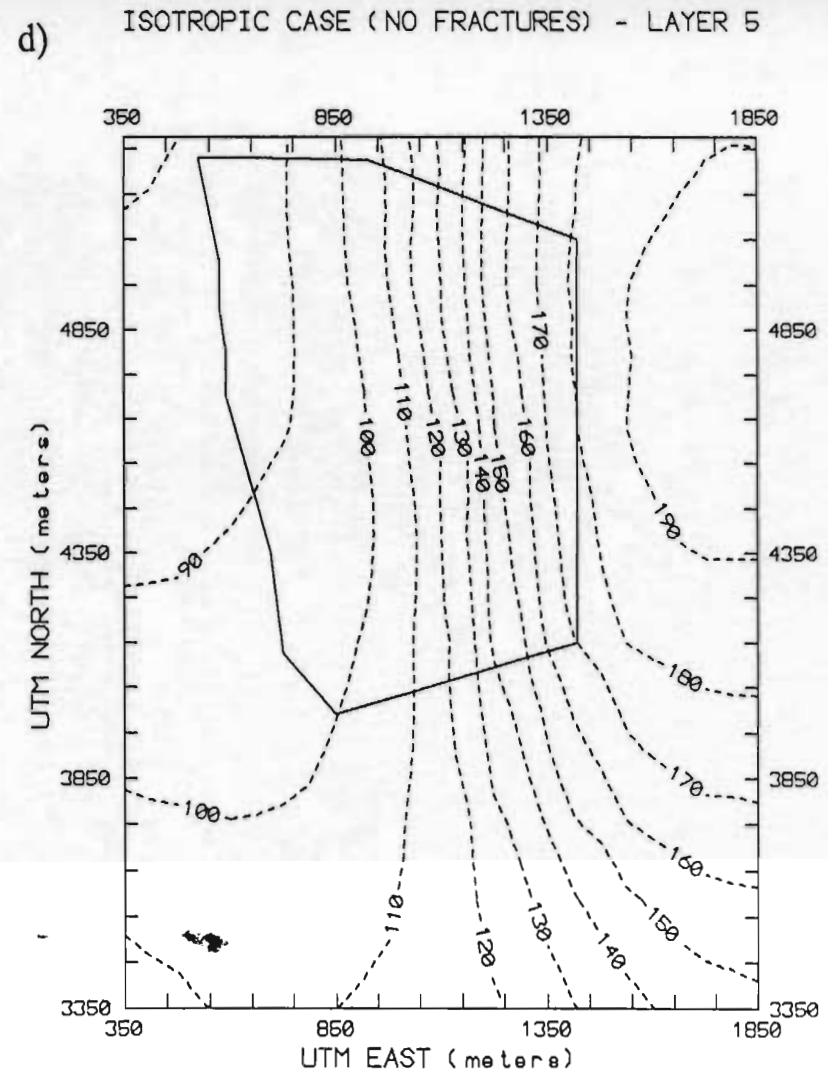
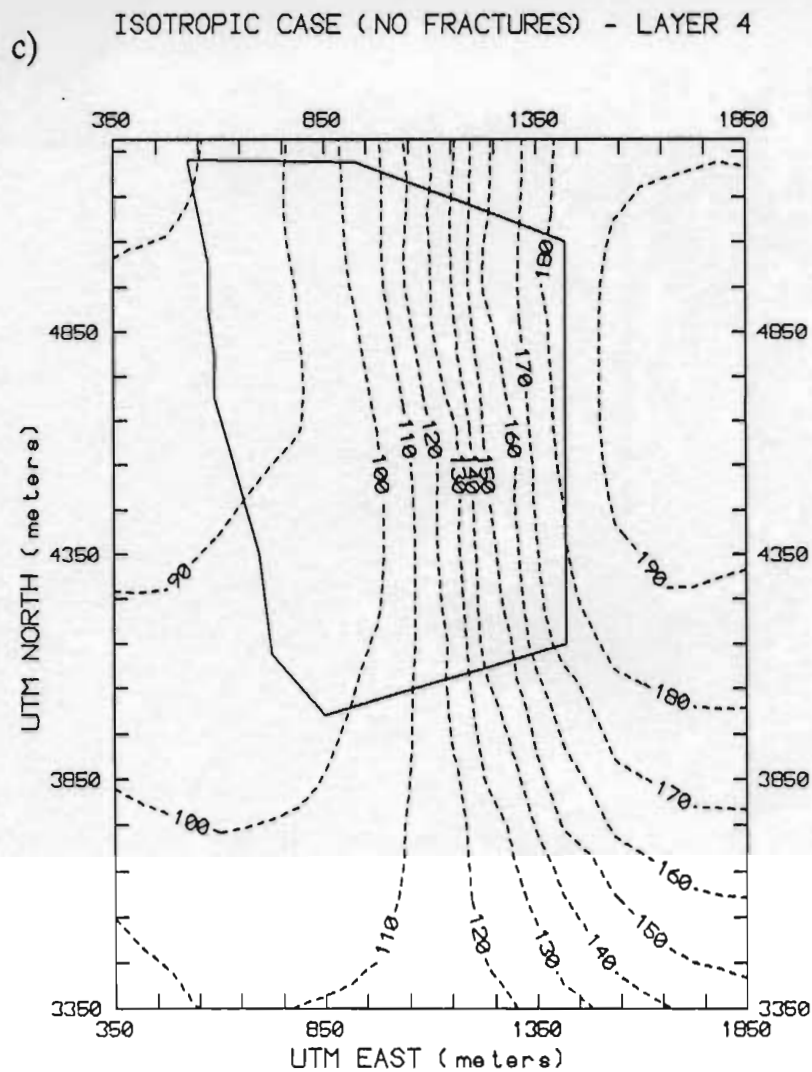


Figure 5.8 - Simulated hydraulic heads (dashed contours) for layers 2 (a), 3 (b), 4 (c), 5 (d) and 6 (e) for the isotropic 3D model (no incorporation of macroscopic fractures). Heads are in meters above sea level. The boundary of the assumed catchment is shown by a solid line.

e) ISOTROPIC CASE (NO FRACTURES) - LAYER 6

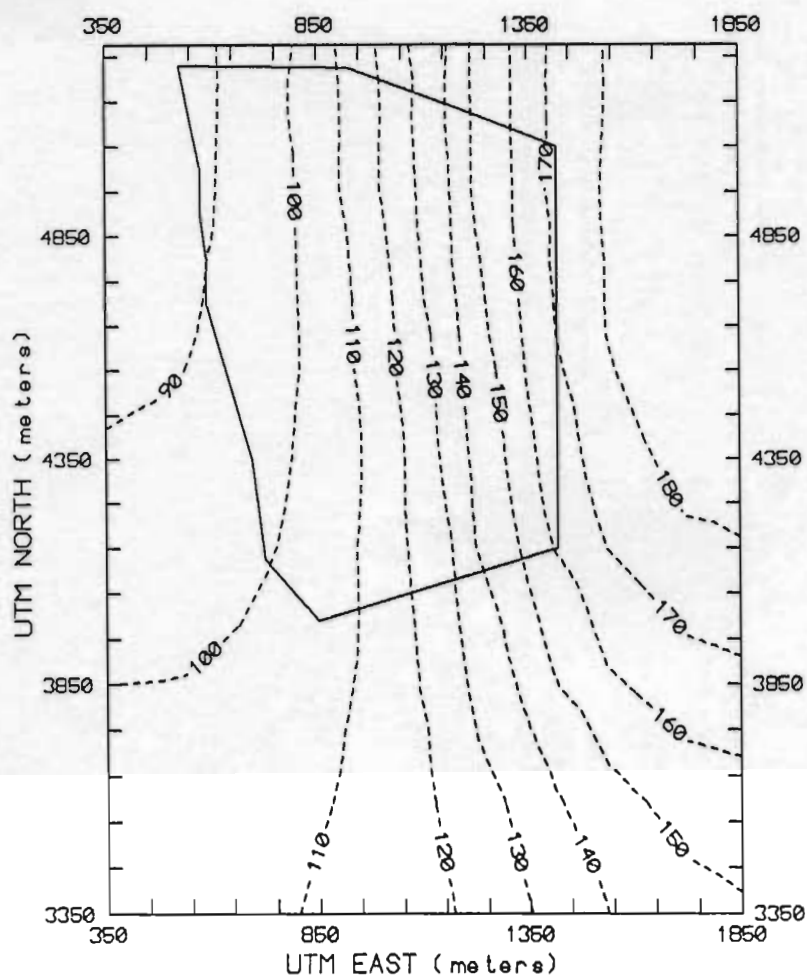
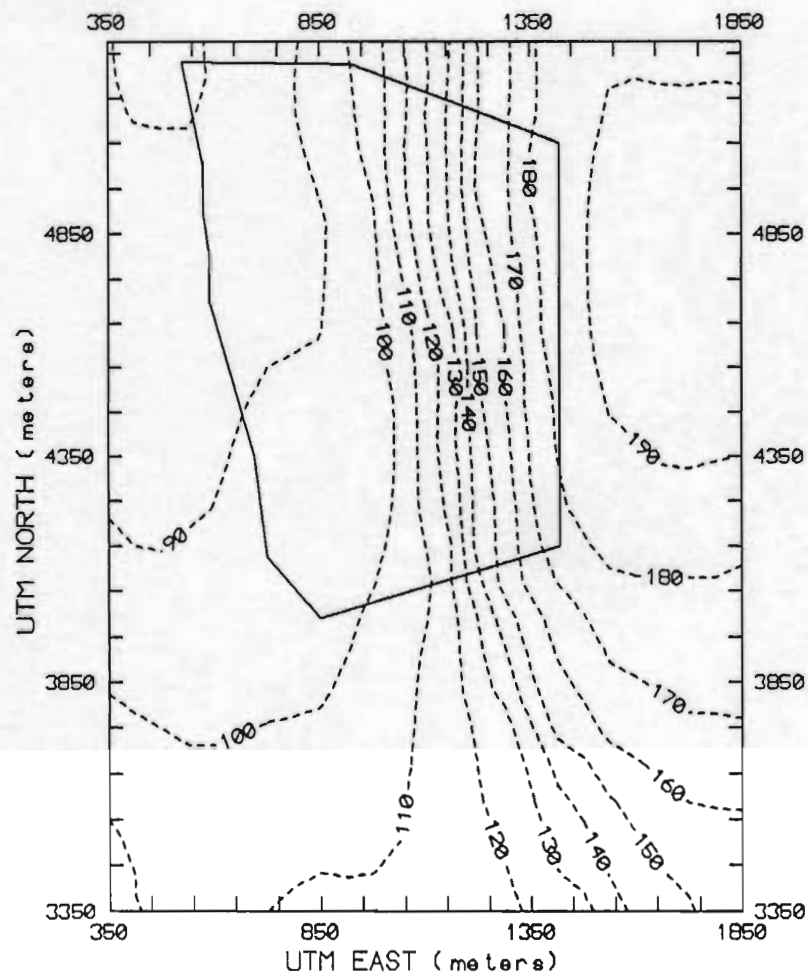


Figure 5.8 - Simulated hydraulic heads (dashed contours) for layers 2 (a), 3 (b), 4 (c), 5 (d) and 6 (e) for the isotropic 3D model (no incorporation of macroscopic fractures). Heads are in meters above sea level. The boundary of the assumed catchment is shown by a solid line.

a) ANISOTROPIC CASE (NO FRACTURES) - LAYER 2



b) ANISOTROPIC CASE (NO FRACTURES) - LAYER 3

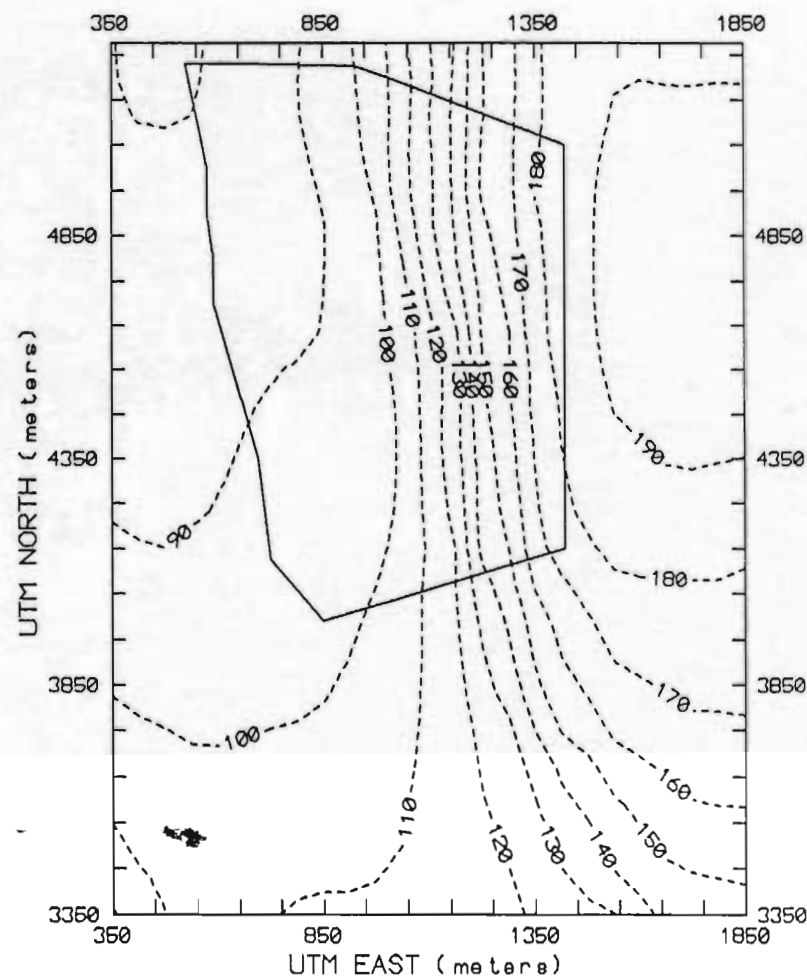
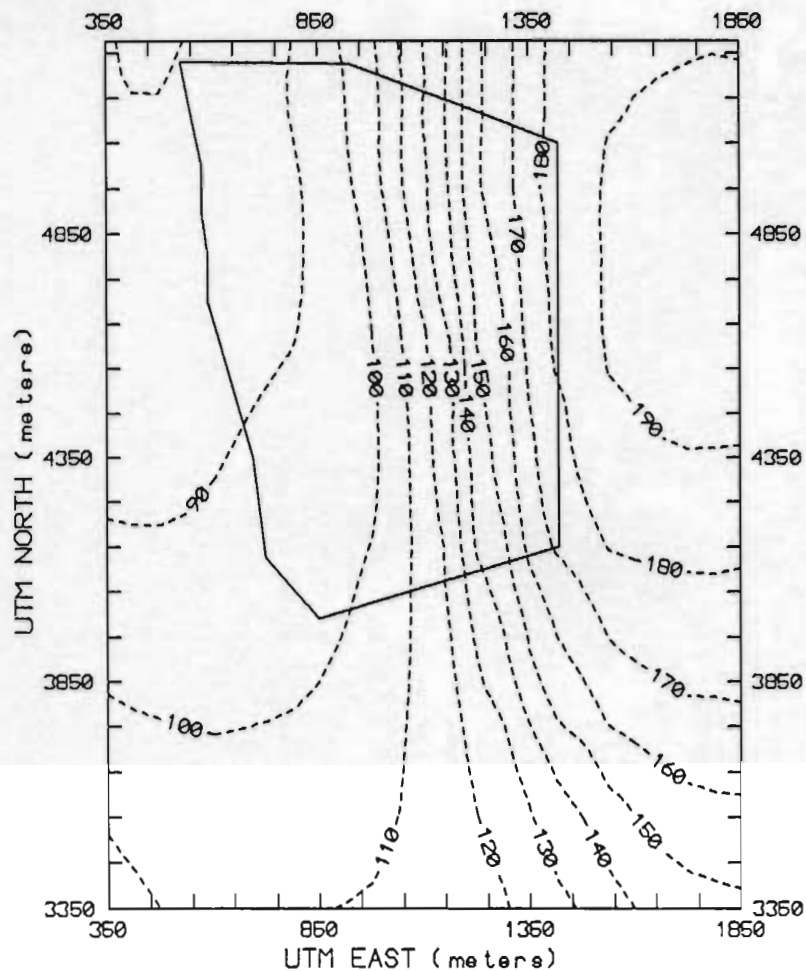


Figure 5.9 - Simulated hydraulic heads (dashed contours) for layers 2 (a), 3 (b), 4 (c), 5 (d) and 6 (e) for the anisotropic 3D model (no incorporation of macroscopic fractures). Heads are in meters above sea level. The boundary of the assumed catchment is shown by a solid line.

c) ANISOTROPIC CASE (NO FRACTURES) - LAYER 4



d) ANISOTROPIC CASE (NO FRACTURES) - LAYER 5

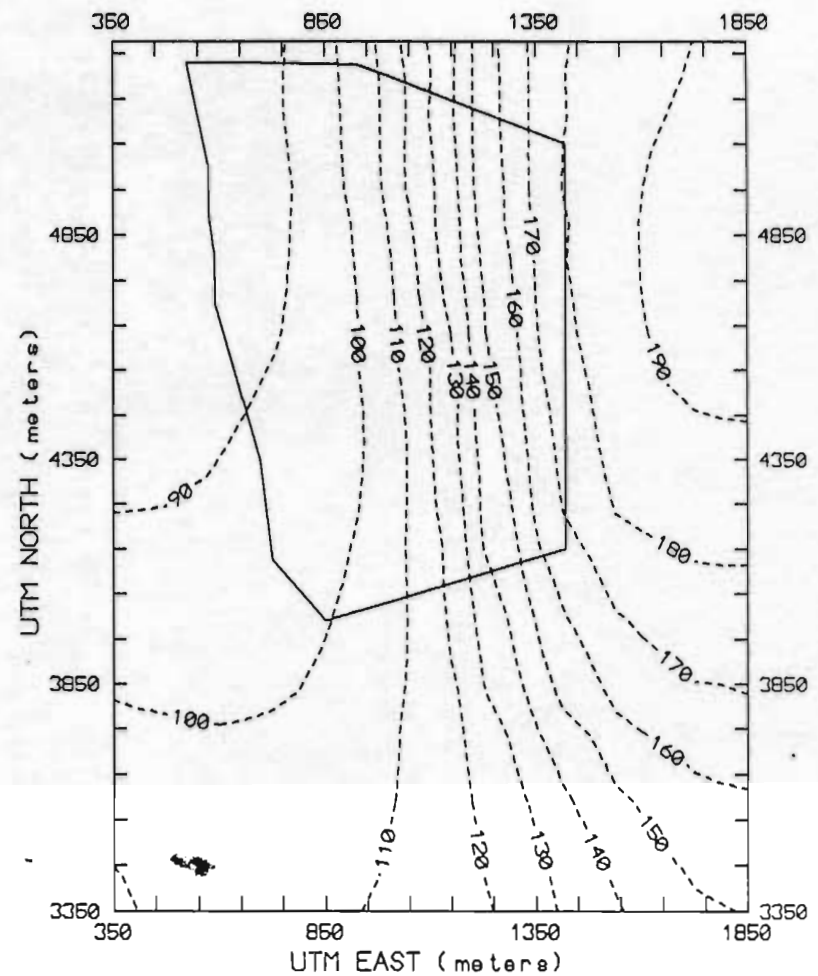


Figure 5.9 - Simulated hydraulic heads (dashed contours) for layers 2 (a), 3 (b), 4 (c), 5 (d) and 6 (e) for the anisotropic 3D model (no incorporation of macroscopic fractures). Heads are in meters above sea level. The boundary of the assumed catchment is shown by a solid line.

e) ANISOTROPIC CASE (NO FRACTURES) - LAYER 6

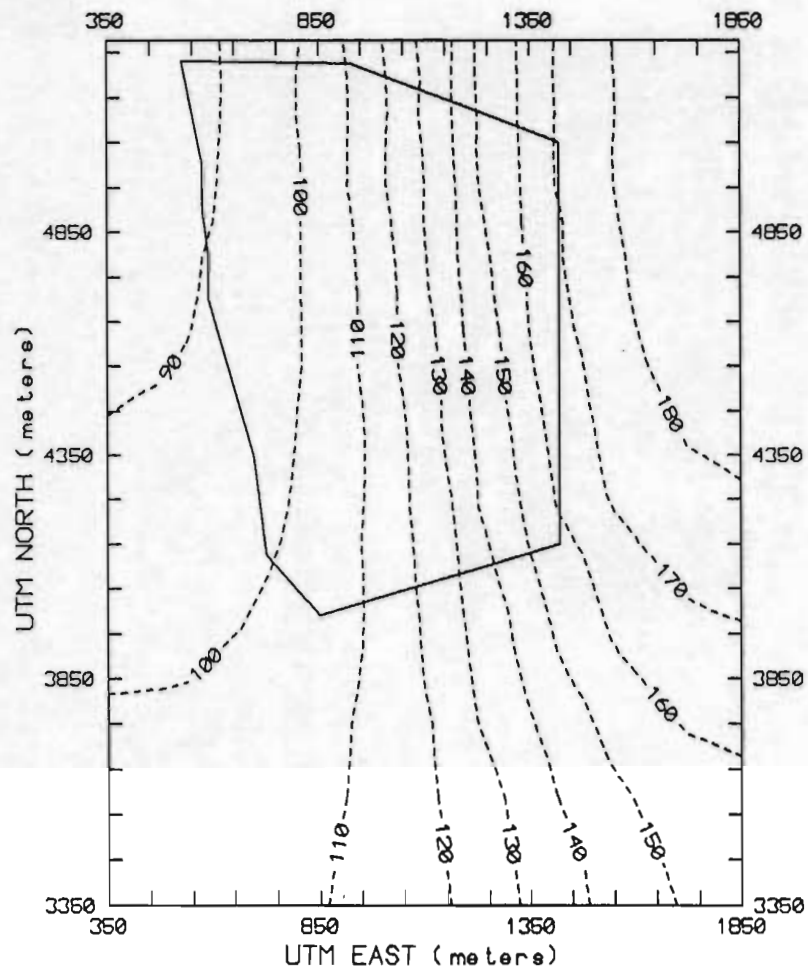
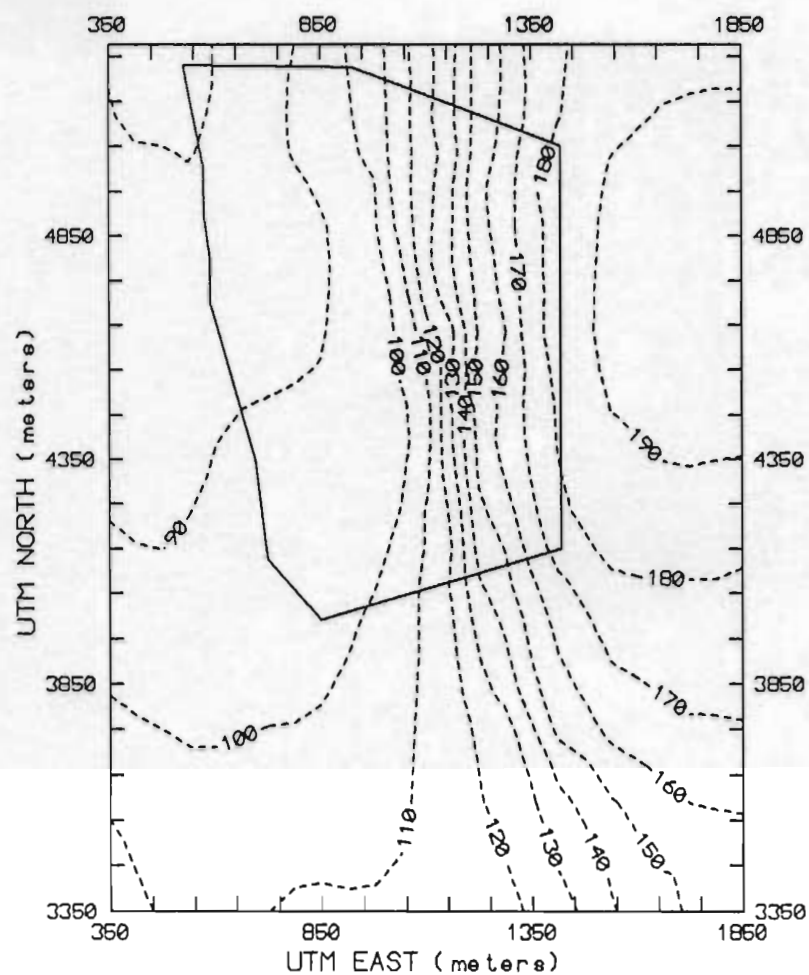


Figure 5.9 - Simulated hydraulic heads (dashed contours) for layers 2 (a), 3 (b), 4 (c), 5 (d) and 6 (e) for the anisotropic 3D model (no incorporation of macroscopic fractures). Heads are in meters above sea level. The boundary of the assumed catchment is shown by a solid line.

a) ANISOTROPIC CASE WITH FRACTURES - LAYER 2



b) ANISOTROPIC CASE WITH FRACTURES - LAYER 3

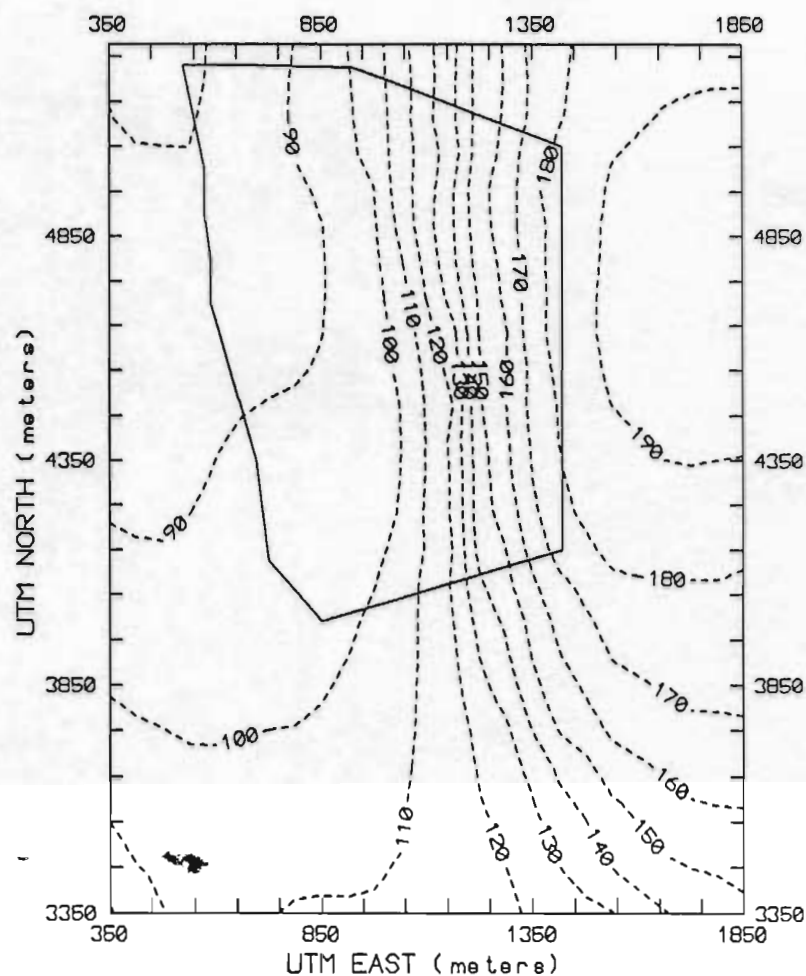
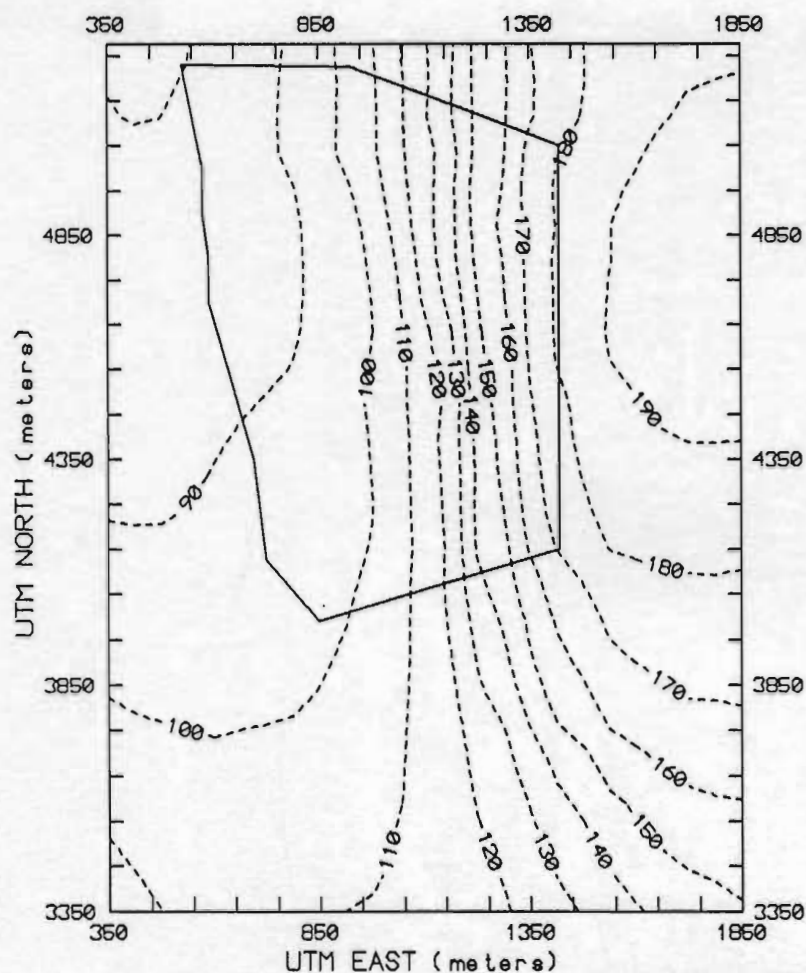


Figure 5.10 - Simulated hydraulic heads (dashed contours) for layers 2 (a), 3 (b), 4 (c), 5 (d) and 6 (e) for the anisotropic 3D model (incorporating macroscopic fractures). Heads are in meters above sea level. The boundary of the assumed catchment is shown by a solid line.



c) ANISOTROPIC CASE WITH FRACTURES - LAYER 4



d) ANISOTROPIC CASE WITH FRACTURES - LAYER 5

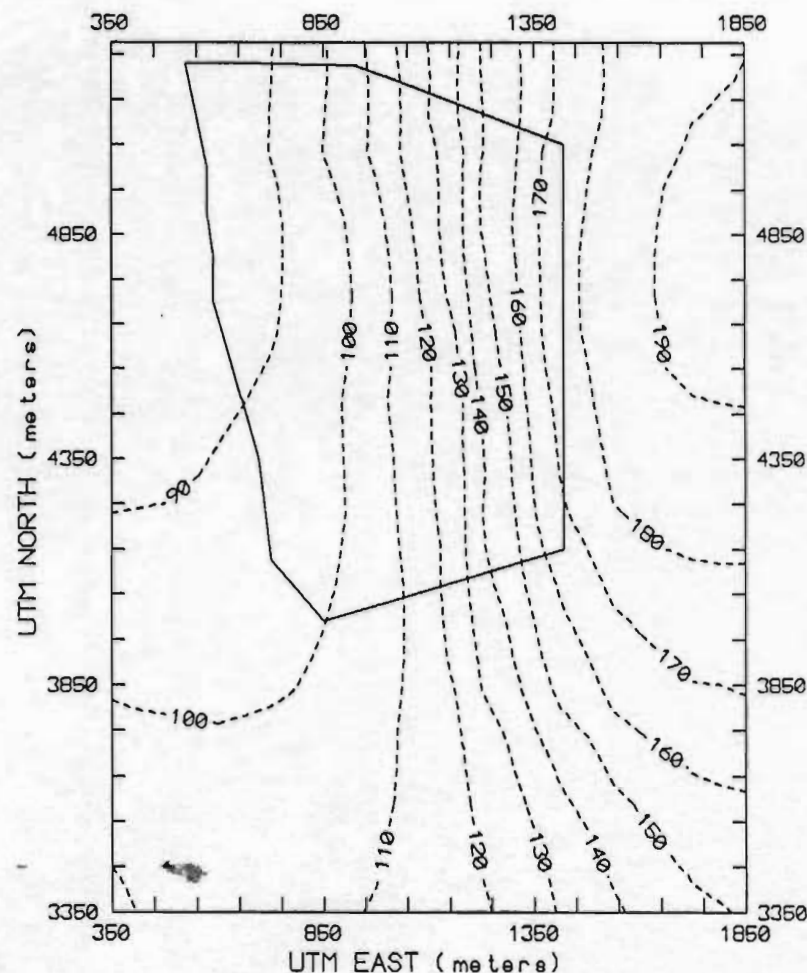


Figure 5.10 - Simulated hydraulic heads (dashed contours) for layers 2 (a), 3 (b), 4 (c), 5 (d) and 6 (e) for the anisotropic 3D model (incorporating macroscopic fractures). Heads are in meters above sea level. The boundary of the assumed catchment is shown by a solid line.

e)

ANISOTROPIC CASE WITH FRACTURES - LAYER 6

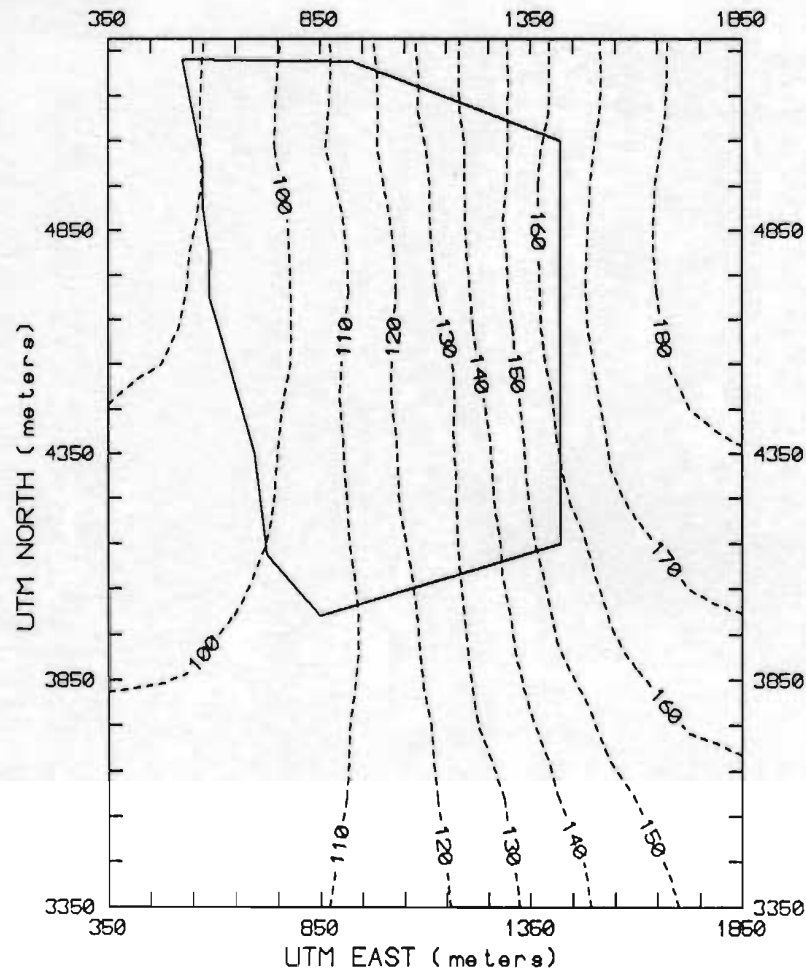


Figure 5.10 - Simulated hydraulic heads (dashed contours) for layers 2 (a), 3 (b), 4 (c), 5 (d) and 6 (e) for the anisotropic 3D model (incorporating macroscopic fractures). Heads are in meters above sea level. The boundary of the assumed catchment is shown by a solid line.

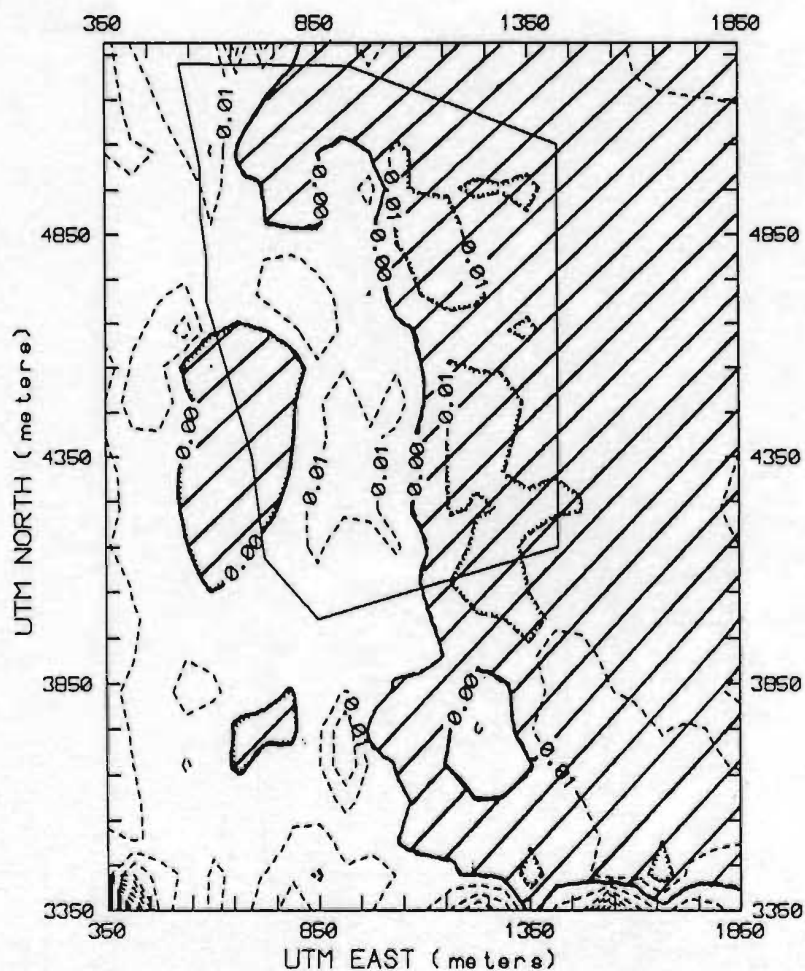
commercially available contouring software (SURFER, Golden Software Inc., Golden, Colorado, U.S.A.), using a standard inverse weighting contouring scheme.

The contoured head patterns for all three cases are grossly similar - near the surface (e.g. layers 2 and 3), the equipotential surface is steeply west-dipping beneath the hill slope and gently west- to northwest-dipping beneath the valley portion of the assumed catchment, while at deeper levels (e.g. layers 5 and 6), the equipotential surface is smoothed and moderately west-dipping. This trend of decreasing complexity in simulated head patterns with depth has been observed in other regional groundwater flow studies (e.g. Gale et al., 1987). The equipotential surface in layer 2 for each model is equivalent to the water table beneath the hill slope on the right side of the model grid and the potentiometric surface along the valley bottom portion of the assumed catchment. For all cases, simulated artesian heads were 0.25-0.5 m above ground surface for the cell containing piezometer M1, which agrees well with observed artesian heads under low flow conditions.

The principal difference between simulated head patterns for the three cases is that the equipotential surface under the hill crest (along the eastern boundary of the assumed catchment) is highest for case 1 (Figure 5.8) and lowest for case 3 (Figure 5.10). Elevation differences are most obvious (on the order of six meters) in deeper layers of cases 1 and 3 (e.g. as shown by the eastward shift of the 170 m contour line in relation to the eastern catchment boundary in Figures 5.8e and 5.10e). For cases 1 and 2, the equipotential patterns are nearly identical in all bedrock layers.

To further investigate the distribution of recharge and discharge areas around the modelled area, Figures 5.11, 5.12 and 5.13 were constructed showing

a) VERTICAL GRADIENT BETWEEN LAYER 2 AND 3



b) VERTICAL GRADIENT BETWEEN LAYER 4 AND 5

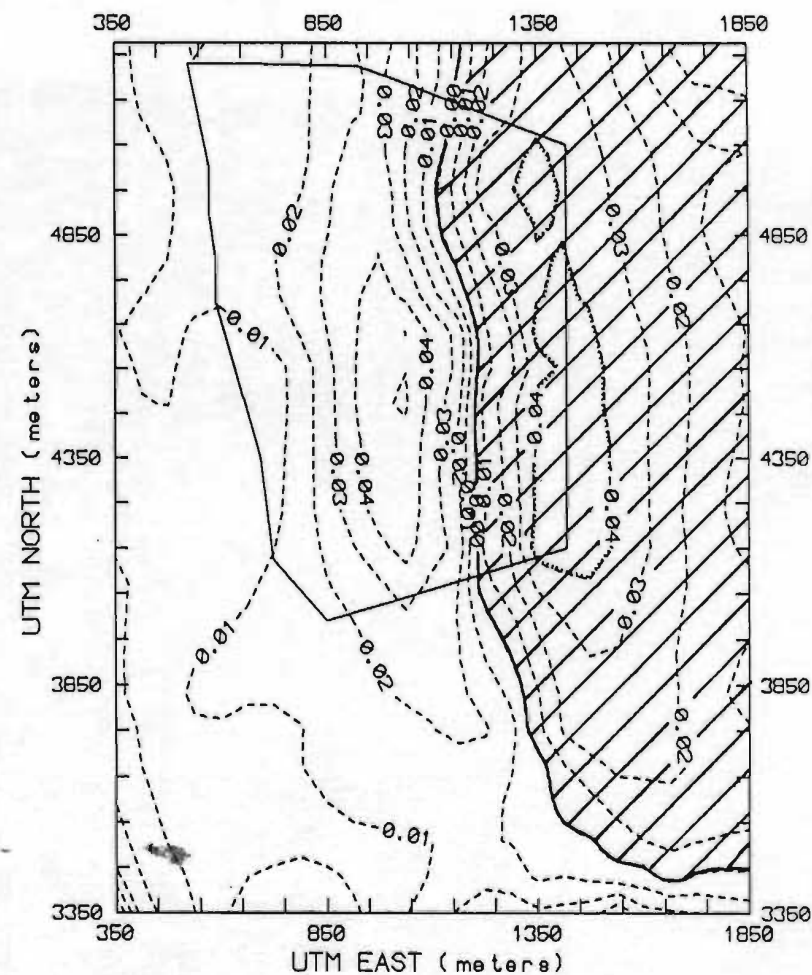
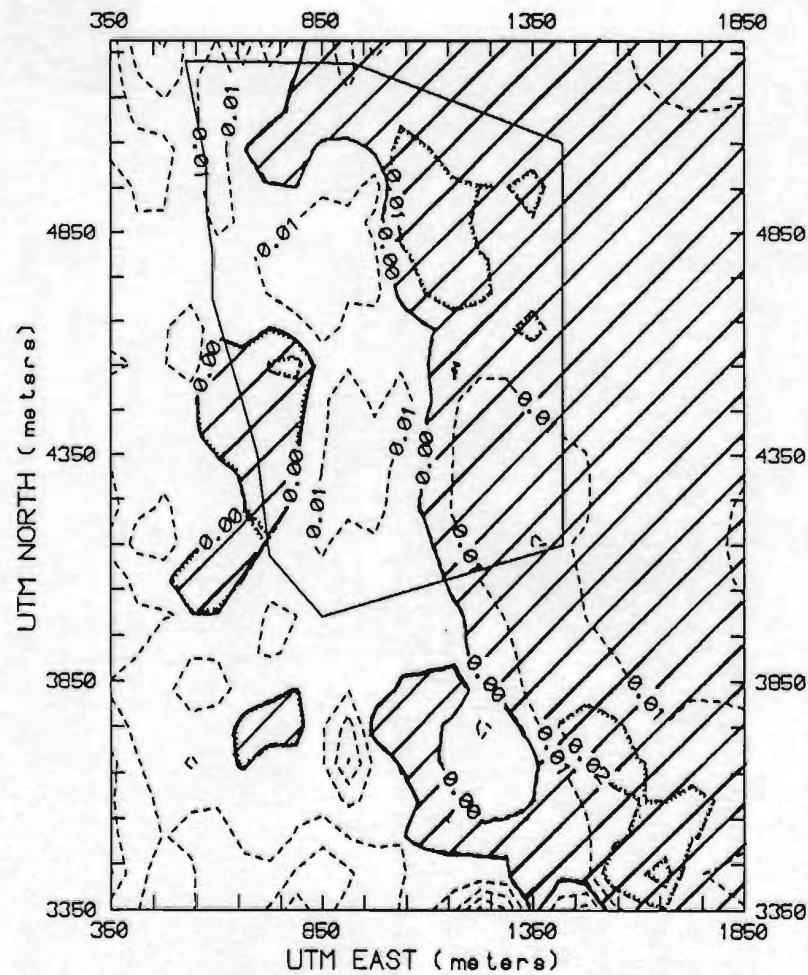


Figure 5.11 - Simulated vertical component of hydraulic gradient (dashed contours) between layers 2 and 3 (a) and between layers 4 and 5 (b) for the isotropic model case (no macroscopic fractures). Negative values indicate recharge areas (cross-hatched); positive values indicate discharge areas. The boundary of the assumed catchment is shown by a solid line.

a) VERTICAL GRADIENT BETWEEN LAYER 2 AND 3



b) VERTICAL GRADIENT BETWEEN LAYER 4 AND 5

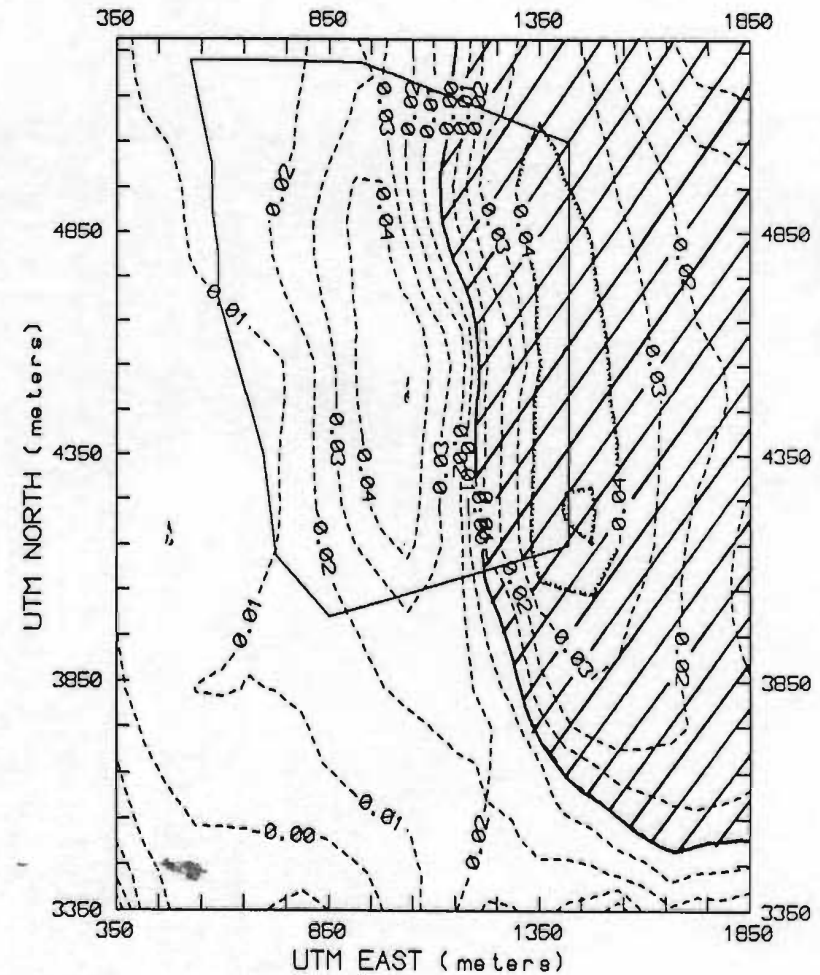
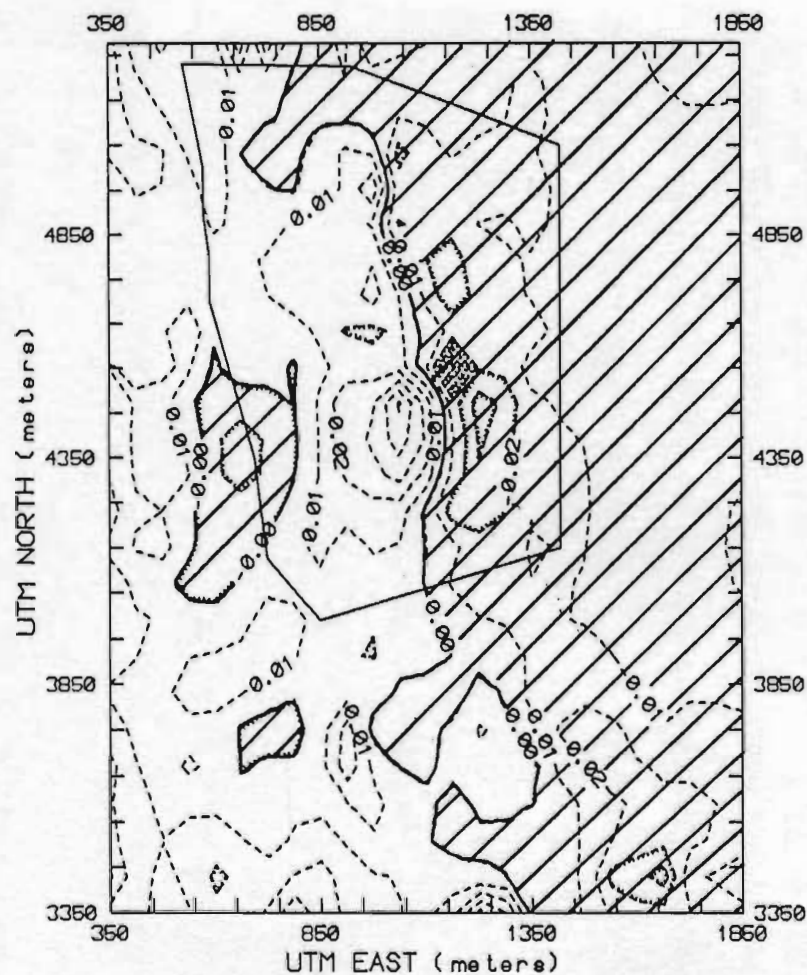


Figure 5.12 - Simulated vertical component of hydraulic gradient (dashed contours) between layers 2 and 3 (a) and between layers 4 and 5 (b) for the anisotropic model case (no macroscopic fractures). Negative values indicate recharge areas (cross-hatched); positive values indicate discharge areas. The boundary of the assumed catchment is shown by a solid line.



a) VERTICAL GRADIENT BETWEEN LAYER 2 AND 3



b) VERTICAL GRADIENT BETWEEN LAYER 4 AND 5

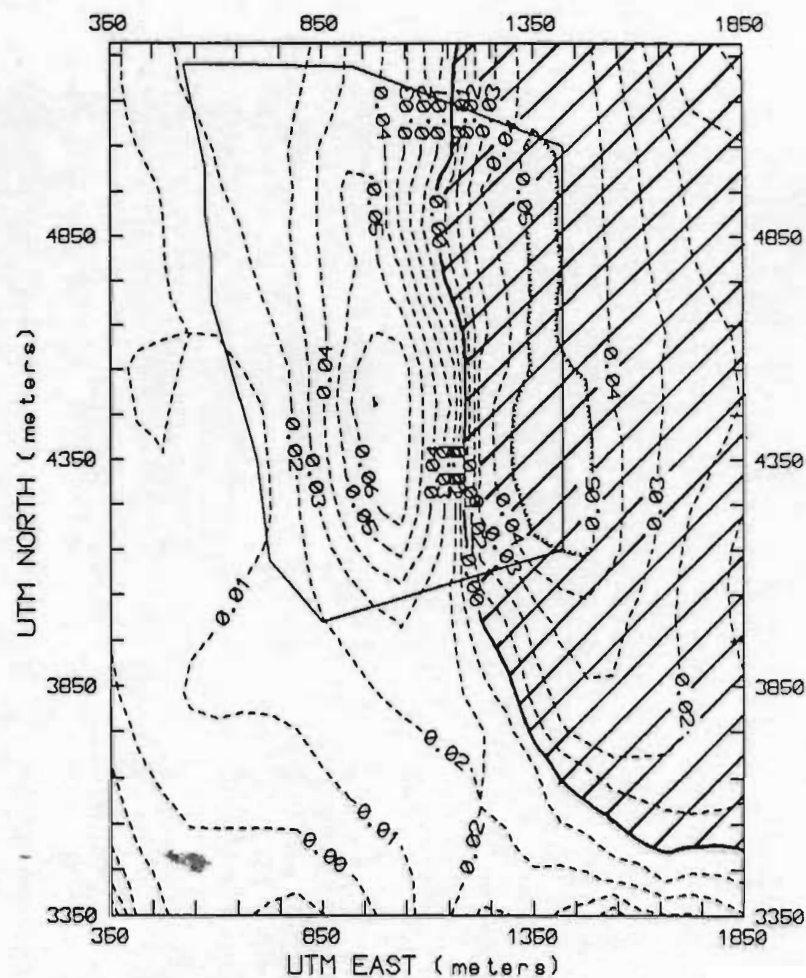


Figure 5.13 - Simulated vertical component of hydraulic gradient (dashed contours) between layers 2 and 3 (a) and between layers 4 and 5 (b) for the anisotropic model case (with macroscopic fractures). Negative values indicate recharge areas (cross-hatched); positive values indicate discharge areas. The boundary of the assumed catchment is shown by a solid line.

simulated vertical components of hydraulic gradient between layers 2 and 3 and layers 4 and 5, for each 3D model case. The vertical components of hydraulic gradient (in units of m/m) were calculated by dividing the simulated head difference for two adjoining layers by the vertical distance between their cell nodes. Negative gradients (decreasing head with depth) indicate recharge areas (cross-hatched areas in the figures), while positive gradients indicate discharge areas. The principal features of these plots are:

- 1) the near-surface gradients for all cases show similar patterns of recharge on the hillside, discharge between the base of the hillslope and the mid-valley area, and a recharge zone along the mid-valley glacial drift ridge at the western boundary of the assumed catchment. This overall pattern is consistent with physical measurements in the SCR V and with assumptions regarding the physical hydrologic setting of the assumed catchment.
- 2) Gradient contour patterns for all three cases become simpler with depth, as did the equipotential patterns. The recharge zone at depth is restricted to eastern portions of the assumed catchment, and gradient magnitudes increase with depth.
- 3) Gradient patterns vary smoothly and are nearly identical for cases 1 and 2, whereas in case 3, near-surface gradients (Figure 5.13a) are more irregular with local high and low values coinciding with areas of dense macroscopic fractures.

The significance of the contoured head and gradient patterns is addressed below, following a discussion of limitations to these 3D model results.

### 5.3.5 Limitations of 3D model results

Interpretation of the 3D model results must be in accordance with limitations imposed by the underlying assumptions and overall modelling approach. The reliance on a simple fracture frequency approach to approximate permeability anisotropy as well as the salient assumption that all subvertical fractures contribute equally to flow at the scale of the model implies that important controls on directional permeability (such as effective normal stress on fractures and varying fracture interconnectivity) are effectively ignored. However, lacking feasible methods to account for such controls using currently available data, this is considered the only justifiable approach at present. Due to this limitation, the 3D model results should be viewed as providing only semi-quantitative information on groundwater flow characteristics at the scale of the assumed catchment. It is notable that results for cases 1 and 2 are nearly identical. This infers that the anisotropy ratio (2:1) really has little effect on catchment-scale groundwater flow. This may be due to the fact that the variability of  $K_r$  values from cell to cell (about 1/2 order of magnitude) is greater than the anisotropy ratio.

A further limitation centers around the incorporation of macroscopic fractures into the 3D model. The approach of incorporating assumed hydraulic properties of macroscopic fractures into effective cell permeabilities amounts to a smoothing process, since the fracture properties are "spread" throughout a cell. As mentioned above, homogeneous properties within a cell are required by MODFLOW (and HETMOD) algorithms. The size of the cell therefore determines how realistic is the incorporation approach. For example, the approach of incorporating the hydraulic properties of macroscopic fractures to



form a diagonal pattern of "fracture" cells (e.g. cells in row 16/column 8, row 15/column 9, etc. in Figure 5.4) effectively breaks long diagonal fractures into shorter segments with no direct hydraulic connection along strike. However, since all fractures in the model are resolved into X- and Y-direction hydraulic components in each cell through which they pass (as per Figure 5.5), there is no attempt to maintain direct hydraulic connection along strike for macroscopic fractures in the modelling approach adopted here. Model grids composed of many tiny cells could incorporate macroscopic fractures as more physically-realistic narrow arrays of fracture-bearing cells, but in turn require exhaustive pre-processing and formulation of input parameters. Larger grid sizes are easier to manage, but may cause the influence of individual macroscopic fractures to be subdued. In retrospect, the grid used in this study may have been somewhat coarse, from the perspective of incorporating macroscopic fractures, judging by the difference in magnitude of fracture width (0.2 m) and cell dimension (50-100 m). This could be proven, as future work, by reconstructing the entire 3D model at a smaller grid size and comparing results with those given here.

## 5.4 Hydrogeological inferences based on numerical modelling results

### 5.4.1 Effective size of catchment area for the study reach

Two-dimensional model results suggested that the catchment area contributing groundwater to the study reach may be smaller than originally assumed (i.e. as indicated by the catchment boundary on Figures 5.8 to 5.13). However, 3D model results tend to suggest that the original catchment boundary is reasonable. This is shown best by the distribution of vertical hydraulic gradients (Figures 5.11, 5.12 or 5.13). In these figures, the principal discharge zone both at shallow and deeper levels coincides with the study reach area, along the western part of the assumed catchment. If substantial underflow was taking place, i.e. with groundwater flowing from the hillslope in the catchment, beneath the study reach and discharging into the western branch of the Seal Cove River, then more pronounced elongate upward gradient contours would be expected along the western branch. In addition, the occurrence of the strongest downward gradient contour exactly underlying the eastern edge of the catchment (e.g. Figure 5.12b) supports the choice of the hillcrest as the logical groundwater flow boundary for the assumed catchment.

The pronounced localized recharge gradient within the catchment in Figure 5.13a coincides with model cells containing multiple macroscopic fractures. This infers that, in sufficient density, these fractures can increase local permeability enough to perturb the gradient field at catchment scale. The lack of obvious gradient or equipotential line perturbations in other fracture-bearing cells (see Figure 5.4) suggests that individual macroscopic fractures have no discernable effect on flow at catchment scale, or that these effects are more subtle and are masked during the contouring process.

#### 5.4.2 Uniformity of groundwater flux along study reach

To investigate the uniformity of groundwater flux along the study reach, Figure 5.14 was constructed using simulated groundwater flow rates into or out of stream reaches within "river" cells, reported in MODFLOW (and HETMOD) output. Fluxes were determined by dividing the flow rate ( $\text{m}^3/\text{s}$ ) by the surface area ( $\text{m}^2$ ) of the stream section within a given river cell. Figure 5.14 shows fluxes from the inflow weir (W1) at the right side of the plot, downstream to the outflow weir (W3) at the left side. Row and column numbers are included for cross-reference to Figure 5.1 and Table 5.2. The cell containing piezometer M1 (row 12, column 10) and the next four cells, representing the beaver pond, are identified, along with calculated discharge flux at M1 and average measured low flow seepage flux at the beaver pond. Fluxes were transformed to log values for convenience of plotting.

The most important feature of Figure 5.14 is the wide ranging flux variability between reach sections (up to two orders of magnitude between adjacent river cells) and the presence of recharge conditions for some cells. This

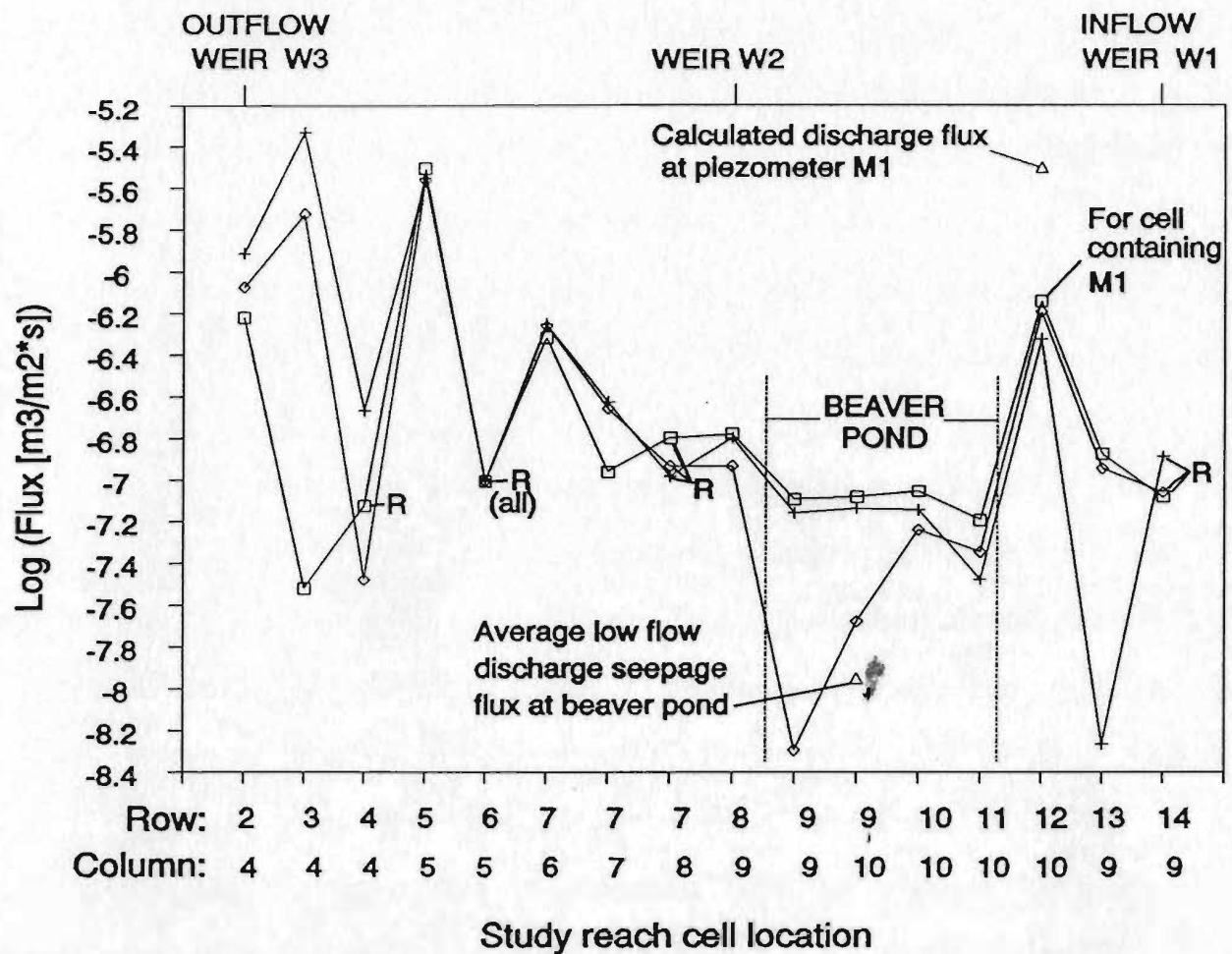


Figure 5.14 - Simulated groundwater flux for sections of the study reach in the SCR. Most points show discharge into the reach section; those with "R" indicate simulated recharge from that reach section. Points representing measured seepage flux, and calculated discharge flux at M1 are also shown. Results for three model cases are shown and are discussed in the text.

indicates that when viewed in many short sections, the reach is not discharging all along its length as originally assumed. However, it is important to note that this original assumption was based on increasing chemical mass influxes at the three successive weirs, with the intervening upper and lower reach half-sections treated as bulk entities. By adding up all the fluxes (both discharge and recharge) for the upper and lower reach sections in Figure 5.14, net discharge fluxes are retained.

Cumulative flow rates for sections of the study reach are presented in Table 5.4. Flow rates for the full reach range from 0.0020 to 0.0030 m<sup>3</sup>/s (depending on the 3D model case). For the upper and lower reach sections, net flow rates for case 3 are the most similar to each other, while flow rates for case 1 are most disparate. Net flow rates for case 3 are interpreted to be lower than for case 2 because of the increased vertical permeability in the model due to inclusion of major fracture hydraulic properties in case 3. Resultant lower elevations for the water table in case 3 lead to decreased flux to the study reach. This is supported by the fact that groundwater flux to the beaver pond cells, which are adjacent to the most dense concentration of fracture lineaments in the model (see Figure 5.4), was lowest for case 3. The net flow rate range for the full reach is close to the value extrapolated from 2D model results (0.0013 m<sup>3</sup>/s), and to the range of actual measured low flow stream discharges along the reach (0.005-0.009 m<sup>3</sup>/s). These results show that 1) the recharge rates and hydraulic conductivities used in the numerical models in this study yield physically reasonable results, and 2) the incorporation of anisotropy or hydraulic properties of macroscopic fractures into the 3D models does not strongly influence net flow rate along the full reach, but has greater effect for smaller reach subsections.

Further indications that model input parameters are physically reasonable

are that all discharge fluxes in the cell containing M1 (regardless of case) are about half an order of magnitude less than calculated discharge flux at M1. In addition, simulated discharge fluxes at the beaver pond are also within an order of magnitude of measured average seepage flux (regardless of case). The best combined match of both M1 and seepage meter fluxes is provided by case 3 results (anisotropic, including macroscopic fractures).

Table 5.4 - Summary of simulated flow rates along sections of the study reach.

<u>Model case</u>	<u>Net flow rates (m<sup>3</sup>/s)</u>		
	<u>Full reach</u>	<u>Upper reach</u>	<u>Lower reach</u>
Case 1: Isotropic (no fractures)	0.0021	0.0015	0.0006
Case 2: Anisotropic (no fractures)	0.0030	0.0011	0.0019
Case 3: Anisotropic (with fractures)	0.0020	0.0009	0.0011

## 5.5 Conclusions

The use of injection test permeabilities in the 2D models produced simulated hydraulic heads and discharge fluxes at the stream which are internally consistent with measured artesian heads (at piezometer M1) and discharge seepage flux at the beaver pond. This supports the use of the injection test data to represent equivalent porous media permeability variations to 60 m depth both in 2D and 3D models at this site.

For the 3D models, the first-order approximation of directional permeability for the granite, based on fracture frequency data, is the only justifiable approach with the available data set in the SCR.V. Results for the 3D models are physically realistic and match (within an order of magnitude) measured hydraulic heads and seepage fluxes at the stream and low flow stream discharges.

The 3D model results also support the size and shape of the assumed catchment and tend to refute inferences, based on 2D model results, that the effective catchment contributing groundwater to the study reach is smaller than originally assumed.

Hydraulic head patterns for isotropic and anisotropic (no fractures) 3D model cases are nearly identical, inferring that the incorporation of an anisotropy ratio of 2:1, as determined from the fracture frequency approach, does not significantly affect model results. Incorporation of hydraulic properties for macroscopic fractures increased the complexity of simulated head patterns in near-surface layers and caused a lowering of the simulated water table (by about 6



m) at the hill crest above the study reach. These relatively minor perturbations suggest that macroscopic fractures in the SCR, as incorporated in 3D modelling here, do not strongly influence the groundwater flow pattern at the scale of the assumed catchment.

## CHAPTER 6

### THESIS SUMMARY AND CONCLUSIONS

#### 6.1 Thesis summary

The contents, principal interpretations and conclusions of Chapters 1-5 of this thesis are summarized here. Conclusions relating to the thesis work as a whole are presented in Section 6.2.

#### Chapter 1

Chapter 1 provides an introduction to this thesis. A background section highlights the need for further understanding of catchment response to hydrologic stress in well-exposed, fractured granitic terrain; the advantages of applying a transient mass balance approach along a stream reach; and the need for incorporating geologic and fracture information in studies of catchment response. The objectives and organization of this thesis are then given, showing how this study in the SCRVT integrates disciplines of geology, hydrogeology and hydrochemistry and involves field, laboratory and numerical modelling components. Finally, previous work is presented regarding the geology of the Holyrood pluton, the characterization and hydrogeological significance of fracture geometry in low-permeability rocks, the response of catchments to hydrologic stress, and the numerical modelling of groundwater flow in hydrologic catchments.

#### Chapter 2

Chapter 2 provides a structural geologic framework of the study region, which is used as a basis for interpretations and conclusions in later parts of this thesis. Data sources include air photo analysis, outcrop mapping and scanline

surveys across the pluton, and core logging in the SCR.V, with scanline data used exclusively for statistical fracture analysis. The regional structural setting of the study region is presented and describes how the Holyrood pluton intrudes volcanic rocks of the Precambrian Harbour Main Group and lies within the north-trending Conception Bay Anticlinorium, bounded to the east and west by major subvertical faults (Topsail and Duffs Faults). Brittle tectonic structures with shear senses of motion predominate in the pluton. Fracture lineament azimuths within the northern part of the pluton are generally consistent with each other and correspond with preferred northerly, northeasterly and southeasterly strikes of mesoscopic fractures. Trace length and fracture frequency patterns show little variation in western parts of the pluton (including the SCR.V area), but greater variability to the east, possibly due to structural complexity near the Topsail Fault. This regional analysis indicates that there are no obvious variations in fracture patterns or structural trends on a macroscopic scale in the western part of the pluton, including the SCR.V.

In the SCR.V, four mesoscopic fracture sets are identified - three subvertical (sets 1, 2 and 3) and one subhorizontal (set 4) - based on cluster analysis techniques and direct observation. The subvertical sets correspond with macroscopic fracture orientations in the SCR.V and with regional fracture orientations. Although the relative dominance of the subvertical sets varies around the SCR.V, set orientations show only minor variation. Subsurface fracture orientations can be matched with the surface fracture sets, with the relative dominance of sets varying within and between boreholes. Analysis of mesoscopic fracture trace lengths and spacings shows that these parameters tend to vary smoothly across the SCR.V without significant variation within or between subvertical fracture sets, and best fit log-normal distributions, as reported for other granite bodies. Most faults and fracture zones in the SCR.V contain porous brittle fault breccia; clayey fault gouge is rare.

A history of brittle deformation in the pluton is presented in which the

large boundary faults are interpreted to predate the pluton, acting as feeders for the sill-like intrusion. Reactivation of these faults during Siluro-Devonian orogenesis is interpreted to have generated the tectonic fracture system in the pluton and the SCR. A kinematic deformation model is presented in which the regional tectonic fracture system formed as Riedel and secondary P-shear fractures during a single phase of progressive, left-lateral bulk simple shear. Subhorizontal fractures are interpreted to be post-tectonic sheeting fractures.

The principal features of fracture variability in the pluton can be summarized as follows: 1) the pluton apparently deformed as a contiguous rigid body without developing strongly contrasting fracture domains, 2) deviations of fracture orientations from regional trends tend to occur locally near faults, although controls due to lithologic changes cannot be ruled out, 3) the fracture system in the SCR is concordant with the regional fracture system in the pluton, and 4) subvertical macroscopic fractures in and around the SCR are interpreted to terminate within the pluton, without extending into underlying host rocks as do the major boundary faults of the pluton.

Chapter 2 ends with a discussion of hydrogeological implications of the structural geologic framework. The inferred lack of major faults in the SCR region implies that there are no high-permeability conduits which could provide preferred pathways between deep groundwater flow systems and the surface in this area. Hence, active groundwater flow in the SCR area is interpreted to occur primarily in shallow or intermediate flow systems within the pluton. Near-surface fractures and subvertical macroscopic fault and fracture zones are the likely principal conduits for shallow groundwater flow in the SCR. Consistency of fracture geometry within the SCR suggests that fracture-controlled rock mass hydraulic properties (e.g. hydraulic conductivity) can be assumed to be uniform around the study area at a scale of tens to hundreds of meters. This, along with the common genetic characteristics for subvertical fractures in the SCR, constitutes a geologic basis for extrapolating fluid flow properties for the rock

mass from a few control points to other areas in the SCR. Finally, biases in scanline spacing data and the lack of statistical description of subhorizontal fractures means that the present fracture data set for the SCR is inadequate for determining directional permeability characteristics of the granite by, for example, calculating a permeability tensor or using a fracture network approach. Simpler approaches are therefore necessary for formulating permeability and anisotropy input parameters for numerical models of groundwater flow in the SCR, as described in Chapter 5.

### Chapter 3

Chapter 3 describes and interprets the groundwater flux and piezometric response to precipitation in the SCR. The physical hydrogeologic setting of the study area is described, incorporating results of surface geophysical surveys conducted for this study. The basis for treating the study area as a hydrologic catchment is presented, in which hydrologic vertical no-flow boundaries are assumed to exist under the catchment boundaries. This is supported by local topography and drainage patterns and by calculations indicating negligible or minimal flows between branches of the Seal Cove River and from upstream areas of the drainage basin into the assumed catchment. Bedrock and overburden permeabilities, based on borehole injection tests and grain size analyses, respectively, show that the glacial drift is more permeable than the fractured bedrock and that bedrock permeabilities show an overall decrease with depth.

Field instrumentation consisted of six multilevel bedrock piezometers installed in granite in the southern part of the SCR to nominal depths of 10-60 m; eight seepage meter/mini-piezometer nests were installed in near-shore locations at roughly 100 m intervals around an elongate shallow pond within the study reach; three rectangular weirs at inflow, mid-reach and outflow locations along the study reach; and a series of recording and standard rain gauges deployed on the valley bottom and hill slope.

Discharge seepage fluxes from the pond in 1987 were low from July to mid-September (3-20 ml/m<sup>2</sup>/hr) then increased during mid-September to November (20-158 ml/m<sup>2</sup>/hr). The increasing flux magnitude and variability during the autumn corresponds with increased rainfall and, by inference, increased groundwater recharge and decreased evapotranspiration. Contour maps of seepage flux for the period October 7-28, 1987, illustrate variability of groundwater discharge to the pond during individual storm events. Immediate flux responses to a light rainfall (13.0 mm, October 8) were slight and sporadic. Cyclical seepage flux variations for 10 days following rainfall may be related to the release and recovery of storm-induced excess pore pressure at the sediment/granite interface beneath the pond. Immediate flux responses to a larger rainfall event (22.6 mm, October 22) were more pronounced, prompt (apparently beginning during rainfall), and short-lived (lasting about one day). Long-term variations due to this storm are uncertain.

Seasonal piezometric response to precipitation shows that hydraulic heads declined during summer, 1987, followed by elevated variable heads during the autumn, correlating with seasonal rainfall, water table and streamflow patterns. Piezometric variations in 1986 followed similar patterns.

Piezometric responses to individual storms (during October, 1987) were marked by 1) prompt rises (within hours of rainfall) and dissipation (within days), 2) increases which were disproportionately greater with increasing rainfall amount, and 3) differing degrees of change with depth in different boreholes (H2 and H4). Delays in piezometric response at piezometer M2 (about 12 hours after rainfall compared with seconds to minutes for other piezometers) may be related to abrupt variations in hydraulic connectivity or increased infiltration times around that hole.

Strong correlation ( $R^2 = 0.80-1.00$ ) of head responses between intervals in individual piezometers indicates that transient heads at the surface were efficiently

transferred to shallow depths in the granite. Moderate to strong correlation of piezometric response with seasonal precipitation ( $R^2 = 0.44-0.97$ ) and with streamflow ( $R^2 = 0.74-0.80$ ) suggests that surface waters and shallow groundwaters in the SCRv interacted closely and responded in similar fashion to hydrologic stress.

The three-dimensional variation of hydraulic head in the instrumented region is investigated by constructing simplified equipotential maps based on interpolation of piezometric measurements. These maps suggest that shallow groundwater flow is directed from the hillslope toward the stream, with equipotential surfaces sloping gently to the northwest, both in response to a storm and under low flow conditions. In addition, the map patterns suggest that the position of hingelines between recharge and discharge zones may be locally controlled by fracture lineaments.

The proposed mechanism of rapid hydraulic head transfer and groundwater displacement in bedrock in the SCRv is the filling and draining of highly permeable fractures in the granite. The principal implications of this mechanism are 1) open, near-surface fractures may allow very high groundwater velocities and greater distances of shallow groundwater movement during storm runoff than would be expected in unfractured porous media, 2) a relatively small number of large permeable fractures with spacings on the order of tens of meters may largely control groundwater response to precipitation in the SCRv, and 3) the water table in the SCRv is likely to be irregular and discontinuous within the fractured bedrock so that the magnitude and timing of water table changes will tend to depend on spacing and hydraulic connectivity of fractures.

Evidence presented in Chapter 3 shows that groundwater plays an active role in the response of the assumed catchment to precipitation and should be included in flow and chemical mass balance analyses of the SCRv (Chapter 4). However, physical hydrologic and hydrogeologic data for the SCRv (e.g. sharp

hydrograph peaks, exposed granite hill slope, low seepage flux magnitudes) infers that stormflow generated along the study reach may be dominated by direct runoff (new event water) from the assumed catchment.

#### Chapter 4

Chapter 4 presents the hydrochemical and isotopic (oxygen-18 and deuterium) responses of surface water and groundwater to precipitation in the SCR. These responses are used to investigate groundwater compositional variations and mixing relationships, determine stormflow components along the study reach, and evaluate the consistency of hydrochemical, isotopic and physical hydrologic responses to precipitation in the study area.

The hydrochemical setting of the SCR reflects the humid temperate marine climate in eastern Newfoundland and the geology of the SCR. Rain waters are Na-Cl type with no obvious seasonal secular oxygen-18 variation. Stream and groundwaters in the SCR are dilute, reflecting the low solubility of silicate minerals in the granite and glacial drift. SCR groundwaters are Ca-HCO<sub>3</sub> type and are undersaturated with respect to calcite suggesting they are only slightly evolved and part of a meteorically-driven, actively-flushed, shallow flow system.

Hydrologic measurements and water sampling for this study were carried out during August-October, 1986, and June-November, 1987, with infrequent preliminary groundwater sampling in 1985. Several hundred stream, groundwater and rain samples were analyzed for oxygen-18 and conductivity, with subsets analyzed for major anion and cation concentrations and deuterium.

A new reach-based mass balance method is presented in Chapter 4 for investigating stormflow generation along a study reach. This reach hydrologic approach differs from conventional mass balance approaches in that transient



equations are used, variations in stream flow generated upstream of a study area can be accounted for, and it is possible to specify varying compositions of pre-storm groundwater (old water) discharging into a study reach during stormflow. Two related methods are developed - one for investigating composition changes in a reach during stormflow (referred to here as bulk inflow analysis) and the other for performing hydrograph separations of storm runoff generated along the reach, utilizing the results of bulk inflow analysis.

Groundwater compositional variations in the SCR V are described in order to identify discharging groundwater compositions during storm runoff and any characteristic groundwater compositional responses to hydrologic stress. Two main groundwater compositional groups are identified in the SCR V - representing valley bottom and hillslope groundwaters (M112-M2 type) and very shallow, near-stream groundwaters (M114 type).

Groundwater compositional variations during periods of low or no rainfall are shown to be generally subtle, around the level of analytical uncertainty. Groundwater compositional variations and mixing relationships during storm stress (for September 27, 1986, September 15, 1987 and October 22, 1987 events) are generally more pronounced and indicate that storm-induced groundwater compositional variations can start within hours of the onset of rainfall. In addition, storm-induced groundwater mixing appears to progress in two stages - an initial response (lasting 1-2 days after start of rainfall) during which groundwater is displaced in stream-ward directions, without mixing with rain water, and a secondary response (lasting up to 4 days after the start of rainfall) during which groundwater may mix with near-surface or recharging groundwaters, or rain water. Rainfall amount and antecedent moisture do not appear to be factors in this process for the storms studied. Possible late-stage discharge of hillslope-derived groundwaters to the stream reach may constitute a third storm response stage. Persistent compositional differences within piezometers also suggests that shallow groundwaters in the SCR V are compositionally heterogeneous and move within

separate fracture plumbing systems at scales of a few meters.

The September 27, 1986 and October 22, 1987 storm runoff events are used for detailed bulk inflow and hydrograph separation analyses. For both events, stream composition changes increased in magnitude down-stream indicating that chemical mass flux was added to the reach from the assumed catchment. Differences in storm hydrograph shape and response time for these two storms are attributed to differences in rainfall distribution within and upstream of the assumed catchment. The September 27, 1986 rainfall was likely concentrated near the study reach, producing prompt stormflow, whereas the October 22, 1987 rainfall was likely concentrated away from the stream (i.e. on the hillslope), with stormflow lagged by increased travel time to the reach.

Bulk inflow analysis for both runoff event suggests that groundwaters discharging into the study reach shifted from M114-type compositions before and during rainfall, to M112,13-type compositions during peak stormflow, then back to M114-type compositions after stormflow. Bulk inflow plots for four additional 1987 runoff events (measured at peak stormflow) show the range of uncertainties in specifying bulk inflow mixing components due to varying degrees of contrast between stream flows along the reach and between runoff component compositions. The best-constrained bulk inflow composition (for the September 17, 1987 event) also infers that groundwater discharging to the reach was a mixture of M114 and M112,13-type compositions.

Based on the above, hydrograph separation results were determined using M114 and M112 groundwater compositions in the mass balance equation. Actual groundwater runoff proportions are interpreted to lie within the separation limits defined by using the M114 and M112 groundwater compositions. For the October 27, 1987 event, separation results using isotopic tracers (oxygen-18 or deuterium) indicate groundwater formed essentially 100% of runoff during rainfall and early stages of the storm hydrograph. Isotopic results during peak flow are unusable

due to inadequate compositional contrast between rain and groundwater. Separation results for this event using conductivity as a tracer also show that groundwater formed 100% of stormflow during rainfall and early stages of the hydrograph, but that this proportion dropped to about 30% (dominated by M112-type groundwater) during peak flow. After peak flow, the return to 100% M114-type groundwater discharge is assumed to have been gradual.

For the September 27, 1986 event, separation results were determined using oxygen-18, conductivity and chloride tracers. Separation results using oxygen-18 or deuterium as a tracer indicate groundwater dominated runoff throughout the storm hydrograph, forming 80-95% of peak stormflow. Groundwater stormflow proportions determined using conductivity as a tracer are much lower overall (maximum of about 40% groundwater at peak flow) than indicated by isotopic tracers and show a significant spread depending on whether M114 or M112 groundwater compositions are used in the separation equation. This pattern is attributed to non-conservative behaviour in the conductivity of surface runoff due to dissolution of surface biosalts during stormflow. This suggests that the conductivity-based separation results for the October 22, 1987 event are also too low to some degree. However, the degree of non-conservative behaviour for conductivity may vary from storm to storm depending on antecedent moisture, pre-storm biosalt concentrations and the distribution of rainfall. Separation results using chloride as a tracer are erratic, with large uncertainties due to low chloride compositional contrasts between flow components and low chloride concentrations in all waters in the SCR.V.

A likely control of the timing of storm runoff in the SCR.V and the composition and proportion of the groundwater component is the location of most concentrated rainfall stress in the assumed catchment. In addition, the predominance of groundwater in early storm runoff described here suggests that storm runoff in the SCR.V may not follow a typical stormflow cycle (e.g. Poinke et al., 1988) in which direct channel precipitation and surface runoff dominate early

runoff and subsurface (groundwater) flow dominates runoff at and after peak flow.

A comparison of hydrochemical, isotopic and physical responses to hydrologic stress in the SCR V are described in terms of the timing and duration of groundwater responses, a comparison of hydrograph separation results with measured physical responses, and the compatibility of hydrochemical variations with proposed physical response mechanisms. Rain-triggered groundwater compositional changes are attributed to the transfer of hydraulic heads into the fractured granite and displacement of heterogeneous groundwater, with both composition and head changes starting promptly with rainfall and persisting for several days. Runoff coefficients determined for the two main study storms (highest for the September 27, 1986 event) are compatible with the hypothesis that the proximity of concentrated rainfall stress strongly controls the timing and amount of stormflow. Measurements of similar stormflows along the upper and lower reach sections are also consistent with similar hydrograph separation results for the reach subsections for the September 27, 1986 event and with numerical modelling results (presented in Chapter 5). In addition, estimated discharge flux into the pond and stream channel (based on seepage meter and piezometric measurements) are very close (with 7.5%) of the calculated groundwater runoff component for the October 22, 1987 event.

Finally, prompt stream-ward displacement of groundwater at the onset of rain and the predominance of groundwater in early stormflow implies that the most active groundwater-surface water interaction occurs primarily in open near-surface fractures. Accordingly, possible late-stage arrival of hillslope-derived groundwater during storm response is physically reasonable only within a regime of rapid flow through such a permeable, near-surface fracture system. However, quantitative analysis of groundwater velocities and residence times were not warranted due to limitations of hydrochemical and physical data in this study.

## Chapter 5

Chapter 5 presents two-dimensional (2D) and three-dimensional (3D) steady-state numerical simulations of groundwater flow in the SCR.V, with the aims of 1) determining the internal consistency of physical hydrologic measurements in the SCR.V, 2) inferring the shape and distribution of discharge and recharge areas in the assumed catchment, and 3) evaluating the influence of major fractures on the shallow groundwater flow system in the SCR.V.

A modular three-dimensional finite-difference groundwater flow code (McDonald and Harbaugh, 1988), incorporating equivalent porous media permeabilities, was used for all simulations. Minor alterations were made to the code (described in Appendix I) to accommodate permeability characteristics of model cells containing fracture zones.

Two parallel 2D model profiles were constructed perpendicular to the stream (through piezometer M1 and the beaver pond), with each model containing six layers of varying thicknesses to a total depth of 500 m. Boundary conditions for the models are as closely related to the local hydrogeologic conditions as possible, with no-flow boundaries at the sides and bottom of each profile. Hydraulic conductivities were assigned to model layers based on measured injection test permeabilities in the SCR.V and granite permeability values reported in the literature. Recharge rates for the models were set at 5% and 1% of average annual precipitation for vegetated areas and bare rock slopes, respectively. The models were calibrated using piezometric and seepage flux measurements at low flow prior to the October 22, 1987 storm.

Results of four cases are presented, representing hydraulic conductivity ranges assigned to the two profiles corresponding with the regression line (cases 1 and 3) and lower 95% confidence limit (cases 2 and 4) for injection test permeability data. This narrow permeability range (about half an order of

magnitude) brackets the hydraulic conductivity values required to produce simulated heads which are reasonable and consistent with measured hydraulic heads throughout the profiles. Equipotential patterns for each case show similar characteristics - recharge areas at the hilltops, a principal discharge area at the west branch of the Seal Cove River, a local discharge area developed around the study reach, and a local water table high between the study reach and west branch of the Seal Cove River. These patterns suggest that 1) groundwater recharging near the hilltop east of the study reach may flow under the study reach and discharge into the west branch of the Seal Cove River, inferring that the catchment area actually contributing groundwater to the study reach may be smaller than originally assumed, and 2) groundwater flow transverse to the valley occurs predominantly at depths on the order of 50-100 m below surface. 2D model results also indicate that measured injection test data adequately represent the range of equivalent porous media permeabilities present in the granite to depths of 60 m in the SCR.V and that the limited number of hydraulic head and seepage flux measurement points in the SCR.V are adequate for constraining models of average groundwater discharge into the study reach.

The 3D modelling expands on the 2D model results to investigate groundwater flow characteristics of the entire assumed catchment, both with and without incorporation of macroscopic fractures in the SCR.V. The 3D model grid contains 21 rows, 21 columns and six layers, extending to 500 m total depth. The sides and bottom of the 3D mesh are designated as no-flow boundaries. The distribution and thickness of the uppermost model layer (overburden) is based in part on the geophysical surveys in the SCR.V.

Formulation of input parameters for the 3D models is discussed in detail. The most notable of these are the assignment of hydraulic conductivities in each layer and anisotropies for the rock mass and for cells containing fracture zones. Hydraulic conductivity for model cells not containing faults or fracture zones ( $K_r$ ) was assigned based on results of the 2D profile models. Hydraulic conductivities

for bedrock cells containing macroscopic fractures were formulated using widths and hydraulic conductivities ( $K_f$ ) assumed for the macroscopic fractures, and  $K_f$  values. The conceptual approach and specific methods for dealing with various geometric configurations are discussed. For simplicity, only known fracture lineaments over 300 m long were used in modelling, and the modelled fractures were assumed to extend vertically from surface to the bottom of the modelled region. A simplified approach for approximating permeability anisotropy of bedrock in the modelled region is presented which is based on fracture frequency determined from scanline data.

Results for three 3D model cases are presented - an isotropic case, with no macroscopic fractures (case 1); an anisotropic case, with no macroscopic fractures (case 2); and an anisotropic case, with macroscopic fractures (case 3). Contoured hydraulic heads for each case in each bedrock layer are presented. The equipotential patterns for each case are grossly similar and show decreased pattern complexity with depth. The principal difference between simulated head patterns for the 3D model cases is that the equipotential surface under the hill crest in the assumed catchment is highest for case 1 and lowest for case 3. Equipotential patterns for cases 1 and 2 are nearly identical.

Vertical components of simulated hydraulic gradients between layers 2 and 3 and layers 4 and 5 are presented for each model case. In all cases, the gradient patterns show recharge areas in near-surface bedrock beneath the hillslope and in mid-valley areas, which is consistent with physical measurements and assumptions regarding the hydrologic setting of the assumed catchment. Gradient patterns vary smoothly for cases 1 and 2, but show irregular local high and low values for case 3 in near-surface layers.

Limitations imposed on the 3D model results are discussed. Because of the use of the simple fracture frequency approach for approximating directional permeability in the fractured granite and the assumption that subvertical fractures

in the SCRV contribute equally to groundwater flow, the 3D model results are viewed as providing only semi-quantitative information on groundwater flow characteristics in the SCRV and only at the scale of the assumed catchment. A further limitation may be a smoothing effect on the influence of individual macroscopic fractures on groundwater flow patterns, due to the method used to determine effective hydraulic conductivities for fracture-bearing model cells.

The effective size of the assumed catchment area in terms of groundwater flow to the study reach is discussed by referring to simulated equipotential patterns and vertical gradient components. The 3D model results support the position of the assumed catchment boundary and tend to refute initial indications from 2D results that the effective catchment was smaller than originally assumed.

The uniformity of groundwater flux along the study reach is investigated by plotting simulated flux to or from river reaches in the 3D model. The most important feature of this plot is strong variability of flux for adjacent river cells (up to two orders of magnitude) and the occurrence of recharge conditions for a few cells. However, cumulative river flow rates for upper and lower half-reaches and the full reach show net discharge to the study reach and are close to measured low flow stream discharges. In addition, simulated discharge fluxes for river cells which include piezometer M1 and the beaver pond match measured artesian heads and discharging seepage fluxes, within an order of magnitude.

The principal conclusions of Chapter 5 are 1) injection test data adequately represent equivalent porous media permeabilities to 60 m depth both for 2D and 3D models; 2) 3D model results, incorporating directional permeability characteristics based on fracture frequency, are physically realistic and reasonably close to measured hydraulic heads, seepage fluxes and stream flows; 3) incorporation of an horizontal anisotropy ratio of 2:1 does not significantly perturb model results compared with the isotropic case; and 4) incorporation of hydraulic properties for macroscopic fractures produced only minor perturbations



in the groundwater flow pattern at the scale of the assumed catchment.

## 6.2 Thesis conclusions

1. A multidisciplinary approach, incorporating the geologic history as well as the physical hydrogeology and hydrochemistry of an area, is appropriate and necessary for investigating groundwater/surface water interaction and stormflow generation in fractured rock terrains, where bedrock geologic factors strongly control groundwater flow.
2. Transient reach mass balance methods were applied with mixed success in the SCR V, with the short-comings largely due to storm-specific inadequacies in flow or compositional contrasts between stormflow components, or non-conservative tracer behaviour. However, these methods can potentially be applied successfully in the SCR V and in other high stream-order settings. This opens up the possibility of investigating stormflow generation in down-stream areas where such information is more practically useful than in headwater regions, to which conventional mass balance methods are confined. Furthermore, while the density of physical hydrologic and hydrochemical measurements in this study was generally sufficient to constrain models of groundwater composition and average flux into the study reach, areas more hydrogeologically complex would likely require greater control. This may constitute the principal limiting factor in practically applying reach hydrologic methods in other settings.
3. A fracture filling and draining mechanism adequately explains rapid hydraulic head transfer and groundwater displacement in the SCR V, and suggests that average groundwater velocities and subsurface flow distances during stormflow generation may be much larger in fractured media than in unfractured porous media. Combined physical, chemical and isotopic results in this study indicate that groundwater and surface waters are strongly coupled during response to hydrologic stress in the SCR V, and suggest that groundwater should not be

ignored in water budgets developed for any well-exposed, fractured rock terrain.

4. Useful inferences regarding groundwater flow characteristics at the scale of the assumed catchment can be obtained from two- or three-dimensional steady state numerical simulations of groundwater flow using data bases such as the one collected for this study. However, interpretation of the model results is limited by simplifying assumptions and methods of formulating input parameters. The principal areas where additional data could improve groundwater flow modelling in the SCR V would be in the characterization of directional bedrock permeability and the hydraulic behaviour of individual macroscopic fractures.

## REFERENCES

- Anderson, M.G. and Burt, T.P., 1982. The contribution of throughflow to storm runoff: an evaluation of a chemical mixing model. *Earth Surf. Processes*, 7: 565-574.
- Baecher, G.B., 1980. Progressively censored sampling of rock joint traces. *Mathematical Geology*, 12: 33-40.
- Baecher, G.B. and Einstein, H.H., 1981. Statistical and probabilistic method in rock engineering; notes for a short course given at the Massachusetts Institute of Technology, Cambridge, MA., June, 1981.
- Baecher, G.B. and Lanney, N.A., 1978. Trace length biases in joint surveys. *Proc. 19th U.S. Rock Mechanics Symposium*, 56-65.
- Balk, R., 1937. Structural behaviour of igneous rocks. *Geol. Soc. Amer. Memoir* 5, 177 pp.
- Barr, M.V. and Hocking, G., 1967. Borehole structural logging employing a pneumatically inflatable impression packer. *Proc. Symposium on Exploration for Rock Engineering, Johannesburg, S. Africa*, 29-34.
- Bencala, K.E., McKnight, D.M. and Zellweger, G.W., 1987. Evaluation of natural tracers in an acidic and metal-rich stream. *Water Resour. Res.*, 23: 827-836.
- Berndtsson, R., 1990. Transport and sedimentation of pollutants in a river reach: a chemical mass balance approach. *Water Resour. Res.*, 26: 1549-1558.
- Bethea, R.M., Duran, B.S. and Boullion, T.L., 1985. Statistical methods for engineers and scientists. Marcel Dekker Pub., New York, 698 pp.
- Boom, R.W., 1983. Superconductive energy storage - Rock Mechanics: Final Technical Report. U.S. Dept. of Energy, DOE/ET/26602-35, Chap. V.
- Bottomley, D., Craig, D. and Johnston, L.M., 1984. Neutralization of acid runoff by groundwater discharge to streams in Canadian Precambrian shield watersheds. *J. Hydrol.*, 75: 1-26.
- Brisbin, W.C., 1980. Fracturing in granitic intrusions. *Atom. Ener. Can. Ltd. Tech. Record TR-37*, 103 p.

- Brueckner, W.D., 1979. Geomorphology of the Avalon Peninsula, Newfoundland. Nfld. Dept. Mines and Energy, Min. Devel. Div., Rept. 79-4, 42 pp.
- Burt, T.P., 1979. The relationship between throughflow generation and the solute concentration of soil and stream water. *Earth Surf. Processes*, 4: 257-266.
- Cherry, J.A. and Johnson, P.E., 1982. A multilevel device for hydraulic head monitoring and groundwater sampling in fractured rock. *Ground Water Mon. Review*, 2: 41-44.
- Christophersen, N., Vogt, R.D., Neal, C., Anderson, H.A., Ferrier, R.C., Miller J.D. and Seip, H.M., 1990. Controlling mechanisms for stream water chemistry at the pristine Ingabekken site in mid-Norway: Some implications for acidification models. *Water Resour. Res.*, 26: 59-67.
- Church, M.R., Hornberger, G.M. and Sorooshian, S., 1990. Catchment hydrogeochemistry. *Water Resour. Res.*, 26: 2947.
- Clark, S.P. Jr. (editor), 1966. Handbook of physical constants. *Geol. Soc. Amer. Memoir* 97, 587 pp.
- Cooley, R.L. and Westphal, J.A., 1974. An evaluation of the theory of groundwater and river-water interchange, Winnemucca reach of the Humboldt River, Nevada. Univ. Nevada, Desert Research Institute, Tech. Report series II-W, Hydrology and Water Resour. Pub. no. 19, 74 pp.
- Cooper, H.H. and Rorabaugh, M.I., 1963. Groundwater movements and bank storage due to flood stages in surface streams. U.S. Geological Survey Water-Supply Paper 1536-J.
- Cruden, D.M., 1977. Describing the size of discontinuities. *Int'l Jour. Rock Mech. Min. Sci. and Geomech. Abst.*, 14: 133-137.
- Dansgaard, W., 1964. Stable isotopes in precipitation. *Tellus*, 16: 436-468.
- de Marsily, G., 1986. Quantitative hydrogeology. Academic Press, Inc., Orlando, Fla., 440 pp.
- DeWalle, D.R., Swistock, B.R. and Sharpe, W.E., 1988. Three-component tracer model for stormflow on a small Appalachian forested catchment. *J. Hydrol.*, 104: 301-310.
- Dincer, T., Payne, B.R., Florkowski, T., Martinec, J. and Tongiorgi, E., 1970. Snowmelt runoff from measurements of tritium and oxygen-18. *Water Resour. Res.*, 6: 110-124.

- Dobrin, M.B., 1976. Introduction to geophysical prospecting. 3rd edition. McGraw-Hill, Inc. Publishers, New York, 630 pp.
- Dugal, J.J.B., Hillary, E.M., Kamineni, D.C., Simandl, G.J. and Sikorsky, R.L., 1981. Drilling and core logging programs at the Atikokan research area. Atom. Ener. Can. Ltd. Tech. Record TR-174, 64 pp.
- Dunne, T. and Black, R.D., 1970. Partial area contributions to storm runoff in a small New England watershed. Water Resour. Res., 6: 1296-1311.
- Dunne, T., Zhang, W. and Aubry, B.F., 1991. Effects of rainfall, vegetation and microtopography on infiltration and runoff. Water Resour. Res., 27: 2271-2285.
- Fisher, N.I., Lewis, T. and Embleton, B.J.J., 1986. Statistical analysis of spherical data. Cambridge Univ. Press, Sydney, 329 pp.
- Forster, C. and Smith, L., 1988a. Groundwater flow systems in mountainous terrain 1. Numerical modeling technique. Water Resour. Res., 24: 999-1010.
- Forster, C. and Smith, L., 1988b. Groundwater flow systems in mountainous terrain 2. Controlling factors. Water Resour. Res., 24: 1011-1023.
- Freeze, R.A., 1971. Three-dimensional, transient, saturated-unsaturated flow in a groundwater basin. Water Resour. Res., 7: 347-366.
- Freeze, R.A., 1972a. Role of subsurface flow in generating surface runoff 1. Base flow contributions to channel flow. Water Resour. Res., 8: 609-623.
- Freeze, R.A., 1972b. Role of subsurface flow in generating surface runoff 2. Upstream source areas. Water Resour. Res., 8: 1272-1283.
- Freeze, R.A., 1980. A stochastic-conceptual analysis of rainfall-runoff processes on a hillslope. Water Resour. Res., 16: 391-408.
- Freeze, R.A., 1990. Water Resources Research and interdisciplinary hydrology. Water Resour. Res., 26: 1865-1867.
- Freeze, R.A. and Banner, J., 1970. The mechanism of natural groundwater recharge and discharge: 2. Laboratory column experiments and field measurements. Water Resour. Res., 6: 138-155.
- Frignet, B., 1981. Two-layer inversion for E-mode VLF. in Manual of geophysical hand-calculator programs (editors E.J. Ballantyne, D.L. Campbell, S.H. Mentemeier, R. Wiggins). Soc. Exploration Geophysicists, Tulsa, Okla.

- Fritz, P., Drimmie, R.J., Frappe, S.K. and O'Shea, K., 1987. The isotopic composition of precipitation and groundwater in Canada. Proc. Int'l Symposium on the use of isotopic techniques in water resources development, Int'l Atomic Energy Agency, Vienna, Mar. 30-Apr. 3, 1987, 539-550.
- Gale, J.E., 1981. Fracture and hydrology data from field studies at Stripa, Preliminary results. Lawrence Berkeley Lab. Report, LBL-13101, SAC-46, 250 pp.
- Gale, J.E., 1982. Assessing the permeability characteristics of fractured rock. Geol. Soc. America, Special Paper 189, 163-181.
- Gale, J.E. and Rouleau, A., 1986. Hydrogeological characterization of the Ventilation Drift (Buffer Mass Test) area, Stripa, Sweden. Stripa Project Internal Report 86-02, SKB, Stockholm.
- Gale, J., MacLeod, R., Welhan, J., Cole, C., and Vail, L., 1987. Hydrogeological characterization of the Stripa site. Stripa Project Tech. Report, TR 87-15, SKB, Stockholm, Sweden.
- Gale, J.E. and Rouleau, A., 1983. Characterizing and interpreting the geometry, permeability and porosity of fractures for repository evaluation. Int'l Symposium on Field Measurements in Geomechanics, Zurich, Sept. 5-8, 1983, 6-28 to 6-54.
- Genereux, D.P. and Hemond, H.F., 1990. Naturally occurring radon-222 as a tracer for streamflow generation: steady state methodology and field example. Water Resour. Res., 26: 3065-3075.
- Gillett, S., 1987. CLUSTRAN - a code to extract clusters from axial data sets using the algorithm of Shanley and Mahtab. Commercial computer code and unpublished instruction manual, S. Gillett, Consulting Geologist, Pasco, Washington, U.S.A.
- Goodman, R.E., 1976. Methods of geological engineering in discontinuous rocks. West Publishing, N.Y., 422 pp.
- Harris, L.B. and Cobbold, P.R., 1984. Development of conjugate shear bands during bulk simple shearing. J. Struc. Geol., 7: 37-44.
- Jacobsen, E.P., 1972. Surficial geology of the Avalon Peninsula, Newfoundland. Geol. Surv. Canada Memoir 368, 121 pp.
- Herrmann, A. and Stiehler, W., 1980. Groundwater-runoff relationships. Catena, 7: 251-263.

- Hewlett, J.D. and Hibbert, A.R., 1967. Factors affecting the response of small watersheds to precipitation in humid areas. In: W.E. Sopper and H.W. Lull (Editors), *Forest Hydrology*, Pergamon, Oxford, pp. 275-290.
- Hodgson, R.A., 1961. Regional study of jointing in Comb Ridge-Navajo Mountain area, Arizona and Utah. *Amer. Assoc. Pet. Geol. Bull.*, 45: 1-38.
- Hodych, J. and Weir, H.C., 1972. A gravity survey across the Holyrood batholith of Newfoundland. *Proc. 24th Int'l Geol. Congress, Montreal, Canada* (abstract), 284.
- Hooper, R.P. and Shoemaker, C.A., 1986. A comparison of chemical and isotopic hydrograph separation. *Water Resour. Res.*, 22: 1444-1454.
- Hsieh, P.A., S.P. Newman, G.K. Stiles and Simpson, E.S., 1985. Field determination of the three-dimensional hydraulic conductivity tensor of anisotropic media, 2. Methodology and application to fractured rocks. *Water Resources Research*, 21: 1667-1676.
- Hudson, J.A., 1982. Computer graphics and printed circuits for studying rock joint patterns. *Geol. Soc. London, Misc. Paper 15*, 69-80.
- Hudson, J.A. and Priest, S.D., 1979. Discontinuities and rock mass geometry. *Int'l J. Rock Mech.*, 16: 339-362.
- Hudson, J.A. and Priest, S.D., 1983. Discontinuity frequency in rock masses. *Int'l Jour. Rock Mech. Min. Sci. and Geomech. Abstr.*, 20: 73-90.
- Hughes, C.J., 1971. Anatomy of a granophyre intrusion. *Lithos*, 4: 403-415.
- Hughes, C.J. and Brueckner, W.D., 1971. Late Precambrian rocks of eastern Avalon Peninsula - a volcanic island complex. *Can. J. Earth Sci.*, 8: 899-915.
- Hvorslev, M.J., 1951. Time lag and soil permeability in groundwater observations. *U.S. Army Corps Engineers Waterways Experimental Station, Vicksburg, Mississippi. Bull. 36*, 47 pp.
- IAEA, 1981. Stable Isotope Hydrology - Deuterium and oxygen-18 in the water cycle. *Int'l Atomic Energy Agency, Tech. Report 210*, 339 pp.
- ISRM, 1977. Suggested methods for determining hydraulic parameters and characteristics of rock masses. *Int'l Soc. Rock Mechanics, Commission on standardization of laboratory and field tests* (prepared by C. Louis). Category II, Part 6, 138 pp.

- ISRM, 1978. Suggested methods for the quantitative description of discontinuities in rock masses. *Int'l Jour. Rock Mech Min. Sci. and Geomech. Abstr.*, 15: 319-368.
- Jahns, R.H., 1943. Sheet structure in granites: its origin and use as a measure of glacial erosion in New England. *J. Geology*, L1: 71-98.
- Johnson, A.M., 1970. *Physical processes in geology*. Freeman and Cooper Pub. Co., San Francisco, 577 pp.
- Kaminen, D.C., Brown, P.A. and Stone, D., 1980. Fracture-filling material in the Atikokan area, northwestern Ontario. *in* Current Research Part A, Geol. Survey Can. Paper 80-1A, 369-374.
- Kennedy, V.C., Kendall, C., Zellweger, G.W., Wyerman, T.A. and Avanzino, R.J., 1986. Determination of the components of stormflow using water chemistry and environmental isotopes, Mattole River basin, California. *J. Hydrol.*, 84: 107-140.
- King, A. (compiler), 1982. Guidebook for Avalon and Meguma zones of Atlantic Canada - The Caledonide Orogen. *Int'l Geological Correlation Project 27*, Memorial Univ. Nfld. Report 9, 308 pp.
- King, A., 1988. Geology of the Avalon Peninsula, Newfoundland (parts of 1K, 1L, 1M, 1N and 2C). Nfld. Dept. Mines and Energy, Min. Develop. Div., Map 88-01.
- Kiraly, L., 1970. Statistical analysis of fractures (orientation and density). *Geologische Rundschau*, 59: 125-151.
- Krabbenhoft, D.P. and Anderson, M.P., 1986. Use of a numerical groundwater flow model for hypothesis testing. *Ground Water*, 24: 49-55.
- Krogh, T.E., Strong, D.F. and Papezik, V.S., 1983. Precise U/Pb ages of zircons from volcanic and plutonic units in the Avalon Peninsula. *Abst. with Prog.*, 18th Annual Meeting, Geol. Soc. Amer., Northeastern Section, 15: 135.
- LaPointe, P., 1980. Analysis of the spatial variation in rock mass properties through geostatistics. *Proc. 21st U.S. Symposium on Rock Mechanics*, Rolla, Mo., U.S.A., 570-580.
- LaPointe, P.R., Belfield, W.C. and Helwig, J.A., 1984. Analysis of fracturing and fluid-flow characteristics of the Monterey Formation, Santa Barbara Channel, CA. *Soc. Petrol. Eng.*, Report SPE 12734, 11 pp.



- LaPointe, P.R. and Ganow, H.C., 1984. Successful prediction of in situ fracture permeability and stiffness characteristics through statistical rock mass characterization. Proc. 25th Symp. on Rock Mech., Evanston, Ill., 8 pp.
- LaPointe, P. and Hudson, J.A., 1985. Characterization and interpretation of rock mass joint patterns. Geol. Soc. Am. Special Paper 199, 37 pp.
- Lee, D.R., 1977. A device for measuring seepage flux in lakes and estuaries. Limnol. and Oceanogr., 22: 140-147.
- Lee, D.R. and Cherry, J.A., 1978. A field exercise on groundwater flow using seepage meters and mini-piezometers. J. Geol. Educ., 27: 6-10.
- Lee, D.R., Cherry, J.A. and Pickens, J.F., 1980. Groundwater transport of a salt tracer through a sandy lakebed. Limnol. and Oceanogr., 25: 45-61.
- Lee, D.R. and Hynes, H.B.N., 1978. Identification of groundwater discharge zones in a reach of Hillman Creek, southern Ontario. Water Pollut. Res. J. Can., 13: 121-133.
- Long, J.C.S., Remer, J.S., Wilson, C.R. and Witherspoon, P.A., 1982. Porous media equivalents for networks of discontinuous fractures. Water Resour. Res., 18: 645-658.
- Long, J.C.S. and Billaux, D.M., 1987. From field data to fracture network modeling: An example incorporating spatial structure. Water Resour. Res., 23: 1201-1216.
- Mahtab, M.A., Bolstad, D.D. and Kendorski, F.S., 1973. Analysis of the geometry of fractures in San Manuel copper mine, Arizona. U.S. Dept. Interior, Bureau of Mines, RI 7715, 24 pp.
- Mahtab, M.A. and Yegulalp, T.M., 1984. A similarity test for grouping orientation data in rock mechanics. Proc. 25th U.S. Symposium on Rock Mechanics, Evanston, Ill., U.S.A., 495-502.
- McCartney, R.D., Poole, W.H., Wanless, E.K., Williams, H. and Loveridge, W.D., 1966. Rb/Sr age and geological setting of the Holyrood Granite, southeastern Newfoundland. Can. J. Earth Sci., 3: 947-957.
- McCartney, R.D., 1967. Whitbourne map-area, Newfoundland. Geol. Surv. Can., Memoir 341, 134 pp.
- McDonald, M.G. and Harbaugh, A.W., 1988. A modular three-dimensional finite-difference ground-water flow model. U.S. Geological Survey, Techniques of Water-Resources Investigations, Chap. A1, Book 6.

- McDonnell, J.J., Bonell, M., Stewart, M.K. and Pearce, A.J., 1990. Deuterium variations in storm rainfall: Implications for stream hydrograph separation. *Water Resour. Res.*, 26: 455-458.
- McKnight, D.M. and Bencala, K.E., 1990. The chemistry of iron, aluminum and dissolved organic material in three acidic, metal-enriched mountain streams, as controlled by watershed and in-stream processes. *Water Resour. Res.*, 26: 3087-3100.
- Miller, H.G., 1983. A geophysical interpretation of the geology of Conception Bay, Newfoundland. *Can. Jour. Earth Sci.*, 20: 1421-1433.
- Miller, H.G. and Pittman, D.A., 1982. Geophysical constraints on the thickness of the Holyrood pluton, Avalon Peninsula, Newfoundland. *Maritime Seds. and Atlantic Geol.*, 18: 75-82.
- Mulholland, P.J., Wilson, G.V. and Jardine, P.M., 1990. Hydrogeochemical response of a forested watershed to storms: Effects of preferential flow along shallow and deep pathways. *Water Resour. Res.*, 26: 3021-3036.
- Neuman, S.P., 1987. Stochastic continuum representation of fractured rock permeability as an alternative to the REV and fracture network concepts. *Proc. 28th U.S. Symposium on Rock Mechanics, Tucson, Az., U.S.A.*, 533-561.
- Odling, N.E. and Webman, I., 1991. A "conductance" mesh approach to the permeability of natural and simulated fracture patterns. *Water Resour. Res.*, 27: 2633-2643.
- Parkhurst, D.L., Thorstenson, D.C. and Plummer, L.N., 1980. PHREEQE - A computer program for geochemical calculations. *U.S. Geol. Survey Water-Resources Invest.* 80-96, 216 pp.
- Pearce, A.J., Stewart, M.K. and Sklash, M.G., 1986. Storm runoff generation in humid headwater catchments: 1. Where does the water come from?. *Water Resour. Res.*, 22: 1263-1272.
- Phillips, F.C., 1972. *The use of stereographic projection in structural geology.* Edward Arnold Pub., London (3rd edition).
- Pilgrim, D.H., Huff, D.D. and Steele, T.D., 1978. A field evaluation of subsurface and surface runoff. *J. Hydrol.*, 38: 319-341.
- Pilgrim, D.H., Huff, D.D. and Steele, T.D., 1979. Use of specific conductance and contact time relationships for separating flow components in storm runoff. *Water Resour. Res.*, 15: 329-339.

- Pinder, G.F. and Jones, J.F., 1969. Determination of the ground-water component of peak discharge from the chemistry of total runoff. *Water Resour. Res.*, 5: 438-445.
- Poinke, H.B., Hoover, J.R., Schnabel, R.R., Grubek, W.J., Urban, J.B. and Rogowski, A.S., 1988. Chemical-hydrologic interaction in the near-stream zone. *Water Resour. Res.*, 24: 1101-1110.
- Priest, S.D. and Hudson, J.A., 1976. Discontinuity spacings in rock. *Int'l Jour. Rock Mech.*, 13: 135-148.
- Priest, S.D. and Hudson, J.A., 1981. Estimation of discontinuity spacing and trace length using scanline surveys. *Int'l Jour. Rock Mech. Min. Sci. and Geomech. Abst.*, 18: 183-197.
- Ragan, D.M., 1973. Structural geology, an introduction to geometrical techniques (2nd edition). John Wiley and Sons, New York, 208 pp.
- Raven, K.G. and Gale, J.E., 1986. A study of the surface and subsurface structural and groundwater conditions at selected underground mines and excavations. *Atom. Ener. Can. Ltd. Tech. Record TR-177*, 81 pp.
- Robin, M.J.L., Dytynshyn, D.J. and Sweeney, S.J., 1982. Two gas-drive sampling devices. *Ground Water Mon. Review*, 2: 63-66.
- Rodhe, A., 1981. Spring flood, meltwater or groundwater?. *Nord. Hydrol.*, 12: 21-30.
- Rodhe, A., 1987. The origin of stream water traced by oxygen-18. Ph.D. thesis, Department Phys. Geogr., Uppsala Univ., Sweden.
- Rose, E.R., 1952. Torbay map-area, Newfoundland. *Geol. Surv. Can., Memoir* 265, 64 pp.
- Rouleau, A., 1984. Statistical characterization and numerical simulation of a fracture system - application to groundwater flow in the Stripa granite. unpub. Ph.D. thesis, Univ. of Waterloo, Waterloo, Ont., 284 pp.
- Rouleau, A., Gale, J.E. and Baleshta, J., 1981. Results of fracture mapping in the ventilation drift, Stripa. Lawrence Berkeley Laboratory report LBL-13071, SAC-42, 60 pp.
- Rouleau, A. and Gale, J.E., 1985. Characterization of the fracture system at Stripa with emphasis on the ventilation drift. Lawrence Berkeley Lab. Report LBL-14875, 115 p.

- Rouleau, A. and Gale, J.E., 1985. Statistical characterization of the fracture system in the Stripa Granite, Sweden. *Int'l Jour. Rock Mech., Min. Sci. and Geomech. Abst.*, 22: 353-367.
- Schillereff, H.S., Miller, H. and Gale, J.E., 1987. Depth to bedrock in the Seal Cove River valley, Newfoundland: a geophysical case study. *Maritime Sediments and Atlantic Geol.*, 23: 123-130.
- Schillereff, H.S., Gale, J.E. and Welhan, J.A., (in prep.). Response of a small catchment in granitic terrain to precipitation: groundwater flux and piezometric levels.
- Seeburger, D.A. and Zoback, M.D., 1982. The distribution of natural fractures and joints at depth in crystalline rock. *J. Geophys. Res.*, 87(B7): 5517-5534.
- Segall, P. and Pollard, D. D., 1982. The process of joint formation in granitic rock near Florence Lake, Sierra Nevada, California. *Geol Soc. Amer. Bull.*, 94: 563-575.
- Shanley, R.J. and Mahtab, M.A., 1976. Delineation and analysis of clusters in orientation data. *Math. Geology*, 8: 9-23.
- Sklash, M.G., Farvolden, R.N. and Fritz, P., 1976. A conceptual model of watershed response to rainfall, developed through the use of oxygen 18 as a natural tracer. *Can. J. Earth Sci.*, 13: 271-283.
- Sklash, M.G. and Farvolden, R.N., 1979. The role of groundwater in storm runoff. *J. Hydrol.*, 43: 45-65.
- Sklash, M.G., Stewart, M.K. and Pearce, A.J., 1986. Storm runoff generation in humid headwater catchments: 2. A case study of hillslope and low-order stream response. *Water Resour. Res.*, 22: 1273-1282.
- Smith, R.E. and Hebbert, R.H.B., 1983. Mathematical simulation of interdependent surface and subsurface hydrologic processes. *Water Resour. Res.*, 19: 987-1001.
- Snow, D.T., 1969. Anisotropic permeability of fractured media. *Water Resour. Res.*, 5: 1273-1289.
- Space, M.L., Ingraham, N.L. and Hess, J.W., 1991. The use of stable isotopes in quantifying groundwater discharge to a partially diverted creek. *J. Hydrol.*, 129: 175-193.
- Stone, D., 1980. Distribution of near-vertical surface fractures in the Dashwa pluton, Atikokan, Ont. *Atom. Ener. Can. Ltd. Tech Record TR-125*, 43 pp.

- Stone, D., Kamineni, D.C. and Brown, P.A., 1984. Geology and fracture characteristics of the Underground Research Laboratory lease near Lac du Bonnet, Manitoba. Atom. Ener. Can. Ltd. Tech. Record TR-243, 41 pp.
- Strong, D.F., Dickson, W.L., O'Driscoll, C.F. and Kean, B.F., 1974. Geochemistry of eastern Newfoundland granitoid rocks. Nfld. Dept. Mines and Energy, Min. Dev. Div., Report 74-3, 140 pp.
- Strong, D.F. and Minatides, D.G., 1975. Geochemistry of the late Precambrian Holyrood plutonic series of eastern Newfoundland. *Lithos*, 8: 283-295.
- Swistock, B.R., DeWalle, D.R. and Sharpe, W.E., 1989. Sources of acidic storm flow in an Appalachian headwater stream. *Water Resour. Res.*, 25: 2139-2147.
- Taylor, J.R., 1982. An introduction to error analysis. University Science Books, Mill Valley, Calif., 270 pp.
- Tchalencho, J.S., 1968. The evolution of kink bands and the development of compression structures in sheared clays. *Tectonophysics*, 6: 159-174.
- Terzaghi, R.D., 1965. Sources of error in joint surveys. *Geotechnique*, 15: 237-304.
- Turner, F.J. and Weiss, L.E., 1963. Structural analysis of metamorphic tectonites. McGraw-Hill, N.Y., 560 pp.
- Warburton, P.M., 1980a. A stereological interpretation of joint trace data. *Int'l Jour. Rock Mech.*, 17: 181-190.
- Warburton, P.M., 1980b. Stereological interpretation of joint trace data: Influence of joint shape and implications for geological surveys. *Int'l Jour. Rock Mech.*, 17: 305-316.
- Ward, R.C., 1984. On the response to precipitation of headwater streams in humid areas. *J. Hydrol.*, 74: 171-189.
- Weaver, D.F., 1967. A geological interpretation of the Bouguer anomaly field of Newfoundland. Publication of Dominion Observ., Ottawa, XXXV: 223-251.
- Wels, C., Cornett, R.J. and LaZerte, B.D., 1990. Groundwater and wetland contributions to stream acidification: an isotopic analysis. *Water Resour. Res.*, 26: 2993-3003.
- Weyer, K.U., 1972. Conceptual models for evaluation of the subterranean water cycle in Paleozoic Highlands. *Proceedings 24th Int'l Geol. Congress*, 107-117.

- Weyer, K.U. and Karrenburg, H., 1970. Influence of fractured rocks on the recession curve in limited catchment areas in hill country: A result of regional research and a first evaluation of runoff at hydrogeological experimental basins. *J. Hydrol. N.Z.*, 9: 177-191.
- Woodcock, N.H. and Naylor, M.A., 1983. Randomness testing in three-dimensional orientation data. *J. Struc. Geol.*, 5: 539-548.
- Yoneda, M., Inoue, Y. and Takine, N., 1991. Location of groundwater seepage points into a river by measurement of radon-222 concentration in water using activated charcoal passive collectors. *J. Hydrol.*, 124: 307-316.

## APPENDIX A

### **Geophysical Surveys in the Seal Cove River Valley - Procedures and Results**

#### **1. Introduction**

Refraction seismic, electromagnetic wave impedance (EM), and direct probe surveys were conducted on the valley floor in the SCRVR to determine thicknesses of overburden (glacial drift and peat deposits) and the topography and orientation of the buried granite surface. Figure A1 shows surface topography, geophysical survey station locations, and the peat and outcrop distribution in the surveyed area. Areas along and east of the gravel road through the SCRVR (including an EM transect toward the power lines in the south) were surveyed in the summer of 1986. Areas west of the road were surveyed in the summer of 1987 using seismic refraction methods only (EM surveys were not done due to time constraints and the greater reliability of refraction compared with EM methods). Procedures and results of these surveys have also been described by Schillereff et al. (1987).

A total of 31 seismic, 101 EM and 44 direct probe field measurements were made. In the boggy northern area east of the study reach, direct probing was used solely for determining depth to bedrock. For many of the southern EM stations and for two seismic stations (6 and 7), direct probe depths or drilling records were used to calibrate geophysical overburden thickness determinations.

## 2. Procedures

For the seismic survey, a Huntco FS-3 refraction seismograph was used, with a 9 kg sledge hammer and 0.3 x 0.3 x 0.025 m steel plate as acoustic source. Maximum step-out distances were nominally 50 meters, with at least ten points defining time-distance curves at each station. Due to time constraints, reverse profiling was not done, although this is not likely to have introduced serious errors in depth determinations since exposed glaciated granite surfaces in the valley are subhorizontal at scales of tens of meters. Overburden thicknesses were calculated using the equation (from Dobrin, 1976):

$$z = (x_c/2) * \{(V_1 - V_0)/(V_1 + V_0)\}^{1/2}$$

where  $z$  is thickness of low velocity layer (m),  $x_c$  is crossover distance from time-distance curves (m),  $V_0$  is lower velocity (m/s) and  $V_1$  is the higher velocity (m/s). In this survey, the low velocity (upper) layer was correlated with overburden and the high velocity (underlying) layer was correlated with bedrock. As described below, at some stations the higher velocity is lower than typically reported for granite and may reflect a three-layer case or more complex subsurface seismic conditions, although this does not substantially alter the overall combined results of these surveys.

For the EM survey, a Geonics EM16R earth resistivity meter was used to measure apparent resistivity,  $\rho_a$ , and the difference in phase angle,  $\phi$ , between magnetic and electrical fields from the 24 KHz very low frequency (VLF) EM transmitter at Cutler, Maine, U.S.A. Electrode spacing used in this EM survey was 19 m and in most cases the ground was damp so that electrical coupling with



the earth was good. EM readings within 150 m of the power lines in the southern part of the survey area were strongly perturbed by local electromagnetic fields around the power lines and were not used in depth determinations.

A two-layer inversion algorithm for programmable TI-59 calculator (Frignet, 1981) was used to calculate thickness ( $z$ ) of the upper layer (interpreted to be overburden) and resistivity ( $\rho_2$ ) of the underlying material (interpreted to be granite bedrock). This algorithm assumes that the resistivity of the upper layer ( $\rho_1$ ) is known. In this survey,  $\rho_1$  was unknown and was found to vary for different types of overburden. Therefore, for each overburden type,  $\rho_1$  was estimated by iteratively varying its value in the algorithm until a depth was calculated which was consistent with the depth found at the same location by probing or seismic methods. Values of  $\rho_1$  used for typical overburden types in the study area are (in ohm-meters): 25 (wet mud); 50 (saturated peat); 100 (wet bouldery peat); 500-700 (gravelly drift). Table A1 shows that  $\rho_2$  is relatively insensitive to variations in  $\rho_1$  (especially for the lower  $\rho_1$  values typical of unconsolidated materials). It is recognized that depth ( $z$ ) is sensitive to  $\rho_1$  with this algorithm, but the approach in this survey of using locally representative  $\rho_1$  values for different overburden types minimizes such sensitivity.

---

Table A1 - Comparison of calculated  $\rho_1$ ,  $\rho_2$  and depth values for EM station 82. For  $\rho_1$  changes of two orders of magnitude,  $\rho_2$  values change by less than a factor of two.

$\rho_1$ (ohm-m)	$\rho_2$ (ohm-m)	depth (m)
10000	86566	127.4
5000	57346	48.4
1000	48418	7.9
500	47663	3.86
100	47099	0.76

Direct probing (primarily in peat deposits) was done using a 1.4 m long, 32 mm O.D. steel pipe, pushed or manually hammered down to depth of refusal (interpreted to be bedrock). At least 0.05 m of the pipe was left exposed to allow recovery, hence the maximum probe depths were 1.35 m. To account for local irregularities in the bedrock surface, an average of four depths, measured at corners of a one meter grid at a given station location, was used to represent depth to bedrock.

### 3. Results

Tables A2, A3 and A4 present survey data and results for the direct probe, refraction seismic and EM surveys, respectively. Direct probe depths to refusal were less than 1.35 m at all stations except no. 28 (Table A2). At several direct probe stations (13, 16, 17, 20-23), thin ( $\leq 0.3$  m) layers of gravelly drift was encountered beneath the peat and above bedrock. The sporadic nature of this gravel occurrence beneath the peat adjacent to the stream reach supports the assertion, expressed in describing the beaver pond sediments (Chapter 3), that glacial drift occurs only in isolated depressions in the granite surface beneath the pond.

In the seismic survey, upper layer velocities ( $V_0$ , Table A3) ranged from 250 - 750 m/s in wet bog and up to 1833 m/s in areas covered by glacial sand and gravel drift. These ranges are consistent with velocities reported for peat and glacial till (Clark, 1966). It is notable that interpretable seismic data were obtained in completely saturated peat bog less than one meter thick. Lower layer velocities ( $V_1$ ) ranged from 1046 - 6154 m/s. The high end of this range is consistent with reported compressional wave velocities for Precambrian granite

(Clark, 1966).  $V_1$  values between about 2000 to 4000 m/s can be attributed to variations in fracture density at the buried granite surface or to a rubbly regolith layer above intact bedrock.  $V_1$  values between 1046 and about 2000 m/s may be due to refraction along a basal till layer (e.g. a lodgment till) overlying actual bedrock.

For the EM survey (Table A4),  $\rho_2$  values range mainly between 10000 - 35000 ohm-m, which are consistent with resistivities for Precambrian granite (Clark, 1966). EM stations where  $\rho_2$  is low (i.e. less than 4000 ohm-m; stations 17, 22, 46, 48, 50, 68, 69, 84, 86, 89-91, 93, 100, 101), generally correspond with areas of low seismic lower layer velocity and may reflect complex subsurface conditions.

Figure A2 depicts comparative results of overburden thicknesses determined at stations where two or all three methods were applied. Points on the horizontal line (squares) show reference depths from direct probe ("DP" stations) or drill records (H3). Ranges of measured values are shown as stippled bars extending from the reference depth points (for H3, true depth (7.01 m from drill records) is assigned an uncertainty of  $\pm 0.5$  m based on steeply dipping bedrock surface and uneven ground elevations at that location). Depths determined by seismic (triangles) or EM (circles) methods show the deviation from the reference depth at each station. For example, at station DP1, the true depth is 0.29 m, while the depths determined by refraction and EM methods are 0.48 m and 0.38 m, respectively. Thus the deviations from true depths (shown on the vertical axis) are 0.19 m and 0.09 m for seismic and EM methods, respectively. Error bars for seismic and EM points (shown by narrow stippled bars) are  $\pm 10\%$  and  $\pm 5\%$ , respectively, based on error analyses of the EM inversion algorithm

and seismic depth equation.

Geophysical depths to bedrock either overlap the range of measured values (within the error range of geophysical results) or deviate nominally by  $\leq 0.28$  m from true depths. This level of agreement supports the application of representative  $\rho_1$  values for different overburden materials at EM stations where ground truth information was not available.

Figures A3 and A4 show contoured bedrock elevations and an overburden isopach map, respectively, for the surveyed area, compiled from combined results of direct probe, seismic and EM surveys. Because the interpretation of the EM measurements requires the most assumptions for determining overburden thickness, a hierarchy of depth reliability was adopted in combining results. Direct probing and drill records were used where available, seismic depths were used in preference to EM depths, and EM depths were used only where no other depth information was available. Figure A3 shows that the buried bedrock surface is essentially flat, sloping gently northwards (on average  $0.5^\circ$ ), with localized depressions and small hummocks. This surface is interpreted to be a continuation of the glaciated granite surface seen at outcrops on the valley floor, with the depressions and hummocks representing glacial erosional features. Figure A5 depicts the buried granite surface in three dimensions (vertical exaggeration 12:1), viewed toward the northeast at an inclination of  $30^\circ$ . Both Figures A3 and A5 show that there are no conspicuous buried bedrock channels which might provide preferred groundwater flow pathways beneath the overburden on the valley floor.

Table A2 – Direct probe survey data and results

Probe station No.	UTM* East (m)	UTM North (m)	Station elevation (m.a.s.l.)	Overburden thickness (m)	Bedrock elevation (m.a.s.l.)	Comment**
1	801	4643	89.8	0.29	89.51	at EM 96, RS 6
2	850	4655	89.0	0.37	88.63	at RS 7
3	896	4654	91.0	0.42	90.58	
4	955	4661	95.0	1.04	93.96	
5	860	4695	89.0	0.48	88.52	
6	840	4700	89.0	0.10	88.90	
7	895	4732	89.5	0.40	89.10	
8	901	4751	89.5	0.82	88.68	
9	879	4765	89.5	0.53	88.97	
10	864	4785	89.5	1.21	88.29	
11	896	4801	89.9	0.75	89.15	
12	872	4850	89.5	1.35	88.15	
13	820	4858	86.0	0.51	85.49	bog + .3m drift
14	801	4850	86.0	0.18	85.82	
15	785	4810	85.5	0.75	84.75	
16	749	4821	85.5	0.93	84.57	bog + .1m drift
17	750	4854	85.5	1.13	84.37	bog + .1m drift
18	805	4902	87.5	0.40	87.10	outcrop visible
19	797	4935	87.7	0.38	87.32	
20	784	4975	88.3	1.02	87.28	bog + .2m drift
21	785	5042	90.0	1.35	88.65	bog + .1m drift
22	740	5009	88.0	0.53	87.47	bog + .3m drift
23	696	5048	87.0	0.55	86.45	bog + .2m drift
24	750	5103	89.0	0.55	88.45	
25	680	5093	86.0	0.43	85.57	
26	641	5141	81.4	0.32	81.08	
27	769	5190	87.5	0.56	86.94	
28	731	5271	81.0	1.35	79.60	max. probe depth
29	668	5290	80.0	0.10	79.90	
30	694	5335	76.5	0.40	76.10	
31	859	4137	95.3	0.48	94.82	
32	861	4159	94.0	0.62	93.38	at EM 4
33	883	4202	94.0	0.45	93.55	at EM 5
34	900	4246	94.0	0.64	93.36	at EM 9
35	933	4240	94.9	0.54	94.36	
36	903	4260	94.0	0.42	93.58	at EM 21
37	880	4270	94.0	0.50	93.50	at EM 22
38	897	4300	93.5	0.37	93.13	at EM 23
39	902	4442	93.0	0.76	92.24	at EM 35
40	940	4421	94.5	0.56	93.94	at EM 34
41	893	4491	92.5	0.65	91.85	at EM 39
42	936	4505	94.0	0.72	93.28	at EM 41
43	905	4525	92.5	0.43	92.07	at EM 42
44	904	4525	92.3	0.60	91.70	

\*UTM (Universal Transverse Mercator) coordinates; for true values add  
344000 m to eastings and 5150000 m to northings

\*\* EM = electromagnetic survey station; RS = refraction seismic survey station

Table A3 – Refraction seismic survey data and results

Station No.	UTM* East (m)	UTM North (m)	Station elevation (m.a.s.l.)	Top layer Veloc. (V <sub>0</sub> ) (m/s)	Bottom layer Veloc. (V <sub>1</sub> ) (m/s)	Crossover distance (m)	Overburden Thickness (m)	Bedrock elevation (m.a.s.l.)	Comment
2	603	4679	91	1058	2100	7.8	2.24	88.76	
3	647	4695	88	1014	2264	7.55	2.33	85.67	
4	693	4696	87	750	1869	4	1.31	85.69	wet bog
6	804	4650	89.5	650	1046	2	0.48	89.02	wet bog
7	850	4655	89	250	2040	0.4	0.18	88.82	wet bog
9	821	4130	95	289	2029	2.65	0.97	94.03	
10	761	4222	94	712	4990	3.65	1.58	92.42	
11	724	4306	94	847	5454	4.4	2.87	91.13	
12	696	4400	94	1000	3930	10	3.85	90.15	
13	645	4497	93.6	933	4444	13.65	5.52	88.08	
14	616	4600	92	1833	3337	4.9	1.85	90.15	
15	595	4705	91	1150	3950	13.1	4.85	86.15	
16	596	4808	90	1101	5208	13.7	5.53	84.47	
17	565	4892	85.5	633	1445	8.05	2.52	82.98	
18	530	5100	89	290	1333	8.08	3.24	85.76	
19	461	5073	80	554	1711	9.2	3.29	76.71	
20	493	5022	87	813	1600	9.42	2.69	84.31	
21	372	4968	85	1099	2056	10.61	2.92	82.08	
23	435	4874	80.5	800	6154	7.65	3.36	77.14	
25	531	4732	84.5	1101	2852	13.6	3.09	81.41	
26	535	4556	85.5	1023	5826	6.18	2.31	83.19	
27	447	4555	85	723	2400	14.05	5.15	79.85	
28	482	4658	83.5	1091	3128	11.26	3.91	79.59	
29	511	4439	88	632	3636	11.15	4.68	83.32	
30	597	4353	90	801	4042	8.57	3.51	86.49	
31	679	4234	92.5	747	2631	4.53	1.69	90.81	

\*UTM (Universal Transverse Mercator) coordinates; for true values add

344000 m to eastings and 5150000 m to northings

Note: Erratic data for stations 1, 5, 8, 22 and 24 show no clear velocity trends

Table A4 – Electromagnetic survey data and results

EM station	UTM* East (m)	UTM North (m)	Station elevation (m.a.s.l.)	Apparent resist. (ohm-m)	Phi angle (deg.)	Rho 1 (ohm-m)	Rho 2 (ohm-m)	Overburden thickness (m)	Bedrock elevation (m.a.s.l.)	Comment
1	877	4065	98.0	8900	34	100	14258	0.00	98.00	outcrop
2	836	4138	95.0	5700	24	-	-	0.00	95.00	outcrop
3	582	4851	85.5	9800	25.5	-	-	0.00	85.50	outcrop
4	861	4159	94.0	3200	27.5	50	7561	0.88	93.12	
5	883	4202	94.0	4000	28.8	50	8660	0.73	93.27	
6	864	4215	94.0	7500	26.9	50	18382	0.59	93.41	
7	840	4210	94.0	7100	27	50	17286	0.60	93.40	
8	856	4246	94.0	5200	27.8	100	12005	0.67	93.33	
9	900	4246	94.0	5700	29.5	50	11791	0.58	93.42	
10	921	4222	94.5	7400	28.5	50	16297	0.54	93.96	
11	920	4248	94.0	10000	29.5	50	20657	0.44	93.56	
12	939	4253	95.0	12000	31	100	22673	0.72	94.28	
13	956	4259	97.5	7600	30.3	100	14992	0.96	96.54	
14	980	4260	102.0	3800	35.5	600	5768	6.15	95.85	H3 site
15	1001	4255	109.0	6400	33	900	10800	0.00	109.00	outcrop
16	1000	4224	107.0	5600	34	100	8982	0.84	106.16	
17	1002	4195	108.5	1810	36.4	100	2585	1.21	107.29	
18	969	4201	100.5	3100	32.6	50	5300	0.20	100.30	
19	940	4209	96.0	5100	30	50	10234	0.00	96.00	outcrop
20	900	4200	94.0	7400	29	900	16000	0.00	94.00	M3 site
21	903	4260	94.0	3100	33	50	5243	0.62	93.38	
22	880	4270	94.0	2320	35.9	50	3382	0.54	93.46	
23	897	4300	93.5	4950	33.6	50	8097	0.46	93.04	
24	931	4308	94.5	4200	32.5	50	7293	0.55	93.95	
25	947	4336	96.5	6600	35.8	700	9778	4.98	91.52	
26	975	4324	102.0	6100	34	700	9772	6.23	95.77	
27	947	4286	97.0	10000	31.3	700	18911	5.76	91.24	
28	957	4355	97.5	6050	35.5	700	9118	5.43	92.07	
29	977	4369	99.0	28000	31	900	50000	0.00	99.01	outcrop
30	947	4377	95.0	7400	35.5	700	11115	4.80	90.20	
31	920	4385	94.0	4950	35	50	7543	0.40	93.60	
32	902	4415	93.5	4600	30	50	9234	0.63	92.87	
33	925	4410	94.0	4100	29.3	50	8599	0.69	93.31	

Table A4 - Electromagnetic survey data and results (continued)

EM station	UTM* East (m)	UTM North (m)	Station elevation (m.a.s.l.)	Apparent resist. (ohm-m)	Phi angle (deg.)	Rho 1 (ohm-m)	Rho 2 (ohm-m)	Overburden thickness (m)	Bedrock elevation (m.a.s.l.)	Comment
34	940	4421	94.5	14000	28	50	31810	0.40	94.10	
35	902	4442	93.0	6950	28	50	15817	0.57	92.43	
36	924	4457	93.7	6950	27.5	50	16354	0.59	93.11	
37	944	4460	94.2	14000	28	700	32511	5.88	88.32	
38	963	4460	96.0	28000	23	900	90000	0.00	96.01	outcrop
39	893	4491	92.5	7100	22	50	25461	0.76	91.74	
40	924	4485	93.5	7500	21.6	50	27849	0.75	92.75	
41	936	4505	94.0	11000	18	50	57965	0.71	93.30	
42	905	4525	92.5	27000	21	50	99999	0.40	92.11	
43	782	4160	94.5	5400	23	100	17959	1.68	92.82	
44	752	4165	94.5	3100	29	700	7394	14.02	80.48	
45	718	4169	94.7	2900	31	700	5998	13.05	81.65	
46	691	4165	94.7	1000	30	50	2035	1.39	93.31	
47	672	4155	94.0	1250	23.3	100	4280	3.63	90.37	
48	660	4169	94.0	1020	24	50	3201	1.90	92.10	
50	648	4196	94.0	750	36	100	1104	2.13	91.87	
51	696	4235	94.0	2010	21.5	100	7870	3.01	90.99	
52	752	4235	94.0	5000	28.5	700	11753	10.41	83.59	
53	765	4197	94.2	6900	22	700	27269	11.61	82.59	
54	516	5248	80.0	9600	24.5	100	28114	1.17	78.83	
55	523	5160	80.2	9200	22.5	300	32339	3.99	76.21	
56	545	5102	80.4	23600	17	700	9999	7.09	73.32	
58	571	4940	83.5	6800	21	700	26879	1.62	81.88	
59	570	4893	86.0	18200	23	700	61587	6.52	79.49	
66	892	3997	99.5	17500	23	50	57447	0.46	99.05	
67	969	3987	104.0	8000	30	25	21602	0.28	103.72	wet mud
68	1025	3980	111.0	2700	37.8	700	3683	7.33	103.67	
69	998	4034	112.0	2300	38.5	700	3042	7.64	104.36	
70	960	4065	108.0	5000	34.3	700	7991	6.76	101.24	
71	930	4102	99.9	5000	30	700	10564	9.52	90.38	
72	950	4158	99.2	9600	28.3	700	22086	7.13	92.07	
73	808	4197	94.3	6100	24.5	50	17836	0.73	93.57	
74	808	4229	94.2	10000	23.6	50	31315	0.60	93.60	
75	830	4262	94.1	7050	25.6	50	18962	0.65	93.45	



Table A4 - Electromagnetic survey data and results (continued)

EM station	UTM* East (m)	UTM North (m)	Station elevation (m.a.s.l.)	Apparent resist (ohm-m)	Phi angle (deg.)	Rho 1 (ohm-m)	Rho 2 (ohm-m)	Overburden thickness (m)	Bedrock elevation (m.a.s.l.)	Comment
76	786	4261	94.0	6000	27.5	50	14127	0.64	93.36	
77	736	4295	94.0	5400	34	100	8662	0.86	93.14	
78	795	4330	94.0	4600	28	50	10486	0.71	93.29	
79	844	4307	94.0	6000	29.8	50	12182	0.55	93.45	
80	881	4350	93.8	7400	25.5	50	20046	0.63	93.17	
81	856	4401	93.5	4500	27.5	50	10609	0.74	92.76	
82	801	4401	93.5	18700	26.5	500	47663	3.86	89.64	
83	745	4402	93.7	24300	35	50	36942	0.18	93.52	
84	727	4350	93.7	2010	40.4	700	2428	6.20	87.50	
85	681	4448	94.0	3800	37.5	700	5216	5.86	88.14	
86	734	4490	92.5	2290	34	50	3676	0.66	91.84	
87	808	4491	91.7	11100	25.8	50	29377	0.51	91.19	
88	862	4460	91.2	4990	27	50	12167	0.72	90.48	
89	850	4539	90.2	890	26	50	2396	1.86	88.34	
90	770	4550	90.5	2470	35	50	3765	0.58	89.92	
91	701	4555	92.0	2900	40	700	3546	4.83	87.17	
92	635	4581	92.3	2990	32.6	700	5515	11.39	80.91	
93	686	4618	91.0	1870	39.5	700	2368	7.97	83.03	
94	754	4619	91.0	2700	32	50	4829	0.72	90.28	
95	807	4582	90.0	20700	23.5	700	66877	5.96	84.05	
96	801	4643	89.8	24100	23.5	50	75907	0.38	89.42	
97	801	4717	89.7	9100	21.5	25	33963	0.34	89.36	wet mud
98	747	4670	90.0	2800	32	50	5008	0.70	89.30	
99	748	4735	87.0	6000	27	50	14617	0.65	86.35	
100	680	4699	87.0	810	48.3	700	813	1.03	85.97	
101	690	4700	87.0	700	38	50	928	0.80	86.20	

\*UTM (Universal Transverse Mercator) coordinates; for true values add 344000 m to eastings and 5150000 m to northings

Note: no data or interference by power lines for stations 49, 57, 60-65.

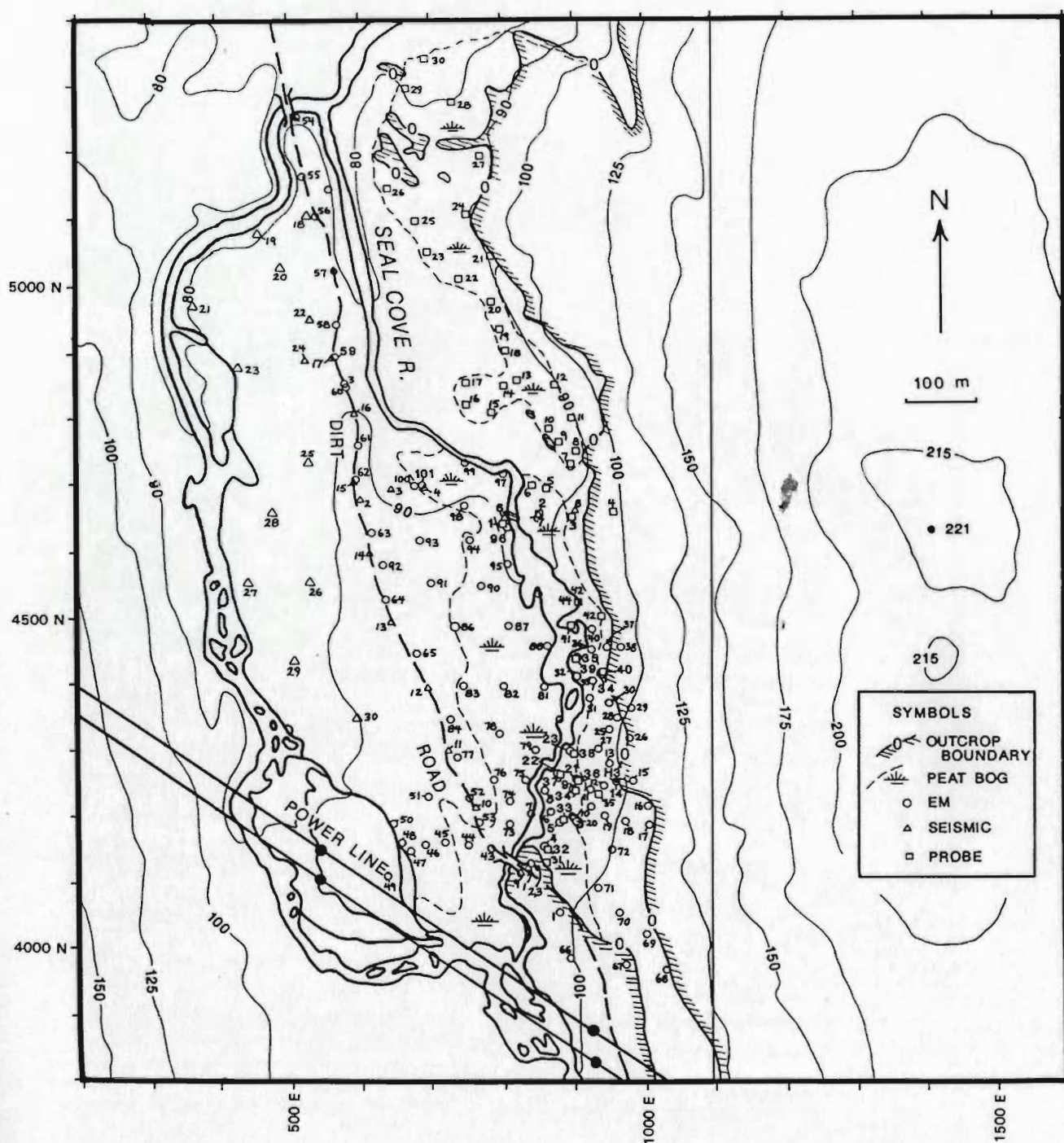


Figure A1 - Surface topography, geophysical survey station locations, and peat and outcrop distribution on the valley floor in the study area.

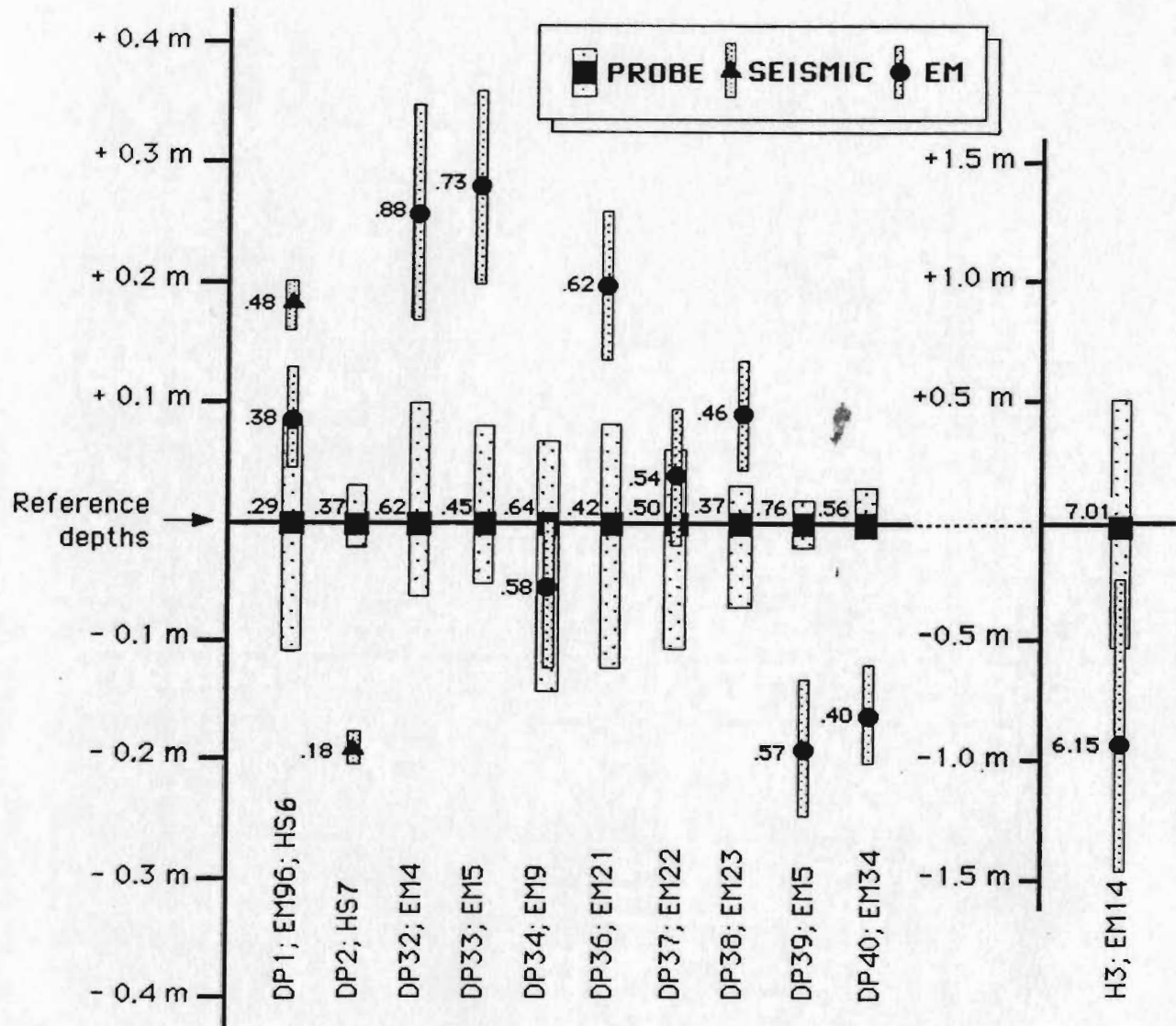


Figure A2 - Comparative results of overburden thicknesses at stations where true depth to bedrock is known. Station abbreviations along bottom: HS (hammer seismic), EM (electromagnetic), DP (direct probe), H3 (borehole H3).

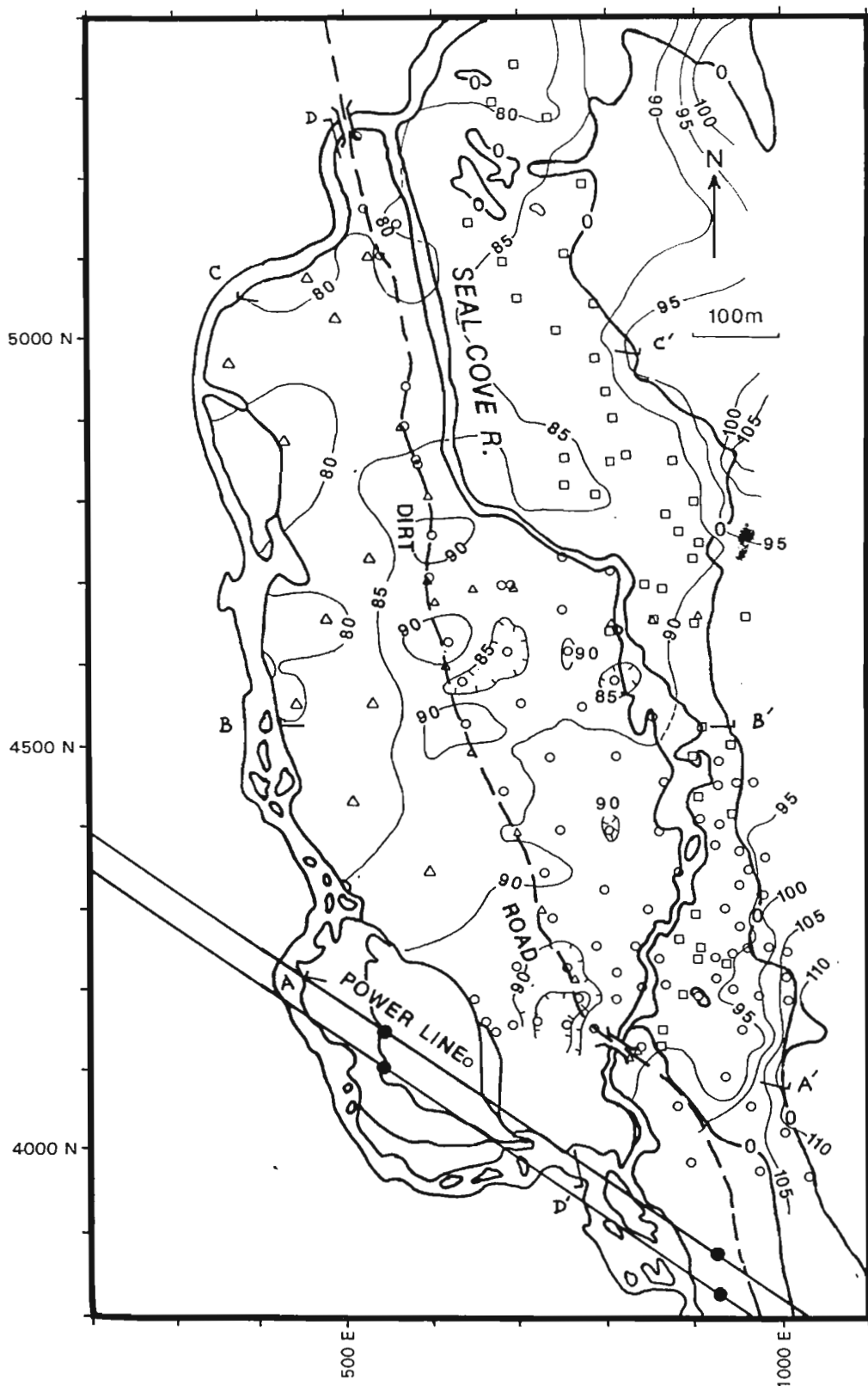


Figure A3 - Contoured bedrock surface elevations (m.a.s.l.) on the valley floor of the Seal Cove River valley, compiled from combined geophysical and direct probe records.

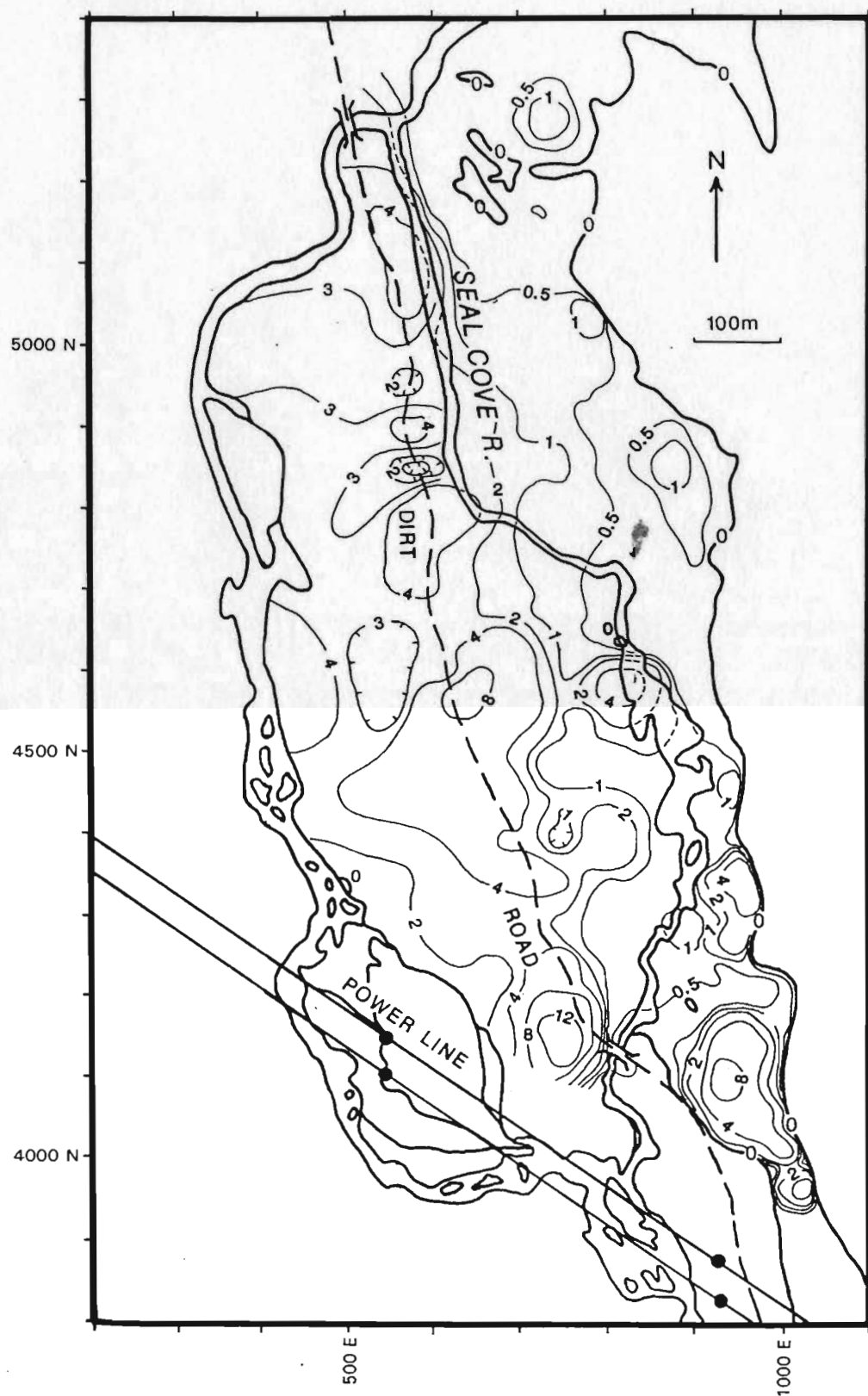


Figure A4 - Overburden isopach map for the valley floor in the study area, compiled from geophysical and direct probe survey data. Contours in meters.



# BURIED GRANITE SURFACE SEAL COVE RIVER VALLEY

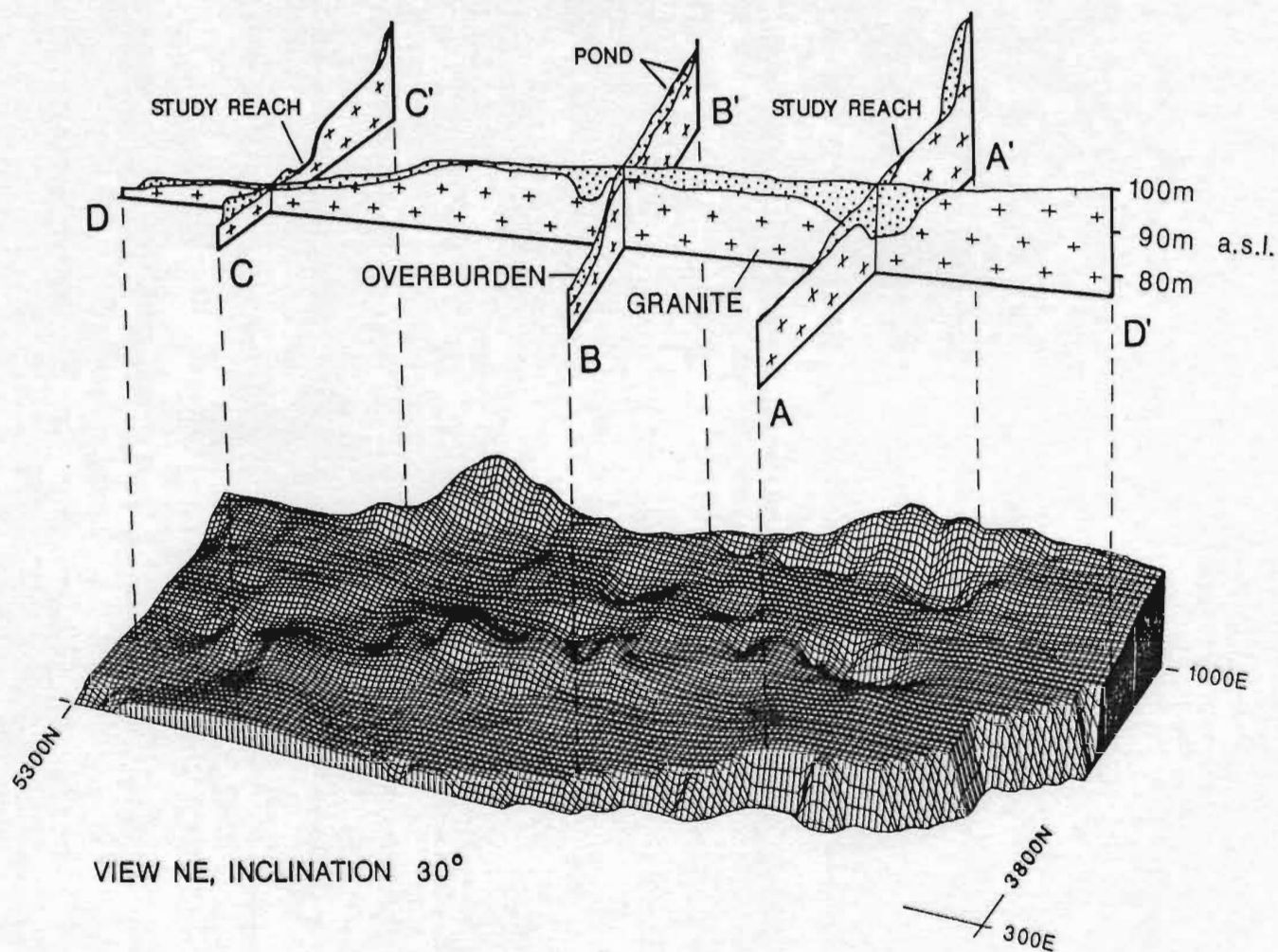


Figure A5 - Perspective view of the buried granite surface on the valley floor, viewed toward the northeast at 30° inclination. Vertical exaggeration is 12:1.

## APPENDIX B

### Scanline Fracture Mapping in the Holyrood Pluton: Procedures and Results

#### 1. Introduction

Scanline fracture mapping in the Holyrood pluton entailed 1) preparation of photographic base maps for each survey site, 2) fracture surveys along multiple scanlines at each site, and 3) encoding fracture data into computer files. Procedures and results of scanline surveys in the Holyrood pluton for this study are presented below.

#### 2. Procedures

A photographic base for each site was compiled from photographs taken using a hand-held 35 mm camera aimed vertically downward from a helicopter hovering 100-200 m above ground surface. Camera settings were adjusted so that outcrop areas of approximately 25 m x 25 m could be shown on a single photograph. Black and white enlargements (0.28 m x 0.36 m; 11" x 14"), with drafting film overlays, were used for field recording. Each photographic base was given a unique identification number which was retained in the computer data files and scanline fracture trace maps.

In conducting fracture surveys, an area shown on a photographic base was first located in the field then a north arrow and bar scale constructed on the film overlay using bearings and distances between natural landmarks. No other measurements

were made directly from base photos, hence aberration effects at the edges of photos had no effect on survey measurements. Two or three crossing scanlines (steel measuring tapes), 15-20 m long, were laid out on the best-exposed portion of the survey site, perpendicular to the principal steeply-dipping fracture sets. An attempt at random preselection of scanline azimuths, to lessen subjectivity in line lay out, proved unworkable due to the distribution of soil cover at the outcrops or the presence of rubbly areas or small scarps (i.e. 1-2 m high) within the outcrops. All surveyed exposures were subhorizontal (slopes of  $\leq 20^\circ$ ). Vertical exposures were avoided due to logistical difficulties and safety risks.

During surveys, angles were measured with a Brunton (R) pocket transit or structural fabric compass. Where fracture surfaces were not sufficiently exposed to be measured directly, fracture orientations were measured from a 0.15 m x 0.3 m aluminum plate held coplanar with the fracture. The following data were recorded on forms for easy entry into computer data files:

**Data flag** - 11 = fracture data line, 33 = comment line

**Locator number** - four-digit number identifying base photo

**Scanline label** - A, B or C letter identification for scanlines

**Scanline trend** - azimuth of scanline in down-plunging direction (0-360°)

**Scanline plunge** - inclination of scanline down from horizontal (0-90°)

**Fracture number** - identification number (1-999), unique and sequential for each site

**Scanline distance** - distance along scanline (to nearest 0.01 m) where fracture crosses scanline

**Fracture type** - Joint (JT), vein (VN), fault or fracture zone (FZ) or lithologic contact (CN)

**Fracture dip direction** - bearing of down-dip direction (0-360°)



**Fracture dip angle** - inclination of fracture in dip direction (0-90°)

**Trace length** - length of exposed fracture trace (to nearest 0.1 m; minimum length = 0.5 m)

**Censoring type** - degree to which fracture trace is exposed: 0 = both ends exposed, 1 = one end covered, 2 = both ends covered

**Mineral infilling type** - Q = quartz, C = calcite, K = chlorite, E = epidote, H = iron oxide or hydroxide minerals (e.g. hematite, limonite, goethite, etc.), U = unknown, R = rock rubble (e.g. along recessively-weathered fault traces). Minerals recorded in order of abundance.

**Fracture surface roughness** - Large size (on scale of meters): 0 = flat planar, 1 = curved planar, 2 = undulating, 3 = stepped; Small size (on scale of mm to cm): 0 = smooth, 1 = slickensided, 2 = rough.

**Rock type** - G = granitoid lithologies, M = microgranite, B = gabbro, granodiorite or diabase, P = pegmatite (dike), A = aplite (dike), F = felsite (dike), O = other

**Fracture termination style** - blank if censoring = 1 or 2 (i.e. if termination style indeterminate), 0 = both ends free (i.e. do not terminate against other fractures), 1 = T-junction (one end of fracture abuts another fracture at nearly 90°), 2 = H-junction (both ends of fracture abut other fractures at nearly 90° angles), 3 = splay (fracture terminates against another fracture at a low angle).

**Comment** - any other information, e.g. age relationships, unusual rock or mineral infilling types, etc.

Scanline fracture trace maps were drawn on the photographic base overlays in the field showing outcrop boundaries, scanline locations, numbered fracture traces and conspicuous or unusual fractures lying off the scanlines.

Field scanline data were encoded as ASCII computer data files for ease of manipulation and transfer between computer environments. Random checks of the composite fracture data file for all sites showed no data entry errors.

### 3. Results

Figures B1-B9 show scanline trace maps for all survey sites in the SCR V study area. Table B1 lists all scanline fracture data collected in the SCR V, subdivided by survey site (in ascending order). To facilitate manipulation by computer, data lines in Table B1 begin with the number 11, while comment lines begin with 33. The FORTRAN format for data lines is listed below.

Format for fracture data lines in Table B1:

<u>Variable</u>	<u>Column</u>	<u>Format</u>
Code	1-2	I2
Locator number	3-6	I4
Scanline label	7	A1
Scanline trend	8-10	I2
Scanline plunge	11-12	I3
Fracture number	13-16	I4
Scanline distance	17-22	F6.2
Fracture type	23-24	A2
Fracture dip direction	25-28	I4
Fracture dip angle	29-30	I2
Trace length	31-35	F5.1
Censoring	36-37	I2
Mineral infilling	38-40	A3
Surface roughness (large, small)	42-43	A1,A1
Rock type	44	A1
Termination style	45	I1
Comment	47-80	17A2

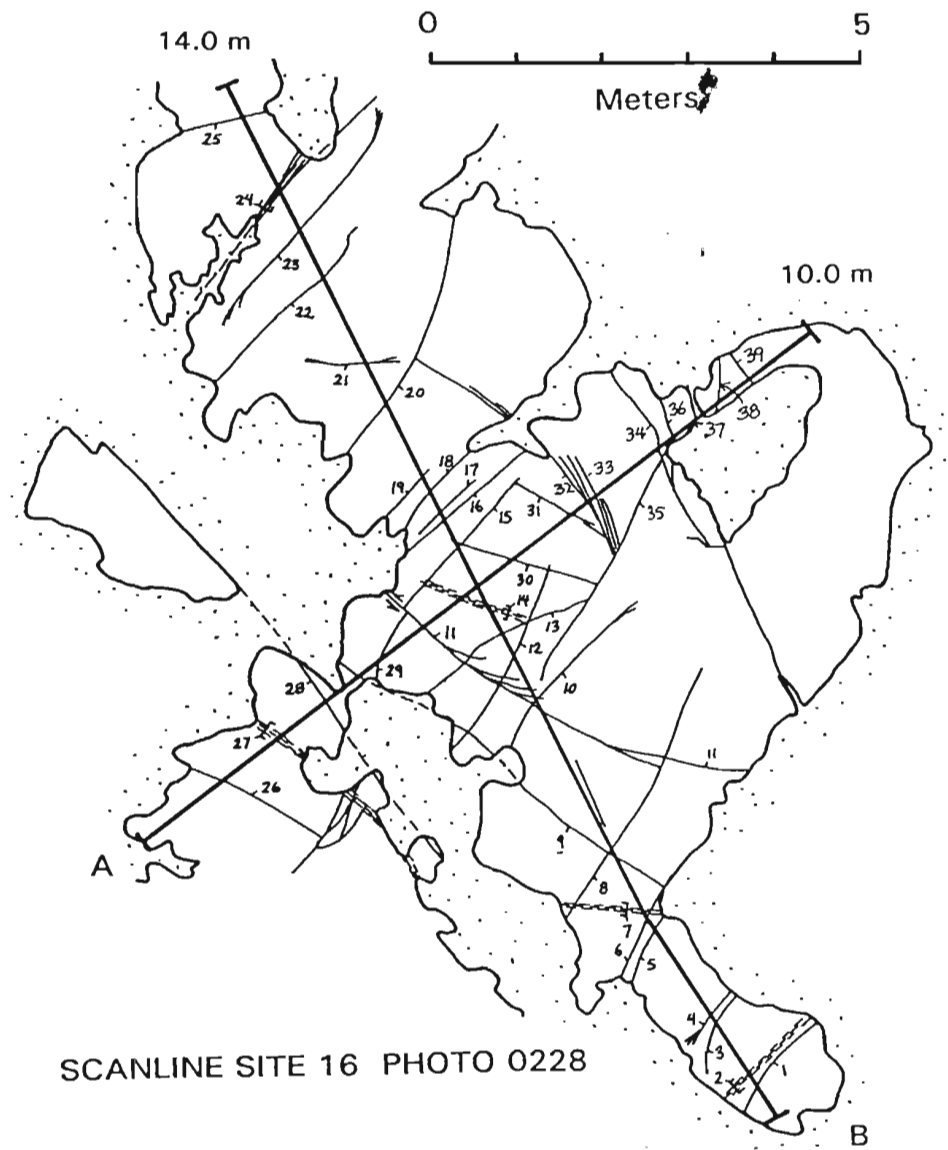
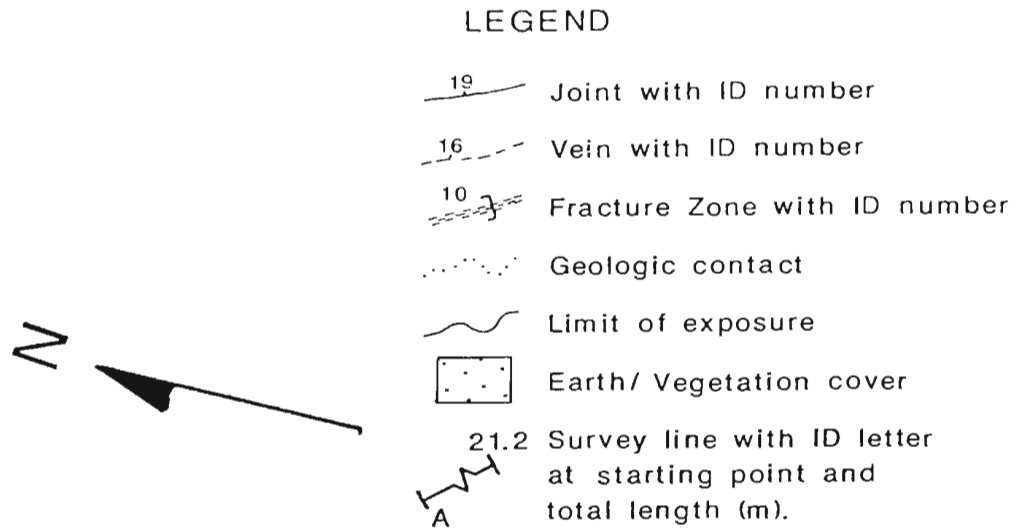


Figure B1a - Scanline trace map for survey site 16 in the Seal Cove River valley

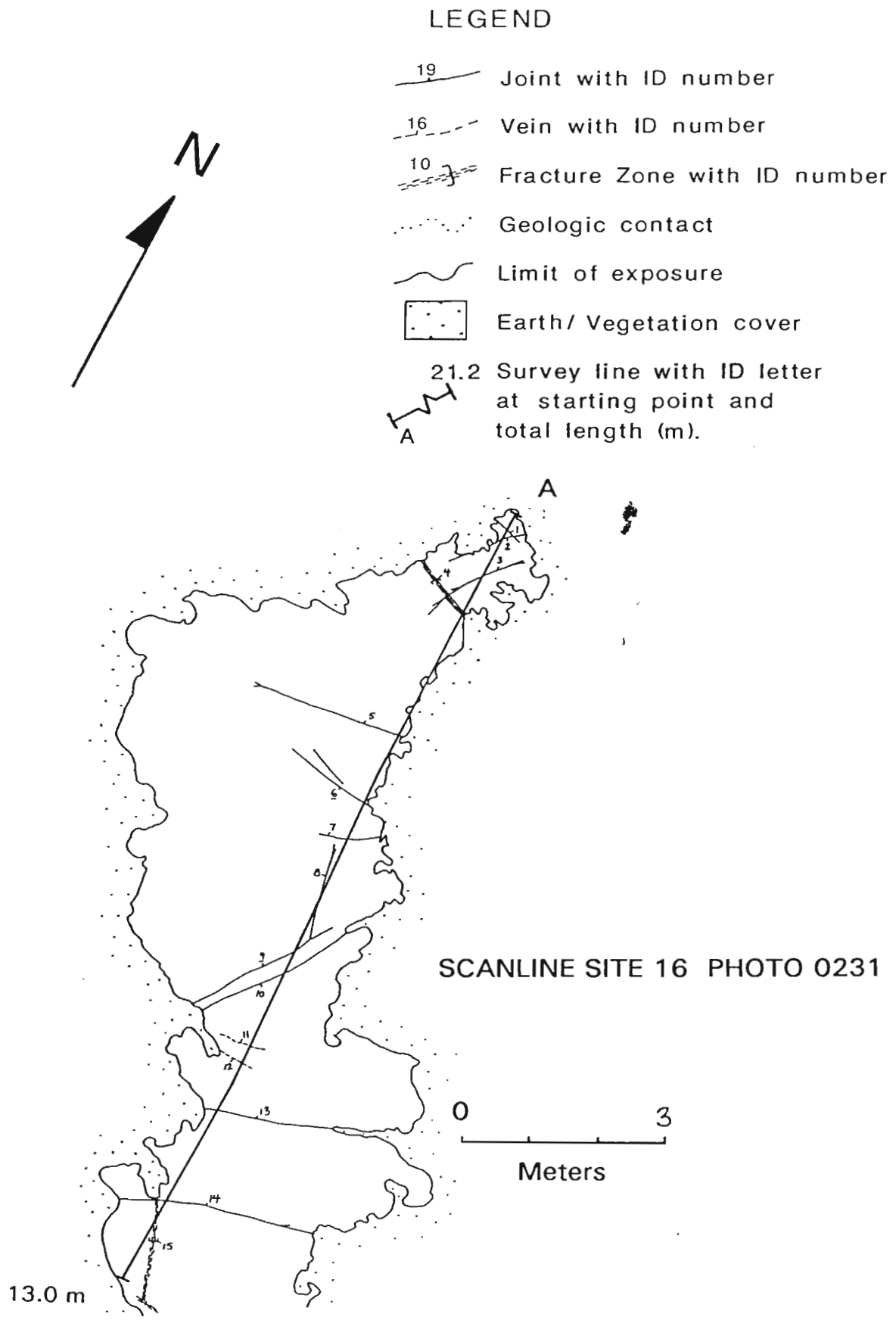





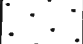
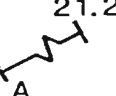


Figure B1b - Scanline trace map for survey site 16 in the Seal Cove River valley

## LEGEND

-  Joint with ID number  
 Vein with ID number  
 Fracture Zone with ID number  
 Geologic contact  
 Limit of exposure  
 Earth/ Vegetation cover  
 21.2 Survey line with ID letter at starting point and total length (m).

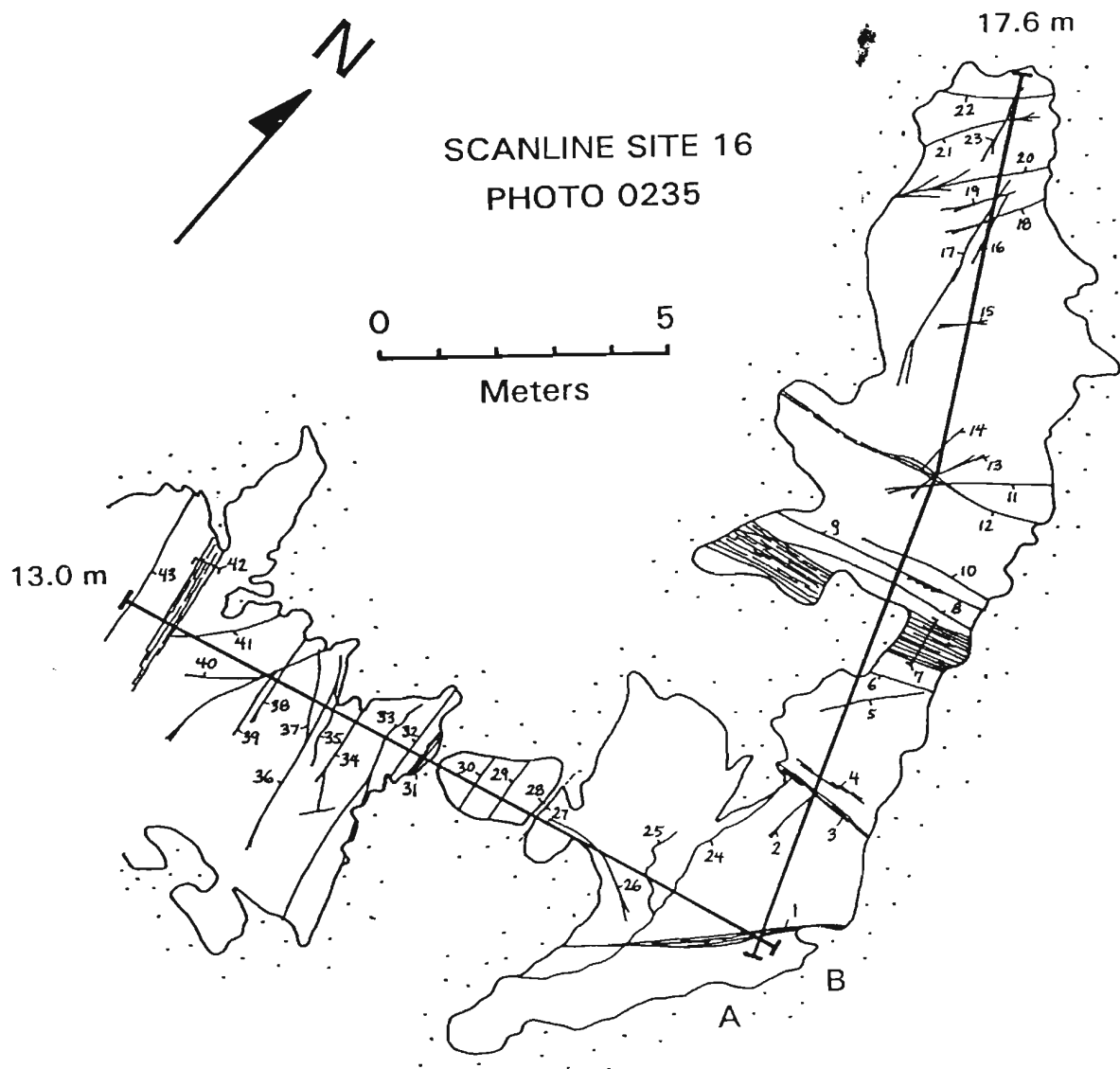


Figure B1c - Scanline trace map for survey site 16 in the Seal Cove River valley

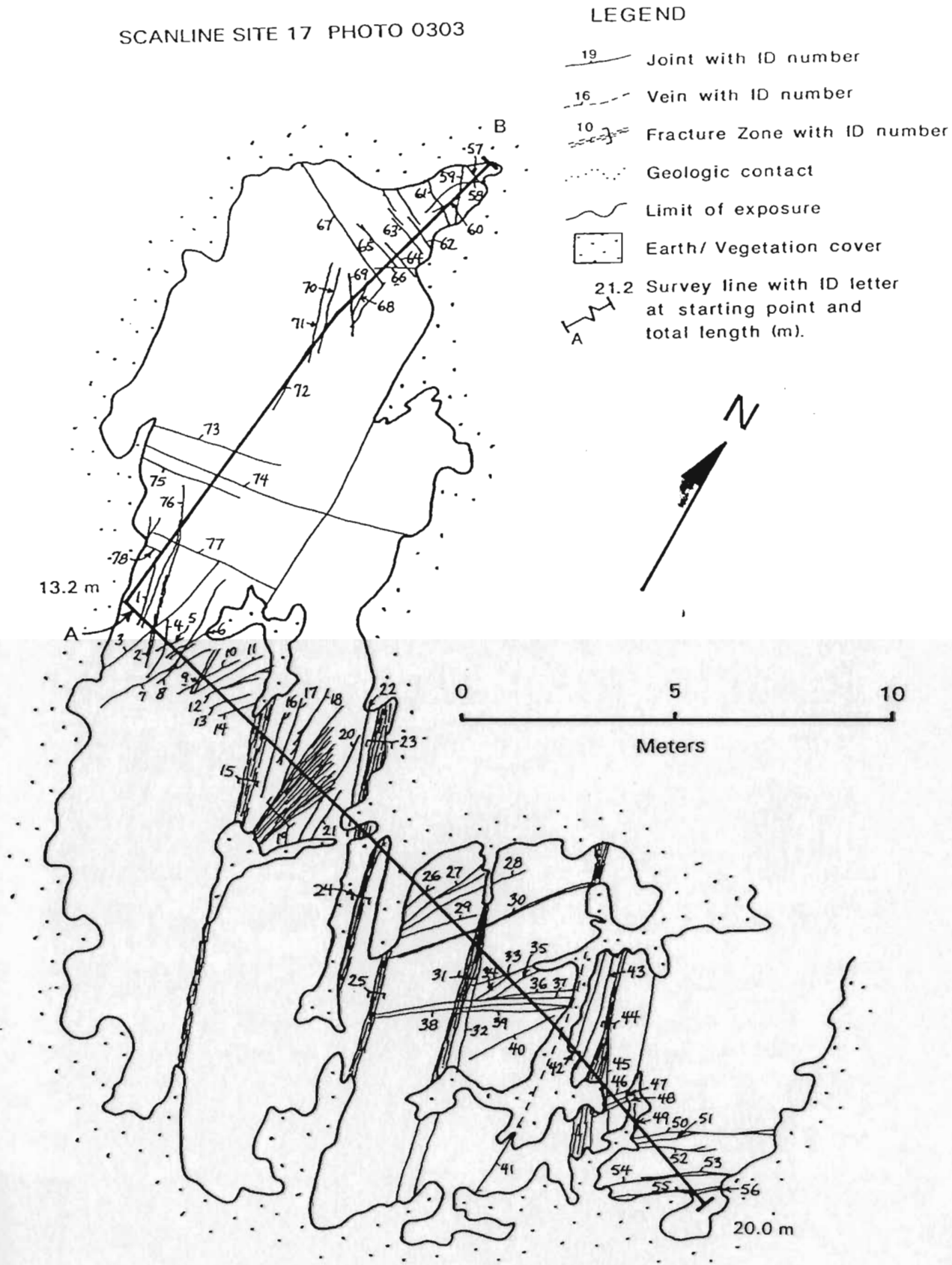


Figure B2 - Scanline trace map for survey site 17 in the Seal Cove River valley

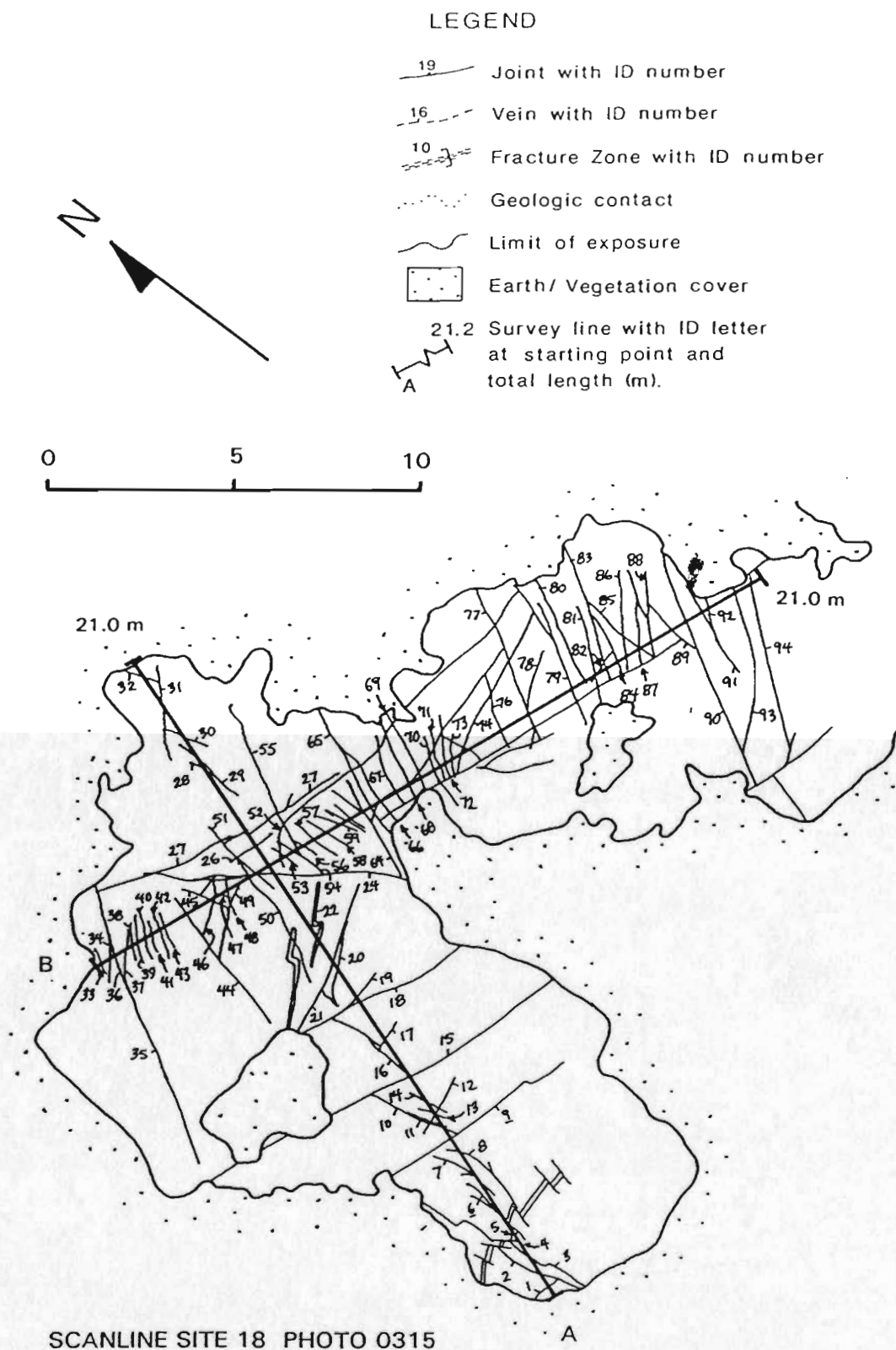


Figure B3 - Scanline trace map for survey site 18 in the Seal Cove River valley

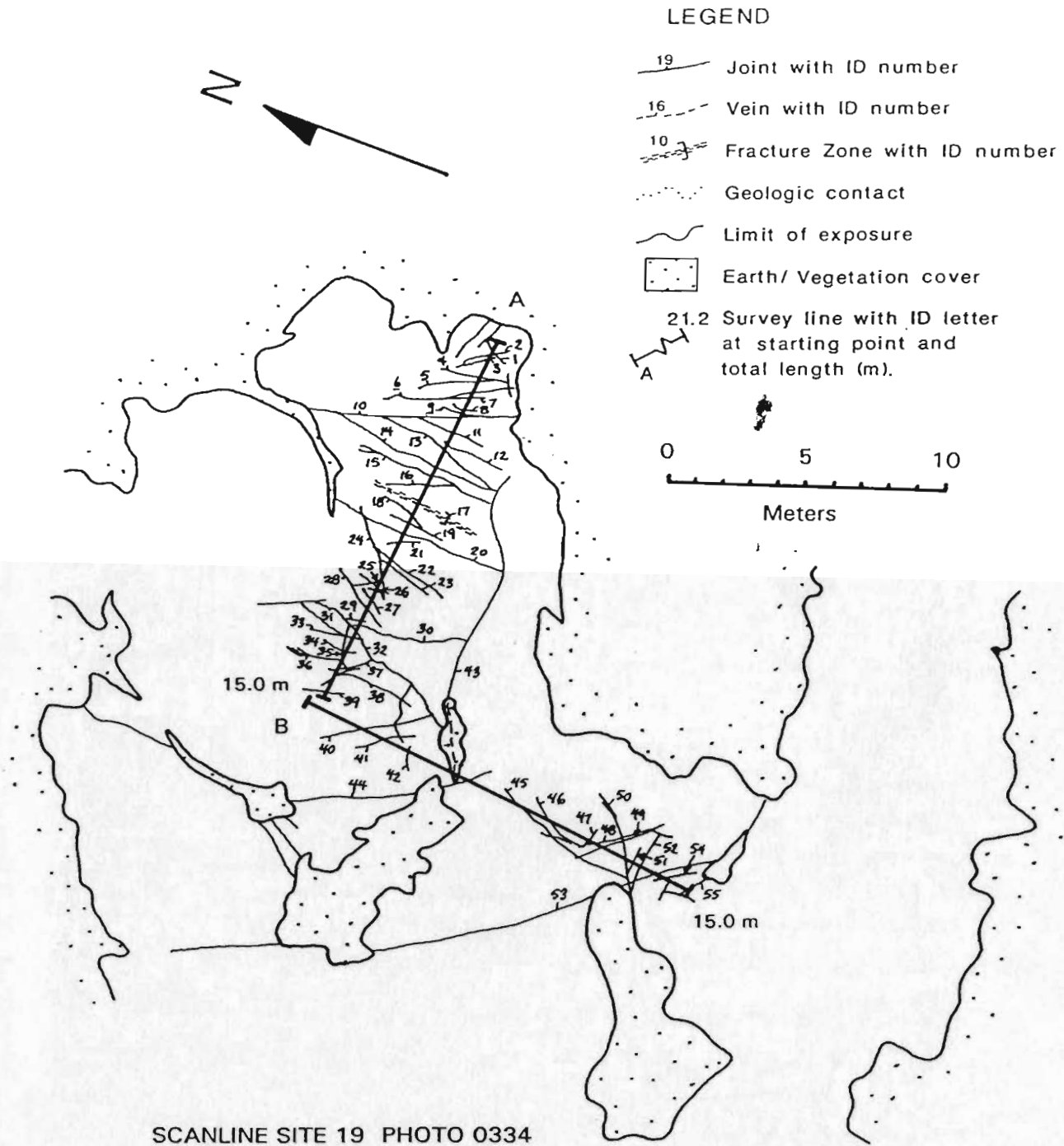


Figure B4 - Scanline trace map for survey site 19 in the Seal Cove River valley



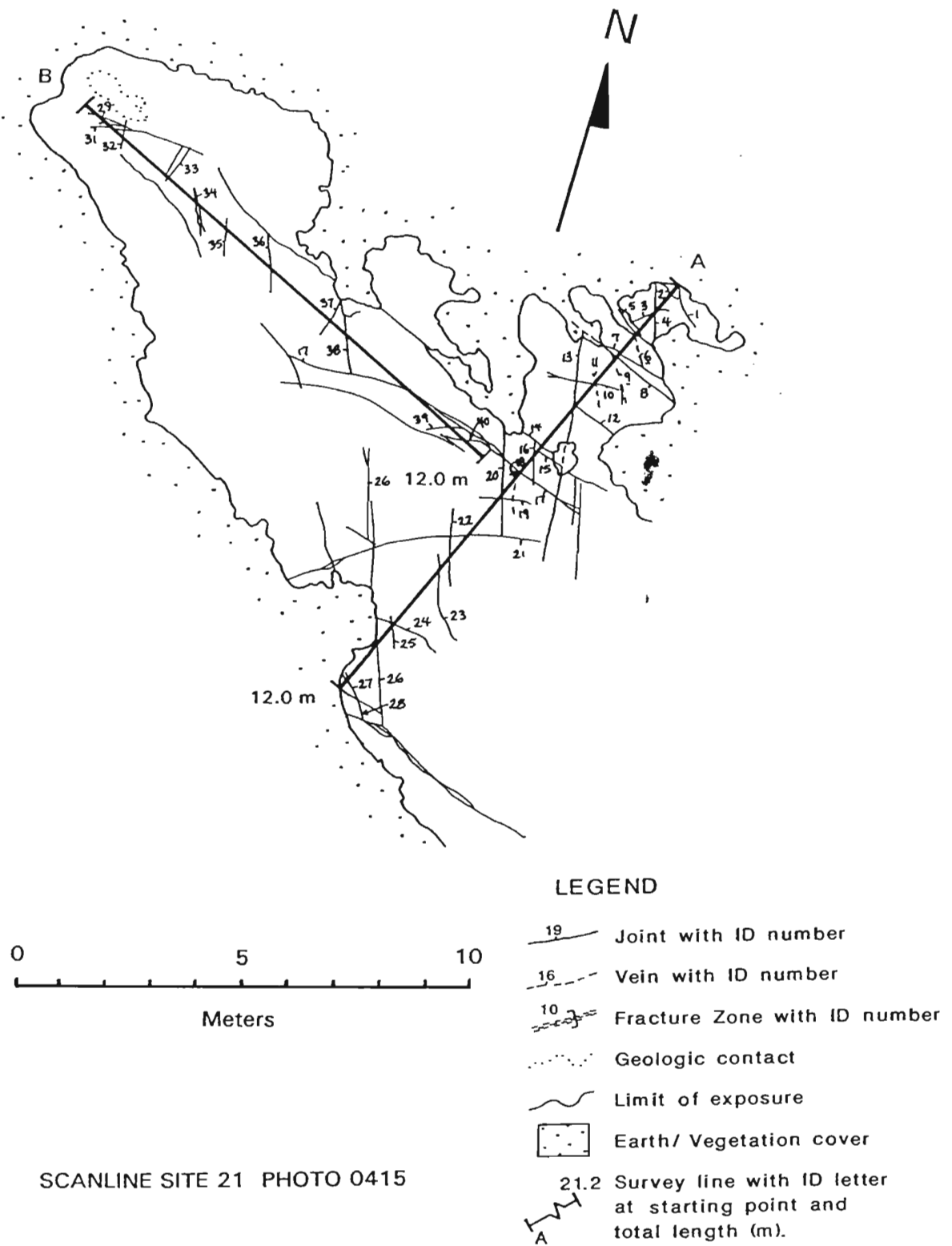


Figure B5a - Scanline trace map for survey site 21 in the Seal Cove River valley

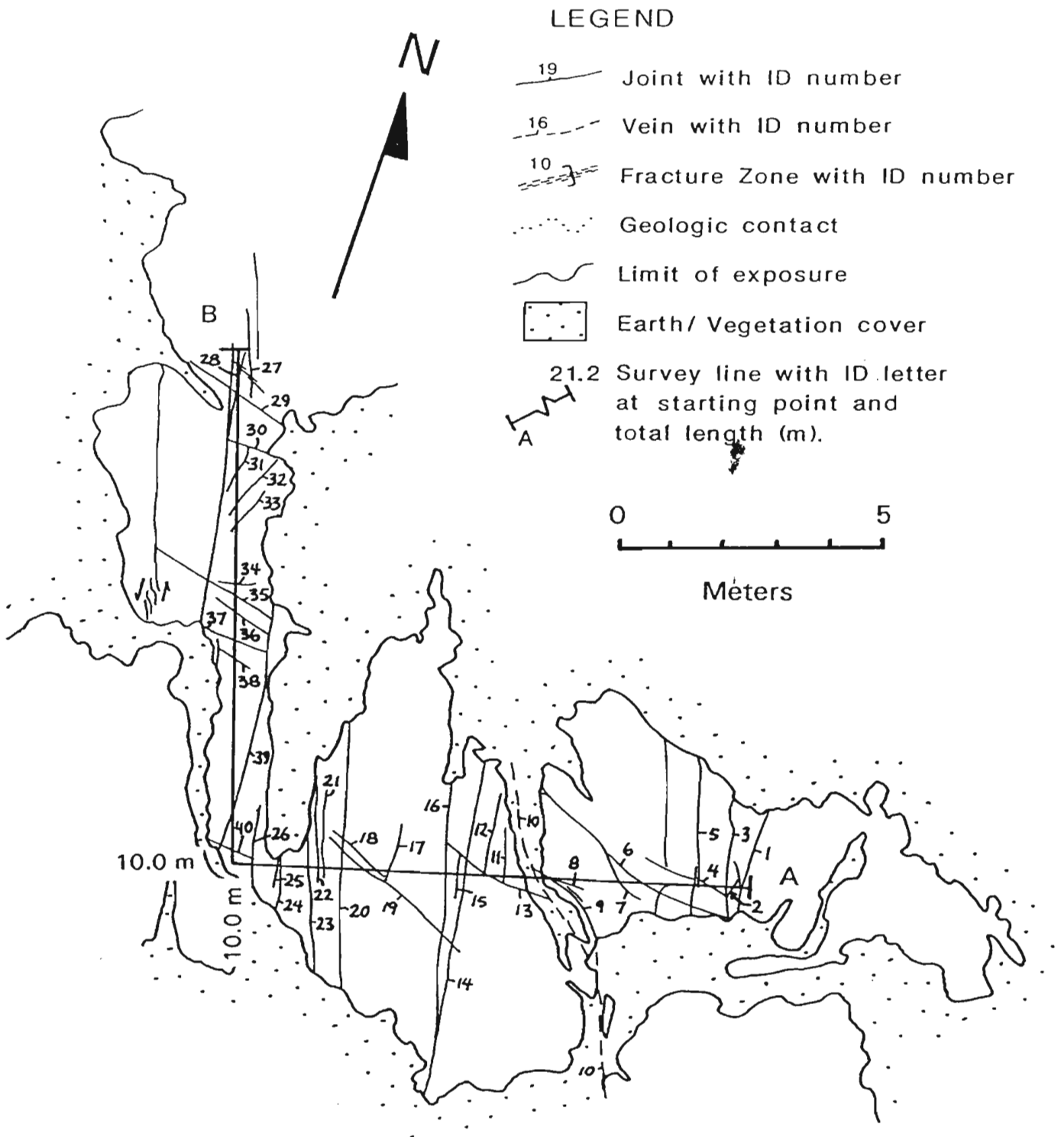


Figure B5b - Scanline trace map for survey site 21 in the Seal Cove River valley

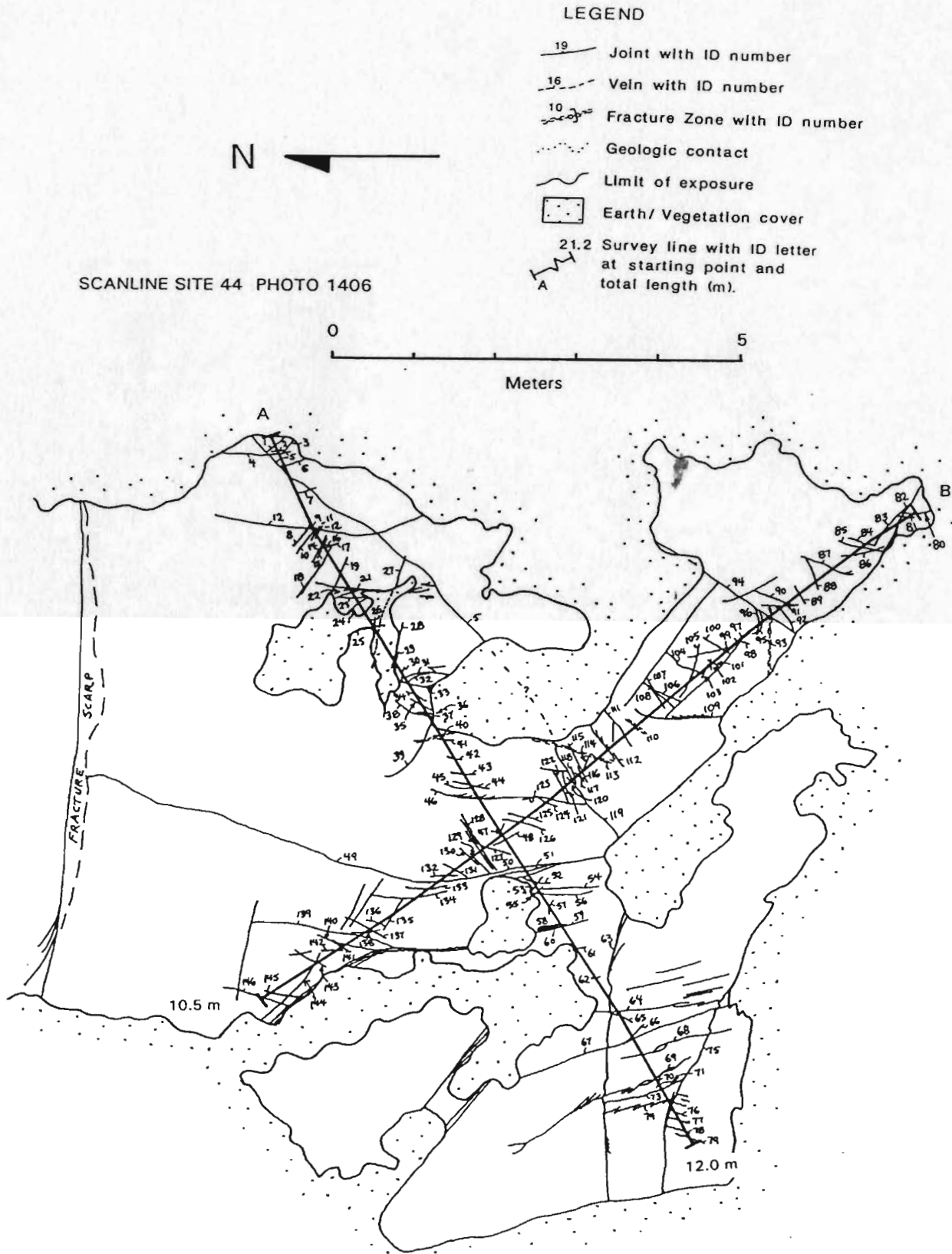


Figure B6 - Scanline trace map for survey site 44 in the Seal Cove River valley

## SCANLINE SITE 49 PHOTO 1229

## LEGEND

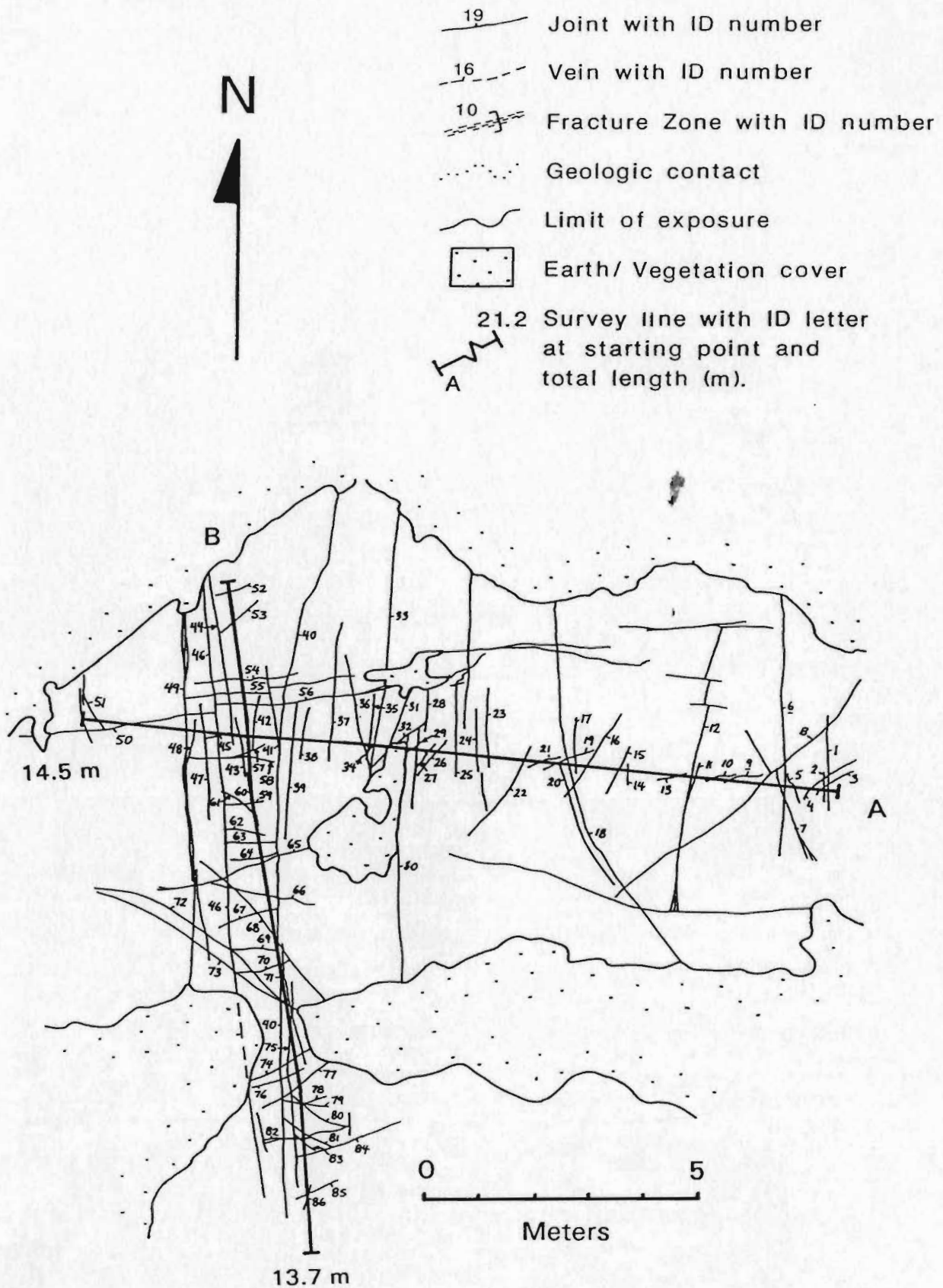
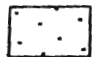
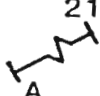


Figure B7 - Scanline trace map for survey site 49 in the Seal Cove River valley

## SCANLINE SITE 54

PHOTO 1321

## LEGEND

- 19 — Joint with ID number
- 16 - - - Vein with ID number
- 10 - - - Fracture Zone with ID number
- ..... Geologic contact
- ~ Limit of exposure
-  Earth/ Vegetation cover
- 21.2  Survey line with ID letter at starting point and total length (m).

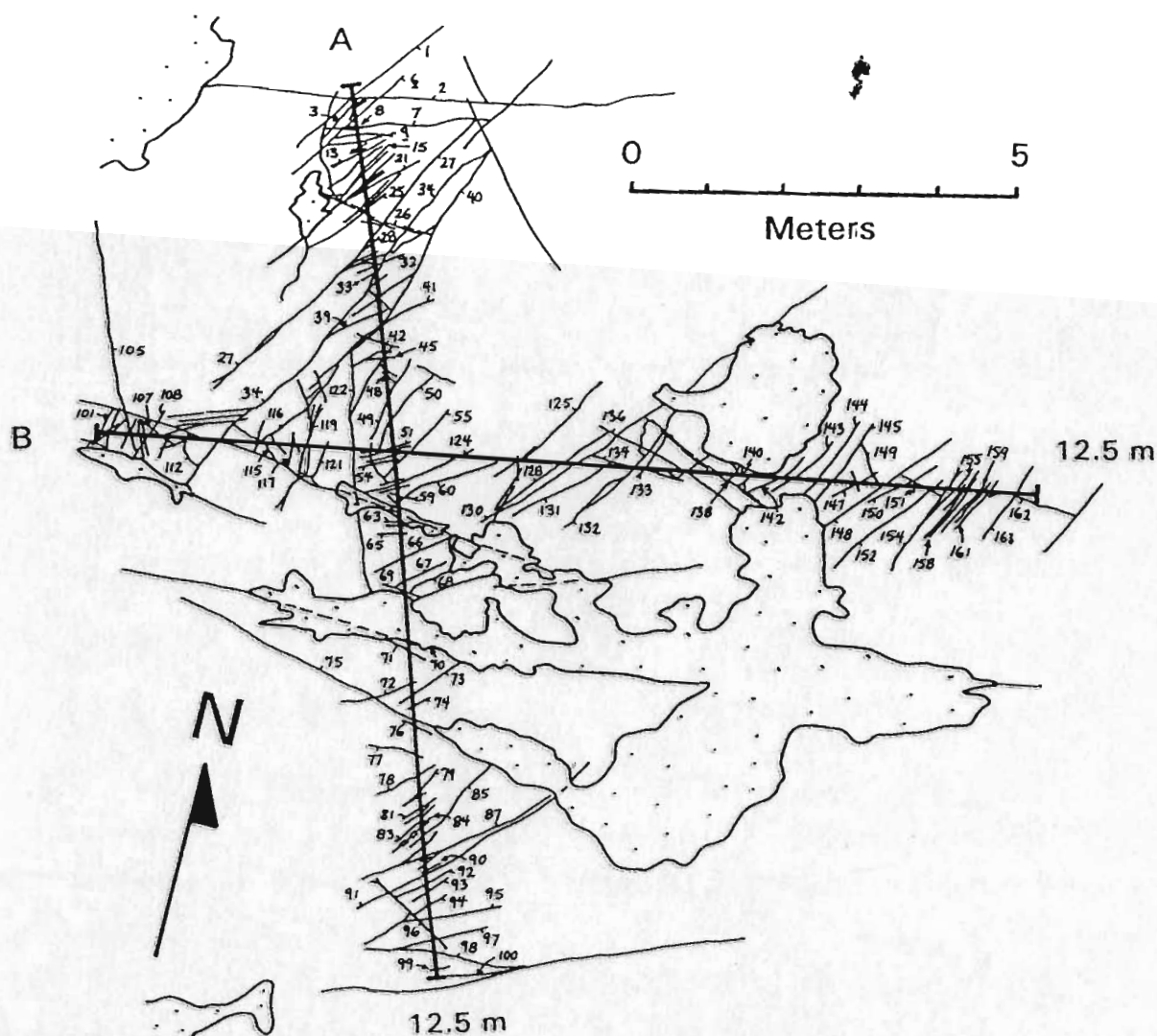


Figure B8 - Scanline trace map for survey site 54 in the Seal Cove River valley

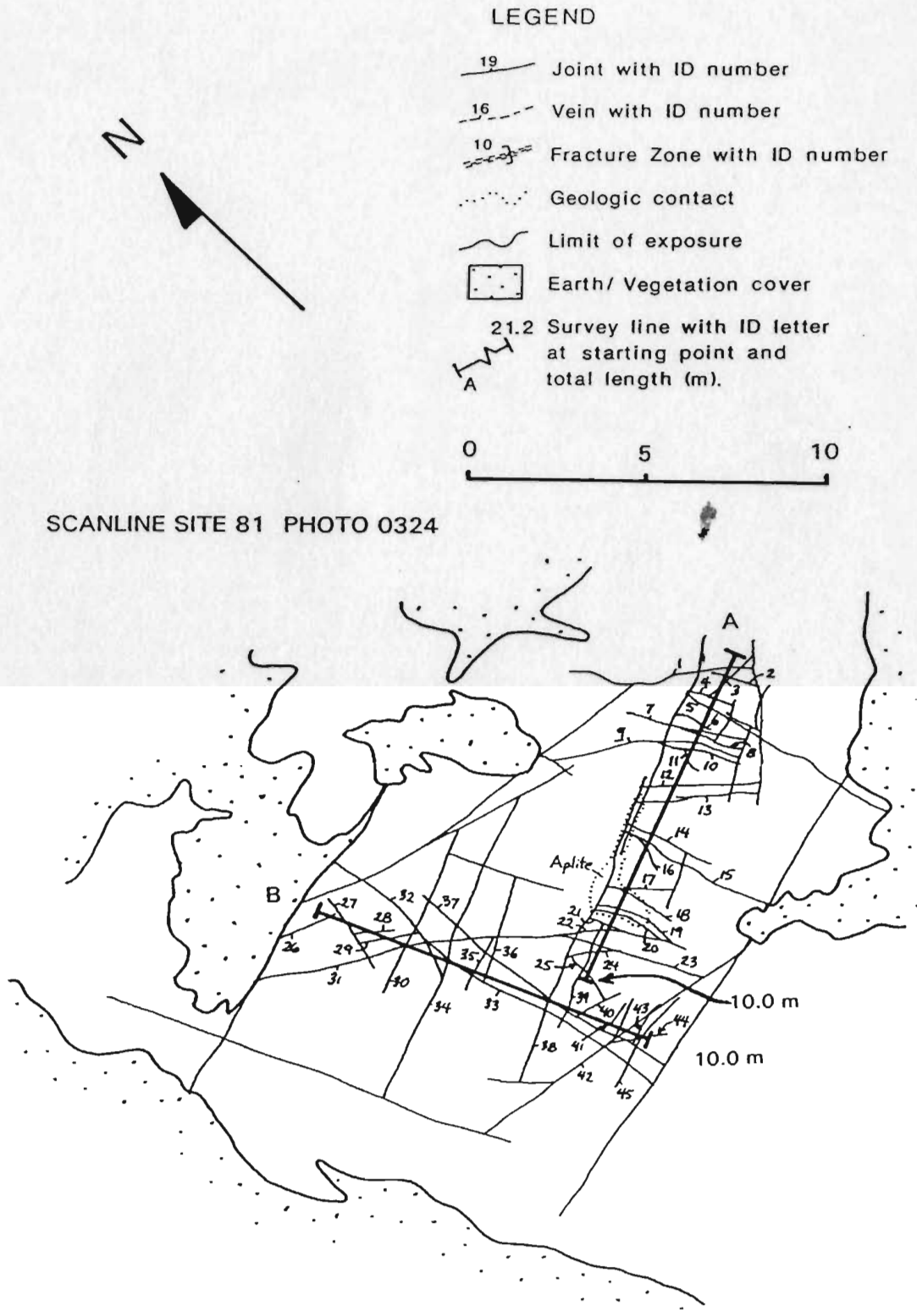


Figure B9 - Scanline trace map for survey site 81 in the Seal Cove River valley

Table B1 - Scanline fracture data for the Seal Cove River valley

```

33-----
33 "SCRVSCAN.DAT" - SCANLINE FRACTURE DATA FOR THE
33 SEAL COVE RIVER VALLEY
33 DATA IS PRESENTED BY INCREASING SURVEY SITE (STOP) NUMBER
33 FORMAT DESCRIBED IN TEXT
33
33 STOP 16 PHOTO 0235 LINE A
33
110235A34009 1 0.35FZ 13885 5.2 2 R USG SPANS:0.25-0.45; BRAIDED
33 TAPERS AT BOTH ENDS TO 5CM
110235A34009 2 2.92JT 8945 1.3 0 R PSG1 STR. SPLAYS AT S END;
33 ABUTS 3
110235A34009 3 3.22FZ 1390 4.0 2 R PSG MOSS; SPANS:3.15-3.28
110235A34009 4 3.49JT 082 1.6 0 PSG0 EN ECHELON AT E END
110235A34000 5 4.87JT 13685 2.0 0 PSG0
110235A34000 6 5.95JT 33884 1.0 2 PRG
110235A34000 7 6.90FZ 35990 5.0 2 R USG SPANS:6.60-7.20;
33 CONTINUES AS STAIR STEPS IN OUTCROP TO W; SPACING 5-10CM
110235A34000 8 7.60VN 35877 5.1 2 QH PSG 5MM WIDE
110235A34000 9 7.79JT 17277 5.0 2 PSG LEFT LAT. SPLAY: S SIDE
110235A34000 10 8.06JT 35671 2.6 2 PSG
110235A34000 11 8.30JT 33173 2.6 1 PSG Fe STAINING AT SCAN LINE
33 SPLAYS AT SCAN LINE
110235A34000 12 9.63FZ 17865 6.9 2 R URG SPANS:9.54-9.72
110235A34000 13 9.60JT 12773 1.5 0 CSGO
110235A34000 14 10.37JT 9482 1.1 0 PSG1 BOTH ENDS STR. SPLAYS
110235A34000 15 12.60JT 33383 1.0 0 PSG0
110235A34000 16 14.15JT 8783 1.8 0 PSG0
110235A34000 17 14.63FZ 8584 5.0 0 R USG1 SPANS:14.55-14.70; CLOSE
33 SPACED, SUBPAR. FRACTURES, SPACING < 1CM; ENDS AT 20
110235A34000 18 14.60JT 30787 1.6 1 USG FeO HALO 3CM EITHER SIDE
110235A34000 19 15.01JT 31390 1.2 0 PSG0
110235A34000 20 15.44FZ 31387 2.7 2 R PRG MOSS; SPANS:15.40-15.47;
33 SPLAYS ON EITHER SIDE AT W END
110235A34000 21 16.57JT 31583 1.9 1 PSG
110235A34000 22 17.07JT 32382 2.1 2 R CRG MOSS
110235A34000 23 17.07JT 8080 1.6 0 PSG1 ENDS AT 22
110235A34000 17.60 90 0 EOL
33
33 PHOTO 0235 LINE B
110235B26400 1 0.33FZ 13885 5.2 2 R USG SPANS:0.20-0.45
110235B26416 24 2.10JT 26978 7.0 1 R SSG MOSS; SHORT STRAIGHT
33 SEGMENTS LINKING SEVERAL PLANAR FRACTURES; ENDS AT 3
110235B26416 25 2.70JT 27016 2.0 0 PSG1 ENDS AT 24
110235B26400 26 4.15JT 250 2.2 0 PSG0
110235B26400 27 4.90JT 8778 3.3 2 PSG
110235B26400 28 5.04JT 27273 0.8 2 PSG 5CM WIDE ZONE OF 1CM
33 SPACED JTS
110235B26400 29 5.61JT 26590 1.0 2 PSG
110235B26400 30 5.90JT 26482 0.5 2 PSG
110235B26400 31 6.83FZ 7956 1.9 2 PSG SPANS:6.70-6.95
110235B26400 32 7.15JT 8480 2.1 2 R PSG SPLAYS ON BOTH SIDES
110235B26400 33 7.78JT 7136 5.0 1 URG SPLAYS AT N END
110235B26400 34 8.48JT 26484 1.7 1 URG
110235B26400 35 8.88JT 26187 2.1 1 URG
110235B26400 36 8.98JT 8082 3.0 0 PSG3 JOINS 35 AT SCAN LINE
110235B26400 37 9.27JT 6085 1.6 0 H CRG3 Fe PATCHY SKINS; JOINS37
110235B26400 38 9.99JT 7558 2.0 1 PSG
110235B26400 39 10.10JT 8083 1.4 0 PSG1 ENDS AT 40
110235B26400 40 10.17JT 31081 3.8 1 CSG FORKS AT SW END
110235B26400 41 11.70JT 31756 2.2 1 CSG
110235B26400 42 12.11FZ 8276 4.0 1 PSG MOSS; SPANS:11.89-12.32;
33 SPACING IN ZONE 3-10CM
110235B26400 43 12.91FZ 7987 6.0 2 R URG MOSS; SPANS:12.82-13.00
110235B26400 13.00 90 0 EOL
33
33 PHOTO 0228 LINE A
110228A23700 1 0.52JT 19080 2.0 1 USG
110228A23700 2 0.88FZ 3890 1.0 2 HR URG SPANS:0.70-1.05; ANGULAR
33 ROCKS FRAGMENTS; BRAIDED
110228A23700 3 1.70JT 35477 1.5 2 CRG ORIENTATION AT SCAN LINE

```

Table B1 (continued)

110228A23700	4	1.90JT	4087	1.1	1	PSG	
110228A23700	5	2.68JT	18384	0.7	2	PSG	MOSS
110228A23700	6	2.90JT	35979	1.7	2	PSG	MOSS
110228A23700	7	3.08FZ	7463	4.0	2	PSG	SPANS:2.95-3.20 ; TRACE
33 INCLUDES FRACTURE UNDERWATER FOR 3 METERS							
110228A23700	8	3.90FZ	19882	3.2	1	USG	MOSS; SPANS:3.85-3.95;
33 SUBPARALLEL DISCONTINUOUS JTS, SPACING = 1-10 CM							
110228A23700	9	4.35JT	12287	8.0	2	USG	MOSS; 3M UNDER WATER
110228A23700	10	5.82JT	20364	2.7	1	R CRG	MOSS
110228A23700	11	6.04JT	11379	4.0	2	R CRG	MOSS
110228A23700	12	6.40JT	981	2.0	1	R PRG	MOSS
110228A23700	13	6.80JT	23472	2.0	1	CRG	
110228A23700	14	7.17FZ	11542	1.1	1	PSG	SPANS:7.09-7.25;ABUTS13
110228A23700	15	7.93JT	21274	1.7	0	USG1	ENDS AT 11
110228A23700	16	8.29JT	21579	2.0	1	R PSG	
110228A23700	17	8.42JT	3484	0.8	1	PRG	
110228A23700	18	8.68JT	20385	1.0	2	R PSG	MOSS
110228A23700	19	8.85JT	21185	1.2	1	R PSG	MOSS
110228A23700	20	9.78FZ	20523	4.0	2	R C-G	MOSS; SPANS:9.66-9.90
110228A23700	21	10.45JT	8575	1.3	0	R PSG0	Fe HALO
110228A23700	22	11.56JT	4586	2.2	1	CSG	
110228A23700	23	12.22JT	21379	4.0	0	R CSG0	MOSS; LEFT LAT. SPLAYS
33 AT SE END							
110228A23700	24	12.78FZ	2887	4.1	2	R PSG	NW END UNDER MOSS
33 SPANS:12.68-12.88							
110228A23700	25	13.74JT	25573	1.0	2	R USG	MOSS
110228A23700		14.00	90 0				EOL
33							
33 PHOTO 0228 LINE B							
110228B30800	26	1.43JT	10562	1.9	1	PSG	
110228B30800	27	2.35FZ	29083	3.0	2	R PRG	MOSS; SPANS:2.27-2.42
110228B30800	28	3.10JT	12877	5.6	2	R P-G	MOSS
110228B30800	9	3.48JT	12287	8.0	2	USG	
110228B30800	29	3.80JT	18779	1.0	0	PSG2	ENDS AT 9 & 10
110228B30800	11	4.45JT	20364	2.7	1	R CRG	
110228B30800	14	4.90FZ	11542	1.1	1	PSG	
110228B30800	30	5.80FZ	10341	1.6	0	PSG1	FZ:2CM WIDE; SPACING 1-2
33 MM IN ZONE							
110228B30800	31	6.57JT	11083	1.2	0	R PSG2	ENDS AT 15 & 32
110228B30800	32	6.94FZ	15077	3.0	0	R PSG2	MOSS; SPANS:6.78-7.10;
33 ABUTS 20							
110228B30800	33	7.80JT	13883	4.0	1	R URG	MOSS
110228B30800	34	8.00JT	33883	1.2	1	R PRG	MOSS
110228B30800	35	8.40JT	33090	4.0	2	--G	MOSS
110228B30800	36	8.80JT	34657	0.7	2	PSG	
110228B30800	37	9.10JT	13283	0.6	2	PSG	MOSS
110228B30800		10.00	90 0				EOL
33							
33 PHOTO 0231 LINE A							
110231A00010	1	0.35JT	3376	0.5	1	PSG	FeO ON FRAC. SURFACE
110231A00010	2	0.81JT	15479	2.4	1	R PSG	
110231A00010	3	1.10JT	30183	1.6	0	RH PSG0	INFILL OF FeO & FINELY
33 CRUSHED ROCK							
110231A00010	4	1.80FZ	3475	1.2	2	R PSG	MOSS; SPANS:1.75-1.85
110231A00010	5	3.94JT	35945	2.1	1	R USG	
110231A00010	6	5.08JT	990	1.7	1	PSG	FeO SKINS
110231A00010	7	5.60JT	35337	0.8	1	PSG	
110231A00010	8	6.50JT	7480	1.8	0	PSG1	ENDS AT 9
110231A00010	9	7.52JT	30381	2.2	1	R PRG	
110231A00010	10	7.91JT	30982	2.8	2	PRG	
110231A00010	11	9.13VN	18279	0.6	0	QH PSG0	ISOLATED Fe CLOTS
110231A00010	12	9.50VN	1090	0.5	1	O PSG	UPTO 1CM THICK
110231A00010	13	10.19FZ	17764	3.0	2	CRG	SPANS:10.13-10.25
110231A00010	14	11.80FZ	25390	1.7	1	R PRG	SPANS:11.75-11.85
110231A00010	15	11.80JT	34590	2.2	1	R PRG	
110231A00010		13.00	90 0				EOL
33							
33 STOP 17 PHOTO 0303 LINE A							
33							
110303A29004	1	0.36JT	7363	1.7	0	PSG1	
110303A29004	2	0.82FZ	9654	3.0	0	PSG0	SPANS:0.75-0.90



Table B1 (continued)

110303A29004	3	0.95CM	26444		PSA	
110303A29004	4	1.28JT	9370	0.8 0	CSA2	
110303A29004	5	1.37JT	14464	0.7 1	PSA	
110303A29004	6	1.57FZ	14554	1.3 0	PSA0	SPANS:1.50-1.65
110303A29004	7	1.72CM	11879		SSA	
110303A29004	8	1.96JT	13563	1.2 1	PSG	
110303A29004	9	2.45FZ	9577	1.5 2	R PSG	SPANS:2.4-2.5; STR.
33 SPLAYS AT N END						
110303A29004	10	2.51JT	13079	1.7 0	PSG0	EN ECHELON AT S END
110303A29004	11	2.70JT	12269	2.0 1	PSG	
110303A29004	12	2.91JT	13555	1.3 1	R PSG	FORKED AT N END
110303A29004	13	3.30JT	13277	0.6 1	PSG	
110303A29004	14	3.55FZ	14260	0.7 2	PSG	SPANS:3.50-3.60
110303A29004	15	4.47FZ	7154	6.0 2	PSG	SPANS:4.0-4.95; INTERNAL
33 5-8CM PAR. FRACS						
110303A29004	16	5.08JT	8173	1.1 0	PSG1	
110303A29004	17	5.24JT	8549	0.9 0	PSG1	RT. LAT. HOOK AT S END
110303A29004	18	5.45JT	9360	1.9 0	PSG1	RT. LAT. SPLAYS ALONG
33 TRACE AT SCAN LINE						
110303A29004	19	6.60FZ	11057	4.0 1	R PSG	SPANS:5.55-7.65;
33 INTERNAL SPACING APPRX. 5CM; TAPERS TO SW						
110303A29004	20	6.80JT	9456	3.0 1	R CSG	
110303A29004	21	7.25JT	34174	0.7 1	PSG	
110303A29004	22	7.40JT	8651	4.0 2	R PSG	MOSS
110303A29004	23	7.80FZ	7967	3.0 2	R PSG	MOSS; SPANS:7.6-8.0;
33 INTERNAL SPACING 0.5-4CM						
110303A29004	24	8.55JT	8658	3.3 2	R PSG	EN ECHELON END AT LINE
33 BECOMES 15CM FZ TO SW						
110303A29004	25	9.10FZ	25485	6.0 2	R PSG	MOSS; SPANS:8.9-9.3;
33 COVERED AT SCAN LINE; EXPOSED TO S						
110303A29004	26	9.67JT	1216	0.5 1	PSG	
110303A29004	27	10.04JT	1351	2.0 2	R PSG	MOSS; FORKS AT N END
110303A29004	28	10.36JT	1328	2.3 1	R PSG	MOSS
110303A29004	29	10.85JT	13966	1.0 2	R PSG	MOSS
110303A29004	30	11.45FZ	13580	4.9 0	R PSG2	MOSS; SPANS: 11.2-11.7;
33 PARALLEL JTS. SPACING IN 2-5CM; ENDS AT 25						
110303A29004	31	11.75FZ	7378	9.0 2	R PSG	MOSS; SPANS:11.5-12.0;
33 SPACING IN ZONE 3-10CM						
110303A29004	32	12.02JT	7374	3.1 2	R PSG	MOSS
110303A29004	33	12.54FZ	13372	1.3 1	R USG	MOSS; SPANS:12.5-12.58;
33 ABUTS 32						
110303A29004	34	12.70JT	30377	1.2 2	USG	ENDS AT 32; JOINS 33
110303A29004	35	12.97JT	29952	1.3 1	PSG	
110303A29004	36	13.20JT	14269	4.1	R PSG	MOSS; ENDS AT 25
110303A29004	37	13.35JT	14262	1.7 1	R PSG	MOSS; JOINS 36
110303A29004	38	13.48JT	13855	4.1 1	R PSG	MOSS; JOINS 25
110303A29004	39	13.77JT	13566	2.3 0	R CSG1	JOINS 38
110303A29004	40	14.08JT	30066	0	PSG1	FREE END AT LINE; ROCK
33 AT 14.10M= Q CLOT WITH PALE GREEN MICA; 0.5MM GRANULAR red						
33 GARNET; MINOR H;						
33 Q GRAINS UP TO 1CM; MINOR E						
110303A29004	41	14.70JT	8864	4.0 2	R PSG	MOSSCOVERED AT SCAN
33 LINE						
33 BASED ON EXPOSED PAR. JTS						
110303A29004	42	15.13JT	8576	2.3 2	R PSG	
110303A29004	43	15.40JT	9077	3.1 2	R PSG	MOSS
110303A29004	44	15.87FZ	8162	5.2 2	R PSG	MOSS; SPANS:15.6-16.15;
33 WIDENS TO S						
110303A29004	45	16.35JT	8056	2.0 1	R PSG	JOINS 44
110303A29004	46	16.45JT	13768	1.0 1	R PSG	MOSS
110303A29004	47	16.68JT	13654	0.8 1	R PSG	MOSS; ENDS AT 45
110303A29004	48	16.80JT	13659	0.8 1	R PSG	MOSS; ENDS AT 44
110303A29004	49	17.25JT	7656	5.0 1	R PSG	MOSS COVERED AT LINE;
33 DIP FROM EXPOSURE AT N END; ENDS AT 50						
110303A29004	50	17.81JT	15481	3.3 1	R PSG	MOSS
110303A29004	51	17.95JT	14075	1.3 1	R PSG	MOSS; JOINS 50
110303A29004	52	18.15JT	15467	2.0 1	R PSG	LEFT LAT. SPLAY AT E END
110303A29004	53	19.00JT	14861	1.7 0	R PSG3	
110303A29004	54	19.10JT	14161	2.8 2	PSG	
110303A29004	55	19.53JT	14582	2.1 2	R PSG	MOSS
110303A29004	56	19.73JT	14386	0.9 2	PSG	

Table B1 (continued)

110303A29004 20.00 90 0 EOL  
33  
33 PHOTO 0303 LINE B  
110303801509 57 0.53JT 3889 1.0 2 R PSG  
110303801509 58 0.65JT 31081 1.6 1 R CSG  
110303801509 59 1.10JT 6878 1.3 2 R PSG  
110303801509 60 1.15JT 28625 1.7 1 R PSG  
110303801509 61 1.64JT 3884 1.2 2 R PSG  
110303801509 62 2.78JT 3977 1.1 1 R SSG  
110303801509 63 3.08JT 2683 1.5 1 PSG W END EN ECHELON  
110303801509 64 3.40JT 2978 1.5 1 PSG MOSS  
110303801509 65 3.68JT 2767 1.2 0 PSG1 STR. SPLAYS TO W;  
33 ABUTS 66  
110303801509 66 3.93JT 13685 0.8 1 PSG MOSS  
110303819005 67 4.35JT 3882 2.5 1 R USG  
110303819005 68 4.75JT 6987 1.1 0 PSG1  
110303819005 69 5.03JT 3767 0.7 0 PSG0 DIFFUSE 5-10CM LONG  
33 BRAIDED MICROJOINTS  
110303819005 70 6.14JT 7569 1.8 0 PSG0  
110303819005 71 6.70JT 7269 1.9 0 PSG0 DIFFUSE SHORT JTS  
110303819005 72 7.40JT 9884 1.2 0 USG0  
110303819005 73 9.74JT 35584 3.1 1 R PSG  
110303819005 74 10.42JT 18090 6.2 2 R PSG  
110303819005 75 10.70JT 282 2.1 1 R PSG  
110303819005 76 11.74JT 9441 3.2 0 R CRG0  
110303819005 77 12.20JT 471 3.3 0 R SSG2 MOSS  
110303819005 78 12.47JT 35685 0.5 2 R PSG MOSS  
110303819005 15.20 90 0 EOL  
33  
33 STOP 18 PHOTO 0315 LINE A  
33  
110315A02005 1 0.15JT 757 0.7 1 USG  
110315A02005 2 0.63JT 7565 1.3 0 H PSG0 DIFFUSE EN ECHELON  
33 MICRO JOINTS  
110315A02005 3 1.20FZ 8678 5.1 2 R SSG FAULT OFFSETS AP DIKE;RT  
33 LAT. OFFSET 30CM  
110315A02005 4 1.25CN 16583 A OFFSET BY NUMEROUS  
33 FAULTS PARALLEL TO 3  
110315A02005 5 1.45CN 16583 G  
110315A02005 6 2.15FZ 9283 3.1 0 R USG3 SPANS:2.0-2.3; INTERNAL  
33 SPACING 1-5MM; FAULT; LEFT LAT. OFFSET OF AP DIKE 30CM; JOINS 3;  
33 LEFT LAT.  
33 SPLAYS AT S END  
110315A02005 7 3.75JT 33475 3.3 0 USG STR.SPLAYS FROM LINE TO  
110315A02005 8 4.66JT 6972 0.9 0 CSG3  
110315A02005 9 5.17JT 1383 4.5 1 CSG  
110315A02005 10 5.35JT 7583 2.4 0 R CSG1  
110315A02005 11 5.55JT 6870 0.9 0 PSG3 JOINS 10  
110315A02005 12 6.13JT 16579 1.2 0 R PSG0  
110315A02005 13 6.20JT 7164 0.9 0 PSG0  
110315A02005 14 6.50JT 7864 1.2 0 PSG0  
110315A02005 15 7.39FZ 20083 10.1 2 R PSG MOSS; SPANS:7.25-7.42  
110315A02005 16 7.60JT 9885 2.1 0 RH PSG1  
110315A02005 17 8.19JT 17374 0.9 0 PSG1 ENDS AT 16  
110315A02005 18 9.36JT 2059 3.1 1 H USG  
110315A02005 19 9.45JT 16138 1.0 0 CSG3 SPLAY FROM 18  
110315A02005 20 10.39JT 15544 1.9 0 USG2  
110315A02005 21 10.73FZ 16671 4.0 1 R USG FAULT  
110315A02005 22 11.50CN 15158 A 9CM WIDE; OFFSET BY  
33 MINOR FAULTS ALONG ITS LENGTH  
110315A02005 23 13.80CN 20545 A  
110315A02005 24 14.30JT 5074 6.0 1 R USG MOSS; ENDS AT 27  
110315A02005 25 14.70CN 2090 A  
110315A02005 26 14.85JT 20758 2.9 0 PSG0 PART OF SPLAY SET  
33 BETWEEN 24+27; EN ECHELON AT MIDSECTION  
110315A02005 27 15.23JT 20070 7.5 1 R SSG  
110315A02005 28 17.80JT 7663 0.6 0 CSG3  
110315A02005 29 18.00JT 8855 2.1 0 USG0  
110315A02005 30 18.40JT 8263 1.2 0 PSG1  
110315A02005 31 19.15FZ 14087 3.2 1 RH USG MOSS; SPANS:19.0-19.3;  
33 SPLAYS AT N

Table B1 (continued)

110315A02005	32	20.64JT	6860	0.7	1	PSG	DIFFUSE PARALLEL MICRO JOINTS
110315A02005		20.90	90	0		EOL	
33							
33 PHOTO 0315 LINE B							
110315B11304	33	0.15JT	10581	0.9	0	H 02G1	
110315B11304	34	.33FZ	11882	1.0	0	H 00G3	SPANS .32 - .35
110315B11304	35	0.51FZ	11075	5.8	1	HR 20G	SPANS .47 - .53
110315B11304	36	0.67JT	11580	1.2	0	00G3	PARALLEL MICROJOINTS IN 1 CM ZONE
110315B11304	37	0.73JT	12680	0.8	0	10G3	
110315B11304	38	0.88JT	13189	0.9	0	H 00G0	
110315B11304	39	0.96JT	13082	1.1	0	10G0	
110315B11304	40	1.22JT	12676	1.0	0	H 00G0	
110315B11304	41	1.33JT	12070	0.8	0	00G1	
110315B11304	42	2.14JT	11577	1.8	0	20G0	CROSSES APLITE DIKE BOUNDARY
110315B11304	43	2.24JT	10464	0.9	0	00G0	
110315B11304	44	3.05CM	11572	6.0	0	20A1	FAULT BOUNDED APLITE DIKE;
33 APPROX 1 M OF LEFT LAT. OFFSET ON 44 SHOWN BY DIKE							
110315B11304	45	3.48JT	9085	1.3	0	00A1	
110315B11304	46	3.68JT	13789	1.5	0	00A2	FEATHER FRACTURES ON W. SIDE SHOW
33 LEFT LAT. STRAIN; 46 ENDS AT DIKE BOUNDARY							
110315B11304	47	3.73JT	8987	0.8	0	00A1	
110315B11304	48	4.02JT	14273	1.0	0	10A1	ENDS AT DIKE BOUNDARY
110315B11304	49	4.63JT	18045	1.6	0	00A2	ENDS AT BOTH DIKE BOUNDARIES
110315B11304	24	4.68					
110315B11304	50	5.13FZ	12184	3.5	0	20G2	SPANS 5.08-5.20; BRAIDED JOINTS
33 SPACED 1 - 3 CM							
110315B11304	51	5.27JT	10584	0.9	0	00G3	SPLAY FROM 50
110315B11304	52	5.63JT	11873	0.6	0	10G3	
110315B11304	53	5.76JT	10183	0.7	0	00G1	
110315B11304	54	6.08JT	8585	1.5	0	00G0	CROSSES DIKE BOUNDARY
110315B11304	55	6.27FZ	11590	4.0	0	H 20G0	SPANS 6.24 - 6.3; CROSSES 33 DIKE BOUNDARY
110315B11304	56	6.49JT	7975	1.0	0	00G3	
110315B11304	57	6.90JT	27085	1.3	0	00A0	
110315B11304	58	7.28JT	9182	0.8	0	00A0	
110315B11304	59	7.52JT	8580	0.5	0	00A0	
110315B11304	60	7.73JT	9085	0.8	0	00A1	ENDS AT DIKE BOUNDARIES
110315B11304	61	7.90JT	26686	1.0	0	00A0	EN ECHELON PATTERN TO LEFT;
33 1 CM SPACING, ENDS WITHIN DIKE							
110315B11304	62	8.36JT	8084	1.1	0	00A2	
110315B11304	63	8.47JT	13655	0.9	0	00A1	
110315B11304	64	8.60FZ	11671	2.6	0	20A1	SPANS 8.57 - 8.62; CROSSES
33 DIKE BOUNDARY TO N.							
110315B11304	65	8.88FZ	30362	6.0	2	20A	SPANS 8.80-8.94; BRAIDED
33 UNDULATING FRACTURES							
110315B11304	66	9.27FZ	11281	2.4	1	02A	SPANS 9.20 - 9.35; SPLAY FROM 65
110315B11304	67	9.62JT	12280	1.9	0	12A1	CROSSES DIKE BOUNDARY
110315B11304	68	9.98FZ	12978	3.4	2	20A	SPANS 9.95 - 10.01; FAULT WITH
33 0.4 M LEFT LAT OFFSET SHOWN BY DIKE							
110315B11304	69	10.39JT	12084	1.9	1	00G	
110315B11304	70	10.72JT	13544	1.0	0	00G0	
110315B11304	71	11.10JT	12535	1.6	0	00G3	
110315B11304	72	11.36JT	13354	1.4	1	00G	
110315B11304	73	11.63JT	33889	0.7	0	00G1	
110315B11304	74	12.00FZ	16550	4.4	0	20G2	SPANS 11.95-12.05; DIP ESTIMATED
110315B11304	75	12.08JT	7587	1.1	0	00G1	
110315B11304	76	12.40JT	13076	2.3	0	10G2	
110315B11304	77	13.70JT	11866	4.3	1	00G	
110315B11304	78	13.76JT	16558	1.3	0	00G1	
110315B11304	79	15.03JT	11185	4.0	1	22G	
110315B11304	80	15.55FZ	11175	3.5	1	20G	SPANS 15.5 - 15.6; FORMS
33 FAULTED DIKE BOUNDARY TO S.							
110315B11304	81	15.75JT	14176	2.2	1	00G	
110315B11304	82	15.90JT	00785	0.9	0	00G2	
110315B11304	83	16.07JT	13884	3.5	1	22G	
110315B11304	84	16.60JT	10680	1.3	0	00G1	MAINLY WITHIN DIKE TO S.
110315B11304	85	16.88JT	27880	2.7	0	02G2	EN ECHELON TO RIGHT
33 WITHIN DIKE							
110315B11304	86	17.02JT	13080	1.8	0	00G2	
110315B11304	87	17.56JT	11588	1.4	0	30G2	
110315B11304	88	17.90JT	30183	1.9	0	00G1	
110315B11304	89	18.27JT	26583	1.4	0	00G2	

Table B1 (continued)

110315B11304	90	18.65JT	12190	7.0	1	OOG	
110315B11304	91	19.83JT	30180	2.0	1	ZOG	
110315B11304	92	20.05JT	13378	1.0	0	10G3	
110315B11304	93	20.31FZ	30075	5.5	2	OOG	SPANS 20.28 - 20.35
110315B11304	94	20.70JT	13280	5.0	0	OOG2	
110315B11304		21.00					END OF LINE
33							
33 STOP 19 PHOTO 0334 LINE A							
33							
110334A26900	1	0.90JT	31472	2.3	0	USG2	
110334A26900	2	1.35JT	5270	0.9	0	PSG0	
110334A26900	3	1.55JT	5572	0.9	0	H PSG0	
110334A26900	4	1.60JT	28274	1.3	0	H PSG1	DIFFUSE MICROJOINTS UP
33 TO 1 CM ZONE							
110334A26900	5	1.81JT	5968	2.0	0	H USG1	DIFFUSE MICROJOINTS UP
33 TO 1 CM ZONE							
110334A26900	6	2.24JT	5682	3.9	0	H PSG1	
110334A26900	7	2.37JT	24286	1.1	0	PSG3	
110334A26900	8	2.86JT	28182	1.1	0	PSG0	
110334A26900	9	3.00JT	28288	1.0	0	PSG3	
110334A26900	10	3.41JT	7075	10.0	2	PSG	
110334A26900	11	3.72JT	8681	2.1	0	USG3	
110334A26900	12	4.21JT	10334	1.6	0	PSG0	
110334A26900	13	4.57JT	29575	3.2	0	USG3	BRAIDED. DIFFUSE. ESTIMATED DIP
33							
110334A26900	14	5.40JT	8287	5.1	0	H USG1	BRAIDED
110334A26900	15	5.72JT	9576	3.6	0	USG0	BRAIDED
110334A26900	16	5.94JT	6285	1.9	0	USG1	
110334A26900	17	6.70FZ	9352	4.4	0	EH USG0	6.60 - 6.80 BRAIDED.
33 SHEAR ZONES. MINOR INFILL							
110334A26910	18	7.28JT	28883	1.5	0	CSG1	
110334A26910	19	7.39JT	26490	1.2	0	PSG0	
110334A26910	20	7.68JT	8774	5.0	0	USG1	
110334A26910	21	8.62JT	6176	0.8	0	H PSG0	1 CM CRUSH ZONE
110334A26910	22	9.10JT	10256	3.5	0	H PSG1	DISCONTINUOUS PARALLEL JOINTS SPACED 3 CM
33							
110334A26910	23	9.30JT	10255	1.7	0	H PSG0	
110334A26910	24	9.85JT	32179	2.5	HR	PSG0	CRUSH ZONES UP TO 1 CM.
33 RIGHT LATERAL SPLAY AT W END							
110334A26910	25	9.96JT	7156	1.3	0	CSG2	
110334A26910	26	10.14JT	29887	1.6	0	CSG2	
110334A26910	27	10.85JT	29476	1.1	0	PSG0	ESTIMATED DIP
110334A26910	28	11.18JT	12078	2.9	1	PSG	
110334A26910	29	11.75JT	25589	1.0	0	CSG3	
110334A26910	30	11.90JT	7373	4.9	0	USG3	
110334A26910	31	12.10JT	10783	2.1	0	PSG3	
110334A26910	32	12.50JT	11378	7.0	0	USG0	BRAIDED
110334A26910	33	12.88JT	27785	2.0	0	USG0	
110334A26910	34	13.19JT	27390	1.1	0	CSG0	
110334A26910	35	13.30JT	34887	1.1	0	PSG2	
110334A26910	36	13.45JT	8389	1.9	0	H USG1	WIDENS TO RIGHT LATERAL SPLAY SET TO N DIP ESTIMATED
33							
110334A26910	37	13.66JT	23982	1.6	0	PSG1	
110334A26910	38	14.10JT	23875	2.3	0	CSG0	
110334A26910	39	14.64JT	8287	1.0	0	USG0	
110334A26910		15.00	90 0				E.O.L.
33							
33 PHOTO 0334 LINE B							
110334B01004	40	1.70JT	5064	2.7	0	H USG1	DIP ESTIMATED
110334B01004	41	2.60JT	4744	1.1	0	H PSG0	
110334B01004	42	3.35JT	30918	2.6	0	URG1	EXFOLIATION
110334B01004	43	5.73JT	32484	10.1	0	U G2	MOSS-COVERED. DIP EST'D.
110334B01004	44	6.40FZ	5170	9.4	0	HR USG1	1 CM FINELY CRUSHED
33 GRAINS, FAULT GOUGE							
110334B01004	45	7.80JT	10881	5.0	0	H CSG1	DIFFUSE MICROJOINTS 1 CM ZONE ESTIMATED DIP
33							
110334B01004	46	8.93JT	11088	2.2	0	H PSG1	DIFFUSE
110334B01004	47	10.43JT	188	0.7	0	PSG0	
110334B01004	48	11.32JT	7373	0.8	0	PSG3	
110334B01004	49	11.57JT	23482	2.4	0	USG	
110334B01004	50	12.00JT	31880	6.2	1	USG	

Table B1 (continued)

110334B01004	51	12.58JT	977	1.4	0	PSG2	
110334B01004	52	12.82JT	2088	1.5	0	HE USG2	
110334B01004	53	14.10FZ	5568	21.0	1	URG	FAULT PROBABLY. MOSS COV
110334B01004	54	14.55JT	4544	0.9	0	PSG0	
110334B01004	55	15.00JT	683	4.1	1	E USG	
110334B01004		15.00	90	0			E.O.L
33							
33 STOP 21 PHOTO C415 LINE A							
33							
110415A02303	1	0.01JT	7485	0.8	1	OK CSG	
110415A02303	2	0.17JT	18866	0.6	1	USG	DIFFUSE PARALLEL MICROJ
110415A02303	3	0.62JT	31362	0.9	0	USG1	
110415A02303	4	0.81JT	26083	1.3	2	PSG	
110415A02303	5	1.30JT	20975	1.0	2	PSG	
110415A02303	6	1.50VN	6449	0.9	1	Q USG	2 MM WIDE
110415A02303	7	2.14JT	1263	1.7	2	H PSG	DIFFUSE MICROJOINTS
110415A02303	8	2.32FZ	2469	2.3	2	PSG	DIFFUSE MICROJOINTS. FAU
33 FAULT ZONE 2-5 CM WIDE, YOUNGER THAN QUARTZ VEINS E.G. Q.							
110415A02303	9	2.37VN	5671	0.9	0	Q PSG1	5 MM WIDE SPLAYS AND
33 TAPERS TO S, CUT OFF BY B							
110415A02303	10	2.95JT	35377	1.6	0	PSG0	DIP ESTIMATED
110415A02303	11	2.96VN	7466	0.8	0	Q PSG0	2 MM WIDE
110415A02303	12	3.81JT	987	1.1	1	H USG	BRAIDED
110415A02303	13	3.97JT	8081	6.0	0	PSG1	PARALLEL AND BRAIDED
33 SPLAY FORM ZONE 5 CM WIDE							
110415A02303	14	4.76JT	1578	0.9	2	USG	
110415A02303	15	4.95JT	1668	0.7	0	PSG1	
110415A02303	16	5.32JT	7876	1.1	0	Q PSG1	
110415A02303	17	5.60FZ	1881	8.4	0	HE USG2	5.50 - 5.70. BRAIDED SHEAR
33 ZONES; 1 - 3 CM CRUSH ZONES							
110415A02303	18	5.97VN	8674	0.7	0	Q PSG1	2 MM WIDE
110415A02303	19	6.25JT	18481	1.0	0	PSG0	
110415A02303	20	6.29JT	25290	2.6	1	PSG	EN PASSANT AT N END
110415A02303	21	7.35JT	34064	6.3	1	CSG	DIP ESTIMATED. JOINT
33 BECOMES 2 CM CRUSHED ZONE ALONG STRIKE							
110415A02303	22	8.33JT	7580	1.7	0	PSG0	
110415A02303	23	8.70JT	7175	2.0	0	USG0	
110415A02303	24	10.32JT	1870	1.7	0	USG1	
110415A02303	25	10.41VN	6376	0.6	0	Q PSG0	2 MM WIDE
110415A02303	26	10.87JT	7466	7.0	0	SSG1	
110415A02303	27	11.77JT	6276	1.3	0	PSG1	
110415A02303	28	12.00JT	2477	1.1	1	USG	DIFFUSE BRAIDED
110415A02303		12.00	90	0			E.O.L
33							
33 STOP 21 LINE B							
110415B29504	29	0.36JT	564	1.1	0	PSG3	DIFFUSE MICROJOINTS
110415B29504	30	0.75JT	34868	0.8	0	PSG3	
110415B29504	31	0.92JT	34187	2.4	0	CSG1	
110415B29504	32	1.25JT	7066	0.7	0	Q PSG0	DIFFUSE MICROJOINTS
110415B29504	33	2.35JT	10478	0.9	0	PSG1	DIP ESTIMATED
110415B29504	34	3.05JT	5565	1.4	0	PSG0	BRAIDED DISCONTINUOUS
33 MICROJOINTS							
110415B29504	35	4.29VN	8366	0.8	0	Q PSG0	5 MM WIDE PRISMATIC
33 TERMINATED MILKY QUARTZ. RADIATING CLUSTERS AND GRANULAR AGGREGATES.							
33 EXTENSIONAL (DILATION) JOINT.							
110415B29504	36	5.64JT	6875	1.2	0	HK PSG1	
110415B29504	37	7.26JT	10233	0.8	0	CSG1	
110415B29504	38	7.88JT	24888	1.7	0	PSG2	
110415B29504		17.10.60	90	0			
110415B29504	39	11.09JT	35042	0.6	0	PSG3	DIP ESTIMATED
110415B29504	40	11.72JT	675	0.8	0	EH USG3	
110415B29504		12.00	90	0			E.O.L
33							
33 STOP 21 PHOTO 0417 LINE A							
110417A25500	1	0.18JT	8372	2.3	2	USG	
110417A25500	2	0.36JT	9380	0.5	0	PSG2	
110417A25500	3	0.53JT	7872	2.5	2	USG	
110417A25500	4	0.81JT	1368	0.7	0	H PSG2	
110417A25500	5	1.13JT	7380	3.3	2	USG	EN ECHELON RIGHT
110417A25503	6	2.43JT	2056	3.5	2	HE USG	CRUSH ZONE UP TO 2 CM
110417A25503	7	2.80JT	4762	0.9	0	CSG3	

Table B1 (continued)

110417A25503	8	3.67JT	059	0.8 0	H	PSG3	FE MATRIX CRUSH ZONE 1
33 CM, NO OFFSET SEEN							
110417A25503	9	3.70JT	20979	1.8 2		CSG	
110417A25503	10	3.90FZ	5580	5.5 2		G	3.75 - 4.05 DIP ESTIMATE
110417A25503	11	4.57JT	7565	0.7 0		PSG1	
110417A25503	12	5.25JT	8382	1.3 0		USG1	
110417A25503	13	5.32JT	1658	2.4 0	E	PSG	INFILL UP TO 1 CM WIDE
110417A25503	14	5.60JT	7583	7.5 2		PSG	
110417A25503	15	5.83JT	7381	0.9 0		PSG1	
110417A25503	16	6.06JT	7783	6.0 1		PSG	FORKS TO S
110417A25503	17	7.04JT	25975	0.7 0		PSG0	
110417A25503	18	7.48JT	1670	1.7 0		PSG0	
110417A25503	19	7.75JT	1281	3.3 0		USG0	
110417A25503	20	8.16JT	7376	6.2 2		PSG	
110417A25503	21	8.55JT	7680	1.5 0		PSG0	
110417A25503	22	8.57JT	25678	1.7 1		PSG	EN ECHELON RIGHT
110417A25503	23	8.71JT	7090	3.0 2		PSG	
110417A25503	24	9.20JT	25090	2.3 2		PSG	
110417A25503	25	9.55JT	7379	0.7 1		USG	
110417A25503	26	9.74JT	7284	1.9 1		PSG	
33		10.00					E.O.L
33							
33 PHOTO 0417 LINE B							
110417B16100	27	0.35JT	18645	0.5 0		PSG1	EN ECHELON RIGHT
110417B16100	28	0.55JT	7778	1.6 0		PSG3	
110417B16100	29	0.87JT	888	1.8 1		PSG	
110417B16100	30	2.27JT	35865	0.9 1		PSG	
110417B16100	31	2.58JT	9775	0.6 0		PSG1	
110417B16100	32	2.95JT	9447	0.9 1		PSG	
110417B16100	33	3.28JT	9038	0.7 0		PSG0	
110417B16100	34	4.98VN	061	0.8 0	Q	PSG0	UP TO 1 CM WIDE. DISCONTINUOUS
33							
110417B16100	35	5.20JT	1767	3.3 0	HE	PSG2	
110417B16100	36	5.69JT	1385	0.8 0		PSG1	
110417B16100	37	6.18JT	34356	1.3 0		PSG2	
110417B16100	38	6.70JT	1776	0.8 0		PSG1	DIP ESTIMATED
110417B16100	39	9.25JT	7788	4.4 2		USG	
110417B16100	40	9.75JT	588	0.7 1		PSG	
110417B16100		10.00	90 0				E.O.L
33							
33 STOP 44 PHOTO 1406 LINE A							
33							
111406A27800	1	0.20JT	6042	0.4 1	H	32M	
111406A27800	2	0.22JT	7185	0.1 0		00M0	
111406A27800	3	0.28JT	9289	0.4 0		00M3	SPLAY FROM 4
111406A27800	4	0.32JT	8864	1.5 1		00M	LEFT LAT. HORSETAIL AT END
111406A27800	5	0.4 JT	31654	4.0 2	E	22M	
111406A27800	6	0.41JT	25975	0.6 1		00M	T-JCT. WITH 5
111406A27800	7	0.88JT	8488	0.3 1		00M	CROSSES 5 WITH NO
33 DISPLACEMENT							
111406A27800	8	1.36JT	21778	0.6 0		00M1	
111406A27800	9	1.4 JT	10155	0.4 0		00M3	
111406A27800	10	1.4 JT	21884	0.5 0		00M0	CROSSES 9, NO
33 DISPLACEMENT							
111406A27800	11	1.44JT	21470	0.2 1	H	00M	
111406A27800	12	1.49FZ	10358	2.3 1	H	10M	SPANS 1.45 - 1.53;
33 BRAIDED JOINTS							
33 0.5 - 1.0 CM SPACING WITHIN ZONE							
111406A27800	13	1.56JT	22280	0.2 0	H	00M1	TRACE 11 AS FILM; ABUTS 12
111406A27800	14	1.58JT	21476	0.3 0	H	00M1	
111406A27800	15	1.58JT	32846	0.1 0		00M1	T-JCT. WITH 14
111406A27800	16	1.62JT	26383	0.1 0		00M1	ABUTS 17
111406A27800	17	1.64JT	11679	0.1 0		00M0	
111406A27800	18	1.68JT	21875	1.4 1		00M	DISCONTINUOUS PARALLEL
33 SHORT							
33 FRACTURES OCCUR ALONG LENGTH OF 18; 0.5 - 1.0 CM SPACING --> TRANSFERS							
111406A27800	19	2.03JT	21570	0.6 1		10M	
111406A27800	20	2.18JT	12489	1.7 0	H	10M0	TRACE H
111406A27800	21	2.23JT	11871	0.1 0		00M3	SPLAY FROM 20 INFERS LEFT LAT.
33 MOTION ON 20							
111406A27800	22	2.27JT	9575	0.5 0		00M3	SPLAY FROM 20

Table B1 (continued)

111406A27800	23	2.41JT	29771	0.3	0	00M1	ABUTS 24
111406A27800	24	2.48JT	8960	0.4	2	20M	
111406A27800	25	2.90JT	8856	1.1	1	30M	
111406A27800	26	3.03JT	20467	0.4	0	00M3	SPLAY FROM 27
111406A27800	27	3.11JT	2688	1.4	0	00M1	
111406A27800	28	3.37JT	2475	0.5	1	30M	
111406A27800	29	3.41JT	2576	0.3	0	00M3	SPLAY FROM 28
111406A27800	30	3.52JT	3653	0.1	0	00M0	
111406A27800	31	3.70JT	8741	0.6	1	10M	
111406A27800	32	3.78JT	9272	0.4	0	00M2	
111406A27800	33	3.78JT	31274	0.5	2	00M	
111406A27812	34	3.98JT	29350	0.3	0	00M0	
111406A27812	35	4.15JT	11165	0.4	1	00M	
111406A27812	36	4.23JT	8269	0.4	0	10M2	
111406A27812	37	4.26JT	11937	0.1	0	00M0	
111406A27812	38	4.32JT	29675	0.5	1	30M	
111406A27812	39	4.40F2	3381	1.2	1	10M	SPANS 4.40-4.43; CLUSTER OF 0.1 M
33 LONG DISCONTINUOUS FRACTURES							
111406A27812	40	4.47F2	28355	1.1	1	00M	SPANS 4.72-4.82; CROSSES 39 WITH
33 NO DISPLACEMENT							
111406A27812	41	4.93JT	29855	0.2	0	10M0	
111406A27812	42	5.08JT	28959	0.1	0	00M0	
111406A27812	43	5.25JT	7176	0.3	0	00M0	
111406A27812	44	5.47JT	10670	0.4	0	00M0	CROSSES 45
111406A27812	45	5.48JT	7781	0.6	0	10M0	
111406A27812	46	5.68JT	27988	0.9	0	10M0	LEFT LAT. HORSETAIL AT S. END
111406A27812	47	6.22JT	3181	0.1	0	00M0	
111406A27812	48	6.35JT	26388	0.6	0	20M0	
111406A27812	49	6.87JT	9181	6.2	1	20M	
111406A27812	50	6.89JT	9184	0.6	0	H 20M3	SPLAY FROM 49
111406A27812	51	7.00JT	8978	0.7	0	10M3	SPLAY FROM 49
111406A27812	52	7.04JT	12076	0.3	0	01M0	
111406A27812	53	7.26JT	3080	0.2	0	00M0	
111406A27812	54	7.35JT	13866	0.1	0	00M1	
111406A27812	55	7.36JT	8174	0.9	2	30M	SPANS 7.35-7.38; EN ECHELON SET
33 OF SHORT SIGMOIDAL FRACTURES INDICATE RIGHT LAT. MOTION; ENVELOPE IS MEASURED							
33 FOR ORIENTATION							
111406A27812	56	7.38JT	9585	1.1	0	00M3	SPLAY WITH 55
111406A27812	57	7.69JT	144	0.2	0	02M0	
111406A27812	58	7.87JT	8679	0.4	1	00M	JOINS 59 BY 1 CM TRANSFER ZONE
111406A27812	59	7.90JT	8681	0.8	1	00M	
111406A27812	60	7.93JT	8673	0.2	0	10M3	
111406A27800	61	8.21JT	7979	0.1	2	00M	
111406A27800	62	8.79JT	9381	0.1	0	H 00M0	TRACE H FILM
111406A27800	63	9.23F2	1079	5.0	1	30M	FAULT WITH SYNTHETIC MINOR FRAC-
33 TURES ON W. SIDE; RIGHT LAT. MOTION; SMOOTH FEATHER FRACTURE PLANE AT E. END							
111406A27800	64	9.31JT	7777	2.5	1	20M	TRANSFER ZONE WITH EN ECHELON
33 STEP TO RIGHT; MINOR HOOKED ENDS TOWARD ADJACENT FRACTURE; I.Z. 5 CM WIDE;							
33 FRACTURES PARALLEL TO 64 DOMINATE THIS END OF OUTCROP							
111406A27832	65	9.38JT	13584	0.3	0	00M1	ABUTS 64
111406A27832	66	9.68JT	5365	0.2	0	00M3	
111406A27832	67	9.72JT	8070	3.8	1	22M	
111406A27832	68	10.06JT	7472	1.3	0	30M0	CLASSIC TRANSFER ZONE TO LEFT;
33 ENVELOPE 3 CM WIDE WITH SIGMOIDAL TRANSFER MICROFRACTURES SHOWING LEFT LAT. MOTION							
111406A27832	69	10.50JT	7360	3.2	0	30M1	SEVERAL TRANSFER ZONE ENVELOPES
33 ALONG LENGTH ON LEFT SIDE OF FRACTURE, SHOWING LEFT LAT. MOTION; SAME AS 68;							
33 FEATHER FRACTURES TO E. SIDE AT S. END ALSO SHOW LEFT LAT. MOTION SENSE							
111406A27832	70	10.63JT	16986	0.2	0	10M2	
111406A27832	71	10.68JT	7480	0.2	0	02M3	SPLAY FROM 72
111406A27832	72	10.72JT	8063	1.1	0	30M2	
111406A27832	73	10.96JT	6664	1.0	0	30M2	EN ECHELON SHORT TRACE FRACTURES
33 STEPPING TO RIGHT							
111406A27832	74	11.13JT	2680	0.4	0	02M3	PART OF DOMINANT PARALLEL SET
111406A27832	75	11.18JT	2477	8.0	2	22M	FORMS OUTCROP SCARP FACE TO NW.
111406A27832	76	11.25JT	13565	0.4	0	00M1	ABUTS 75; PROBABLY PARASITIC
33 (ANTITHETIC) TO 75							
111406A27832	77	11.44JT	11651	0.3	0	00M1	
111406A27832	78	11.63JT	31090	0.4	0	00M1	
111406A27832	79	12.00JT	13070	0.5	0	10M0	
111406A27832		12.00					E.O.L. END OF LINE

Table B1 (continued)

```

33
33 LINE B STOP 44
33
111406833213 80 0.04JT 10081 0.3 0 10M2
111406833213 81 0.11JT 8690 0.2 0 00M1
111406833213 82 0.34FZ 2869 1.0 2 R 20M SPANS 0.29-0.37
111406833213 83 0.42JT 3585 0.4 0 00M3 SPLAY FROM 82
111406833213 84 0.64JT 11672 0.4 0 20M0 BRAIDED MICROJOINTS IN 1 CM ZONE
111406833213 85 0.78JT 14389 0.5 0 30M1 ABUTS 82
111406833213 86 0.95JT 9076 0.4 0 00M0 CROSSES 85 WITH NO OFFSET
111406833213 87 1.33JT 13857 0.4 0 00M0 VERY FINE FEATHER MICROJOINTS
33 ON LEFT (N.) SIDE AT W. END INDICATE LEFT LAT. STRAIN SENSE ON THIS SHEAR
33 JOINT
111406833213 88 1.45JT 35255 0.3 0 00M1 ABUTS 87
33 RELOCATED ON LINE SEPT. 11, 1987 WEATHER COLD AND WINDY, SHOWERY - THE PITS
111406833213 89 1.59JT 33890 0.2 0 00M0
111406833213 90 1.70JT 29163 0.8 0 00M1 ORIENTATION ESTIMATED
111406833213 91 1.82JT 9976 0.3 0 M 00M0 MINOR H, ORIENTATION ESTIMATED
111406833213 92 1.91JT 31270 0.9 0 10M3
111406833213 93 2.03JT 33944 1.0 1 20M BRAIDED UNDULATING SHORT JTS.
33 ALONG LENGTH
111406833213 94 2.14FZ 13571 2.7 2 20M SPANS 2.12 - 2.16 M
111406833213 95 2.24JT 35224 0.6 0 00M1
111406833213 96 2.40JT 35224 0.7 0 00M1
111406833213 97 2.52FZ 4679 1.7 0 00M0 EN ECHELON MICROJOINTS STEP TO
33 RIGHT INFERS LEFT. LAT. MOTION; 1-2 MM SPACING WITHIN 1 CM WIDE ZONE
111406833213 98 2.63JT 12379 0.1 0 00M0
111406833213 99 2.72JT 27185 0.5 0 02M1 ABUTS 97
111406833213 100 2.79JT 11574 0.5 0 02M1 ABUTS 97
111406833213 101 3.03JT 12770 0.1 0 02M2
111406833213 102 3.06JT 21059 0.1 0 00M0
111406833213 103 3.16JT 22675 0.7 0 00M3 SPLAY FROM 97
111406833213 104 3.28JT 12559 0.5 0 00M2
111406833213 105 3.37JT 3284 1.1 0 00M0 CROSSES 104, NO OFFSET
111406833213 106 3.87JT 28461 0.7 0 00M1 ABUTS 97
111406833213 107 3.97JT 12475 0.6 0 00M2
111406833213 108 4.07JT 13453 0.3 0 10M3 SPLAY FROM 106
111406833213 109 4.20JT 27988 1.6 1 10M FEATHER FRAC. 5 CM LONG ON
33 SE. SIDE INFERS RIGHT LAT. MOTION (HOOKS TO RIGHT)
111406833213 110 4.28FZ 13581 0.4 0 10M0 SPANS 4.23-4.33; BRAIDED SMOOTH
33 JTS. 1-2 CM SPACING WITHIN ZONE
111406833213 111 4.58JT 13389 0.5 1 10M
111406833213 112 4.82JT 14586 0.6 1 00M EN ECHELON; STEP TO RIGHT INFERS
33 LEFT LAT. MOTION; 2 CM SPACING WITHIN ZONE
111406833213 113 4.88JT 4562 0.2 0 EH 00M0 FEATHER FRACTURE ON E. SIDE SHOWS
33 LEFT. LAT. MOTION
111406833213 114 5.05JT 1980 0.3 0 00M0
111406833213 115 5.06JT 15188 0.5 0 00M0 CROSSES 114, NO OFFSET
111406833213 116 5.13JT 14978 0.1 0 00M0
111406833213 117 5.22JT 30532 0.5 0 20M0
111406833213 118 5.32JT 17078 0.2 0 00M0
111406833213 119 5.42JT 34390 2.1 1 20M PROBABLE CONTINUATION OF 5
111406833213 120 5.45JT 15076 0.2 0 00M3 SPLAY FROM 119
111406833213 121 5.48JT 34480 0.7 0 00M1
111406833213 122 5.51JT 14880 0.3 0 00M1
111406833225 123 5.80JT 10168 1.9 0 00M1 ABUTS 119; CONTINUATION OF 46
111406833225 124 5.86JT 11640 0.4 0 00M3 SPLAY FROM 123
111406833225 125 6.19JT 12864 0.4 0 00M0
111406833225 126 6.45JT 13069 0.6 0 00M0
111406833225 127 6.89JT 29783 0.6 0 10M0
111406833225 128 6.95FZ 33989 1.2 0 00M1 SPANS 6.89-7.00; SPACING 1.2 CM
111406833225 129 7.15JT 14879 0.6 0 00M1
111406833225 130 7.25JT 14669 0.5 0 00M0
111406833225 131 7.52JT 14571 0.4 0 00M0
111406833225 132 7.78JT 9054 0.3 0 00M0
111406833225 49 7.86
111406833225 133 8.14JT 11864 0.7 0 20M0
111406833225 134 8.20JT 10254 1.0 0 00M1
111406833225 135 8.50JT 5071 0.8 0 00M0
111406833225 136 8.80JT 30470 0.2 0 00M1
111406833241 137 8.88JT 30162 0.7 0 02M0

```



Table B1 (continued)

111406833241	138	9.00JT	27284	0.4 0	OOM1	ABUTS 139; CROSSES 137, NO OFFSET
111406833241	139	9.11JT	12080	2.2 0	02M2	
111406833241	140	9.24JT	30276	1.2 0	10M3	
111406833241	141	9.60JT	14362	0.3 0	OOM0	
111406833241	142	9.82JT	9079	0.3 0	OOM0	
111406833241	143	10.02JT	14375	0.4 0	OOM0	
111406833241	144	10.02JT	3978	1.2 1	10M	
111406833241	145	10.30JT	30266	0.4 1	10M3	
111406833241	146	10.50JT	11265	1.4 0	OOM3	
111406833241		10.50				END OF LINE
33						
33						
33						STOP 49 PHOTO 1229 LINE A
111229A27418	1	.03JT	28475	2.2 0	00G0	
111229A27418	2	.07JT	28575	0.7 0	00G0	
111229A27418	3	.17JT	33685	0.6 0	00G0	
111229A27418	4	.29JT	32685	1.3 0	10G0	
111229A27418	5	.48JT	8475	0.7 0	00G0	
111229A27418	6	.70JT	9676	4.4 1	00G	
111229A27418	7	.84FZ	06558	3.8 0	HE 20G1	SPANS .82-.86; CRUSHED ZONES UP
33						TO 1 CM; PARALLEL OVERLAPPING JOINTS CLEARLY TRUNCATED BY 8
111229A27418	8	1.13FZ	31680	6.1 0	20G0	SPANS 1.12-1.15; POSSIBLE EXTEN
33						SLOW OF 7 SHOWS 20 CM RIGHT LAT. OFFSET ALONG 8
111229A27418	9	1.62JT	33988	0.7 0	20G0	
111229A27418	10	1.95JT	32671	0.5 0	20G0	
111229A27418	11	2.37JT	10751	0.5 0	00G3	SPLAY FROM 12
111229A27418	12	2.44FZ	10067	6.0 0	32G2	SPANS 2.42-2.46; THIS IS A FAULT
33						WITH 1.- 3 CM RUSTY GRANULATED GOUGE, BRAIDED SHORT JOINTS AND PROBABLE
33						SENSE RIGHT LAT.; AT N. END, 12 IS OFFSET TO LEFT BY E.-W. FAULTS, SO CLEARLY
33						THESE N.-S. FRACTURES PREDATE THE EAST-WEST ONES.
111229A27418	13	2.60JT	35275	0.5 0	00G0	
111229A27418	14	3.60JT	8883	0.5 0	00G0	
111229A27418	15	3.78JT	29486	1.2 0	00G0	
111229A27418	16	4.44JT	30469	1.7 0	00G0	
111229A27418	17	4.64JT	8575	1.1 0	00G1	
111229A27418	18	4.77FZ	6659	7.0 2	22G	SPANS 4.73-4.80; BRAIDED PLANAR
33						JOINTS AND LENSOIDAL CRUSHED ZONES INFER SHEAR ORIGIN
111229A27418	19	4.85JT	32986	1.2 0	22G0	IN PART BRAIDED ZONE
111229A27418	20	4.95JT	6952	2.1 0	00G1	
111229A27418	21	5.10JT	34678	0.5 0	00G0	
111229A27418	22	5.52JT	12481	1.8 0	00G0	
111229A27418	23	6.26JT	8887	1.5 0	00G0	
111229A27418	24	6.54JT	27489	1.1 0	00G0	
111229A27418	25	6.93JT	8782	1.9 0	00G1	JOINS LONGER PARALLEL JOINT BY
33						UNDULATING TRANSFER ZONE FRACTURE
111229A27418	26	7.30JT	12173	0.8 0	00G0	
111229A27418	27	7.47JT	12270	0.7 0	30G1	
111229A27418	28	7.85JT	10088	2.9 0	00G1	
111229A27418	29	7.87JT	32789	0.5 1	00G	
111229A27414	30	8.02JT	9785	4.5 1	00G	ENDS AT E.-W. FRACTURE BY SCAN
33						LINE
111229A27414	31	8.32JT	10071	1.3 2	00G	
111229A27414	32	8.35JT	33683	1.8 0	32G1	
111229A27414	33	8.45JT	9190	4.8 2	00G	
111229A27414	34	8.55JT	31674	0.5 0	00G1	ABUTS 33
111229A27414	35	8.65JT	27678	1.2 0	00G0	
111229A27414	36	9.00JT	7972	2.3 0	00G1	
111229A27414	37	9.63JT	10178	3.0 0	00G0	SEVERAL PARALLEL JOINTS; IN
33						PLACES UP TO 1 CM SPACING
111229A27414	38	10.07JT	10881	1.1 0	00G1	
111229A27414	39	10.29JT	9369	2.4 0	00G2	
111229A27414	40	10.58JT	28385	14.5 1	02G	
111229A27414	41	10.71JT	26881	1.1 0	00G3	SPLAY FROM 40
111229A27414	42	11.02JT	9989	1.2 0	00G0	2 MM WIDE LENSOID CRUSHED ZONES
33						SLOW LENGTH INFERS SHEAR ORIGIN
111229A27414	43	11.40JT	8583	1.2 0	00G0	
111229A27414	44	11.52FZ	9090	3.1 1	20G	2-12 MM E.-W. FAULT; GOUGE HEALED
111229A27414	45	11.65JT	35579	0.8 0	20G0	
111229A27414	46	11.79JT	9390	12.0 1	00G	
111229A27414	47	12.07JT	9090	2.2 0	00G0	
111229A27414	48	12.27JT	28085	0.9 0	00G3	

Table B1 (continued)

111229A27414	49	12.47FZ	9669	8.0	2	ZOG	SPANS 12.42-12.55
111229A27414	50	13.80JT	17184	5.0	1	ZOG	
111229A27414	51	14.23JT	6366	0.8	0	OOG2	
111229A27414		14.5					E.O.L.
33							
33							STOP 49 LINE B
33							
111229B17300	52	0.30JT	32122	0.7	0	OOG0	
111229B17300	53	0.74JT	13876	0.8	0	OOG0	
111229B17300	54	1.74JT	20337	2.7	0	OOG0	
111229B17300	55	2.12JT	19946	2.0	0	OOG2	
111229B17300	56	2.64FZ	19562	5.0	0	ZOG3	SPANS 2.57-2.72; CURVED PLANAR
33							SMOOTH JOINTS SPACED APPROX. 2-4 CM.
111229B17300	57	3.32JT	18643	0.6	0	10G3	
111229B17300	58	3.42JT	19278	1.8	0	OOG2	
111229B17300	59	4.36JT	19450	0.7	0	OOG2	
111229B17300	60	4.60JT	8586	1.2	0	OOG0	
111229B17300	61	4.70JT	2081	0.7	0	OOG1	
111229B17311	62	5.07JT	31231	0.7	0	10G1	
111229B17311	63	5.30JT	33945	1.1	0	OOG2	
111229B17311	64	5.33JT	17950	0.6	0	OOG2	
111229B17311	65	5.85JT	33378	3.0	1	ZOG	
111229B17311	66	6.35JT	19082	1.4	0	ZOG1	
111229B17311	67	6.58JT	19540	1.3	0	OOG1	
111229B17311	68	7.17FZ	6065	4.0	1	ZOG	SPANS 7.05-7.30; BRITTLE FRACTURE
33							ZONE WITH ANGULAR CRUSHED FRAGMENTS, NO FINE GOUGE
111229B17311	69	7.57JT	32134	1.1	0	OOG2	
111229B17311	70	7.60JT	19439	1.1	0	10G2	
111229B17311	71	8.25JT	27085	1.0	0	OOG3	
111229B17311	72	8.65JT	22187	4.5	0	OOG3	
111229B17311	73	8.83JT	3582	4.5	1	ZOG	
111229B17307	74	9.50JT	20021	1.2	2	ZOG	EXFOLIATION JOINT
111229B17307	75	9.95JT	9577	5.0	0	OOG0	SIDENS TO 3 CM PARALLEL JOINT
33							ZONE ALONG LENGTH
111229B17307	76	10.36JT	17590	1.0	1	ZOG	
111229B17307	77	10.55JT	32868	1.8	1	10G	
111229B17307	78	10.71JT	16975	0.7	0	H 10G3	
111229B17307	79	10.71JT	19970	1.0	0	OOG0	
111229B17307	80	10.82JT	2988	1.3	0	10G2	DIFFUSE MICROJOINTS IN 1-2 CM
33							ZONE
111229B17307	81	11.32FZ	3166	1.1	0	OOG1	3 CM WIDE
111229B17307	82	11.49JT	19452	1.5	0	OOG1	
111229B17307	83	11.60JT	3569	0.5	0	OOG1	
111229B17307	84	11.94FZ	32758	2.1	1	ZOG	RUSTY CRUSHED ZONES 2 CM WIDE
111229B17307	85	12.61JT	17156	1.0	0	OOG1	
111229B17307	86	12.80JT	27076	0.6	0	OOG0	
111229B17307		13.70					END OF LINE
33							
33							STOP 54 PHOTO 1321 LINE A
33							
111321A32707	1	0.02JT	29786	2.4	0	OOG0	
111321A32707	2	0.08JT	16164	12.0	2	ZOG	NUMEROUS SMALL SPLAYS
33							ON N. SIDE INFER RIGHT LAT. MOTION
111321A32707	3	0.12JT	11161	0.9	0	H OOG3	
111321A32707	4	0.18JT	30764	0.2	0	10G3	
111321A32707	5	0.24JT	9570	0.3	0	H 20G3	
111321A32707	6	0.33JT	12065	2.0	0	H 10G0	
111321A32707	7	0.40JT	16879	2.0	0	ZOG2	CROSSES 6 WITH 1 CM RIGHT LAT.
33							OFFSET
111321A32707	8	0.46JT	32276	0.3	0	10G3	SPLAY FROM 7
111321A32707	9	0.63JT	32677	0.6	0	ZOG1	
111321A32707	10	0.70JT	32690	0.6	0	OOG1	
111321A32707	11	0.80JT	14882	0.1	0	OOG0	
111321A32707	12	0.87JT	18790	0.2	0	OOG0	
111321A32707	13	0.90JT	30490	0.9	0	H OOG0	FEATHER FRACS. ON N. SIDE AT W.
33							END INFER RIGHT LAT. MOTION
111321A32707	14	1.05JT	30487	1.0	0	H 20G0	
111321A32707	15	1.15JT	29786	1.3	0	ZOG0	
111321A32707	16	1.16JT	30489	1.0	0	OOG0	
111321A32707	17	1.21JT	12879	0.2	0	10G3	
111321A32707	18	1.27JT	11871	2.5	0	H 20G0	BRAIDED 20 CM JOINTS ALONG LENGTH

Table B1 (continued)

111321A32707	19	1.30JT	12078	0.7 0	10G3	
111321A32707	20	1.35JT	12078	0.8 0	10G3	
111321A32707	21	1.39JT	12078	1.4 0	10G3	
111321A32707	22	1.57JT	29170	0.9 0	00G0	
111321A32707	23	1.60JT	29665	1.1 0	00G0	EN ECHELON TO RIGHT ALONG LENGTH
111321A32707	24	1.67JT	29575	1.3 0	00G1	
111321A32707	25	1.67F2	35585	1.7 0	20G2	SPAN FROM 1.63-1.74; 2CM SPACING
33 EN ECHELON TO RIGHT						
111321A32707	26	1.85JT	16675	0.6 0	00G0	
111321A32707	27	2.07F2	28476	5.3 0	H 20G1	SPAN FROM 2.03-2.12
111321A32707	28	2.18JT	29767	0.3 0	12G3	SPLAY FROM 27
111321A32707	29	2.25JT	31481	0.6 0	H 00G2	
111321A32707	30	2.32JT	15687	0.3 0	10G1	
111321A32707	31	2.42JT	15381	0.5 0	10G3	SPLAY FROM 27
111321A32707	32	2.45JT	14085	0.8 0	00G0	
111321A32707	33	2.52JT	13985	0.3 0	00G1	
111321A32707	34	2.62F2	9890	7.0 0	22G2	SPANS 2.57-2.65; BRAIDED
33 EN ECHELON AND STEPPED SMALL FRACTURES						
111321A32707	35	2.70JT	10872	0.3 0	00G3	SPLAY FROM 34
111321A32707	36	2.89JT	29477	1.3 0	H 00G3	
111321A32707	37	2.90JT	1968	0.5 0	00G2	DIFFUSE MICROJOINTS IN 1 CM ZONE
111321A32707	38	2.98JT	1478	0.2 0	00G0	
111321A32707	39	3.10JT	30382	1.0 0	H 00G3	
111321A32707	40	3.28F2	29182	3.8 0	22G2	SPAN FROM 3.25-3.33; ZONE CONTAINS
33 BRAIDED SHORT JOINTS AND FE-RICH CRUSH ZONES 5 MM WIDE						
111321A32707	41	3.40JT	30786	1.5 0	10G3	SPLAY FROM 40
111321A32707	42	3.46JT	380	0.8 0	00G0	
111321A32707	43	3.63JT	27072	0.2 0	00G0	
111321A32707	44	3.71JT	14365	0.6 0	H 10G1	
111321A32707	45	3.77JT	14981	0.7 0	00G3	SPLAY FROM 44
111321A32707	46	3.90JT	28177	1.0 0	20G2	
111321A32707	47	4.01JT	35084	0.3 0	00G0	
111321A32707	48	4.11JT	16888	0.2 0	00G0	
111321A32707	49	4.37JT	27086	1.1 0	20G0	
111321A32707	50	4.67JT	28075	1.2 0	00G1	1 CM WIDE TRANSFER ZONES; SENSE?
111321A32707	51	4.93JT	33076	0.6 0	00G0	
111321A32707	52	4.99JT	16287	0.6 0	00G0	
111321A32707	53	5.06JT	16685	0.4 0	00G0	
111321A32707	54	5.14JT	16084	0.5 0	H 00G0	
111321A32707	55	5.28JT	11288	1.2 0	00G0	
111321A32707	56	5.39JT	33183	0.6 0	00G3	SPLAY FROM 57
111321A32707	57	5.45JT	32589	1.6 0	10G0	
111321A32707	58	5.53JT	14481	0.5 0	00G0	
111321A32707	59	5.65JT	18890	0.6 0	00G0	
111321A32707	60	5.80JT	11082	1.7 0	20G1	
111321A32707	61	5.83JT	2382	0.4 0	10G3	
111321A32707	62	5.90JT	35588	12.0 1	R 00G	DIP ESTIMATED
111321A32707	63	6.07JT	33684	0.5 0	00G3	SPLAY FROM 62
111321A32707	64	6.19JT	34580	0.8 0	00G3	SPLAY FROM 62
111321A32707	65	6.37JT	16380	0.4 0	00G0	
111321A32707	66	6.57JT	12874	1.5 0	00G1	
111321A32707	67	6.88JT	13276	0.8 0	00G0	
111321A32707	68	7.05F2	12081	0.9 2	32G	2 CM CRUSHED ZONES: COMMINUTED
33 QTZ. GRAINS IN FINE FE-FELDSPAR MATRIX						
111321A32707	69	7.15JT	13875	1.5 2	00G	
111321A32707	70	7.72JT	34986	20.0 2	02G	
111321A32707	71	7.93JT	35580	0.9 0	10G3	SPLAY FROM 70
111321A32707	72	8.29JT	13459	1.1 0	00G0	
111321A32707	73	8.51JT	12855	1.7 0	00G1	
111321A32707	74	8.75JT	31284	0.3 0	00G0	
111321A32707	75	8.88JT	18576	7.0 2	00G	
111321A32707	76	8.97JT	00090	0.6 0	30G0	
111321A32707	77	9.35JT	17782	0.8 0	30G0	
111321A32707	78	9.58JT	11462	0.8 0	20G0	
111321A32707	79	9.88JT	8061	0.7 0	20G0	
111321A32707	80	9.98JT	13164	0.2 0	00G1	
111321A32707	81	10.05JT	11745	0.7 0	00G0	
111321A32707	82	10.15JT	11148	0.6 0	10G0	
111321A32707	83	10.23JT	10265	0.9 0	10G0	LENSOIDAL CRUSHED ZONES 5 CM LONG
33 AND 1 CM WIDE; INFER THESE ARE SHEAR JOINTS						
111321A32707	84	10.37F2	11489	0.9 0	00G0	SPANS 10.34-10.39; BRAIDED JOINTS

Table B1 (continued)

33 2-5 MM SPACING						
111321A32707	85	10.48JT	11487	1.9	1	20G
111321A32707	86	10.67JT	28666	0.6	0	00G3
111321A32707	87	10.75JT	13278	3.0	0	22G0 LENSOIDAL CRUSHED ZONES AND
33 FEATHER FRACTURES INDICATE THIS IS SHEAR JOINT						
111321A32707	88	10.79JT	14382	0.3	0	10G3 SPLA FROM 87
111321A32707	89	10.87JT	10876	0.7	0	20G0
111321A32707	90	10.98JT	10850	0.4	0	20G3 LENSOIDAL CRUSHED ZONES
111321A32707	91	11.03JT	13636	3.5	0	00G0 CRUSHED ZONES 1-5 CM LONG ALONG
33 LENGTH						
111321A32707	92	11.15JT	29772	0.9	0	00G0
111321A32707	93	11.29JT	29084	0.6	0	20G0
111321A32707	94	11.38JT	10858	0.7	0	00G1
111321A32707	95	11.61JT	15254	1.8	0	00G1
111321A32707	96	11.88JT	19385	1.4	0	00G1
111321A32707	97	11.94JT	14366	1.4	0	00G3 1 MM CRUSHED ZONE INFERS SHLAR
33 JOINT						
111321A32707	98	12.12FZ	16369	2.1	0	22G3 SPAN 12.10-12.13; CRUSHED ZONE
33 1-2 CM WIDE + MANY FINE FEATHER FRACTURES ON N. SIDE INFER LEFT LAT. MOTION						
111321A32707	99	12.29JT	11446	0.4	0	12G0
111321A32707	100	12.50JT	14145	0.8	0	00G3 CRUSHED ZONES UP TO 1 CM WIDE
33		12.50				END OF LINE
33 STOP 54 LINE B						
111321B24812	101	0.04JT	28179	0.5	0	00G2
111321B24812	102	0.10FZ	30879	0.4	0	00G0 SPANS 0.08-0.11
111321B24812	103	0.10JT	9732	0.7	1	00G0 DIFFUSE MICROJOINTS IN 2 CM ZONE
111321B24812	104	0.29JT	11363	0.4	0	00G0
111321B24812	105	0.39FZ	5469	3.3	0	H 00G0 SPANS .38-.41; 1-2 MM SPACING;
33 DIP ESTIMATED						
111321B24812	106	0.49JT	5475	0.5	0	00G0
111321B24812	107	0.57JT	5466	0.4	0	00G0
111321B24812	108	0.65JT	27982	0.8	0	00G0
111321B24812	109	0.70JT	30571	0.8	0	00G3
111321B24812	110	0.95JT	10466	0.5	0	00G1
111321B24812	111	1.00JT	18571	0.5	0	20G0
111321B24812	112	1.18JT	7136			H 00G2
111321B24812	113	1.22JT	30962	0.6	0	H 00G0 1 MM CRUSHED ZONE UP TO 5 CM LONG
111321B24812	4	1.58				
111321B24812	62	1.89				
111321B24812	114	2.15JT	25761	0.5	0	00G1
111321B24812	115	2.29FZ	21580	0.6	0	20G3 4 MM RUSTY CRUSHED ZONE CLEARLY
33 OFFSETS FZ EXTENDING NE.; WITH LEFT LAT. MOTION						
111321B24812	116	2.45JT	3678	0.2	0	00G1
111321B24812	117	2.55JT	26571	0.6	0	00G1
111321B24812	118	2.60JT	25567	0.1	0	00G3 SPLAY FROM 117
111321B24812	119	2.77JT	27670	1.8	0	00G0 BRAIDED IN PLACES; FEATHER FRAC-
33 TURES AT BOTH ENDS.						
111321B24812	120	2.83JT	25478	0.4	0	00G1
111321B24812	121	3.06JT	26780	0.6	0	00G1
111321B24812	122	3.48FZ	5971	4.1	0	H 20G1 SPAN 3.47-03.49
111321B24812	123	3.83JT	23157	1.2	0	20G0
111321B24812	52	4.1				
111321B24812	55	4.15				
111321B24812	57	4.8				
111321B24812	124	4.80JT	25671	0.1	0	00G1 PARASITIC FROM 57
111321B24812	60	5.37				
111321B24812	125	5.65JT	11663	1.8	0	H 00G0 FEATHER FRACTURES ON SE. SIDE AT
33 NE. END						
111321B24812	126	5.76JT	9826	0.2	0	00G1
111321B24812	127	5.95JT	12866	0.4	0	00G3
111321B24812	128	6.22JT	11962	1.7	0	00G0
111321B24812	129	6.36JT	7085	0.1	0	00G2
111321B24812	130	6.41FZ	11985	12.0	1	20G SPANS 6.36-6.46; RUSTY CRUSHED
33 ZONES AND MICROJOINTS SPACED UP TO 1 CM						
111321B24802	131	6.83FZ	12872	1.3	0	00G1 SPANS 6.8 - 6.85; RUSTY CRUSHED
33 ZONES; 131 CLEARLY TRUNCATED BY 134						
111321B24802	132	7.20FZ	11586	2.7	0	22G3 SPANS 7.18 - 7.22
111321B24802	133	7.37JT	8568	0.6	0	00G0
111321B24802	134	7.44JT	17566	1.1	0	00G1
111321B24802	135	7.63JT	18469	0.3	0	10G3 SPLAY FROM 134
111321B24802	136	8.00JT	20483	2.2	1	20G

Table B1 (continued)

111321B24802	137	8.01JT	11339	0.5	1	H	ZOG	
111321B24802	138	8.37FZ	1475	2.1	1		ZOG	SPANS 8.27-8.47; BRAIDED RUSTY
33 CRUSH ZONES								
111321B24802	139	8.64JT	10451	0.3	1		OOG	
111321B24802	140	8.72JT	13481	0.3	0		OOG3	
111321B24802	141	8.77JT	12265	0.4	1		OOG	
111321B24802	142	9.07JT	11350	0.6	0		OOG0	
111321B24802	143	9.43JT	10880	0.8	0		OOG1	
111321B24802	144	9.67JT	10864	1.3	1		OOG	
111321B24802	145	9.92FZ	10039	1.5	1		OOG	SPANS 9.9-9.95; 2 CM RUSTY CRUSHED
33 ZONES								
111321B24802	146	10.17JT	24081	0.1	0		OOG0	
111321B24802	147	10.18JT	12164	0.5	0		OOG0	
111321B24802	148	10.46FZ	11760	2.1	1		OOG	SPANS 10.43-10.5
111321B24802	149	10.47JT	22855	0.6	0		12G2	
111321B24802	150	10.82JT	13381	0.8	0		OOG0	
111321B24802	151	11.00JT	25582	0.4	0		OOG1	
111321B24802	152	11.02JT	12075	1.5	0		OOG0	
111321B24802	153	11.11JT	880	0.5	0		OOG1	
111321B24802	154	11.25JT	10360	1.5	0	H	OOG0	
111321B24802	155	11.30JT	10360	1.0	0		OOG3	
111321B24802	156	11.42JT	10776	0.3	0		OOG0	
111321B24802	157	11.48JT	10459	1.0	0		OOG0	
111321B24802	158	11.53JT	10459	1.7	0		OOG0	
111321B24802	159	11.60JT	11166	0.4	0		OOG3	
111321B24802	160	11.63JT	10065	0.7	0		OOG0	
111321B24802	161	11.81JT	11059	0.8	0		OOG0	
111321B24802	162	12.07JT	15252	1.3	0		ZOG0	
111321B24802	163	12.20JT	7588	1.0	0		OOG0	
111321B24802		12.50						END OF LINE
33								
33 STOP 81 PHOTO 0324 LINE A								
33								
110324A10000	1	0.35JT	7974	5.1	0		USG0	
110324A10000	2	0.52JT	9280	0.9	0		PSG1	
110324A10000	3	0.60JT	20290	1.9	0		CSG2	
110324A10000	4	1.34JT	9484	1.2	0	HR	PSG2	CRUSH ZONE UP TO 1 CM
110324A10000	5	1.66JT	11082	6.4	1		USG	
110324A10000	6	1.97JT	10090	0.8	0		USG0	
110324A10000	7	2.22JT	7563	4.1	0		USG2	
110324A10000	8	2.45JT	9874	1.4	0		USG2	
110324A10000	9	2.98JT	7678	4.2	0		PSG1	PARALLEL DISCONT. JOINTS
110324A10000	10	3.20JT	7871	2.3	0		PSG3	
110324A10000	11	3.30JT	11870	1.3	0		PSG0	LEFT LAT. SPLAYS @S END
110324A10000	12	3.50JT	7077	2.6	0	H	PSG2	
110324A10000	13	3.95JT	6866	2.9	0		USG2	EN PASSANT AT SCAN LINE
110324A10000	14	5.67JT	29786	2.1	0		PSG2	
110324A10000	15	5.98JT	11471	4.5	0		PSG2	
110324A10000	16	6.45JT	13864	1.8	0		PSG1	
110324A10000	17	7.19JT	8069	1.6	0	HR	PSG2	CRUSH ZONE UP TO 1 CM
110324A10000	18	7.50JT	10934	2.5	0		USG1	SEVERAL SHORT JOINTS
110324A10000	19	7.99CN	8565	2.4	0		CSA1	JOINT AT CONTACT
110324A10000	20	8.13JT	9467	2.0	0		CSA2	
110324A10000	21	8.45JT	9978	2.6	0		USA1	
110324A10000	22	8.80JT	24285	0.9	0		PSG2	
110324A10000	23	9.27JT	10945	3.3	0		CSG2	
110324A10000	24	9.55JT	6773	2.0	0		PSG0	
110324A10000	25	9.70JT	33516	1.1	0		PSG2	
110324A10000		10.00	90	0				E.O.L
33								
33 STOP 81 LINE B								
110324B01907	26	0.45JT	3568	1.2	0		PSG2	
110324B01907	27	0.90JT	14583	2.2	1		CSG	
110324B01907	28	1.45JT	7582	0.8	0		CSG1	
110324B01907	29	1.85JT	6757	1.5	0		PSG1	
110324B01907	30	2.83JT	685	6.8	0		PSG1	
110324B01907	31	2.85JT	8474	5.4	0		USG2	
110324B01907	32	3.40JT	13049	3.9	0		CSG1	
110324B01907	33	3.75JT	11958	6.0	0		PSG3	
110324B01907	34	4.29JT	075	9.0	0		PSG2	
110324B01907	35	4.86JT	1779	1.9	0		PSG1	

Table B1 (continued)

110324801907	36	5.21JT	1385	3.0 0	CSG2	
110324801907	37	6.90JT	10771	6.0 0	USG1	
110324801907	38	7.10JT	19484	13.4 0	q PSG2	5 MM WIDE. SPLITS TO
33						FRACTURE ZONE 30CM WIDE
33						AT E END.
110324801907	39	7.65JT	1388	4.0 0	PSG0	
110324801907	40	8.99JT	1973	1.6 0	PSG3	
110324801907	41	9.17JT	19985	1.5 0	PSG3	
110324801907	42	9.40JT	3879	8.0 0	USG2	
110324801907	43	9.74JT	2181	0.8 0	PSG0	
110324801907	44	9.76JT	27072	1.2 0	USG1	
110324801907	45	9.95JT	2486	2.9 0	PSG0	
110324801907		10.00	90 0			E.O.L
33						
33						END OF SCANLINE FRACTURE DATA FOR THE SEAL COVE RIVER VALLEY

## APPENDIX C

### Core Logging in the Seal Cove River Valley: Procedures and Results

#### 1. Introduction

Core was logged for all boreholes in the study area, focusing on measurement of fracture characteristics. Graphical fracture logs for boreholes M1, M2, M3, H2 and H4 were compiled and are presented here. Borehole H3 was unintentionally drilled within a fault zone, producing mainly fragmental fault breccia (with abundant calcite, hematite and chlorite fracture coatings) and clay-rich fault gouge. Due to poor core recovery and lack of good depth control on intact core sections, it was not possible to compile a detailed fracture log for borehole H3.

Impression packing was conducted in boreholes H2 and H4 in order to reorient fractures in those cores to in situ orientations. Impression packing methods used here follow the approach of Barr and Hocking (1967). Impression packing procedures and detailed core logs including reoriented fracture orientations for boreholes H2 and H4 are also presented below.

#### 2. Procedures

##### Core logging

The following characteristics were recorded during borehole fracture

logging:

**Borehole information** - name, location, orientation of borehole

**Rock type** - G = granite or quartz monzonite, M = microgranite, B = gabbro, granodiorite or diabase, O = other; dike lithologies: P = pegmatite, A = aplite, F = felsite

**Depth to fracture** - distance to center of fracture along length of hole below top of casing

**Fracture number** - unique sequential identification number for each fracture

**Fracture type** - natural joint (JT), fracture zone (FZ), vein (VN) or contact (CN) or induced by drilling (fresh helical break or ground core perpendicular to core axis)

**Fracture surface roughness** - 0 = smooth, 1 = slickensided, 2 = rough; (on scale of mm to cm; analogous to small size roughness in scanline data)

**Mineral fracture coatings** - (same abbreviations as for scanline data) Q = quartz, C = calcite, K = chlorite, E = epidote, H = iron oxide or hydroxide minerals, U = uncertain; minerals recorded in order of abundance

**Fracture orientation** - the acute angle between a fracture plane and the core axis (alpha angle) and the angle, measured clockwise looking down-hole, between a line corresponding with the underside of the inclined borehole (hole reference line) and the tip of a fracture ellipse (beta angle). The hole reference line is further described below and is used with the alpha and beta angles to reorient fractures.

**Comment** - any other pertinent information, e.g. fracture age relationships, unusual rock fabric or mineralogy, etc.

The core was examined in the original core boxes and all records entered on coding forms for easy encoding into computer data files. Alpha angles were measured with a contact goniometer and beta angles measured with graduated plastic sleeves which match the diameter of the core, as described by Goodman (1976) and Gale (1981).



### Impression packing and fracture reorientation

Fractures in core from boreholes H2 and H4 were reoriented using the following steps:

- 1) Core was reconstructed as much as possible within core boxes and depths noted for zones where reconstruction was not possible (due to core being ground during drilling, missing or brecciated).
- 2) Impression packing intervals were selected (14 in borehole H2, 18 in borehole H4) to bridge these zones and include adjacent fractures in reconstructed zones.
- 3) Impression packing was carried out (as described below), providing impressions of fractures intersecting the borehole walls, the location of the actual underside of the borehole (hole reference line) in relation to the impressions, and the actual orientation of the borehole.
- 4) Fracture impressions were matched with corresponding reconstructed fractures and the hole reference line transferred from impression tracings onto the reconstructed core sections. Beta angles for fractures to be reoriented were measured with respect to the hole reference line.
- 5) Finally, the in situ orientation of core fractures was calculated using alpha and beta angles (described above) and the known orientation of the inclined borehole, following recalculation methods described by Gale (1981).

Figure C1 shows the geometric relationships between components of the impression packer apparatus used in this study. The three major components (Figure C1a) were, from top to bottom, an indenter apparatus for determining the hole reference line and relating this line to the impression sleeves, the impression sleeves for taking fracture impressions, and a borehole compass for recording the actual trend and plunge of the borehole at each impression interval. The indenter device consisted of a pneumatically-driven steel ram (not shown in Figure C1a)

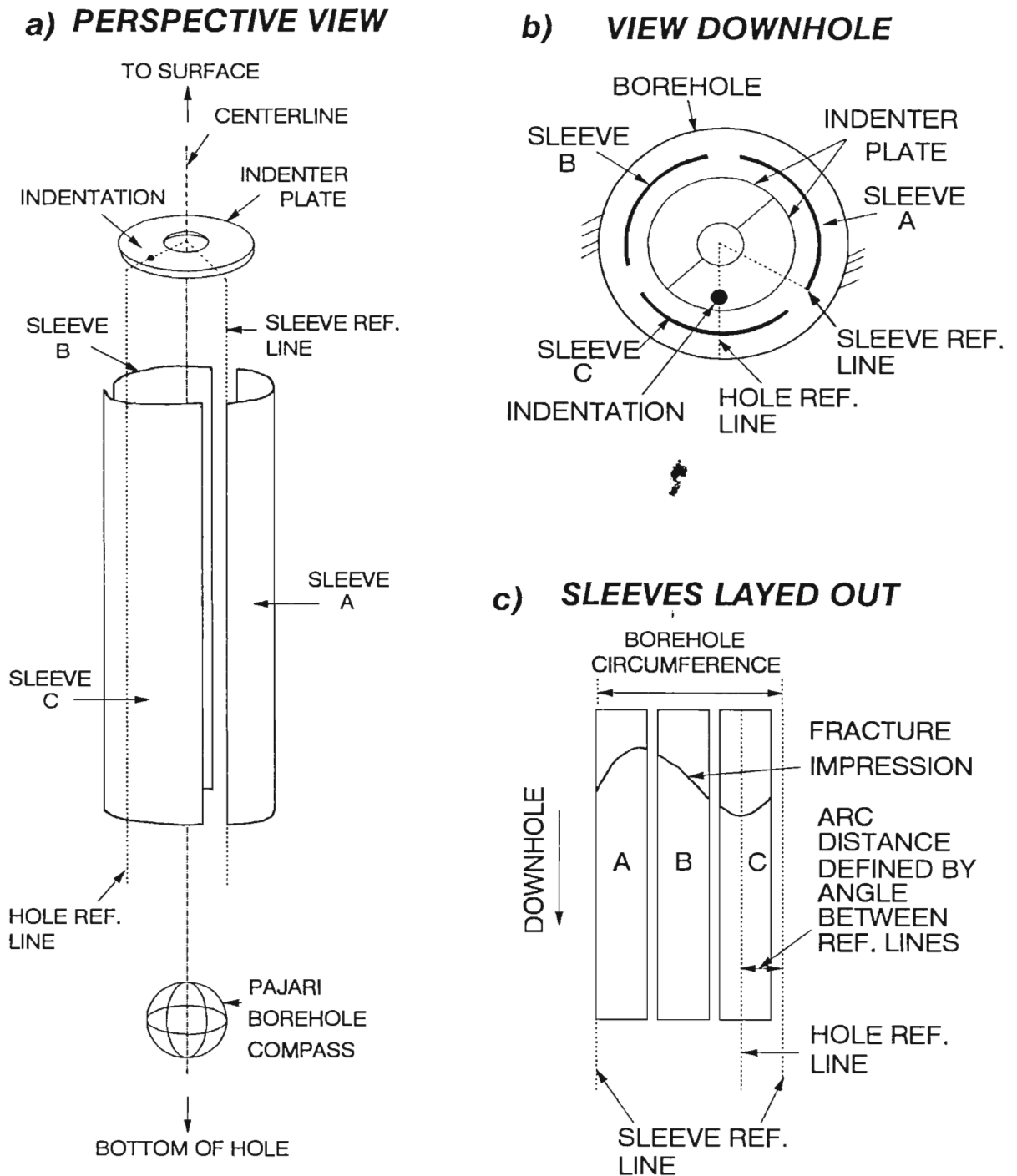


Figure C1 - Schematic diagram showing the geometric relationships between components of the impression packer used in this study. Packer, pipe mandrel mounting string, indenter hardware and related hardware are omitted for clarity.

which pressed a free-rolling ball bearing into an aluminum indenter plate (shown in Figures C1a and C1b), marking the underside of the inclined borehole. This mark defined the position of the hole reference line, which was transferred to a tracing of the fracture impressions (Figure C1c) and ultimately to the reconstructed core sections. A set screw mark on the edge of the indenter plate (Figure C1a) allowed alignment of the plate (hence the hole reference line) with the impression sleeves, via the sleeve reference line.

Three impression sleeves were mounted radially about a 1.4 m long pneumatic packer (not shown). The sleeves consisted of 1.4 m long strips of uncured rubber (1.6 mm thick) glued with contact cement to curved steel strips (Venetian window blind material) 0.05 m wide and 1.5 m long, with the strips held in place by screws into collars mounted on the mandrel pipe above and below the packer (not shown). When the packer was inflated, the sleeves were equally spaced around the circumference of the borehole.

A Pajari<sup>®</sup> timed locking borehole compass was mounted at the bottom of the impression packer string. To maintain a manageable packer string length, a single 1.52 m (5 foot) aluminum drill rod was used as a non-magnetic buffer above the compass (instead of three 5-foot rods as recommended by the manufacturer). Laboratory tests showed that this configuration still produced accurate orientations.

In the field, the impression string was lowered to the desired depth and the packer inflated (to 2.48-3.31 MPa, 360-480 psi) for 15-30 minutes. The borehole compass was preset to lock during impression time, and the indenter was activated with a high-pressure nitrogen pulse after the compass locked. On retrieval,

impression sleeves were removed and laid out to correspond with the circumference of the borehole and tracings made on drafting film (Figure C1c). Reference line information and borehole orientations were also recorded for use in fracture orientation calculation, as described above.

### 3. Results

Figures C2 - C6 are fracture logs for boreholes M1, M2, M3, H2 and H4, respectively. Symbols and terms pertaining to these logs are given below.

Key to fracture core logs:

Fracture inclination to core axis

———— 0-45 degrees  
 ----- 46-90 degrees

Fracture characteristics

c: crushed zone (brittle fragments, little coating)  
 h: healed autobrecciation zone  
 ~: shear zone (ductile strain, mylonitization)  
 #: slickensides on fault plane or in fault zone  
 =: fracture zone with coated surfaces  
 ? or r: missing core or overcored rubble, respectively  
 solid dot: induced fracture

Fracture infilling material

K - Chlorite	C - Calcite	I - Clay	E - Epidote
H - iron oxide or hydroxide minerals	Q - Quartz, silica minerals		
S - Sericite	M - MnO <sub>2</sub> minerals (dendrites)		

Table C1 and C2 present reoriented fracture orientations and other fracture information for core from boreholes H2 and H4, respectively. As with the scanline fracture data (Appendix B), these data were coded for manipulation by computer. The FORTRAN format for the core fracture information is as follows.

**Format for Tables C1 and C2:**

<u>Variable</u>	<u>Column</u>	<u>Format</u>
Line flag (11 = data line, 33 = comment line)	1-2	I2
Depth to fracture along hole	3-8	F6.2
Rock type	10	A1
Fracture characteristic flags (1 = yes)		
Natural fracture	12	I1
Induced fracture	13	I1
Open fracture	14	I1
Closed (sealed) fracture	15	I1
Planar surface	16	I1
Curved surface	17	I1
Irregular surface	19	I1
Roughness (scale 1-5)	20	I1
Mineral infilling	23-25	3A1
Infilling thickness (mm)	29-32 (H2) 33-36 (H4)	F4.1
Infilling colour (H4 only)	27-32	3A2
Fracture inclination (dip angle if reoriented, alpha angle if not reoriented)	40-41	I2
Fracture dip direction (999 if not reoriented)	43-45	I3
Comment	46-80	17A2

It should be noted that fractures along certain sections of each borehole could not be reoriented due to impression apparatus configuration (preventing impressions at the very top and bottom of each hole), inconclusive impressions, occurrence of rubbly or brecciated zones, or problems related to drilling or core recovery. Zones which could not be reoriented in boreholes H2 and H4 are listed below (in meters of borehole length):

Borehole H2: 0-2.52, 8.08-8.22, 14.63-23.90, 38.57-39.73, 46.04-48.15, 55.75-78.06.

Borehole H4: 0-4.07, 6.81-8.02, 22.22-22.52, 37.96-38.56, 39.84-40.02, 42.24-42.74, 51.66-52.30.

The proportion of successfully reoriented core was 52% for borehole H2 and 88% for borehole H4.

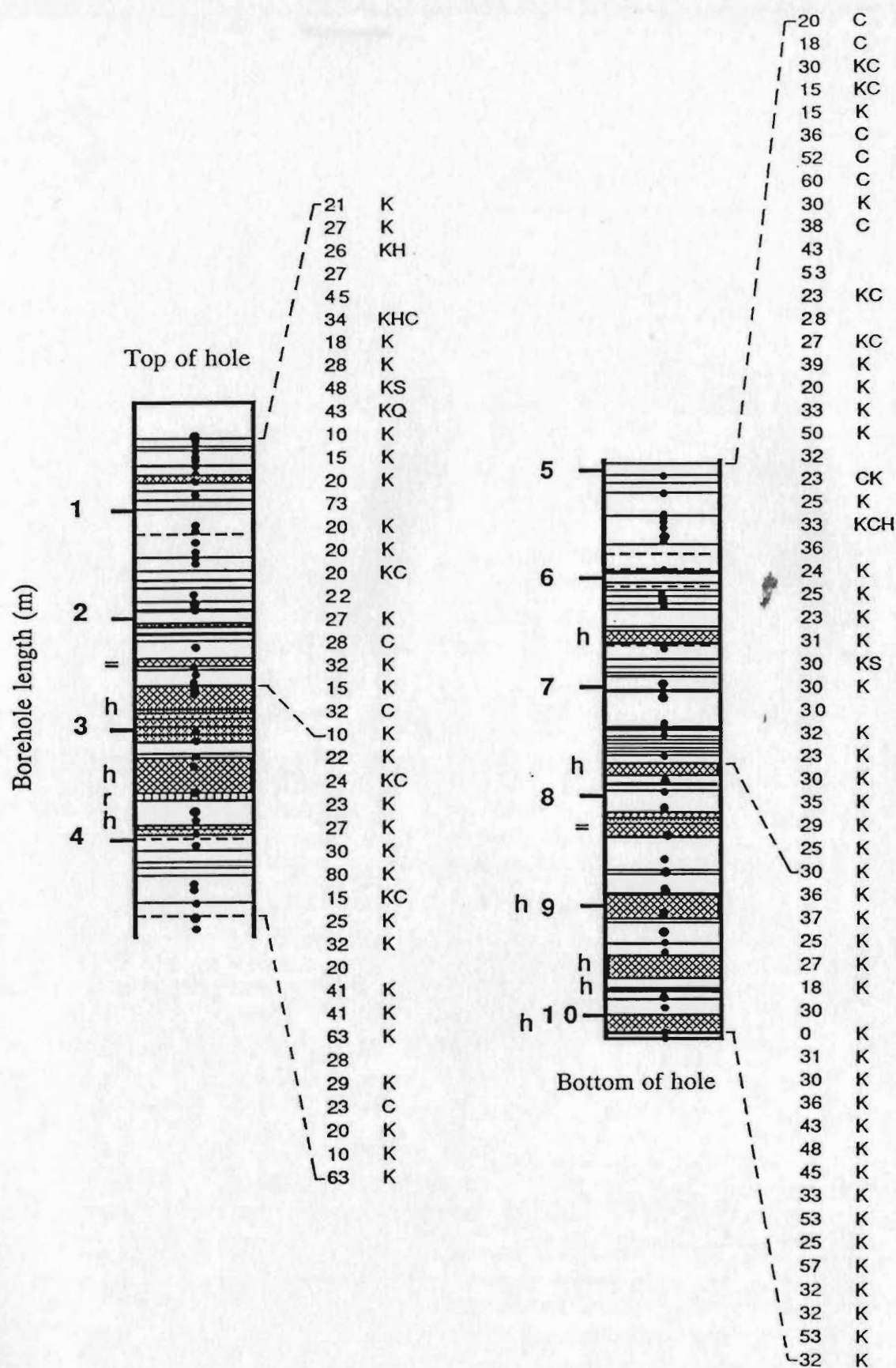


Figure C2 - Fracture core log for borehole M1

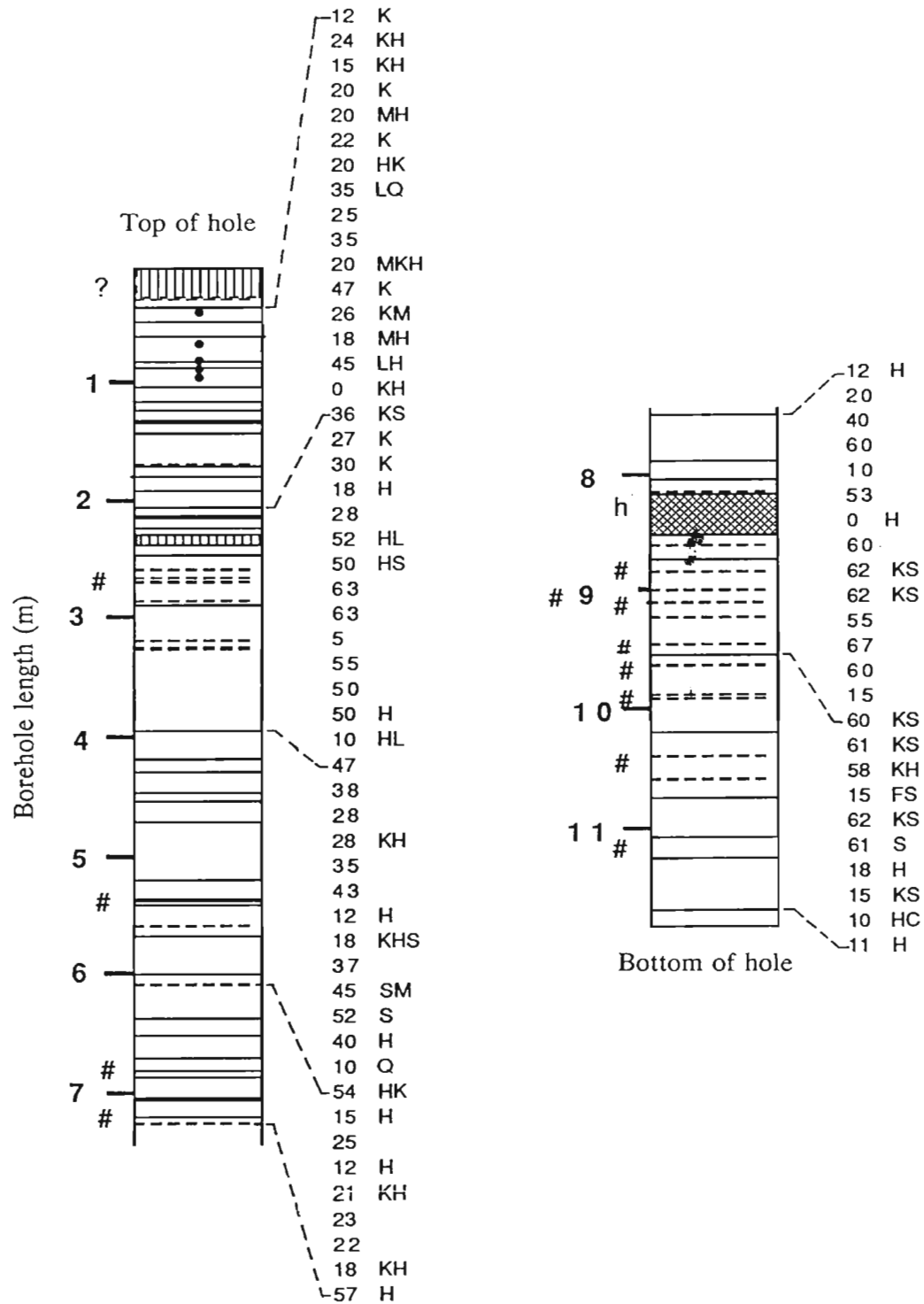


Figure C3 - Fracture core log for borehole M2

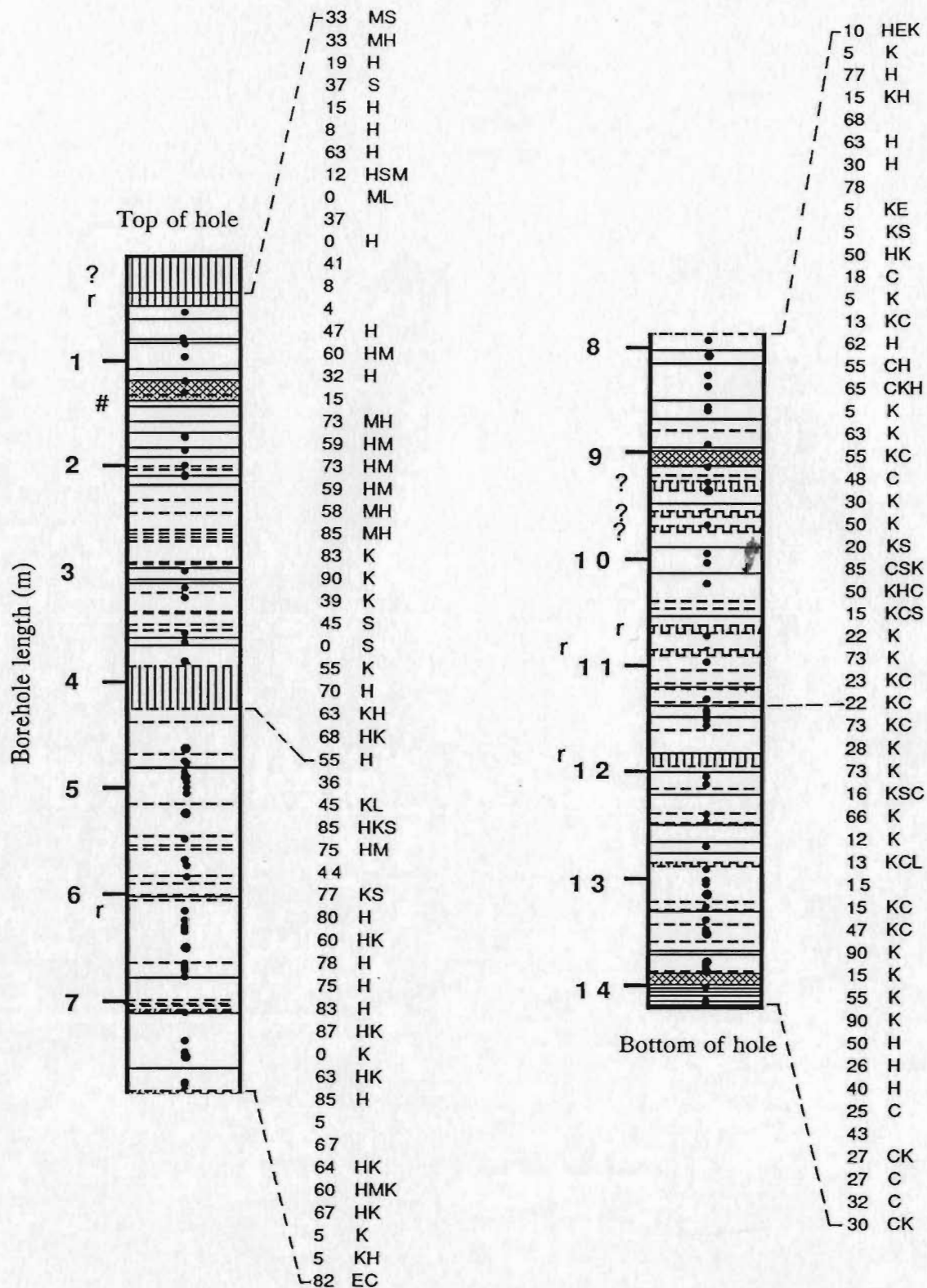


Figure C4 - Fracture core log for borehole M3



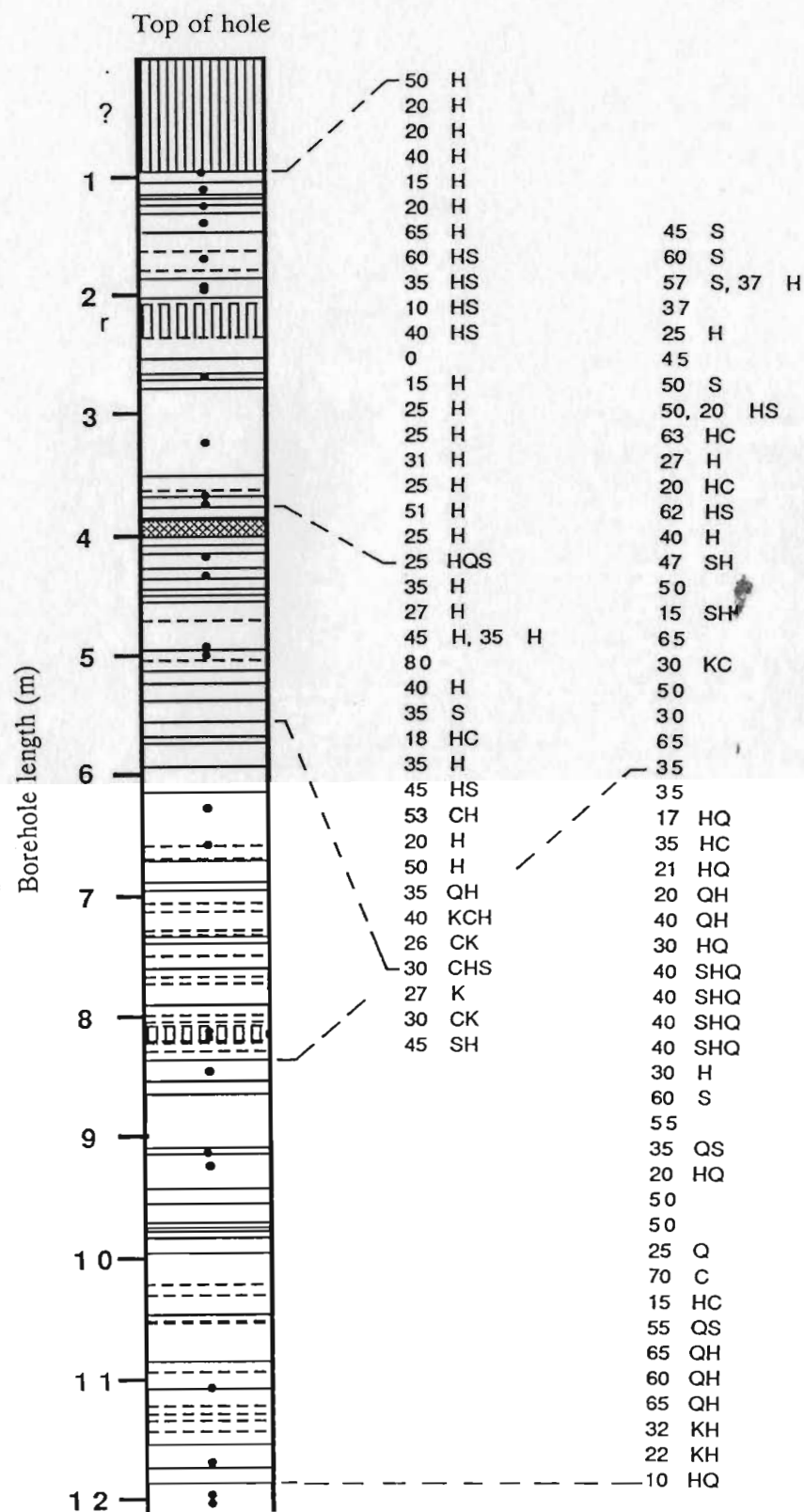


Figure C5 - Fracture core log for borehole H2

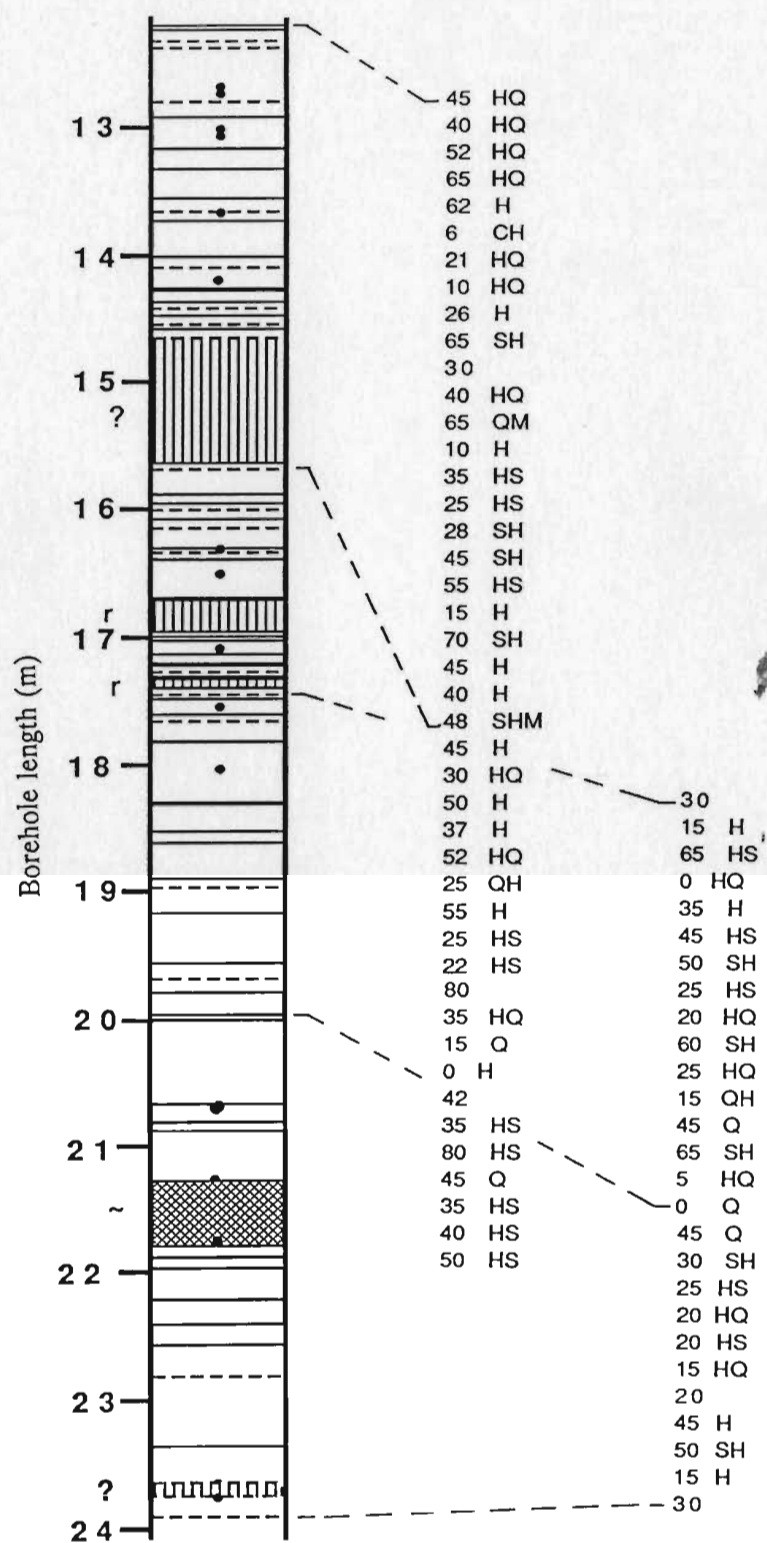


Figure C5 (continued)

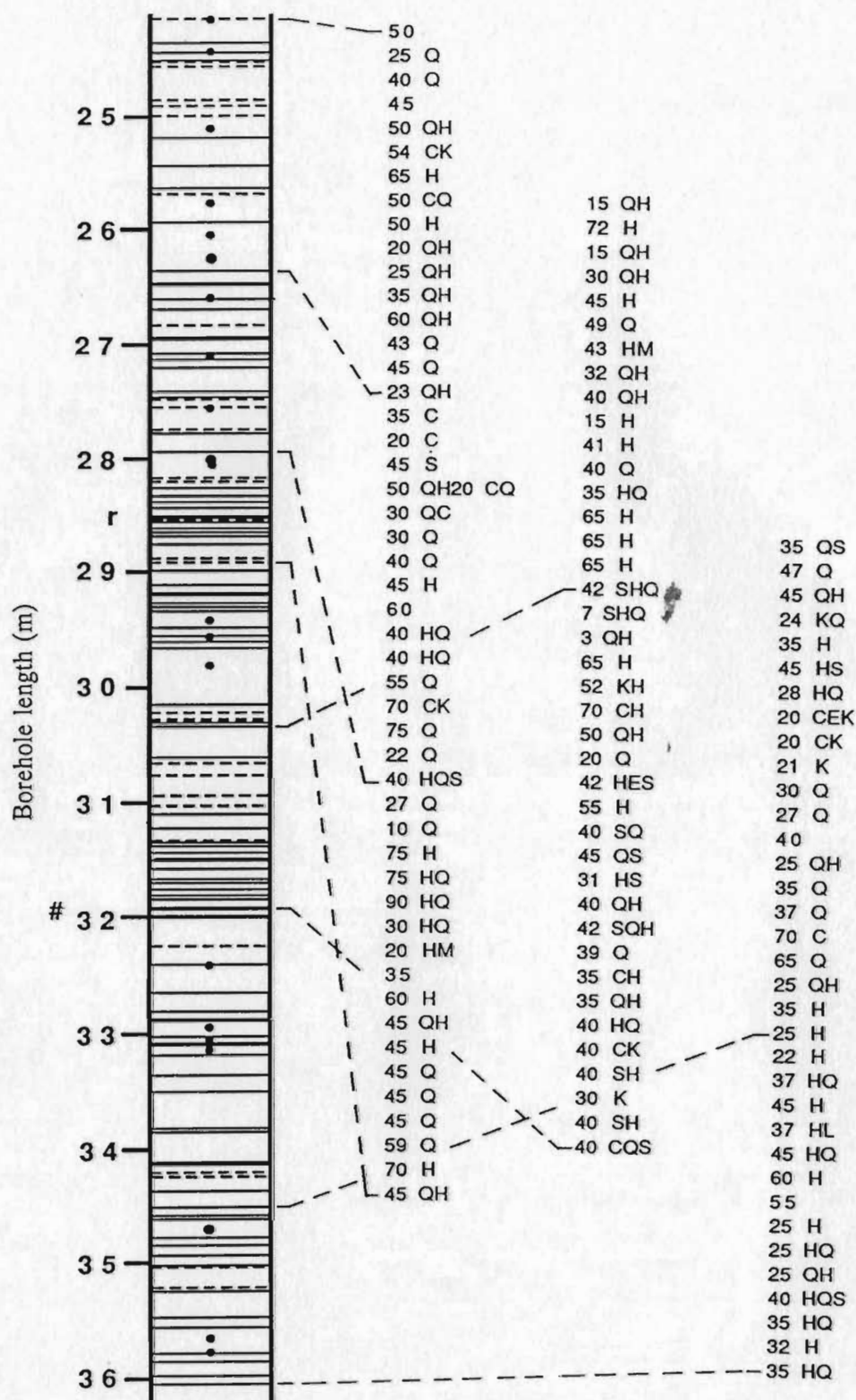
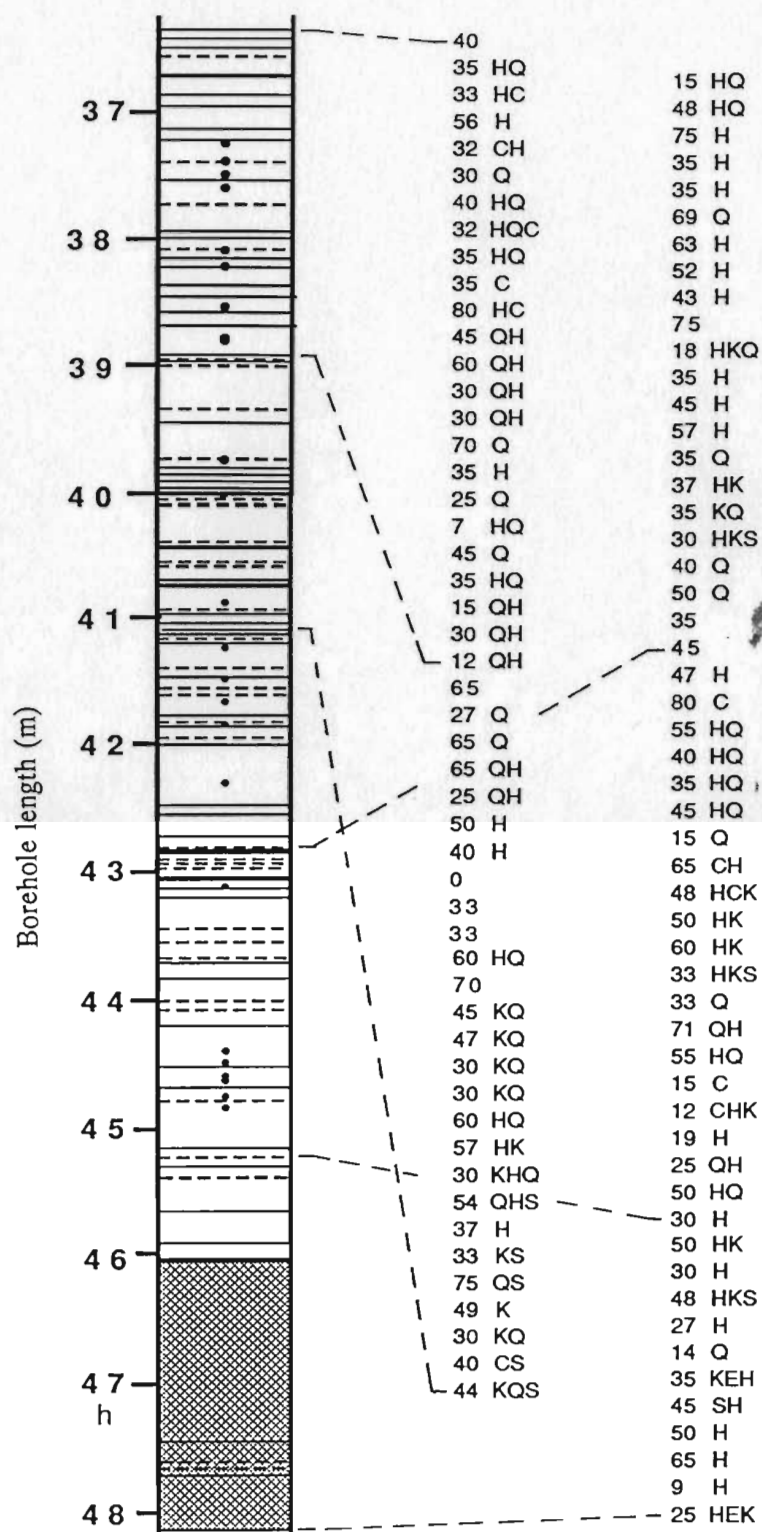


Figure C5 (continued)



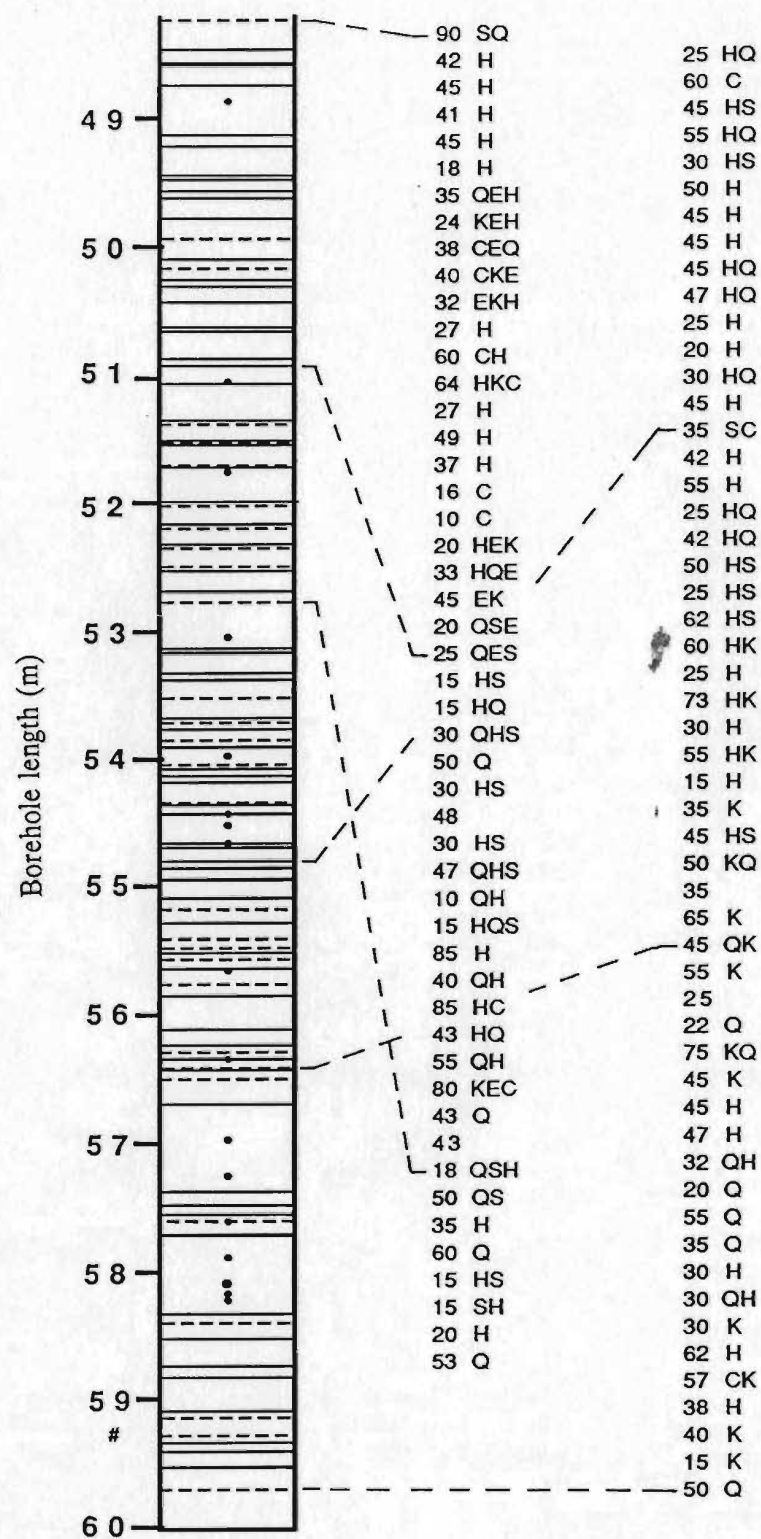


Figure C5 (continued)

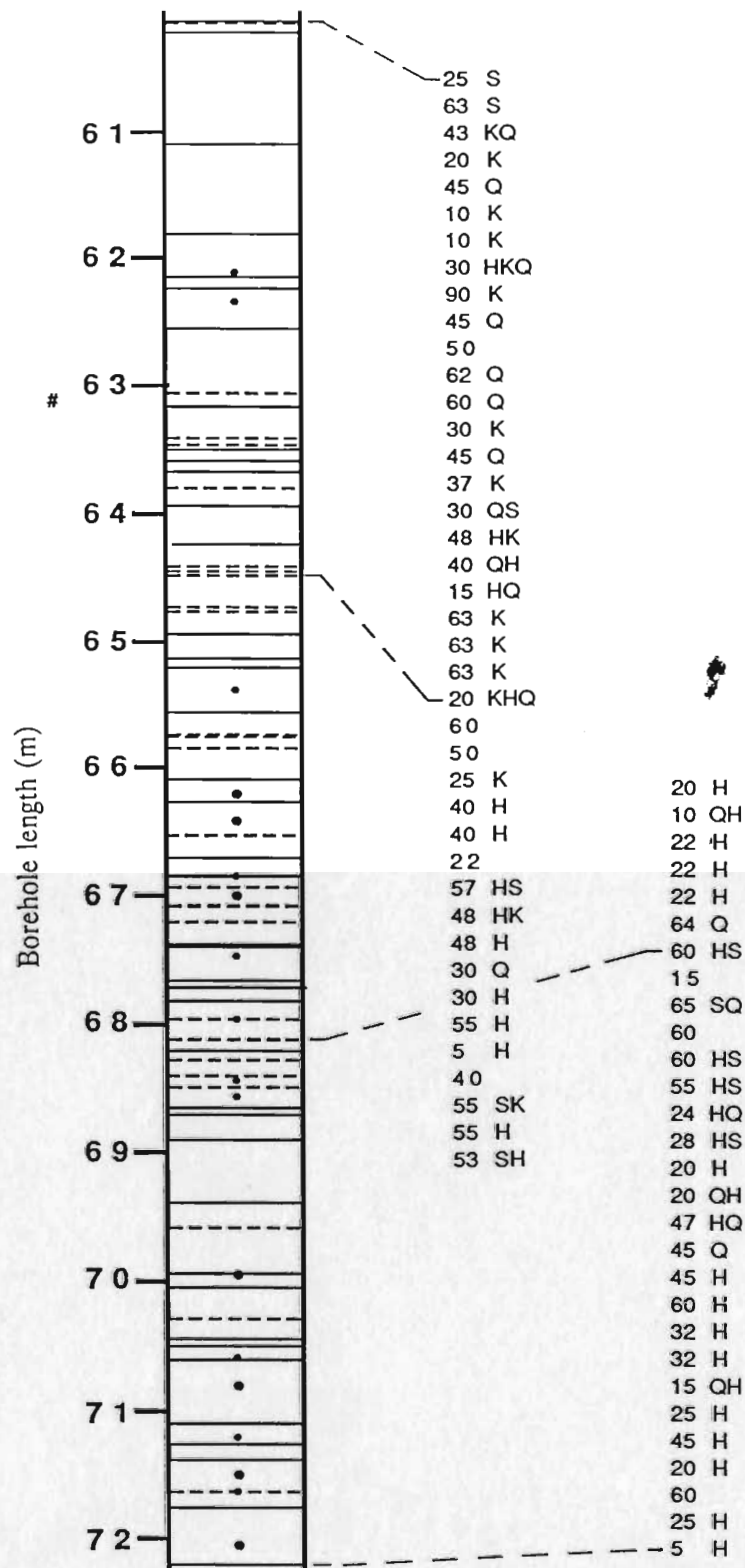


Figure C5 (continued)

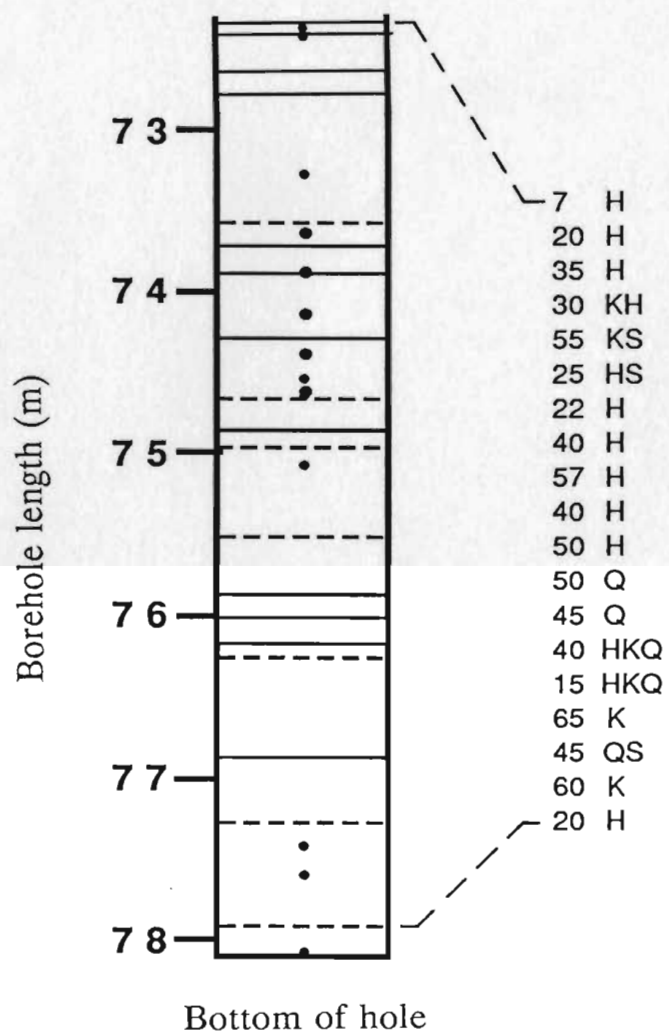


Figure C5 (continued)



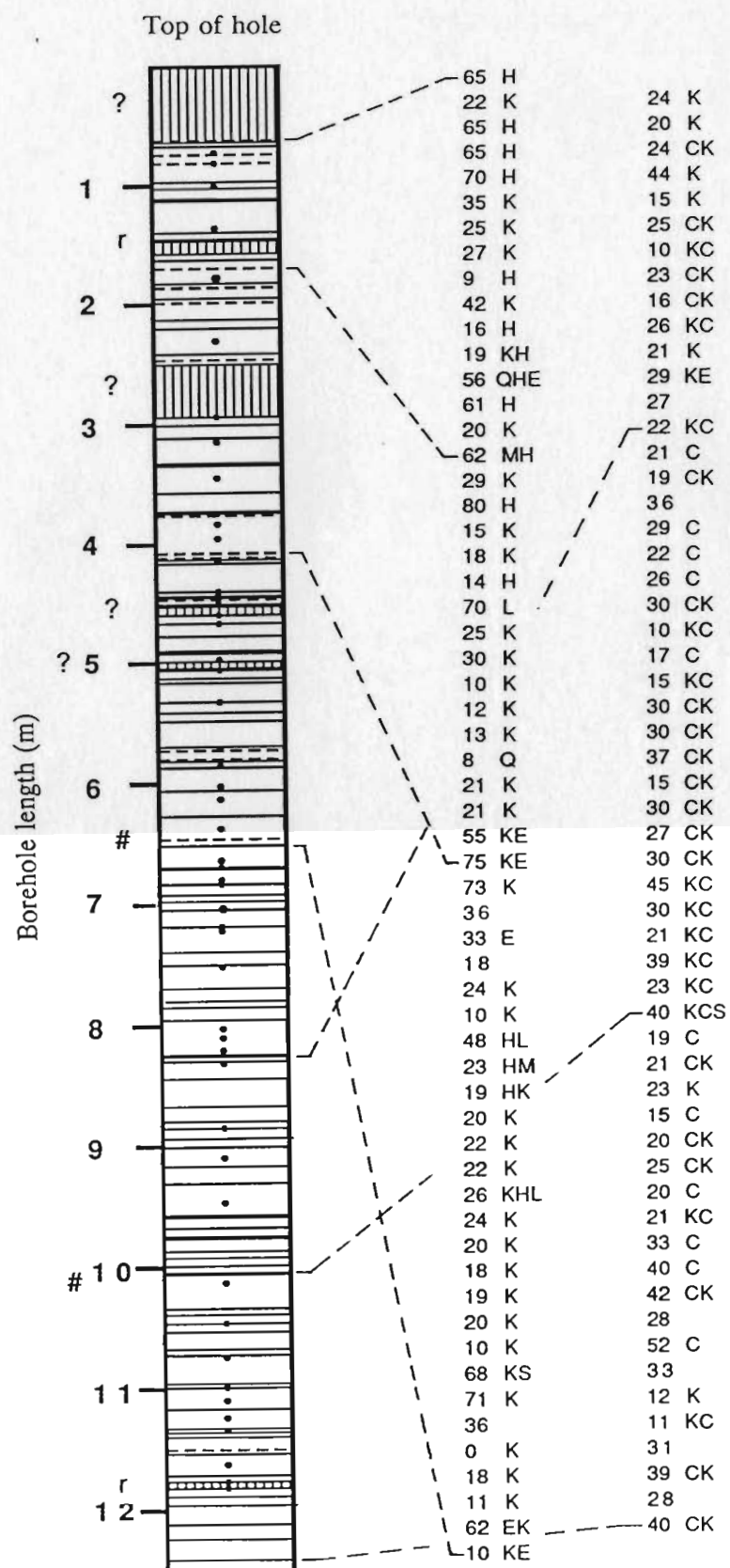


Figure C6 - Fracture core log for borehole H4



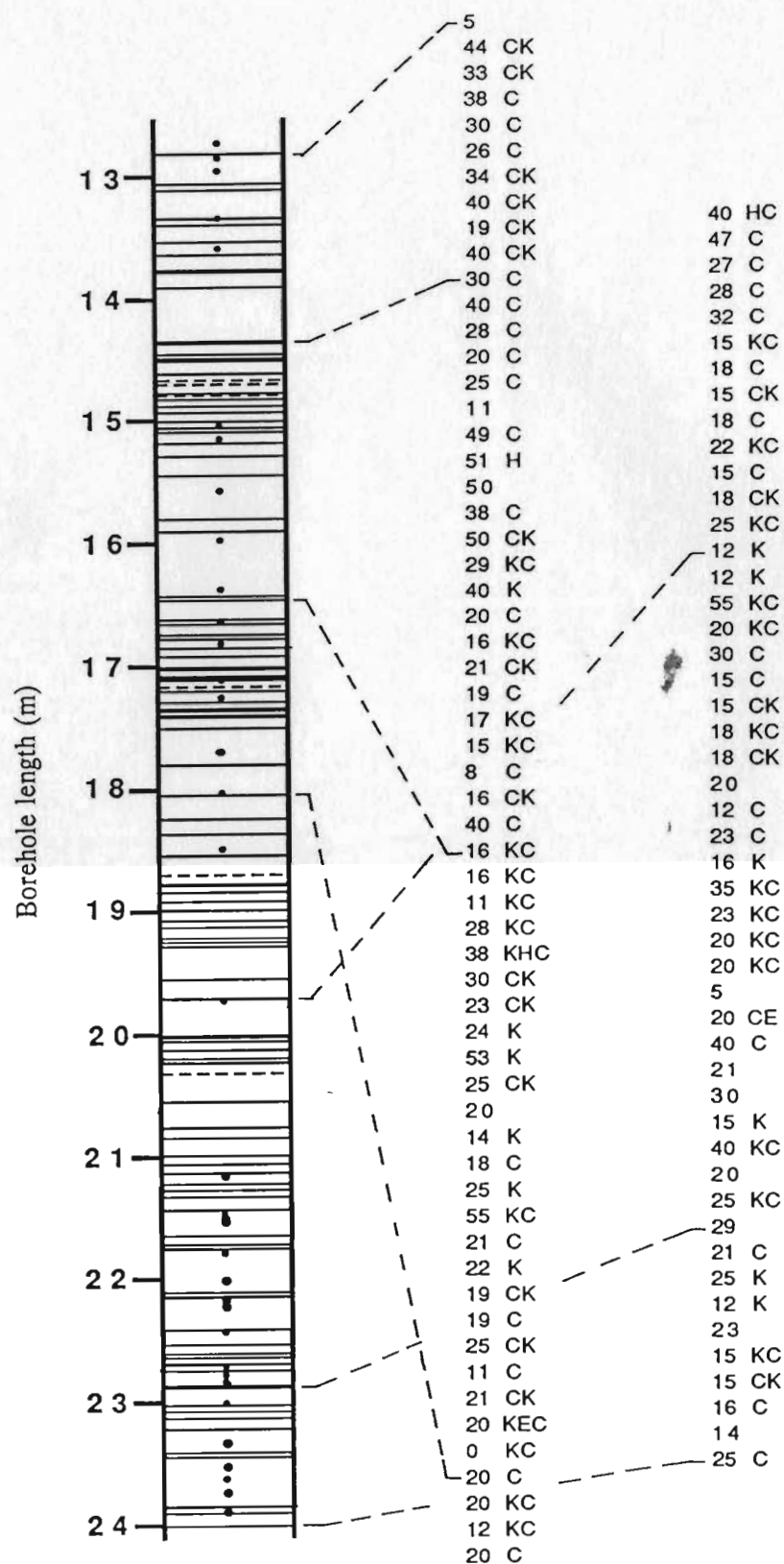


Figure C6 (continued)

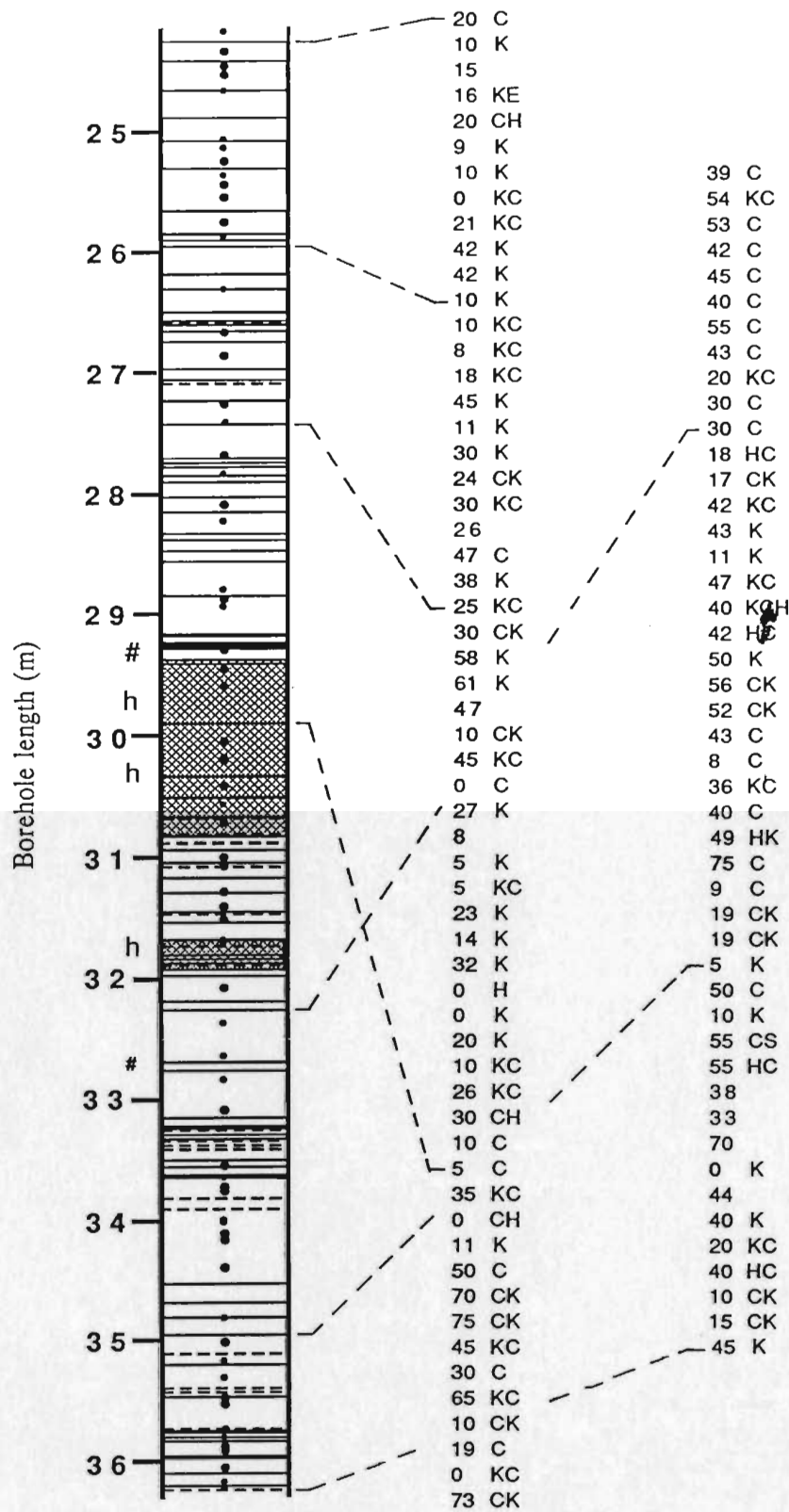


Figure C6 (continued)

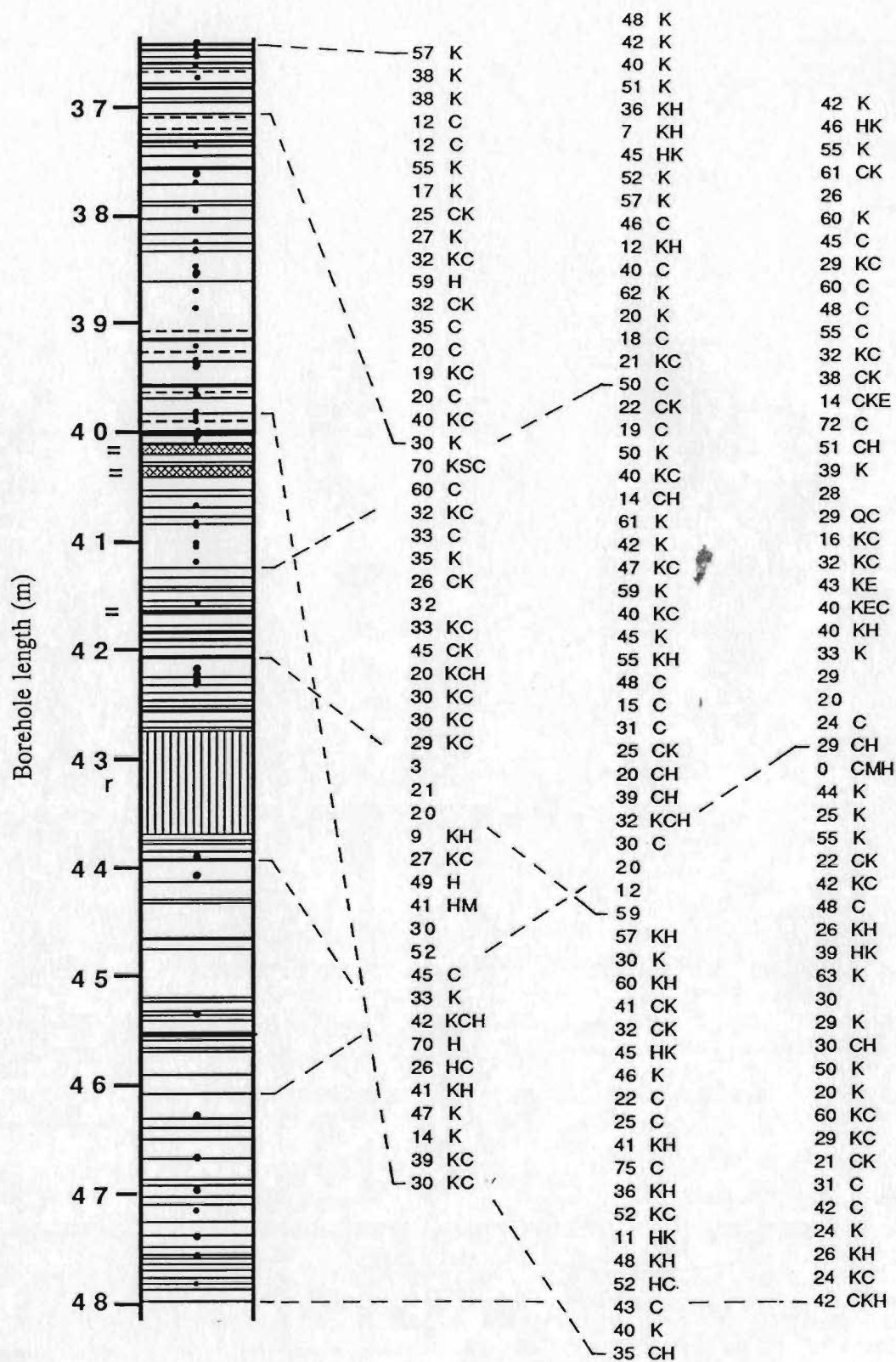


Figure C6 (continued)

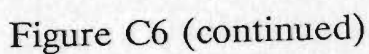


Figure C6 (continued)

Table C1 - Fracture data for borehole H2 in the Seal Cove River valley

```

33      H2CORE.DAT - ORIENTED FRACTURE DATA FOR BOREHOLE H2
33      IN THE SEAL COVE RIVER VALLEY
33      IMPRESSION PACKER ZONES LABELLED AS "IP #" (e.g. IP5)
33      FORMAT FOR FRACTURE DATA DESCRIBED IN TEXT
33
11      .95 G 1 1 14S H 50 999
11      .95 G 1
11      1.04 G 1 1 1 H 20 999
11      1.10 G 1
11      1.14 G 1 11 H 4 20 999
11      1.17 G 1 1 15 HS .1 0 999
11      1.23 G 1 GC
11      1.23 G 1 11 H 1 40 999
11      1.31 G 1 11 H 1 15 999
11      1.39 G 1
11      1.46 G 1 1 15 H 1 20 999
11      1.62 G 1 11 H 1 65 999
11      1.69 G 1
11      1.77 G 1 1 1 2 HS .1 60 999
11      1.80 G 1 1 13 0 999
11      1.84 G 1 1 1 5 HS 35 999
11      1.86 G 1 1 1 4 HS 10 999
11      1.90 G 1 GC
11      1.95 G 1
11      1.95 G 1
11      2.01 G 1 1 1 4 HS 1 40 999
11      2.06 G 1 1 1 4 0 999
33
33      2.06 - 2.35 BLOCKY RUBBLE AND GC AT EOR
11      2.52 G 1 1 13 H 1 85 89
11      2.65 G 1 1 13 H 1 55 233
11      2.67 G 1
11      2.70 G 1 11 4 H .5 43 215
11      2.77 G 1 11 4 H 1 85 285
11      3.20 G 1
11      3.49 G 1 11 1 H 1 33 103
11      3.61 G 1 11 2 H 1 51 999
11      3.63 G 1
11      3.66 G 1 1 1 2 H .1 55 233
11      3.73 G 1
11      3.75 G 1 1 1 HQS 5 40 209
11      3.84 G 1 1 14 H 10 70 270
33      3.87 - 4.00 SHEAR ZONE AND EOR
11      4.07 G 1 11 3 H 2 44 221
11      4.14 G 1 1 1 H 2 79 309
11      4.14 G 1 11 H 1.5 62 259
11      4.17 G 1
33      stub mismatch leadto original wrong ref. line drawn on core
33      2.52 - 4.17: 115 added to beta
11      4.28 G 1 11 H .1 71 14
11      4.34 G 1
11      4.36 G 1 1 13S S 75 276
11      4.45 G 1 11 3 HC .5 84 259
11      4.51 G 1 11 H 2 45 238
11      4.55 G 1 1 1 2 HS .1 71 4
11      4.71 G 1 1 1 2 CH 1.5 17 249
11      4.93 G 1
11      4.95 G 1 11 H 1 82 104
11      5.00 G 1
11      5.05 G 1 11 2 H .5 59 280
11      5.14 G 1 1 QH 5 62 259
11      5.24 G 1 1 1 KCH 1 73 10
11      5.39 G 1 11 3 CK 5 30 183
11      5.56 G 1 11 CHS 1 63 252
11      5.68 G 1 11 2 K .1 39 211
11      5.73 G 1 1 1 2 CK .2 34 208
11      5.93 G 1 1 1 2 SH 1 30 240
33      tie mark mismatch lead to wrong ref. line drawn on core - corrected betas
33      in this data file. 4.28 - 5.93: 35 added to beta
11      6.15 G 1 1 1 3 S 62 17
11      6.27 G 1

```

SHEAR ZONE, MULTIPLE FRACS

FIRST OCCUR. OF CALCITE

TOP OF 6 CM FELSITE DIKE

Table C1 (continued)

11	6.57	G	1						GC
11	6.57	G	1	1	1	2	S	50	6
11	6.69	G	1	1	1	2	S	56	5
33	END OF BOX 1								
33	START OF BOX 2								
11	6.69	G	1	11	5	H	2	76	281
11	6.70	G	1	11	3			81	292
11	6.88	G	1	11		H	1	89	103
11	6.95	G	1	1				69	286
11	7.06	G	1						SHEAR ZONE 6.88 - 7.03
11	7.06	G	1	1	1	3	S	57	16
11	7.12	G	1	1	1	2		74	310
11	7.12	G	1	11	2	HS	.5	34	121
11	7.29	G	1						GC
11	7.32	G	1	11	2	HC	2	63	319
11	7.34	G	1	11	2	H	.5	29	184
11	7.39	G	1	11	2	HC	1.5	33	147
11	7.50	G	1	1	1	HS	3	32	277
11	7.61	G	1	11	4	H	3	14	178
11	7.68	G	1	1	1	SH	3	26	54
11	7.73	G	1	1	1	3		68	295
11	7.90	G	1	1	1	SH	2	38	147
11	8.00	G	1						
11	8.04	G	1	11				14	300
11	8.08	G	1						
33	8.08 - 8.22 BLOCKY RUBBLE - NO ORIENTATION								
11	8.08	G	1	11	2	KC	.5	54	52
11	8.12	G	1						
11	8.16	G	1						
33	6.15 - 8.16: original beta OK								
33	8.20 - 11.55: 5 added to orig. beta								
11	8.20	G	1	1	1	3		21	50
11	8.23	G	1	11	2		.5	39	219
11	8.30	G	1	11	3		.5	58	343
11	8.36	G	1	11	3		.5	88	142
11	8.46	G	1						
11	8.53	G	1	11	3			88	155
11	8.64	G	1	1	1	HQ	18	80	190
11	9.08	G	1	11	2	HC		39	63
11	9.13	G	1						
11	9.14	G	1	11	2	HQ		88	198
11	9.23	G	1						
11	9.42	G	1	11	4	QH	3	53	73
11	9.55	G	1	11	3	QH	3	32	61
11	9.70	G	1	11	5	HQ	4	89	0
11	9.73	G	1	1	1	4	SHQ	69	276
11	9.76	G	1	11	4	SHQ		71	279
11	9.79	G	1	1	1	4	SHQ	71	279
11	9.83	G	1	11	4	SHQ		69	276
11	9.95	G	1	11	3	H	8	39	74
11	10.22	G	1	1	13	S		23	23
11	10.30	G	1	1	1	4		20	37
11	10.30	G	1	1	1	3	QS	68	266
11	10.46	G	1	11	2	HQ		38	107
11	10.51	G	1	1	14			21	50
11	10.53	G	1	1	14			21	50
11	10.86	G	1	1		Q		88	279
11	10.94	G	1	1	1	3	C	56	320
11	11.07	G	1						EOR
11	11.08	G	1	1	1	2	HC	1	78
11	11.23	G	1	11	3	QS	5	59	4
11	11.29	G	1	11	2	QH	.5	61	329
11	11.34	G	1	11	4	QH	1	58	355
11	11.44	G	1	11	2	QH	2	60	338
11	11.55	G	1	11	2	KH	.5	88	172
33	tiemark mismatch lead to wrong orig. beta - corrected								
33	11.68 - 13.72: 15 added to orig. beta								
11	11.68	G	1						
11	11.73	G	1	11	3	KH	3	76	161
11	11.84	G	1	11	5	HQ	3	83	210

Table C1 (continued)

11 11.96 G 1						EOR
11 12.01 G 1						GC
11 12.20 G 1	11 4 HQ	3		74 358		
11 12.22 G 1	11 2 HQ	.5		84 345		
11 12.30 G 1	1 1 HQ	.5		74 320		
11 12.37 G 1	1 14 HQ	.5		61 334		
11 12.67 G 1						
11 12.73 G 1						
11 12.79 G 1	11 2 H	4		62 342		
11 12.91 G 1	11 3 CH	1.5		88 49	BETA APPROX.	
11 13.00 G 1					GC	
11 13.06 G 1						
11 13.16 G 1	11 2 HQ	3		87 196		
11 13.33 G 1	1 1 HQ	1		83 210	HEALED BRAIDED FAULT GOUGE	
11 13.56 G 1	11 3 H			83 22		
11 13.64 G 1	1 1 3 SH			60 338	ref. FRAC. FOR IP5 #1	
11 13.65 G 1						
11 13.72 G 1	11	.5		34 85		
11 14.01 G 1	1 1 HQ	3		40 999		
11 14.09 G 1	1 1 2 QM			65 999		
11 14.09 G 1	11 3 H	.5		49 106		
11 14.20 G 1						
11 14.25 G 1	11 3 HS	1		57 40		
11 14.28 G 1	11 HS	5		75 33	REF. FRAC. FR IP5 #2	
11 14.36 G 1	1 1 2 SH			82 129		
11 14.36 G 1	1 1 2 SH			76 354		
11 14.42 G 1	11 3 HS	1		34 29		
11 14.47 G 1	11 2 H	.5		39 124		
11 14.53 G 1	1 1 3 SH			54 313		
11 14.57 G 1	1 1 2 H	.5		38 250		
33 14.63 - 15.64 BLOCK CORE RUBBLE, SOME MISSING CORE IN VERY FINE						
33 GRAINED GRANITE - D.CAMERON NOTED METASOMATIC ALTERATION						
33						
33 NO ORIENTATIONS FOR 15.64 - 16.31 - OLD INCORRECT BETAS RETAINED						
33 FOR REFERENCE INFO.. IP6 IMPRESSIONS INCONCLUSIVE.						
11 15.64 M 1	1 1 15 H			40 999 200		
11 15.69 M 1	1 1 3 SHM	.1		48 999 45	DENDRITIC MNO2	
11 15.88 M 1	1 1 2 H			45 999 45		
11 15.94 M 1	11 2 HQ	2		30 999 275		
11 16.00 M 1	1 1 2 H	1		50 999 260	SLICKS	
11 16.07 M 1	1 1 2 H	1		37 999 195		
11 16.14 M 1	1 1 2 HQ			52 999 270		
11 16.30 M 1	1 1 4 QH	2		25 999 80		
11 16.31 M 1						
33 16.31-16.33 BLOCKY CORE						
33						
33 NO REFERENCE LINE POSSIBLE FROM 16.31 - 23.90 M - NO IMPRESSIONS DONE						
33						
11 16.33 M 1	1 1 2 H			55 999		
11 16.38 M 1	1 1 HS			25 999		
11 16.50 M 1						
11 16.69 M 1	1 1 3 HS			22 999		
33 16.69 - 16.96 BLOCKY RUBBLE						
11 16.96 M 1	1 13			80 999	GC PART	
11 16.99 M 1	11 HQ	.5		35 999		
11 17.02 M 1	11 3 Q	.5		15 999		
11 17.07 A 1						
11 17.13 M 1	1 1 3 H	.5		0 999	EOR	
11 17.20 M 1	1 1 2			42 999	BLOCKY CORE	
11 17.22 M 1	1 1 5 HS	.1		35 999		
11 17.28 M 1	1 1 2 HS			80 999	BLOCKY	
11 17.30 M 1	11 3 Q	1		45 999	BLOCKY	
11 17.33 M 1	1 1 4 HS			35 999	BLOCKY	
33 17.33 - 17.40 BLOCKY RUBBLY						
11 17.40 M 1	1 1 2 HS			40 999	BLOCKY	
11 17.43 M 1	1 1 3 HS			50 999	BLOCKY	
11 17.48 M 1	1 1			30 999		
11 17.55 M 1					EOR	
11 17.60 M 1	1 1 H	5		15 999		
11 17.66 M 1	1 1 3 HS			65 999		
11 17.82 M 1	1 1 HQ	2		0 999		

Table C1 (continued)

11 18.03 M 1						
11 18.29 M 1	11	H	1	35	999	
11 18.31 M 1	1 1	HS		45	999	
11 18.31 M 1	1 1	SH		50	999	
11 18.53 M 1	1 1	HS	2	25	999	
11 18.61 M 1	11	HQ		20	999	
11 18.96 M 1	1 1	SH		60	999	
11 18.90 M 1	1	HQ		25	999	
11 19.15 M 1	11	QH	1	15	999	
11 19.54 M 1	11	Q	1	45	999	
11 19.58 M 1	1 1	SH	1	65	999	
11 19.77 M 1	1	HQ		53	147	SHEAR ZONE 19.60-19.94
11 19.96 M 1	1	Q	1	0	999	
11 20.68 M 1	1 1	Q	1	45	999	POROUS APER. - IRREG. AL
11 20.68 M 1						EOR
11 20.69 M 1						
11 20.82 M 1	11	SH	1	30	999	POROUS APER.
11 20.88 M 1	11	HS	2	25	999	
11 21.25 M 1						
33 21.28 M 21.78	SHEAR ZONE					
11 21.74 M 1						EOR
11 21.87 M 1	11	HQ	2	20	999	
11 21.96 M 1	11	HS	2	20	999	
11 22.20 M 1	1	HQ	5	15	999	
11 22.40 M 1	11	2	.1	20	999	OPEN CHANNELS IN APER
11 22.56 M 1	1 1	H	.1	45	999	
11 22.70 M 1	1			53	147	OPEN CHANNELS
11 22.80 M 1	1 1	SH		50	999	
11 23.03 M 1						
11 23.36 M 1						
11 23.36 M 1	11	H	1	15	999	
11 23.64 M 1						EOR
33 MISSING CORE STICK 23.64 - 23.74						
11 23.74 M 1						
11 23.90 M 1	11	Q	.5	27	106	
11 24.13 M 1						
11 24.13 M 1	1 1	2		36	36	
11 24.33 M 1	11	Q	1	52	64	
11 24.41 M 1						GC
11 24.43 M 1	1 1	3	Q	64	23	GC
11 24.50 M 1	1 1	2		50	31	GC
11 24.56 M 1	11	QH	1	30	42	
11 24.51 M 1	11	CK	1	34	30	
11 24.85 M 1	11	H		15	359	PART GC
33 END OF BOX 4						
33						
33 START OF BOX 5						
11 24.98 M 1	11	CQ		41	31	POROUS APER
11 24.90 M 1	1 1	H		41	31	
11 25.10 M 1						BADLY GC
11 25.19 M 1	11	QH	.5	71	48	
11 25.43 M 1	11	QH	.5	52	229	
11 25.63 M 1	11	QH	.1	42	234	
11 25.76 M 1						BADLY GC
11 25.69 M 1	11	QH	15	12	277	SHEAR ZONE
11 25.95 M 1	11	Q		14	96	DIALTIONAL Q-FILLED JT.
11 26.03 M 1						GC POLISHED
11 26.25 G 1						GC POLISHED
11 26.36 M 1	11	Q	.5	15	213	
11 26.46 M 1	11	QH		68	247	GC POLISHED
11 26.47 M 1	11	C		19	121	
11 26.58 M 1						
11 26.66 M 1	1 1	2	.1	62	60	
11 26.68 M 1	1 1	2	S	27	57	
11 26.82 M 1	1 1	3	QH	.1	18	239
11 26.94 M 1	11	3	CQ	.1	33	164
11 26.92 M 1	11	2	QC	1	27	187
11 27.06 M 1	11	2	Q	.5	27	187
11 27.11 M 1						SLIGHT GC
11 27.12 M 1	11	2	Q	.5	59	30
11 27.20 M 1	11	3	H	.5	76	299



Table C1 (continued)

11 27.20 M 1	11 2		17 21	
11 27.41 M 1	1 1 2 HQ		80 297	
11 27.45 M 1	1 1 2 HQ		82 300	POROUS APER.; CREAM RUST CON
11 27.49 M 1	11 2 Q	.5	69 309	
11 27.55 M 1				SLIGHT GC
11 27.55 M 1	1 1 2 CK	.5	56 318	SLIGHT GC
11 27.75 M 1	1 1 Q		51 330	
11 27.78 M 1	1 1 3 Q	1	72 43	POROUS APER
11 27.94 M 1	1 1 2 HQS		85 311	PALE GREEN SHEEN; MINOR SLICK
11 28.01 M 1				POLISHED GC
11 28.03 M 1	1 1 3 Q		44 72	WIDE CHANNEL
11 28.03 M 1	1 1 2 Q		76 235	POROUS APERTURE
11 28.03 M 1				
11 28.17 M 1	1 1 2 H		28 304	
11 28.21 M 1	11 5 HQ		28 304	WIDE CHANNEL
11 28.21 M 1	1 HQ		90 999	GC; DENDRITIC FEO
11 28.25 M 1	11 2 HQ		88 176	
11 28.33 M 1	1 1 5 HM		74 249	WIDE CHANNEL - CONDUIT -
11 28.38 M 1				GC
11 28.45 M 1	11 2	.5	83 2	FEW SMALL CHANNELS
11 28.54 M 1	11 3 H	.1	57 357	
11 28.50 M 1	11 5 QH	1	45 999	
11 28.63 M 1	1 1 2 H		27 57	
33 28.51 - 28.56 BLOCKY CORE - CONDUIT LIKELY				
11 28.68 M 1	11 2 Q		10 103	FRAC. ZONE WTH DENDRITIC
11 28.75 M 1	11 2 Q	2	10 103	1/2 OPEN CAVITIES WITH TERMIN
33 QUARTZ CRYSTALS INTO TORTUOUS EXFOLIATION JTS. - DILATIONAL - GOOD PHOTO				
33				
33 IP8 #1 NOT CERTAIN - BUT FITS IF USE VUGGY EXFOLIATION JTS. AS HORIZONTAL.				
33 THIS FITS GEOLOGY AND LIKELY GEOMETRY. THIS WAS USED TO ORIENT FRACS				
33 FROM 23.74 - 29.27.				
11 28.65 M 1	11 2 Q	2	78 348	OPEN CHANNELS
11 28.87 M 1	11 3 Q		60 300	
11 28.92 M 1	1 1 2 H		17 321	SLIGHT GC; DENDRITIC MIN
11 28.98 M 1	11 2 QH	10	76 354	OPEN CHANNELS
11 29.10 M 1	11 4 QH	.5	86 257	
11 29.10 M 1	1 1 2 H		55 327	DENDRITIC MnO2 AND H
11 29.16 M 1	11 2 QH	.5	60 72	DENDRITIC INFILL
11 29.20 M 1	1 1 2 QH	.5	31 202	
11 29.27 M 1	1 1 3 H		27 57	PATCHY FEO DENDRITES
33 29.27 - 29.42 BLOCKY CORE RUBBLE				
11 29.27 M 1	1 1 5 Q		69 359	
11 29.30 M 1	1 1 3 HM		74 2	
11 29.33 M 1	1 1 5 QH	1.5	88 293	
11 29.41 M 1				
11 29.46 M 1	11 2 QH	1	77 290	DILATIONAL QTZ-FILLED JT.
11 29.53 M 1				
11 29.55 M 1	11 3 H	.5	68 136	
11 29.60 M 1	11 2 H	.5	72 283	VUGGY QTZ. IN OPENINGS
33 TERMINATED QTZ. XTALS.				
11 29.65 M 1	1 1 Q	.5	71 279	
11 29.80 M 1				EOR
33				
33 29.80 - END OF BOX 5: BRITTLE FAULT BRECCIA ZONE - ANGULAR SHARDS IN				
33 PURPLE FILMY MATRIX - HEALED - AUTOBRECCIA				
33				
11 30.13 M 1	1 14 HQ	.1	88 302	
11 30.21 M 1	1 1 3 H		25 282	
11 30.26 M 1	11 2 H	.5	25 282	
33 END OF BOX 5				
33				
33 START OF BOX 6				
11 30.28 M 1	1 1 2 H		31 282	
11 30.30 M 1	1 13 SHQ	.5	46 252	
11 30.34 M 1	1 13 SHQ	.5	84 241	
11 30.60 M 1	11 4 QH	.5	56 135	POROUS APER
11 30.66 M 1	1 1 3 H	1	27 11	SLIGHT GC
11 30.77 M 1	11 3 KH	1	74 330	
11 30.94 M 1	1 1 2 CH		31 1	
11 31.01 M 1	11 4 QH	1	75 313	
11 31.10 M 1	11 2 Q	1	75 166	SLIGHT POROUS APER

Table C1 (continued)

11 31.22 M 1 1 1 2 HES	10	62 271	LIKELY CONDUIT 1CM FAUL
33 BRECCIA WITH SLICKS WITH STRONG H COATING			
11 31.33 M 1 11 2 H	1.5	62 295	
11 31.34 M 1 11 4 SQ	2	73 10	POROUS APERTURE
11 31.38 M 1 11 2 QS	4	73 292	
11 31.43 M 1 11 2 HS	2	89 293	
11 31.48 M 1 11 2 QH	.8	75 286	
11 31.51 M 1 11 2 SQH	.5	71 9	
11 31.58 M 1 11 2 Q	2	74 282	OPEN CHANNEL
11 31.66 M 1 1 1 2 CH		77 13	
11 31.68 M 1 11 2 QH	1	77 13	
11 31.74 M 1 11 2 HQ	1	83 304	
11 31.81 M 1 1 1 2 CK	.5	83 304	
11 31.84 M 1 1 1 1 SH		47 250	LIKELY CONDUIT
11 31.91 M 1 11 2 K	1	54 241	
11 31.93 M 1 11 3 SH	3	53 257	
11 31.97 M 1 11 2 COS	2	71 14	CONDUIT: SILKY FAULT PLANE W/
33 GREEN CALCITE AND SLICKS			
11 32.00 M 1 11 1 QS	6	88 134	
11 32.24 M 1 11 2 Q		79 337	
11 32.41 M 1 1 1 4 QH		50 262	
11 32.41 M 1			
11 32.65 M 1 11 3 KQ		82 27	
11 32.80 M 1 1 1 4 H		75 17	
11 32.87 M 1 1 13 HS	15	80 312	HEALED PURPLE SHEAR ZONE
11 32.94 M 1			SLIGHTLY GC
11 33.03 M 1 11 3 HQ		50 231	BRAIDED ZONE 1-2 CM - Q17.FIL
11 33.04 M 1			EOR
11 33.08 M 1 1 1 3 CEK		47 210	BETA EST'D IN RUBBLE ZONE
11 33.10 M 1 1 1 4 CK		40 100	BETA EST'D
11 33.13 M 1			
11 33.17 M 1 11 3 K		75 132	
11 33.36 M 1 11 Q	3	66 37	
11 33.48 M 1 11 2 Q	1	81 133	
11 33.82 M 1 11 3	2	38 240	
11 33.84 M 1 11 3 QH	8	78 147	FAULT BRECCIA SLIGHTLY POROUS
11 34.11 M 1 11 3 Q	1	88 147	
11 34.13 M 1 11 2 Q	.5	80 288	
11 34.20 M 1 1 1 3 C	1	24 358	
11 34.23 M 1 1 1 2 Q	.5	31 11	
11 34.37 M 1 1 1 3 QH	.5	64 48	POROUS APERTURE
11 34.50 M 1 11 4 H	.5	57 40	
11 34.56 M 1 1 1 3 H		58 56	REF. FRAC FOR IP9 #3 - TWO
33 RUSTY PATCHES ARE DIAGNOSTIC BOTH ON CORE AND IMPRESSION TRACING.			
33 THIS IS BEST IMPRESSION CERTAINTY FOR ENTIREHOLE.			
11 34.61 M 1 11 2 H	.5	72 43	
11 34.69 M 1			GC
11 34.76 M 1 11 5 HQ	1	55 39	OPEN CHANNEL
11 34.84 M 1 1 13 H	.1	38 250	OPEN CHANNEL
11 34.93 M 1 1 1 2 HL		55 254	
11 35.01 M 1 11 3 HQ		50 262	GC
11 35.02 M 1 11 3 H		41 279	
11 35.20 M 1 11 3		71 323	GC
11 35.36 M 1 11 3 H	2	61 52	
11 35.46 M 1 11 3 HQ	1	78 30	
11 35.55 M 1 1 1 3 QH		58 56	
11 35.66 M 1			GC
33 END OF BOX 6			
33			
33 START OF BOX 7			
11 35.66 M 1			GC
11 35.78 M 1			EOR
33 35.78 - 38.45 : 220 ADDED TO ORIG. BETA			
11 35.78 M 1 11 3 HQS	2	35 57	5 MM CRUSH HALO
11 35.85 M 1 11 3 HQ	2	18 160	
11 35.99 M 1 11 4 H	2	41 67	
11 36.06 M 1 1 1 5 HQ	4	33 73	
11 36.35 M 1 11 2	.1	41 50	
11 36.42 M 1 1 1 HQ	5	18 147	SMALL OPEN CHANNELS
11 36.50 M 1 1 1 4 HC	3	29 88	
11 36.54 M 1 11 3 H		6 25	

Table C1 (continued)

11	36.70	M	1	1	1	4	CH	.1	53	50	
11	36.73	M	1	1	1	2	Q	.2	57	48	
11	36.87	M	1	1	1	2	HQ	2	35	236	
11	36.95	M	1	1	1	3	HQC	5	32	211	
11	37.13	M	1	1	1	1	HQ	20	39	63	
11	37.22	G	1	1	1	2	C	.5	19	121	SHEAR ZONE 37.09-37.20
11	37.24	G	1								GC
11	37.37	G	1								
11	37.38	G	1	1	1	5	HC		44	338	
11	37.43	G	1								
11	37.49	G	1								
11	37.53	G	1	1	1	2	QH	.1	21	226	
11	37.60	G	1								EOR
11	37.72	G	1	1	1		QH		22	23	REF. FRAC FOR IP10 #1, USED T
33	CORRECT ORIG. WRONG BETA LINE (NOW DRAWN ON CORE)										CORE)
11	37.94	G	1	1	1		QH	1	29	195	
11	38.00	G	1	1	1		QH	1.5	37	214	
11	38.07	G	1	1	1	3	Q	.5	17	338	
11	38.09	G	1								
11	38.15	G	1	1	1	3	H		22	193	
11	38.22	G	1								GC
11	38.22	G	1	1	1		Q	3	46	220	
11	38.37	G	1	1	1		HQ	.1	46	160	
11	38.45	G	1	1	1		Q	1.5	27	236	
11	38.53	G	1								GC
11	38.57	G	1	1	1	2	HQ		35	999	
11	38.68	G	1	1	1		QH	5	15	999	
11	38.77	G	1								GC
11	38.80	G	1								GC
11	38.90	G	1	1	1	3	QH	2	30	999	
11	38.90	G	1	1	1	3	QH		12	999	
11	38.96	G	1	1	1	4			65	999	
11	38.96	G	1	1	1	4	Q	.5	27	999	
11	39.00	G	1	1	1	3	Q	.5	65	999	
33	38.98 - 39.78 BRECCIA ZONE										
11	39.33	G	1	1	1	2	QH		65	999	
11	39.45	G	1	1	1	4	QH	1	25	999	
11	39.73	G	1	1	1	3	H		50	999	
11	39.73	G	1								GC
33	39.80 - 50.93 EXTRAPOLATED BACK FROM IP12 REVISED REF. LINE AT 54.66										
11	39.80	G	1	1	1	3	H		53	36	
11	39.84	G	1	1	1	4			0	999	
11	39.90	G	1	1	1	3			43	61	
11	39.95	G	1	1	1	3			20	147	
11	40.02	G	1								GC
11	40.06	G	1	1	1	2	HQ		57	296	
11	40.10	G	1	1	1	14			47	353	
11	40.21	G	1	1	1	3	KQ	.5	15	80	CLOTTY MASSIVE CHLORITE AND C
11	40.40	G	1	1	1	4	KQ	1	72	296	
11	40.45	G	1	1	1	4	KQ	.5	29	98	
11	40.47	G	1	1	1	3	KQ	.5	24	168	
11	40.57	G	1	1	1	3	HQ		64	343	GC
11	40.60	G	1	1	1	2	HK	1	17	31	
11	40.71	G	1	1	1	3	KNQ	2	24	168	
11	40.73	G	1	1	1	2	QHS		14	43	
11	40.74	G	1	1	1	2	H	.5	19	186	
11	40.77	G	1	1	1	2	KS	.5	21	123	
11	40.88	G	1								
11	40.93	G	1	1	1	2	QS		52	327	
11	40.93	G	1	1	1	2	K	.5	13	66	
11	40.97	G	1	1	1	2	KQ	.5	27	106	POROUS APERTURE
11	41.04	G	1	1	1	2	CS		77	290	
11	41.10	G	1	1	1	3	KQS		50	32	
11	41.13	G	1	1	1	3	HQ		15	999	
11	41.14	G	1	1	1	2	HQ		48	999	
33	END OF BOX 7										
33	START OF BOX 8										
11	41.17	G	1	1	1	3	H	1	51	333	

Table C1 (continued)

11 41.21 G 1	11 2 H	.1	19 172	
11 41.24 G 1				GC
11 41.46 G 1	1 1 H		36 68	
11 41.40 G 1	1 1 2 Q		17 345	
11 41.48 G 1				
11 41.56 G 1	1 1 3 H		11 350	
11 41.60 G 1	11 3 H	2	6 231	
11 41.66 G 1				
11 41.76 G 1	11 3 H	.5	12 184	
11 41.81 G 1	1 15		22 333	
11 41.84 G 1				
11 41.83 G 1	11 3 HKQ	.1	35 163	
11 41.86 G 1	11 3 H	1	22 193	SMALL OPEN CHANNELS
11 41.86 G 1	11 4 H	2	15 213	
11 41.96 G 1	1 1 3 H		41 20	
11 42.00 G 1	11 3 Q	.5	57 40	POROUS APERTURES
11 42.30 G 1				
11 42.84 G 1	1 1 3 HK		21 97	
11 42.48 G 1	1 14 KQ	.1	22 100	
11 42.63 G 1	11 3 HKS	3	39 219	
11 42.72 G 1	11 2 Q	1	13 147	
11 42.80 G 1	11 2 Q	1	6 78	
11 42.82 G 1	1 1 4		36 68	
11 42.84 G 1	11	5	18 73	
11 42.89 G 1	11 2 H	1	26 54	
11 42.94 G 1	1 1 4 C		45 335	
11 42.96 G 1	11 4 HQ	2	11 39	
11 43.03 G 1	11 4 HQ	3	16 102	
11 43.06 G 1	11 4 HQ	5	20 110	
11 43.10 G 1				GC
11 43.13 G 1	11 3 HQ	1	8 147	
11 43.20 G 1	11 Q	.1	41 177	OPEN CHANNELS
11 43.44 G 1	11 2 CH	1	27 11	
11 43.54 G 1	11 4 HCK	2	31 45	
11 43.68 G 1	11 4 HK	1	33 254	
11 43.70 G 1	1 1 3 HK		37 17	
11 43.70 G 1	1 1 3 HKS	1	55 46	OPEN CHANNELS
11 43.84 G 1	11 3 Q	.5	52 49	OPEN CHANNELS
11 44.01 G 1	1 1 4 QH	.5	54 338	
11 44.08 G 1	11 2 HQ	1	34 29	
11 44.20 G 1	11 4 C	1	38 162	OPEN CHANNELS
11 44.20 G 1	1 1 CMK	30	51 200	BRECCIA ZONE IN FEO MATR
11 44.39 G 1				
11 44.48 G 1				
11 44.52 G 1	1 1 4 H	1	80 256	
11 44.58 G 1				
11 44.62 G 1				
11 44.67 G 1	11 3 QH	1	46 220	
11 44.75 G 1				
11 44.78 G 1	11 2 HQ	1	57 277	
11 44.85 G 1				
11 45.15 G 1	11 2 H	1	57 48	
11 45.22 G 1	11 2 HK	.5	36 257	
11 45.29 G 1	11 3 H	.1	54 241	
11 45.38 G 1	1 1 2 HKS	1.5	58 276	
11 45.65 G 1	11 2 H	.5	84 276	
11 45.90 G 1	11 2 Q	.5	47 195	VEIN
11 46.01 G 1	11 1 KEH	5	22 193	

33  
33 MISSING CORE 46.01 - 46.21 END OF BOX 8

33  
33 END OF BOX 8

33  
33 START OF BOX 9

33  
33 46.04 - 48.15 BRECCIA ZONE - HEALED AUTOBRECCIA - MAINLY QTZ GRAINS AND ROC  
33 FRAGMENTS LESS THAN 1 CM IN PURPLE RUSTY BRECCIA MATRIX - 46.21 - 47.60 ONE  
33 LONG STICK, SO ROCK IS COMPETENT; MOST FRACTURES INTERCONNECTED, MOST DO NO  
33 PASS COMPLETELY THROUGH CORE; HEAVY PATCHY HEM. DEPOSITS

33  
33 FOR BOX 9, DEPTH MARKS INKED ON CORE ARE 6-9 CM HIGHER THAN THOSE LISTED HE

Table C1 (continued)

33 ORIGINALLY LOGGED IN FIELD). I RETAINED ORIGINAL DEPTHS TO STAY CONSISTENT  
33 WITH REST OF DATA FILE

33									
11	47.43	G	1	11	3	SH		33	243
11	47.61	G	1	1	1	H		76	320
11	47.65	G	1	1	1	3	H	59	312
11	47.72	G	1	11	3	H	2	70	226
11	48.15	G	1	11	2	HEK	.5	81	267
11	48.22	G	1	1	1	3	SO	37	327
11	48.45	G	1	11	2	H	.5	65	274
11	48.56	G	1	11	2	H	1	55	268
11	48.58	G	1	11	2	H	.5	68	277
11	48.74	G	1	11	3	H	1	65	279
33									
11	48.87	G	1						
11	49.13	G	1	11	2	H	.1	46	204
11	49.22	G	1	11	3	QEH	15	27	208
11	49.43	G	1	11	2	KEQ	3	53	228
11	49.47	G	1	1	1	4	CEQ	25	213
11	49.56	G	1	1	1	2	CKE	14	115
11	49.62	G	1	11	3	EKM	1	35	216
11	49.77	G	1	11	2	H	1	29	184
11	49.94	G	1	1	1	2	CH	57	357
11	50.09	G	1	1	1	5	HKC	56	350
11	50.09	G	1	11	2	H	.1	29	184
11	50.17	G	1	1	1	2	H	69	294
11	50.25	G	1	11	2	H	4	71	274
11	50.31	G	1	11	2	C	.5	53	213
11	50.43	G	1	11	2	C	.1	64	218
11	50.66	G	1	1	1	2	HEK	3	79
11	50.62	G	1	11	2	HQE	1	64	258
11	50.86	G	1	1	15	EK		60	273
11	50.92	G	1	1	1	4	QSE	1	36
11	50.92	G	1	11	3	QES	2	46	220
11	50.93	G	1	1	1	3	HS	.5	49
11	51.04	G	1					201	
33									
33 51.07 - 54.44: 70 ADDED TO ORIG. BETA BASED ON IP12 IMPRESSION AT 54.66									
33									
11	51.07	G	1	11	2	HQ	1	51	207
11	51.34	G	1	11	3	QHS	.5	89	293
11	51.38	G	1	1	1	3	Q	76	333
11	51.50	G	1	11	4	HS	.5	87	121
11	51.53	G	1	1	1	4		53	23
11	51.53	G	1	1	14	HS	.5	87	121
11	51.70	G	1	11	5	QHS	3	49	264
11	51.71	G	1	11	3	QH	2	10	999
33 BOTTOM OF BOX 9									
33									
33 START OF BOX 10									
11	51.75	G	1						
11	51.99	G	1	11	3	HQS	3	66	230
11	52.01	G	1	1	1	4	H	33	333
11	52.16	G	1	11	5	QH	2	83	349
11	52.20	G	1	1	1	3	HC	41	329
11	52.32	G	1	11	2	HQ	1	83	334
11	52.35	G	1	11	5	QH	10	64	297
11	52.50	G	1	1	1	5	KEC	41	341
11	52.53	G	1	1	1	3	Q	59	24
11	52.69	G	1	1	1	4		68	12
11	52.69	G	1	11				73	127
11	52.78	G	1	11	2	QS	2	75	313
33									
11	53.13	G	1	11				19	121
11	53.16	G	1	1	1	4	Q	17	272
11	53.16	G	1	11	3	HS	1	74	111
11	53.32	G	1	11	3	SH	.5	81	250
11	53.37	G	1	11	5	H	10	77	118
11	53.52	G	1	1	1	3	Q	71	308
11	53.67	G	1	1	1	5	HQ	61	241
11	53.71	G	1	1	1	3	C	22	270
11	53.76	G	1	1	14	HS	3	12	203

POROUS APERTURE

GC

OPEN CHANNELS

BETA APPROX.

BETA APPROX.

SLIGHT GC

OPEN CHANNELS

OPENED BY DRILLING

SMALL OPEN CHANNELS

SMALL OPEN CHANNELS 1CM BRECC

Table C1 (continued)

11 53.85 G 1	1 1 5 HQ	2	28 261	
11 53.90 G 1	11 4 HS	3	39 219	
11 53.98 G 1				EOR
33	END OF BOX 10			
33				
33	START OF BOX 11			
11 54.05 G 1	11 2 H	.5	76 320	
11 54.08 G 1	1 1 3 H	.5	27 236	
11 54.13 G 1	11 4 H	3	27 236	
11 54.20 G 1	1 15 HQ	2	36 246	
11 54.35 G 1	1 1 3 HQ	2	34 249	
11 54.37 G 1	11 3 H	1	49 224	
11 54.44 G 1	11 4 H	3	50 215	
11 54.44 G 1				
33	TIE MARK MISMATCH MEANS 70 ADDED TO OLD BETA ABOVE, 100 SUBTRACTED			
33	FROM BETA BELOW, FRM 54.53 - 55.63.			
11 54.53 G 1				GC EOR
33	54.10- 56.12 FRACTURE ZONE WITH IRREGULAR CLOSED FRACTURES			
33				
11 54.66 G 1	1 15 HQ	10	66 256	REF. FRAC. FOR IP12 #1
11 54.66 G 1				
11 54.70 G 1	11 3 H	1.5	44 256	
11 54.80 G 1	1 1 5 SC	3	39 63	
11 54.85 G 1	11 3 H	.5	71 284	
11 54.94 G 1	11 3 H	.1	62 295	
11 54.94 G 1	11 5 HQ	5	64 245	
11 55.08 G 1	11 4 HQ	5	73 287	
11 55.17 G 1	1 1 2 HS	.5	44 264	
11 55.28 G 1	1 1 3 HS	.5	40 209	SMALL OPEN CHANNELS
11 55.41 G 1	11 3 HS	3	62 311	
11 55.47 G 1	1 1 3 HK		41 279	
11 55.50 G 1	1 1 5 H	1	31 183	
11 55.56 G 1	1 1 2 HK	.5	47 306	SLIGHT GC POLISHED SLICK
11 55.63 G 1	11 3 H	2.5	87 121	
11 55.64 G 1				GC
11 55.75 G 1	11 3 HK	3	55 999	
11 55.85 G 1	1 1 5 H	3	15 999	
11 56.12 G 1	11 2 K	5	35 999	
11 56.23 G 1	1 1 3 HS		45 999	
11 56.28 G 1	11 KQ	2	50 999	
11 56.34 G 1	1 1 3		35 999	
11 56.34 G 1				
11 56.40 G 1	1 1 2 K	5	65 999	
11 56.43 G 1	11 4 QK	3	45 999	
11 56.50 G 1	1 1 2 K		55 999	
11 56.70 G 1	11 2	.1	25 999	
11 56.97 G 1				
11 57.26 G 1				
11 57.38 G 1	11 4 Q	3	22 999	
11 57.38 G 1	1 1 2 KQ		75 999	
11 57.49 G 1	11 5 K	2	45 999	
11 57.55 G 1	11 3 H	1.5	45 999	
11 57.60 G 1	11 2 H	.5	47 999	
11 57.60 G 1				
11 57.72 G 1	11 2 QH	.5	32 999	
11 57.88 G 1				GC
11 58.09 G 1				
11 58.17 G 1				GC
11 58.23 G 1				GC
33				
33	58.34 - 59.71 NOT ORIENTED - IMPRESSIONS INCONCLUSIVE -			
33	ORIGINAL BETAS RETAINED FOR INFO ONLY			
33				
11 58.34 G 1	11 3 Q		20 999 110	
11 58.41 G 1	1 1 2 Q		55 999 350	
11 58.53 G 1	11 3 Q	.5	35 999 355	
11 58.72 G 1	11 4 H	.5	30 999 80	
11 58.82 G 1	11 4 QH	15	30 999 10	
11 59.10 G 1	11 2 K	.5	30 999 225	
11 59.15 G 1	1 1 3 H		62 999 350	
11 59.28 G 1	1 1 5 CK	4	57 999 185	EOR; FAULT PLANE WIT

Table CI (continued)

33 DEVELOPED SLICKS WITH RAMP AND RISER STRUCTURE OF CALCITE AND SILKY PALE									
33 GREEN CHLORITE OR SERICITE									
11 59.34	G 1	1 1	4	H				38 999	320
11 59.41	G 1	1 1	3	K				40 999	295
11 59.53	G 1	1 1	3	K	4			15 999	150
11 59.71	G 1	1 1	3	Q				50 999	190
33									
33 END OF REFERENCE LINE FOR CORE ORIENTATION. NO ORIENTATION BELOW BECAUSE									
33 SAMPLES WERE REMOVED (FOR JOHN ANDREWS), BREAKING LINK OF MESHING CORE									
33 PIECES, AND BECAUSE THE DEEPER IMPRESSION (NO. 14) HAD NO IMPRESSIONS									
33									
11 60.12	G 1	11 3	S		.5			25 999	
11 60.14	G 1	1 1	2	S				63 999	
11 60.21	G 1	11 5	KQ		25			43 999	
11 61.10	G 1	11 4	K		10			20 999	
11 61.80	G 1	11 2	Q		.5			45 999	
11 62.10	G 1								
11 62.13	G 1	11 2	K		2			10 999	
11 62.23	G 1	11 2	K		10			10 999	
11 62.33	G 1								
11 62.54	G 1	11 2	HQ		1			30 999	EOR
11 63.04	G 1	1 1	1	K	2			90 999	SLICKS
11 63.16	G 1	11 2	Q		.1			45 999	
11 63.40	G 1	1 1	3					50 999	
11 63.46	G 1	1 1	3	Q				62 999	
11 63.50	G 1	1 1	3	Q				60 999	
11 63.50	G 1	1 1	2	K				30 999	
11 63.60	G 1	1 1	2	Q				45 999	
11 63.60	G 1	1 1	2	K				37 999	
11 63.67	G 1	1 1	3	QS	2			30 999	OPEN CHANNELS
11 63.79	G 1	1 1	3	HK				48 999	
11 63.94	G 1	11 4	QH		2			40 999	
11 64.24	G 1	11 5	HQ		10			15 999	
11 64.42	G 1	1 1	2	K	2			63 999	
11 64.44	G 1	1 1	2	K	2			63 999	
11 64.49	G 1	11 2	K		3			63 999	
11 64.63	G 1	11 2	KHQ		.5			20 999	OPEN CHANNELS
11 64.72	G 1	1 1						60 999	
11 64.76	G 1	1 1	3					50 999	
11 64.95	G 1	11 5	K					25 999	
11 65.14	G 1	11 2	H		5			40 999	
11 65.21	G 1	1 1	3	H	.5			40 999	
11 65.38	G 1								EOR
11 65.57	G 1	11 2						22 999	
11 65.73	G 1	1 1	2	HS				57 999	
11 65.75	G 1	11 2	HK		1			48 999	
11 65.85	G 1	11 3	H		.5			48 999	
11 66.10	G 1	11 2	Q					30 999	
11 66.20	G 1								GC
11 66.26	G 1	11 2	H		.1			30 999	
11 66.42	G 1								
11 66.52	G 1	11 3	H		2			55 999	
11 66.70	G 1	1 1	2	H	.1			5 999	
11 66.84	G 1	11 2						40 999	
11 66.84	G 1								
11 66.92	G 1	11 5	SK		10			55 999	
11 66.99	G 1								
11 67.07	G 1	11 4	H		.1			55 999	
11 67.20	G 1	11 3	SH		1			53 999	
11 67.37	G 1	11 3	H		.1			20 999	OPEN CHANNELS
11 67.40	G 1	11 2	QH		1			10 999	
11 67.46	G 1								GC
11 67.66	G 1	11 3	H		.5			22 999	
11 67.72	G 1	11 2	H		1			22 999	
11 67.82	G 1	11 5	H		10			22 999	
11 67.96	G 1	11 2	Q					64 999	
11 67.96	G 1								GC
11 68.11	G 1	1 1	2	HS	1			60 999	
11 68.20	G 1	11 3						15 999	
11 68.27	G 1	1 1	3	SQ				65 999	
11 68.27	G 1	11						60 999	

Table C1 (continued)

11 68.40 G 1	1 1 5 HS		60 999	
11 68.43 G 1				
11 68.50 G 1	11 2 HS	.5	55 999	EOR
11 68.55 G 1				OPEN CHANNELS
11 68.64 G 1	11 5 HQ	5	24 999	
11 68.70 G 1	11 4 HS	.5	28 999	
11 68.90 G 1	11 4 H		20 999	
11 69.38 G 1	11 3 QH	1	20 999	
11 69.58 G 1	11 5 HQ	5	47 999	
11 69.94 G 1				
11 69.94 G 1	1 1 2 Q	3	45 999	
11 70.04 G 1	11 5 H	1.5	45 999	
11 70.29 G 1	1 1 3 H		60 999	SLIGHT GC
11 70.43 G 1	11 3 H	1	32 999	
11 70.49 G 1	11 4 H	2.5	32 999	
11 70.58 G 1				
11 70.60 G 1	11 3 QH	1	15 999	
11 70.80 G 1				GC
11 71.10 G 1	11 2 H	2	25 999	
11 71.20 G 1				GC
11 71.26 G 1	11 3 H	2	45 999	
11 71.36 G 1	1 13 H	1.5	20 999	
11 71.48 G 1				
11 71.62 G 1	11 4		60 999	
11 71.63 G 1				
11 71.75 G 1	11 H	2	25 999	
33 71.50 - 72.20	BLOCKY ZONE CHECK-			
11 72.04 G 1				
11 72.20 G 1	11 3 H	5	5 999	
11 72.32 G 1	1 1 3 H	1	7 999	
11 72.35 G 1				
11 72.40 G 1	11 2 H	.5	20 999	
11 72.40 G 1				
11 72.61 G 1	1 1 3 H	1	35 999	
11 72.75 G 1	1 1 2 KH	3	30 999	
11 73.26 G 1				GC
11 73.56 G 1	11 5 KS	1	55 999	
11 73.63 G 1				
11 73.71 G 1	11 5 HS	2	25 999	
11 73.88 G 1				
11 73.89 G 1	1 1 H	12.5	22 999	
11 74.14 G 1				
11 74.30 G 1	1 1 2 H		40 999	
11 74.38 G 1				
11 74.53 G 1				FOR
11 74.61 G 1				
11 74.64 G 1				
11 74.67 G 1	11 3 H	1.5	57 999	
11 74.84 G 1	11 3 H	3	40 999	
11 74.96 G 1	11 4 H	10	50 999	
11 75.06 G 1				
11 75.51 G 1	1 1 2 Q	.1	50 999	
11 75.85 G 1	1 1 2 Q	.1	45 999	
11 76.00 G 1	11 5 HKQ	10	40 999	
11 76.16 G 1	1 1 5 HKQ	5	15 999	
11 76.25 G 1	1 1 4 K		65 999	
11 76.87 G 1	11 3 QS	4	45 999	
11 77.28 G 1	1 1 4 K		60 999	
11 77.41 G 1				SLIGHT GC
11 77.58 G 1				EOR
11 77.90 G 1	11 3 H	10	20 999	HEM. VEIN
11 78.06 G 1				
33				
33	BOTTOM OF HOLE			



Table C2 - Fracture data for borehole H4 in the Seal Cove River valley

```

33 H4COPE.DAT - ORIENTED FRACTURE DATA FOR BOREHOLE H4
33 IN THE SEAL COVE RIVER VALLEY
33
33 IMPRESSION PACKER ZONES LABELLED AS "IP #1" (e.g. IP5)
33 FORMAT FOR FRACTURE DATA DESCRIBED IN TEXT
33
11 00.61 G 1 1 1 4M H WH .1 65 999 NO CORE FROM 0-.61 M;
33 ROUGH DULL SHEETING JT
11 .66 G 1 1 1 2 K GR 2 22 999
11 .71 G 1 1 1 1
11 .72 G 1 1 1 3M H BRWH 65 999
11 .74 G 1 1 1 2M H BR 65 999
11 .80 G 1 1
11 .80 G 1 1 1 3H H BR 5 70 999 WEATHERING HALO
11 .95 G 1 1 1 2 K GR .5 35 999 CHLOR. HALO
11 1.00 G 1 GC
11 1.02 G 1 1 1 1 K GR 1 25 999
11 1.09 G 1 1 1 2 K GR 5 27 999 5MM BRECCIA ZONE
11 1.11 G 1 1 1 2L H BR .5 9 999
11 1.35 G 1 14
11 1.39 G 1 1 1 2 K GR .5 42 999
11 1.44 G 1 1 1 2M H BR .5 16 999
33 1.44 - 1.55 M RUBBLE AND GC, NO ORIENTATION POSSIBLE
11 1.62 G 1 1 1 2L KH GP .5 19 999 SPLAYS INTO 2 CM FAULT ZONE
11 1.68 G 1 1 1 3H QHE WBRGR 3.0 56 999
11 1.76 G 1
11 1.80 G 1 1 1 3H H BR .5 61 999
11 1.81 G 1 1 1 2 K GR 20 999 SPLAYS TO 3CM FAULT ZONE
11 1.84 G 1 1 1 3H MH BLBR .8 62 999
11 1.95 G 1 1 1 2 K GR 2 29 999 MINOR BRECCIA POCKETS
11 1.97 G 1 1 1 14M H BR .5 80 999
11 2.10 G 1 1 1 3 K GR 1 15 999
11 2.18 G 1 1 1 2 K GR .5 18 999
11 2.28 G 1 GC
11 2.38 G 1 1 1 4 H BR 2 14 999 OPEN APERTURE, CONDUIT
11 2.44 G 1 1 1 3M L BU 1 70 999
33 2.47-2.91 M RUBBLE AND MISSING CORE
33
11 2.91 G 1 GC
11 2.91 G 1 1 1 2 K GR 1 25 999 1CM WIDE FAULT ZONE
11 3.00 G 1 1 1 5 K GR 2 30 999
11 3.09 G 1 1 1 2 K GR .2 10 999
11 3.13 G 1
11 3.30 G 1 1 1 2 K GR 1 12 999
11 3.31 G 1 1 1 2 K GR .3 13 999
11 3.43 G 1
11 3.55 G 1 1 1 2 Q WH 1.5 8 999
11 3.71 G 1 1 1 2 K GR 1 21 999
11 3.72 G 1 1 1 2 K GR 1 21 999
11 3.72 G 1 PART GC
11 3.73 G 1 1 1 3 KE GR .5 55 999
11 3.81 G 1 GC
33 3.81-3.93 OVERCORED RUBBLE AND GC (MOST MISSING)
11 3.93 G 1 GC
33
33 4.07 - 4.95: ORIENTED USING IP3
33
11 4.07 G 1 1 1 14 KE GR .5 20 322
11 4.10 G 1 1 1 3 K GR .3 18 324
11 4.12 G 1 1 1 3 1.5 82 283 POSSIBLE CONDUIT
11 4.14 G 1 1
11 4.15 G 1 1 1 2 E GR 2 35 203
11 4.38 G 1 1
11 4.38 G 1 1 1 2 74 120
11 4.41 G 1 1
11 4.41 G 1 1 1 4 K GR 1 80 116
11 4.43 G 1 1 1 3 K GR .7 65 135
11 4.43 G 1 1
11 4.46 G 1 SLIGHT GC
11 4.46 G 1 1 1 2M HL BR .5 74 332
11 4.49 G 1 1 1 3L HM BRBL .5 82 107

```





Table C2 (continued)

33  
 33 START OF BOX 3  
 33  
 33 OK ORIENTATIONS BASED ON IP7 #1 FROM 11.80 - 13.51  
 33  
 11 11.80 M 1 GC CONE  
 11 11.88 M 1 1 1 2 KC GRWH 2 68 156 FAULT + BRITTLE BRECCIA 2CM WI  
 33  
 33 ROCK FROM 11.80 - 13.51 M ARE VARIETIES OF MICROGRANITE WITH CLOTS OF MILKY  
 33 QUARTZ AND CHLORITE UP TO 1 CM ACROSS IN 1MM SIZE ROCK MINERAL MATRIX  
 11 11.95 M 1 11 2 86 147  
 11 12.11 M 1 11 1 CK WH .2 76 352  
 11 12.22 M 1 1 1 2 83 148 SHEAR JT WITH 3MM OFFSET OF QT  
 11 12.40 M 1 11 2 CK WHGR .5 82 334  
 11 12.70 M 1  
 11 12.80 M 1 11 3 62 112 PALE PINK MICROGRANITE WITH CL  
 11 12.83 M 1  
 11 12.93 M 1  
 11 13.04 M 1 11 2 CK WHGR 1 73 346  
 11 13.10 M 1 1 1 3 CK WH .3 83 351 LARGE SER. OR MUSC CLOT ON SUR  
 11 13.32 M 1 WHITE MICROGRANITE WITH Q-CHL  
 11 13.32 M 1 1 1 2 C .3 85 299  
 11 13.38 M 1 1 1 3 C .2 86 117  
 11 13.51 M 1 11 3 C ORWH 2 83 157  
 33 RUBBLE OF REGULAR GRANITE - DOESN'T LOOK LIKE ADJACENT MICROGRANITE ABOVE  
 33 AND BELOW, SO MAY BE OUT OF PLACE  
 33  
 33 13.57 - 15.90 ORIENTATIONS OK BASED ON IP7 #2  
 33  
 11 13.57 M 1  
 11 13.62 M 1 11 1 CK ORWHGR 1.5 79 358  
 11 13.74 M 1 1 1 2 CK WHORGR 3 75 352 BRITTLE FAULT ZONE  
 11 13.76 M 1 11 2 CK WH 1 78 163 PINK MICROGRANITE  
 11 13.89 M 1 11 2 CK WHGR 1 75 352  
 11 14.33 M 1 1 1 2 C WH .3 80 4 PINK FINE-GRAINED GRANITE FROM  
 33 HERE TO 14.79M  
 11 14.35 M 1 11 2 C WH .5 77 348 TAN FILM  
 11 14.43 M 1 11 2 C WHBR .5 86 161  
 11 14.47 M 1 11 2 C .2 84 176  
 11 14.49 M 1 11 2 C .2 87 170 SHEAR JT OFFSETS Q-CHL CLOT  
 11 14.60 M 1 1 1 2 82 193  
 11 14.64 M 1 11 2 C WH 1 60 359  
 11 14.68 M 1 11 3 H RE .5 54 4 RED HEM SPOTS  
 11 14.70 M 1 11 2 46 16  
 11 14.75 M 1 1 1 2 C WH 2 64 14  
 11 14.76 M 1 1 1 2 CK GRWH 2 63 353  
 11 14.79 M 1 1 1 1 KC GR 1 86 156  
 11 14.85 M 1 11 3 K GR 35 67 5 FAULT BRECCIA ZONE 14.83-14.87  
 33 3.5 CM WIDE - HEALED WITH DARK GR CHL MATRIX  
 11 14.91 G 1 1 1 2 C WH 1.5 77 158 FRACS TRUNCATED BY FAULT ABOVE  
 11 14.98 G 1 11 4 KC GRWH 1 74 161  
 11 15.02 G 1  
 11 15.03 G 1 11 2 CK GRWH .3 78 158  
 11 15.06 G 1 11 2 C WH .5 77 159 FILMY COATING  
 11 15.12 G 1  
 11 15.16 G 1 11 3 KC GRWH 50 75 159 FAULT BRECCIA 5MM ZONE HEALED  
 11 15.28 G 1 11 3 KC GRWH .8 63 213  
 11 15.42 G 1 11 4 C WH .5 69 172  
 11 15.54 G 1 GC  
 33 15.60M 2CM QTZ VEIN- NO BOUNDARY JTS  
 11 15.78 G 1 11 3 CK WHGR 2 73 155  
 11 15.90 G 1 11 3 C WH 1 77 348  
 33  
 33 15.96 - 22.22 ORIENTATIONS OK BASED ON IP8 #3  
 33  
 11 15.96 G 1 GC  
 11 16.36 G 1  
 11 16.40 G 1 11 2 KC GRWH 2 76 169 SHEAR JTS WITH SMALL CRUSH ZON  
 11 16.44 G 1 11 2 KC GRWH .3 76 169  
 11 16.60 G 1 11 4 KC 69 161  
 11 16.63 G 1

Table C2 (continued)

11 16.63 G 1	11 3 KC GRWH	1.5	84 152	
11 16.73 G 1	11 2 KHC GRBRWH	2	77 353	SPLAYS TURN PARALLEL TO CORE AXIS
11 16.76 G 1	11 3 CK WHGR	1.2	84 356	SHEAR JTS WITH OFFSET ASPERITIES
11 16.80 G 1				
33	END OF BOX 3			
33				
33	START OF BOX 4			
11 16.84 G 1	11 3 CK WHGR	2	80 158	SHEAR JT OR MINOR FAULT
11 16.91 G 1	11 2 K GR	3	87 175	
11 16.95 G 1	11 3 K GR	2	39 17	BRITTLE BRECCIA ZONE
11 16.97 G 1	11 4 CK WHGR	1.5	87 170	
11 17.01 G 1	11 2	1	75 144	BRITTLE BRECCIA 1CM ZONE
11 17.05 G 1	11 2 K GR	.2	69 135	
11 17.08 G 1	11 3 C WH	2	74 149	
11 17.10 G 1				
11 17.10 G 1	11 2 K GR	2	81 150	
11 17.15 G 1	11 2 KC GRWH	2	22 28	1 CM BRITTLE BRECCIA ZONE - BR
11 17.18 G 1	11 2 C WH	1	77 154	
11 17.24 G 1				
11 17.26 G 1	11 2 K GR	1	78 153	
11 17.32 G 1	11 2 CK WHGR	.5	75 154	
11 17.34 G 1	1 1 2 C ORWH	15	78 163	FAULT BRECCIA - HEALED - BRAIDED
33	LENSOID FRAGMENTS OVER SPAN	17.33-17.36		
11 17.38 G 1	11 3 CK WHGR	3	84 162	
11 17.40 G 1	11 2 C WH	1	69 214	
11 17.40 G 1	11 3 CK WHGR	3	80 163	1CM FAULT BRECCIA - BRAIDED
11 17.50 G 1	11 2 KEC GRWHGR	.5	86 181	
11 17.67 G 1				
11 17.68 G 1				
11 17.78 G 1	11 2 KC GRWH	.5	55 135	
11 18.01 G 1				
11 18.04 G 1	11 1 C WH	.3	68 228	
11 18.23 G 1	11 3 KC GRWH	1	79 163	
11 18.36 G 1	11 2 KC GRWH	1	69 155	
11 18.38 G 1	11 2 C WH	.5	79 163	EN ECHELON TENSION CRACKS
33	18.40 RUSTY RED MICROGRANITE WITH QTZ AND CHL CLOTS			
11 18.48 M 1				
11 18.52 M 1	11 4 HC BRWH		36 221	
11 18.68 G 1	11 2 C WH	1	26 223	
11 18.76 G 1	11 2 C ORWH	.5	87 358	
11 18.78 G 1	11 2 C WH	1	86 357	
11 18.82 G 1	11 2 C WH	1.5	47 48	
11 18.90 G 1	11 2 KC GRWH	.5	74 165	
11 18.96 G 1	11 2 C ORWH	1.5	80 173	
11 19.07 G 1	11 2 CK GRWH	10	72 155	1.5 CM FAULT ZONE WITH FINE
33	COMMUNUTED GOUGE			
11 19.10 G 1	11 2 C WH	.5	82 177	
11 19.24 G 1	11 2 KC GRWH	1.5	81 162	THIN FAULT BRECCIA ZONE HEALED
11 19.27 G 1	11 2 C WH	.5	70 145	
11 19.20 G 1	11 2 CK GR	5	74 149	FAULT ZONE WITH FINE PALE GR.
11 19.52 G 1	1 1 3 KC GRWH	2	30 125	SLICKENSIDED
11 19.69 G 1	11 2 K GR	3	70 161	GRANITE WITH 1CM PINK FELDSPAR
11 19.71 G 1				
11 20.02 G 1	11 2 C WH	.5	87 180	
11 20.06 G 1	11 3 CK WHGR	3	84 171	
11 20.13 G 1	11 3 KC GRWH	1	79 153	BRAIDED SHEAR JT IN 5MM ZONE
11 20.19 G 1	1 1 3 C	.5	74 351	DULL GRAY COATING
33	END OF BOX 4			
33				
33	START OF BOX 5			
33	START OF BOX 5 (19.99M) IS 0.21 M HIGHER THAN END OF BOX 4 (20.23M). THESE			
33	DEPTHS WERE TAKEN FROM DRILLERS MARKERS - SO THIS REFLECTS POOR DRILLING			
33	PRACTICE. SINCE ONLY ONE FRACTURE OCCURS UP TO 20.2M IN BOX 5 THIS FIRST 2			
33	CM IS DISREGARDED AND BOX 5 EFFECTIVELY "STARTS" AT 20.2 M. CORE BELOW IS			
33	STILL MARKED BASED ON DRILLERS REFERENCE MARKS, SO 20 CM OF CORE IS IGNORED			
11 20.24 G 1	11 3 K GR	.5	71 166	JT SPLAYS INTO TWO PARTS
11 20.32 G 1	11 2 KC GR	1	19 239	
11 20.55 G 1	11 3 KC GR	10	75 125	1CM BRITTLE BRAIDED BRECCIA ZONE
11 20.76 G 1	11 2 C WH	.8	86 352	
11 20.86 G 1	11 2 C WH	.5	76 169	
11 21.00 G 1	1 1 2 CK	1	74 165	

Table C2 (continued)

11 21.06 G 1	1 1 2	KC	2	77 164	
11 21.13 G 1	111 2	CK GR	1.5	76 159	FAULT BRECCIA ZONE
11 21.16 G 1					
11 21.23 G 1	11 3			88 185	
11 21.28 G 1	11 2	C WH	.3	73 170	
11 21.33 G 1	11 2	C WH	.2	83 167	
11 21.43 G 1	11 2	K GR	.5	84 187	
11 21.44 G 1	1 1 2	KC GRWH	.5	78 358	
11 21.47 G 1					
11 21.51 G 1					
11 21.53 G 1					PART GC
11 21.64 G 1	1 1 2	KC GRWH	1	79 120	
11 21.71 G 1	11 3	KC GRWH	4	89 260	1 CM FAULT BRECCIA BRITTLE ZONE
11 21.75 G 1	11 2	KC GRWH	.5	86 88	
11 21.78 G 1					
11 22.00 G 1					WH. QTZ. VEIN WITH CHL-EPI CLOTS
11 22.09 G 1	11 2			61 117	
11 22.13 G 1	11 2	CE WHGR	1	35 151	
11 22.16 G 1					
11 22.22 G 1	1 1 2	C WH	1	74 274	
11 22.22 G 1					
33					
33	NO ORIENTATIONS FROM 22.22 - 22.52				
33					
11 22.42 G 1					
11 22.52 G 1	11 2			21 999 250	
11 22.52 G 1					GC
33					
33	22.60 - 25.35 ORIENTATIONS OK BASED ON IP9 #3				
33					
11 22.60 G 1	11 2			60 34	
11 22.64 G 1	11 4	K GR	.8	77 233	
11 22.67 G 1	1 1 2	KC GRWH	3	79 284	
11 22.70 G 1					
11 22.73 G 1	11 2			76 240	1 CM BRECCIA ZONE
11 22.77 G 1					
11 22.82 G 1					
11 22.85 G 1					
11 22.87 G 1	11 3	KC GRWH	1	30 135	BETA EST.
11 22.89 G 1	1 1 3			28 106	
11 23.00 G 1					GC
11 23.03 G 1	11 2	C ORWH	1	83 253	
11 23.07 G 1	11 2	K GR	.5	80 255	
11 23.12 G 1	11 4	K GR	.5	83 76	
11 23.23 G 1	11 2			79 250	
11 23.33 G 1					
11 23.40 G 1	11 2	KC GRWH	.5	81 86	
11 23.45 G 1	1 1 4	CK GRBR	.5	88 73	
11 23.52 G 1					
11 23.62 G 1					
11 23.73 G 1					
11 23.85 G 1	11 2	C WH	.3	39 135	
11 23.85 G 1	11 2			89 249	FINE EN ECHELON FRACTURES
11 23.89 G 1					GC
11 23.90 G 1	1 1 3	C WH	1	30 135	
11 24.01 G 1	11 2	C WHOR	.5	82 97	
11 24.15 G 1					PART GC
11 24.24 G 1	11 2	K GR	5	75 88	FAULT ZONE - ROCK FRAGMENTS IN
33	COMMINUTED CHLORITIC CRUSH GOUGE - HEALED - NO CONDUIT				
11 24.32 G 1					
11 24.39 G 1	11 2			77 95	CRUSH ZONE WITH COMMINUTED CHL
11 24.44 G 1					
11 24.51 G 1					
11 24.63 G 1	11 2	KE GR	1	71 135	
11 24.64 G 1	11 2	CH WHRE	.5	76 120	ABUTS ABOVE FRAC.
11 24.64 G 1					GC
11 24.87 G 1	11 2	K GR	10	64 124	FAULT ZONE - 1CM BRITTLE
11 25.05 G 1					
11 25.07 G 1	11 3	K GR	5	68 161	BRAIDED FRAC. ZONE 5 CM WIDE
11 25.12 G 1					
11 25.23 G 1					PART GC

Table C2 (continued)

11 25.29 G 1	1 1 2	KC GRWH	63 180
11 25.35 G 1			
11 25.43 P 1			
11 25.53 G 1			
33			
33 25.65 - 33.64	ADDED 50 TO OLD BETA (BASED ON IP9)		
33			
11 25.65 G 1	11 3	KC GRWH 2	88 8 1 CM FAULT ZONE HEALED BRAIDED
33	SHEAR JTS AND FAULT PLANES INTERWOVEN		
11 25.74 G 1			GC
33	END OF BOX 5		
33			
33	START OF BOX 6		
33 25.74 - 25.80	HEALED FAULT BRECCIA		
11 25.84 G 1	11 2	K GR	54 20
11 25.86 G 1			
11 25.90 G 1	11 2	K	51 24
11 25.95 G 1	1 1 2	K	70 214
11 26.18 G 1	1 1	KC	77 185 SPANS 26.12-26.25 COARSE ANG.
33	FAULT BRECCIA WITH GREEN COMMUNUTED GOUGE		
11 26.30 G 1			
11 26.30 G 1	11 2	KC	75 186
11 26.50 G 1	1 1 4	KC	58 59 2 CM FAULT BRECCIA ZONE WITH GRAN.
33	FRAGS. UP TO 1 CM IN CHL. MATRIX		
11 26.56 G 1	11 3	K	32 41 4 MM WIDE FAULT BRECCIA ZONE
11 26.60 G 1	11 3	K	64 63
11 26.66 G 1	1 1	K	65 26 1-3 CM CHL-SPHALERITE(?) CLOT
33	BRECCIA ZONE		
11 26.66 G 1			GC
11 26.75 G 1	11 3	CK	86 171
11 26.85 G 1			
11 26.98 G 1	11 3	KC	32 82
11 27.06 G 1	11 4		41 73 NARROW BRECCIA ZONE
11 27.09 G 1	1 1 2	C	26 46
11 27.23 G 1	11 3	K	21 88
11 27.26 G 1			
11 27.42 G 1			
11 27.43 G 1	1 1 4	KC	52 54
11 27.46 G 1	1 1 2	CK	48 50
11 27.50 G 1	11 4	K	37 10
11 27.58 G 1	11 2	K	21 12 2 CM BRAIDED FRACTURE ZONE
11 27.60 G 1	1 1 3		72 287
11 27.68 G 1			
11 27.71 G 1	11 2	CK	87 238
11 27.72 G 1	11 2	KC	32 41
11 27.77 G 1	1 1 2	C	84 216 BETA EST'D
11 27.84 G 1			
11 27.85 G 1	11 2	K	40 197
11 27.90 G 1	1 1 2		66 204 CURVED FAULT WITH FINE SPLAYS;
33	LEFT-LATERAL SENSE		
11 28.03 G 1	1 1 3	K	88 56 1.5 CM BRITTLE CRUSH ZONE
11 28.09 G 1			
11 28.16 G 1	11 2	KC	88 231
11 28.22 G 1			GC
11 28.34 G 1	1 1 3	K	74 242 BRAIDED FRAC. ZONE 5 MM WIDE
11 28.36 G 1	11 2	K	81 237
11 28.46 G 1	1 1	K	61 241 1 CM BRITTLE CRUSH ZONE SPANS
33 28.43 - 28.49	WITH CHL RICH GOUGE		
11 28.57 G 1	1 1 2	H	89 225 SPANS 28.47 - 28.76 M11
11 28.79 G 1			
11 28.85 G 1	1 1 3	K	89 44
11 28.87 G 1			
11 28.93 G 1			
11 29.16 G 1	11 2	K	35 118 FUZZY 1 CM CHL HALO AROUND FRACTURE
11 29.17 G 1	1 1 3	KC	59 74
11 29.24 G 1	11 1	KC	32 100
11 29.26 G 1	1 1 3L	CH	26 114 3 CM FAULT ZONE SPANS 29.24-29
33	RARE OCCURRENCE OF HEMATITE (RUSTY BROWN, SOFT) - SLICKENSIDES - PROBABLE		
33	CONDUIT FOR WATER FLOW.		
11 29.29 G 1			
11 29.40 G 1	11 2	C	.8 76 222

Table C2 (continued)

33 29.38 - 30.82 ANASTOMOSING BRITTLE CRUSH ZONE PARALLEL TO CORE AXIS -									
33 MOSTLY 0 ALPHA; BRAIDED CHLORITE AND COMMINUTED GOUGE AROUND ANGULAR									
33 GRANITE FRAGMENTS 10 CM WIDE.; ZONE CRUSHES AND OFFSETS APLITE DIKE FROM									
33 30.47 - 30.60 ; SEVERAL PLANAR FRACTURES OFFSET THE BIG CRUSH ZONE; LARGE									
33 ZONE IS HARD AND HEALED - PROBABLY AN AUTOBRECCIA									
33 THIS ZONE IS NOT LIKELY A CONDUIT.									
11 29.45 G	1								
11 29.59 G	1								
11 29.90 G	1	11 5 C	2		72	188			
11 30.05 G	1						PART GC		
11 30.19 G	1						PART GC		
11 30.21 G	1						PART GC		
11 30.33 G	1	11 5 KC	3		33	64			
11 30.42 G	1								
33 30.47 - 30.60 SUGARY APLITE									
11 30.52 G	1	15M CH WHRE2			87	49	KNOCKED OPEN WITH HAMMER TO SE		
33 INSIDE - WELL PRESERVED ZONAL MINERAL INFILLING, WITH RUSTY HEMATITE ALONG									
33 THE FRACTURE WALLS, AND WHITE CALCITE DOWN THE CENTER. FRAC. IS VERY									
33 IRREGULAR, TAKING SHARP BENDS UP TO 90 DEGREES, AND CROSSING ALL EARLIER									
33 STRUCTURES. A MOST UNUSUAL FRAC - DUE TO SHAPE AND PRESENCE OF HEM. AT									
33 THIS DEPTH. MAY BE A PALEOCONDUIT AS SHOWN BY EARLY HEM. COATINGS.									
11 30.57 G	1						PART GC		
11 30.68 G	1	11 2 K	3		58	73	FAULT ZONE, 1IN WITH FINE CHL		
33 COMMINUTED GOUGE - LOOKS LIKE A REACTIVATED ZONE WITHIN LARGER CRUSH ZONE									
33 DESCRIBED ABOVE.									
11 30.70 G	1	1 15 C	1		73	148	BETA EST'D		
11 30.72 G	1						GC CONE		
11 30.82 G	1	1 1 5 CK	1		39	282			
11 30.89 G	1	11 5 CK	2		44	296			
11 30.94 G	1	11 3 KC	3		67	273			
11 31.00 G	1								
11 31.04 G	1	11 2 C	1		85	126			
33 END OF BOX 6									
33									
33 START OF BOX 7									
11 31.06 G	1						GC		
11 31.09 G	1	11 2 KC	2		45	350			
11 31.17 G	1	1 1 2 CK	1		65	124	CURVED AND EN ECHELON IN PART		
11 31.29 G	1	11 2 C	2		82	247			
11 31.29 G	1						GC		
11 31.41 G	1						GC		
11 31.46 G	1	1 13 KC	4		89	225			
11 31.48 G	1	11 2 CK	5		24	342	5 MM CRUSH ZONE WITH FINE CHL		
11 31.51 G	1						GC		
11 31.54 G	1	11 2 C	1		83	295			
11 31.67 G	1	11 4 KC			66	290	BORDER OF 1 CM CRUSH ZONE		
33 31.67 - 31.92 ANASTOMOSING LARGE CRUSH ZONE - LARGE AREAS OF MASSIVE CHL									
33 AND CALCITE PALE GREEN GOUGE WITH ANGULAR GRAN. FRAGS. - INDIVIDUAL									
33 THROUGH-GOING FRACS. LISTED BELOW. THIS IS HEALED AUTOBRECCIA AS ABOVE									
33 LARGE ZONE. CROSSCUT BY YOUNGER CAL/CHL FILLED FRACS.									
11 31.68 G	1								
11 31.71 G	1								
11 31.74 G	1	11 2 C	1		72	315			
11 31.81 G	1	11 2 C	1		83	315			
11 31.84 G	1	11 2 C	.5		80	315			
11 31.87 G	1	11 2 C	.3		84	307			
11 31.89 G	1	11 2 C	.5		69	308			
11 31.93 G	1	11 2 C	.5		81	307			
11 31.97 G	1	11 3 KC	5		79	25	3 MM WIDE FAULT ZONE		
11 32.08 G	1								
11 32.19 G	1	11 2 C	10		85	135	1 CM CRUSH ZONE VERY CALCITE RICH		
11 32.26 G	1	11 3 C	.5		68	247	OFFSETS LARGE CRUSH ZONE		
11 32.37 G	1						GC		
33 32.35 - 32.45 brecciated aplite dike in calcite matrix									
33 6 MM SHEAR ZONE WITH CHL AND CAL COATED REACTIVATED FRACTURES IN CENTER									
33 THIS ZONE OFFSETS A 3MM CALCITE FILLED FRACTURE (SO YOUNGER)									
11 32.63 G	1						GC		
11 32.69 G	1	1 1 2 HC	2		77	105	POSSIBLE CONDUIT - FAULT		
33 PLANE WITH SLICKS									
11 32.76 G	1	1 1 3 CK	3		76	105			
11 32.83 G	1								



Table C2 (continued)

11 33.08 G 1					
11 33.14 G 1	11 2	KC	2	82 311	
11 33.21 G 1	11 3	K	1	76 343	BETA EST'D
11 33.24 G 1	11 2	K	.3	69 214	
11 33.24 G 1	11 4	KC	1.5	72 342	
11 33.29 G 1	1 1 3	KCH	10	84 307	1 CM FAULT WITH SLICKS
11 33.32 G 1	1 1 3	HC	4	79 337	3 MM FAULT PLANE WITH SLICKS
33 POSSIBLE CONDUIT					
11 33.34 G 1	11 2	K	.5	72 334	
11 33.37 G 1	1 1 4	CK	1	67 326	
11 33.41 G 1	1 1 4	CK	.5	67 340	
11 33.49 G 1	11 2	C	.8	78 336	
11 33.54 G 1					
11 33.54 G 1	11 2	C		89 237	SHEAR JT.
11 33.63 G 1	11 2	KC	.5	89 315	
11 33.64 G 1	11 2	C	.8	60 15	
11 33.64 G 1					GC NO TM
11 33.72 G 1					"
11 33.74 G 1					"
11 33.81 G 1	11 3	HK	.8	49 999	
11 33.90 G 1	1 1 4	C	1	75 999	
11 33.99 G 1					TM
11 34.01 G 1					TM
11 34.10 G 1					NO TM
11 34.15 G 1					NO TM
11 34.39 G 1					GC TM
11 34.52 G 1	11 2	C	1	9 999	
33					
33 34.69 - 34.95 OK ORIENT.					
33					
11 34.69 G 1	11 3	CK	1.5	80 244	
11 34.80 G 1					
11 34.80 G 1	1 1 3	CK	2.5	74 135	
11 34.95 G 1	1 1 3	K	.8	60 135	BETA EST'D
33					
33 35.00 - 35.45 ADDED 110 TO OLD BETA BASED ON IP13 #2					
33					
11 35.00 G 1					
11 35.10 G 1	1 1 4	C	.3	73 301	
11 35.15 G 1					
11 35.19 G 1	11 3	K	.5	45 141	
11 35.30 G 1					
11 35.38 G 1	1 1 4	CS	.8	5 229	
11 35.41 G 1	1 1 3	HCH	1.5	70 315	CONDUIT?
11 35.45 G 1	11 2		.3	86 307	
11 35.45 G 1	11 1		.1	26 175	HAIRLINE TRACE, VY. SMOOTH
11 35.46 G 1					
11 35.47 G 1					GC NO TM
11 35.52 G 1					RUBBLE AND GC - NO TM
33					
33 35.72 - 35.79 ADDED 180 TO OLD BETA BASED ON IP13 #2					
33					
11 35.72 G 1	1 1 3			33 350	
11 35.73 G 1	1 1 2	K	3	68 79	FAULT ZONE 3 MM WITH FINE
33 ROCK FRAGMENTS IN GOUGE					
11 35.73 G 1					
11 35.76 G 1	1 1 4		.5	33 42	
11 35.79 G 1	11 2	K	.5	24 200	
11 35.79 G 1					GC TM
33					
33 35.83 - 36.28 ADDED 110 TO OLD BETA BASED ON IP13 #2					
33					
11 35.83 G 1	11 2	KC	.3	35 118	FINE TRACE
11 35.83 G 1	1 1 2	HCH	1	41 40	
11 35.87 G 1					GC TM
11 35.90 G 1					GC TM
11 35.95 G 1	1 1 3	CK	8	54 84	1 CM BRAIDED FAULT ZONE
33 WITH COMMUNUTED GOUGE					
11 36.05 G 1					
11 36.08 G 1	11 3	CK	6	50 81	8 MM BRITTLE FAULT ZONE
11 36.17 G 1					

Table C2 (continued)

11 36.19 G 1	11 3 K		27 49 SHEAR JT OR MINOR FAULT
11 36.22 G 1			
11 36.23 G 1	11 3 K	4	11 26 4 MM FAULT GOUGE
11 36.28 G 1			GC TM
11 36.32 G 1			GC NO TM
11 36.40 G 1			GC NO TM
11 36.40 G 1	11 2 K		38 999
11 36.42 G 1	11 2 K	.5	38 999 OFFSET BY NEXT FRACTURE
11 36.46 G 1	11 2 C	.5	12 999
11 36.46 G 1			NO TM
11 36.49 G 1	11 2 C	.3	12 999
11 36.49 G 1	11 3 K	2	55 999
11 36.52 G 1			GC TM
33 END OF BOX 7			
33			
33 START OF BOX 8			
33			
33 36.54 - 37.94 ORIENT. OK BASED ON IP14 #1			
33			
11 36.54 G 1	11 2 K	.8	72 145
11 36.58 G 1	11 2 CK	.8	84 162 EW ECHELON SHOWS LEFT. LA1 SENSE
11 36.61 G 1	11 2 K	.5	85 161
11 36.62 G 1			TM, WEDGE OF CORE MISSING
11 36.63 G 1	11 2 KC	.5	88 151
11 36.66 G 1	1 1 3 H		11 253 FLECS OF FEO
11 36.73 G 1			TM
11 36.78 G 1	11 3 CK	2.5	86 348 SHEAR JT
11 36.81 G 1	11 4 C		80 354 SHEAR JT
11 36.84 G 1	11 4 C	2.5	76 154 SHEAR JT - GOOD PHOTO SPECIMEN
11 36.92 G 1	11 3 KC	3	75 154 3 MM FAULT PLANE BRECCIA
11 36.93 G 1	11 3 C	2	76 154
11 36.95 G 1	1 1 3 KC	1	50 240
11 37.05 G 1	11 2 K	.5	86 352
11 37.09 G 1	1 1 3 KSC	.5	51 298
11 37.21 G 1	11 3 C	2.5	64 320 SHEAR JT
11 37.25 G 1	1 1 3 KC	1	87 143
11 37.30 G 1	11 2 C	.3	89 335
11 37.32 G 1	11 2 K	.5	86 339
11 37.36 G 1			GC TM
11 37.37 G 1	11 2 CK		84 161
11 37.46 G 1	11 2		86 348
11 37.55 G 1	1 1 3 KC	.5	89 151
11 37.57 G 1	1 1 2 CK	2	18 203
11 37.61 G 1			GC TM
11 37.69 G 1			GC TM
11 37.72 G 1	1 1 2 KCH	1	76 115
11 37.87 G 1	11 2 KC	2	88 109 SHEAR JT
11 37.88 G 1	11 2 KC	1.5	88 109 SHEAR JT
11 37.91 G 1	11 2 KC	2.5	85 117 BRAIDED ZONE
33 PEGMATITE DIKE 37.90- 37.96			
11 37.94 G 1			NO TM
11 37.96 G 1			GC NO TM
33			
33 37.96 -38.56 NO ORIENTATION POSSIBLE - IMPRESSIONS INCONCLUSIVE			
33			
11 38.03 G 1	11 2	.1	3 999 270
11 38.18 G 1	11 2	.5	21 999 270
11 38.24 G 1			GC TM
11 38.26 G 1	11 2	.2	20 999 320
11 38.31 G 1			GC TM
11 38.33 G 1			GC TM
11 38.33 G 1	11 2 KH	.5	9 999 260
11 38.47 G 1			GC TM
11 38.53 G 1			GC NO TM
11 38.54 G 1			GC TM
11 38.56 G 1			GC NO TM
33			
33 38.61 - 39.34 80 SUBTRACTED FROM OLD BETA BASED ON IP14 #3			
33			
11 38.61 G 1	11 2 KC	.8	82 139
11 38.69 G 1			GC TM

Table C2 (continued)

11 38.70 G 1					TM
11 38.86 G 1					
11 39.07 G 1 1 1 3 H	.3	6 135			
11 39.14 G 1 1 1 2 HM		62 258	MnO DENDRITES ON FRACTURE SURFACE		
11 39.17 G 1 1 1		86 117	POROUS; POSSIBLE CONDUIT		
11 39.21 G 1			GC TM		
11 39.27 G 1 1 1 3		6 202			
11 39.34 G 1			TM		
33					
33	TIE MARK MISMATCH LEAD TO WRONG BETA LINE DRAWN ON CORE				
33	39.35 - 39.81 SUBTRACTED 180 FROM OLD BETA				
33					
11 39.35 G 1 1 1 3 C	.5	44 27			
11 39.38 G 1			TM		
11 39.41 G 1			GC TM		
11 39.57 G 1 11 2 K	.5	71 256			
11 39.59 G 1 11 2 KCH	.8	23 66			
11 39.60 G 1			GC TM		
11 39.64 G 1 1 1 2 H	.3	51 298			
11 39.66 G 1			TM		
11 39.70 G 1 1 1 3 HC	1	66 33	CONDUIT?		
11 39.81 G 1			GC TM		
33					
33	NO ORIENTATION FROM 39.34 - 40.02 - IMPRESSION INCONCLUSIVE				
33					
11 39.84 G 1 11 2 KH	1.5	41 999	205 FAULT ZONE FROM 39.82-39.8		
11 39.86 G 1			GC TM		
11 39.90 G 1			GC TM		
11 39.91 G 1 11 2 K	.8	47 999	240		
11 39.92 G 1 11 2 K	.8	14 999	330		
11 39.98 G 1 11 2 KC	3	39 999	230 FAULT WITH POROUS GOUGE IS		
33	POSSIBLE CONDUIT				
11 39.99 G 1			TM		
11 39.99 G 1 11 2 KC	.8	30 999	220		
11 40.02 G 1					
11 40.02 G 1 11 3 K	8	48 999	220 8 MM BRITTLE BRECCIA - POROUS		
33	PROBABLE CONDUIT				
33					
33	40.02 - 42.22 ORIENT. OK BASED ON IP16 #1				
33					
11 40.04 G 1					
33	40.07-40.18 DENSE PARALLEL FRACTURE ZONE - INDIVIDUAL CHLORITE FILLED				
33	JTS SPACED 1-20 MM; SLIGHTLY BRAIDED - PRINCIPAL FRACS. REPORTED BELOW				
11 40.08 G 1 11 2 K	1	56 252			
11 40.09 G 1 11 3 K	3	33 217			
11 40.16 G 1 11 3 K	.8	24 232			
11 40.18 G 1 11 2 KH	1	38 216	POROUS FRAC. - CONDUIT?		
11 40.24 G 1 11 4 KH	.5	66 102			
11 40.28 G 1 1 1 5 HK	.8	27 220	BRIGHT RUST PATCHES ON SURFACE		
33	POSSIBLE CONDUIT				
33					
33	40.29-40.39 ANOTHER DENSE FRACTURE ZONE LIKE ABOVE - BRAIDED, HEALED,				
33	CHL-FILLED FRACS PARALLEL TO CONDUIT AT 40.28, SO WHOLE ZONE INTERPRETED				
33	TO HAVE BEEN (BE) A CONDUIT				
11 40.29 G 1 11 4 K	3	17 227			
11 40.38 G 1 11 4 K	1.5	19 245			
33	FINE COMMUNUTED ZONES IN ABOVE TWO FRACS.				
11 40.44 G 1 11 4 C	3	60 264			
11 40.51 G 1 11 4 KH	2.5	45 107			
11 40.58 G 1 1 1 3 C	.5	16 106			
11 40.63 G 1 1 1 2 K		28 261			
11 40.66 G 1			PART GC TM		
11 40.68 G 1 11 2 K	1	62 220			
11 40.77 G 1 11 2 C	.3	86 18			
11 40.81 G 1			TM		
11 40.84 G 1 11 2 KC	.3	55 212			
11 40.85 G 1			GC TM		
11 40.92 G 1			PART GC TM		
11 41.01 G 1			GC TM		
11 41.04 G 1			GC TM		
11 41.18 G 1			TM		

Table C2 (continued)

11 41.22	G 1	1 1 2	C	.5	51	10
11 41.25	G 1	1 1 2	CK	1	72	31
11 41.33	G 1	1 1 2	C		36	150
11 41.37	G 1	1 1 3	K	.5	53	262
11 41.42	G 1	1 1 2	KC	.5	52	243 TWO PARALLEL FRACS 3MM SPACED
11 41.46	G 1	1 1 4	CH	.3	41	127 OFFSETS CHL-FILLED FRACS
11 41.52	G 1	1 1 3	K	1	26	258 THIN BRECCIA
11 41.54	G 1	1 1 2	K	.5	48	242
11 41.56	G 1	1 1 2	KC	.8	37	238
11 41.57	G 1					RUBBLE ZONE
11 41.58	G 1	1 1 2	K	.3	26	254
11 41.60	G 1	1 1 3	KC	4	36	221 4 MM FAULT BRECCIA
33 41.63-41.67	CHLORITE RICH	FAULT ZONE				
11 41.64	G 1	1 1 2	K	3	38	235
11 41.68	G 1	1 1 5	KH		33	250 RUSTY FEO PATCHES
11 41.74	G 1	1 1 2	C	2	39	242
11 41.77	G 1	1 1 2	C	1.5	55	70
11 41.77	G 1	1 1 2	C	.1	31	999
11 41.81	G 1	1 1 3	CK	1	49	211
11 41.83	G 1	1 1 2	CH	.3	62	220 POROUS APERTURE
11 41.89	G 1	1 1 2	CH	.5	42	228
11 41.91	G 1	1 1 4	KCH	.5	53	229
11 41.97	G 1	1 1 2	C		32	187
33	END OF BOX 8					
33	START OF BOX 9					
11 42.04	G 1	1 1 3			38	166
11 42.05	G 1	1 1 2			68	215
11 42.09	G 1	1 1 3			41	5
11 42.16	G 1					GC TH
11 42.22	G 1	1 1 3	KH	.5	42	8
11 42.22	G 1					GC NO TH
33	NO ORIENTATION FROM 42.24 - 42.74					
33						
11 42.24	G 1	1 1 3	K	.3	30	999 135
11 42.26	G 1					TM
11 42.29	G 1					TM
11 42.31	G 1	1 1 2	KH	.5	60	999 290
11 42.31	G 1					TM
11 42.32	G 1	1 1 3	CK	.5	41	999 250
11 42.38	G 1	1 1 3	CK	.3	32	999 270
11 42.45	G 1	1 1 3	HK	.8	45	999 285
11 42.49	G 1	1 1 2	K	.5	46	999 300
11 42.51	G 1	1 1 2	C	.5	22	999 290
11 42.54	G 1	1 1 2	C	.5	25	999 235
11 42.57	G 1	1 1 2	KH	.8	41	999 210
11 42.60	G 1	1 1 5	C	.3	75	999 90
11 42.65	G 1	1 1 3	KH	.3	36	999 305
11 42.68	G 1	1 1 3	KC	.5	52	999 305
11 42.70	G 1	1 1 3	HK	.8	11	999 140
11 42.74	G 1	1 1 3	KH	.3	48	999 240
33 42.74 - 43.69	INDUCED RUBBLE, CORE FRAGS AND OVERCORED STUBS - NO					
33	ORIENTATIONS POSSIBLE					
33						
33	END OF BQ3 DRILLING AT 42.8M; START OF BQ2 DRILLING DOWN TO B.O.H.					
33	NOTICABLE IMPROVEMENT OF CORE RECOVERY AND LESS GROUND CORE					
11 43.69	G 1	1 1 5	HC	.3	72	321
11 43.75	G 1	1 1 3	C	.3	77	272 POROUS APERTURE - CONDUIT?
11 43.79	G 1	1 1 2	C	.3	76	286
11 43.85	G 1	1 1 2	K	.8	84	322
11 43.89	G 1					
11 43.92	G 1	1 1 2	CH	.3	88	331
11 43.94	G 1	1 1 1	K	10	82	322 1 CM FAULT ZONE HEALED
11 44.01	G 1	1 1 2	HK	.8	76	332
11 44.05	G 1	1 1 2	K	.8	70	315
11 44.07	G 1					TM
11 44.08	G 1					TM
11 44.11	G 1	1 1 3	CK	.3	61	299
11 44.14	G 1	1 1 4			41	196
11 44.24	G 1	1 1 5	K	.2	55	283

Table C2 (continued)

11 44.28 G 1	11 3 C	.1	78 329
11 44.32 G 1	11 3 KC	.3	89 280 BRAIDED FRACS IN 5MM ZONE THAT
33 SEEMS TIGHT - NOT LIKELY CONDUIT			
11 44.37 G 1	11 2 C	.3	59 339
11 44.51 G 1	11 2 C		75 328
11 44.60 G 1	11 3 C	1	62 345
11 44.65 G 1	11 2 KC	.5	88 151
11 44.67 G 1	11 2 CK	.3	86 322
11 44.75 G 1	11 3 CKE	5	73 104 POROUS ZONE 5 MM - CONDUIT?
11 44.93 G 1	11 3 C	.8	52 309
11 45.13 G 1	11 3 CH	1	72 328 BETA EST'D
11 45.19 G 1	11 1 K	.3	85 322
11 45.23 G 1	11 1	.3	86 161
11 45.32 G 1	11 2 QC	3	85 152
11 45.34 G 1			TM
11 45.36 G 1	11 2 KC	.3	73 114 LOWER BOUND OF 1 CM BRITTLE F.
11 45.40 G 1	11 1 KC	1	89 156
11 45.50 G 1	11 2 KE	.5	73 350
11 45.52 G 1	11 1 KEC	8	80 341 BORDER OF 8 MM BRITTLE CRUSH ZONE
11 45.54 G 1	11 2 KM	.5	67 5
11 45.57 G 1	11 2 K	.8	83 351
11 45.65 G 1	11 3	1	84 143 8 MM BRAIDED FRACTURE ZONE
11 45.68 G 1	11 13	.5	75 144
11 45.90 G 1	11 2 C	.3	78 135
11 46.08 G 1	11 13 CH	.5	76 12
33 FRAC AT 46.12 HAS NO ALPHA ANGLE			
11 46.27 G 1			TM
11 46.31 G 1	11 12 CMH	2.5	57 111 APPROX. CENTER OF AXIAL FRACTURE
33 DENDRITES ABUNDANT ON SURFACE SHOWS OXYGENATED WATERS DESCEND TO THIS DEPTH			
11 46.38 G 1	11 3 K	.5	77 336
11 46.50 G 1	11 2 K	.3	85 6
11 46.57 G 1	11 2 K	.2	67 333
11 46.66 G 1			TM
11 46.67 G 1	11 3 CK	1	78 116
11 46.86 G 1	11 2 KC	.2	78 340
11 46.87 G 1	11 3 C	.2	73 335
11 46.91 G 1	11 3 KM	1	81 125
11 46.96 G 1			TM
11 47.02 G 1	11 2 HK	.3	78 349
11 47.07 G 1	11 2 K	.2	53 344
11 47.09 G 1	11 2		85 122 8 MM CRUSHED ZONE
11 47.14 G 1			TM GC
11 47.25 G 1	11 2 K	.8	87 109
11 47.38 G 1	11 3 CH	1.5	89 344
11 47.38 G 1			TM
33 END OF BOX 9			
33			
33 START OF BOX 10			
11 47.43 G 1	11 3 K	1	51 10
11 47.48 G 1	11 4 K	.8	82 172
11 47.50 G 1	11 13 KC	4	62 331 DIFFUSE GREEN HALO
11 47.55 G 1	11 2 KC	1.5	84 143
11 47.56 G 1			TM
11 47.59 G 1	11 3 CK	1	76 139 BRAIDED THIN JOINTS
11 47.65 G 1	11 4 C	1.5	86 143
11 47.69 G 1	11 2 C	1	79 337
11 47.76 G 1	11 3 K	.5	80 153
11 47.82 G 1			TM
11 47.82 G 1	11 3 KH	1	36 85 DIFFUSE RUSTY GREEN JTS.
11 47.86 G 1	11 2 KC	2.5	85 7
11 47.98 G 1	11 4 CKH	1.5	79 337 FAULT PLANE WITH SLICKS
33 PERPENDICULAR TO AXIS - CONDUIT?			
33 47.08 - 47.17 MICROGRANITE DIKE WITH DARK MIN. CONCENTRATIONS AT BORDERS			
33 FRACS. AT BOTTOM BORDER OF ZONE			
11 48.20 G 1	11 2 CK	1	71 13 FAULT PLANE WITH 1.5 CM HALO
11 48.25 G 1	11 4 C	1.5	33 227
11 48.31 G 1	11 2 C	.1	76 352
11 48.41 G 1	11 12 C	.5	89 340
11 48.54 G 1	11 2 C	1.5	74 343
11 48.66 G 1	11 2 HK	.5	88 298 BRAIDED 5 MM FRAC. ZONE
11 48.72 G 1	11 2 CK	.2	89 340

Table C2 (continued)

11 48.81 G 1	1 1 2 C	.5	33 205 SLICKS
11 48.93 G 1	11 2 K	.1	62 1
11 49.08 G 1	1 1 3 KH	.5	65 283 RUSTY SPOTS
11 49.16 G 1	11 3 K	4	64 335 NARROW FAULT PLANE, 4 MM BRECC
11 49.20 G 1	11 1 K	.1	79 345
11 49.24 G 1	11 2 K		84 338 SHEAR JT.
33 49.17 - 49.22 APLITE DIKE CUT BY MINOR FAULTS AND SHEAR JTS.			
11 49.32 G 1	11 2 K	.1	83 338
11 49.36 G 1	1 1 3 CK	1.5	73 335
11 49.43 G 1	11 2 K	.1	83 330
11 49.54 G 1	11 2 KH	1	81 337 VY. PLANAR JT
11 49.60 G 1	11 2 KC	.5	84 152
11 49.66 G 1	1 1 3 CK	.4	80 341
11 49.76 G 1	11 3 C	.1	87 353
11 49.80 G 1	11 2 CK	.5	87 180
11 49.89 G 1	11 2 K	.5	68 348 3 MM CHL HALO
11 49.92 G 1	11 2 KC	.5	80 173
11 49.93 G 1	11 3 KC	.2	81 172 BRAIDED OVER 3 MM ZONE
11 49.98 G 1	11 2 HK	.5	50 95 1 CM HALO OF BLOOD RED (Fe?) MINERAL
11 50.05 G 1	1 1 3 HC	3	84 171 CONSPICUOUS POROUS CONDUIT
11 50.24 G 1	1 1 2 CHK	.5	83 152
11 50.34 G 1	11 2 H	1	47 148 8 MM BLOOD RED MEM. ZONE
11 50.41 G 1	1 1 3 HC	.2	81 337
11 50.43 G 1	1 1 3 KCH	.5	41 229
33 50.49 - 50.52 MISSING CORE - PRESUMED WASHED OUT DURING DRILLING			
11 50.52 G 1			GC
11 50.52 G 1	11 2 KH	.5	85 130
11 50.59 G 1	1 15 CH	1	59 312 HEM-CAL-HEM LAYERED INFILLING
11 50.67 G 1	11 2 HCH	2	89 344
11 50.71 G 1	11 2 KH	.5	85 334
11 50.75 G 1	1 1 3 KHC		72 63 DIFFUSE RUSTY GREEN HALO
11 50.77 G 1	11 2 C		76 149
11 50.79 G 1	1 15 HC	1.5	84 318
11 50.80 G 1	11 3 HC	.2	85 122
11 50.94 G 1	11 3 CK	3	75 139
11 50.96 G 1	11 1 KC	.2	84 311
11 50.98 G 1	11 1 KC	.1	84 311
11 51.03 G 1	11 2 KC	.3	84 318
11 51.09 G 1	1 1 2 CK	.5	42 171
11 51.13 G 1	11 2 C	2	65 135
11 51.15 G 1	11 2 KC	1	87 160
11 51.19 G 1	11 2 KC	.1	72 338
11 51.21 G 1	11 2 K	.2	75 339
11 51.28 G 1	1 1 3 KC	.8	74 318 5 MM BRAIDED ZONE
11 51.33 G 1	11 4 KC	1	86 318
11 51.41 G 1	11 2 K	.2	84 311 5 MM BRAIDED ZONE
11 51.42 G 1	1 1 3 HK	.2	15 220
11 51.44 G 1	1 1 3 C	.5	14 235
11 51.51 G 1	11 2 K	.3	84 318
11 51.56 G 1	11 2 K	.2	88 143
11 51.56 G 1	1 13	10	79 56 1 CM HEALED CRUSH ZONE PARA.
11 51.66 G 1	1 1 3	2	2 227
33 51.66 - 52.30 MISSING CORE - NO RUBBLE - PRESUMED A LOST STICK, SINCE THERE			
33 IS A GAP IN CORE BOX. REFERENCE LINE DRAWN ACROSS GAP BASED ON SIMILARITY			
33 OF DOMINANT FRACTURE ORIENTATIONS ON EITHER SIDE.			
11 52.36 G 1	11 3 KC	1.5	80 139
11 52.44 G 1	11 2 C	.2	88 302
11 52.58 G 1	11 3 K	.5	80 296 DIFFUSE CHL. HALO
11 52.63 G 1	11 2 KC	.5	85 126
11 52.77 G 1	11 2 K	.5	81 341
11 52.80 G 1	1 1 4 C	1	74 318
33 END OF BOX 10			
33			
33 start OF BOX 11			
11 52.90 G 1	11 3 KC	8	74 52 HEALED FAULT 8 MM
11 53.05 G 1	11 2 K	.5	82 130
11 53.07 G 1	1 1 4 C	.5	63 328
11 53.10 G 1	11 3 KC	2	87 3 BRITTLE FRACTURE ZONE BRAIDED
11 53.22 G 1	11 4 K	3	69 119 SHEAR JT
11 53.28 G 1	11 2 K	.1	76 120
11 53.30 G 1	11 3 KC	3	88 315

Table C2 (continued)

11 53.31 G 1				TM	
11 53.37 G 1	11 2 K	2.5	86 139	DIFFUSE BRN-PURP ZONE	
11 53.38 G 1	11 3 K	3	80 139	LARGE QTZ XTAL OFFSET BY JT.	
11 53.47 G 1	11 3		82 126		
11 53.73 G 1	11 2 K	1	78 139		
11 53.79 G 1	11 2		61 214		
11 53.84 G 1	11 3 KCH	.5	61 221		
11 53.96 M 1	11 4 C	.5	24 255		
11 54.06 M 1	11 3 C	4	70 129	BRITTLE BRAIDED FRAC. ZONE	
11 54.15 M 1	11 2 K	.5	76 120		
11 54.20 M 1			TM		
11 54.27 M 1	11 3		39 157		
11 54.48 M 1	11 2		58 217		
11 54.53 M 1	11 2		84 356		
11 54.55 M 1	11 2 CH		21 280		
11 54.81 M 1	11 2		46 55	DIFFUSE PALE GREEN 3 MM ZONE	
33 HEALED					
11 54.89 M 1	11 2 CH	2	64 19		
11 54.90 M 1	11 2 CK	.3	42 187		
11 54.92 M 1	11 3 KH	.3	24 229		
11 54.96 M 1	11 2 K	.5	85 139		
11 55.00 M 1	11 2 K	.5	61 228		
11 55.14 M 1	11 2 K	.2	65 129		
11 55.14 M 1	11 2 KH		44 142		
11 55.31 M 1	11 3 K	.2	74 120		
11 55.31 M 1	11 5 KH	.5	58 66	RAGGED BRITTLE BRECCIA ZONE UP	
33 1 CM - TRUNCATES MANY SMALLER JTS. ALONG HALF OF CORE - POROUS APERTURE					
33 LOOKS LIKE CONDUIT					
11 55.51 M 1	11 15 Q	2	76 251		
11 55.60 M 1	11 2 QKC		66 279		
11 55.63 M 1	11 3 K	.3	64 275		
11 55.64 M 1	11 2 K	.5	71 261		
11 55.66 M 1	11 2 CK	1.5	39 282		
11 55.69 M 1	11 2 K	1	47 264	BRAIDED 5 MM ZONE	
11 55.71 M 1	11 2 KH	.2	37 283		
11 55.73 M 1	11 2 KH	.5	40 274	BRAIDED 5 MM ZONE	
11 55.74 M 1	11 3 KH	.2	38 299		
11 55.75 M 1	11 2	.1	39 277		
11 55.78 M 1	11 2 K	.2	38 281		
11 55.83 M 1	11 2 KHC	.5	35 252		
11 55.90 M 1	11 5 KH	1	89 243		
11 56.10 M 1	11 2 K	.5	32 218		
11 56.18 M 1	11 3 K		77 139	BRITTLE FRAC. ZONE HEALED	
11 56.28 G 1	11 2 K	1	79 116	MEDIUM GRAINED GRANITE	
11 56.30 G 1	11 2 H	.3	83 326		
11 56.46 G 1			TM		
11 56.50 G 1	11 3 K	1	58 66		
11 56.68 G 1	11 1 QK	1	48 27		
11 56.73 G 1	11 2 Q	1	50 29	BRAIDED 5 MM ZONE	
11 56.78 G 1	11 3 C	.2	55 220		
11 56.80 G 1	11 3 K	1.5	65 359		
11 56.87 G 1			TM		
11 56.93 G 1	11 2 K	.3	57 331		
11 56.95 G 1			TM		
11 56.95 G 1	11 3 Q	3	82 0	FILLED SHEAR JT.	
11 56.98 G 1	11 3 QK	2.5	86 13	SHEAR JT. HEALED	
11 57.06 G 1	11 5 CH	1	31 244		
11 57.16 G 1	11 3 CH	1.5	72 135	POROUS FRACTURES SPLIT IN 2	
33 SPLAYS WITHIN CORE					
11 57.24 G 1	11 2 Q	1	78 168	SHEAR JT.	
11 57.26 G 1	11 3 H	1	84 322	POROUS - LIKELY CONDUIT	
11 57.36 G 1	11 3 CHK	.8	80 337		
11 57.60 G 1	11 2 C	.3	71 349		
11 57.69 G 1	11 2		88 344		
11 57.73 G 1	11 3 H	3	89 160	DIFFUSE ORANGE HALO ZONE	
11 57.83 G 1	11 2 KC		82 0		
11 57.90 G 1	11 3 KCQ	1	78 2	SHEAR JT.	
11 58.06 G 1	11 3 CK	1	75 11	SHEAR JT.	
11 58.15 G 1	11 15 C	.5	44 322		
11 58.18 G 1	11 2 C	.2	76 350		
11 58.46 G 1	11 1 CH	.2	65 350		

Table C2 (continued)

11 58.51 G 1 11 3 HK	5	77 154 5MM FAULT BRECCIA ZONE
11 58.54 G 1 1 1 4 HCK	1	63 30 SLICKS ON FAULT PLANE
33 END OF BOX 11		
33		
33 START OF BOX 12		
11 58.62 G 1 11 2 C	.2	51 60
11 58.91 G 1 11 2 KC	.1	50 353
11 59.06 G 1 11 2 C	.3	24 54
11 59.15 G 1 11 4 C	.1	85 246
11 59.15 G 1 11 2 C	1	73 254
11 59.17 G 1 11 2 C	.5	25 58
11 59.22 G 1 11 2 CKH	.5	88 179 3 MM ZONE OF MICROFRACTURES
11 59.26 G 1 11 2 CK	1.5	60 34 SHEAR JT.
11 59.27 G 1 11 2 CK	.2	51 17
11 59.31 G 1 11 2 CK	1	89 179
11 59.44 G 1 11 3 K	.5	80 349
11 59.46 G 1 1 1 4		44 269
11 59.48 G 1 1 1 2 KC	.5	75 181 FRAC. ZONE 1 CM WIDE
11 59.54 G 1 11 2 KCL	1.5	79 349
11 59.57 G 1 11 2 KL	.1	89 3
11 59.63 G 1 11 2 C	1	87 3
11 59.74 G 1 1 14 KC	4	71 171 BRAIDED FRAC. ZONE UP TO 2 CM
33 HEALED		
11 59.84 G 1 11 2 C	.1	58 250
11 59.88 G 1 1 1 C	.3	73 181
11 59.96 G 1 11 2 C	1.3	85 352 SHEAR JT.
11 60.02 G 1 11 2 C	1	89 179 SHEAR JT. WITH LENSOIDAL INFILL
11 60.06 G 1 11 2 C	.2	51 346
11 60.09 G 1 11 2 C	.1	51 354 SHEAR JT.
11 60.09 G 1 11 2 C	.1	83 82
11 60.13 G 1 11 2 C	1	50 353 SHEAR JT. WITH EN ECHELON SPLAYS
11 60.21 G 1 11 3 KC	1	82 326
11 60.28 G 1 1 1 2 C	.5	48 256
11 60.33 G 1 11 2 CK	.1	83 157
11 60.58 G 1 1 1 K	1	43 127 FINE SPLAYS
11 60.60 G 1		TM
11 60.62 G 1 11 2 CK	1	13 151
11 60.65 G 1 11 5 CK	1	78 344
11 60.72 G 1 11 2 CK	1.5	86 348
11 60.79 G 1		
11 60.81 G 1 11 2 KC	.5	47 64
11 60.81 G 1 11 3 C	.5	80 168
11 60.97 G 1 11 3 K	.3	50 30 PARALLEL MICROCRACKS
11 60.99 G 1		
33 BOTTOM OF BOREHOLE H4.		



## APPENDIX D

### Method for Correction of Orientation Bias in Fracture Surveys in the Seal Cove River Valley

#### 1. Introduction

Terzaghi (1965) described a type of orientation bias in fracture surveys where fractures are less and less well-sampled as the angle between a fracture and the sampling line (borehole or scanline) decreases. Where such angles are small (about  $25^\circ$  or less), fractures are not likely to be adequately sampled at all. On a stereoplot of fracture poles, the region from about  $65^\circ$  to  $115^\circ$  away from the point representing the sampling line is thus referred to as a blind zone. Terzaghi suggested that fractures outside of a blind zone can be corrected for orientation bias (i.e. fracture abundances increased over actual counts) using a cosine weighting function. This approach assumes that fractures which are coplanar with those actually measured also occur beyond the ends of the sampling line. This is reasonable for the regular fracture sets in granite in the SCR, at least on the sampling scale of several tens of meters. The Terzaghi correction was implemented in this study using a FORTRAN computer code (TERZAGHI). This code is a revised version of an unpublished code, written and developed by the author in collaboration with Mr. R. MacLeod and Dr. J. Gale.

#### 2. Description of FORTRAN code TERZAGHI

The Terzaghi correction is implemented in the code TERZAGHI by a three-step process. Firstly, an equal-angle stereoplot is subdivided into sectors,

each  $10^\circ$  in azimuth by  $10^\circ$  in inclination, to form segmented rings emanating from the point representing the sample line and extending to  $70^\circ$  away from the sampling line (i.e. to within the blind zone). Secondly, poles to measured fractures within a given sector are counted, and new fracture poles are generated for that sector based on this count and the cosine of the mean angle between poles to measured fractures and the sample line. Thirdly, the new fractures are assigned orientations corresponding with the mean orientation of measured fractures in that sector.

In practice, very few measured fractures occur in the blind zone. Thus, while the cosine weighting factor mathematically increases as the angle away from the sample line increases, the diminishing number of measured "seed" fractures means that the number of new fractures generated by the correction algorithm actually drops off to nil around the blind zone limits. A complete listing of the code is given in Table D1.

Table D1 - Listing of FORTRAN code "TERZAGHI" used for implementing the Terzaghi orientation bias correction

```

C-----
C   "TERZAGHI"
C
C   FORTRAN CODE FOR IMPLEMENTING CORRECTION FOR
C   ORIENTATION BIAS IN FRACTURE SAMPLING SURVEYS
C   (AFTER TERZAGHI, 1965)
C-----
C
C DESCRIPTION OF VARIABLES AND TERMS (IN ORDER OF APPEARANCE IN CODE):
C
C HTREND: TREND OF SAMPLING LINE, AZIMUTH 0-360 DEG.
C HPLUNG: PLUNGE OF SAMPLING LINE, INCLINATION 0-90 DEG.
C CLEN(): DISTANCE WHERE FRACTURE CROSSES SAMPLE LINE
C CDIPD(): DIP DIRECTION OF MEASURED FRACTURE, AZIMUTH 0-360 DEG.
C CDIP(): DIP ANGLE OF MEASURED FRACTURE, INCLINATION 0-90 DEG.
C POLEAZ(): TREND OF POLE TO A FRACTURE, AZIMUTH 0-360 DEG.
C POLEPL(): PLUNGE OF POLE TO A FRACTURE, INCLINATION 0-90 DEG.
C PH,QH,RH: DIRECTION COSINES OF THE SAMPLE LINE
C PF,QF,RF: DIRECTION COSINES OF A POLE TO A FRACTURE
C ALPHA(): ANGLE (RADIAN) BETWEEN SAMPLE LINE AND FRACTURE POLE
C NUMDAT: NUMBER OF MEASURED FRACTURES (IN INPUT FILE)
C SECTALPHA(): ALPHA ANGLE OF A FRACTURE IN A SECTOR
C SECTPOLEAZ(): AZIMUTH OF A FRACTURE POLE IN A SECTOR
C SECTPOLEPL(): PLUNGE OF A FRACTURE POLE IN A SECTOR
C NSECTFRAC: NUMBER OF MEASURED FRACTURES IN A SECTOR
C AZSUM: SUM OF AZIMUTHS FOR FRACTURE POLES IN A SECTOR
C PLSUM: SUM OF PLUNGES FOR FRACTURE POLES IN A SECTOR
C ALPHASUM: SUM OF ALPHA ANGLES FOR FRACTURES IN A SECTOR
C MEANALPHA: MEAN ALPHA ANGLE FOR FRACTURES IN A SECTOR
C MEANSECTAZ: MEAN AZIMUTH FOR FRACTURE POLES IN A SECTOR
C MEANSECTPL: MEAN PLUNGE FOR FRACTURE POLES IN A SECTOR
C NTERZ: CALCULATED NUMBER (REAL) OF FRACTURES IN A SECTOR AFTER
C   TERZAGHI CORRECTION
C NTERZINT: NTERZ VALUE ROUNDED TO INTEGER
C NEWNUM: NUMBER OF NEW FRACTURES ADDED TO A SECTOR AFTER CORRECTION
C ALPHADEG(): ALPHA ANGLE IN DEGREES FOR MEASURED AND NEW FRACTURES
C   INCLUDED IN OUTPUT FILE
C-----
C DECLARATION STATEMENTS
C
C   CHARACTER*80 FILE1,FILE2,ACARD
C   INTEGER AZSUM,PLSUM,MEANSECTAZ,MEANSECTPL,HTREND,HPLUNG,
C   INTEGER CDIPD(1000),CDIP(1000),POLEAZ(1000),NUMDAT,ALPHASUM
C   INTEGER POLEPL(1000),SECTPOLEPL(1000),SECTPOLEAZ(1000),NTERZINT
C   REAL CLEN(1000),ALPHA(1000),ALPHADEG(1000),SECTALPHA(1000)
C   REAL PH,QH,RH,PF,QF,RF,MEANALPHA,NTERZ
C 1 FORMAT (A40)
C
C   WRITE (6,*)
C   WRITE (6,*) ' TYPE INPUT DATA FILE TO BE CORRECTED'
C   READ(5,1) FILE1
C   OPEN (UNIT=10,FILE=FILE1,STATUS='OLD')
C   WRITE (6,*)
C
C   WRITE (6,*) ' TYPE NAME OF OUTPUT FILE TO BE CREATED'
C   READ (5,1) FILE2
C   OPEN (UNIT=11,FILE=FILE2,STATUS='NEW',CARRIAGECONTROL='LIST')
C   WRITE(6,*)
C
C   WRITE (6,*) ' TYPE TREND OF SAMPLE LINE; 0-360 DEG. (INTEGER)'
C   READ (5,*) HTREND
C   WRITE (6,*)

```

```

C      WRITE (6,*) ' TYPE PLUNGE OF SAMPLE LINE; 0-90 DEG. (INTEGER)'
      READ (5,*) HPLUNG
      WRITE (6,*)
C
C READ IN DATA AND COUNT NUMBER OF FRACTURES
C
      I=1
      8 READ (10,1) TITLE
      READ (10,1) TITLE
      5 READ (10,40,END=25) CLEN(I), CDIPD(I), CDIP(I)
      40 FORMAT (F7.2,5X,I4,1X,I3)
      POLEAZ(I) = 180 + CDIPD(I)
      IF (POLEAZ(I).GE.360) THEN
        POLEAZ(I) = POLEAZ(I) - 360
      END IF
      POLEPL(I) = 90 - CDIP(I)
      I=I+1
      GO TO 5
C
C      COMPUTE DIRECTION COSINES (PH,QH,RH) OF SAMPLE LINE
C
      25 RAD = 57.2957795
      PH = COS(HTREND/RAD)*COS(HPLUNG/RAD)
      QH = SIN(HTREND/RAD)*COS(HPLUNG/RAD)
      RH = SIN(HPLUNG/RAD)
C
C      COMPUTE DIRECTION COSINES AND ALPHA ANGLES FOR EACH FRACTURE POLE
C
      DO J=1,I-1
C
C      COMPUTE DIRECTION COSINES FOR POLE TO FRACTURE PLANE
C
      PF = COS(CDIPD(J)/RAD)*COS((CDIP(J)-90)/RAD)
      QF = SIN(CDIPD(J)/RAD)*COS((CDIP(J)-90)/RAD)
      RF = SIN((CDIP(J)-90)/RAD)
C
C      COMPUTE ALPHA ANGLE BETWEEN SAMPLE LINE AND FRACTURE POLE
C
      ALPHA(J) = ACOS((PH*PF)+(QH*QF)+(RH*RF))
      ALPHA(J) = 3.14159 - ALPHA(J)
      END DO
C
C      DO LOOP TO DEFINE 10X10 DEGREE SECTORS
C
      NUMDAT = I-1
      DO JJ=0,350,10
      DO J=0,70,10
C
C      COUNT FRACTURES IN SECTORS AND PUT IN WORKING ARRAY, i.e. SECT*(L)
C      FIRST ZERO SECTALPHA, SECTPOLEPL AND SECTPOLEAZ VALUES
C
      DO KK = 1, NUMDAT
        SECTALPHA(KK) = 0.
        SECTPOLEAZ(KK) = 0
        SECTPOLEPL(KK) = 0
      END DO
      NSECTFRAC = 0
C
      L = 1
      DO K = 1, NUMDAT
        IF((POLEAZ(K).GE.JJ).AND.(POLEAZ(K).LT.JJ+10).AND.
          *(POLEPL(K).GE.J).AND.(POLEPL(K).LT.J+10).AND.
          *(ALPHA(K).LE.1.22173047)) THEN
          SECTALPHA(L) = ALPHA(K)
          SECTPOLEPL(L) = POLEPL(K)
          SECTPOLEAZ(L) = POLEAZ(K)
C
C          L = L + 1
        END IF
      END DO
      NSECTFRAC = L-1

```

```

C
C IF NO FRACTURES IN SECTOR, MOVE ON TO NEXT SECTOR
C
C   IF (NSECTFRAC.LE.0) THEN
C     GO TO 35
C   END IF
C
C CALCULATE MEAN ALPHA ANGLE, MEAN POLE AZ. AND
C PLUNGE IN SECTOR. FIRST ZERO TERMS.
C
C   AZSUM = 0
C   PLSUM = 0
C   ALPHASUM = 0.
C   MEANSECTAZ = 0
C   MEANSECTPL = 0
C   DO M = 1, L-1
C     ALPHASUM = ALPHASUM + SECTALPHA(M)
C     AZSUM = AZSUM + SECTPOLEAZ(M)
C     PLSUM = PLSUM + SECTPOLEPL(M)
C   END DO
C   MEANALPHA = ALPHASUM/NSECTFRAC
C   MEANSECTAZ = AZSUM/NSECTFRAC
C   MEANSECTPL = PLSUM/NSECTFRAC
C
C CALCULATE TERZAGHI CORRECTION AND NUMBER OF NEW FRACTURES IN SECTOR
C
C   NEWNUM = 0
C   NTERZ = NSECTFRAC/COS(MEANALPHA)
C   NTERZINT = ABS(JNINT(NTERZ))
C   NEWNUM = NTERZINT - NSECTFRAC
C
C IF NO NEW FRACTURES GENERATED, GO ON TO NEXT SECTOR
C
C   IF (NEWNUM.EQ.0) THEN
C     GO TO 35
C   END IF
C
C ASSIGN NEW FRACTURES TO MEAN POLE LOCATION IN SECTOR
C
C   DO M = 1, NEWNUM
C     CDIPD(1) = MEANSECTAZ + 180
C     IF (CDIPD(1).GE.360) THEN
C       CDIPD(1) = CDIPD(1) - 360
C     END IF
C     CDIP(1) = 90 - MEANSECTPL
C     ALPHA(1) = MEANALPHA
C     I = I+1
C   END DO
C
C CONTINUE ON TO NEXT SECTOR UNTIL ALL ARE PROCESSED
C
C 35 CONTINUE
C   END DO
C   END DO
C
C WRITE OUT FINAL EXPANDED DATA SET
C
C   DO N = 1, I-1
C     ALPHADEG(N) = ALPHA(N)*RAD
C     WRITE (11,200) CLEN(N),CDIPD(N),CDIP(N),ALPHADEG(N)
C     WRITE (6,*)
C   END DO
C
C 100 CONTINUE
C
C 200 FORMAT (F7.2,1X,14,1X,13,1X,F5.1)
C
C   STOP
C   END
C-----

```

## APPENDIX E

### Injection Testing in the Seal Cove River Valley - Procedures and Results

#### 1. Introduction

Bedrock permeabilities in the SCRIV were determined using constant head injection tests in boreholes M1, M2, M3 and H2, and using falling head injection tests in boreholes H4 and M2. Hole H3 was not tested due to caving hole conditions. All tests were conducted in the fall of 1985 or the summer of 1986 in open holes prior to instrumentation with multilevel piezometers. Water from the stream reach was used for injection testing for all but the upper parts of borehole H4, where pre-pumped groundwater was used.

#### 2. Procedures

##### Constant head injection tests

Constant head injection testing involved isolating a test interval within a borehole with two pneumatic packers (Figure E1), then injecting water into the packed off interval (and hence the rock mass between the packers) from a calibrated pressure tank at the surface. Manometers terminating within (P2) and below (P1) the test interval were used to monitor injection head stability and interaction with untested deeper portions of the hole. A series of tests, each lasting 5-15 minutes, were conducted at each interval using nominal pressures of 0 MPa, 0.138 Mpa (20 psi), 0.276 MPa (40 psi) and 0.414 MPa (60 psi) applied to the pressure tank using compressed nitrogen. For each test, average flow rate from the tank was measured, and the hydraulic head of the injected water was determined from the difference of injection interval pressure and stabilized shut-in

pressure. Equivalent porous media hydraulic conductivity over the test interval was calculated using the following equation for constant head flow from a well (ISRM, 1977):

$$K = Q \cdot (\ln r_e - \ln r_w) / h_i \cdot L \cdot 2\pi$$

where,  $K$  = equivalent porous media hydraulic conductivity [ $L/T$ ],  $Q$  = flow rate from the pressure tank [ $L^3/T$ ],  $r_e$  = effective radius of flow into the rock mass [ $L$ ] (assumed to be 5 m),  $r_w$  = borehole radius [ $L$ ],  $h_i$  = hydraulic head of injected water [ $L$ ], and  $L$  = vertical length of injection test interval [ $L$ ].

#### Falling head injection tests

Falling head injection testing involved isolating a test interval within a borehole with two pneumatic packers mounted on a mandrel string of 19 mm (0.75 inch) I.D. steel pipe (Figure E2), then injecting water into the packed off interval (and hence the rock mass between the packers) from calibrated falling head tanks at the surface through the mandrel. This gravity-driven, passive system does not require heavy pressure tanks or nitrogen cylinders and was selected for testing in H4 because of difficult access to that site. A custom-made mechanical in-line valve for this system (Figure E2) was designed to start and stop flow, by manually pushing down or pulling up on the mandrel at the surface, without generating any substantial pressure transients in the test cavity during opening or closing. This ensured that early time data were usable in the falling head tests.

The tests were conducted according to the following steps:

- 1) shut-in hydraulic head ( $h_s$ ) was determined by measuring stabilized water level within the mandrel;

2) a calibrated falling head tank was connected to the top of the mandrel (in-line valve closed) and both mandrel and tank were filled with water;

3) the in-line valve was opened and the drop in excess head ( $h_e$ ) with time was measured (the components of  $h_e$  are shown in Figure 1E2).

Tanks of several sizes were available. The appropriate tank was selected (by trial and error) so that tests lasted approximately 5-15 minutes. Values of excess head and their corresponding times, early and late in the test, were used to determine equivalent porous media hydraulic conductivity over the test interval using the following equation for falling head flow from a well (ISRM, 1977):

$$K = \{ \ln(h_e^0/h_e^1) * (r_f)^2 * \ln(r_e/r_w) \} / \{ (t^1 - t^0) * 2L \}$$

where,  $K$  = equivalent porous media hydraulic conductivity [ $L/T$ ],  $h_e^0$  and  $h_e^1$  = early and late excess heads, respectively [ $L$ ],  $r_f$  = radius of calibrated falling head tank [ $L$ ],  $r_e$  = effective radius of flow into the rock mass [ $L$ ] (assumed to be 5 m),  $r_w$  = borehole radius [ $L$ ],  $t^0$  and  $t^1$  = early and late times [ $T$ ] corresponding with  $h_e^0$  and  $h_e^1$ ,  $L$  = vertical length of test interval [ $L$ ].

Intrinsic permeability values were calculated from both constant head and falling head hydraulic conductivity values using the equation (Freeze and Cherry, 1979)  $k = K * \mu / \gamma$ , where,  $k$  = intrinsic permeability [ $L^2$ ],  $K$  = equivalent porous media hydraulic conductivity [ $L/T$ ],  $\mu$  = fluid dynamic viscosity [ $M/LT$ ],  $\gamma$  = fluid unit weight [ $M/T^2L^2$ ]. For typical groundwater temperatures in the SCRV during the test periods (10° C),  $\mu = 1.307 \text{ E-3 Pa-s}$  and  $\gamma = 9804 \text{ N/m}^3$ , so that  $k [\text{m}^2] = K [\text{m/s}] * 1.333 \text{ E-7}$ .



### 3. Results

Tables E1 - E5 present injection test data for boreholes M1, M2, M3, H2 and H4, respectively. The data were stored as ASCII computer data files for ease of manipulation and transfer between computer environments.

The numbered lines in these tables contain the following information:

Line 99: General comments

Line 88: Location and reference data. For constant head tests, line 88 lists nominal reference depth (NRD) to middle of injection interval (meters below top of casing, BTOC), number of tests at that interval, depth to top of interval, and depth to bottom of interval. For falling head tests, line 88 lists nominal reference depth, packer pressure (psi), stabilized shut-in head (vertical meters above NRD), stabilization time (minutes), excess head at start of test (vertical meters above shut-in head), and flow tank radius (mm). Depths to top and bottom of interval are given in a comment line above the data for that interval.

Line 11: Falling head injection test data. These lines contain data pairs of elapsed time of test (seconds) and excess head values (m) measured during each test. Each data line contains up to five time/head data pairs.

Line 21-31: Constant head injection test data. These lines contain shut-in pressure (MPa), injection pressure applied to interval (MPa), average flow rate (Q) during test (ml/s), effective injection pressure in interval (MPa), effective head in interval (m), test number for each interval, and nominal pressure (psi) applied to flow tank.

Table E6 summarizes calculated permeability values for the tested intervals in each borehole, which were used in compiling Figure 3.2.

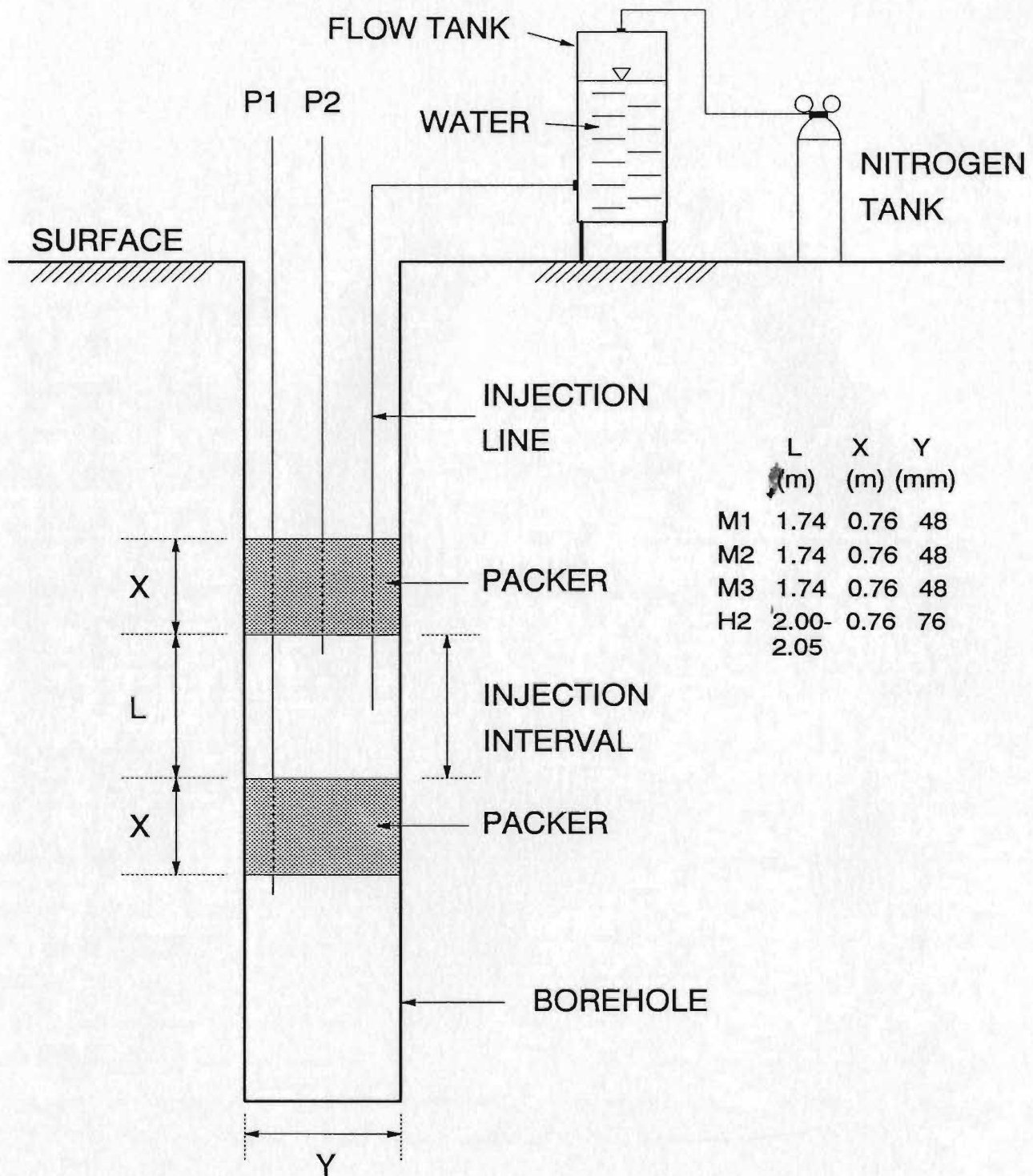


Figure E1 - Schematic diagram of constant head injection test setup

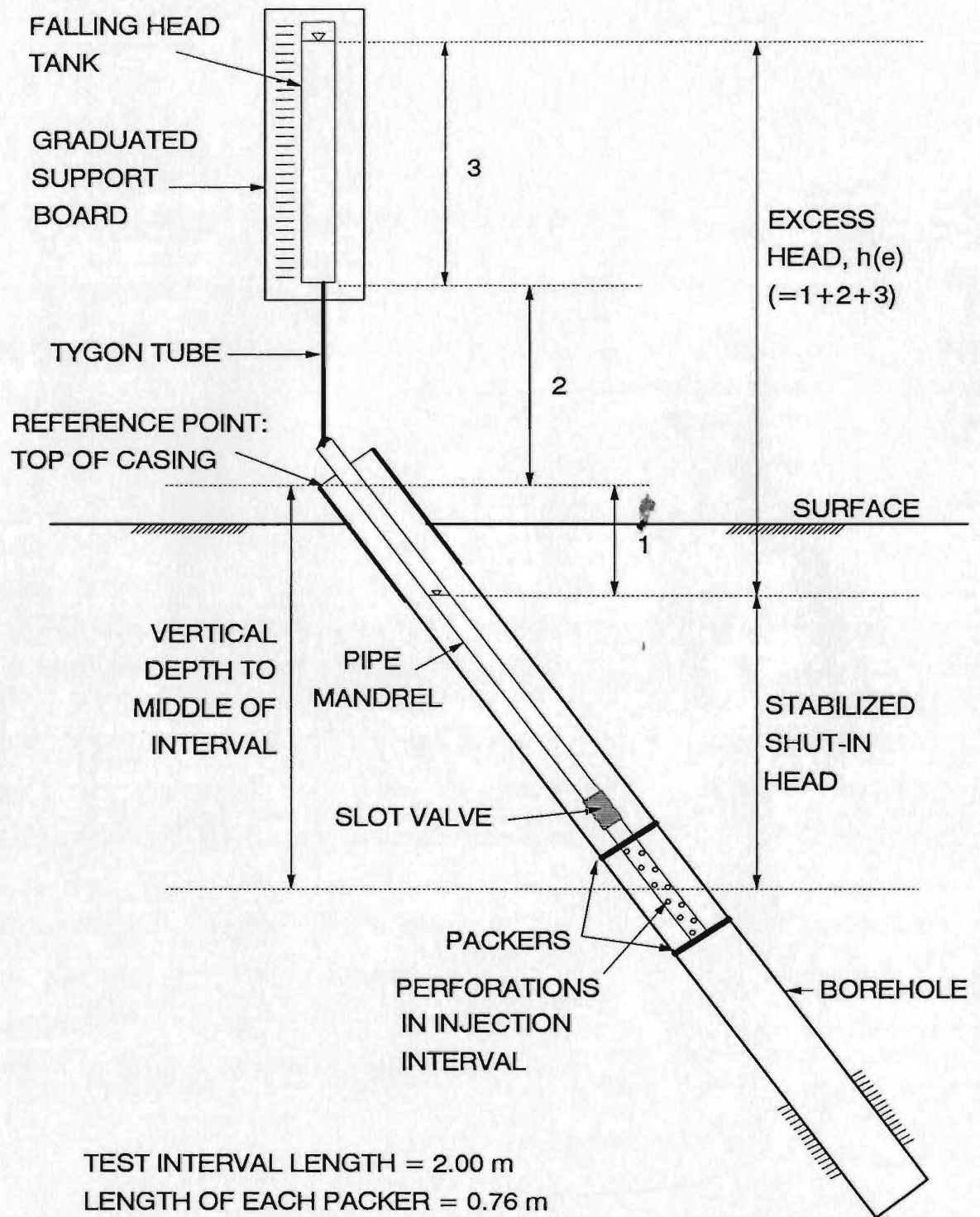


Figure E2 - Schematic diagram of falling head injection test setup in inclined borehole H4. Setup for borehole M2 was identical except borehole was vertical.

Table E1 – Injection test data for borehole M1  
in the Seal Cove River valley

99 Constant head injection test data for borehole M1

	NRD	# tests	Top Int.	Bot. Int.			
	(m BTOC)		(m BTOC)	(m BTOC)			
88	2.07	3	1.2	2.94			
99							
99	Shutin P	Inj. P	Q	Effect. P	Effect. h	Test	Tank P
99	(MPa)	(MPa)	(ml/sec)	(MPa)	(m)	no.	(psi)
21	0.0220	0.02235	2.352	0.00035	0.036	1	0
22	0.0220	0.02289	7.840	0.00089	0.091	2	25
23	0.0220	0.02329	12.278	0.00129	0.132	3	40
99							
88	3.81	3	2.94	4.68			
21	0.0390	0.03922	2.777	0.00022	0.022	1	0
22	0.0390	0.03966	6.720	0.00066	0.067	2	25
23	0.0390	0.04033	12.362	0.00133	0.136	3	40
99							
88	5.55	3	4.68	6.42			
21	0.0560	0.05625	2.847	0.00025	0.025	1	0
22	0.0560	0.05669	7.084	0.00069	0.070	2	25
23	0.0560	0.05726	12.495	0.00126	0.129	3	40
99							
88	7.29	3	6.42	8.16			
21	0.0740	0.07455	2.555	0.00055	0.056	1	0
22	0.0740	0.07506	7.714	0.00106	0.108	2	25
23	0.0740	0.07621	12.705	0.00221	0.225	3	40
99							
99	END OF TESTING IN BOREHOLE M1						

Table E2 — Injection test data for borehole M2  
in the Seal Cove River valley

99 Constant and falling head injection test data for borehole M2

99

99 Note: top interval 3.95 – 5.69 m tested by constant head methods

99	NRD	# Tests	Top Int.	Bot. Int.
99	(m BTOC)		(m BTOC)	(m BTOC)
88	4.82	2	3.95	5.69

99

99	Shutin P	Inj. P	Q	Effect. P	Effect. h	Test	Tank P
99	(MPa)	(MPa)	(ml/sec)	(MPa)	(m)	no.	(psi)
21	0.00853	0.01098	6.790	0.00245	0.2502	1	27
22	0.00853	0.01173	8.148	0.00320	0.3268	2	36

99

99 Remaining tests by falling head methods

99 Note change in variables on line 88 and format on line 11

99 Interval = 5.69 – 7.43 m

99	NRD	Packer P	Shutin	Stabil'n	Start h(e)	Tank radius
99	(m BTOC)	(psi)	head (m)	time (min)	(m)	(mm)
88	6.56	200	3.763	20	5.312	4.725
99	Elapsed t	h(e)	Elapsed t	h(e)	Elapsed t	h(e)
99	(sec)	(m)	(sec)	(m)	(sec)	(m)
11	0	5.312	90	5.237	150	5.194
11	180	5.174	240	5.128	300	5.084
11	360	5.045	480	4.972	600	4.900
11	900	4.730				

99 End of test

99

99 Interval = 7.43 – 9.17 m

88	8.3	200	5.294	20	3.812	4.725
11	0	3.812	30	3.791	60	3.780
11	90	3.772	120	3.764	180	3.749
11	240	3.742	360	3.720	600	3.650
11	1200	3.561				

99 End of test

99

99 Interval = 9.14 – 10.88 m

88	10.01	200	6.81	20	4.48	4.725
11	0	4.480	30	4.238	60	4.023
11	90	3.826	120	3.655	180	3.361
11	240	3.095	360	2.639	600	1.882
11	960	0.979	1260	0.395		

99 End of test

99

99 END OF TESTING IN BOREHOLE M2

**Table E3 – Injection test data for borehole M3  
in the Seal Cove River valley**

99 Constant head injection test data for borehole M3							
99	NRD	# Tests	Top Int.	Bot. Int.			
99	(m BTOC)		(m BTOC)	(m BTOC)			
88	2.07	2	1.2	2.94			
99							
99	Shutin P	Inj. P	Q	Effect. P	Effect. h	Test	Tank P
99	(MPa)	(MPa)	(ml/sec)	(MPa)	(m)	no.	(psi)
21	0.0102	0.02029	16.800	0.01009	1.030	1	30
22	0.0102	0.02176	18.600	0.01156	1.180	2	40
99							
88	3.81	2	2.94	4.68			
21	0.0277	0.02820	3.710	0.00050	0.051	1	0
22	0.0277	0.02872	5.964	0.00102	0.104	2	25
99							
88	5.55	3	4.68	6.42			
21	0.0443	0.04453	7.930	0.00023	0.023	1	0
22	0.0443	0.04471	7.230	0.00041	0.042	2	10
23	0.0443	0.04497	15.400	0.00067	0.068	3	20
99							
88	7.29	3	6.42	8.16			
21	0.0607	0.06330	4.890	0.00260	0.265	1	0
22	0.0607	0.06472	9.594	0.00402	0.410	2	10
99							
88	9.03	3	8.16	9.90			
21	0.0776	0.08037	3.276	0.00277	0.283	1	0
22	0.0776	0.08693	11.725	0.09330	0.952	2	20
23	0.0776	0.08713	11.880	0.09530	0.972	3	42
99							
99	END OF TESTING IN BOREHOLE M3						

Table 1-4 - Injection test data for borehole H2 in the  
Seal Cove River valley.

99 INJECTION TEST DATA FOR BOREHOLE H2 IN THE SEAL COVE RIVER VALLEY

```

99
99 No testing from 0-14.00 m
88 15.03 2 14.00 16.05
21 0.1960 0.1983 5.833 0.0023 0.235 1 40
22 0.1960 0.2003 11.200 0.0043 0.439 2 60
99
88 16.98 2 15.95 18.00
21 0.2126 0.2137 15.000 0.0011 0.111 1 50
22 0.2126 0.2145 16.000 0.0019 0.190 2 65
99
88 18.98 3 17.95 20.
21 0.2299 0.2573 2.847 0.0274 2.795 1 10
22 0.2299 0.2870 6.300 0.0571 5.824 2 30
23 0.2299 0.3813 10.650 0.1514 15.443 3 60
99
88 19.03 1 18.00 20.05
21 0.1399 0.1552 1.388 0.0153 1.561 1 0
99
88 22.98 2 21.95 24.
21 0.2638 0.1261 0.152 - 1 10
22 0.2638 0.1712 8.700 0.0451 4.600 2 40
99
88 25 1 24. 26.
21 0.1988 0.2153 0.011 0.0165 1.680 1 3
99
88 27 2 26. 28.
21 0.1858 0.2011 4.981 0.0153 1.560 1 0
22 0.1777 0.1905 7.327 0.0127 1.295 2 0
99
88 29 2 28. 30.
21 0.2107 0.2108 5.262 0.0001 0.012 1 0
22 0.2107 0.2117 9.222 0.0010 0.109 2 0
99
88 31 1 30. 32.
21 0.2581 0.2581 0.061 0.0001 0.004 1 0
99
88 33.03 3 32. 34.05
21 0.2635 0.2641 9.975 0.0005 0.055 1 20
22 0.2635 0.2640 14.350 0.0005 0.051 2 40
23 0.2635 0.2645 18.250 0.0009 0.094 3 60
99
99 NO TESTING 34.05-36.00 m
99
88 37.03 3 36. 38.05
21 0.2956 0.3024 10.185 0.0044 0.447 1 20
22 0.2956 0.3024 12.513 0.0067 0.687 2 40
23 0.2956 0.3033 16.836 0.0077 0.786 3 60
99
88 35.24 3 34.21 36.26
21 0.2778 0.2830 8.051 0.0052 0.525 1 20
22 0.2778 0.2844 10.060 0.0066 0.673 2 40
23 0.2778 0.2845 12.280 0.0067 0.681 3 60
99
88 37.24 3 36.21 38.26
21 0.3000 0.3001 8.169 0.0002 0.019 1 20
22 0.3000 0.3002 10.804 0.0003 0.025 2 40
23 0.3000 0.3007 12.284 0.0008 0.081 3 60
99
99 NO TESTING 38.26-40.00 M
99
88 41.03 2 40. 42.05
21 0.4206 0.5234 0.002 0.1028 10.485 1 40
22 0.4206 0.6953 0.004 0.2747 28.018 2 60
99
88 43.03 3 42. 44.05

```

Table E4 (continued)

21	0.4328	0.3404	6.248	-	-	1	10
99	SHUTIN P2 DATA SUSPECT (HIGHER THAN INJECTION P2);						
99	USE DELTA Q AND DELTA H VALUES TO CALCULATE PERMEABILITY.						
22	0.4328	0.3424	10.027	0.0020		0.204	2 40
23	0.4328	0.3429	13.692	0.0005		0.051	3 60
99							
88	45.03	2	44.	46.05			
21	0.5002	0.5422	-	0.0420		4.283	1 30
22	0.5002	0.8563	0.014	0.3141		36.322	2 60
99							
88	47.03	3	46.	48.05			
21	0.4910	0.6400	-	-		-	1 20
22	0.4910	0.7566	1.700	0.2656		27.091	2 40
23	0.7566	0.8407	2.730	0.0841		8.578	3 60
99	NOTE: ONLY 60 PSI DATA WERE FULLY STABILIZED.						
99							
88	49.03	3	48.	50.05			
21	0.4888	0.0400	-	-		-	1 20
22	0.4888	0.7553	0.025	0.2665		27.183	2 40
99	NOTE: DELTA Q VALUE NEGATIVE BETWEEN 20 AND 40 PSI						
99	RUNS. USED ONLY 40-60 PSI DELTA Q VALUE FOR CALCS.						
23	0.7553	0.8712	0.009	0.1159	0.016	11.822	3 60
99							
88	49.24	3	48.21	50.26			
21	0.5820	-	-	-		-	1 20
22	0.5820	0.8307	0.042	0.2486		25.361	2 50
23	0.8307	0.8968	0.021	0.0661		6.745	3 60
99							
99	NO USEABLE DATA FOR 50.26-52.00 M						
99							
88	53.03	3	52.	54.05			
21	0.5426	0.2200	-	-		-	1 20
22	0.5426	0.6680	0.410	0.1254		12.791	2 40
23	0.6880	0.9110	0.653	0.2230		24.786	3 60
99							
88	55.03	3	54.	56.05			
21	0.4526	-	6.627	-		-	1 20
22	0.4526	0.4542	9.240	0.0016		0.163	2 40
23	0.4542	0.4544	13.113	0.0002		0.002	3 60
99							
88	57.08	3	56.05	58.10			
21	0.4790	-	5.334	-		-	1 20
22	0.4790	0.4877	9.193	0.0087		0.887	2 40
23	0.4877	0.4983	13.253	0.0106		1.081	3 60
99							
88	59.03	3	58.00	60.05			
21	0.4922	-	6.510	-		-	1 20
22	0.4922	0.4949	9.648	0.0027		0.275	2 40
23	0.4949	0.4990	13.773	0.0041		0.418	3 60
99							
99	NO TESTING FROM 60.05-62.00 M						
99							
99	FOR INTERVAL 62.00-64.05, NO SIGNIFICANT INCREASE						
99	OF INJECTION PRESSURE WITH INCREASED TANK PRESSURE.						
99	ALL FLOWRATES AROUND ZERO.						
99							
88	65.03	2	64.	66.05			
21	0.6566	0.0050	-	-		-	1 20
22	0.6566	1.0360	0.009	0.3794		38.698	2 60
99							
88	67.03	3	66.	68.05			
21	0.5715	-	4.813	-		-	1 20
22	0.5715	0.5842	8.488	0.0127		1.295	2 40
23	0.5842	0.5990	13.193	0.0148		1.510	3 60
99							
88	67.24	3	66.21	68.26			
21	0.5694	0.5849	6.132	0.0155		1.579	1 20
22	0.5694	0.5945	9.472	0.0251		2.560	2 40
23	0.5694	0.5988	10.458	0.0294		2.998	3 60
99							
88	69.24	1	68.21	70.26			
21	0.5800	1.0909	0.001	0.5109		52.110	1 65



Table I-4 (continued)

```

99
99 INTERVAL 70.21 - 72.26 M: NO TEST DATA DUE TO
99 HYDRAULIC SHUNT BETWEEN P1 AND P2.
99 SAME CASE FOR INTERVAL 70.71 - 72.76 M.
99
88 72.24      3  71.21  73.26
21 0.6110  0.8568  0.616 0.2458      25.072 1 20
22 0.6110  1.0040  0.825 0.3929      40.084 2 40
23 0.6110  1.1804  1.078 0.5693      58.07  3 60
99
88 73.24      3  72.21  74.26
21 0.6208  0.7838  0.408 0.1630      16.628 1 20
22 0.6208  1.0299  0.852 0.4091      41.729 2 40
23 0.6208  1.2851  1.132 0.6643      67.759 3 60
99
99 END OF INJECTION TEST DATA IN BOREHOLE H2.

```

Table E5 - Injection test data for borehole H4 in the  
Seal Cove River valley.

99 INJECTION TEST DATA FOR BOREHOLE H4 IN THE SEAL COVE RIVER VALLEY

99

99 Note: no testing from 0-5.59 m

99

99 Interval 5.59-7.19 m

88 6.39 210 5.154 5 3.727 15.9  
11 000 3.727 010 3.553 020 3.443 030 3.379 045 3.295  
11 060 3.183 090 3.061 120 2.918 150 2.778 180 2.643  
11 210 2.505 240 2.374

99 End of test

99

99 Interval 7.19-8.78 m

88 7.99 205 4.434 4 6.210 38.2  
11 000 6.210 010 6.112 020 6.068 030 6.038 45 5.978  
11 060 5.936 080 5.877 100 5.819 120 5.767 150 5.690  
11 180 5.619 210 5.555 240 5.480 300 5.340 360 5.216  
11 420 5.090

99 End of test

99

99 Interval 8.79-10.38 m

88 9.584 200 6.509 32 5.767 4.8  
11 000 5.767 20 5.762 30 5.758 40 5.703 60 5.681  
11 80 5.659 100 5.637 120 5.616 150 5.586 180 5.556  
11 210 5.525 240 5.493 300 5.438 360 5.381 480 5.277  
11 720 5.091

99 End of test

99

99 Interval 10.38-11.98 m

88 11.19 200 8.676 12 5.203 4.8  
11 000 5.203 30 5.190 70 5.174 90 5.167 120 5.155  
11 200 5.125 260 5.104 320 5.082 450 5.040 680 4.967  
11 1290 4.788

99 End of test

99

99 Interval 11.98-13.58 m

88 12.78 200 10.066 20 5.416 4.8  
11 000 5.416 20 5.389 40 5.369 70 5.337 90 5.319  
11 120 5.290 160 5.255 180 5.237 210 5.213 240 5.189  
11 300 5.143 360 5.097 480 5.011 720 4.854

99 End of test

99

99 Interval 13.58-15.17 m

88 14.38 200 11.712 6 5.158 4.8  
11 000 5.158 030 5.142 045 5.135 060 5.129 090 5.117  
11 125 5.103 180 5.081 240 5.062 300 5.041 420 5.002

99 End of test

99

99 Interval 15.17-16.77 m

88 15.98 200 12.667 30 6.069 4.8  
11 000 6.069 040 6.055 080 6.030 180 5.966 300 5.894  
11 420 5.834 540 5.775

99 End of test

99

99 Interval 16.77-18.37 m

88 17.68 200 14.920 4 5.083 4.8  
11 000 5.083 030 5.048 070 5.018 120 4.982 180 4.940  
11 290 4.874 360 4.828 450 4.778 720 4.631

99 End of test

99

99 Interval 18.37-19.97 m

88 19.18 225 15.676 17 5.855 4.8  
11 000 5.855 010 5.751 020 5.659 030 5.577 040 5.493  
11 060 5.349 090 5.145 105 5.053 120 4.948 135 4.857  
11 150 4.765 180 4.595

99 End of test

99

99 Interval 19.97-21.56 m

88 20.77 230 17.960 6 5.428 4.8  
11 000 5.428 060 5.413 090 5.401 120 5.392 150 5.383

Table E5 (continued)

11	180	5.372	210	5.363	240	5.354	270	5.344	300	5.336
11	330	5.327	360	5.318						
99	End of test									
99	Interval 21.56-23.16 m									
88	22.37	300	20.410	15	4.442	17.2				
11	000	4.442	010	4.420	020	4.397	030	4.370	060	4.310
11	090	4.261	120	4.219	150	4.180	180	4.145	210	4.107
11	240	4.081	300	4.025	360	3.971	480	3.869		
99	End of test									
99	Interval 23.16-24.76 m									
88	23.97	310	20.755	10	5.898	4.8				
11	000	5.898	008	5.768	020	5.568	030	5.403	040	5.253
11	050	5.104	060	4.970	075	4.761	090	4.592	105	4.413
11	116	4.298								
99	Note: Following readings in tube (radius 7.1 mm) below tank									
11	150	4.095	180	4.010	210	3.929	240	3.860	300	3.718
11	360	3.583	420	3.460						
99	End of test									
99	Interval 24.76-26.35 m									
88	25.57	300	22.738	10	5.563	4.8				
11	000	5.563	030	5.537	060	5.516	090	5.501	120	5.484
11	150	5.469	210	5.445	270	5.418	300	5.405	420	5.354
11	600	5.286								
99	End of test									
99	Interval 26.35-27.95 m									
88	27.17	300	23.871	22	5.890	38.2				
11	000	5.890	020	5.849	033	5.819	045	5.798	060	5.773
11	120	5.674	180	5.589	240	5.501	300	5.412	420	5.245
11	660	4.933	900	4.649						
99	End of test									
99	Interval 27.95-29.55 m									
88	28.76	300	25.499	11	5.988	4.8				
11	000	5.988	015	5.933	030	5.719	045	5.583	060	5.475
11	080	5.318	100	5.173	120	5.028	150	4.822	180	4.629
11	210	4.439	226	4.348	270	4.176	300	4.125	360	4.040
11	420	3.954								
99	End of test									
99	Interval 29.55-31.15 m									
88	30.36	300	27.096	12	5.890	4.8				
11	000	5.890	009	5.569	015	5.394	020	5.262	030	5.062
11	040	4.854	050	4.658	060	4.461	067	4.349		
99	Note: Following readings in tube (7.1 mm radius) below tank									
11	090	4.130	120	3.998	150	3.869	180	3.747	195	3.553
11	240	3.525	300	3.324						
99	End of test									
99	Interval 31.15-32.74 m									
88	31.95	300	30.096	16	4.453	38.2				
11	000	4.453	010	4.402	020	4.373	030	4.337	040	4.301
11	050	4.271	060	4.242	090	4.155	120	4.065	150	3.980
11	180	3.899	210	3.818	240	3.739	300	3.585	360	3.442
11	420	3.314								
99	End of test									
99	Interval 32.74-34.34 m									
88	33.56	305	31.909	9.5	4.369	4.8				
11	000	4.369	010	4.344	020	4.318	030	4.297	045	4.265
11	060	4.239	090	4.176	122	4.113	150	4.070	183	4.013
11	220	3.954	240	3.923	300	3.828	360	3.741	420	3.653
99	End of test									
99	Interval 34.34-35.94 m									
88	35.16	305	33.426	15	4.252	17.2				
11	000	4.252	010	4.198	020	4.143	030	4.084	045	4.005
11	060	3.928	090	3.782	120	3.639	152	3.494	180	3.374
11	210	3.253	240	3.142	273	3.017	300	2.925		

Table E5 (continued)

```

99 End of test
99
99 Interval 35.94-37.54 m
88 36.74 305 35.018 12 4.500 4.8
11 000 4.500 010 4.238 020 4.056 030 3.911 040 3.759
11 050 3.615 060 3.479 080 3.228 090 3.110 100 3.001
11 110 2.906 113 2.862
99 End of test
99
99 Interval 37.54-39.13 m
88 38.34 340 36.938 22 4.147 4.8
11 000 4.147 010 3.885 020 3.858 030 3.840 040 3.825
11 050 3.814 060 3.802 090 3.776 120 3.749 155 3.722
11 180 3.700 240 3.658 300 3.617 360 3.575 480 3.501
99 End of test
99
99 Interval 39.13-40.73 m
88 39.93 340 38.267 6 4.291 38.2
11 000 4.291 010 3.998 020 3.762 030 3.527 040 3.320
11 050 3.124 060 2.950 070 2.795
99 End of test
99
99 Interval 40.73-42.33 m
88 41.55 305 39.816 23 4.464 4.8
11 000 4.464 010 4.322 020 4.203 030 4.072 040 3.950
11 050 3.844 060 3.736 080 3.531 100 3.335 120 3.156
11 140 2.986 154 2.866
99 End of test
99
99 Interval 42.33-43.92 m
88 43.15 305 41.484 14 4.342 4.8
11 000 4.342 010 3.989 020 3.781 030 3.592 040 3.405
11 050 3.240 060 3.084 070 2.935 080 2.795
99 End of test
99
99 Interval 43.92-45.52 m
88 44.74 305 43.550 5 3.935 4.8
11 000 3.935 040 3.924 060 3.920 090 3.912 120 3.907
11 180 3.895 240 3.883 300 3.876
99 End of test
99
99 Interval 45.52-47.12 m
88 46.34 355 45.212 7 3.870 4.8
11 000 3.870 060 3.862 150 3.868 250 3.872 360 3.883
99 End of test
99 END OF INJECTION TESTING IN BOREHOLE H4.

```

Table E6 – Summary of bedrock permeabilities calculated from injection test data in the Seal Cove River valley  
(note: \*BTOC\* = below top of casing).

HOLE ID	Depth to top of interval (m BTOC)	Depth to bottom of interval (m BTOC)	Nom. Ref. Depth (vert.) (m BTOC)	Hydraulic Conductivity K (m/s)	log K	Intrinsic Permeability k (m2)	log k
M1	1.2	2.94	2.07	4.21E-05	-4.3757	5.61E-12	-11.2509
	2.94	4.68	3.81	4.90E-05	-4.3098	6.53E-12	-11.1850
	4.68	6.42	5.55	4.94E-05	-4.3063	6.59E-12	-11.1814
	6.42	8.16	7.29	2.76E-05	-4.5591	3.68E-12	-11.4343
(bottom of hole at 10.20 m depth; 80.96 m elevation)							
M2	3.95	5.69	4.82	1.22E-06	-5.9136	1.63E-13	-12.7888
	5.69	7.43	6.56	4.32E-08	-7.3645	5.76E-15	-14.2397
	7.43	9.17	8.3	2.67E-08	-7.5735	3.56E-15	-14.4487
	9.17	10.91	10.04	4.35E-07	-6.3615	5.80E-14	-13.2367
(bottom of hole at 11.84 m depth; 97.24 m elevation)							
M3	1.2	2.94	-2.07	7.83E-06	-5.1062	1.04E-12	-11.9814
	2.94	4.68	-3.81	3.18E-05	-4.4976	4.24E-12	-11.3727
	4.68	6.42	-5.55	9.73E-05	-4.0119	1.30E-11	-10.8871
	6.42	8.16	-7.29	1.02E-05	-4.9914	1.36E-12	-11.8666
	8.16	9.9	-9.03	5.88E-06	-5.2306	7.84E-13	-12.1058
	9.9	11.64	-10.77	1.03E-05	-4.9872	1.37E-12	-11.8623
(bottom of hole at 13.55 m depth; 81.67 m elevation)							
H2	11.25	12.9	-12.08	9.55E-06	-5.0200	1.27E-12	-11.8952
	12.82	14.47	-13.65	4.15E-05	-4.3820	5.53E-12	-11.2571
	14.43	16.08	-15.23	3.52E-07	-6.4535	4.69E-14	-13.3286
	14.47	16.12	-15.26	3.37E-07	-6.4724	4.49E-14	-13.3475
	17.64	19.29	-18.47	7.04E-07	-6.1524	9.38E-14	-13.0276
	19.29	20.9	-20.09	2.64E-09	-8.5784	3.52E-16	-15.4536
	20.9	22.51	-21.7	2.20E-06	-5.6576	2.93E-13	-12.5327
	22.51	24.12	-23.31	3.29E-05	-4.4828	4.39E-12	-11.3580
	24.12	25.72	-24.92	5.88E-06	-5.2306	7.84E-13	-12.1058
	25.72	27.37	-26.55	7.11E-05	-4.1481	9.48E-12	-11.0233
	27.5	29.15	-28.33	6.10E-06	-5.2147	8.13E-13	-12.0898
	28.94	30.54	-29.77	7.88E-06	-5.1035	1.05E-12	-11.9786
	29.11	30.76	-29.94	1.28E-04	-3.8928	1.71E-11	-10.7680
	32.15	33.8	-32.98	6.52E-11	-10.1858	8.69E-18	-17.0609
	33.76	35.41	-34.59	3.55E-05	-4.4498	4.73E-12	-11.3249
	35.37	37.02	-36.2	1.46E-10	-9.8356	1.95E-17	-16.7108
	36.98	38.63	-37.81	4.55E-08	-7.3420	6.07E-15	-14.2172
	38.59	40.23	-39.42	5.03E-10	-9.2984	6.70E-17	-16.1736
	38.75	40.4	-39.58	6.27E-10	-9.2027	8.36E-17	-16.0779
	41.8	43.45	-42.63	4.67E-09	-8.3307	6.23E-16	-15.2059
	43.41	45.06	-44.24	6.07E-06	-5.2168	8.09E-13	-12.0920
	45.06	46.7	-45.89	1.54E-06	-5.8125	2.05E-13	-12.6876
	46.62	48.27	-47.45	4.03E-06	-5.3947	5.37E-13	-12.2699
	51.45	53.09	-52.28	4.50E-11	-10.3468	6.00E-18	-17.2220

Table E6 (continued)

53.05	54.7	-53.88	1.13E-06	-5.9469	1.51E-13	-12.8221
53.22	54.87	-54.05	1.40E-06	-5.8539	1.87E-13	-12.7290
54.83	56.48	-55.66	1.00E-11	-11.0000	1.33E-18	-17.8752
57.24	58.89	-58.07	8.05E-09	-8.0942	1.07E-15	-14.9694
58.05	59.69	-58.88	7.79E-09	-8.1085	1.04E-15	-14.9836

(bottom of hole at 62.34 m depth; 34.34 m elevation)

H4	5.59	7.19	-6.39	7.56E-07	-6.1215	1.01E-13	-12.9966
	7.19	8.79	-7.99	9.31E-07	-6.0311	1.24E-13	-12.9062
	8.79	10.38	-9.58	5.91E-09	-8.2284	7.88E-16	-15.1036
	10.38	12	-11.19	2.12E-09	-8.6737	2.83E-16	-15.5488
	12	13.58	-12.78	4.91E-09	-8.3089	6.55E-16	-15.1841
	13.58	15.18	-14.38	2.18E-09	-8.6615	2.91E-16	-15.5367
	15.18	16.78	-15.98	3.04E-09	-8.5171	4.05E-16	-15.3923
	16.78	18.38	-17.58	4.13E-09	-8.3840	5.51E-16	-15.2592
	18.38	19.98	-19.18	2.74E-06	-5.5622	3.65E-13	-12.4374
	19.98	21.57	-20.77	1.95E-09	-8.7100	2.60E-16	-15.5851
	21.57	23.17	-22.37	1.20E-07	-6.9208	1.60E-14	-13.7960
	23.17	24.77	-23.97	8.80E-08	-7.0555	1.17E-14	-13.9307
	24.77	26.37	-25.57	8.59E-10	-9.0660	1.15E-16	-15.9412
	26.37	27.97	-27.17	4.22E-07	-6.3747	5.63E-14	-13.2499
	27.97	29.56	-28.76	4.41E-08	-7.3556	5.88E-15	-14.2307
	29.56	31.16	-30.36	1.35E-07	-6.8697	1.80E-14	-13.7448
	31.16	32.76	-31.94	1.28E-06	-5.8928	1.71E-13	-12.7680
	32.76	34.36	-33.56	1.12E-08	-7.9508	1.49E-15	-14.8260
	34.36	35.96	-35.16	5.36E-07	-6.2708	7.14E-14	-13.1460
	35.96	37.55	-36.74	1.24E-07	-6.9066	1.65E-14	-13.7817
	37.55	39.15	-38.34	6.99E-09	-8.1555	9.32E-16	-15.0307
	39.15	40.75	-39.93	7.58E-04	-3.1203	1.01E-10	-9.9955
	40.75	42.35	-41.55	9.46E-08	-7.0241	1.26E-14	-13.8993
	42.35	43.95	-43.15	9.06E-08	-7.0429	1.21E-14	-13.9180
	43.95	45.54	-44.74	-	-	1.00E-16	-16.0000
	45.54	47.14	-46.34	-	-	1.00E-16	-16.0000

(bottom of hole at 49.97 m depth; 45.21 m elevation)

## APPENDIX F

### **Estimation of Permeability of Glacial Drift in the Seal Cove River Valley - Procedures and Results**

#### **1. Introduction**

Permeabilities of glacial drift overburden in the valley bottom were estimated using the method of Masch and Denny (1966), which relates hydraulic conductivity with grain-size distribution curve characteristics. Grain-size was determined by mechanical sieve analysis of drift samples collected on the valley floor in the study area. A description of the drift samples, grain size analysis procedures, and a summary of results and calculated hydraulic conductivities for these samples are presented below.

#### **2. Glacial drift sample collection and description**

Eight 2.5 kg samples of glacial drift were collected from embankments exposed by construction of the gravel road through the SCR V (locations D1-D8 in Figure 3.1). Each sample was a composite sample of drift material over a freshly exposed 1-2 m face at each site. Large cobbles and boulders ( $\geq 0.1$  m) were not collected but were present at all sites, constituting approximately 5% of the drift by volume. The samples consisted of light brown to tan sand and fine gravel, made up of sub-angular particles of quartz, feldspar, granitic and volcanic lithic fragments, clay minerals, and minor organic debris.

### 3. Grain-size analysis procedures

In preparation for mechanical sieve analysis, minor amounts of roots and organic debris were removed and the bulk samples thoroughly mixed before splitting into 2-4 test samples. Each test sample was passed through a nest of sieves with mesh sizes ranging from 50.8 to 0.074 mm (U.S. Standard Sieve sizes 2, 1, 1/2, 4, 10, 20, 40, 60, 100, 200, pan), following standard sieve analysis procedures. The weight percent passing each sieve was calculated and grain size distribution curves plotted for each test sample. Effective grain-size, defined as the grain diameter such that 10% of the sample is finer, was determined from the grain size distribution curve. In addition, coefficients of uniformity,  $C_u$ , and curvature,  $C_c$ , were determined to quantify the degree of grading and gaps in grain size, respectively, for the samples.

### 4. Results and method

The Masch and Denny method involves determining the median grain-size,  $d_{50}$ , from a grain-size distribution curve (expressed in phi units, where  $\phi = -\log_2 \times d(\text{mm})$ ), and inclusive standard deviation,  $\sigma_1$ . Knowing  $d_{50}$  and  $\sigma_1$ , hydraulic conductivity,  $K$ , is determined using type curves.

Figure F1 shows grain size distribution curves for glacial drift samples collected in the Seal Cove River valley. These samples range from gravelly sands to sandy gravels (using American Society of Testing and Materials (ASTM) grain size divisions). The curves show that these samples are well-graded (i.e. poorly sorted in geological terms). The generally high values for coefficient of uniformity ( $C_u$ , mean of 47.07) and low values for coefficient of curvature ( $C_c$ , mean of 1.37)



confirm that the samples are well-graded, with no significant gaps in grain size.

Table I-1 summarizes grain-size analysis characteristics and hydraulic conductivities estimated for the samples. Hydraulic conductivities for the drift samples range from  $9.4 \times 10^{-6}$  to  $2.8 \times 10^{-5}$  m/s, with a geometric mean of  $1.6 \times 10^{-5}$  m/s. These values are within the range of K values commonly reported for glacial drift materials (e.g. Freeze and Cherry, 1979).

# GRAINSIZE ANALYSIS

## ASTM SIZE DIVISIONS

GRAVEL	SAND		SILT	CLAY
	COARSE TO MEDIUM	FINE		

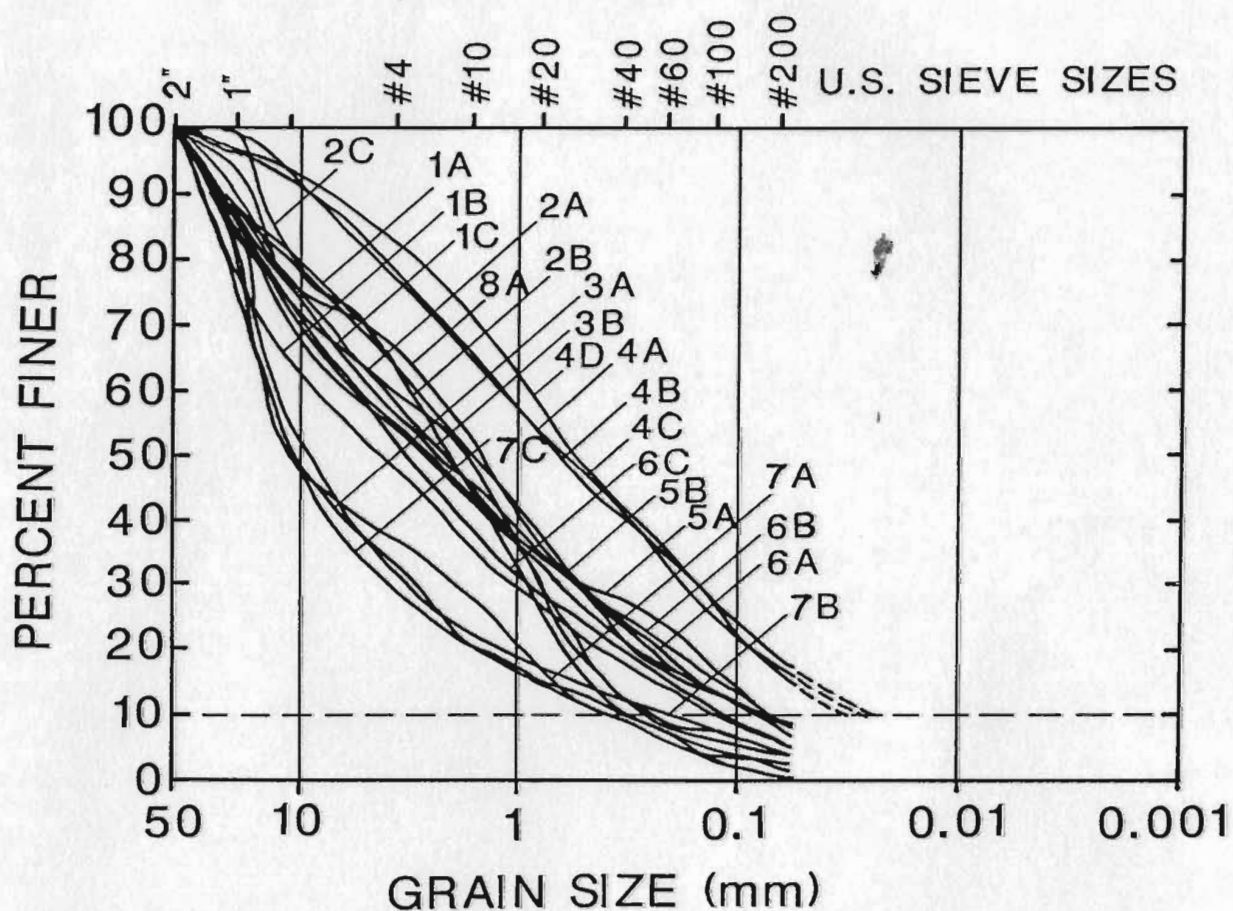


Figure F1 - Grainsize distribution curves for glacial drifts samples collected in the Seal Cove River valley

Table F1 - Summary of grain-size distribution characteristics and estimated hydraulic conductivities for glacial drift from the SCR

Grain-sizes (e.g. d50) are expressed in phi units,

where  $\phi = -\log(\text{base } 2) \times d(\text{mm})$ .

Cu is the coefficient of uniformity.

Cz is the coefficient of curvature.

Sigma(i) is inclusive standard deviation (Masch and Denny, 1966).

Sample	Cu	Cz	d5	d16	d50	d84	d95	Sigma(i)	K (m/s)
1A	39.7	1.2	4.62	2.00	-1.00	-4.35	-5.35	3.10	1.5E-05
1B	62.4	1.2	3.75	1.62	-2.40	-4.90	-5.40	3.02	1.1E-05
1C	40.3	0.9	3.75	1.75	-1.70	-4.35	-5.35	2.90	1.4E-05
2A	13.3	0.4	2.35	0.87	-1.20	-4.65	-5.35	2.55	2.0E-05
2B	2.2	0.6	2.00	0.73	-1.35	-4.15	-5.35	2.33	2.4E-05
2C	12.5	0.7	3.37	1.00	-1.10	-3.90	-4.48	2.41	2.3E-05
3A	34.6	1.8	2.35	0.15	-3.70	-5.00	-5.37	2.46	1.7E-05
3B	61.1	0.9	5.65	2.05	-1.50	-4.40	-5.00	3.23	1.2E-05
4A	41.2	0.9	5.65	1.62	3.62	-2.80	-4.35	2.62	2.8E-05
4B	55.6	1.2	5.65	1.62	0.50	-2.90	-4.15	2.61	2.3E-05
4C	27.3	0.8	5.05	3.62	3.62	-3.00	-4.35	3.08	2.7E-05
4D	25.0	1.2	5.65	3.75	0.50	-2.40	-3.85	2.98	1.8E-05
5A	83.3	0.9	3.75	3.00	-1.62	-4.35	-4.73	3.12	1.3E-05
6A	92.9	1	4.62	2.05	-1.90	-4.70	-5.35	3.20	1.2E-05
6B	109.1	1.4	5.65	2.70	-1.62	-4.90	-5.49	3.59	9.4E-06
6C	74.4	2.2	4.62	2.20	-2.10	-4.78	-5.49	3.28	1.0E-05
7A	35.7	0.5	3.62	0.15	-3.60	-4.74	-5.30	2.57	1.6E-05
7B	50.0	4.9	3.50	0.50	-3.30	-4.85	-5.35	2.68	1.5E-05
7C	47.6	3.3	2.75	0.25	-3.70	-4.74	-5.20	2.45	1.7E-05
8A	33.2	1.5	3.75	2.25	-0.85	-4.75	-5.35	3.13	1.5E-05

Geometric Mean: 1.6E-05

Max. value: 2.8E-05

Min. value: 9.4E-06

## APPENDIX G

### **Construction and Installation of Multilevel Piezometers in the Seal Cove River Valley**

#### **1. Introduction**

Two types of multilevel piezometer were used in this study. Piezometers in boreholes M1, M2, M3, H2 and H4 consisted of a central PVC pipe string with standpipes rising through the pipe from intervals (3-5, depending on hole size) isolated with chemical packers (after Cherry et al., 1984). Due to caving hole conditions in borehole H3, it was deemed too risky to attempt to install a chemical packer type multilevel piezometer. Instead, two individual standpipes were installed in a silica sand filter pack and isolated by bentonite seals.

Piezometric intervals were selected to include high permeability zones (defined by injection testing) in order to obtain the highest groundwater inflow rates for piezometer development and groundwater sampling. Lacking injection test data in H3, piezometric intervals were made as long as possible to maximize inflow rates.

Table G1 (below) summarizes the locations, depths and orientations of boreholes instrumented with multilevel piezometers in the SCRV.

#### **2. Construction and Installation of Chemical Packer Type Multilevel Piezometers**

Figure G1 shows schematic diagrams of piezometric interval locations and

depths, and plumbing details for multilevel piezometers in boreholes M1, M2, M3, H2 and H4. All of these multilevel piezometers were custom-made for this study using standard polyvinyl chloride (PVC) pipe and fittings. Ports into the isolated piezometric intervals consist of 90° elbows of 1/4 inch Schedule 80 PVC pipe fed through the PVC pipe string wall and PVC-welded in place. Standpipes of 6 mm or 12 mm O.D. polyethylene tubing extend from these elbows to the surface on the inside of the PVC pipe string. Piezometers M1, M2 and M3 have single (12 mm) standpipes, leading from the middle of each piezometric interval.

Piezometers H2 and H4 have two standpipes per interval (above I1) - one at the top and one at the bottom (Figure G1). This configuration was used in an attempt to sample groundwaters by applying pressure to the bottom port (using compressed nitrogen from the surface) and displacing water through the upper port and standpipe. However, field tests after installation showed that groundwater was preferentially driven back into bedrock rather than through the upper port and this technique was abandoned. Subsequently, monitoring and sampling for such double-port intervals were done using only the upper port standpipe. 12 mm O.D. tubing was connected to the top portions of the upper port standpipes to admit coaxial water level tapes. The 12 mm O.D. standpipe for interval I1 in H2 (Figure G1) was used to allow space for introduction of a thermistor probe in an attempt to measure ambient temperatures at various depths. This proved unworkable (due to friction within the tube), so the I1 standpipe was used for monitoring only.

The chemical packers were custom-made using Dowell Chemical Seal Ring<sup>R</sup> (CSR), a rubber-like, synthetic organic compound which expands on contact with water. Packers were fabricated following the approach described by Cherry

et al. (1984), with the design down-sized for smaller diameter (A and B-sized) boreholes in the SCR.V. The packers were nominally 0.3 m long and one or two were used at the top and bottom of each interval. The packers were either glued into the PVC pipe string (M1, M2, M3) or built into integral packer/interval sections (H2, H4).

Installation of the chemical packer multilevel piezometers proceeded by laying out all the pre-assembled packers, PVC pipe string pieces and pre-cut standpipe tubing lengths in the field, then incrementally threading the appropriate packer or pipe string pieces onto the bundled tubing, gluing the components together and lowering into the open boreholes. For the deep H2 and H4 boreholes, water was poured into the PVC pipe string to counteract buoyancy (the M-holes were shallow enough to push the piezometer string down by hand). Because this ballast water also began activating the CSR packers, it was important to install these deep multilevel piezometers in a single session. While there were no installation difficulties, this approach introduces the risk that the piezometer may get stuck partway in the borehole due to premature packer expansion. Alternate ballast materials, such as coarse sand, are therefore more advisable.

Once the piezometers were at the desired depth, they were anchored and filled completely with water to activate the packers. Piezometric monitoring showed that the packers expanded and sealed the intervals within two days after installation.

### 3. Construction and Installation of the Sand and Bentonite Piezometer at H3

Figure G2 shows a schematic diagram of piezometric interval locations and

depths, and plumbing details for the multilevel piezometer in borehole H3. The two standpipes in borehole H3 consist of 1/2-inch (nominal) schedule 80 PVC pipe with the tips consisting of a 1.5 m long perforated zone (6 mm holes drilled on staggered 50 mm centers) covered with two layers of nylon mesh (panty hose fabric).

The standpipes were installed in H3 by the following steps:

- 1) medium grained silica sand was placed in the bottom of H3, up to the depth of the base of the tip of I1, using water entrainment in a Tremie tube;
- 2) the I1 standpipe was lowered in the hole, then sand packed around the tip and up to the depth of the first bentonite seal;
- 3) crushed bentonite pellets were emplaced above the sand filter pack by repeatedly lowering and releasing small quantities in tear-away plastic bags (water-entrainment in a Tremie tube was unsuccessful due to bridging of the pellets in the inclined hole). Each seal is approximately 1 m long.
- 4) the process was repeated for standpipe I2, then the hole was backfilled to surface.

Table G1 - Summary of locations, orientations and depths for boreholes instrumented with multilevel piezometers in the Seal Cove River valley

Borehole:	M1	M2	M3	H2	H3	H4
Diameter (mm)	48	48	48	76	60	60
Collar location:						
UTM E <sup>1</sup>	884	1019	900	859	975	974
UTM N <sup>1</sup>	4275	4272	4200	4120	4245	4368
Elev. (m.a.s.l.)	91.16	109.08	95.22	96.68	96.83	95.18
Bottom of hole location:						
UTM E <sup>1</sup>	884	1019	900	893	982	996
UTM N <sup>1</sup>	4275	4272	4200	4100	4238	4237
Elev. (m.a.s.l.)	80.96	97.24	81.67	34.34	73.61	45.21
Trend/plunge (degrees)	vertical	vertical	vertical	147/53	135/55	135/55
Hole length (m)	10.20	11.84	14.20	78.06	28.35	61.00
Vertical hole depth (m)	10.20	11.84	14.20	62.34	23.22	49.97

<sup>1</sup> partial Universal Transverse Mercator coordinates; for complete values, add 344000 m to eastings and 5150000 m to northings



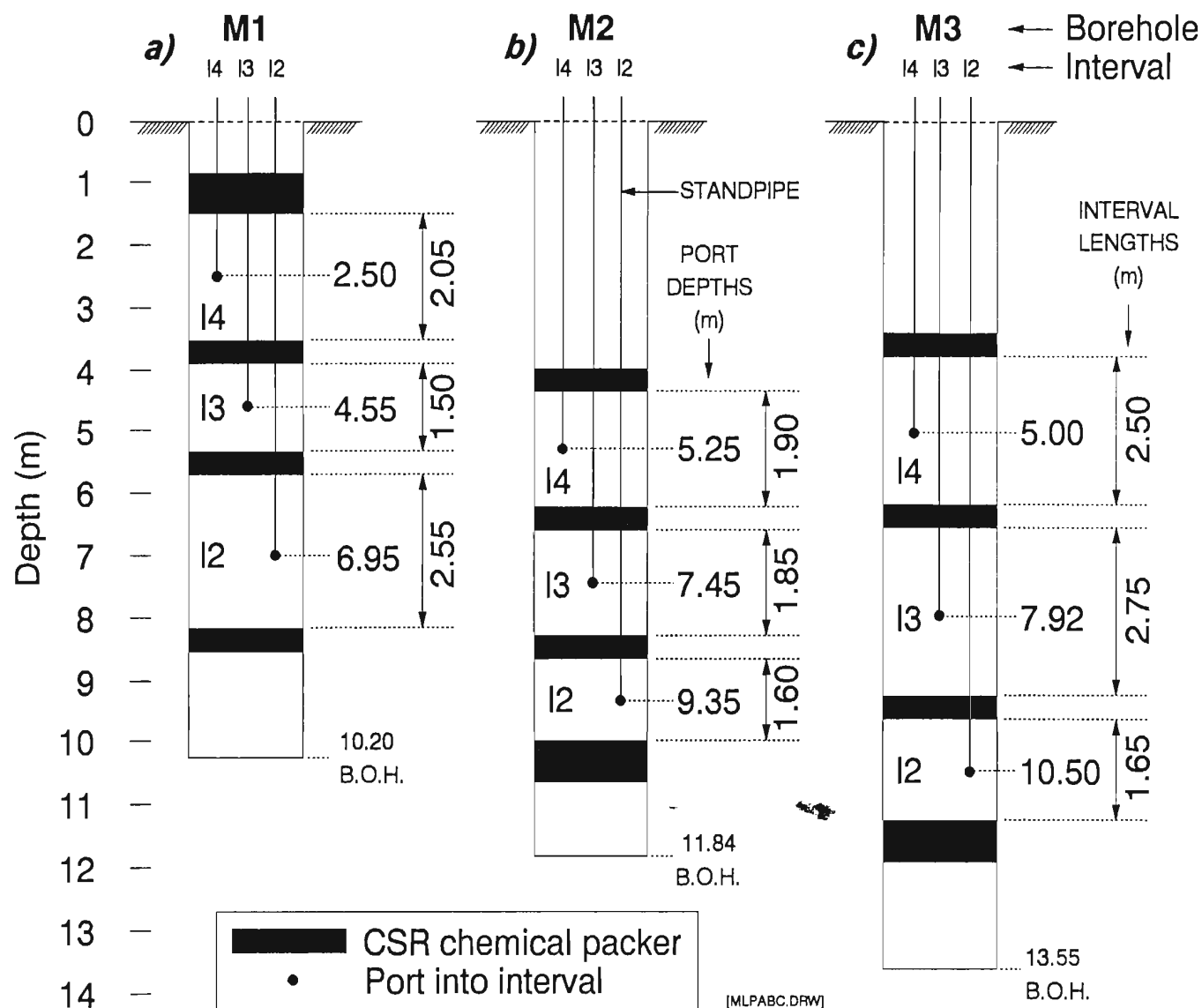


Figure G1 - Schematic diagrams of piezometric interval locations and depths, and plumbing details for multilevel piezometers in boreholes M1 (a), M2 (b), M3 (c), H2 (d) and H4 (e).

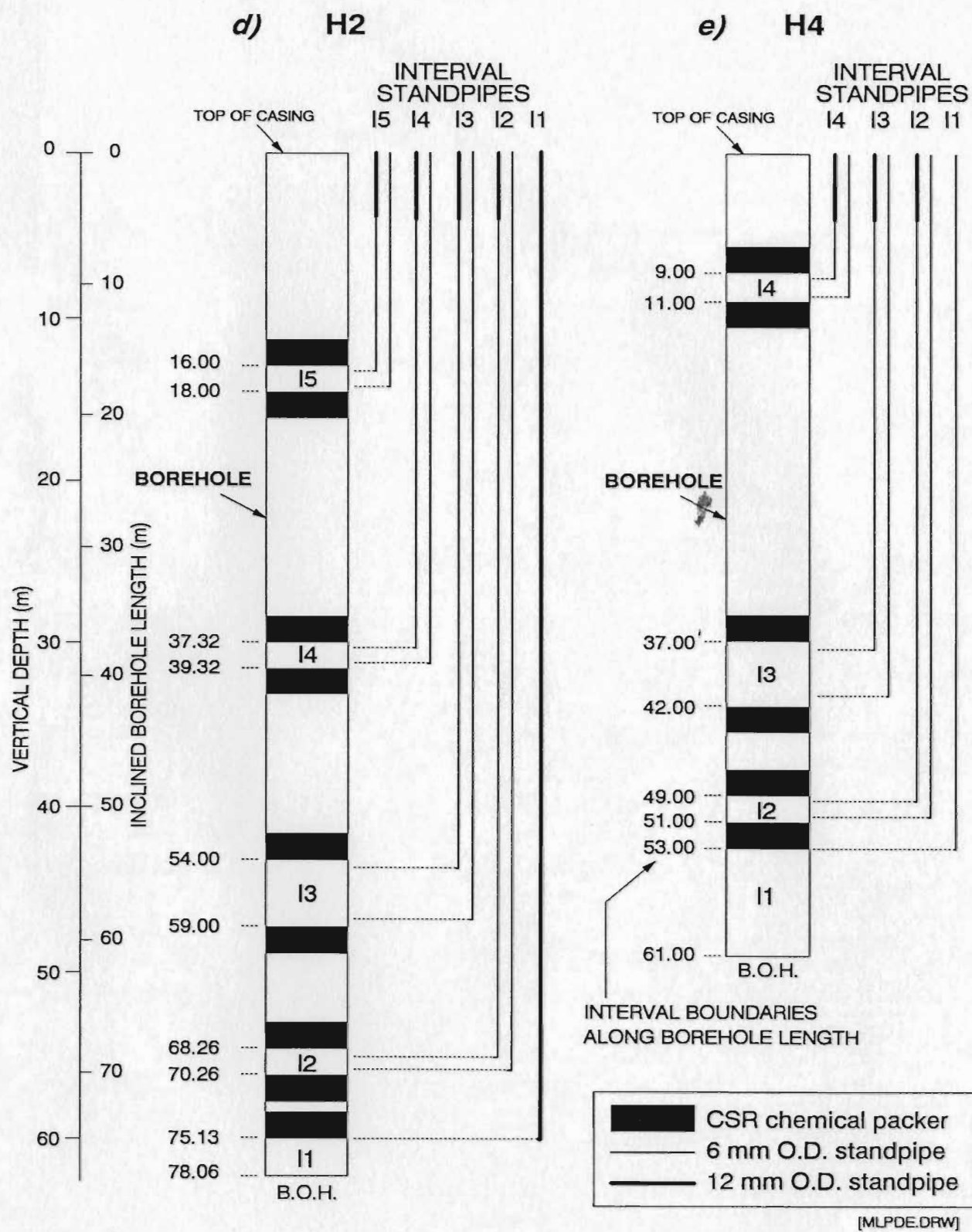


Figure G1 (continued)

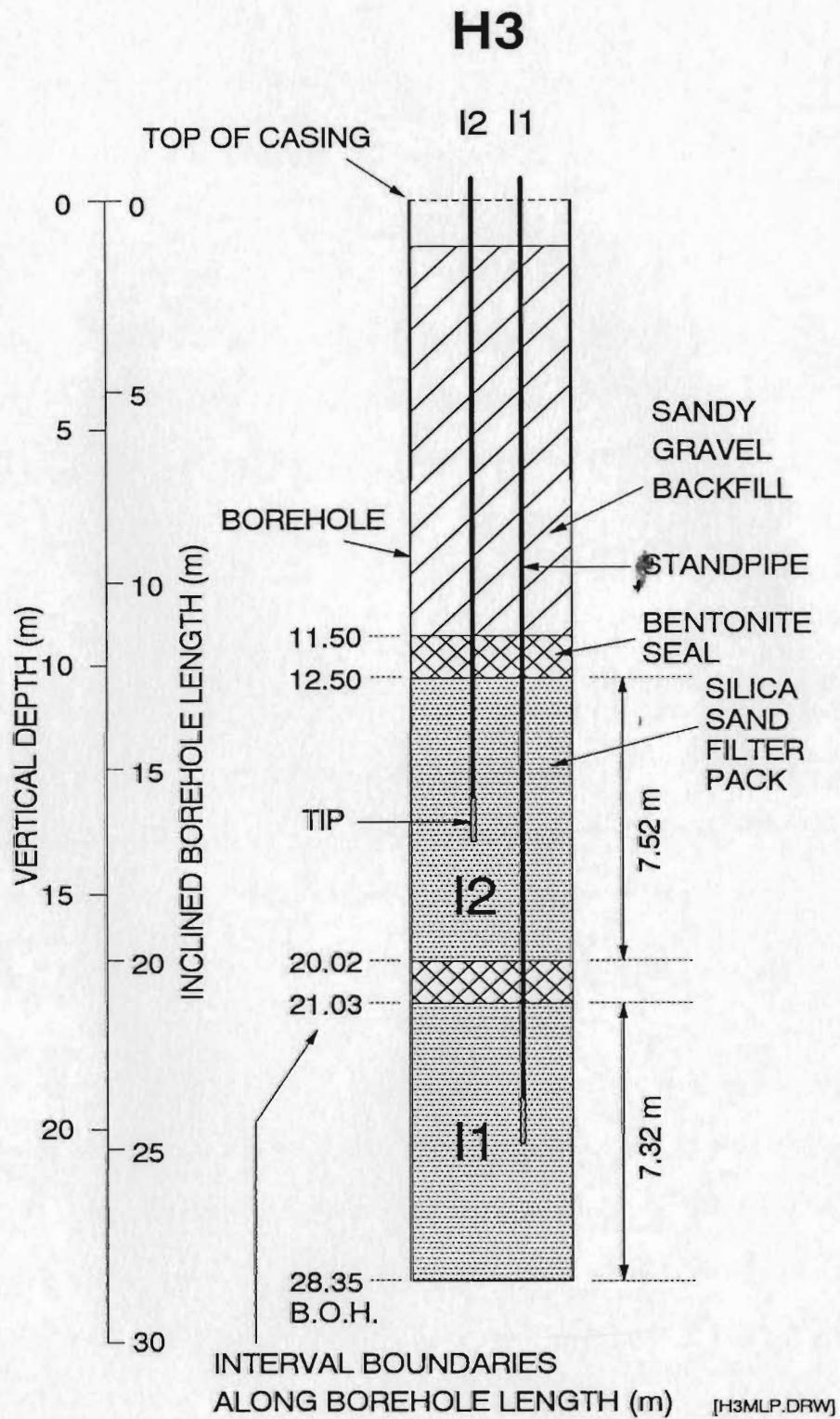


Figure G2 - Schematic diagram of piezometric interval locations and depths, and construction details for the multilevel piezometer in borehole H3.

## APPENDIX H

### Factors Affecting the Implementation of Reach Mass Balance Methods

#### 1. Introduction

The principal factors affecting the implementation of reach mass balance methods relate to assumptions which underlie the development of bulk inflow and reach hydrograph separation equations and to methods used to determine transient storage term values for use in those equations. These factors are i) evaporation effects, ii) the adequacy of contrasts in runoff composition and stream flow terms, iii) flow and mass routing along the reach, iv) effects of influent stream flow conditions, and v) determination of transient storage terms. These are discussed below in reference to the SCR V study area, along with implications for other study areas and different hydrologic conditions.

#### 2. Evaporation Effects

The assumption that evaporation flow and mass losses from the study reach are negligible during stormflow is reasonable based on small evaporation loss rates ( $<0.3$  % of typical reach stormflows), estimated from Class-A evaporation pan measurements made at a weather station in St. John's 20 km from the study area. Supporting this, calculated  $Q_g$  values equal total reach discharge ( $Q_o - Q_i$ ), within error limits, indicating that possible evaporation losses from the stream reach are less than the uncertainty levels in stream flow measurements.

Evaporation effects in the SCR V are further shown by relationships

between selected rain, stream and M114 groundwaters on a deuterium-oxygen-18 plot (Figure H1). The global meteoric water line (GMWL) lies above most of the groundwater and rain data suggesting that precipitation in the SCRIV region defines a local meteoric water line (LMWL) with lower slope. The LMWL in Figure H1 is a regression line through all groundwaters and all rain waters, except point no. 8, and is defined by the relation  $\delta^2\text{H} = 7.52 (\delta^{18}\text{O}) + 3.05$ . The SCRIV LMWL is well-constrained ( $R^2 = 0.96$ ) and compares well with a LMWL defined elsewhere in Atlantic Canada (at Truro, Nova Scotia,  $\delta^2\text{H} = 7.30 (\delta^{18}\text{O}) + 3.59$ ; Fritz et al., 1987).

Other principal features relating to Figure H1 are as follows:

- 1) Point 4 (September 27, 1986 rain) is tightly constrained (by duplicate oxygen-18 and deuterium analyses) and is located close to the GMWL (suggesting it has not undergone significant evaporative fractionation). This justifies its inclusion in the data set used to define the SCRIV LMWL.
- 2) The deviation of point 8 (September 17, 1987 rain) from the SCRIV LMWL suggests that this rain sample either underwent evaporative fractionation or that one or both of the isotopic analyses are bad. Detailed review of handling and analysis records indicates that evaporative fractionation during sampling, storage or analysis leading to an enriched oxygen-18 value is unlikely. Supporting this, the bulk inflow plot for the September 17, 1987 storm (Figure 4.10) shows that the measured rain oxygen-18 value (-2.65 ‰) leads to physically reasonable mixing relationships with M1 groundwaters, whereas a more depleted oxygen-18 value, corresponding with a rain composition before supposed evaporative fractionation, would not. Since calculated bulk inflow composition is a function only of stream

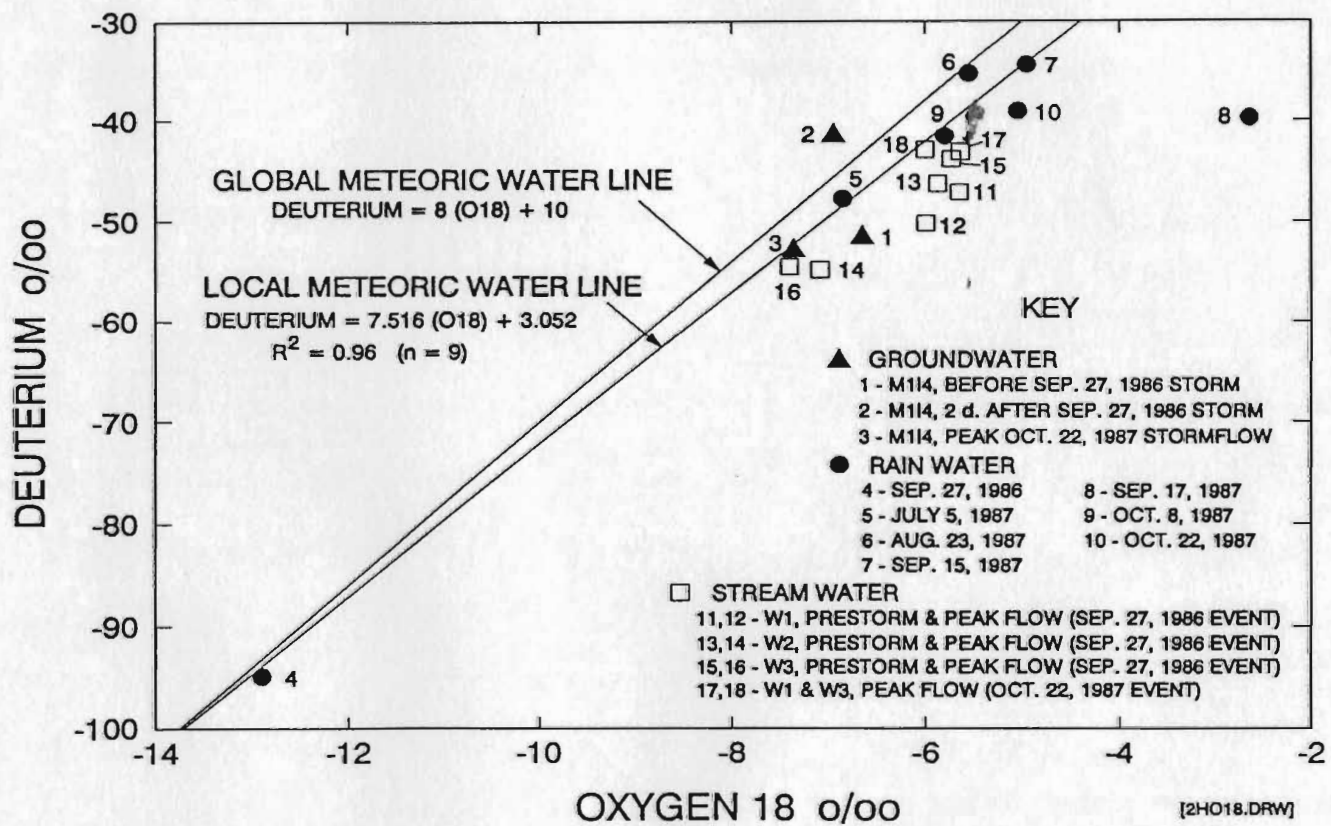


Figure H1 - Plot of deuterium versus oxygen-18 showing the location of selected rain, stream and groundwaters from the Seal Cove River valley with respect to global and local meteoric water lines.

compositions and stream flow terms, reflecting runoff compositions generated from actual rainfall, this independently suggests that the rain composition for this storm was naturally enriched in oxygen-18. The anomalous position of point 8 is therefore attributed to a bad deuterium analysis.

3) Stream waters (open squares) tend to plot below the LMWL and, for low flow (pre-storm) conditions, are enriched with respect to M14 groundwaters. This supports the assertion that waters entering the study reach from Gull Pond East are isotopically enriched due to evaporation in the pond and therefore cannot be used to infer discharging groundwater compositions along the study reach.

4) The tight cluster of low flow stream compositions for all three weirs (points 11, 13 and 15), with no trend toward enrichment for progressive downstream locations, indicates that evaporative fractionation from the reach channel and beaver pond is negligible. However, in other settings, where water residence times in a reach are high or included surface water bodies are large, or where dry climatic conditions prevail, isotopic enrichment of reach waters may become significant.

### 3. Adequacy of Contrasts in Composition ( $C_g$ - $C_r$ ) and Flow ( $Q_o$ - $Q_i$ )

Most workers using chemical or isotopic hydrograph separation methods highlight the need for sufficient contrast between composition of flow components for acceptable separation precision, yet none have set quantitative guidelines. To objectively assess the adequacy of contrasts between  $C_g$  and  $C_r$  and between  $Q_o$  and  $Q_i$  values in this study, the contrasts are quantitatively expressed as unitless

contrast/error ratios, defined as:

$$\text{Magnitude of contrast} / \text{Propagated error of contrast.}$$

For example, at the peak of September 27, 1986 stormflow,  $Q_o$  (weir W3) was  $0.4819 \text{ m}^3/\text{s}$ ,  $Q_i$  (weir W1) was  $0.1120 \text{ m}^3/\text{s}$ , and the measurement uncertainty at both weirs was  $\pm .005 \text{ m}^3/\text{s}$ . Hence, the contrast/error ratio is:

$$(0.4819 - 0.1120) / (.005^2 + .005^2)^{1/2} = \underline{52}.$$

Minimum ratios can be considered as those which yield separation precision (i.e. the uncertainty in the calculated groundwater proportion of total stormflow) of at least  $\pm 15 \%$ , a level of precision generally attained and accepted in the literature (e.g. Sklash et al. 1976; Rodhe, 1981; Hooper and Shoemaker, 1986).

Analysis of runoff data used in this study (Table H1) and in the literature (e.g. Sklash et al., 1976; Sklash and Farvolden, 1979; Bottomley et al., 1984; Hooper and Shoemaker, 1986) lead to the following conclusions regarding composition and stream flow contrasts:

- 1) Contrast/error ratios of at least 10-15 are required for contrasts of runoff component compositions in conventional separations and for both component composition and stream flow contrasts in reach hydrograph separations in order to achieve  $\pm 15 \%$  separation precision;
- 2) In this study, adequate contrasts existed for the main study storms (September 27, 1986 and October 22, 1987) and one ancillary storm (September 17, 1987),



Table H1 - Contrast/error ratios for flow ( $Q_o-Q_i$ ) and composition ( $C_g-C_r$ ) contrasts at peak flow for storm runoff data sets used in this study.

Date	Contrast/error ( $Q_o-Q_i$ ) (full reach)	Contrast/error ( $C_g-C_r$ )	Separation precision <sup>1</sup>
<u>Main study storms</u>			
September 27, 1986	52 <sup>2</sup>	56 (Conductivity) 34 (Deuterium) 29 (Oxygen-18) 6.7 (Chloride)	+3 % 5 % 6 % 39 %
October 22, 1987	12.2	152 (Conductivity) 11 (Oxygen-18) 9.9 (Deuterium)	12 % 16 % 19 %
<u>Ancillary storms</u>			
Aug. 23, 1987	2	126 (Conductivity) 7 (Oxygen-18)	76 % 107 %
September 17, 1987	10	168 (Conductivity) 22 (Oxygen-18)	8 % 14 %
September 26, 1987	3	115 (Conductivity) 20 (Oxygen-18)	63 % 96 %
October 8, 1987	3	123 (Conductivity) 9 (Oxygen-18)	65 % 117 %

<sup>1</sup> Equal to [absolute uncertainty in  $Q_g$ / value of ( $Q_o-Q_i$ )] x 100, at peak flow

<sup>2</sup> Flow contrast/error ratio for upper reach = 29; for lower reach = 24

except where precision were poor using chloride as a tracer for the 1986 storm and marginal using oxygen-18 as a tracer for the Oct 22, 1987 storm. Runoff for the other ancillary storms in 1987 (on Aug. 23, September 26, and October 8) had inadequate combined flow and composition contrasts, but are retained here to illustrate the effects of this inadequacy.

3) Storm runoff events with adequate composition contrasts appear to be common in a variety of hydrogeologic and climatic settings. However, due to lack of corresponding reach stream flow data, it is unknown if runoff events with sufficient flow contrasts are equally common.

In the SCR<sub>V</sub>, storms with adequate composition contrasts may be expected at any time during summer or fall periods, in light of seasonally unpredictable isotopic (and chemical) rainfall compositions observed in this study. However, high discharge contrasts are most likely to occur during fall (and, by inference, spring) periods when rainfalls tend to be heavier and more frequent. The few storms cited in this study seem to indicate that runoff events in the SCR<sub>V</sub> with acceptable flow contrasts correspond with rainfall amounts above about 20 mm.

Flow contrasts are also controlled in part by the level of stream flow measurement precision. Thus, if 1987 stream flows had been measured with precision available in 1986, the 1987 flow contrast/error ratios in Table H1 would increase by a factor of 2.2. However, trial hydrograph separations for the September 17 and October 22, 1987 storms, using 1986 stream flow precision, indicate that improvements in separation precision would only be marginal ( $\leq 2\%$ ). This indicates that while stream flow measurement precision is important, it is the adequacy of both flow and composition contrasts which determines overall

separation precision and hence the suitability of a runoff data set for analysis by reach methods. Finally, contrast requirements described above have important practical uses in applying reach methods in that minimum flow contrasts can be used in evaluating potential new study sites and in screening runoff data sets before costly and time-consuming chemical analyses are performed.

#### 4. Flow and Mass Routing along the Reach

The assumption that flow and mass routing times along the study reach are negligibly small compared with the duration of stormflow is reasonable based on average stream velocity (about 0.5 m/s) which results in rapid throughput times (less than one hour) along the reach compared with typical stormflow durations of 1-3 days. Lag times between hydrograph peaks at weirs W2 and W3 during runoff from the assumed catchment are short (typically  $\leq 1$  hour), which can be attributed to runoff entering the reach almost simultaneously along its length. In addition, abundant turbulence along the reach suggests that mixing within the channel is rapid and thorough.

In the SCR V study reach, flow routing times may be significant for short periods during the steep rising limb of flood waves which pass through the study reach from upstream. However, durations of such rising limbs in the SCR V are short (on the order of a few hours) and should not affect the overall analysis of storm runoff events. Routing times may be significant in other settings, e.g. where a study reach is very long or stream velocities are very low. Theoretical and practical difficulties of incorporating routing into reach mass balance equations suggest that such site conditions should be avoided in applying the reach methods described here.

## 5. Effects of Influent Stream Flow Conditions

Influent flow along a stream reach, in the form of groundwater recharge through the stream bed or flow to bank storage, or both, introduces extra terms into the flow and mass balance equations. Ignoring significant influent flow would result in underestimated bulk inflow compositions and groundwater inflow to a reach. Direct measurement of influent flow into a reach would not generally be feasible because the spatial and temporal variability of influent flow processes would require prohibitively time-consuming and costly monitoring and sampling. Alternatively, influent flow can theoretically be treated as an additional unknown or can be approximated from other measurements (as is done below for bank storage along the study reach).

Treating influent flow as an additional unknown would require expanded hydrograph separation and bulk inflow equations, with increased propagated error, and, more importantly, would rely on knowledge of water compositions involved in ephemeral departure from and return to a stream channel. In general, such exchange would tend to have variable starting times, flow rates and residence times along a reach, leading to complex mixing relationships with shallow groundwater, making it difficult to determine actual compositions of discharging subsurface water once effluent conditions resumed. Hence, storm runoff events or study areas in which substantial influent flow is suspected to occur should be avoided in applying the reach mass balance methods described here.

In the SCRVS, groundwater recharge through the stream bed is unlikely to occur based on 1) persistent discharge gradients and seepage fluxes at the stream, 2) groundwater mixing trends showing no tendency for mixing with stream water

and 3) the fact that storm-induced piezometric rises commence before the start of storm hydrographs so that abrupt stream stage increases, leading to temporary reversals of stream bed gradients, do not occur. In addition, bank storage effects in the SCR<sub>V</sub> are negligible, based on very small bank storage flow rates and volumes (less than the uncertainties in stream Q and V values) and short residence times (on the order of 1-2 days), estimated from hydrologic and physiographic features of the study reach using the methods of Cooper and Rorabaugh (1963). The negligible effect of bank and channel storage is supported by the lack of substantial changes to hydrograph shapes for floodwaves passing through the study reach.

#### 6. Determination of Transient Storage Terms

In this study, the transient storage terms  $V$ ,  $\Delta V/\Delta t$ ,  $C_v$  and  $\Delta C_v/\Delta t$  were approximated using the following expressions:

$$V = A(h^0 + h(t))$$

$$\Delta V/\Delta t = A\{(\Delta h/\Delta t_i + \Delta h/\Delta t_o)/2\}$$

$$C_v = (C_i + C_o)/2$$

$$\Delta C_v/\Delta t = (\Delta C/\Delta t_i + \Delta C/\Delta t_o)/2$$

where  $A$  is reach channel area,  $h^0$  is average stream stage at low flow,  $h(t)$  is average increase in stream stage above  $h^0$  during stormflow,  $\Delta h/\Delta t$  is the rate of change of stream stage at a weir,  $\Delta C/\Delta t$  is rate of change of stream composition at a weir and other terms and subscripts are as defined above. Area  $A$  was digitized from enlarged air photos and was assumed to be constant during small stage changes (0.1 m or less) developed during stormflow. The term  $h^0$  was

determined from stream profiles at the weirs and observations of stream morphology along the reach. Stream stage terms  $h(t)$  and  $\Delta h/\Delta t$  were determined from float recorder records.

The least well-constrained of these terms is reach volume,  $V$ , due mainly to uncertainties in the volume of the beaver pond upstream of weir W2. However, sensitivity analyses show that calculated  $Q_g$  is very insensitive to changes in  $V$  compared with changes in stream flow or composition terms. This is because  $V$  appears in the product term  $V \cdot \Delta C_v / \Delta t$  in the equation for  $Q_g$  and, for stormflows in the SCR, the value of this product is very small compared with other product terms. In other settings, however, where either  $V$  or  $\Delta C_v / \Delta t$  values may be much larger, the  $V \cdot \Delta C_v / \Delta t$  product term may influence  $Q_g$  more strongly, requiring more precise methods for determining  $V$ .

## APPENDIX I

**Alterations to the Computer Code used for Three-Dimensional Numerical  
Simulations of Groundwater Flow in the Study Area**

An altered version of the U.S. Geological Survey groundwater flow computer code MODFLOW (McDonald and Harbaugh, 1988) was used for some three-dimensional (3D) simulations of groundwater flow in this study. The current version of MODFLOW requires that the term describing the hydraulic conductivity anisotropy ratio  $K_y/K_x$  (labelled in the code as "TRPY") be assigned a constant value within a given layer in the model mesh. In order to incorporate large fracture zones with different anisotropy characteristics than the surrounding rock mass into the 3D simulations, it was necessary to alter MODFLOW so that different TRPY values could be assigned to any individual cell in the model mesh. The altered version of MODFLOW is referred to here as HETMOD.

Alterations to MODFLOW to produce HETMOD are summarized in Table I1. Verification of HETMOD was assessed by comparing results produced by HETMOD and MODFLOW for the sample problem provided with the MODFLOW documentation. HETMOD and MODFLOW produced identical hydraulic head values and solution precisions when the factor TRPY (for a given layer) was assigned a value of 1.0 (i.e.  $K_x = K_y$ ) or a range of values less than one. This agreement infers that results from HETMOD, for cases where TRPY values for individual cells within a given layer are not constant, are also mathematically correct and internally consistent.

---

Table 11 - Alterations to the computer code MODFLOW to produce HETMOD. The revisions are easily recognizable in the context of the subroutine listings provided in the MODFLOW documentation.

<u>Subroutine:</u>	<u>MODFLOW line:</u>	<u>HETMOD line:</u>
<u>BCFIAL</u>	ISUM = ISUM + NLAY	ISUM = ISUM + (NROW*NCOL*NLAY)
<u>BCFIRP</u> <sup>1</sup>	DIMENSION...TRPY(NLAY)	DIMENSION...TRPY(NODES)
	CALL U1DREL(TRPY,...)	(line removed)
	(after comment 2A)	CALL U2DREL(TRPY(LOC),ANAME(1,8), NROW,NCOL,KK,IN,IOUT)
<u>BCFIFM</u>	DIMENSION...TRPY(NLAY)	DIMENSION...TRPY(NCOL,NROW,NLAY)
<u>SBCFIC</u>	DIMENSION...TRPY(NLAY)	DIMENSION...TRPY(NCOL,NROW,NLAY)
	YX = TRPY(K)*2.	(line removed)
	(after comment 1)	(put new YX line inside DO LOOP: ...DO 40 I = 1, NROW DO 40 J = 1, NCOL YX = TRPY(J,I,K)*2. T1 = CC(J,I,K)...
<u>SBCFIH</u>	DIMENSION...TRPY(NLAY)	DIMENSION...TRPY(NCOL,NROW,NLAY)
<u>SBCFIN</u>	DIMENSION...TRPY(NLAY)	DIMENSION...TRPY(NCOL,NROW,NLAY)

---

<sup>1</sup> Removal of 1D reader (used for original global assignment of TRPY value to a layer) and insertion of 2D reader (for assigning individual TRPY values for each cell layer by layer) requires a revised order for lines in the BCF file.



## APPENDIX J

## Hydrochemistry Data

Hydrochemistry data used in this thesis is presented below. It is subdivided by the Figure number where it is presented. Following the data, the input parameters and constraints used for PHREEQE modelling are presented.

## Rain data for Figure 4.1

Location	Julian Date	O-18 (o/oo)	Cond. uS/cm
R6	189.563	-6.85	15.0
R6	235.290	-5.55	7.0
R4	240.506	-2.67	15.0
R6	257.800	-4.95	7.3
R6	260.514	-2.65	22.4
R6	271.000	-11.56	11.7
R4	271.680	-12.90	26.4
R6	281.420	-5.80	8.5
R6	294.448	-2.97	14.4
R6	295.396	-5.05	6.0

## Data for Figure 4.4a

Location	Chloride mg/l	Cond. uS/cm
M1I2	8.1	138.6
M1I2	7.64	140.0
M1I2	7.97	141.0
M1I2	7.83	131.0
M1I2	6.25	131.2
M1I3	8.32	149.0
M1I3	8.65	152.5
M1I3	8.86	151.4
M1I3	8.14	141.1
M1I4	6.31	39.8
M1I4	5.96	41.6
M1I4	5.78	44.5
M1I4	6.16	41.6
M2I2	12.37	263.3
M2I3	12.43	242.6
M3I2	8.56	85.2
M3I3	7.47	105.3
M3I4	8.48	86.6
H2, 25m, 1985	5.2	140.0
H2, 25m, 1985	5.2	137.0
H2, 25m, 1985	6.2	150.0
H2, 25m, 1985	7.4	190.0

Location	Chloride mg/l	Cond. uS/cm
H2, 25m, 1985	6.2	140.0
H2, 25m, 1985	8.6	130.0
H2, 25m, 1985	5.2	139.0
H2, 62m, 1985	13.3	370.0
H2, 62m, 1985	14.4	440.0
H2, 62m, 1985	17.8	395.0
H3	8.1	520.0
H4, 8m, 1985	8.2	168.0
H4, 8m, 1985	8	169.0
H4, 8m, 1985	9.6	169.0

## Data for Figure 4.4b

Location	Date or Time	Ca mg/L	Mg mg/L	K mg/L	Na mg/L
M114	SEP 5 '86	2.4	0.5	0.32	4.4
M114	JUL 9 '87	4.7	0.7	0.25	3.9
M114	JUL 16 '87	3.8	0.6	0.26	4.0
M114	SEP 15 '87	3.8	0.7	0.45	4.7
M114	SEP 17 '87	4.6	0.8	0.34	4.7
M114	268.67	2.0	0.7	0.30	4.5
M114	271.667	2.4	0.8	0.30	4.5
M114	275.688	2.6	0.7	0.30	4.7
M113	SEP 5 '86	11.8	2.3	0.55	7.9
M113	SEP 29 '86	18.3	2.5	0.68	8.5
M113	271.669	21.3	3.0	0.70	8.2
M113	268.668	20.3	3.0	0.60	8.4
M113	275.689	20.1	2.8	0.70	8.3
M112	SEP 29 '86	19.0	2.7	0.47	7.4
M112	271.67	19.0	3.3	0.40	7.0
M112	JUL 9 '87	10.4	1.5	0.39	6.1
M112	JUL 16 '87	16.6	2.5	0.52	7.1
M112	SEP 16 '87	10.3	2.1	0.64	7.1
M112	272.691	17.8	3.1	0.50	7.2
M112	268.667	18.3	3.3	0.50	7.1
M214	SEP 5 '86	34.2	2.4	2.48	15.3
M214	JUL 9 '87	24.3	2.3	1.11	6.8
M214	SEP 17 '87	11.4	2.3	0.72	6.3
M212	SEP 5 '86	38.6	2.6	2.04	24.0
M212	SEP 12 '86	31.3	2.5	2.73	20.4
M212	SEP 15 '87	22.6	2.3	2.56	35.5
M212	SEP 17 '87	10.0	2.0	1.82	29.4
M314	SEP 12 '86	9.8	1.3	0.93	5.8
M314	JUL 9 '87	7.2	1.0	1.39	5.6
M314	SEP 15 '87	6.8	1.0	0.48	5.0
M314	SEP 22 '87	5.5	0.9	0.60	5.0
M314	SEP 17 '87	6.1	1.0	0.48	4.9
M313	SEP 12 '86	13.5	1.7	0.79	6.1
M312	SEP 12 '86	10.1	1.2	0.79	6.4
M312	JUL 9 '87	13.6	1.7	1.10	6.4
M312	JUL 16 '87	13.6	1.7	1.06	6.1
M312	SEP 15 '87	11.0	1.6	0.63	5.8
M312	SEP 22 '87	7.6	1.5	0.44	5.8
M312	SEP 17 '87	7.8	1.4	0.63	5.7
H215	SEP 15 '87	18.3	1.6	0.48	6.5
H215	SEP 17 '87	9.7	1.4	0.47	6.4
H212	SEP 17 '87	9.1	1.3	0.76	12.2
H212	SEP 17 '87	15.4	1.5	0.75	12.4
H312	SEP 15 '87	13.9	2.9	0.66	6.8

Location	Date or Time	Ca mg/L	Mg mg/L	K mg/L	Na mg/L
H3I2	SEP 17'87	5.9	1.3	0.59	6.1
H3I1	SEP 15'87	22.1	3.9	0.58	9.7
H3I1	SEP 17'87	4.1	3.3	0.60	9.4
H3I1	SEP 17'87	5.9	3.4	0.60	9.5
H4I4	SEP 15'87	29.5	1.3	1.06	9.2
H4I4	SEP 15'87	29.3	1.4	1.06	9.2
H4I4	SEP 17'87	25.1	1.8	3.70	38.2
H4I1	SEP 15'87	24.3	1.8	0.81	14.8
H4I1	SEP 17'87	8.6	1.3	0.75	14.4
R4	271.679	0.00	0.40	0.10	2.70
R4	SEP 29'86	1.30	0.30	0.11	2.60
R6	SEP 16'87	0.20	0.10	0.05	0.29
R6	SEP 16'87	0.00	0.08	0.04	0.30
R4	SEP 4 86	0.24	0.37	0.07	1.17
R4	SEP 12 86	0.17	0.24	0.04	0.70
R4	SEP 17 86	0.14	0.15	0.08	0.96
R6	JUL 9 87	0.19	0.14	0.10	1.22
R6	SEP 3 87	0.33	0.26	0.43	1.34
R6	SEP 10 87	0.34	0.26	0.16	1.05
R6	SEP 18 87	0.23	0.30	0.12	1.41
R6	OCT 1 87	0.20	0.10	0.29	0.85
R6	OCT 9 87	0.19	0.17	0.08	0.88
R6	OCT 30 87	0.34	0.28	0.17	1.22
R6	OCT 27 87	0.29	0.21	0.08	1.15
R6	SEP 29 87	0.20	0.07	0.07	0.93
R6	OCT 23 87	0.21	0.10	0.08	0.80
R6	OCT 22 87	0.40	0.44	0.20	1.37

## Data for Figure 4.5a and 4.5b

Julian Date	Sample Location	O-18 (o/oo)	Cond. (uS/cm)
236.513	M1I2		140.7
239.606	M1I2	-7.873	138.4
240.497	M1I2	-7.772	138.9
240.718	m1i2		137.3
246.703	M1I2	-7.646	131.2
247.462	M1I2	-7.772	131.2
236.501	M1I3	-7.634	144.0
239.604	M1I3	-7.954	144.0
240.495	M1I3	-7.898	
240.719	M1I3		143.3
246.740	M1I3	-7.705	140.1
247.400	M1I3	-8.157	137.1
236.497	M1I4		36.8
239.599	M1I4		39.0
240.495	M1I4	-7.262	38.1
246.790	M1I4	-7.664	37.6
247.458	M1I4	-7.765	39.1
247.572	M2I2	-7.315	256.4
247.547	m2i4		208.7
240.547	M3I2	-8.103	82.5

Julian Date	Sample Location	O-18 (o/oo)	Cond. (uS/cm)
247.468	M312	-7.892	80.5
240.500	M313	-8.252	106.9
247.472	M313	-8.087	103.2
240.556	M314	-7.899	85.9
247.476	M314	-7.700	81.7
240.506	R4	-2.674	15.0

## Data for Figure 4.5c and 4.5d

Julian Date	Sample Location	O-18 (o/oo)	Cond. (uS/cm)
257.625	H212	-7.653	119.0
259.609	H212	-7.868	130.9
257.601	H214	-7.987	197.1
259.568	H214	-8.105	123.4
257.596	H215	-7.286	106.8
258.563	H215	-7.759	117.2
259.566	H215	-7.533	90.5
257.625	H311	-7.577	131.9
259.626	H311	-7.698	114.2
257.625	H312	-7.375	108.0
259.631	H312	-6.702	76.1
257.625	H411	-7.336	183.0
258.663	H411	-7.834	184.0
259.702	H411	-7.560	131.4
257.583	H414	-6.823	
258.666	H414	-7.370	
259.666	H414	-7.344	
257.542	M114	-6.648	46.7
258.542	M114	-7.309	48.9
259.708	M114	-7.195	47.9
257.625	M212	-7.451	291.0
259.656	M212	-6.586	242.0
257.625	M214	-7.800	202.0
259.638	M214	-7.727	137.4
257.625	M312	-7.39	91.8
258.576	M312	-8.036	93.4
259.613	M312	-8.053	75.4
264.665	M312	-7.789	89.6
257.625	M314	-7.508	65.4
258.573	M314	-6.744	65.9
259.607	M314	-7.632	62.9
264.668	M314	-7.212	65.4
257.800	R6	-4.961	7.3

## M114 conductivity data for Figure 4.5d

Location	DATE	Julian Date	Cond. (uS/cm)
M114	SEP 11	253.490	42
M114	SEP 15	257.542	46.7
M114	SEP 15	257.708	45.2
M114	SEP 15	257.875	45.3
M114	SEP 16	258.042	46.3
M114	SEP 16	258.208	47.6
M114	SEP 16	258.375	48.6
M114	SEP 16	258.542	48.9

Location	DATE	Julian Date	Cond. (uS/cm)
M1I4	SEP 16	258.708	48.9
M1I4	SEP 16	258.875	48.7
M1I4	SEP 17	259.042	48.5
M1I4	SEP 17	259.208	48.5
M1I4	SEP 17	259.375	48.3
M1I4	SEP 17	259.542	47.9
M1I4	SEP 17	259.708	47.9
M1I4	SEP 18	260.042	47.7
M1I4	SEP 18	260.208	47.1
M1I4	SEP 18	260.375	46.8
M1I4	SEP 18	260.542	46.9
M1I4	SEP 18	260.708	47.1

Data for Figure 4.6b and 4.6c

Julian Date	Sample Location	O-18 (o/oo)	Cond. (uS/cm)	Chloride (mg/L)
268.667	M1I2	-7.503	140.0	7.64
271.670	M1I2	-7.621	141.0	7.97
273.500	M1I2	-7.771	123.1	
275.691	M1I2	-7.695	131.0	7.83
268.668	M1I3	-7.181	152.5	8.65
271.669	M1I3	-7.512	151.4	8.86
273.500	M1I3	-7.799	135.2	
275.689	M1I3	-7.689	141.1	8.14
268.670	M1I4	-6.646	41.6	5.96
271.667	M1I4	-6.956	44.5	5.78
273.500	M1I4	-7.304	40.9	
275.688	M1I4	-7.119	41.6	6.16
271.679	R4	-12.901	26.4	4.95
268.625	W1	-5.649	37.7	8.68
268.958	W1	-5.410	38.5	8.55
269.125	W1	-5.890	38.5	8.66
269.292	W1	-5.910	38.5	8.57
269.458	W1	-6.030	37.7	8.70
269.625	W1	-6.119	37.3	8.56
269.875	W1	-5.988	38.5	
269.958	W1	-5.910	38.5	8.45
270.125	W1	-5.933	38.5	8.45
270.292	W1	-5.806	38.5	8.81
270.375	W1	-6.055	38.5	
270.458	W1	-5.640	38.5	8.75
270.542	W1	-5.681	38.1	
271.646	W1	-6.079	37.6	
271.813	W1	-6.064	37.6	
272.146	W1	-5.730	37.6	8.52
272.396	W1	-6.120	37.6	8.88
273.563	W1	-6.010	38.3	
268.708	W2	-5.873	38.1	8.50
268.958	W2	-5.618	38.1	8.30
269.292	W2	-5.584	38.9	8.84
269.458	W2	-5.619	38.5	8.66
269.625	W2	-5.902	36.9	8.32
269.792	W2	-6.483	35.6	8.23
269.875	W2	-7.087	34.4	7.55
269.958	W2	-7.632	36.3	7.50

Julian Date	Sample Location	0-18 (o/oo)	Cond. (uS/cm)	Chloride (mg/L)
270.125	W2	-7.328	37.3	7.56
270.292	W2	-7.125	37.3	7.85
270.375	W2	-6.705	36.9	
270.458	W2	-6.388	37.7	8.07
270.625	W2	-5.894	37.7	8.03
271.625	W2	-6.022	36.8	
272.375	W2	-5.796	38.0	8.36
272.958	W2	-6.064	37.6	8.09
268.604	W3	-5.728	38.5	8.35
269.021	W3	-5.780	38.9	
269.188	W3	-5.470	38.5	
269.354	W3	-5.660	37.7	8.60
269.521	W3	-6.810	37.3	8.33
269.604	W3	-6.357	36.0	
269.688	W3	-6.810	34.8	7.55
269.854	W3	-7.402	33.6	6.96
269.938	W3	-7.550	35.6	7.04
270.271	W3	-7.735	36.0	7.61
270.354	W3	-7.252	36.9	
270.438	W3	-6.870	36.9	8.10
270.521	W3	-6.630	36.9	
271.604	W3	-6.761	36.8	

## Data for Figure 4.7b and 4.7c

Julian Date	Sample Location	0-18 (o/oo)	Cond. (uS/cm)
292.604	M112	-7.425	128.1
293.604	M112	-7.544	128.4
294.438	M112	-6.784	127.0
294.688	M112	-6.825	127.9
294.938	M112	-7.314	127.5
295.188	M112	-7.178	127.0
295.438	M112	-7.580	128.0
295.688	M112	-7.550	126.5
295.938	M112	-7.478	127.5
296.188	M112	-7.514	127.9
296.438	M112	-7.454	127.6
296.688	M112	-7.474	128.0
296.938	M112	-7.571	128.0
297.438	M112	-7.341	128.2
292.502	M114	-7.368	46.1
294.434	M114	-7.409	48.2
294.542	M114	-7.435	47.4
294.688	M114	-7.362	48.4
295.438	M114	-7.590	52.0
295.500	M114	-7.278	51.2
295.396	R6	-5.053	6.0
294.375	W1	-5.145	40.8
294.875	W1	-5.231	39.4
294.958	W1	-5.430	40.2
295.083	W1	-5.635	41.1
295.167	W1	-5.644	41.3
295.208	W1	-5.532	41.4
295.250	W1	-5.546	41.2
295.542	W1	-5.330	40.7

Julian Date	Sample Location	O-18 (o/oo)	Cond. (uS/cm)
296.042	W1	-5.070	41.2
296.542	W1	-5.297	41.2
297.375	W1	-5.339	41.5
293.417	W1	-5.532	41.3
294.333	W3	-5.651	41.4
294.375	W3	-5.686	41.3
294.625	W3	-5.660	40.2
294.792	W3	-5.630	40.1
294.875	W3	-5.540	39.7
294.958	W3	-6.320	38.1
295.000	W3	-6.070	39.2
295.083	W3	-5.994	40.0
295.167	W3	-5.662	40.2
295.250	W3	-5.487	40.9
295.469	W3	-5.820	42.5
295.552	W3	-5.640	42.8
296.052	W3	-5.340	40.7
297.052	W3	-5.537	39.5
293.438	W3	-5.250	43.1

#### Data for Figure H1

Location	Deuterium (o/oo)	O-18 (o/oo)	Date/ID info
w1	-47.08	-5.649	Sep 27, 1986 prestorm
w1	-50.25	-5.988	Sep 27, 1986 peak
w2	-46.28	-5.873	Sep 27, 1986 prestorm
w2	-54.78	-7.087	Sep 27, 1986 peak
w3	-43.94	-5.728	Sep 27, 1986 prestorm
w3	-54.45	-7.402	Sep 27, 1986 peak
W1	-43.06	-5.635	OCT 22, 1987 PEAK
W3	-42.85	-5.994	OCT 22, 1987 PEAK
M1I4	-51.64	-6.646	Sep 27, 1986 prestorm
M1I4	-41.55	-6.956	Sep 27, 1986 post-storm
R6	-94.88	-12.90	Sep. 27, 1986 rain
R6	-38.99	-5.053	OCT 22, 1987 RAIN
M1I4	-53.00	-7.362	OCT 22, 1987 PEAK
R6	-41.50	-5.80	OCT.8, 1987 RAIN
R6	-34.49	-4.961	SEP. 15, 1987 RAIN
R6	-47.67	-6.85	JUL 5, 1987 RAIN
R6	-35.39	-5.554	AUG. 23, 1987 RAIN
R6	-39.76	-2.651	SEP. 17, 1987 RAIN

#### PHREEQE Model Input Parameters and Constraints

Only H-hole hydrochemical data, collected in 1985 as part of initial site investigations, were used for solution modelling using the PHREEQE geochemical code (Parkhurst et. al., 1980). This was because only these groundwater data in

the SCRV included measurements of pH and Eh. These groundwaters were collected using a positive-displacement down-hole pump. Field geochemical parameters (including pH, Eh and temperature) were measured before the groundwater samples were exposed to the atmosphere, using measurement probes connected to a flow-cell apparatus.

Data sets for four groundwater samples were analyzed. Sample information and principal PHREEQE model results are summarized below.

Location	H2	H2	H3	H4
Vertical Sample Depth	21.0 m	50.2 m	20.4 m	6.7 m
Sampling Date	3 July 85	11 July 85	1 Nov. 85	6 Dec 85
Log IAP/KT from PHREEQE modelling:				
Calcite	-5.330	-2.519	-0.256	-3.632
SiO <sub>2</sub> (anh.)	-1.119	-0.994	-0.789	-1.070
Quartz	+0.280	+0.405	+0.632	+0.367
Hydrochemical data:				
Temp. (°C)	12.8	15	7.6	5
pH	4.78	6.03	7.8	6.12
Eh (mV)	263	216	282	313
Alkalinity (mg/L)	10.45*	59.6*	128.1	14
Na (mg/L)	3.8	8.1	8.4	4.8
K (mg/L)	0.7	1.0	0.6	0.5
Ca (mg/L)	2.5	17.9	32.7	5.2
Mg (mg/L)	0.6	1.4	3.7	1
Cl (mg/L)	5.2	13.3	8.1	8.2
SO <sub>4</sub> (mg/L)	2.6	2.5	3.8	3.6
Si** (mg/L)	3	4	6	3
Fe (mg/L)	0.4	0.2	0.05	0.1
Mn (mg/L)	0.43	0.84	0.07	0.09

Note:

\* Estimated based on other cation and anion concentrations.

\*\* Entered in PHREEQE as H<sub>4</sub>SiO<sub>4</sub> equivalent.







